
Let there be Light
Quantitative Imaging of
Nanoscale Dynamics
in Polymer Materials
Hanne van der Kooij
FzbL 2020

Propositions

1. Laser speckle imaging is the most versatile, accessible, and time-effective technique for spatially resolved quantification of dynamics inside everyday polymer materials. (This thesis)

2. The d_2 structure function should replace the widely used g_2 correlation function as an indicator of nanoscale dynamics derived from scattered light intensity fluctuations. (This thesis)

3. In agricultural water management, simple solutions and positive incentives for farmers are currently lacking; yet they are essential to improve the water quality in the Netherlands.

4. Flow of scientific funds is as non-transparent as flow of pigmented paints.

5. Essential oils are the solution to the impending antimicrobial resistance crisis.

6. In the competitive scientific community, "making love, not war" is vital for conceiving fertile research ideas and subsequent growth of brainchildren.

7. The Dutch government direly needs a Ministry of Futurology focused on game-changing discoveries.

8. As of 2035, electricity will be virtually free of charge.

Propositions belonging to the thesis, entitled

Let there be light
Quantitative imaging of nanoscale dynamics in polymer materials

Hanne M. van der Kooij
Wageningen, 24 August 2020

Let there be light

Quantitative imaging of nanoscale dynamics in polymer materials

Hanne M. van der Kooij

Thesis committee

Promotors

Prof. Dr J. Sprakel
Personal chair, Physical Chemistry and Soft Matter
Wageningen University & Research

Prof. Dr J. van der Gucht
Professor of Physical Chemistry and Soft Matter
Wageningen University & Research

Other members

Prof. Dr C.G.P.H. Schroën, Wageningen University & Research
Prof. Dr J.L. Keddie, University of Surrey, Guildford, United Kingdom
Prof. Dr N. Katsonis, Stratingh Institute for Chemistry, Groningen
Dr W. G. Ellenbroek, Eindhoven University of Technology

This research was conducted under the auspices of Graduate School VLAG
(Advanced studies in Food Technology, Agrobiotechnology, Nutrition and Health Sciences).

Let there be light

Quantitative imaging of nanoscale dynamics in polymer materials

Hanne M. van der Kooij

Thesis
submitted in fulfillment of the requirements for the degree of doctor
at Wageningen University
by the authority of the Rector Magnificus,
Prof. Dr A.P. J. Mol,
in the presence of the
Thesis Committee appointed by the Academic Board,
to be defended in public
on Monday 24 August 2020
at 4 p.m. in the Aula.

Hanne M. van der Kooij
Let there be light — Quantitative imaging of nanoscale dynamics in polymer materials
356 pages

PhD thesis, Wageningen University, Wageningen, The Netherlands (2020)
With references, with summary in English

ISBN: 978-94-6395-422-8
DOI: https://doi.org/10.18174/523168

Contents

Chapter 1

General introduction

"Look at how a single candle can both defy and define the darkness."

Anne Frank (1929–1945) knew the power of a light source to illuminate phenomena. For most of human history, mankind has remained in the dark regarding the inner workings of materials. People envisioned materials as black boxes, and believed in invisible spirits as the source of all natural phenomena in order to make sense of their world. Everything one did not understand was considered supernatural. The complexity of matter was reduced to only four elements that humans could grasp: air, fire, water and earth (Figure 1.1a).[1]

Since the scientific revolution in the 16th century, the prevailing view of nature has changed radically and fundamentally, from one that revolved around deduction and assumption, to one dedicated to induction and objective observation. Development of experimental methods and theoretical models gained momentum.[5] The father of microscopy, Antoni van Leeuwenhoek (1632–1723), discovered micro-organisms that no human eye had ever seen by using his self-constructed microscopes (Figure 1.1b).[6] He provided a glimpse into the previously unseen world of 'wee animalcules' (little animals), and exposed a diversity of 'cavorting beasties' (bacteria and protozoa) in a drop of fresh water (Figure 1.1c).[7] Researchers and society realized how pivotal it is to cast light on small-scale phenomena beneath the surface of materials, where the naked eye cannot see. A vast multitude of imaging methods have thenceforth been developed with the aim

Figure 1.1. Towards an enlightened view of matter. **(a)** From 450 BC, the concept of four classical elements – air, fire, water and earth – was the cornerstone of science.[2] This paradigm persisted throughout the Middle Ages and into the Renaissance, until the scientific revolution transformed human's perception of materials. **(b)** Antoni van Leeuwenhoek used a self-constructed microscope to see the previously unimagined and unseen microcosmos **(c)**.[3,4]

to elucidate the microscopic patterns underlying tangible material properties such as strength, appearance or motility. Indeed, gaining a fundamental understanding of how dynamics, structure and interactions in the molecular world are expressed in the macroscopic world is one of the key challenges in materials science.

This quest has proven successful for optically transparent materials, in which light can easily penetrate. However, as evident when looking around, most everyday materials are highly opaque and coloured, and therefore their core is unreachable for light. These materials can thus be considered 'white boxes' that diffusely reflect all the incident light from the surface. To nevertheless reach the core, a common workaround is to strongly dilute these opaque materials such that optical transparency is achieved. In this thesis, we have applied that strategy to water-based coatings in Chapters 3 and 4. Although insightful for gaining knowledge on larger-scale and superficial phenomena, the legitimate question arises how representative the analysis of dilute systems is for realistic, concentrated analogues. Alternatively, transparent model systems comprising the main features of the material of interest are frequently synthesized in the lab, by carefully tuning the refractive indices of the constituents.[8–11] This procedure is, however, a laborious task that inevitably introduces artefacts.

The need for such workarounds is circumvented if a method would exist that benefits from the diffuse scattering inside opaque materials. A technique that enables us to literally and figuratively switch on the light within a material. Indeed, such a technique exists: *laser speckle imaging* (LSI). This method utilizes the interaction of laser light with scattering centres inside a material to visualize dynamics and mechanics at the nanoscale (see Section 1.4). We have advanced and tailored this method, and thus 'let light be' in a variety of soft materials.

1.1 Bridging length scales in soft materials

Finding microscopic explanations for macroscopic phenomena is a central theme in soft matter science. Soft materials live up to their name: they are 'soft', meaning that they can easily be deformed by an external force. Hence, they are no rigid solids (such as steel or ice), yet no simple liquids either (such as petrol or water) thanks to their soft elasticity and integrity.[12–14] Soft matter is ubiquitous, ranging from plastics and personal care products to food and biological substances. These materials are exceedingly complex. They are bipolar in the sense that they exhibit a convoluted mixture of solid- and liquid-like behaviour depending on the conditions, notably the magnitude and rate of the applied force. For example, a glob of mayonnaise appears solid-like on top of a sandwich, but like a liquid it can

be squeezed from a bottle or spread with a knife. Paint becomes readily flowable when brushed, but resists running down a vertical wall.

The origin of this schizophrenic behaviour lies in the relatively large size of the building blocks – much larger than an atom – and relatively weak interactions between them. These features not only provide soft materials with characteristic time-dependent softness, but also with high sensitivity towards external stimuli such as heat and pH, non-trivial heterogeneity, spontaneous pattern formation, and proneness to kinetic trapping in non-equilibrium states. It is therefore a daunting

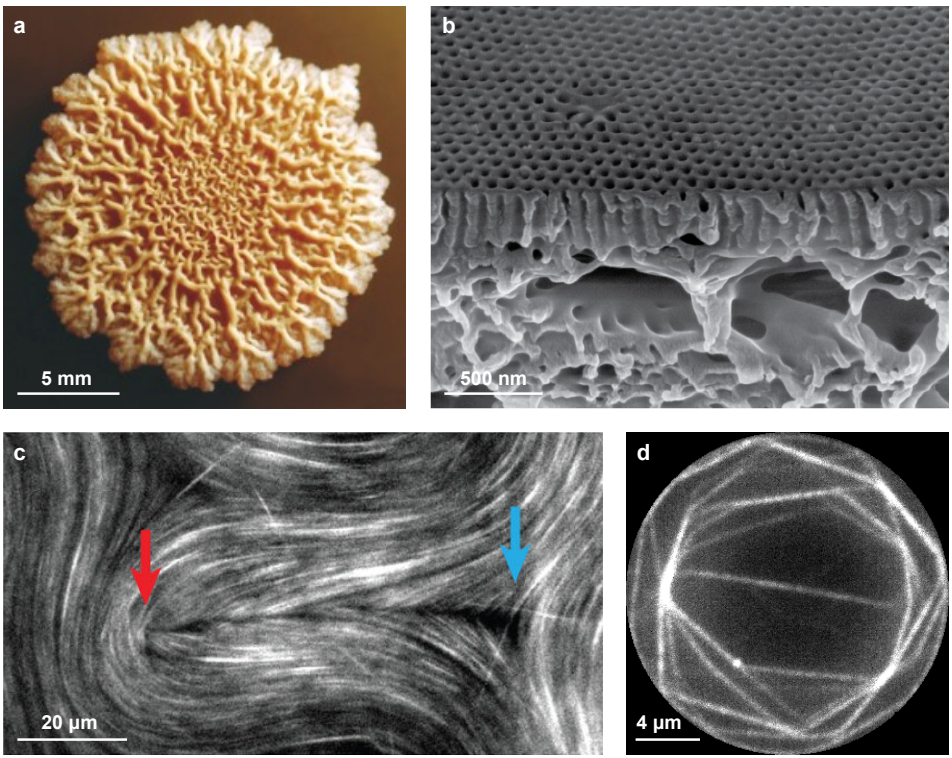

Figure 1.2. Emergence in soft materials. **(a)** *Bacillus subtilis* biofilm, a colony of bacteria, showing an ill-understood pattern of branched wrinkles.[15] Reprinted with permission from ref. 16. Copyright 2015 by the American Physical Society. **(b)** Scanning electron micrograph of the cross-section of an asymmetric polystyrene-*block*-poly(2-vinylpyridine) membrane. Adapted with permission from ref. 17. **(c)** Active liquid crystals, confined to a fluid interface, display unexpected internally driven motion such as buckling, folding, and internal fracture. The arrows point to a pair of topological defects. Adapted with permission from ref. 18. **(d)** Spindle-like network of actin bundles in confinement, induced by depletion interaction. Adapted with permission from ref. 19.

task to precisely predict their properties by considering the individual structural units. In fact, *collective* behaviour of large numbers of building blocks gives rise to complex emergent properties. This emergence cannot easily be rationalized. Biofilms form a fascinating example of emergence: these thin layers of surface-bound micro-organisms, embedded within a slime matrix, can display mosaic-like wrinkling patterns that are not readily predictable from detailed knowledge of the microbes and matrix alone (Figure 1.2a).[15,16] Certain polymers (see Section 1.2) can form puzzling asymmetric superstructures, which have unforeseen potential as highly selective membranes (Figure 1.2b).[17,20,21] Active materials exhibit novel modes of behaviour and organization that often cannot be forecasted, such as folding and fracture in active liquid crystals (Figure 1.2c).[18] Life itself is the most mind-boggling, quintessential and intricate form of emergence. Yet also at a smaller scale, the cellular framework or cytoskeleton can organize in a remarkable manner (Figure 1.2d).[19,22] To connect all phenomena from the nanoscopic to the macroscopic world, we must unravel the complexity that arises across multiple time and length scales.

1.2 Synthetic polymer materials

A prototypical example of complex soft matter are polymers.[23,24] Synthetic polymers are widely found in plastics, elastomers, gels, and various types of dispersions and solutions. In recent decades, the rapid development of polymer materials has made a substantial contribution to society. The global production of plastics alone amounted to 359 million metric tons in 2018.[25]

Polymers are long, chain-like molecules that consist of many repeated subunits, resembling a nanoscopic necklace. Individual polymer chains can take different conformations, ranging from flexible and coil-like to stiff and rod-like. An assembly of flexible polymer chains easily gets physically entangled or chemically tied together. In contrast to macroscopic necklaces, for polymers this property can be highly beneficial, as explained in Sections 1.2.1 and 1.2.2. Dedicated synthesis strategies allow the chemistry and number of subunits to be precisely tuned, and thereby the chain architecture and physical interactions. An astonishing variety of bespoke polymer materials have thus been designed.

Polymer phases are characterized by viscoelasticity, large-strain nonlinear behaviour, and a broad range of relaxation times and length scales. In this thesis, we focus on two types of polymer materials: (i) dispersions, in which the polymer phase is distributed as small (order 100 nm) spheres in a continuous medium (Chapters 2–6), and (ii) solvent-free, percolated networks, in which the polymer chains form the continuous phase (Chapters 7–10). The former are called latex

dispersions or water-borne paints if the medium is water. The latter are commonly known as rubbers or elastomers.

In view of the rapidly growing polymer demand worldwide, the need for more sustainable polymer materials is rising. Environmental pollution and shortage of resources are two alarming issues, which urge researchers to develop durable alternatives of excellent quality. This quest is imperative yet challenging. Most polymer materials are intrinsically complex and thus not well-understood, impeding the discovery of rational design principles. Properties accessible to the human eye cannot simply be explained based on individual polymer chains. Instead, unravelling the collective 'dance' of the polymeric building blocks is pivotal. Experimental methods that visualize the complex dance at the microscale are thus crucial to fathom the origin of macroscopic phenomena. This necessity is even greater when it comes to non-equilibrium processes, which is a thread running through all chapters of this thesis. We here distinguish passive out-of-equilibrium systems such as drying water-borne paints (Chapters 2–6), enforced fracture (Chapter 7), and spontaneous self-healing (Chapter 8), from active systems that are inherently out of equilibrium as they continuously consume energy to drive their motion (Chapters 9 and 10). Both for water-borne coatings, which have been around for many decades, and for recent advanced technologies, the fabrication is still largely empirical and artisanal. Many questions regarding the fundamental microscopic mechanisms remain unanswered. Although the structure and functioning of the individual components are often known thanks to numerous ingenious experiments, truly understanding the operational principles requires comprehensive insight into the cooperativity between building blocks.

1.2.1 Towards greener paints

Coatings form a protective layer on virtually all surfaces around us, ranging from furniture, walls and appliances, to cars, buildings and satellites.[26] These thin films of typically $0.01 - 1$ mm thick are used to confer various functional and aesthetic properties to a surface, including colour, opacity, gloss, weather resistance, abrasion protection, insect repellency, or electrical conductance. Currently, almost half of the global coatings market is water-based; these so-called latex dispersions are predominantly applied indoors for decorative purposes. Approximately a quarter is formulated in organic solvents such as turpentine and acetone; their use is limited to demanding and outdoors applications, because the solvents are volatile organic compounds (VOCs) that are released into the atmosphere. 15–20% of all coatings is powder-based, mainly used to coat metals; see Chapter 11 for detailed information and experimental analysis of this category. The remaining

15–20% are less common yet emerging technologies including high-solids and radiation-cured coatings.[27] The percentage of solvent-borne paints has gradually declined over the past decades, as VOCs have been shown to be hazardous for both the environment and the user. These compounds contribute to smog and the greenhouse effect, while additionally causing severe brain damage to professional painters who inhale the fumes daily.

The environmental and consumer concerns have led to increasingly stringent legislation regarding the allowed VOC content, which in turn has incentivized industry to produce more water-based paints. However, the performance and longevity of water-borne systems are still inferior to those of solvent-borne analogues. Improving the paint quality is particularly vital for high-performance applications such as cars, airplanes and satellites, which have to withstand extreme conditions. Solvent-borne paints are currently still the standard for those applications. Considering the abundance of coatings, with 37 billion litres of coating products sold worldwide in 2018 at a total market value of 140 billion euro,[28,29] not only the environment but also the economy will benefit significantly from improved water-based paints. This improvement is, however, a challenging endeavour. Water-borne paints are extremely complex systems consisting of dozens of components that migrate, interact and evolve during drying.[30,31]

Complexity of latex drying

Chapter 2 further elaborates on the intricate processes governing paint drying, highlighting the principal challenges that preclude a thorough understanding of film formation, and how these can be addressed. In Chapters 3 and 4, we circumvent some of the complexity by preparing well-defined model paints. Synthesis of dispersions with well-known properties allows us to reduce the number of variables that affect the drying dynamics. These systems consist of only the two main latex ingredients: water and dispersed binder particles (Figure 1.3a). The water serves to reduce the viscosity of the paint and thereby facilitates application of a uniform thin coating. The binder particles form the final coherent film after evaporation of the water. These particles are ~100 nm spheres made of hydrophobic polymer assemblies stabilized by charges on the surface.[32] At some moment during latex drying, the individual binder particles must all deform and subsequently fuse together or 'coalesce' to form a homogeneous polymer film (Figure 1.3).[33] Successful film formation is crucial in establishing the desired appearance and performance of the final dry coating.

Although the drying stages in Figure 1.3a are drawn consecutively and distinctly, in reality all drying phenomena are intimately linked. It is therefore challenging to

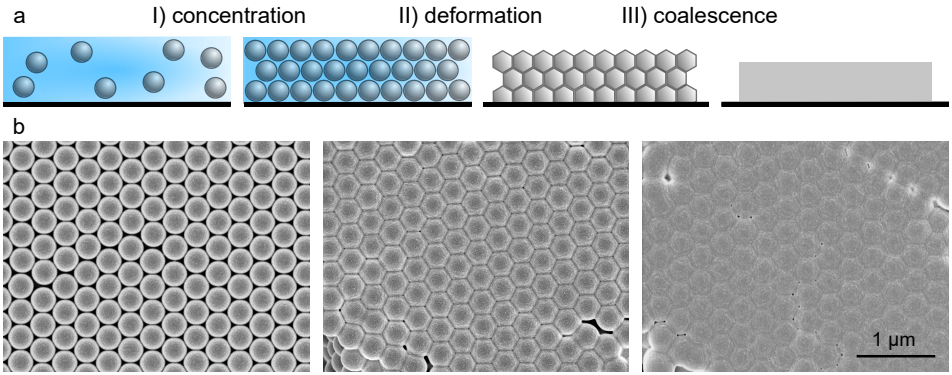

Figure 1.3. Film formation in a drying latex dispersion. In an ideal world, three well-defined stages occur, shown schematically in **(a)** and using scanning electron microscopy (SEM) on a dry film surface in **(b)**. I) First, the polymer particles concentrate, until they are closely packed. II) Second, the rising capillary pressure causes the particles to squeeze together and deform, driven by surface tension, thus gradually closing the interparticle voids. III) At a certain moment, the pressure is so high that the particles coalesce. This leads to a more or less uniform film depending on the polymer viscosity. The scale bar applies to all SEM images.

disentangle their individual effects. The interaction map in Figure 1.4 emphasizes the wide variety of physical and chemical aspects which come into play during film formation in a latex dispersion. The inner ring represents the typical time scales of the main processes, and the outer ring shows the numerous parameters affecting these. The arrows indicate relations between processes and parameters. Strikingly, this web is not even close to complete, disregarding the particular polymer chemistry as well as the behaviour of surfactants, rheology modifiers and other additives.

At the core of film formation is the process of phase inversion, in which the continuous water phase with dispersed polymer particles transitions into a continuous polymer phase with interstitial water.[35] Only soft binder particles can deform and coalesce, which are prerequisites for film formation. Yet, soft particles give rise to an unacceptably poor coating after drying. This clearly poses a paradox: hard particles exclude film formation, whereas soft particles preclude film functionality.[30]

Solutions to the film formation dilemma

Resolving this conundrum is not a trivial task. The traditional, easiest answer has been to temporarily soften hard particles by a plasticizer that evaporates after film

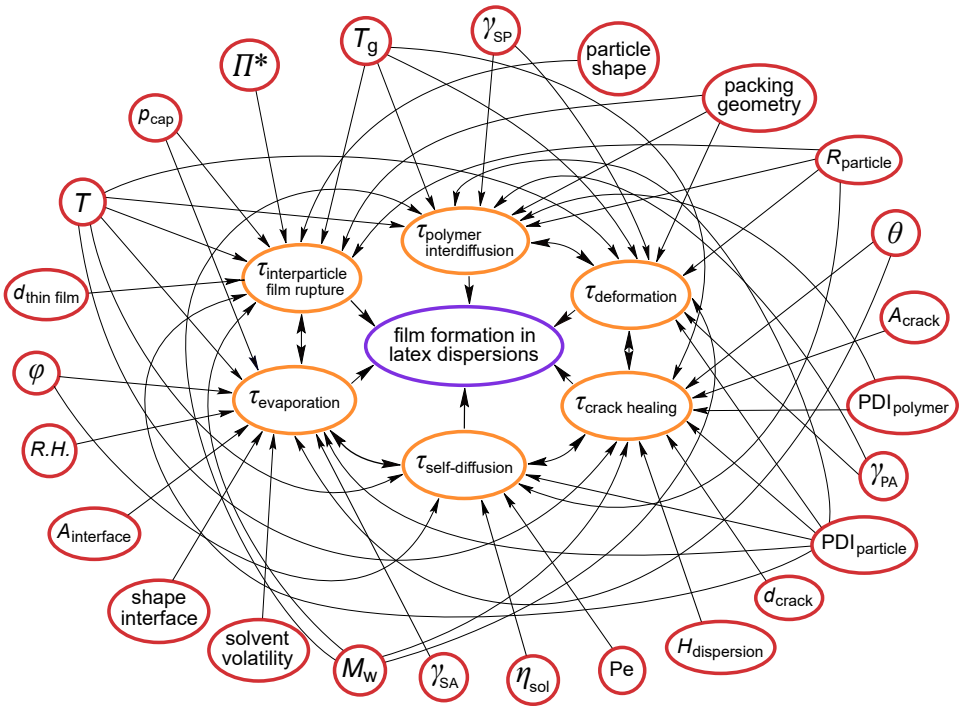

Figure 1.4. Complexity of latex film formation. A myriad of physico-chemical parameters (outer ring) influence the six most important time scales (inner ring). The subscripts S, P and A denote solvent, polymer and air, respectively. γ is the interfacial tension, θ is the contact angle, Pe is the Péclet number, φ is the volume fraction, and Π^* is the critical disjoining pressure. Adapted significantly with permission from ref. 34.

formation. However, most plasticizers are VOCs, which renders them harmful and unfavourable. More recent strategies are blending high- and low-T_g particles,[36–38] harnessing hydroplasticization to soften the polymer phase,[39–41] synthesizing core–shell particles comprising both hard and soft portions (or related morphologies, e.g. multi-domain, multi-lobe or raspberry),[32,42–44] and leveraging radiation-assisted curing or sintering.[45,46] Although effective, each of these approaches requires tailored modification of the polymer chemistry. In this thesis, we choose to take a different course and focus on enhancing our understanding of drying and film formation phenomena in water-based coatings. In order to advance the development of high-quality water-borne paints, we use laser speckle imaging to shed light on the inner workings of drying latex dispersions and unravel the mechanisms of film formation. We believe that these new insights will help

achieve the ultimate goal to reduce the amount of VOCs and thereby protect the environment and painters' health.

Above, we mentioned that laser speckle imaging is particularly suitable when it comes to opaque systems. Indeed, most latex dispersions are highly scattering and coloured. The majority of 'model paints' in the literature are transparent and cannot be considered as realistic formulations, because they lack pigments, which give the coating its opacity and colour. In Chapters 5 and 6, we therefore add commonly used titanium dioxide pigments to our dispersions, thus creating representative paints while simultaneously bringing them into a regime where LSI thrives. In addition, the dynamics that govern paint drying are highly heterogeneous and characterized by a broad spectrum of time and length scales. Imaging methods such as LSI are therefore indispensable. In fact, one of the main reasons for the inferiority of water-borne coatings compared to their solvent-based counterparts is a more inhomogeneous morphology of the final film, featuring voids, gradients in constituent concentrations, and possibly cracks or other defects. Visualizing the development of such heterogeneous structures during drying is essential, as the evolution of their appearance provides insight into the underlying root issue. Knowing the origin of imperfections is the primary step towards new and sustainable water-based paints.

1.2.2 Towards high-performance elastomers

Elastomers form another subclass of polymers which are prevalent in society. These synthetic, flexible, rubber-like elastic solids were first introduced in the 1920s, when inventor and physician Joseph C. Patrick discovered the polysulphide 'Thiokol' thanks to serendipity.[47] Elastomers are used in diverse areas, including tyres, tubes, gaskets, adhesives, raincoats, footwear, belts, electrical insulators and many more. The global elastomers market was valued at over 60 billion euro in 2017.[48] Elastomers consist of crosslinked polymer chains; these crosslinks can be entanglements, covalent (permanent) intermolecular connections, and/or supramolecular (transient) bonds (Figure 1.5a). The crosslink density principally dictates the elastomer stiffness.[49]

Failure prevention is better than cure?

Traditionally, research has revolved around the concept that elastomers should first and foremost be stiff and strong to grant a long lifetime. Prevention of material failure has been the central tenet in polymer science. All everyday materials inevitably suffer from damage during their use, resulting from scratching, cutting, cracking, abrasion, impact, corrosion, wear or tear. This damage starts

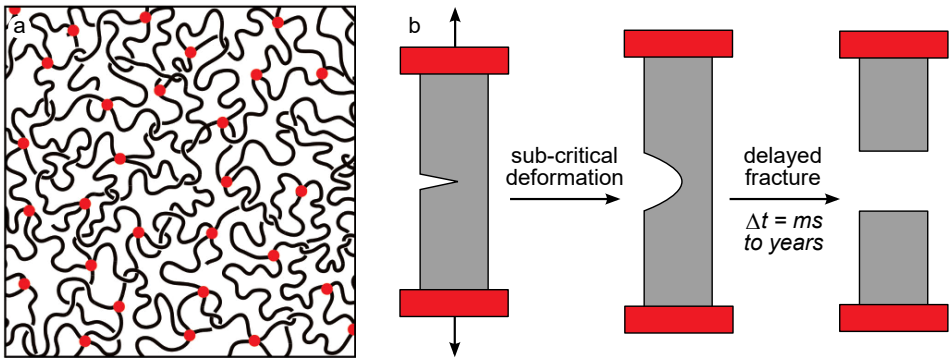

Figure 1.5. (a) Schematic of an elastomer at the molecular level. The red circles designate cross-links, and the knots indicate entanglements. Reprinted with permission from ref. 50. **(b)** Schematic of delayed fracture of a step-strained, notched elastomer. After application of a sub-critical tensile strain, a period of seeming stability follows that can vary from milliseconds to hours or even years, yet unavoidably culminates in macroscopic failure.

at the Ångström scale with local bond scission. Often these breaking events are irreversible, and accumulation of broken molecules over time ultimately causes failure of the material as a whole, for example by fracture or fatigue.[51,52] In Chapter 7 of this thesis, we make an important contribution to mitigating one of the most elusive forms of elastomer failure, namely delayed fracture (Figure 1.5b). This phenomenon – the sudden and catastrophic failure after an extended period of apparent stability – is a common feature in a wide variety of materials.[53–59] It occurs continuously around us and within us. While our tissues and skin have evolved sophisticated mechanisms to heal such damage, for elastomers it typically means the end of functionality. Despite the immense ubiquity, the reasons why, when and where a delayed crack will nucleate have remained largely obscure. Contrasting hypotheses have been presented in the literature, but these have remained speculative as experimental evidence of the nature of delayed failure has remained absent. In Chapter 7, we use LSI to create very precise micromechanical maps deep within an elastomer, of the moments prior to catastrophic failure. We prove how delayed failure may in fact be detectable and predictable well before the tipping point is reached. Our new insights may have significant consequences for safeguarding the operational safety of materials and structures, as well as for the rational design of new and tough materials.

Self-healing functionality

In recent years, material science has undergone a paradigm shift. Instead of impeding failure, a relatively new strategy is to impart self-healing capabilities to polymers, thus stopping material damage in its track.[62,63] Autonomous self-healing polymers spontaneously repair broken bonds from the inside out, without any human intervention,[64] and thereby evade the otherwise inescapable route towards failure.[65] Indeed, nature teaches us that curing damage is invariably more reliable than prevention. This approach is particularly relevant in situations where safety is key, damage readily occurs, yet repair is troublesome or expensive. A diversity of self-healing designs have thus materialized in the past two decades.[66–72] In all invented systems, broken intermolecular bonds can reform in such a way that the original material properties are restored from the nano- to the macroscale (Figure 1.6). To date, the development of these materials has been partially empirical, as the precise mechanisms underlying this unique behaviour have remained speculative. The main reason is the lack of a suitable method to visualize, quantify and interpret the nanoscale dynamics involved in autonomous self-healing at the relevant time and length scales. To address this question, we have collaborated with Prof. Sybrand van der Zwaag, Dr. Santiago García and Dr. Arijana Susa from the Novel Aerospace Materials group of the TU Delft, who develop elastomeric coatings that spontaneously repair damage at room temperature while also displaying a remarkably high strength and stiffness.[73] By

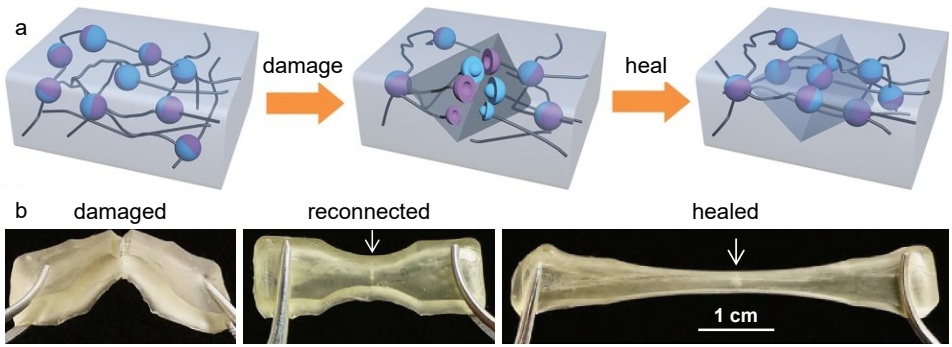

Figure 1.6. Autonomous repair of a self-healing polymer. **(a)** Molecular-scale schematic. Damage, in the form of broken supramolecular crosslinks, is spontaneously repaired from the inside out by reformation of reversible bonds. Adapted with permission from ref. 60. **(b)** Autonomous self-repair at the macroscopic level. After reunion of two damaged surfaces, self-healing starts instantly and restores the original mechanical properties. The arrows point to the cut location. Adapted with permission from ref. 61.

performing bulk mechanical experiments they have established the conditions of self-healing in great detail,[74–77] but they could not provide direct insight into the molecular mechanisms. In Chapter 8, we bring these to light using laser speckle imaging. For the first time, we spatially unveil the internal nanoscale motions with unprecedented displacement resolution across almost six decades in frequency. These findings may form a stepping stone for a new generation of self-healing polymers.

Active liquid crystal networks

A whole new world of possibilities unfolds when a material is driven out of equilibrium by an external perturbation. The interplay between a vast number of active entities can lead to complex patterns of cooperative motion and self-organized structures.[78] A way to introduce activity is by means of responsive molecules, i.e. molecules that react to changes in environmental stimuli such as temperature, light, pH, external fields, or mechanical forces.[79] The resulting 'smart' materials display even richer dynamics than their passive counterparts and can be designed to create an astonishing variety of shape-shifting, force-generating, locomotive and interactive responses.[80] Creating these materials is as much an art as a science. The holy grail is to decipher the rules that govern the complex behaviour of active matter, and the principles by which controlled molecular motion can be transmitted across length scales.

Liquid crystal molecules are particularly promising candidates for active matter because of their highly anisotropic order and rapid response to a wide range of stimuli (Figure 1.7).[83] Numerous different types of liquid crystals exist, which have been exploited ingeniously in display technologies.[84] This has led to an industry worth over 100 billion a year.[85] Thanks to the long-range liquid-crystalline organization, small changes in the individual molecules are amplified over orders of magnitude, and can thus convey remarkably large-scale reconfiguration. Although this amplification is at the heart of many applications, the underlying mechanisms are not well understood.

When liquid crystal molecules are embedded in a crosslinked polymeric solid, the orientational order and responsiveness of liquid crystals are merged with the versatile viscoelasticity of a polymer network.[86] These materials can exhibit large, yet reversible, changes of dimension and shape (Figure 1.7a3 and b3).[81,87–89] Responsive liquid crystal polymer networks have shown great potential in various applications, including soft robotics,[82,90] self-cleaning solar cells,[91,92] tuneable separation membranes[93] and bio-interfacing.[94,95] In almost all cases, the macroscopic functionality of the material arises from nanoscopic changes

in shape and/or volume in response to an external trigger, such as an electric field.[90,92,95–99] The engineering of these stimuli-responsive polymers has taken flight in recent years, which all hinges on the fundamental premise that the nonuniform electric field locally transforms the glassy solid into a rubbery elastomer to enable the programmed shape and/or volumetric changes. Yet, the existence of such an electric-field-induced glass transition has never been proven directly and unambiguously. Moreover, the exact route from the nanoscale, where energy is continuously consumed, to macroscopic functionality has long remained unknown.

To answer these open questions, we have collaborated with Dr. Danqing Liu and Prof. Dirk Broer from the Laboratory of Stimuli-Responsive Functional Materials and Devices of the TU Eindhoven, who have created a diversity of shape-morphing liquid crystal networks.[82,90,92,98,99] In Chapter 9, we use LSI to reveal how an alternating electric field can set in motion a hierarchical cascade of activated and collective molecular rearrangements. In Chapter 10, we prove the existence of a true field-induced glass-to-rubber transition. Using extensive quantitative analysis, we evidence that actuation involves three distinct stages, amongst which the – to date elusive – stage of 'electroplasticization'. Our results thus lay a foundation

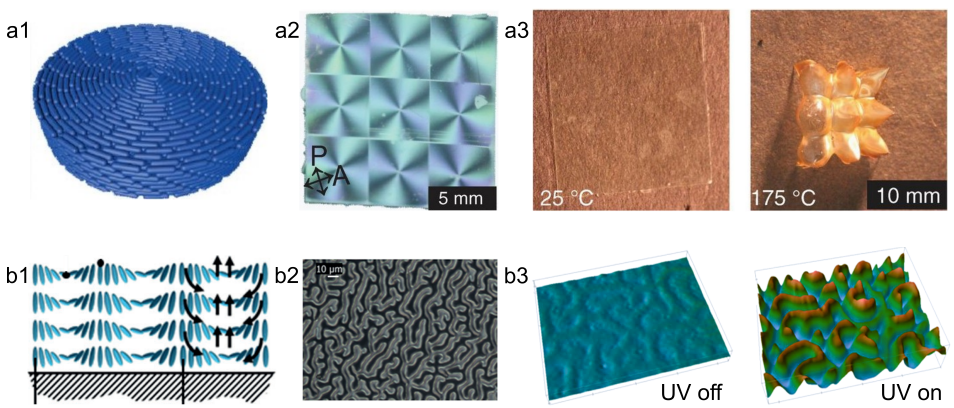

Figure 1.7. Examples of responsive liquid crystal networks in free-standing form **(a)** and surface-constrained **(b)**. **(a1)** Rod-like LC building blocks can be oriented in a concentric cylindrical manner. **(a2)** A polymer film comprising nine such coaxial packings displays an array of four-lobed patterns between crossed polarizers. **(a3)** The spatially heterogeneous LC ordering allows for pre-programmed, reversible shape changes, here between a flat film at room temperature and nine protruding cones at elevated temperature. Reprinted from ref. 81 with permission from AAAS. **(b1)** Cholesteric alignment of the LC units on a surface results in **(b2)** a 'fingerprint' texture between crossed polarizers. **(b3)** Upon UV exposure, the initially flat topography morphs into a corrugated state. Adapted with permission from ref. 82.

for the future development of these active and interactive materials and resolve a fundamental question in the field.

1.3 Visualization of dynamics

In all of the above-mentioned cases, establishing a deep understanding of the internal dynamics in space and time is essential. With the growing societal focus on sustainable and sophisticated technologies, research must go the extra mile and reach beyond empirical knowledge of polymer materials. In order to advance this aim, it is imperative to develop new imaging tools and instrumentation with quantitative access to heterogeneous material properties. The pursuit of such imaging capabilities is far from easy, as researchers face many obstacles along the way. The most demanding are listed below.

1.3.1 Challenges

- The majority of everyday polymer materials are turbid, and therefore light cannot pass through them. These materials appear as pitch dark under a standard microscope, which makes imaging underneath the sample surface quite challenging.

- The material may not be free-standing, but rather substrate-constrained. This substrate will likely obstruct or interfere with the illuminating beam.

- Polymer materials are intrinsically complex and feature a very broad spectrum of time and length scales. Complete characterization thus requires visualization of dynamics from the level of individual molecules to the macroscopic level.

- Preferably, the material is not modified upon imaging, nor needs extensive prior preparation. A non-invasive imaging modality is accordingly preferred.

- Although qualitative data are useful for identifying trends, they entail subjectivity in the evaluation and limit reproducibility. Quantitative imaging is most powerful for extracting tangible properties that can be connected to physical phenomena without observer bias.

- Imaging equipment is often costly, non-adjustable and difficult to operate. An inexpensive, modular and accessible technique is highly desired.

1.3.2 Commonly used methods

"You can't study the darkness by flooding it with light." – Edward Abbey (1927–1989)

Conventional non-contact imaging methods therefore employ a well-defined illuminating beam, made of white light (bright-field microscopy), laser light (fluorescence-based microscopy), electrons (scanning electron microscopy), X-rays (X-ray scattering), or radio waves (magnetic resonance imaging). Each of these techniques has proven its merit for imaging polymer materials over the past decades. Examples of their application to latex dispersions are shown in Figures 1.8 and 1.9. Nevertheless, all methods suffer from non-negligible drawbacks, which we outline below.

Bright-field microscopy

Bright-field microscopy is the simplest, most direct and inexpensive means to visualize material structure and dynamics.[100] Since the image contrast is based on variations in scattered or transmitted intensity, acquired images are easily interpreted. However, only heterogeneities with dimensions larger than approximately 200 nm can be detected, and strong scattering renders bright-field microscopy ineffective.[6] Molecular-scale heterogeneities and deep layers in opaque materials therefore remain invisible. For colloidal dispersions such as water-based paints, which feature microscopic inhomogeneities and instabilities, this technique may be perfectly useful if the dispersion is (semi-)transparent. Emulsion coalescence, for instance, can beautifully be visualized (Figure 1.8a).[101] We benefit from this method in Chapters 3 and 4, where the dispersion films are sufficiently dilute and thin to allow for rather detailed insight into the drying processes. By measuring spatio-temporal changes in the transmitted light intensity, we can connect the latex properties to evaporation-induced instabilities and final film homogeneity, which ultimately enables a deeper mechanistic understanding of paint drying.

The temporal resolution of bright-field microscopes is limited only by the camera frame rate and the required exposure time, and can reach beyond µs under optimal conditions.[102] Even though the resultant images are intuitively interpretable, their information content is only semi-quantitative and limited with respect to further processing.

Fluorescence-based microscopy

One of the most common real-space optical methods in soft matter research is the confocal laser scanning microscope (CLSM).[104] Confocal microscopy relies on variations in fluorescence intensity for its contrast, which already emphasizes

the limitation that fluorescent components are required. Nevertheless, CLSM is unsurpassed in providing particle-level information about a material. With the advent of three-dimensional imaging capabilities, including high-speed cameras and software, nowadays confocal microscopy allows measuring individual particles in three dimensions with sub-second temporal resolution and even down to a millisecond in two dimensions. The particle locations can afterwards be tracked with outstanding accuracy using sophisticated computer algorithms, thus providing

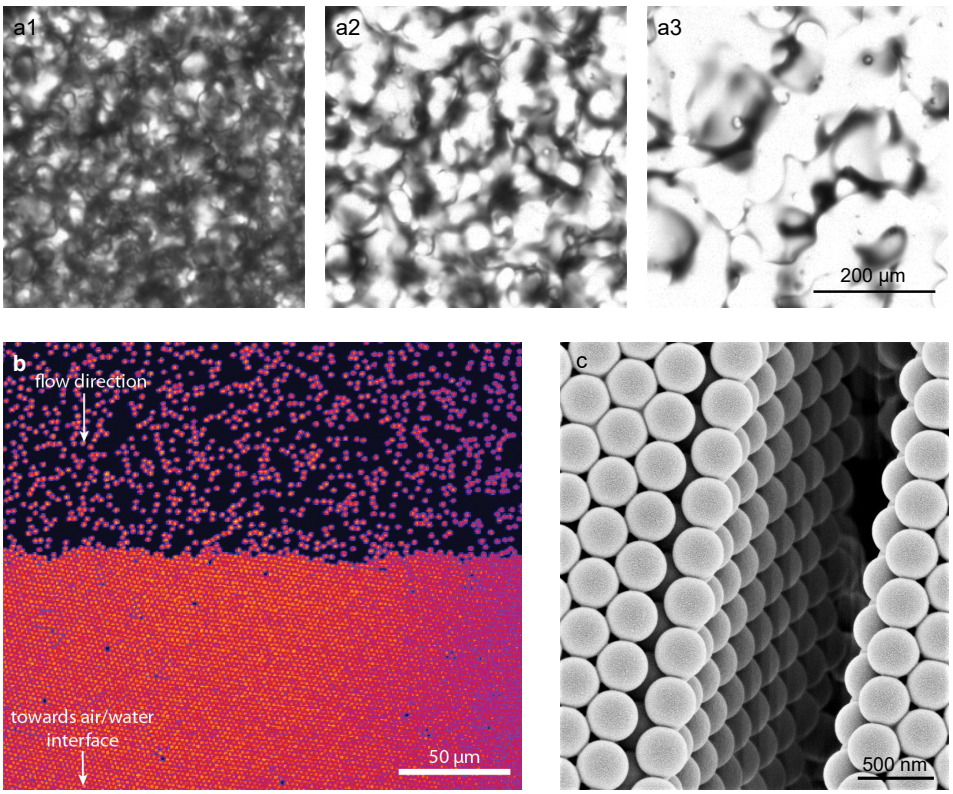

Figure 1.8. Typical imaging methods applied to latices. **(a)** Time-lapse transmission optical micrographs showing coalescence in a film of poly(*n*-butyl acrylate) particles. Δt_{a1-a2} = 200 s and Δt_{a2-a3} = 700 s. Coalesced regions appear as bright, while non-coalesced areas scatter rather than transmit the light. The scale bar applies to all images. **(b)** Confocal micrograph of a partially-dried suspension of fluorescent 1.1 µm latex particles inside a unidirectional drying geometry. The particles accumulate at the open air/water interface. Reprinted with permission from ref. 103. Copyright 2017 by the American Physical Society. **(c)** Scanning electron micrograph of the surface of an air-dried polystyrene latex film, showing three-dimensional crystalline packing.

access to the instantaneous sample structure and its evolution over time. However, analogous to bright-field microscopy, the spatial resolution cannot significantly beat the diffraction limit. Particle-level information can thus be achieved only for a limited number of specific systems, e.g. micron-sized fluorescent colloids (Figure 1.8b). Moreover, optical transparency is an essential prerequisite, which thus excludes many everyday polymer materials. In those cases, either the aqueous medium must be reformulated into a refractive-index-matched solvent, or the imaging remains limited to superficial layers.

In recent years, a wealth of fluorescence-based super-resolution microscopy (SRM) methods have seen the light.[105,106] These techniques provide unprecedented information about features smaller than the excitation wavelength, down to single molecules. Super-resolution microscopy has revolutionized imaging by thoroughly breaking the diffraction limit. The potential and power of SRM are undeniable, although applications to soft matter beyond biology are still relatively scarce. Possible explanations are the high equipment cost, lack of flexibility, and proneness to image artefacts. A review of the wide variety of SRM variants is beyond the scope of this thesis.

Scanning electron microscopy

When it comes to direct nanoscale glimpses of the material surface, SEM is unparalleled. This technique uses accelerated electrons, which have a much smaller de Broglie wavelength than light, to image a sample.[107] The application of a high vacuum prevents interactions of the electrons with surrounding gases and thereby ensures a high lateral resolution – down to a few nanometres, depending on the diameter of the electron beam. The image contrast is mainly determined by the so-called 'edge effect': secondary electrons are generated mostly at edges in the sample, resulting in an increased brightness at those positions. This allows visualizing the morphology of the sample surface in great detail. In addition, elemental mapping is possible, and fragile morphologies can be studied in their original state by employing cryogenic conditions. Representative examples of the surface of a dry paint film are shown in Figures 1.3b and 1.8c. Chapters 3 and 4 feature more high-resolution SEM images of a wide variety of dried latex films, where we systematically evaluate the local particle packing and crack morphology for different systems. These images, combined with complementary bright-field micrographs and theory, provide comprehensive insight into the governing drying stresses, mechanisms and regimes.

The major disadvantage of SEM is the restriction to surface or cross-sectional information. Furthermore, the technique is destructive in the sense that sputter-

coating of the sample with conductive metal is required. A third drawback is the lack of truly quantitative information in scanning electron micrographs: different images cannot accurately be compared in a quantitative manner, as the contrast depends strongly on the used acceleration voltage, digital contrast and brightness. Finally, the material dynamics are unattainable using typical scanning electron microscopes, which operate only under high vacuum. In-situ analysis of the sample surface *is* possible using so-called environmental SEM,[108,109] but the corresponding resolution is suboptimal because of the lower vacuum.

X-ray scattering

X-ray scattering methods, such as small-angle X-ray scattering (SAXS)[112] and X-ray photon correlation spectroscopy (XPCS),[113] are commonly used because of their high sensitivity to multiple length scales in a single measurement – down to the

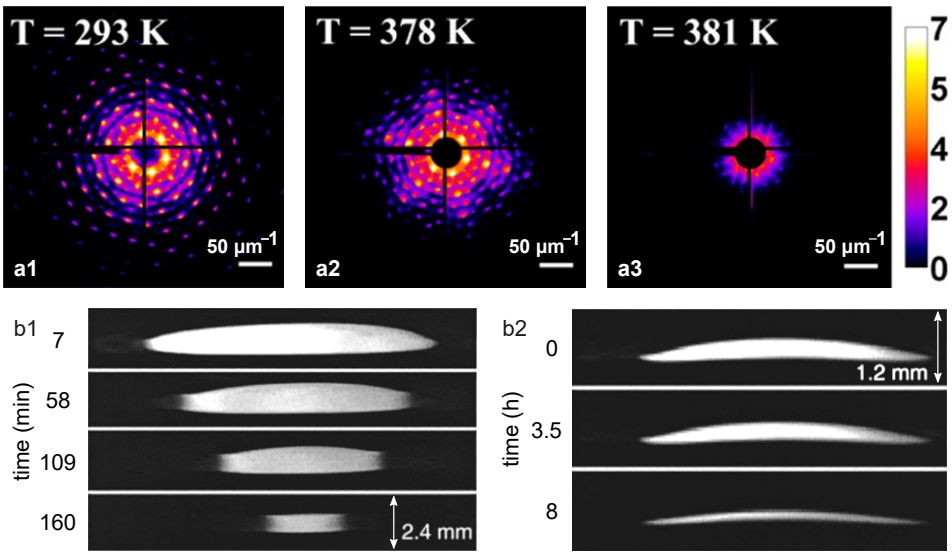

Figure 1.9. Typical imaging methods applied to latices. **(a)** In-situ X-ray diffraction patterns obtained during incremental heating of a polystyrene latex crystal. The intensity values on the colour scale are logarithmic. At the melting temperature T = 381 K **(a3)**, the Bragg peaks and six-fold symmetry disappear. Adapted with permission from ref. 110. **(b)** Magnetic resonance images of the cross-sections of drying latex films. The grey level scales with the local water concentration. For small particles **(b1)**, the water rapidly recedes from the film edge, whereas for large particles **(b2)**, it remains pinned at the edge for a prolonged period. Adapted with permission from ref. 111.

nanoscale. Some laboratories have in-house SAXS equipment, but to achieve the maximum signal, high-brilliance X-rays produced by (costly) synchrotrons are recommended. The temporal resolution is typically of the order of minutes, i.e. not real-time. Both an advantage and disadvantage is the inherent volumetric averaging; on the one hand, this affords ample ensemble statistics over a vast number of scatterers, yet on the other hand, it impedes spatially resolved information. Instead, scattering methods probe the structure and dynamics as a function of scattering vector q, which inversely reflects length scales $\sim 1/q$. In a latex film, loss of small-scale structure by coalescence or melting thus involves a shift towards smaller q values (Figure 1.9a).[110,114,115] The fact that samples are studied in reciprocal space makes it rather challenging to extract meaningful and intuitive quantities.

Magnetic resonance imaging

Although traditionally used in the medical field, magnetic resonance imaging (MRI) has progressively entered the toolbox of soft matter experimentalists.[116–118] MRI allows non-invasive investigation of microscopic structure and dynamics of both transparent and opaque samples in complex geometries. It combines a strong magnetic field with intricate sequences of radiofrequency pulses, for which the optimization possibilities are virtually endless. Using two-dimensional slices, three-dimensional reconstructions can be made, albeit with relatively poor spatial resolution of ~10–100 μm. Application examples in polymer materials include establishing water concentration profiles in a drying paint film (Figure 1.9b),[111,119,120] measuring polymer swelling kinetics,[121,122] and imaging stress in strained elastomers.[123,124] Unfortunately, the method is time-consuming and expensive, and demands a thorough understanding of pulse sequences, signal acquisition and data processing. The time resolution is also limited compared to the aforementioned techniques, typically in the range of 10–1000 ms. A final drawback of MRI is its intrinsically low signal-to-noise ratio.

Novel imaging methods

This list is by no means exhaustive. In recent decades, various more 'exotic' imaging techniques have emerged with applications in polymer science. Worth mentioning are optical coherence tomography (an interferometric technique most widely applied in the medical field), digital holography microscopy (for computational reconstruction of holograms), light-sheet fluorescence microscopy (for three-dimensional mapping of fluorophores), and digital photoelasticity (for visualization of stress-induced birefringence). Yet again, these methods only function optimally

in the limit of weak scattering. A notable exception is X-ray tomography, which indeed permits capturing the three-dimensional dynamic properties of a broad variety of turbid systems. Nevertheless, the technique is quite costly, and with a time resolution of seconds at best, it is unsuitable for real-time imaging.

1.4 Laser speckle imaging

Despite the proven value of each of the techniques above, none of them fulfils all the conditions listed in Section 1.3.1. We therefore took a leap in the dark to develop a method that *does* allow the spatially resolved quantification of nanoscale dynamics inside highly turbid, heterogeneous and complex materials, in situ, non-invasively, over a wide range of time scales, irrespective of the sample substrate, and in an affordable and accessible way: laser speckle imaging.

1.4.1 Background

Laser speckle imaging (LSI) has its origin in the medical world, emerging in the 1980s as a new diagnostic tool for non-invasive imaging of microvascular blood flow velocities *in vivo*.[125] This technique is essentially an extremely sensitive motion-detection method. It relies on the quasi-elastic interaction of laser photons with a large number of scattering centres inside a turbid material.[126] As a result of the multitude of scattering events, the photons follow a diffusive trajectory, with statistical properties identical to a random walk (Figure 1.10a).[127,128]

Remarkably few components are needed for an LSI set-up (Figure 1.10b): (i) a coherent light source, typically a laser, which illuminates the turbid material of interest; (ii) an array of photodetectors, generally a CCD or CMOS camera, which records the multiply scattered light; (iii) an objective lens, which focuses the scattered light onto the camera sensor; and (iv) a linear polarizer perpendicular to the laser polarization, which filters most of the reflected and weakly scattered photons. Finally, a beam expander is required if the laser beam is collimated, to widen the beam diameter and thus illuminate a larger area of the sample. Interestingly, these components strongly resemble the parts of a (polarization) optical microscope if the laser would be replaced by a white-light source. It is indeed the coherence of the illuminating beam that is crucial for LSI. While white light yields commonly known images, laser light results in a speckle pattern on the camera: a spatial structure of randomly distributed intensity minima and maxima (Figure 1.10c1). This peculiar pattern arises from the interference between numerous photons that all have traversed a unique scattering path inside the opaque sample, leading to a multitude of photon path lengths and phase

differences.[132] White-light images are in a sense superpositions of an infinite number of laser speckle patterns.

A single speckle pattern is rather boring and does not contain significant information. The detailed granular structure bears no relation to the macroscopic properties of the illuminated object.[133] By contrast, *temporal sequences* of speckle patterns, i.e. speckle movies, harbour a wealth of dynamic information. In the early 1980s, it was discovered that motion inside the sample leads to blurring of the speckles, provided the exposure time is of the order of the speckle decorrelation time.[125] This blurring was translated into dynamic information using the contrast function K:

$$K = \frac{\sigma_I}{\mu_I} = \frac{\sqrt{\langle I^2 \rangle - \langle I \rangle^2}}{\langle I \rangle} \tag{1.1}$$

where σ_I is the standard deviation of the speckle intensity I and μ_I is the mean intensity. The brackets $\langle ... \rangle$ refer to an average over time and/or space.[134] Under ideal conditions, a static speckle pattern features an intensity distribution with σ_I

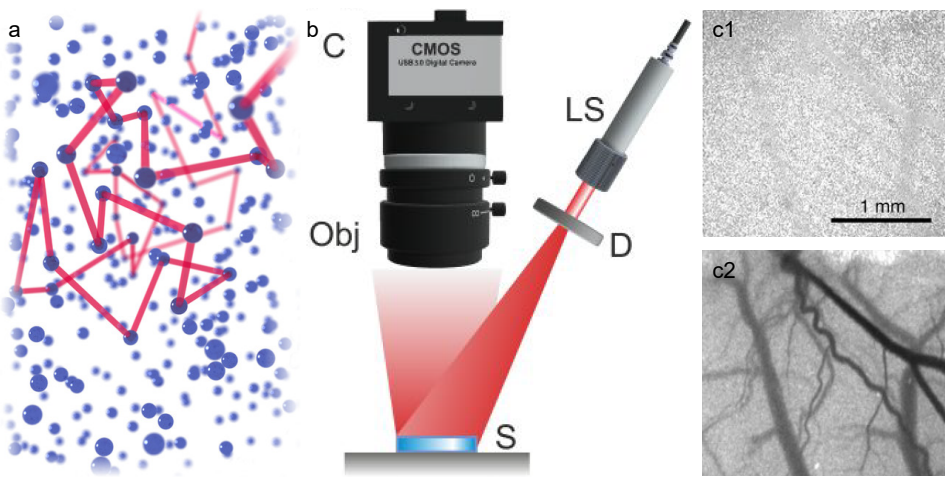

Figure 1.10. Principle of laser speckle imaging. **(a)** Artist's impression of diffusive light propagation through a material with randomly distributed scattering centres (blue spheres). A single photon path is drawn in pink. Reprinted with permission from ref. 129. **(b)** Schematic of a laser speckle imaging apparatus. C = camera, Obj = objective lens and polarizer, S = sample, D = diverging lens, LS = laser source. Reprinted with permission from ref. 130. **(c1)** Typical raw speckle image of microvascular blood flow inside a rat brain. Very few features are visible, except for slightly blurred blood vessels. Speckle contrast analysis of a time series of such speckle patterns yields the corresponding K map **(c2)**, in which hidden capillaries come to light. The grey level is inversely proportional to the blood flow velocity. Adapted with permission from ref. 131.

equal to μ_I, which gives a theoretical maximum contrast of unity. Such a speckle pattern is termed 'fully developed'.[132,135] In practice, the light is not perfectly polarized and monochromatic, the dynamic range of the camera is imperfectly used, background noise interferes, and the exposure time is not infinitesimally small, giving rise to $K < 1$. This value will decrease further if the scatterers move and cause blurring of the speckles, i.e. a reduction of σ_I.[134] A blurry speckle image can thus be transformed into a sharp flow velocity map using this simple and fast image processing algorithm (Figure 1.10c2).

In the 1990s, new digital methods enabled the development of a real-time version of laser speckle contrast imaging.[136] Even though in parallel, truly quantitative algorithms were developed to analyse speckle fluctuations via correlation functions, the required computing power was too large to allow for on-line image processing. As a result, the K analysis routine became firmly embedded and widespread. Laser speckle imaging has thenceforth matured into a well-established medical imaging modality.[137–140]

Although the K algorithm is fast and intuitive, its quantitative potential is limited. Some progress has been made in semi-quantitative analysis of flow velocities using 'multi-exposure LSI'.[140,141] The amount of speckle blurring depends not only on the movement of the scattering centres, but also on the exposure time L; specifically, on the ratio of L to the intensity fluctuation time. By measuring K for multiple exposure times, and fitting $K(L)$ to intricate equations, the typical relaxation time τ_0 of the scatterers can be obtained and inversely related to the flow velocity v. Most commonly using $v = \lambda/2\pi\tau_0$ with λ the laser wavelength.[134] Yet, this equation has limited physical foundation and neglects Brownian motion. A multitude of mathematical models have been derived over the years, which incorporate the fraction of static scattered light, different velocity distributions, and the noise contribution.[142,143] Although the results empirically correlate with blood perfusion, they remain far removed from light scattering physics.

1.4.2 Theory

The lack of a solid physical basis for most LSI analysis is remarkable, since the theory connecting speckle fluctuations quantitatively to scatterer dynamics has been established since the late 1980s. Theoretical frameworks were developed using the diffusive nature of light transport to derive expressions for the temporal intensity correlation function.[144–146] This theory has laid the foundation for diffusing wave spectroscopy (DWS), which is essentially LSI of a single speckle, i.e. not spatially resolved. In fact, outside the medical field, LSI is frequently referred to as 'space-resolved DWS'.[147–151] One central assumption of DWS is that photons are scattered

a very large number of times inside the material. This method thus operates in the opposite limit of traditional dynamic light scattering (DLS), which features highly transparent samples that satisfy the condition that each photon is scattered only once.[152,153]

The most widely used, truly quantitative alternative to the K function is the well-established intensity correlation function g_2:

$$g_2(t,x,y,\tau) = \frac{\left\langle I(t,x,y)\cdot I(t+\tau,x,y)\right\rangle}{\left\langle I(t,x,y)\right\rangle\left\langle I(t+\tau,x,y)\right\rangle} \tag{1.2}$$

where x and y are the spatial coordinates or pixels, t is the experimental time, and τ is the correlation or lag time between the two correlated speckle patterns. The numerator represents the speckle correlation, while the denominator ensures the correct normalization by the absolute intensity. The angular brackets denote averaging over multiple speckle correlations in order to achieve sufficient statistics. Experimentally this is achieved either by time averaging at a single pixel in space, or at a fixed point in time over a window in space i.e. an ensemble of different speckles.[154]

Assuming Gaussian field statistics,[152] $g_2(t,\tau)$ can be directly linked to the electric field correlation function $g_1(t,\tau) = \langle E(t)\cdot E^*(t+\tau)\rangle / \langle |E(t)|^2\rangle$ via the Siegert relation: $g_2(t,\tau) = 1 + \beta\,|g_1(t,\tau)|^2$. For clarity, we have omitted the spatial dependence here. The quantity β is a constant which is proportional to the inverse of the number of detected speckle modes. In an ideal experiment, $\beta = 1$, but camera-based detection invariably involves $0 < \beta \leq 1$ due to the detection of multiple speckle modes at the same time.[155,156]

In conventional DWS, the correlation function is typically computed as a function of τ. Fitting $g_1(\tau)$ to well-known equations subsequently allows to extract characteristic time scales of the internal dynamics. Moreover, different types of movement can be disentangled, such as diffusion from ballistic transport. We discuss these possibilities extensively in Chapters 5–11.

The two main physical quantities hidden in the scattering statistics are the deformation field $f(\mathbf{U})$, given by the tensor $\mathbf{U}$, and a non-affine motion, characterized by the mean-square displacement $\langle \Delta r^2\rangle$ of the scattering centres during the correlation time used. g_1 can be expressed as a superposition of the two.[148,149] This expression is not trivial, since the multiply scattered photons traverse a wide diversity of path lengths inside the material. Each path length s has a certain probability or statistical weight $P(s)$ and contributes to the overall correlation function $g_1(\tau)$ by means of a single-exponential decay function: $g_{1,s}(\tau,s) = \exp\left(-s{k_0}^2\left[\ell^* f(\mathbf{U}) + \langle \Delta r^2(\tau)\rangle/3\ell^*\right]\right)$. Here, $k_0 = 2\pi n/\lambda_0$ is the wave

vector with n the refractive index of the medium and λ_0 the laser wavelength in vacuum. ℓ^* is the transport mean free path, which constitutes the step length in the photon random walk (see Chapter 11, Section 11.2.7 for more details).[127,146] As the equation shows, longer path lengths cause $g_{1,s}(\tau, s)$ to decay faster. The total field correlation function is an integral over all possible path lengths: $g_1(\tau) = \int_0^\infty P(s)\, g_{1,s}(\tau, s)\, \mathrm{d}s$.[154]

The decay rate of a given path can be physically interpreted as the time it takes for s to change by a wavelength.[127] Long photon paths involve many scattering events and thus cause accelerated speckle decorrelation, as each individual scatterer needs only to move by a small fraction of λ in order to change the cumulative path length by a full wavelength. The exceptional sensitivity of LSI stems from this unique feature. Under single-scattering conditions, nanometric displacements of scattering centres cannot be detected, yet numerous minute displacements rapidly add up to measurable changes in the photon propagation. Provided the resulting intensity fluctuation exceeds one grey value – out of the typically 256 shades of grey for an 8-bit camera – it gives rise to signal decorrelation and a concomitant decrease of g_2.

For two particular experimental geometries, the photon path length distribution $P(s)$ has been explicitly derived. The first is the back-scatter geometry, depicted in Figure 1.10a, where the laser and camera are on the same side of the sample. We use this geometry in Chapters 5, 6 and 8–10. A surprisingly simple approximation for the corresponding correlation function is:[148,149]

$$g_1 \approx \exp\left(-\gamma\, k_0 \sqrt{3\ell^{*2} f(\mathbf{U}) + \langle \Delta r^2 \rangle}\right) \tag{1.3}$$

where γ is a numerical constant which has been experimentally observed to vary between 1.5 and 2.7.[154] Specifically, $\gamma = z_0/\ell^* + 2/3$, with z_0 a depth inside the material of the order of ℓ^*, from which the light is assumed to originate.[127]

The second relevant experimental geometry is forward-scatter LSI, where the laser and camera are on opposite sides of the sample. This variant is generally called the 'transmission' geometry – somewhat inaccurately in our opinion, because all straightforwardly transmitted photons are filtered out by the linear polarizer in the detection path. We utilize this geometry in Chapter 7. Again, the probability distribution $P(s)$ has been determined with excellent accuracy by solving the photon diffusion equation for a slab of thickness $h \gg \ell^*$ illuminated with a plane wave in the forward-scatter geometry:[149,157]

$$g_1 \approx \frac{k_0 h\sqrt{3f(\mathbf{U}) + \langle \Delta r^2 \rangle / \ell^{*2}}}{\sinh\left[k_0 h\sqrt{3f(\mathbf{U}) + \langle \Delta r^2 \rangle / \ell^{*2}}\right]} \tag{1.4}$$

The main advantages of the back-scatter geometry are easy alignment and applicability to any sample, regardless of whether the substrate is opaque or transparent. The forward-scatter geometry is superior when it comes to displacement resolution, which can go down to the Ångström scale, contrary to the ~10 nm motion resolution obtained using back-scatter LSI. The origin of this difference is the larger contribution of short photon paths in the latter case, where the light remains more superficial.[127] In the forward-scatter geometry, the minimum path length equals the sample thickness, and thus involves many more scattering events on average. Consequently, the correlation function decays much faster.

Related to this, the spatial resolution is somewhat poorer, i.e. the area over which the dynamics are averaged. A larger number of diffusive steps also leads to greater spreading of the light inside the material. Photons will often exit the sample from a different location than their entry point, and this distance is proportional to the average path length. Generally, the spatial resolution of LSI is of the order of 10 μm, but this value depends strongly on the geometry, ℓ^* and speckle size. Chapters 5, 7 and 11 further elaborate on this topic.

Finally, a third type of resolution crucial in LSI is the temporal resolution, which also dictates the τ resolution. The high end of this resolution is entirely determined by the frame rate of the camera, which in turn cannot exceed $1/L$ and thus also depends on the laser power. Using a minimally divergent 1 Watt laser, we have ultimately reached a frame rate of 100 kHz. The low end of the temporal resolution is set by the total duration of the speckle movie. This can in principle be as long as the researcher's patience.

In discussing the data analysis, we have thus far limited ourselves to the contrast function K and correlation functions g_2 and g_1. Indeed, these are used in 99.9% of all light scattering experiments. The K routine is commonly employed in medical LSI applications, and correlators are standard in DLS and DWS measurements. However, yet a third gauge for the local mobility exists – the intensity structure function d_2:[153]

$$d_2(t, x, y, \tau) = \frac{\left\langle \left[I(t, x, y) - I(t + \tau, x, y)\right]^2 \right\rangle}{\left\langle I(t, x, y)\right\rangle \left\langle I(t + \tau, x, y)\right\rangle} \tag{1.5}$$

The structure function reflects *changes* in the intensity, with high values indicating fast decorrelation of the signal and hence a large mobility. In the case of a stationary ergodic process with sufficient sample size, d_2 and g_2 are inversely related,[158,159] as

can be derived by expanding Equation (1.5) (again omitting the spatial dependence for brevity):

$$
\begin{aligned}
d_2(t,\tau) &= \frac{\left\langle I(t)^2\right\rangle + \left\langle I(t+\tau)^2\right\rangle - 2\left\langle I(t)\cdot I(t+\tau)\right\rangle}{\left\langle I(t)\right\rangle\left\langle I(t+\tau)\right\rangle} \\
&= \frac{\left\langle I(t)^2\right\rangle + \left\langle I(t+\tau)^2\right\rangle}{\left\langle I(t)\right\rangle\left\langle I(t+\tau)\right\rangle} - 2\,g_2(t,\tau) \\
&= \frac{2\left\langle I(t)^2\right\rangle}{\left\langle I(t)\right\rangle^2} - 2\,g_2(t,\tau) \qquad\qquad \text{if } \left\langle I(t)\right\rangle = \left\langle I(t+\tau)\right\rangle \\
&= 2\left[g_2(t,0) - g_2(t,\tau)\right] \qquad\qquad (1.6)
\end{aligned}
$$

We are strong advocates of using d_2 as the dynamic indicator of choice, because it is not sensitive to low-frequency noise nor to spurious drift in the mean intensity, thanks to the subtraction in the numerator. In fact, one to two orders of magnitude fewer data points are needed to achieve the same accuracy and convergence for d_2 compared to g_2. The computing time and hardware investment are very similar for the two.[158] Virtually the only disadvantage of d_2 is its indirect relationship to g_1. Despite the apparent superiority of the structure function, it is surprisingly unknown and underrated in soft matter science, with very few accounts of its application.[153,160–163] While 'correlators' are prevalent, we recommend designing and implementing 'structurators' instead, either as software or as hardware products.[159,161] The term structurator was first coined in ref. 158, yet this proposal never gained momentum.

A similar conservative attitude exists in the medical world, where fully quantitative LSI is one of the grand challenges, but K-based analysis prevails in most applications – with a few interesting exceptions, primarily from the group of S. K. Nadkarni.[143,155,164–168] Yet, computing capacity nowadays is sufficient for real-time image processing and visualization using d_2 algorithms. In this thesis, we hope to reveal the ease and power of the structure function in visualizing dynamics.

1.4.3 Quantitative LSI of polymer materials

"If I have seen further than others, it is by standing upon the shoulders of Giants."
– Sir Isaac Newton (1642–1727)

To relate the LSI chapters of this thesis to the international state-of-the-art, let us examine the pioneering work and recent advances in the application of LSI to polymer materials. Such research is actually surprisingly limited, as evid-

enced in the next sections. Note that we exclude most work from the groups of J. Crassous and L. Cipelletti, who have performed beautiful series of experiments on non-polymeric soft materials using LSI analogues, notably granular materials,[148,149,169–171] aqueous foams[172] and chocolate.[151] A review of these applications is beyond the scope of this thesis.

We subdivide the LSI literature into imaging of nanodynamics and nanomechanics. However, this distinction is not black and white, hence our choices are debatable. In fact, realistic experiments often entail a complex convolution of a non-ideal strain field $f(\mathbf{U})$ and different contributions of non-affine motion $\langle \Delta r^2 \rangle$, although in most cases either of the two is negligible on the time scale of observation. A paper worth mentioning in this respect is by Nagazi *et al.*[150] In a comprehensive, rigorous and truly quantitative manner, the authors are capable of disentangling an affine deformation field from random nanoscopic displacements during tensile strain tests. We exclude this work from the following review because no displacement images are presented – only one-dimensional plots of coarse-grained regions of interest. Yet, the authors find an excellent and relevant agreement between their results and those obtained using a conventional stereo-digital image correlation method. In addition, they are able to detect distinct deviations from linear elasticity and the onset of localized plasticity well before any macroscopic sign of weakening. We believe that this approach is promising for development into a higher-resolution, two-dimensional equivalent.

Imaging of nanodynamics

The term nanodynamics can denote a variety of nanoscale processes, including diffusion, evaporative flux, particle deformation, coalescence, crack propagation, paint delamination, etc. Unravelling and quantifying these diverse phenomena is a challenging endeavour that we will tackle in this thesis.

Of the very few papers using LSI on paints,[175,176] the most prominent employs a variation of LSI called 'echo speckle imaging' (ESI).[163] The hallmark of this method is the potential for ensemble-averaged imaging of dynamics without sacrificing spatial resolution. ESI thus offers a workaround for the intrinsic non-ergodicity of drying paints; meaning that on most time scales, paints do not satisfy the condition that the spatial dynamic average equals the temporal average. Single-pixel time traces may thus be insufficient to obtain a correct d_2 value, and the g_1 function may not decay to zero on an experimental time scale. The solution proposed by Zakharov and Scheffold utilizes a spinning ground glass disk in the incident laser beam (Figure 1.11a1).[163] The rough, matte finish of the ground glass scrambles the laser light on purpose. Rather than averaging over time, this permits averaging

over statistically independent illumination geometries, which vary in a temporally controlled manner. Hence, the scattered light will fluctuate not only by internal sample motion, but also at a well-defined rate imposed by the ground glass revolution. After integer multiples of the ground glass period, the incident speckle pattern is retrieved, giving rise to so-called echoes in the signal. For static samples, the height of these echo peaks is constant over time. Yet, for dynamic samples, the motion within the sample induces additional decorrelation, resulting in a decrease of the echoes. The rate with which the echo peak height declines is a measure for the internal dynamics of the sample – in a fully ergodic way. Averaging over different phases of the ground glass, i.e. over statistically independent realizations of the speckle pattern, yields sufficient statistics without any spatial averaging.[126]

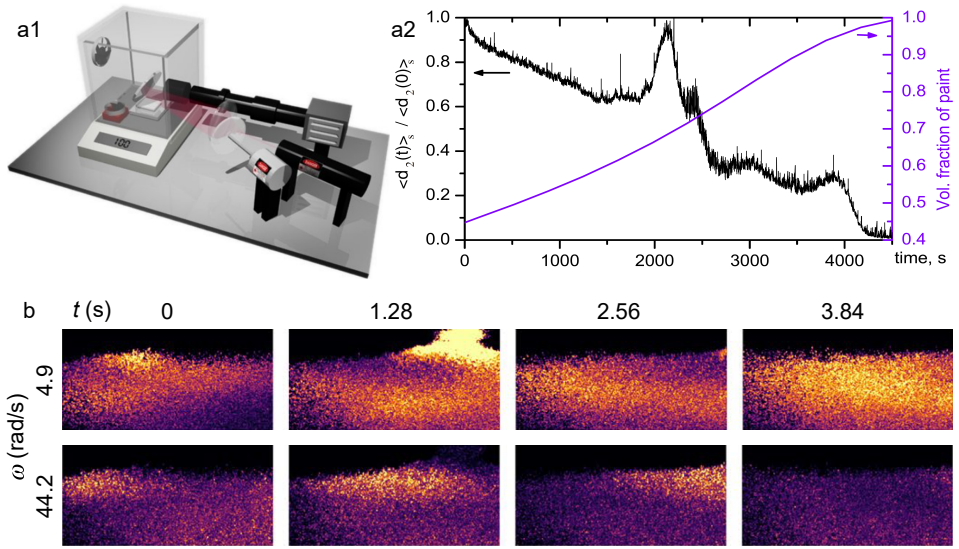

Figure 1.11. LSI of nanodynamics inside synthetic polymer materials. **(a)** Monitoring paint drying by a variant of LSI: echo speckle imaging. **(a1)** The paint film is placed on an analytical balance inside a humidity chamber. The incident laser beam is diffused by a rotating ground glass mounted on a stepper motor, which provides access to ensemble-averaged dynamic properties without spatial averaging. Adapted with permission from ref. 173. **(a2)** Time evolution of the normalized mobility and solids fraction. d_2 peaks when the water front retreats intermittently into the packing of particles. Adapted with permission from ref. 163. **(b)** On-line imaging of ABS plastic extrusion from a 3D printer. The hot nozzle propagates to the right and deposits a 200 μm layer of molten plastic onto the 3 mm thick existing structure. An FFT algorithm enables real-time quantitative visualization at different characteristic frequencies ω. Adapted with permission from ref. 174.

In this single paper, echo speckle imaging has been developed and applied to elucidate the different stages of paint drying. Interestingly, the average mobility in the centre of a paint film appears to not decrease monotonically, but peaks after ~2000 s (Figure 1.11a2). Spatially resolved d_2 maps manifest intermittent events in both space and time, probably arising from rapid bursts of liquid receding into the porous bed of particles. The volume fraction of solids, by contrast, evolves very smoothly over time. Although ESI certainly has its merits, the technique is rather advanced and involved. In fact, we have endeavoured to develop an ESI set-up ourselves. Synchronization of the ground glass rotation and camera turned out to be an insurmountable task. Stable spinning of the ground glass, mounted on a stepper motor, is practically impossible at high revolution rates, which are desired for imaging fast processes. This hindrance is exacerbated by the question whether ESI is really necessary for watching paint dry. In spite of the unavoidable non-ergodicity, largely correct results can also be acquired using 'standard' LSI routines, as we demonstrate in this thesis. We elaborate on the ergodicity problem in Chapter 11, Section 11.2.8.

Another noteworthy feature of LSI is its potential for frequency-resolved imaging. As Equation (1.5) shows, d_2 is a four-dimensional function of t, x, y and τ, with $\tau \propto f^{-1}$. The correlation time can thus be considered as a frequency selector in d_2 maps. By choosing a longer τ in the image analysis, we can shift our focus to slower dynamics. We clarify and illustrate this capability in Chapters 5, 8 and 11, but also in recent literature an exemplary example is presented using a portable LSI set-up developed in our group.[174] This apparatus has been successfully applied to visualize the 3D printing of acrylonitrile-butadiene-styrene plastic in situ. Furthermore, the authors have developed a fast Fourier transform (FFT) routine that permits real-time analysis of the printing process (Figure 1.11b). The FFT is several orders of magnitude faster than existing quantitative analysis methods.[153] The reciprocal Fourier space contains a frequency counterpart of the correlation time: $\omega = 2\pi f \propto \tau^{-1}$. Varying ω allows discriminating different types of motion (compare the two rows in Figure 1.11b): while the transient deposition of a new fluid layer is visible at both low and high frequencies as a superficial zone of enhanced mobility, only at low frequency (top row) a much deeper and longer-lasting perturbation of the previously printed material is manifest. These results emphasize the extraordinary sensitivity of LSI and the power of frequency-resolved imaging. We utilize the full capacity of Fourier-transform-LSI in Chapters 9 and 10.

Imaging of nanomechanics

As mentioned above, the differentiation between nanodynamics and nanomechanics is not clear-cut. We here choose to assign two types of experiments to the nanomechanics category: (i) measuring internal strains induced by an externally imposed force field; and (ii) establishing the viscoelastic modulus of a material at equilibrium.

Visualizing the local mechanical response of polymers under applied stress is vital to improve the material performance and lifetime. Laser speckle imaging is ideally suited for measuring the minute deformations that ensue from an external mechanical perturbation of a (non-transparent) polymer material.

An excellent paper in this regard seeks to unravel the remarkable fracture toughness of nacre. Verho *et al.* have synthesized a nacre-inspired polymer/clay nanocomposite and used LSI to illuminate the inelastic deformations in the process zone prior to crack propagation.[177] Such energy dissipating mechanisms are crucial for dispersing the stress concentration and delaying fracture. By integrating an LSI set-up into a three-point bending tester, the macroscopic strain of the notched specimen could be determined in parallel with the spatially resolved LSI signal at the notch tip (Figure 1.12a). The authors use a semi-quantitative measure for the amplitude of the local displacements: $S(x, y, t, \tau) = \left|\tilde{I}(x, y, t) - \tilde{I}(x, y, t - \tau)\right| / \tilde{I}(x, y, t)$ where $\tilde{I}$ is the smoothed intensity. This indicator thus reflects the normalized change in speckle intensity. Plotting S as a function of imposed strain and distance perpendicular to the notch tip X unveils a millimetric

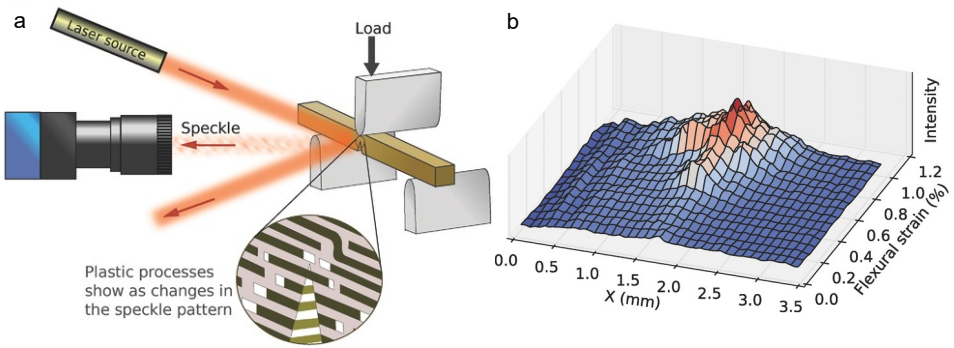

Figure 1.12. LSI of polymer nanomechanics. **(a)** Schematic of a set-up to image inelastic deformations during single-edge-notched bending of a nacre-inspired polymer/clay nanocomposite. **(b)** 'Speckle difference signal' S (see text) perpendicular to the notch tip (located at X = 1.7 mm) versus increasing macroscopic strain, showing a steadily growing process zone. Adapted with permission from ref. 177.

process zone that develops and grows intermittently (Figure 1.12b). In-situ SEM confirms the presence of inelastic deformations in the process zone, including various forms of micro-cracking. Such toughening mechanisms are invaluable for enhancing the fracture resistance.

The validity and potential of the correlation function for mapping internal strains has been further demonstrated by Erpelding *et al*.[147,178] During a quasi-static loading/unloading cycle of a slab of teflon, the authors could accurately measure the g_1 correlation map, which shows a pronounced Boussinesq strain field beneath the applied point force (Figure 1.13a, top row).[147] These deformations prove largely reversible: the image sequence, representing point forces of 0, 2.7, 8.1, 2.7 and 0 N, is almost symmetric. Moreover, correlation maps based on the analytical Boussinesq solution for the strain tensor U,[147,178] yield strikingly similar contours (Figure 1.13a, bottom row). These results highlight the accuracy of LSI to image displacement fields both qualitatively and quantitatively.

Also in the absence of an external force, LSI can provide insight into viscoelastic properties. To achieve this, a small fraction of strongly scattering nanoparticles must be embedded in a (semi-)transparent polymer, and the particle vibrations are subsequently measured to determine the modulus of the surrounding matrix. In a sense, the nanoparticles serve as tracers that probe the local rigidity of the quiescent polymer network. A relevant application of this approach is proposed in refs. 165 and 167. The authors have created various synthetic tissue mimicks with heterogeneous moduli, and successfully generate corresponding nanomechanical maps using LSI – or 'laser speckle rheology' as the authors coin their methodology.[164,165,167,168,179] In this work, the well-established idea of the generalized Stokes–Einstein equation is adopted, which forms the basis of the microrheology formalism.[180] This equation states that the amplitude of the thermal fluctuations of inert, monodisperse particles in an elastic solid is inversely proportional to the microscopic rigidity. More specifically, it directly relates the particle mean-square displacement to the complex viscoelastic shear modulus $G^*(\omega)$ via the approximation:

$$G^*(\omega) \approx \frac{k_B T}{\pi a \langle \Delta r^2(1/\omega) \rangle \Gamma[1 + \alpha(\omega)]} \tag{1.7}$$

where ω is the frequency, k_B is the Boltzmann constant, T is the temperature, a is the nanoparticle radius, Γ is the gamma function, and $\alpha = \mathrm{d} \ln \left\langle \Delta r^2(t) \right\rangle / \mathrm{d} \ln t$ is the logarithmic slope of the mean-square displacement at $\omega = 1/t$.[181]

For example, Wang *et al.* have mimicked the luminal wall by a gel phantom of eight compartments with different viscoelasticities, thus realizing both circumferentially and longitudinally varying mechanical properties (Figure 1.13b1).[167] The eight cells were alternating gels of PEG (polyethylene glycol), PA (polyacrylamide)

and PDMS (polydimethylsiloxane), with 0.6 % w/v embedded titanium dioxide particles. Conventional macrorheology at an oscillation frequency of 1 Hz yielded for the three polymer gels $G^* = 18$ Pa, 77 Pa and 9.5 kPa, respectively. Subsequently, the authors brought a catheter into the centre of the phantom, which acquired laser speckle patterns in four channels. Finally, they computed the g_2 function, converted this to $\langle \Delta r^2 \rangle$ of the nanoparticles via Equation (1.3) assuming absence

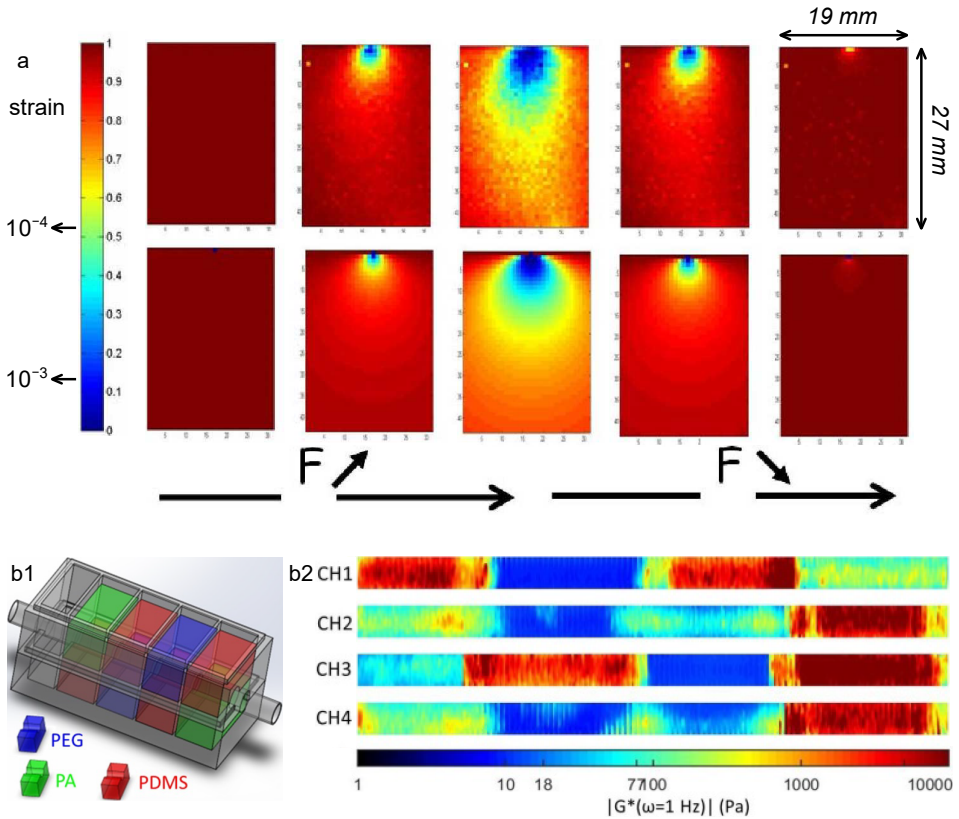

Figure 1.13. LSI of polymer nanomechanics. **(a)** Experimental (top) and analytical (bottom) back-scatter g_1 maps during a linear point-loading/unloading cycle of teflon. The colour coding represents the correlation, and the corresponding strains are indicated. Adapted with permission from ref. 147. **(b)** Mapping heterogeneous mechanical properties of a tissue phantom. **(b1)** Design of an eight-cell polymer phantom which mimics the lumen wall. The centre is imaged using of a four-faceted catheter. **(b2)** Nanomechanical maps for the four channels (CH1–CH4) representing the top, left, bottom and right of the phantom core, inverted horizontally with respect to (b1). The colour coding indicates the complex shear modulus. Three orders-of-magnitude different moduli are found, in good agreement with macroscopic rheology. Adapted with permission from ref. 167.

of a strain field, and substituted the mean-square displacement into Equation (1.7). The outcome is quite remarkable (Figure 1.13b2). Both qualitatively and quantitatively, the resultant nanomechanical $G^*(\omega = 1\ \text{Hz})$ maps are in excellent agreement with predictions – although we do have some reservations concerning the data interpretation by the authors, notably their confusion of g_1 and g_2, the quality of their speckle patterns, and the validity of their microrheology approach.

These examples give a tiny glimpse of the broad application potential and versatility of laser speckle imaging, both in the type of materials to investigate and in the type of information to extract. Yet, LSI has still gathered surprisingly little momentum outside the medical field. Moreover, its full capacity to quantitatively visualize motions has remained unrealized, especially the great frequency-resolving capability and high spatio-temporal resolution. We will venture into this uncharted territory.

1.5 Outline of this thesis

The chapters in this thesis are written as independent scientific papers, yet each of them is centred on the title: *'Quantitative imaging of nanoscale dynamics in polymer materials'*. This title consists of two distinct aims: (i) the development of new imaging methods to uncover nanoscopic processes that have long remained obscure; and (ii) understanding how the complex properties of polymer materials emerge from the collective dance of their nanometric building blocks. In each chapter, we amalgamate these two aims, although the specific imaging methods and polymer materials vary from chapter to chapter. Additional to the title, two recurring themes in this thesis are non-equilibrium processes and sustainability.

This thesis is divided into three parts. In Parts I and II (Chapters 2–6), we paint a quantitative picture of drying polymer dispersions at the nanoscale, starting with a review on watching paint dry. In Part III (Chapters 7–10), we visualize and quantify the molecular origins of a variety of complex mechanical processes inside polymer networks, including fracture nucleation in elastomers, spontaneous self-healing in polymers, and shape-shifting of active liquid crystal networks. The difference between Parts I and II lies in their focus on different imaging methods: Chapters 3 and 4 revolve around conventional bright-field microscopy, whose quantitative potential for studying paint drying phenomena we exploit to the fullest. Chapters 5 and 6 introduce LSI as an experimental tool to unveil the inner workings of coatings across a wide range of time scales, in a spatially resolved manner, even in complex and realistic formulations. The final chapter of this thesis is an overarching discussion which reflects upon all chapters, identifies limitations, and highlights many bright future avenues.

References

[1] R. Bartlett, *The natural and the supernatural in the Middle Ages* (Cambridge University Press, 2008).

[2] *Ovide moralisé en prose (BnF, Français 137, fol. 1r)* (1470–1480).

[3] Leeuwenhoek with his microscope. Oil painting by Ernest Board. Credit: Wellcome Collection. CC BY.

[4] Bacteria from Leeuwenhoek. *Arcana naturae detecta*, 1695. Credit: Wellcome Collection. CC BY.

[5] J. Henry, *The scientific revolution and the origins of modern science* (Macmillan International Higher Education, 1997).

[6] B. R. Masters, *Superresolution optical microscopy* (Springer).

[7] A. L. Gillen, *The genesis of germs: the origin of diseases and the coming plagues* (New Leaf Publishing Group, 2007).

[8] M. Stöhr, K. Roth, B. Jähne. *Exp. Fluids* **35**, 159–166 (2003).

[9] C. P. Royall, W. C. K. Poon, E. R. Weeks. *Soft Matter* **9**, 17–27 (2013).

[10] T. E. Kodger, R. E. Guerra, J. Sprakel. *Sci. Rep.* **5**, 14635 (2015).

[11] J. M. van Doorn, J. Bronkhorst, R. Higler, T. van de Laar, J. Sprakel. *Phys. Rev. Lett.* **118**, 188001 (2017).

[12] M. Doi, *Soft matter physics* (Oxford University Press, 2013).

[13] S. R. Nagel. *Rev. Mod. Phys.* **89**, 025002 (2017).

[14] J. van der Gucht. *Front. Phys.* **6**, 87 (2018).

[15] J. N. Wilking, T. E. Angelini, A. Seminara, M. P. Brenner, D. A. Weitz. *MRS Bull.* **36**, 385–391 (2011).

[16] D. R. Espeso, A. Carpio, B. Einarsson. *Phys. Rev. E* **91**, 022710 (2015).

[17] A. Jung, S. Rangou, C. Abetz, V. Filiz, V. Abetz. *Macromol. Mater. Eng.* **297**, 790–798 (2012).

[18] T. Sanchez, D. T. N. Chen, S. J. DeCamp, M. Heymann, Z. Dogic. *Nature* **491**, 431–434 (2012).

[19] S. Deshpande, T. Pfohl. *PLoS One* **10** (2015).

[20] K.-V. Peinemann, V. Abetz, P. F. Simon. *Nat. Mater.* **6**, 992 (2007).

[21] M. Mocan, H. Wahdat, H. M. van der Kooij, W. M. de Vos, M. Kamperman. *J. Membr. Sci.* **548**, 502–509 (2018).

[22] S. Jalal, S. Shi, V. Acharya, R. Y.-J. Huang, V. Viasnoff, A. D. Bershadsky, Y. H. Tee. *J. Cell Sci.* **132**, jcs220780 (2019).

[23] T. A. Witten, P. A. Pincus, *Structured fluids: polymers, colloids, surfactants* (Oxford University Press on Demand, 2004), chap. 3. Polymer molecules, pp. 41–82.

[24] M. Kleman, O. D. Laverntovich, *Soft matter physics: an introduction* (Springer, 2007), chap. 15. Polymers: structural properties, pp. 560–593.

[25] M. Garside, Global plastic production from 1950 to 2018 (2019). www.statista.com/statistics/282732/global-production-of-plastics-since-1950.

[26] M. Wen, K. Dušek, *Protective coatings* (Springer, 2017).

[27] S. Kumari, Global paints and coatings market (2019). www.medium.com/@savitrics.96/global-paints-and-coatings-market-global-industry-analysis-and-forecast-2018-2026-by-resin-by-13585a3ce06f.

[28] M. Garside, Global paints and coatings market volume 2015–2018 (2019). www.statista.com/statistics/1042799/paints-and-coatings-market-volume-worldwide.

[29] M. Garside, Global paint and coatings industry market value 2017–2027 (2019). www.statista.com/statistics/745160/global-paint-and-coatings-industry-market-value.

[30] J. Keddie, A. F. Routh, *Fundamentals of latex film formation: processes and properties* (Springer, 2010).

[31] A. F. Routh. *Rep. Prog. Phys.* **76**, 046603 (2013).

[32] S. Jiang, A. van Dyk, A. Maurice, J. Bohling, D. Fasano, S. Brownell. *Chem. Soc. Rev.* **46**, 3792–3807 (2017).

[33] J. L. Keddie. *Mater. Sci. Eng. R Rep.* **21**, 101–170 (1997).

[34] M. de Kool, Watching paint dry... Multiple regimes of coalescence, cracking and self-healing in drying dispersion droplets, Master's thesis, Wageningen University (2014).

[35] H. Feng, J. Sprakel, D. Ershov, T. Krebs, M. A. Cohen Stuart, J. van der Gucht. *Soft Matter* **9**, 2810–2815 (2013).

[36] A. Tzitzinou, J. L. Keddie, J. M. Geurts, A. C. I. A. Peters, R. Satguru. *Macromolecules* **33**, 2695–2708 (2000).

[37] D. Colombini, H. Hassander, O. J. Karlsson, F. H. J. Maurer. *Macromolecules* **37**, 6865–6873 (2004).

[38] K. B. Singh, G. Deoghare, M. S. Tirumkudulu. *Langmuir* **25**, 751–760 (2009).

[39] M. Soleimani, J. C. Haley, W. Lau, M. A. Winnik. *Macromolecules* **43**, 975–985 (2010).

[40] J. G. Tsavalas, D. C. Sundberg. *Langmuir* **26**, 6960–6966 (2010).

[41] B. Voogt, H. P. Huinink, S. J. F. Erich, J. Scheerder, P. Venema, J. L. Keddie, O. C. G. Adan. *Langmuir* **35**, 12418–12427 (2019).

[42] M. J. Devon, J. L. Gardon, G. Roberts, A. Rudin. *J. Appl. Polym. Sci.* **39**, 2119–2128 (1990).

[43] P. A. Steward, J. Hearn, M. C. Wilkinson. *Adv. Colloid Interface Sci.* **86**, 195–267 (2000).

[44] S. Kirsch, A. Pfau, J. Stubbs, D. Sundberg. *Colloids Surf., A* **183-185**, 725–737 (2001).

[45] A. Georgiadis, P. A. Bryant, M. Murray, P. Beharrell, J. L. Keddie. *Langmuir* **27**, 2176–2180 (2011).

[46] A. Javadi, H. S. Mehr, M. Sobani, M. D. Soucek. *Prog. Org. Coat.* **100**, 2–31 (2016).

[47] E. R. Bertozzi. *Rubber Chem. Technol.* **41**, 114–160 (1968).

[48] C. Smith, Elastomers market 2018–2026 (2019). www.marketwatch.com/press-release/elastomers-market-2018-2026-size-share-opportunities-and-forecast-credence-research-2019-04-05.

[49] P. M. Visakh, S. Thomas, A. K. Chandra, A. P. Mathew, *Advances in elastomers* (Springer, 2013).

[50] L.-H. Cai, T. E. Kodger, R. E. Guerra, A. F. Pegoraro, M. Rubinstein, D. A. Weitz. *Adv. Mater.* **27**, 5132–5140 (2015).

[51] E. Ducrot, Y. Chen, M. Bulters, R. P. Sijbesma, C. Creton. *Science* **344**, 186–189 (2014).

[52] B. Talamini, Y. Mao, L. Anand. *J. Mech. Phys. Solids* **111**, 434 - 457 (2018).

[53] N. J. Petch, P. Stables. *Nature* **169**, 842–843 (1952).

[54] S. Pearson. *Proc. Phys. Soc. B* **69**, 1293 (1956).

[55] L. Pauchard, H. Meunier. *Phys. Rev. Lett.* **70**, 3565–3568 (1993).

[56] D. Bonn, H. Kellay, M. Prochnow, K. Ben-Djemiaa, J. Meunier. *Science* **280**, 265–267 (1998).

[57] N. Shahidzadeh-Bonn, P. Vié, X. Chateau, J.-N. Roux, D. Bonn. *Phys. Rev. Lett.* **95**, 175501 (2005).

[58] O. Lengliné, R. Toussaint, J. Schmittbuhl, J. E. Elkhoury, J. P. Ampuero, K. T. Tallakstad, S. Santucci, K. J. Måløy. *Phys. Rev. E* **84**, 036104 (2011).

[59] J. Sprakel, S. B. Lindström, T. E. Kodger, D. A. Weitz. *Phys. Rev. Lett.* **106**, 248303 (2011).

[60] D. Chen, D. Wang, Y. Yang, Q. Huang, S. Zhu, Z. Zheng. *Adv. Energy Mater.* **7**, 1700890 (2017).

[61] H. Ying, Y. Zhang, J. Cheng. *Nat. Commun.* **5**, 3218 (2014).

[62] Y. Yang, M. W. Urban. *Chem. Soc. Rev.* **42**, 7446-7467 (2013).

[63] J. F. Patrick, M. J. Robb, N. R. Sottos, J. S. Moore, S. R. White. *Nature* **540**, 363–370 (2016).

[64] Y. Chen, A. M. Kushner, G. A. Williams, Z. Guan. *Nat. Chem.* **4**, 467–472 (2012).

[65] L. Zhai, A. Narkar, K. Ahn. *Nano Today* p. 100826 (2019).

[66] P. Cordier, F. Tournilhac, C. Soulié-Ziakovic, L. Leibler. *Nature* **451**, 977–980 (2008).

[67] C. Wang, H. Wu, Z. Chen, M. T. McDowell, Y. Cui, Z. Bao. *Nat. Chem.* **5**, 1042–1048 (2013).

[68] C.-H. Li, C. Wang, C. Keplinger, J.-L. Zuo, L. Jin, Y. Sun, P. Zheng, Y. Cao, F. Lissel, C. Linder, X.-Z. You, Z. Bao. *Nat. Chem.* **8**, 618–624 (2016).

[69] M. W. Urban, D. Davydovich, Y. Yang, T. Demir, Y. Zhang, L. Casabianca. *Science* **362**, 220–225 (2018).

[70] H. Wang, Y. Yang, M. Nishiura, Y. Higaki, A. Takahara, Z. Hou. *J. Am. Chem. Soc.* **141**, 3249–3257 (2019).

[71] L. Zhang, Z. Liu, X. Wu, Q. Guan, S. Chen, L. Sun, Y. Guo, S. Wang, J. Song, E. M. Jeffries, C. He, F.-L. Qing, X. Bao, Z. You. *Adv. Mater.* **31**, 1901402 (2019).

[72] D. Wang, J. Xu, J. Chen, P. Hu, Y. Wang, W. Jiang, J. Fu. *Adv. Funct. Mater.* **30**, 1907109 (2020).

[73] A. Susa, R. K. Bose, A. M. Grande, S. van der Zwaag, S. J. Garcia. *ACS Appl. Mater. Interfaces* **8**, 34068–34079 (2016).

[74] A. Susa, A. Mordvinkin, K. Saalwächter, S. van der Zwaag, S. J. Garcia. *Macromolecules* **51**, 8333–8345 (2018).

[75] A. Susa, J. Bijleveld, M. Hernandez Santana, S. J. Garcia. *ACS Sustain. Chem. Eng.* **6**, 668–678 (2018).

[76] V. Montano, S. J. Picken, S. van der Zwaag, S. J. Garcia. *Phys. Chem. Chem. Phys.* **21**, 10171–10184 (2019).

[77] V. Montano, M. M. B. Wempe, S. M. H. Does, J. C. Bijleveld, S. van der Zwaag, S. J. Garcia. *Macromolecules* **52**, 8067–8078 (2019).

[78] F. Lancia, A. Ryabchun, N. Katsonis. *Nat. Rev. Chem.* **3**, 536–551 (2019).

[79] P. J. Roth, A. B. Lowe. *Polym. Chem.* **8**, 10–11 (2017).

[80] M. R. Aguilar, J. San Román, *Smart polymers and their applications* (Woodhead Publishing, 2019).

[81] T. H. Ware, M. E. McConney, J. J. Wie, V. P. Tondiglia, T. J. White. *Science* **347**, 982–984 (2015).

[82] D. Liu, D. J. Broer. *Angew. Chem., Int. Ed.* **53**, 4542–4546 (2014).

[83] E. Bukusoglu, M. Bedolla Pantoja, P. C. Mushenheim, X. Wang, N. L. Abbott. *Annu. Rev. Chem. Biomol. Eng.* **7**, 163–196 (2016).

[84] D. J. Broer. *Adv. Mater.* p. 1905144 (2019).

[85] H. Yokoyama, Annual report, *Tech. rep.*, Liquid Crystal Institute, Kent State University (2012).

[86] T. J. White, D. J. Broer. *Nat. Mater.* **14**, 1087–1098 (2015).

[87] M. Camacho-Lopez, H. Finkelmann, P. Palffy-Muhoray, M. Shelley. *Nat. Mater.* **3**, 307–310 (2004).

[88] S. Iamsaard, S. J. Aßhoff, B. Matt, T. Kudernac, J. J. Cornelissen, S. P. Fletcher, N. Katsonis. *Nat. Chem.* **6**, 229 (2014).

[89] A. H. Gelebart, D. J. Mulder, M. Varga, A. Konya, G. Vantomme, E. Meijer, R. L. Selinger, D. J. Broer. *Nature* **546**, 632–636 (2017).

[90] W. Feng, D. J. Broer, D. Liu. *Adv. Funct. Mater.* p. 1901681 (2019).

[91] A. H. Gelebart, D. Liu, D. J. Mulder, K. H. J. Leunissen, J. van Gerven, A. P. H. J. Schenning, D. J. Broer. *Adv. Funct. Mater.* **28**, 1705942 (2018).

[92] W. Feng, D. J. Broer, D. Liu. *Adv. Mater.* **30**, 1704970 (2018).

[93] A. Cao, R. J. H. van Raak, X. Pan, D. J. Broer. *Adv. Funct. Mater.* **29**, 1900857 (2019).

[94] G. Koçer, J. ter Schiphorst, M. Hendrikx, H. G. Kassa, P. Leclère, A. P. H. J. Schenning, P. Jonkheijm. *Adv. Mater.* **29**, 1606407 (2017).

[95] A. Agrawal, H. Chen, H. Kim, B. Zhu, O. Adetiba, A. Miranda, A. C. Chipara, P. M. Ajayan, J. G. Jacot, R. Verduzco. *ACS Macro Lett.* **5**, 1386–1390 (2016).

[96] W. Lehmann, H. Skupin, C. Tolksdorf, E. Gebhard, R. Zentel, P. Krüger, M. Lösche, F. Kremer. *Nature* **410**, 447–450 (2001).

[97] Z. S. Davidson, H. Shahsavan, A. Aghakhani, Y. Guo, L. Hines, Y. Xia, S. Yang, M. Sitti. *Sci. Adv.* **5**, eaay0855 (2019).

[98] D. Liu, N. B. Tito, D. J. Broer. *Nat. Commun.* **8**, 1526 (2017).

[99] W. Feng, D. J. Broer, D. Liu. *Adv. Funct. Mater.* **30**, 1901681 (2020).

[100] S. Bradbury, B. Bracegirdle, *Introduction to light microscopy* (BIOS Scientific Publishers, 1998).

[101] H. Feng, N. A. L. Verstappen, A. J. C. Kuehne, J. Sprakel. *Polym. Chem.* **4**, 1842–1847 (2013).

[102] X. Chen, J. Wang, M. Versluis, N. de Jong, F. S. Villanueva. *Rev. Sci. Instrum.* **84**, 063701 (2013).

[103] C. Noirjean, M. Marcellini, S. Deville, T. E. Kodger, C. Monteux. *Phys. Rev. Materials* **1**, 065601 (2017).

[104] V. Prasad, D. Semwogerere, E. R. Weeks. *J. Phys.: Condens. Matter* **19**, 113102 (2007).

[105] A. Aloi, I. K. Voets. *Curr. Opin. Colloid Interface Sci.* **34**, 59–73 (2018).

[106] S. Pujals, N. Feiner-Gracia, P. Delcanale, I. Voets, L. Albertazzi. *Nat. Rev. Chem.* **3**, 68–84 (2019).

[107] J. I. Goldstein, D. E. Newbury, J. R. Michael, N. W. M. Ritchie, J. H. J. Scott, D. C. Joy, *Scanning electron microscopy and X-ray microanalysis* (Springer, 2017).

[108] J. L. Keddie, P. Meredith, R. A. L. Jones, A. M. Donald. *Macromolecules* **28**, 2673–2682 (1995).

[109] E. Gonzalez, C. Tollan, A. Chuvilin, M. J. Barandiaran, M. Paulis. *ACS Appl. Mater. Interfaces* **4**, 4276–4282 (2012).

[110] E. A. Sulyanova, A. Shabalin, A. V. Zozulya, J.-M. Meijer, D. Dzhigaev, O. Gorobtsov, R. P. Kurta, S. Lazarev, U. Lorenz, A. Singer, O. Yefanov, I. Zaluzhnyy, I. Besedin, M. Sprung, A. V. Petukhov, I. A. Vartanyants. *Langmuir* **31**, 5274–5283 (2015).

[111] J. M. Salamanca, E. Ciampi, D. A. Faux, P. M. Glover, P. J. McDonald, A. F. Routh, A. C. I. A. Peters, R. Satguru, J. L. Keddie. *Langmuir* **17**, 3202–3207 (2001).

[112] N. Stribeck, *X-ray scattering of soft matter* (Springer, 2007).

[113] O. Bikondoa, *X-ray photon correlation spectroscopy for the characterization of soft and hard condensed matter*, X-ray and neutron techniques for nanomaterials characterization (Springer, 2016), chap. 3, pp. 95–156.

[114] A. V. Zozulya, J.-M. Meijer, A. Shabalin, A. Ricci, F. Westermeier, R. P. Kurta, U. Lorenz, A. Singer, O. Yefanov, A. V. Petukhov, M. Sprung, I. A. Vartanyants. *J. Appl. Cryst.* **46**, 903–907 (2013).

[115] A. Vagias, Q. Chen, G. H. ten Brink, D. Hermida-Merino, J. Scheerder, G. Portale. *ACS Appl. Polym. Mater.* **1**, 2482–2494 (2019).

[116] C. J. Elkins, M. T. Alley. *Exp. Fluids* **43**, 823–858 (2007).

[117] R. Stannarius. *Rev. Sci. Instrum.* **88**, 051806 (2017).

[118] N. B. Abdelouahab, A. Gossard, S. Rodts, B. Coasne, P. Coussot. *Eur. Phys. J. E* **42**, 66 (2019).

[119] A. M. König, T. G. Weerakkody, J. L. Keddie, D. Johannsmann. *Langmuir* **24**, 7580–7589 (2008).

[120] F. T. Carter, R. M. Kowalczyk, I. Millichamp, M. Chainey, J. L. Keddie. *Langmuir* **30**, 9672–9681 (2014).

[121] W. E. Baille, C. Malveau, X. X. Zhu, R. H. Marchessault. *Biomacromolecules* **3**, 214–218 (2002).

[122] M. Gajdošová, D. Pěček, N. Sarvašová, Z. Grof, F. Štěpánek. *Int. J. Pharm.* **500**, 136–143 (2016).

[123] M. Klinkenberg, P. Blümler, B. Blümich. *Macromolecules* **30**, 1038–1043 (1997).

[124] E. W. Abel, K. I. Wheeler, J. A. Chudek, G. Hunter, F. M. Som. *Biomaterials* **19**, 55–60 (1998).

[125] A. F. Fercher, J. D. Briers. *Opt. Commun.* **37**, 326–330 (1981).

[126] A. C. Völker, P. Zakharov, B. Weber, F. Buck, F. Scheffold. *Opt. Express* **13**, 9782–9787 (2005).

[127] Pine, D. J., Weitz, D. A., Zhu, J. X., Herbolzheimer, E. *J. Phys. France* **51**, 2101–2127 (1990).

[128] L. Vitomir, J. Sprakel, J. van der Gucht. *Sci. Rep.* **7**, 16879 (2017).

[129] R. Schittny, A. Niemeyer, F. Mayer, A. Naber, M. Kadic, M. Wegener. *Laser Photonics Rev.* **10**, 382–408 (2016).

[130] A. Sdobnov, A. Bykov, A. Popov, E. Zherebtsov, I. Meglinski, *Biophotonics: Photonic Solutions for Better Health Care VI* (2018), vol. 10685, p. 1068509.

[131] A. Ponticorvo, A. K. Dunn. *J. Vis. Exp.* **45**, e2004 (2010).

[132] J. C. Dainty, ed., *Laser speckle and related phenomena* (Springer, 1984).

[133] J. W. Goodman, *Statistical properties of laser speckle patterns* (Springer, 1975), pp. 9–75.

[134] M. Draijer, E. Hondebrink, T. van Leeuwen, W. Steenbergen. *Lasers Med. Sci.* **24**, 639–651 (2009).

[135] P. Jain, S. E. Sarma. *Sci. Rep.* **9**, 11157 (2019).

[136] J. D. Briers, S. Webster. *J. Biomed. Opt.* **1**, 174–179 (1996).

[137] H. Bolay, U. Reuter, A. K. Dunn, Z. Huang, D. A. Boas, M. A. Moskowitz. *Nat. Med.* **8**, 136–142 (2002).

[138] D. A. Boas, A. K. Dunn. *J. Biomed. Opt.* **15**, 011109 (2010).

[139] D. Briers, D. D. Duncan, E. Hirst, S. J. Kirkpatrick, M. Larsson, W. Steenbergen, T. Stromberg, O. B. Thompson. *J. Biomed. Opt.* **18**, 066018 (2013).

[140] W. Heeman, W. Steenbergen, G. M. van Dam, E. C. Boerma. *J. Biomed. Opt.* **24**, 080901 (2019).

[141] A. B. Parthasarathy, W. J. Tom, A. Gopal, X. Zhang, A. K. Dunn. *Opt. Express* **16**, 1975–1989 (2008).

[142] A. Nadort, K. Kalkman, T. G. van Leeuwen, D. J. Faber. *Sci. Rep.* **6**, 25258 (2016).

[143] D. D. Postnov, J. Tang, S. E. Erdener, K. Kılıç, D. A. Boas. *BioRxiv* p. 626515 (2019).

[144] G. Maret, P. E. Wolf. *J. Phys. B Condens. Matter* **65**, 409–413 (1987).

[145] M. J. Stephen. *Phys. Rev. B* **37**, 1–5 (1988).

[146] D. J. Pine, D. A. Weitz, P. M. Chaikin, E. Herbolzheimer. *Phys. Rev. Lett.* **60**, 1134–1137 (1988).

[147] M. Erpelding, B. Dollet, A. Faisant, J. Crassous, A. Amon. *Strain* **49**, 167–174 (2013).

[148] A. Le Bouil, A. Amon, J.-C. Sangleboeuf, H. Orain, P. Bésuelle, G. Viggiani, P. Chasle, J. Crassous. *Granul. Matter* **16**, 1–8 (2014).

[149] A. Amon, A. Mikhailovskaya, J. Crassous. *Rev. Sci. Instrum.* **88**, 051804 (2017).

[150] M.-Y. Nagazi, G. Brambilla, G. Meunier, P. Marguerès, J.-N. Périé, L. Cipelletti. *Opt. Lasers Eng.* **88**, 5–12 (2017).

[151] M.-Y. Nagazi, P. Dieudonné-George, G. Brambilla, G. Meunier, L. Cipelletti. *Soft Matter* **14**, 6439–6448 (2018).

[152] B. J. Berne, R. Pecora, *Dynamic light scattering: with applications to chemistry, biology, and physics* (Courier Corporation, 2000).

[153] P. Zakharov, F. Scheffold, *Light scattering reviews 4: single light scattering and radiative transfer* (Springer, Berlin, Heidelberg, 2009), chap. Advances in dynamic light scattering techniques, pp. 433–467.

[154] D. Orsi, F. Salerni, E. Macaluso, E. Santini, F. Ravera, L. Liggieri, L. Cristofolini. *Colloids Surf., A* **580**, 123574 (2019).

[155] C. Zhou, G. Yu, D. Furuya, J. H. Greenberg, A. G. Yodh, T. Durduran. *Opt. Express* **14**, 1125–1144 (2006).

[156] P. Zakharov, A. C. Völker, M. T. Wyss, F. Haiss, N. Calcinaghi, C. Zunzunegui, A. Buck, F. Scheffold, B. Weber. *Opt. Express* **17**, 13904–13917 (2009).

[157] L. Djaoui, J. Crassous. *Granul. Matter* **7**, 185–190 (2005).

[158] E. O. Schulz-DuBois, I. Rehberg. *Appl. Phys.* **24**, 323–329 (1981).

[159] K. Schätzel. *Opt. Acta: Int. J. Opt.* **30**, 155–166 (1983).

[160] G. F. Lorusso, A. Minafra, V. Capozzi. *Appl. Opt.* **32**, 3867–3870 (1993).

[161] D. Brogioli, F. Croccolo, V. Cassina, D. Salerno, F. Mantegazza. *Opt. Express* **16**, 20272–20282 (2008).

[162] A. Brun, H. Dihang, L. Brunel. *Prog. Org. Coat.* **61**, 181–191 (2008).

[163] P. Zakharov, F. Scheffold. *Soft Mater.* **8**, 102–113 (2010).

[164] Z. Hajjarian, M. M. Tripathi, S. K. Nadkarni. *J. Biophotonics* **8**, 372–381 (2015).

[165] Z. Hajjarian, H. T. Nia, S. Ahn, A. J. Grodzinsky, R. K. Jain, S. K. Nadkarni. *Sci. Rep.* **6**, 37949 (2016).

[166] Z. Hajjarian, D. M. Tshikudi, S. K. Nadkarni. *Biomed. Opt. Express* **8**, 3502–3515 (2017).

[167] J. Wang, M. Hosoda, D. M. Tshikudi, Z. Hajjarian, S. K. Nadkarni. *Biomed. Opt. Express* **8**, 137–150 (2017).

[168] S. K. Nadkarni, *Semin. Thromb. Hemost.* (2019), vol. 45, pp. 264–274.

[169] M. Erpelding, A. Amon, J. Crassous. *Europhys. Lett.* **91**, 18002 (2010).

[170] A. Amon, V. B. Nguyen, A. Bruand, J. Crassous, E. Clément. *Phys. Rev. Lett.* **108**, 135502 (2012).

[171] A. Amon, R. Bertoni, J. Crassous. *Phys. Rev. E* **87**, 012204 (2013).

[172] D. A. Sessoms, H. Bissig, A. Duri, L. Cipelletti, V. Trappe. *Soft Matter* **6**, 3030–3037 (2010).

[173] P. Zakharov, Echo Speckle Imaging (ESI) (2007). sites.google.com/site/pzoptics/projects/echo-speckle-imaging.

[174] J. Buijs, J. van der Gucht, J. Sprakel. *Sci. Rep.* **9**, 13279 (2019).

[175] M. Z. Ansari, A. K. Nirala. *J. Optics* **45**, 357–363 (2016).

[176] M. Z. Ansari, A. Mujeeb. *Laser Phys.* **28**, 085603 (2018).

[177] T. Verho, P. Karppinen, A. H. Gröschel, O. Ikkala. *Adv. Sci.* **5**, 1700635 (2018).

[178] M. Erpelding, A. Amon, J. Crassous. *Phys. Rev. E* **78**, 046104 (2008).

[179] Z. Hajjarian, S. K. Nadkarni. *J. Biomed. Opt.* **25**, 050801 (2020).

[180] T. G. Mason, D. A. Weitz. *Phys. Rev. Lett.* **74**, 1250 (1995).

[181] T. G. Mason. *Rheol. Acta* **39**, 371–378 (2000).

Part I

Drying model coatings

Chapter 2

Watching paint dry; more exciting than it seems

This chapter is based on: Hanne M. van der Kooij and Joris Sprakel, 'Watching paint dry; more exciting than it seems', *Soft Matter* **11**, 6353–6359 (2015).

Abstract

With an ever-increasing demand for sustainable alternatives to solvent-borne coatings and paints, the pressure to develop aqueous alternatives that match or exceed the performance of their traditional counterparts rises. A crucial step in this sustainability challenge for the years to come is to arrive at a deep, and complete, understanding of how water-borne paints dry and form their final protective films. As it turns out, this is no minor challenge. Yet, understanding drying and film formation is a prototypical soft matter problem at heart, displaying a rich variety of complex non-equilibrium phenomena that are waiting to be understood. Watching paint dry is far from the boring activity the saying suggests.

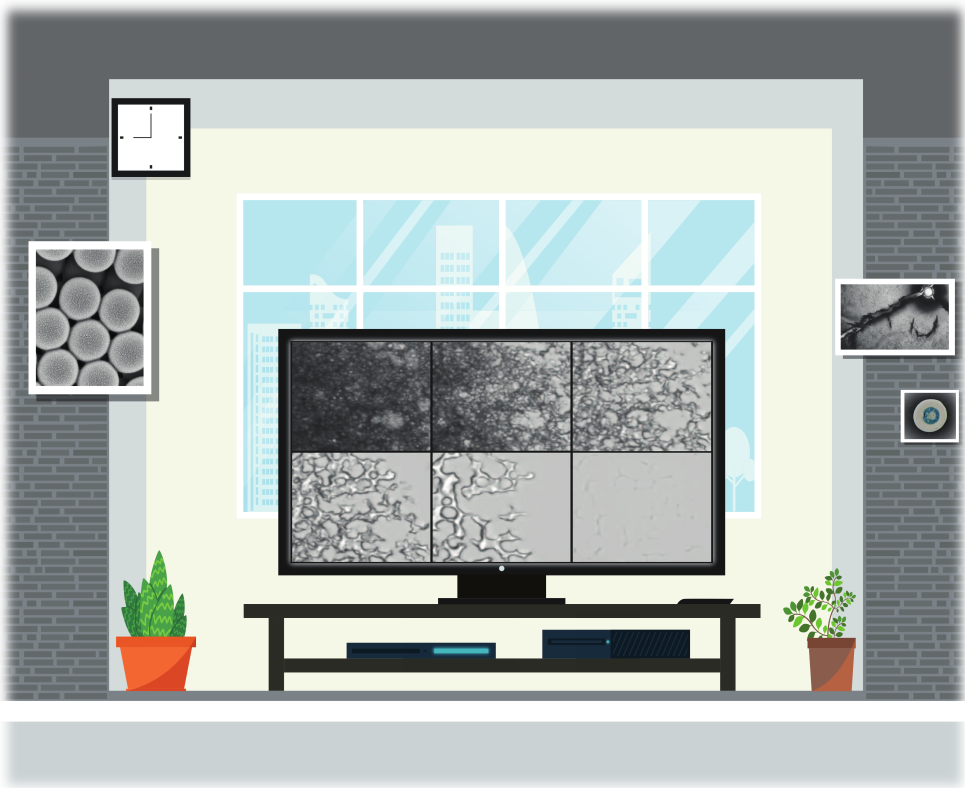

2.1 Introduction

Traditional paints are composed of a polymeric binder dissolved in an organic solvent, with additional paint ingredients, such as pigments or fillers, suspended in the medium. Upon drying, the polymer forms a solid layer which shields the material underneath from environmental conditions, while simultaneously trapping the pigments to generate an aesthetically appealing surface. During drying, the solvent evaporates into the air and atmosphere. These volatile organic compounds (VOCs) emitted from paints and adhesives are among the main contributors to greenhouse gases in the earth's atmosphere, and simultaneously endanger the health of consumers or professionals applying the paints. Prolonged exposure to VOCs emitted from paint can lead to severe brain damage, impairing sensory, motor, and behavioural functions, in a disease known as 'painters' syndrome'.[1] Not surprisingly, this has motivated paint manufacturers and policy makers to embark on a road to phase out the use of solvent-borne paints.

Effectively eradicating solvent-borne paints across the wide variety of applications where they find use, requires the availability of sustainable and non-toxic alternatives that offer the same quality of performance and appearance. One of the key technologies to replace solvent-based paints are water-based coatings, in which the organic solvent has been replaced, partially or completely, by water. For most applications however, the final film must be resistant to water irrespective of the carrier medium that the paint was formulated for. The water-insoluble binder polymer, which was traditionally dissolved in an organic medium, is now added to the water-borne paint as a dispersion of colloidal polymer particles, known as a latex.[2]

Film formation in solvent-based paints, in which the binder is molecularly dissolved, involves the continuous thickening of the paint as the solvent evaporates, until it leaves behind a homogeneous polymer layer in which pigments and opacifiers are embedded. By contrast, in water-based systems, in which the binder is dispersed rather than dissolved, film formation proceeds completely differently: as the aqueous continuous phase dries, the particles become close-packed, until at some point phase inversion takes place, during which the binder phase forms a continuous film through coalescence. This process of film formation is at the core of determining the resilience and aesthetics of the final coating.

While it has been a subject of intense study for decades, much remains to be understood before water-borne and VOC-free paints can be rationally designed to offer the high-quality performance we have come to know and expect from traditional solvent-borne paints. Our deep understanding of the film formation process is obscured by its inherent complexity, which arises from the multitude

of phenomena that come into play as soon as a paint starts drying. It requires us to connect knowledge on colloidal interactions in multicomponent mixtures, the thermodynamic and kinetic stability of thin liquid films, fluid flows through porous media induced by evaporative fluxes, the yielding and flow of highly viscoelastic matter which simultaneously undergoes chemical curing, the mechanics of thin paint layers that gradually transition from particulate to continuous, and much more. It is this fascinating complexity, emerging in an everyday situation, that makes understanding film formation a prototypical soft matter challenge.

As elaborated in Chapter 1, one of the central paradigms in soft matter science is the connection of phenomena acting on the relevant microscopic length scales, be it molecular or colloidal, to phenomena observable in the macroscopic realm. Applying this approach to film formation requires detailed experimental investigation into the structure and dynamics on the smallest length scales across a wide range of time scales: from the moment a paint is applied, throughout its drying and ageing, until the moment it becomes so brittle that it may fracture or delaminate from the surface onto which it was applied. While spectroscopic, resonance-based methods such as magnetic resonance imaging (MRI) and Förster Resonance Energy Transfer (FRET) are invaluable, direct visualization at the colloidal scale in real space and time is ideally suited for this task. With the wide range of imaging methods available this is now excellently feasible.

Below, we will highlight several of the key challenges we face in understanding film formation, and sketch how a combination of smart chemistry, quantitative imaging, and emerging techniques such as microfluidics, may allow us to watch paint dry with fresh eyes. Please note that the scientific foray into drying dispersions and film formation extends far beyond what we discuss here; for a comprehensive overview we refer to the excellent reviews of Keddie,[3] Winnik,[4] Steward *et al.*,[5] and Routh.[6]

2.2 Thin film stability

A crucial part of the transformation of a dispersion of liquid-like latex colloids into a homogeneous coating film is the coalescence of the individual particles or droplets to form a macroscopic polymer phase. We can divide coalescence into two characteristic processes: (i) rupture of the thin liquid film that initially separates the colloids and (ii) subsequent mixing of the contents of the colloids.

The stability of thin liquid films has been intensively studied for many years using a variety of experimental techniques, such as the surface force apparatus, atomic force microscopy, and the thin film pressure balance.[7,8] These methods allow for careful measurement of the interactions between two fluid phases separated

by a thin, nanometre-thick, film of a liquid. Upon decreasing the film thickness, and consequently increasing the disjoining pressure Π, the thin film becomes unstable when the critical disjoining pressure Π^* is exceeded.[9,10] While there are strong links between well-established knowledge of colloidal interactions and the stability and rupture of thin films separating emulsion droplets, a predictive understanding of what sets the exact magnitude of Π^* remains lacking. For example, it is well established that surfactant adsorption reaches a plateau around the critical micelle concentration (CMC) of the surfactant in solution.[11] If the critical disjoining pressure of a thin surfactant film would depend only on the amount of adsorbed surfactants – which provides the film stability by means of electrostatic and/or steric repulsion – we may expect a plateau in Π^* as well. However, we recently showed that Π^* continues to rise with increasing surfactant concentration, and reaches a plateau at a concentration several decades above the CMC.[12] While the origins of this surprising finding are unclear, we speculate that diffusion-limited surfactant exchange at the interface plays a role. Moreover, while the critical disjoining pressure describes film stability in the thermodynamic limit, in practice fluid kinetics may also be important. The rupture of a thin film involves temporary expansion of the interface, thus creating an energy barrier, and drainage of the thin film such that hydrodynamic and lubrication forces come into play.[13–15]

In drying paints, film rupture is caused by the increasing osmotic and/or capillary pressure gradients that develop as water evaporates. Moreover, in these scenarios also solute concentrations rise and may lead to spatial heterogeneities throughout the coating. Experimentally disentangling the interplay between various thermodynamic and kinetic parameters is difficult, and requires creative strategies.

One approach involves the use of responsive surfactants, so that the stability of the liquid films separating droplets can be tuned during an experiment. For example, thermoresponsive surfactants, composed of a hydrophobic tail and a thermoresponsive polymeric head group, can be switched between soluble and insoluble by means of a small temperature change. Triggering the surfactant renders the emulsion droplets adhesive, which can be measured with atomic force microscopy (Figure 2.1a),[16] and simultaneously increases the interfacial tension[17] and decreases the critical disjoining pressure (Figure 2.1b–c).[18] This allows creating emulsions which are highly stable at room temperature, even when densely packed, yet can be made to coalesce within seconds.[17]

This tuneable system can be combined with new tools to study the stability of emulsion layers, for example a microfluidic centrifuge combined with high-speed synchronized imaging, as illustrated in Figure 2.1d. For a given system, the pressure applied to the emulsion can be easily varied by changing the rotation

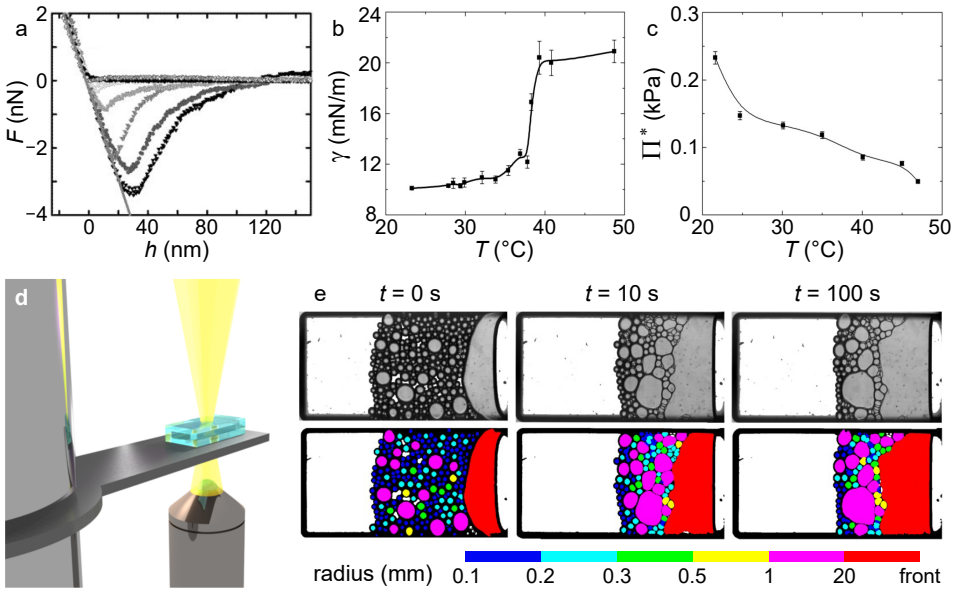

Figure 2.1. Measuring and manipulating thin film stability. With a thermoresponsive surfactant, exhibiting a lower critical solution temperature, droplets can be made adhesive upon increasing the temperature, as demonstrated using colloidal probe atomic force microscopy **(a)**,[16] while simultaneously increasing the interfacial tension **(b)**[17] and decreasing the critical disjoining pressure **(c)**.[18] In combination with microfluidic centrifugation and synchronized high-speed imaging, as illustrated in **(d)**,[18] this allows direct observation and quantitative analysis of triggered coalescence in emulsions, as shown in raw (top) and processed (bottom) images **(e)**.[18] Reproduced from refs. 16–18 with permission from Wiley and The Royal Society of Chemistry.

speed. By means of image processing algorithms, detailed information down to the single particle or droplet level can be quantitatively extracted (Figure 2.1e).[18] This makes it possible to begin to unravel the effects of thermodynamic stability, emulsion properties and osmotic pressure (or packing density) on film rupture and coalescence in a clean and reproducible manner.

2.3 Content mixing

After the rupture of the liquid film that separates two latex particles, the inner phases begin to mix. For simple viscous liquids, this process occurs on very short time scales, accessible only with high-speed imaging[19] or high-frequency conductometry[20] and can be described by hydrodynamics alone. However, for aqueous paints, the latex particles are composed of a highly viscoelastic entangled

polymer melt with a glass–liquid transition temperature T_g at or around the relevant application temperature of the coating. As a result, the mixing process following film rupture occurs over much longer time scales, and may continue well after the coating has dried. Routh and Russel have described several regimes of film formation depending on the relative rates of particle deformation – which precedes content mixing – and water evaporation.[2,21–23] These regimes have also been identified experimentally,[24] for example by MRI, which allows measuring local water concentrations in a drying paint layer.[25–28] With a typical resolution of approximately 10 μm, MRI profilometry does not give direct insight into particle deformation and coalescence at the single-particle scale. By contrast, polymer intermixing upon coalescence can be studied at the molecular scale using FRET,[29–31] in which lateral and depth information are usually lost.

Highly entangled polymer phases, such as those forming typical latex particles, may show not only a very high viscosity but in some cases, depending on the ratio between processing temperature and T_g, will also exhibit an effective yield stress. As a result, coalescence may never reach completion if the yield stress outweighs

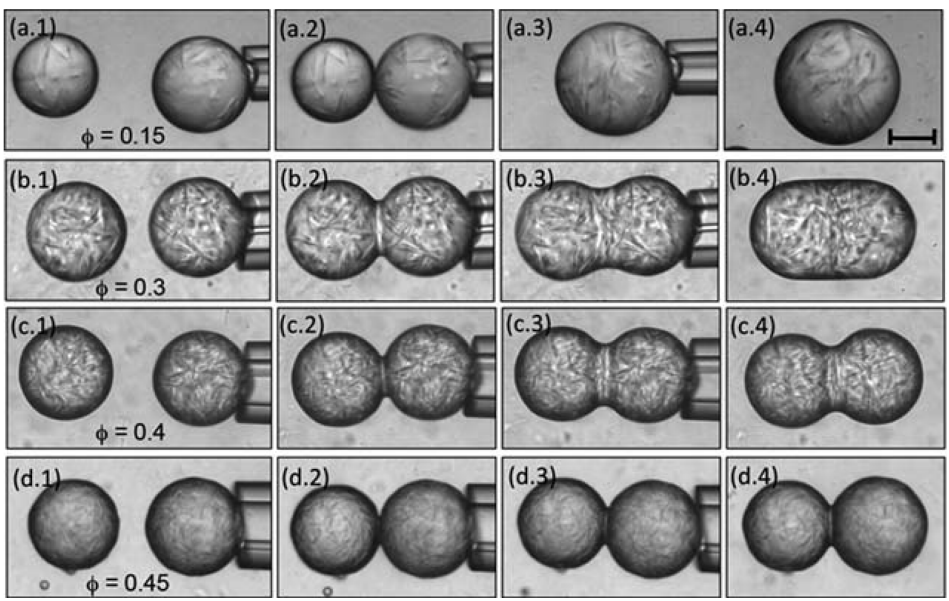

Figure 2.2. Transition from complete coalescence **(a)** to partial coalescence **(b–d)** of droplets of a yield stress fluid upon increasing the yield stress from top to bottom. The scale bar in (a.4) is 50 μm and applies to all images. Reproduced from ref. 32 with permission from The Royal Society of Chemistry.

the interfacial pressure which drives coalescence. This was demonstrated elegantly for the coalescence of two isolated droplets of yield stress fluids (Figure 2.2).[32] However, it remains unclear how these effects are manifest in dense systems, in which each particle is surrounded by many others, and how this influences the ultimate fate of a drying paint layer. Our knowledge is particularly incomplete when it comes to aqueous dispersions which do not only dry and coalesce but also undergo chemical curing when applied, as is the case for alkyd dispersions or two-component latices. In these systems, an additional time variable which describes the gradual increase in particle viscoelasticity due to the chemical reactions occurring, needs to be considered. We may expect that the relative rates of drying, polymer intermixing and chemical crosslinking give rise to new regimes of film formation, analogous to those described by the Routh–Russel model.[2,21,22]

2.4 Complex suspensions

The phenomena of film rupture and content mixing described above are already significantly complex when studied in the simplest limit of two interacting droplets or particles. However, additional complexity emerges, even in simple systems, when the particle concentration is increased. During paint drying, as solvent evaporates, the initially liquid-like dispersion reaches particle volume fractions where glassy dynamics prevail, and ultimately reaches a close-packed state, which can be ordered or disordered dependent on the particle interactions, polydispersity and drying rate.

Under these conditions, film rupture is no longer a problem merely depending on the thermodynamic stability of a single film, but collective effects must be taken into account. The first film to rupture in a homogeneously compressed packing of equally sized droplets is a problem of symmetry breaking governed by thermal or external fluctuations. However, once coalescence has nucleated, geometrical effects come into play in deciding which film will rupture next. This can lead to propagating coalescence fronts,[12,33] governed by local curvature effects and recoil of the fluid interfaces.[34] On a global scale, these effects can be ideally studied by for example water profilometry using MRI,[26,28] while insight into phenomena on smaller scales requires the use of higher-resolution methods such as optical microscopy, including confocal microscopy,[35] and electron microscopy.[36–39] Also here, the use of microfluidic tools to manipulate and in situ visualize the fate of droplets on their way to instability has proven invaluable.[33,40]

Direct imaging gives us access to details of the film formation process which are not accessible in other techniques. For example, using confocal fluorescence imaging, we have shown how coalescence in emulsion films subjected to a uni-

directional drying stress manifests itself in two distinct modes:[12] coalescence either occurs by the propagation of a coherent coalescence front from the dry end of the dispersion towards the wet region, or as a sequence of random nucleation-and-growth steps throughout the bulk of the dispersion. Using the same images, not only can the sequence of nucleation events be traced, but also can local capillary pressures be measured by analyzing the curvature of the Plateau borders. In this way, we have related these two distinct modes of coalescence in a drying emulsion to the temporal development of a pressure gradient across the drying emulsion. This example illustrates how direct imaging can provide new insights and reveal new phenomena that remain hidden with methods in which all data is spatially averaged.

In a typical aqueous paint formulation, the dispersed phase comprises a mixture of polymeric particles which coalesce, known as the binder as it provides the final film with its mechanical integrity, and solid colloids which do not coalesce, typically inorganic, such as pigments, opacifiers and fillers. This gives rise to new

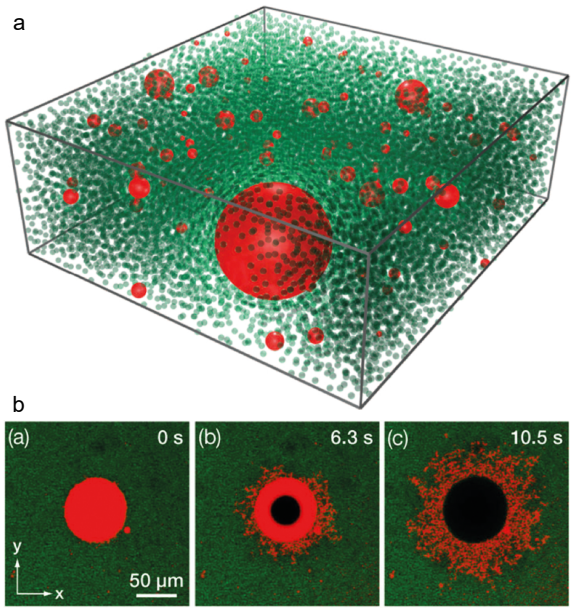

Figure 2.3. Confocal fluorescence microscopy of a drying mixture of hard particles (green) and emulsion droplets (red). **(a)** Three-dimensional reconstruction of the particle mixture and **(b)** time sequence showing break-up of a single emulsion drop and invasion into the surrounding matrix during drying. Reprinted with permission from ref. 41. Copyright 2010 by the American Physical Society.

phenomena as is beautifully illustrated in experiments by Xu *et al*.[41] These authors studied the drying of a mixture of small hard particles and larger liquid emulsion droplets using three-dimensional confocal fluorescence microscopy (Figure 2.3a). As drying progressed, and a densely packed state was reached, air invaded the structure. When the Laplace pressure within the droplets exceeded the osmotic pressure of the bath of small particles, air invasion caused the spontaneous break-up of emulsion droplets and their dispersal into the porous surroundings (Figure 2.3b), showing a distinct departure from the classical picture of droplet coalescence upon drying. Moreover, in drying dispersions containing particles of very different sizes, a distinct layering, or stratification, can occur, resulting in an inhomogeneous distribution of the different particle species across the final film.[42,43]

Water-borne paints typically also contain large amounts of dissolved components, such as surfactants and/or polymeric stabilizers, and thickeners such as network-forming associative polymers. Upon drying, the concentration of these solutes increases; as a result, the interactions between each of these species evolve over time, as well as the interactions between the solid or liquid particles mediated by the presence of polymers and surfactants, which in turn affects the phase behaviour and dynamics of the system. No clear understanding exists so far to what extent this will affect the structure and properties of the final film; for example, in some cases films are known to exhibit a heterogeneous distribution of inorganic pigment particles. It is not clear whether this structure is already present in the liquid state or if it emerges during drying, for example due to increasing depletion attractions between the particles as the polymer concentration increases. Water flow during drying can also transport dissolved species to the dry end of the paint layer, potentially leading to accumulation of solutes at the paint–air boundary, depending on the relative rates of water flux and thermal diffusion of the solutes. Modelling of the water and solute flows through the porous particle network may provide insight into this matter.[12]

2.5 Instabilities

The design of a new generation of sustainable water-based coatings requires not only control over the deformation and coalescence of individual particles during drying, but equally vitally requires the effective mitigation of large-scale instabilities which occur during the application, drying and ageing of these coatings. Typical instabilities include cracking and delamination,[44] wrinkling,[45] and the formation of exposed areas of the substrate, either in small spots known as pinholes,[46] or in larger domains, for example by dewetting or by Marangoni-stress-induced delevelling.[47] These instabilities, which significantly deteriorate the performance

and appearance of the coating, occur on length scales much larger than the scale of individual particles. They must arise from collective effects within the paint and from paint–substrate interactions. Identifying the origins of such instabilities is therefore a major challenge, especially for formulations containing a variety of components. This challenge is exacerbated by the fact that some instabilities may not manifest directly but appear gradually during ageing of the coating. For example, the cracking and delamination of paint films composed of air-curing polymers such as in artist oil paints pose a significant threat to the preservation of many seminal artworks, yet these cracks only become visible decades or even centuries after the paintings were first created.

The complete suppression of cracking requires an understanding spanning multiple length and time scales. Crack nucleation is a highly localized event, but once it leads to a propagating crack, this strongly influences the nucleation and growth of subsequent cracks[48] as well as the internal stresses throughout the coating.[49–52] Because of the directional release of stresses around the growing cracks, fracture networks typically display distinct statistical features, such as polygonal cracks in dried silica suspensions and mud[53,54] or regularly spaced radial cracks in dried colloidal droplets.[45,55]

The majority of literature on cracking in colloidal coatings is centred around two topics: the propagation mechanism of individual cracks, and the correlation between dispersion parameters and the final fracture pattern. Imaging of propagating cracks has provided a wealth of information about the stress distribution and particle arrangement around the cracks,[37,39,56,57] the reversibility and trajectory of crack opening,[56–60] and the characteristic crack spacing.[39,51,61,62] Furthermore, a variety of strategies have been proposed to prevent cracking, such as reducing the interparticle adhesion,[45,57] increasing the elastic modulus of the particle network,[53,63] and mitigating stress build-up by adding soft colloids.[55,64,65] Despite the great fundamental and practical value of these insights, it remains difficult to predict *a priori* íf and how a coating will fracture. Typical unanswered questions concern the extent of brittle versus plastic fracture and the moment of crack nucleation, either following the drying front or throughout the coating after consolidation. In-depth knowledge of the collective phenomena occurring at all scales is therefore desired.

As mentioned above, instabilities may develop well after drying of a coating, suggesting the need for long-term measurements. A simple yet effective technique for this purpose is bright-field microscopy. In Chapter 3 of this thesis, we show how measuring the transmitted light intensity through semi-transparent latex droplets allowed us to visualize and quantify local changes in droplet homogeneity over extended periods. Using this method, we uncovered that in many cases,

pronounced cracks show self-healing over longer periods of time (Figure 2.4a). Scanning electron microscopy revealed how crack healing occurs: first particles deform and form facets (Figure 2.4b1), subsequently they coalesce (b2), upon which the cracks heal by creep of the now coherent polymer film (b3). Surprisingly, this gradual self-healing persisted up to relatively high $T_g - T$ values of 13 °C, where by common definition the polymer is in a glassy state. Thanks to the universality of the self-healing mechanism, independent of particle softness, we could fit the accompanying rise in the transmitted intensity by a single function from which we obtained a typical time scale of crack healing τ_{heal}. Increasing the T_g of the

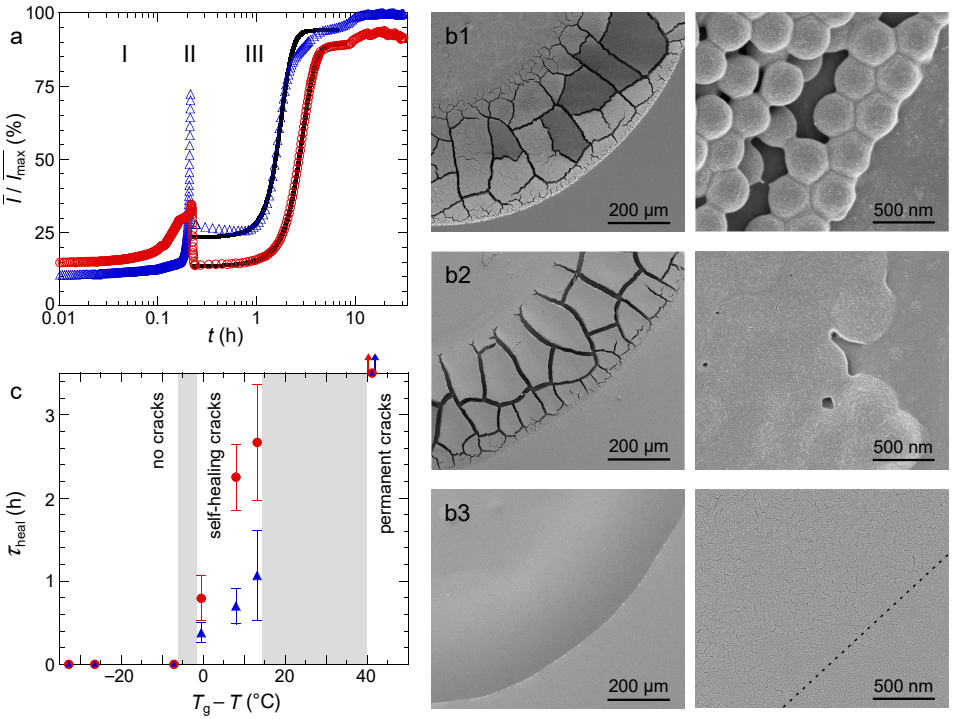

Figure 2.4. Cracking and crack healing. **(a)** Transmitted light intensity through a drying droplet of poly(styrene-*co*-butyl acrylate) colloids with a T_g at room temperature, measured using bright-field microscopy. Distinct stages of drying (I), cracking (II), and crack healing (III) are visible. **(b)** Scanning electron microscopy time series showing particle deformation, coalescence and crack healing at the edge of a dried droplet of particles with $T_g - T = 13$ °C at $t = 4$ h **(b1)**, 24 h **(b2)** and 48 h **(b3)** after deposition. **(c)** Typical time scale of crack healing as a function of the difference between the glass transition and room temperature, showing three regimes. Adapted with permission from ref. 66 (Chapter 3). Copyright 2015 American Chemical Society.

polymer phase allowed us to tune τ_{heal} from zero (no cracks) to several hours (self-healing cracks) to more than ten days (presumed permanent cracks) (Figure 2.4c).[66] Although the practical applicability of long ageing times is questionable, and preventing cracking may be preferred over curing them slowly, these results suggest that in polymeric films cracking may be a transient phenomenon when the film is relatively soft.

2.6 Outlook

Much of the effort in improving and innovating sustainable water-borne coatings is dedicated to fine-tuning formulations, developing new types of particles and stabilizers, and redesigning application procedures. However, with so many unknowns regarding the mechanisms with which complex colloidal dispersions dry and form films, these efforts remain largely empirically driven. Extending our fundamental insight into the governing mechanisms of film formation will pave the way for a more rational approach towards improving water-based paints and replacing environmentally unfriendly solvent-based systems. With the advent of a plethora of novel imaging techniques and enabling technologies such as microfluidics, and the rise of new types of soft responsive materials to control and tune film formation, this challenge, although complex, can now be effectively addressed.

Future challenges lie primarily in connecting the interactions among the different components of multicomponent aqueous paints to the complexity that emerges when particle and solute concentrations rise and couple to non-equilibrium phenomena such as fluid flows, thin film rupture and particle coalescence. Quantitative imaging, combined with complementary methods, may provide a crucial tool to span the length scales from individual particles to the properties of entire systems. This leaves the challenge of capturing dynamics on a wide range of time scales for which not one single technique may be suitable; for example, while three-dimensional confocal microscopy may resolve processes in unprecedented detail, the acquisition time of a single three-dimensional image stack may be too slow to capture fast processes such as coalescence. Another pressing challenge is to develop methods which allow for imaging of inherently turbid dispersions, especially their internal structure and dynamics. Although designing systems for microscopy through refractive index matching most certainly has its merits, similar studies could ideally be performed on realistic formulations which are typically highly scattering and coloured. In Chapters 5 and 6 of this thesis, we show that laser speckle based imaging tools may provide the solution.

In addition, film formation is in part so complex, and ill-controlled in certain circumstances, because drying and the associated flows of solvent and solute occur simultaneously with coalescence of the particles. The use of responsive, or triggerable, surfactants or particles, could in principle enable the formulation of systems which are extremely stable against coalescence, allowing the system to dry without particle destabilization, after which coalescence can be triggered by means of an external impulse, such as temperature [12,18] or light. At least for the study of film formation, such an approach may have merit, but even for certain industrial applications the decoupling of various stages in the coating process may prove to be useful.

Finally, all of the issues discussed here originate from the fact that conventional solvent-based paints, in which the binder is molecularly dissolved, have been reformulated in a colloidal dispersion for their application in water-based systems. Clever polymer chemistry may allow circumventing the issues associated with the formation of a film from a dispersed system by rethinking this strategy in its entirety, for example by using dissolved polymers which become hydrophobic upon drying, or through the use of solvent-free systems.

With these challenges ahead, many of which lie at the heart of the soft matter field, much needs to be done before a full replacement of toxic and harmful solvent-based coatings can take place. Nevertheless, studying these problems offers an opportunity to reveal and unravel fascinating phenomena that remain to be explained, with a clear societal relevance. In short: watching paint dry is hardly a boring or idle endeavour.

References

[1] G. Triebig, J. Hallermann. *Occup. Environ. Med.* **58**, 575–581 (2001).

[2] J. Keddie, A. F. Routh, *Fundamentals of latex film formation: processes and properties* (Springer, 2010).

[3] J. L. Keddie. *Mater. Sci. Eng. R Rep.* **21**, 101–170 (1997).

[4] M. A. Winnik. *Curr. Opin. Colloid Interface Sci.* **2**, 192–199 (1997).

[5] P. Steward, J. Hearn, M. Wilkinson. *Adv. Colloid Interface Sci.* **86**, 195–267 (2000).

[6] A. F. Routh. *Rep. Prog. Phys.* **76**, 046603 (2013).

[7] T. D. Dimitrova, F. Leal-Calderon, T. D. Gurkov, B. Campbell. *Langmuir* **17**, 8069–8077 (2001).

[8] C. Stubenrauch, R. von Klitzing. *J. Phys. Condens. Matter* **15**, R1197–R1232 (2003).

[9] H. M. Princen. *J. Colloid Interface Sci.* **71**, 55–66 (1979).

[10] J. Bibette, D. C. Morse, T. A. Witten, D. A. Weitz. *Phys. Rev. Lett.* **69**, 2439–2442 (1992).

[11] J. Lyklema, *Fundamentals of interface and colloid science: soft colloids*, vol. 5 (Academic Press, 2005).

[12] H. Feng, J. Sprakel, D. Ershov, T. Krebs, M. A. Cohen Stuart, J. van der Gucht. *Soft Matter* **9**, 2810–2815 (2013).

[13] Z. Zapryanov, A. K. Malhotra, N. Aderangi, D. T. Wasan. *Int. J. Multiphase Flow* **9**, 105–129 (1983).

[14] D. Y. C. Chan, R. G. Horn. *J. Chem. Phys.* **83**, 5311–5324 (1985).

[15] A. Oron, S. H. Davis, S. G. Bankoff. *Rev. Mod. Phys.* **69**, 931–980 (1997).

[16] T. E. Kodger, J. Sprakel. *Adv. Funct. Mater.* **23**, 475–482 (2013).

[17] H. Feng, N. A. L. Verstappen, A. J. C. Kuehne, J. Sprakel. *Polym. Chem.* **4**, 1842–1847 (2013).

[18] H. Feng, D. Ershov, T. Krebs, K. Schroen, M. A. Cohen Stuart, J. van der Gucht, J. Sprakel. *Lab Chip* **15**, 188–194 (2015).

[19] S. T. Thoroddsen, T. G. Etoh, K. Takehara. *Annu. Rev. Fluid Mech.* **40**, 257–285 (2008).

[20] J. D. Paulsen, J. C. Burton, S. R. Nagel. *Phys. Rev. Lett.* **106**, 114501 (2011).

[21] A. F. Routh, W. B. Russel. *Langmuir* **15**, 7762–7773 (1999).

[22] A. F. Routh, W. B. Russel. *Ind. Eng. Chem. Res.* **40**, 4302–4308 (2001).

[23] J. M. Salamanca, E. Ciampi, D. A. Faux, P. M. Glover, P. J. McDonald, A. F. Routh, A. C. I. A. Peters, R. Satguru, J. L. Keddie. *Langmuir* **17**, 3202–3207 (2001).

[24] E. Gonzalez, M. Paulis, M. J. Barandiaran, J. L. Keddie. *Langmuir* **29**, 2044–2053 (2013).

[25] S. J. F. Erich, O. C. G. Adan, L. Pel, H. P. Huinink, K. Kopinga. *Chem. Mater.* **18**, 4500–4504 (2006).

[26] P. J. McDonald, J. L. Keddie. *Europhys. News* **33**, 48–51 (2002).

[27] E. Ciampi, U. Goerke, J. L. Keddie, P. J. McDonald. *Langmuir* **16**, 1057–1065 (2000).

[28] F. T. Carter, R. M. Kowalczyk, I. Millichamp, M. Chainey, J. L. Keddie. *Langmuir* **30**, 9672–9681 (2014).

[29] J. C. Haley, Y. Liu, M. A. Winnik, W. Lau. *J. Coat. Technol. Res.* **5**, 157–168 (2008).

[30] M. Soleimani, S. Khan, D. Mendenhall, W. Lau, M. A. Winnik. *Polymer* **53**, 2652–2663 (2012).

[31] E. Odrobina, M. A. Winnik. *Macromolecules* **34**, 6029–6038 (2001).

[32] A. B. Pawar, M. Caggioni, R. W. Hartel, P. T. Spicer. *Faraday Discuss.* **158**, 341–350 (2012).

[33] A. R. Thiam, N. Bremond, J. Bibette. *Phys. Rev. Lett.* **107**, 068301 (2011).

[34] P. S. Stewart, S. H. Davis, S. Hilgenfeldt. *Colloids Surf., A* **436**, 898–905 (2013).

[35] J. C. Cabanelas, B. Serrano, M. G. Gonzalez, J. Baselga. *Polymer* **46**, 6633–6639 (2005).

[36] J. L. Keddie, P. Meredith, R. A. L. Jones, A. M. Donald. *Macromolecules* **28**, 2673–2682 (1995).

[37] Y. Ma, H. T. Davis, L. E. Scriven. *Prog. Org. Coat.* **52**, 46–62 (2005).

[38] E. Gonzalez, C. Tollan, A. Chuvilin, M. J. Barandiaran, M. Paulis. *ACS Appl. Mater. Interfaces* **4**, 4276–4282 (2012).

[39] C. C. Roberts, L. F. Francis. *J. Coat. Technol. Res.* **10**, 441–451 (2013).

[40] N. Bremond, J. Bibette. *Soft Matter* **8**, 10549–10559 (2012).

[41] L. Xu, A. Berges, P. J. Lu, A. R. Studart, A. B. Schofield, H. Oki, S. Davies, D. A. Weitz. *Phys. Rev. Lett.* **104**, 128303 (2010).

[42] R. E. Trueman, E. L. Domingues, S. N. Emmett, M. W. Murray, A. F. Routh. *J. Colloid Interface Sci.* **377**, 207–212 (2012).

[43] R. E. Trueman, E. Lago Domingues, S. N. Emmett, M. W. Murray, J. L. Keddie, A. F. Routh. *Langmuir* **28**, 3420–3428 (2012).

[44] F. Giorgiutti-Dauphiné, L. Pauchard. *Soft Matter* **11**, 1397–1402 (2015).

[45] Y. Zhang, Y. Qian, Z. Liu, Z. Li, D. Zang. *Eur. Phys. J. E* **37**, 84 (2014).

[46] J. Domnick, D. Gruseck, K. Pulli, A. Scheibe, Q. Ye, F. Brinckmann. *Chem. Eng. Proc. Proc. Intens.* **50**, 495–502 (2011).

[47] V. R. Gundabala, C.-h. Lei, K. Ouzineb, O. Dupont, J. L. Keddie, A. F. Routh. *AIChE J.* **54**, 3092–3105 (2008).

[48] S. Bohn, L. Pauchard, Y. Couder. *Phys. Rev. E* **71**, 046214 (2005).

[49] C. J. Martinez, J. A. Lewis. *Langmuir* **18**, 4689–4698 (2002).

[50] M. S. Tirumkudulu, W. B. Russel. *Langmuir* **20**, 2947–2961 (2004).

[51] M. S. Tirumkudulu, W. B. Russel. *Langmuir* **21**, 4938–4948 (2005).

[52] H. N. Yow, M. Goikoetxea, L. Goehring, A. F. Routh. *J. Colloid Interface Sci.* **352**, 542–548 (2010).

[53] F. Boulogne, F. Giorgiutti-Dauphiné, L. Pauchard. *Soft Matter* **11**, 102–108 (2015).

[54] L. Goehring, R. Conroy, A. Akhter, W. J. Clegg, A. F. Routh. *Soft Matter* **6**, 3562–3567 (2010).

[55] Q. Jin, P. Tan, A. B. Schofield, L. Xu. *Eur. Phys. J. E* **36**, 28 (2013).

[56] K. I. Dragnevski, A. F. Routh, M. W. Murray, A. M. Donald. *Langmuir* **26**, 7747–7751 (2010).

[57] L. Goehring, W. J. Clegg, A. F. Routh. *Phys. Rev. Lett.* **110**, 024301 (2013).

[58] E. R. Dufresne, E. I. Corwin, N. A. Greenblatt, J. Ashmore, D. Y. Wang, A. D. Dinsmore, J. X. Cheng, X. S. Xie, J. W. Hutchinson, D. A. Weitz. *Phys. Rev. Lett.* **91**, 224501 (2003).

[59] E. R. Dufresne, D. J. Stark, N. A. Greenblatt, J. X. Cheng, J. W. Hutchinson, L. Mahadevan, D. A. Weitz. *Langmuir* **22**, 7144–7147 (2006).

[60] L. Goehring, W. J. Clegg, A. F. Routh. *Langmuir* **26**, 9269–9275 (2010).

[61] W. P. Lee, A. F. Routh. *Langmuir* **20**, 9885–9888 (2004).

[62] W. Man, W. B. Russel. *Phys. Rev. Lett.* **100**, 198302 (2008).

[63] J. Qiao, J. Adams, D. Johannsmann. *Langmuir* **28**, 8674–8680 (2012).

[64] A. Tzitzinou, J. L. Keddie, J. M. Geurts, A. C. I. A. Peters, R. Satguru. *Macromolecules* **33**, 2695–2708 (2000).

[65] K. B. Singh, G. Deoghare, M. S. Tirumkudulu. *Langmuir* **25**, 751–760 (2009).

[66] H. M. van der Kooij, M. de Kool, J. van der Gucht, J. Sprakel. *Langmuir* **31**, 4419–4428 (2015). **(Chapter 3)**

Chapter 3

Coalescence, cracking and crack healing in drying dispersion droplets

This chapter is based on: Hanne M. van der Kooij, Marleen de Kool, Jasper van der Gucht and Joris Sprakel, 'Coalescence, cracking, and crack healing in drying dispersion droplets', *Langmuir* **31**, 4419–4428 (2015).

Abstract

The formation of a uniform film from a polymer dispersion is a complex phenomenon involving the interplay of many processes: evaporation and resulting fluid flows through confined geometries, particle packing and deformation, coalescence, and cracking. Understanding this multidimensional problem has proven challenging, precluding a clear understanding of film formation to date. This is especially true for drying dispersion droplets, where the particular geometry introduces additional complexity such as lateral flow towards the droplet periphery. We study the drying of these droplets using a simplified approach in which we systematically vary a single parameter: the glass transition temperature (T_g) of the polymer. We combine bright-field with scanning electron microscopy to elucidate these processes from the macroscopic down to the single-particle level, both qualitatively and quantitatively, over times ranging from seconds to days. Our results indicate that the polymer T_g has a marked influence on the time evolution of particle deformation and coalescence, giving rise to a distinct and sudden cracking transition. Moreover, in cracked droplets it affects the frequently overlooked time scale of crack healing, giving rise to a second transition from self-healing to permanently cracked droplets. These findings are in line with the classical Routh–Russel model for film formation, yet extend its scope from particle-level dynamics to long-range polymer flow.

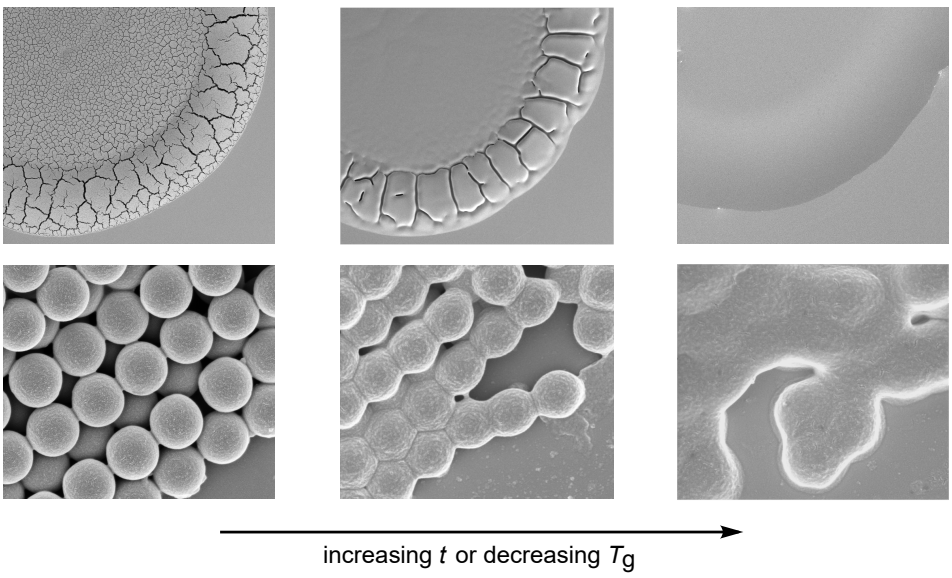

3.1 Introduction

The formation of a homogeneous film from a droplet containing dispersed colloidal particles is a crucial stage in techniques such as inkjet printing[1] and spray painting.[2] After this droplet has been discharged from the spray nozzle and impinged on a substrate, the dispersing fluid evaporates to yield a solid circular deposit. The assembly of many thousands of these closely deposited droplets forms the complete print or coating. In traditional coatings cast from a polymer solution, film formation is relatively straightforward because the polymer is homogeneously distributed throughout the drying process. However, for water-based inks and paints, forming a film not only requires evaporation of the solvent but also deformation and coalescence of the dispersed polymer particles. These processes usually do not reach completion for high-viscosity polymers, resulting in porous films that are prone to cracking.[3] Consequently, purely water-based coatings cannot yet compete with their solvent-based counterparts in terms of durability and performance. Improving the quality of water-based inks and paints to allow for the ultimate replacement of all solvent-based systems requires a deeper understanding of the film formation process.

Film formation in drying dispersion droplets involves the intricate interplay of many processes, including fluid flow, particle deformation, coalescence, and cracking. Each of these processes has been individually investigated in some detail,[4–10] yet crucial connections between them are lacking. Particle deformation is effectively described in the Routh–Russel model, which identifies distinct deformation regimes depending on the relative time scales of particle deformation and evaporation.[11,12] However, the Routh–Russel model makes several simplifying assumptions regarding fluid flow and does not take into account particle coalescence and cracking, while especially these phenomena, governed not only by the properties of single particles but also by collective effects spanning much larger length scales, determine the properties of the dried film.

In reality, the rates of evaporation and fluid flow within a drying film vary considerably, both in time and in space. For drying droplets, the spatial variation of the evaporative flux is manifest in the so-called 'coffee-ring effect': dispersion droplets whose contact line is pinned to the substrate produce ring-like deposits upon drying. This pattern arises from a capillary flow towards the contact line, which carries particles and other solutes along, to replenish fluid evaporated from the edges. The evaporative flux from the droplet surface has both experimentally[4] and theoretically[6] been shown to diverge near the contact line. In addition to the spatial divergence, the radial flow velocity diverges towards the end of drying, which has illustratively been called the 'rush hour'. This temporal singularity gives

rise to a sharp structural transition in the stain, from ordered crystals near the contact line to disordered packings in the centre.[5] All of these conclusions apply to hard, undeformable particles, whose behaviour during drying is governed largely by the velocity with which they arrive at the contact line. However, when the particles are soft, allowing them to deform and coalesce within the deposit at the contact line, the evolution of the droplet must be governed by the dynamic interplay of all processes involved. While of crucial importance to understanding droplet drying during printing and spray painting, this scenario has not been studied in detail; consequently, it remains unknown which factors influence the subtle balance of time scales and how this affects the homogeneity of the final film.

The softness of the particles can be conveniently tuned by changing the glass transition temperature (T_g) of the polymer phase.[13] This parameter affects not only the dynamics of particle deformation and coalescence but also the formation and fate of cracks. Coatings typically crack when the T_g is above or just below room temperature,[14,15] in which cases particle deformation is too slow to release the contractile stresses that develop during drying.[16] The low polymer mobility in the bulk of these coatings has led to a general belief that formed cracks are incapable of spontaneous self-healing. However, a considerable body of work suggests that interdiffusion of polymers across interfaces may persist at temperatures well below the T_g, albeit at a reduced rate.[17–22] This must have significant implications for the long-term ageing of films, during which deformation and coalescence may proceed and cracks and defects may heal. Yet, this healing remains virtually unexplored. A full understanding of the associated processes requires their visualization by techniques spanning length scales of nano- to millimetres and time scales of seconds to days.

In this chapter, we systematically study the effects of the polymer T_g on both the drying and ageing of polymer dispersion droplets. We combine bright-field and scanning electron microscopy with quantitative image analysis to provide a scale-spanning overview of the key processes in film formation. Our results highlight the wide-ranging importance of the polymer T_g: it markedly influences not only coalescence and cracking during drying but also the frequently overlooked potential for crack healing after drying. We show that the factors T_g and time are inextricably linked in determining the homogeneity of dried dispersion droplets on all length scales.

3.2 Experimental details

3.2.1 Particle synthesis

Styrene, *n*-butyl acrylate, 4,4′-azobis(4-cyanovaleric acid) (ACVA), and 1.0 M sodium hydroxide solution are purchased from Sigma-Aldrich. All chemicals are used as received. Polymer particles with varying ratios of styrene and butyl acrylate are synthesized according to a one-step surfactant-free emulsion polymerization described previously.[23] The polymer dispersions will be referred to as S_x-B_y, where x and y designate the percentages of styrene and butyl acrylate, respectively. In a 150 mL one-neck round-bottom flask, the following components are mixed: $x/100 \times 12.5$ g of styrene, $y/100 \times 12.5$ g of *n*-butyl acrylate, 62.5 g of Milli-Q water, and 0.0125 g of 1-octanethiol. The latter serves as a chain-transfer agent and allows us to control the mean molecular weight of the polymer and its distribution (see Appendix 3.A.1 and Figure 3.A.1 for details). A 2.5 cm magnetic stirring bar is included, and the flask is sealed with a rubber septum. The reaction mixture is subsequently flushed with dry nitrogen for 15 min while stirring at 500 rpm. Simultaneously, the initiator solution is prepared by dissolving 140 mg of ACVA in 2.5 mL of 0.4 M sodium hydroxide. The flask is then transferred to an oil bath at 85 °C, and the reaction mixture is flushed with dry nitrogen while stirring at 500 rpm for another 15 min. Finally, the initiator solution is injected quickly into the reaction mixture, after which the nitrogen inlet and outlet are removed. The reaction is left for approximately 20 h at 85 °C with continued stirring at 500 rpm. The reaction mixture is then filtered to remove the coagulum, yielding a dispersion with polymer concentration of ∼10 wt% and a pH of ∼7.

3.2.2 Characterization of particles

Dynamic light scattering

The hydrodynamic radii (R_h) of the particles are determined using dynamic light scattering (DLS). These measurements are performed on an ALV instrument equipped with an ALV-7002 external correlator and a 300 mW Cobolt Samba-300 DPSS laser operating at a wavelength of 532 nm. The dispersions are diluted to a concentration of $\sim 1 \times 10^{-3}$ wt% and filtered through a 0.20 μm poly(ether sulphone) membrane syringe filter (Advanced Microdevices Pvt. Ltd.). They are measured in polycarbonate capillaries of 1.9 mm diameter (Enki SRL) at a detection angle of 90° and a temperature of 20 ± 1 °C. Reported radii are the average of 30 independent measurements of 30 s each.

Gel permeation chromatography

The size distribution of the polymers is measured using an Agilent Technologies 1200 series gel permeation chromatograph (GPC) equipped with a PLgel 5 μm Mixed-D column (M_w range 200–400,000 Da, Polymer Laboratories Ltd.) and an Agilent 1200 differential refractometer. The column is calibrated using polystyrene standards (Fluka, ReadyCal set 400–200,000,000 Da). The samples are prepared by drying the polymer dispersions in an oven at 65 °C overnight and dissolving the dry polymer fraction at a concentration of 2 mg/mL, after which the solutions are filtered through 0.20 μm polytetrafluoroethylene (PTFE) membrane syringe filters (Advanced Microdevices Pvt. Ltd.). 100 μL of each sample is injected into the tetrahydrofuran (THF) flowstream of the GPC system at 30 °C and a flow rate of 1 mL/min.

Differential scanning calorimetry

The glass transition temperatures of the polymers are measured by differential scanning calorimetry (DSC), after drying the dispersions in an oven at 65 °C overnight to remove residual water and unreacted monomer. DSC thermograms are recorded with a PerkinElmer Diamond DSC using dry nitrogen as carrier gas. Approximately 10 mg of each polymer is weighed and sealed into a stainless steel pan. The DSC is calibrated with indium, and an empty stainless steel pan is used as a reference. Two heating runs are performed per sample, from −60 to 150 °C at a rate of 10 °C/min; in between these runs, the sample is rapidly quenched to −60 °C at a rate of 100 °C/min and maintained at that temperature for 10 min, to release strain stored in the sample and promote heat transfer between the sample and the pan. The T_g is determined from the second heating thermogram as the temperature at the midpoint of the change in heat capacity.

3.2.3 Drying and ageing of dispersion droplets

For all drying and ageing experiments, the dispersions are diluted to a concentration of 7.4 wt%. 0.5 μL droplets of these dispersions are deposited on glass (bright-field microscopy) or silicon wafers with a natural oxide layer (scanning electron microscopy, SEM) and dried in an enclosed, transparent chamber at a controlled temperature of 23 ± 1 °C and relative humidity of 48 ± 4%. Using bright-field microscopy, the transmitted light intensity through the droplets is measured in a continuous manner; for the SEM measurements the samples are removed from the climate chamber at distinct times and imaged shortly afterwards.

Bright-field transmission microscopy

The transmission through the drying and ageing droplets is monitored with a Nikon eclipse Ti-U inverted microscope in bright-field mode, using a 10× air objective (NA = 0.30, WD = 16.0 mm). For each dispersion, experiments are performed in triplicate, with a duration of ~15 min and a frame rate of 5.2 fps. For droplets that crack, additional experiments are performed in triplicate, with a duration of ~30 h and a frame rate of 1.0 fps. The resulting time-lapse image sequences are analysed by measuring the time evolution of the average transmitted intensity in a square area of 50×50 μm^2 at two locations: 120 μm from the contact line of the droplet, which we refer to as the 'edge', and 600 μm from the contact line, which we refer to as the 'centre'. We denote this pixel-averaged transmitted intensity as $\bar{I}$. Because of the inherent delay involved in the sample deposition and camera focusing steps, the image acquisition cannot be started at exactly $t = 0$, with the delay ranging from 10 to 30 s. To allow for reliable averaging of the intensity curves of the different experiments per dispersion, each curve is adjusted in two steps: first, from all t a single value is subtracted such that the local maxima of the curves recorded at the droplet edge overlap, thereby eliminating the variations in induction time. Second, all $\bar{I}$ are divided by the maximum $\bar{I}$ ($\overline{I_{\max}}$) to account for variations in the initial transmission resulting from differences in the pre-acquisition drying of the samples and temporal variations in illumination power. The same transformations are performed to the curves recorded at the centre and edge of each sample.

Scanning electron microscopy

To analyse the evolution of particle deformation, coalescence, cracking and crack healing in detail, SEM images are taken at distinct times after deposition of the droplets. The samples are mounted on flat aluminium stubs with double-sided adhesive, conducting carbon tape. Charging of the samples is prevented by coating them with a 12 nm layer of iridium using a Leica EM SCD 500 sputter-coater. The SEM images are recorded on an FEI Magellan 400 field-emission SEM at an acceleration voltage of 2.0 kV.

3.3 Results and discussion

To study the effects of the polymer T_g on the drying and ageing of dispersion droplets, we synthesize a series of aqueous polymer dispersions with varying ratios of styrene to butyl acrylate. The main characteristics of these dispersions are given in Table 3.1. Most importantly, we find that the T_g increases approximately

Table 3.1. Specifications of the polymer dispersions used in this study. R_h is the hydrodynamic radius of the particles. M_n, PDI, and T_g are the number-average molecular weight, polydispersity index, and glass transition temperature of the polymer phase, respectively.

Dispersion	R_h (nm)	M_n (±5 kDa)	PDI (±0.5)	T_g (±1 °C)
S_{36}-B_{64}	235 ± 10	39	2.1	−10
S_{40}-B_{60}	247 ± 6	41	2.4	−3
S_{50}-B_{50}	216 ± 4	33	3.1	16
S_{60}-B_{40}	241 ± 9	40	2.1	23
S_{64}-B_{36}	242 ± 1	40	2.9	31
S_{67}-B_{33}	195 ± 3	42	3.2	36
S_{80}-B_{20}	214 ± 7	50	3.3	64

linearly with increasing percentage of styrene and is consistent with literature values.[24] All DSC heating curves show a single, relatively narrow glass transition, indicating a negligible composition drift during the copolymerization and a resultant homogeneous distribution of the monomers along the polymer chains (Appendix Figure 3.A.2 and Table 3.A.2). Other important characteristics of the dispersions that influence film formation – specifically the hydrodynamic radius (R_h) of the particles, and the number-average molecular weight (M_n) and polydispersity index (PDI) of the polymer chains – are relatively constant among the dispersions; this allows us to attribute observed differences and trends to changes in the glass transition temperature alone. We note that the polymer chains have relatively high polydispersities, which is inherent of the radical polymerization that we use and common for water-based polymer dispersions.

3.3.1 Droplet drying

We monitor the drying dynamics of dispersion droplets using bright-field transmission microscopy. Typical time-lapse sequences for relatively soft ($T_g - T$=−7 °C) and hard ($T_g - T$=13 °C) particles are presented in Figure 3.1a and b, respectively, with the corresponding full time series available as Supplementary Movies 1 and 2 in ref. 25. These images show the transmitted light intensity through the droplets, which is inversely proportional to the turbidity. Clearly, in both cases the contact line remains pinned to the glass substrate throughout the experiment, giving rise to the coffee-ring effect: a net outward flow of fluid carries particles towards the edges and transforms the initially spherical-cap-shaped droplets into ring-shaped

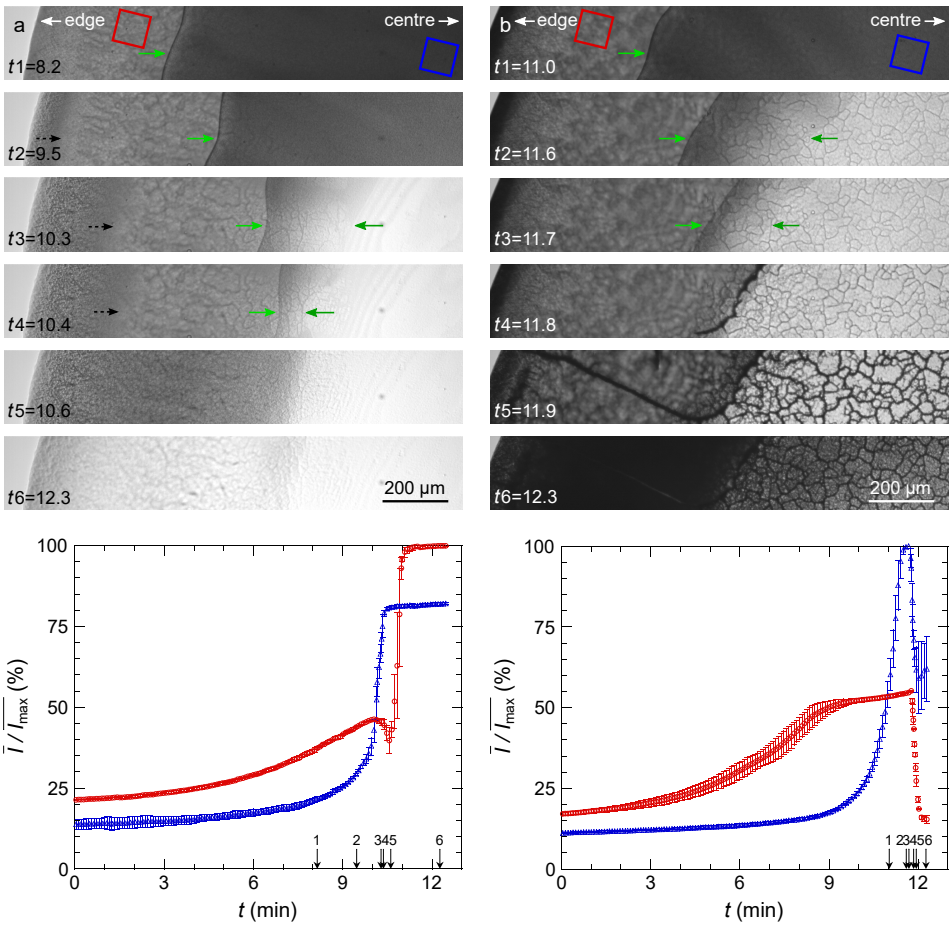

Figure 3.1. Top: time-lapse bright-field transmission micrographs of a fragment of a drying droplet of **(a)** S_{50}-B_{50} ($T_g - T = -7$ °C) and **(b)** S_{67}-B_{33} ($T_g - T = 13$ °C). See Supplementary Movies 1 and 2 in ref. 25 for the full time series. The numbers after $t1$–6 indicate the drying times in minutes. The arrows point to different propagating fronts: a coalescence front (⇢), inward moving drying fronts (→), and outward moving drying fronts (←). **Bottom:** the corresponding normalized intensity versus time, averaged over the squares depicted in the top frame at the edge (●) and centre (▲), and averaged over three measurements. The error bars represent the standard deviations. The numbered arrows indicate the drying times for the top frames.

stains.[4,6] Furthermore, in both experiments we observe a distinct drying front propagating from the contact line towards the centre of the droplet. This drying front indicates the boundary between two concentric regions: a consolidated yet moist outer ring containing a closely packed bed of particles and a wet central region containing the dilute dispersion.[9,26] Towards the end of drying, the inward moving drying front becomes accompanied by an outward moving drying front, when the water in the centre has been depleted. These two fronts meet exactly at the transition between the edge and centre of the droplet.

The velocity of the drying front is proportional to the evaporative flux in the radial direction and therefore provides information about the evaporation rate. We obtain this velocity from the image sequence using a custom-made MATLAB code. A typical example of the velocity of the inward moving drying front (v_{dry}) over time is presented in Figure 3.2a, corresponding to particles with $T_{\mathrm{g}} - T = -7$ °C. The shape of the curve is similar for other dispersions, albeit with different absolute values. Clearly, the velocity increases strongly near the end of drying, which arises from the rapid increase in the surface-to-volume ratio of the droplet while the evaporation rate remains approximately constant.[5,27] To compare the evaporation rates of the different dispersions, we extrapolate v_{dry} to $t = 0$ and plot these extrapolated linear velocities (${v_{\mathrm{dry}}}^0$) against $T_{\mathrm{g}} - T$ (Figure 3.2b). We find that for $T_{\mathrm{g}} - T > 0$ °C, that is for relatively hard particles, ${v_{\mathrm{dry}}}^0$ is constant around 0.33 µm/s, whereas for $T_{\mathrm{g}} - T < 0$ °C the velocity of the drying front decreases with decreasing T_{g}. This transition reflects the particle deformability: softer particles

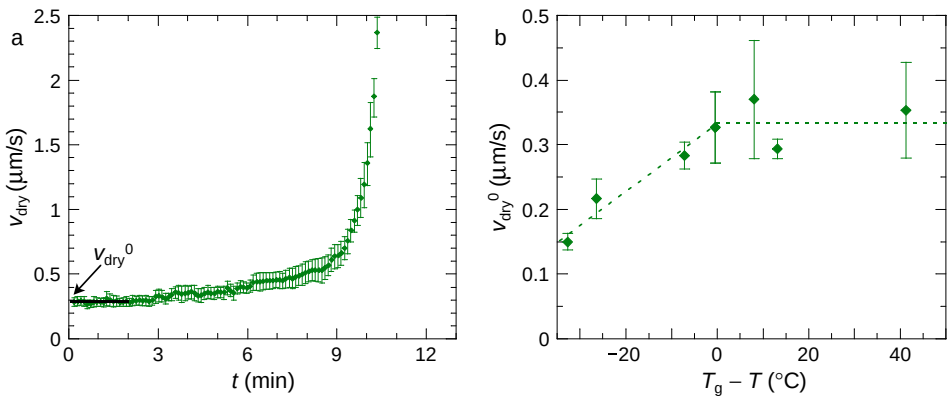

Figure 3.2. (a) Velocity of the inward moving drying front versus time for S_{50}-B_{50} ($T_{\mathrm{g}} - T = -7$ °C), averaged over three measurements. The error bars represent the standard deviations. The solid horizontal line shows the extrapolation of v_{dry} to $t = 0$ to give ${v_{\mathrm{dry}}}^0$, which is plotted in **(b)** versus $T_{\mathrm{g}} - T$. The dashed lines are guides to the eye.

deform to a greater extent during drying, resulting in a lower porosity of the packed particle beds at the droplet periphery and surface, which in turn limits evaporation and consequently the velocity of the drying front is lower.[28,29] In other words, the rate-limiting step in the evaporation shifts from the transport of water across the particle shell when $T_g < T$ to the diffusion of water vapour out of the saturated region around the droplet when $T_g > T$.

At the drying front of a high-T_g droplet, air invades the packed bed of particles, creating interparticle voids separated by pendular liquid bridges. If the packed particles are sufficiently soft, they can deform by the compressive capillary forces these bridges generate and thereby reduce the void volume. This likely occurs during drying of the low-T_g droplet in Figure 3.1a. Although we cannot differentiate between deformed and undeformed yet closely packed particles with the bright-field microscope, we observe a clear coalescence front propagating from the edge inwards after ~8.5 min, which typically occurs following extensive particle deformation and in the presence of a steep pressure gradient.[30] Such a coalescence front trailing behind a drying front has been reported earlier for low-T_g films, both microscopically by cryo-SEM[26] and molecularly by fluorescence resonance energy transfer (FRET).[9] We note that the coalesced region initially appears rather rough, which is probably due to the fact that the particles coalesce into progressively larger, polydisperse clusters.[31] This transient roughness causes a dip in the transmitted intensity at the edge (Figure 3.1a, *t*2–5), but at the end of drying the entire film has become rather homogeneous and transparent (Figure 3.1a, *t*6). The homogenization process gradually continues after drying: SEM images taken after 4 h of ageing reveal no other discontinuities than the difference in thickness between the edge and centre (Figure 3.3).

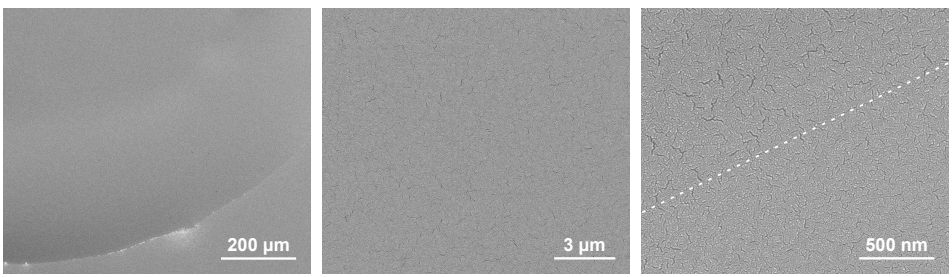

Figure 3.3. Typical SEM images of a droplet of S_{50}-B_{50} ($T_g - T = -7$ °C) after 4 h of ageing. The first image displays a quadrant of the droplet, the second gives a magnification of the centre, and the last image shows a high magnification of the contact line (indicated by a dashed line). The tiny cracks are artefacts caused by the sputter-coating.

The drying process of a high-T_g droplet is strikingly different: instead of a coalescence front during drying, the droplet cracks prodigiously when evaporation is complete (Figure 3.1b). The first cracks nucleate approximately 2 s following the disappearance of the drying fronts, after which they rapidly propagate and branch into progressively smaller secondary cracks over a period of 20–30 s. Most of the cracks run along a path of defects in the crystalline structure. Because of the extensive branching, individual cracks at the edge eventually cannot be discerned and the light transmission is severely reduced (Figure 3.1b, $t6$).

Interestingly, the cracks do not trail behind the drying fronts, which is the most commonly observed mechanism of fracture in dried dispersions.[32,33] Instead, we observe crack nucleation only after the entire droplet has consolidated, indicating that the capillary stresses near the drying front are insufficient to cause cracking.[34] This delayed mode of cracking is preceded by a divergence of the in-plane tensile stresses near the culmination of drying.[16,35] These tensile forces are exerted by the rigid substrate to oppose the compressive capillary forces. For hard particles, developed stresses cannot be relaxed other than by cracking because the particles are undeformable on the time scale of drying: even after 4 h of ageing, these particles have deformed only to a limited extent, as is apparent from the SEM images in Figure 3.4a. By contrast, soft particles can deform towards the substrate and thereby reduce the tensile stresses.[36] The interconnection of these particles by coalescence causes additional relaxation of the stresses through viscous flow; the extent thereof depends on the time scales of crack nucleation and propagation relative to those of coalescence flows.

Remarkably, the first cracks nucleate along the inner edge of the coffee ring, where the two drying fronts meet upon complete evaporation. A likely explanation is the concentration of stresses in this zone, due to the locally low packing density and crystallinity that originate from the diverging rate of particle deposition.[5] An additional contribution may be the discontinuity in the height of the film across the inner ring: this ring is in fact a large circular defect where different crystalline arrays meet, facilitating the formation of cracks.

To enable a quantitative comparison of the drying process of different dispersions, we measure the pixel-averaged transmitted intensity ($\bar{I}$) both at the edge and centre of each droplet, and plot this against the drying time. The resulting intensity curves for S_{50}-B_{50} and S_{67}-B_{33} are shown in the bottom frames of Figure 3.1a and b, respectively. These data confirm the above-described difference between low- and high-T_g droplets: for soft particles, drying ends with a rapid rise in $\bar{I}$ due to coalescence and a concurrent increase in the film homogeneity (Figure 3.1a, $t5$–6), whereas for hard particles it culminates in a sharp drop in $\bar{I}$ due to the formation of a vast number of cracks that scatter the light (Figure 3.1b, $t4$–6). Despite these

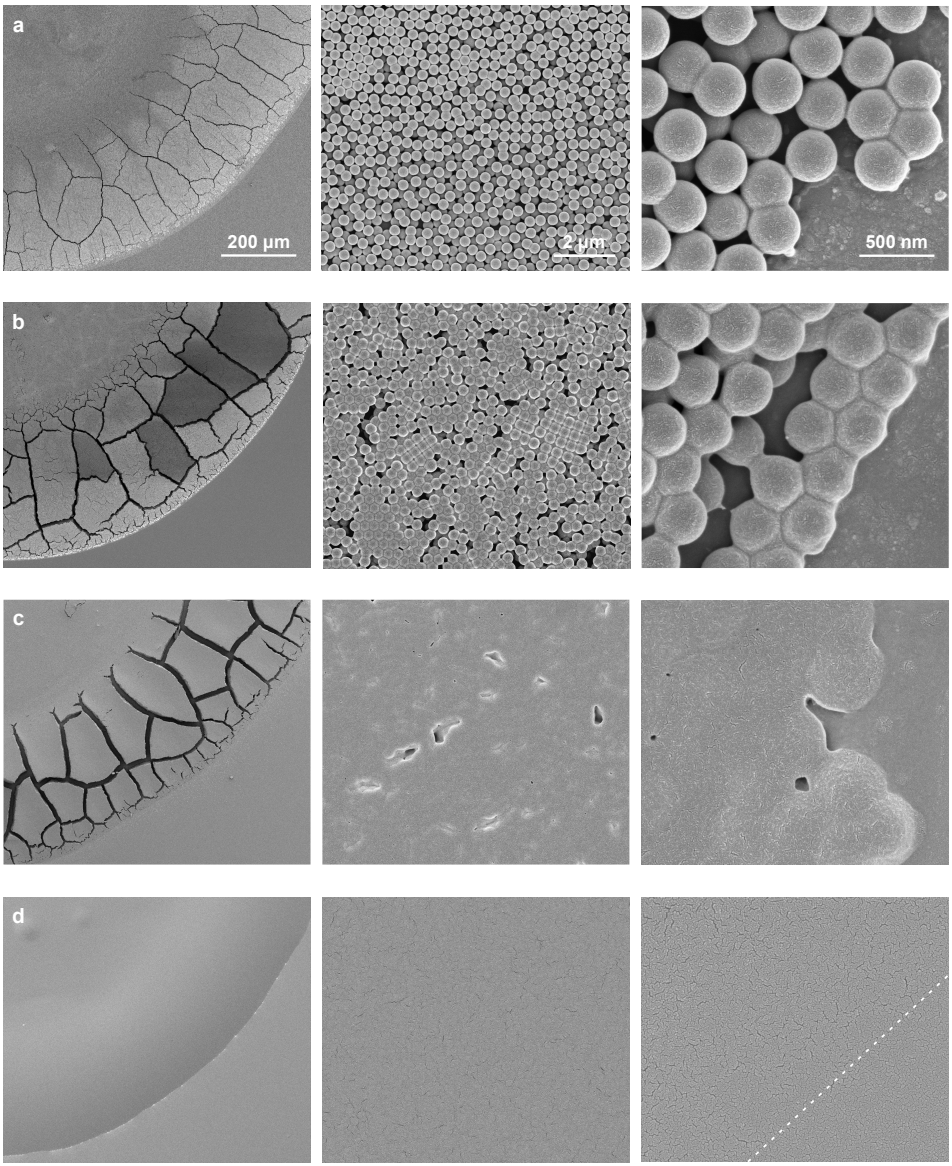

Figure 3.4. Typical SEM images showing the post-drying evolution of a droplet of S_{67}-B_{33} ($T_g - T$ = 13 °C). The ageing times are **(a)** 4 h, **(b)** 24 h, **(c)** 48 h, and **(d)** 10 days. The first column displays a quadrant of the droplet, the second column gives a magnification of the centre, and the last column shows a high magnification of the contact line (indicated in (d) by a dashed line). The scale bars apply to all rows. The tiny cracks are artefacts caused by the sputter-coating.

distinct outcomes, the stage of drying preceding close packing is similar for all samples and involves a gradual increase in the transmitted intensity with time. This reflects a net decrease in scattering due to the decreasing droplet thickness, which dominates the concurrent increase in particle concentration. Note that both the absolute intensity and the slope start higher at the edge than in the centre because of the lower droplet thickness and faster drying at the edge.

As a measure for the crack density, we normalize the decrease in intensity upon cracking ($\Delta\overline{I_{\mathrm{crack}}}$) by the minimum intensity after cracking ($\overline{I_{\mathrm{min}}}$). Both for the edge and centre of the droplets, we find an abrupt transition in the crack density at $T_{\mathrm{g}} - T = -5\,^{\circ}\mathrm{C}$: below this transition, no visible cracks form, whereas above it, a high density of cracks is observed (Figure 3.5). The crossover is remarkably sharp, which we attribute to the steep change in polymer viscosity across the glass transition.

Interestingly, the samples just above the transition point, with $T_{\mathrm{g}} - T = 0\,^{\circ}\mathrm{C}$, show a significantly higher crack density in the centre than at the edge. This suggests that partial particle deformation and coalescence precede the cracking at the edge, relieving part of the tensile stresses. We indeed observe a coalescence front at the edge of these droplets, which does not reach the centre before the onset of cracking.

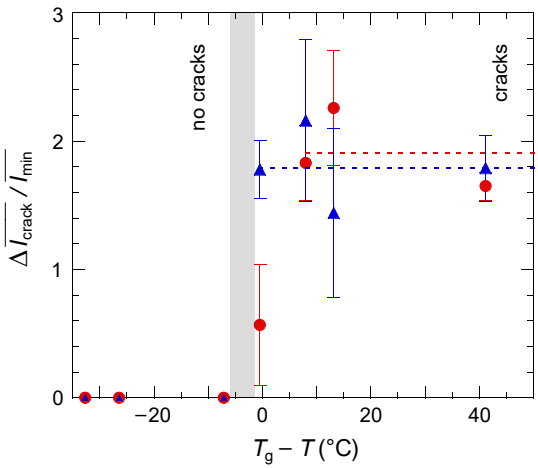

Figure 3.5. Normalized decrease in intensity due to cracking for both the edge (●) and centre (▲), averaged over three measurements. The error bars represent the standard deviations. The dashed horizontal lines indicate the average $\Delta\overline{I_{\mathrm{crack}}}/\overline{I_{\mathrm{min}}}$ in the regions where they are approximately constant. The grey vertical bar indicates the transition region between absence and presence of cracks.

3.3.2 Droplet ageing

In practical applications, the formation of cracks is highly undesired because of their deteriorative effects on the aesthetic appearance, durability, and mechanical properties of the coating. We therefore study the fate of cracks during prolonged ageing of the dried droplets. We visualize the ageing of all cracked droplets with a bright-field transmission microscope, which for a droplet with $T_g - T = 0\,^{\circ}\mathrm{C}$ is displayed in Figure 3.6a. The corresponding full time series is available as Supplementary Movie 3 in ref. 25. Clearly, the droplet contains many cracks after drying (Figure 3.6a, $t1$), yet these cracks show a surprising capacity of self-healing

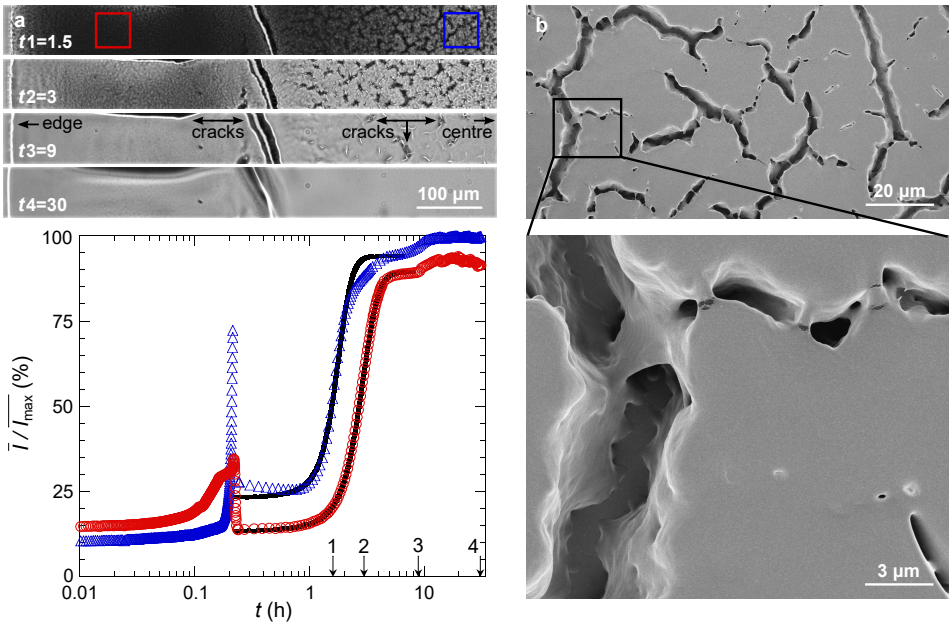

Figure 3.6. (a) Top: bright-field transmission micrographs of a fragment of a droplet of S_{60}-B_{40} ($T_g - T = 0\,^{\circ}\mathrm{C}$) at different times after deposition, specified in hours after $t1$–4. The double-headed arrow points to large cracks that initially expand over time; the triple-headed arrow points to smaller cracks that start healing shortly after their formation. See Supplementary Movie 3 in ref. 25 for the full time series. **Bottom:** normalized intensity versus time, averaged over the squares depicted in the top frame at the edge (●) and centre (▲). The numbered arrows indicate the drying times for the top frames. The black solid lines are fits to Equation (3.1), with $t_{1/2} = 2.8$ h and $\tau_{heal} = 0.59$ h for the edge, and $t_{1/2} = 1.7$ h and $\tau_{heal} = 0.36$ h for the centre. **(b)** Scanning electron micrographs of healing cracks in the centre of the droplet in (a) at $t2$. The bottom image is a magnification of the delineated region in the top image.

over time. The droplet becomes progressively more homogeneous upon the healing of increasingly large cracks, and after 30 h (Figure 3.6a, $t4$) all the smaller cracks have vanished and a largely transparent film remains. Initially, the two large cracks in the middle and top left expand, caused by a net flow of polymer away from these large cracks towards the smaller cracks, but even these largest cracks heal eventually.

Crack healing is driven by the minimization of the polymer surface energy, analogous to so-called 'dry sintering' of particles. However, sintering usually refers to the fusion of particle pairs, implying closure of cracks with a length scale on the order of the particle size.[37,38] The typical time scales of this short-range polymer interdiffusion are much smaller than the time scales of macroscopic crack closure; for the latter, long-range creeping polymer flow is required. This scale-dependent variation in healing rate becomes apparent upon zooming in to healing cracks, as shown in Figure 3.6b for the centre of the droplet in Figure 3.6a at $t2$ = 3 h. In the high-magnification image (bottom panel), the small cracks at the lower right have almost disappeared and have a smooth circumference, whereas the large crack at the left still shows the substrate underneath it and has rather rough walls. Note that the polymer bridges do not originate from polymer diffusion across opposing faces but from coalescence within bridges of particles. Instead, the cracks heal by polymer flow from the sides into the crevice upwards and from the crack tips inwards, culminating in a completely levelled film.

Remarkably, we find a similar sequence of crack healing for the droplets with $T_g - T$ = 8 °C and 13 °C, which are well below the polymer glass transition temperature (Figure 3.4, first column). At first the smaller cracks self-heal while the largest cracks expand – up to a width of ~15 μm. However, after 10 days of ageing also the largest cracks disappear, and the film is indistinguishable from the low-T_g film in Figure 3.3. Remnants of the coffee-ring effect are still visible in the thicker outer ring relative to the centre. It appears that this sequence of crack healing is universal among our droplets, with only the absolute times being different, implying a universal mechanism governed by a single time scale. As the rate of crack healing increases with decreasing $T_g - T$ (compare e.g. Figure 3.4 with Figure 3.6), this time scale is likely associated with viscous flow.

The potential for crack healing is generally not considered for polymer films with T_g above room temperature because of the low polymer mobility in the glassy state. However, the glass transition is continuous and therefore involves a continuous change in the polymer mobility, which suggests that polymer flow at $T_g > T$ may still occur at a reduced rate. Earlier research has demonstrated that polymer interdiffusion across interfaces may indeed persist up to $T_g - T$ as high as 50–126 °C for sufficiently thin films.[17–22]

Using time-lapse sequences recorded at long intervals with electron microscopy, we can closely probe the progression of particle deformation and coalescence that accompany the self-healing of cracks. Both in the centre and at the edge of the droplet with $T_g - T = 13$ °C, we find that the particles become increasingly deformed over time and gradually close all the voids (Figure 3.4, the second and third column, respectively). Concurrently, the particles start to coalesce: whereas after 4 h of ageing still all the interparticle boundaries are visible, after 48 h individual particles are not discernible any more. Earlier reports using environmental SEM demonstrate the universality of this sequence of deformation, void closure and coalescence,[15,39,40] yet always at T_g close to or below room temperature.

Strikingly, these self-healing sequences are even observed to some extent for particles with $T_g - T = 41$ °C, which are highly glassy and rigid. After 10 days of ageing, most particles are connected by small 'necks' (Figure 3.7a, last column), implying that some polymer chains have interdiffused across the particle boundaries. These necks are not artefacts because their appearance is independent

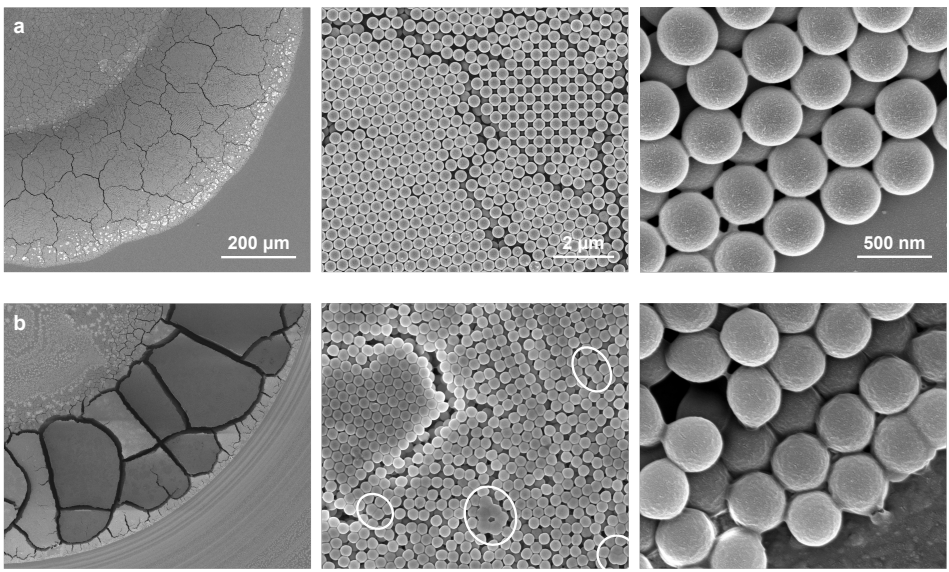

Figure 3.7. Typical SEM images of a droplet of S_{80}-B_{20} ($T_g - T = 41$ °C) after **(a)** 10 days and **(b)** 6 years of ageing. The first column displays a quadrant of the droplet, the second column gives a magnification of the centre, and the last column shows a high magnification of the contact line. The scale bars apply to both rows. The ellipses in (b) indicate partially coalesced groups of particles. The tiny cracks are artefacts caused by the sputter-coating.

of the SEM accelerating voltage. Considering the relatively high polydispersity index of this polymer of 3.3, these interdiffused polymer chains are probably the lowest-M_w species that are usually near the particle surface.[41] Nevertheless, the polymer mobility goes beyond superficial chains when given ample time: after 6 years of ageing, signs of long-range particle deformation and even sintering are apparent (Figure 3.7b). Furthermore, the primary cracks have significantly expanded up to ten times their original width, due to particle deformation and consequent compression of the inter-crack regions. These findings clearly illustrate the concept of the Deborah number (De); defined as the ratio between the characteristic relaxation time and the observation time. Low Deborah numbers indicate fluid-like behaviour. Considering a single experimental time scale, De rapidly increases with increasing polymer T_g, yet even the most slowly relaxing polymer may flow when given enough patience.

As noted above, we suspect a single mechanism of crack healing governed by the typical time scale of viscous flow. To determine this time scale, we again measure $\overline{I}$ at the edge and centre of droplets, but over extended periods, as shown in the bottom panel of Figure 3.6a for a sample with $T_g - T = 0$ °C. After drying and cracking, we observe an initial transient, yet this is followed by a gradual increase in the transmitted intensity due to crack healing, ultimately reaching a plateau. All curves of crack healing are well described by the following sigmoidal function:

$$\overline{I(t)} = \overline{I_{\text{min}}} + \frac{\Delta\overline{I_{\text{heal}}}}{1 + \exp\left(\frac{t_{1/2} - t}{\tau_{\text{heal}}}\right)} \tag{3.1}$$

where $\Delta\overline{I_{\text{heal}}}$ is the difference between the plateau $\overline{I}$ after crack healing and $\overline{I_{\text{min}}}$; $t_{1/2}$ is the time at which $\overline{I} = \overline{I_{\text{min}}} + \Delta\overline{I_{\text{heal}}}/2$; and τ_{heal} determines the slope at $t = t_{1/2}$.

A possible explanation for this sigmoidal shape is the wide distribution of crack sizes and the concomitant wide range of self-healing times: first, the tiniest cracks heal, but their small size prevents observing this process with the bright-field microscope, causing the initially constant intensity after cracking; then, progressively larger cracks heal, leading to a steady increase in $\overline{I}$; finally, all the small and intermediate cracks have healed and the intensity reaches a plateau. The intensity at this plateau is considerably higher than the intensity before cracking, which reflects the dissolving of the initially present crystal defects into a continuous polymer film. Note that we exclude the evolution of the largest cracks from this measurement because of their dissimilar healing sequence.

Equation (3.1) contains two characteristic parameters that quantify the crack healing: $t_{1/2}$, which is the time after which half of the small and intermediate cracks have healed, and τ_{heal}, which is the typical time scale of healing of the

intermediate cracks. We obtain $t_{1/2}$ from the unfitted data and τ_{heal} from the most optimal sigmoidal fit. In the following, we focus on τ_{heal} because it is a direct measure of the rate of crack healing, whereas $t_{1/2}$ is in fact a convolution of the rate of healing and the crack density.

We observe a clear increase in the characteristic time scale of crack healing with increasing $T_g - T$ (Figure 3.8), which confirms the positive relation between τ_{heal} and the viscosity; an increase of the latter slows down the viscous flow required for cracks to heal. For $t_{1/2}$ we find very similar trends (Appendix Figure 3.A.3). We cannot specify the exact τ_{heal} and $t_{1/2}$ for the highest-T_g droplet, because the polymer mobility is so low that even after 6 years of ageing the cracks have not visibly healed. Despite distinct evidence of particle-level plasticity, this droplet remains completely cracked and opaque. We do not observe crack healing at any level (Figure 3.7b). On the basis of this observation, we make a distinction between self-healing and presumed permanent cracks, with the tentative transition region marked grey in Figure 3.8. The broadness of this transition is due not only to the lack of data points but also to the exceeding difficulty in measuring the precise transition point, as experiments at $t = \infty$ are not possible. We therefore use the word 'permanent' to denote absence of self-healing on an experimental time scale. Using this definition, we can subdivide the development of cracks into three distinct regimes: no crack formation, crack self-healing, and permanent cracks.

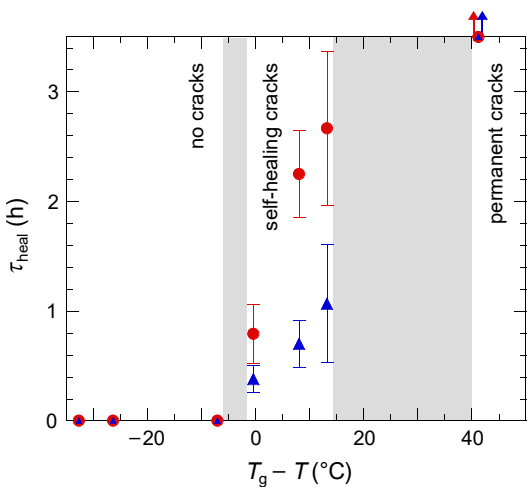

Figure 3.8. Typical time scale of healing of intermediate cracks, as obtained from the fits of Equation (3.1) to the sigmoidal increase in intensity after cracking, both for the edge (●) and centre (▲). Each point is the average of three measurements; the error bars represent the standard deviations. The grey vertical bars mark the transition regions between absence and presence of cracks, and between self-healing and permanent cracks.

These three regimes are schematically depicted in the flow diagram in Figure 3.9. In addition, the diagram includes the laterally inhomogeneous drying profile that is characteristic of the droplet geometry. The first transition from absence to presence of cracks occurs at $T_g - T = -5$ °C: particles below this transition deform and coalesce already during drying to yield a continuous film, whereas particles above this transition do not deform considerably during drying, and the droplets crack massively. The second transition cannot be defined precisely, and therefore we use the approximate average between the self-healing and permanently cracked regimes in Figure 3.8, which is $T_g - T \approx 30$ °C. Above this transition, formed cracks are permanent, yet cracks below this transition show a surprising potential for self-healing. The crack healing is accompanied by continued particle deformation and coalescence after drying, culminating in a film devoid of defects. Nevertheless, further research into the molecular-scale homogeneity is needed to assess the full extent of self-healing. Although the cracks and interstitial voids have morphologically healed, the mechanical and barrier properties of the healed films may be compromised.

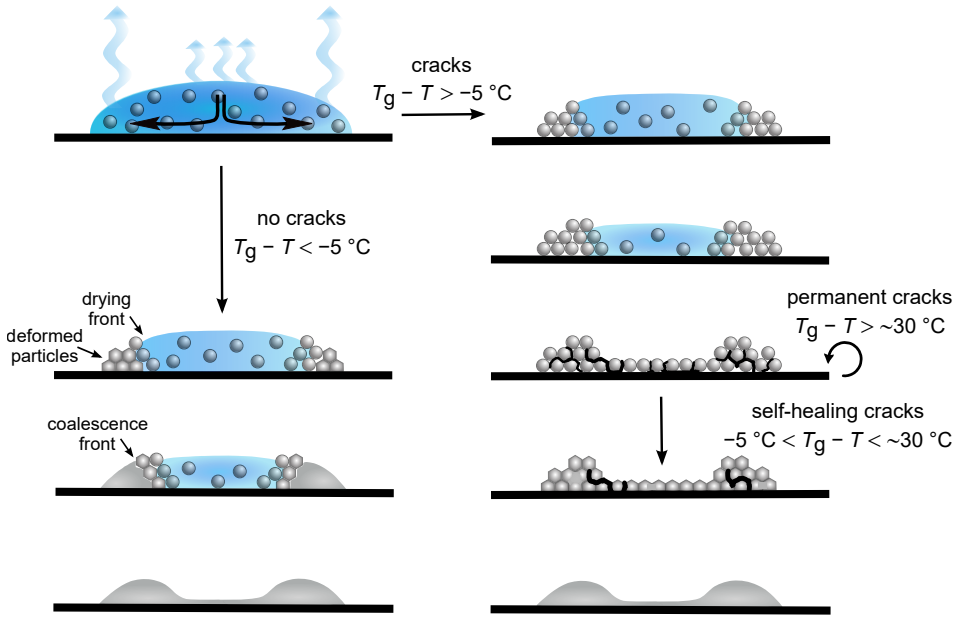

Figure 3.9. Schematic of the different regimes of crack development observed in drying dispersion droplets. The transition temperatures are estimated from Figure 3.8. The top left image illustrates the coffee-ring effect: increased evaporation at the edges gives rise to a net outward flow of solvent which drags particles towards the contact line.

3.4 Concluding remarks

Both the drying and ageing of polymer dispersion droplets depend strongly on the polymer T_g. During drying, the T_g affects the subtle interplay of evaporation, particle deformation and coalescence, leading to either crack-free or severely cracked droplets. However, this distinction is not necessarily permanent, as formed cracks may self-heal over time. The rate of crack healing decreases with increasing T_g, yet the typical sequence of healing appears to be universal and governed by the time scale of viscous flow. We therefore conclude that the factors T_g and time cannot be considered separately from each other: by giving high-T_g droplets more time to age, these droplets may reach the same homogeneity as low-T_g droplets shortly after drying. Our research thus provides a way to produce relatively strong and non-sticky films on the long term. We also believe that the subdivision into distinct regimes of coalescence, cracking, and crack healing is more general and can be extended to similar systems with variations in the polymer chemistry and film geometry.

Acknowledgements

We thank Marcel Giesbers, Elbert van der Klift, and Herman de Beukelaer for technical assistance. We thank the Wageningen Electron Microscopy Centre (WEMC) of Wageningen University & Research for access to their facilities.

3.A Appendix

3.A.1 Effects of the concentration of chain-transfer agent

During the particle synthesis, we add not only styrene, *n*-butyl acrylate and ACVA initiator to the reaction mixture, but also the chain-transfer agent 1-octanethiol, which allows controlling the molecular weight of the polymer. A chain-transfer agent (CTA) continuously transfers the polymerization reaction from one polymer chain to another, thus decreasing the average polymer length, without significantly altering the polymerization rate. In addition, it suppresses undesirable crosslinking.

In this chapter, we systematically investigate the effects of the polymer T_g at a fixed CTA concentration of 0.10 wt% (relative to the dry weight). Yet, we have also varied the CTA concentration from 0 to 0.20 wt% for the S_{50}-B_{50} dispersion, yielding a range in polymer molecular weight. The molecular weight distribution is an often overlooked factor in tuning the polymer viscosity.

Using dynamic light scattering, we find that the chain-transfer agent has a negligible effect on the particle size: at all CTA concentrations, the particles have approximately the same hydrodynamic radius and are close to monodisperse (Figure 3.A.1a). Also the polydispersity index of the polymers, measured using gel permeation chromatography, is roughly constant throughout this series (Figure 3.A.1b). By contrast, the number- and weight-average molecular weights of the polymers clearly confirm the predicted effect of the chain-transfer agent: higher 1-octanethiol concentrations indeed result in shorter polymer chains, with a dependence that is approximately linear (Figure 3.A.1c,d). This trend is likely not caused by different crosslinking densities, because Soxhlet extraction reveals a gel fraction smaller than 4% for polymer without added CTA, where the highest crosslinking density is expected.

This well-defined series of dispersions could serve to systematically evaluate the effects of polymer molecular weight. Even though M_n and M_w vary by only a factor 2 over the range of tested CTA concentrations, this difference may result in an order-of-magnitude change in viscosity, as reptation theory predicts for the zero-shear viscosity of entangled linear polymer melts[42] that $\eta_0 \sim M^3$. According to experiments,[43] $\eta_0 \sim M^{3.4}$. A ten times higher viscosity may result in considerably different polymer flow properties, yet it is uncertain whether these differences are macroscopically measurable on the experimental time scale. We leave this exploration to future research. In this chapter, we fix the CTA concentration at an intermediate value of 0.10%.

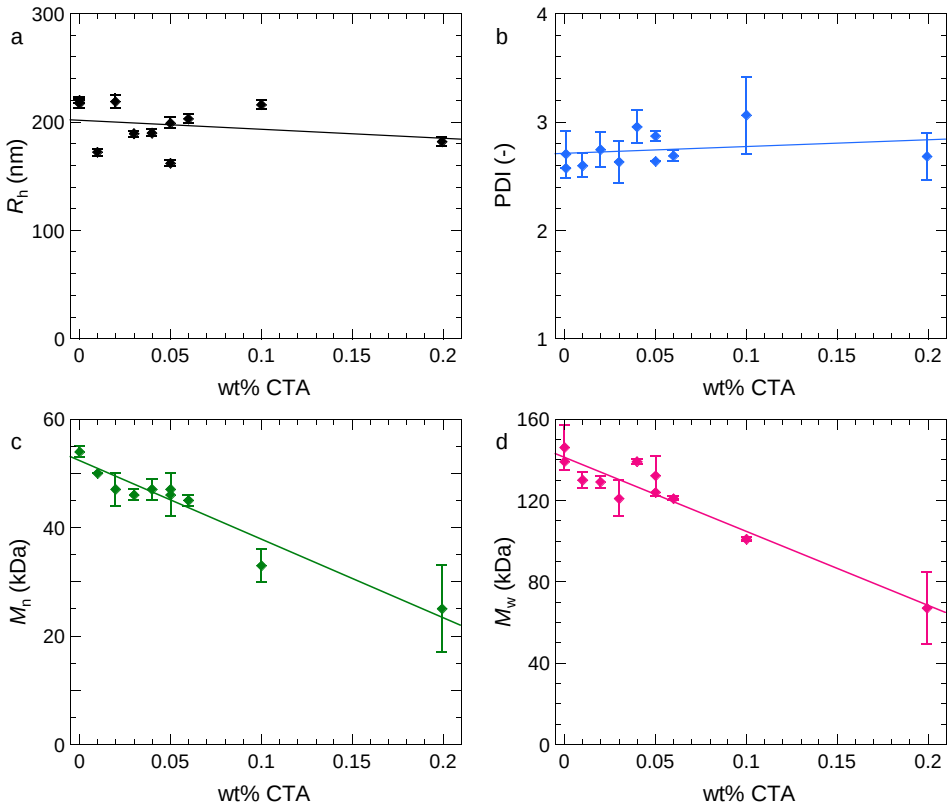

Figure 3.A.1. Effects of the concentration of chain-transfer agent 1-octanethiol on the properties of dispersion S_{50}-B_{50} ($T_g - T = -7$ °C). **(a)** Hydrodynamic radius of the particles, **(b)** polydispersity index of the polymer, **(c)** number-average molecular weight of the polymer, and **(d)** weight-average molecular weight of the polymer. The solid lines are linear fits to the data. The error bars represent the standard deviations, determined from 30 independent DLS measurements per sample (a) or from 3 independent GPC runs (b–d). The double points at 0 wt% and 0.05 wt% CTA represent different particle batches synthesized under the same conditions.

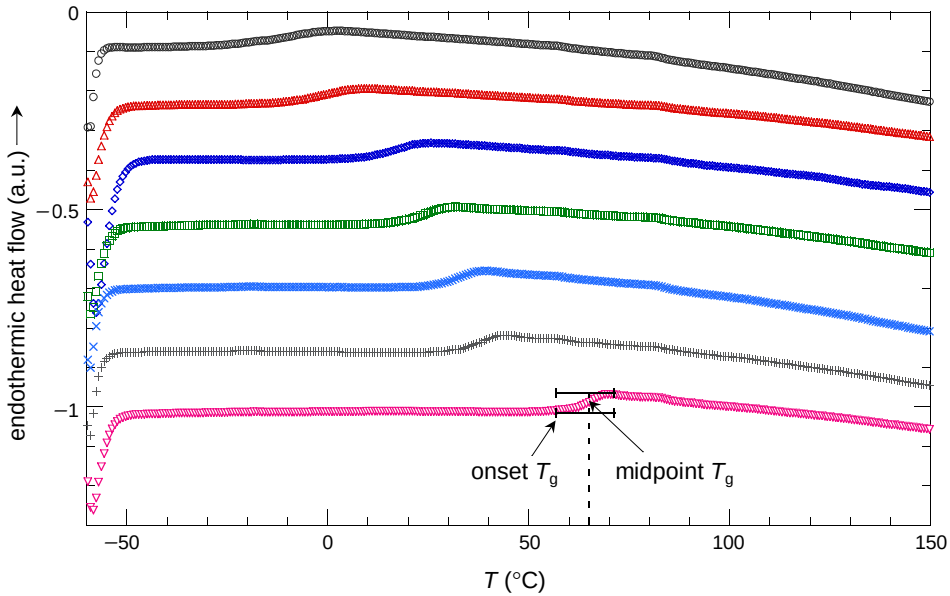

Figure 3.A.2. Second DSC heating runs of the polymers listed in Table 3.A.2 from top to bottom. The onset T_g is determined as the start of the change in heat capacity, and the midpoint T_g as the temperature at the midpoint of the change in heat capacity.

Table 3.A.2. Onset and midpoint T_g values obtained from the DSC thermograms in Figure 3.A.2.

Dispersion	Onset T_g (±2 °C)	Midpoint T_g (±1 °C)
S_{36}-B_{64}	−23	−10
S_{40}-B_{60}	−15	−3
S_{50}-B_{50}	8	16
S_{60}-B_{40}	16	23
S_{64}-B_{36}	24	31
S_{67}-B_{33}	29	36
S_{80}-B_{20}	57	64

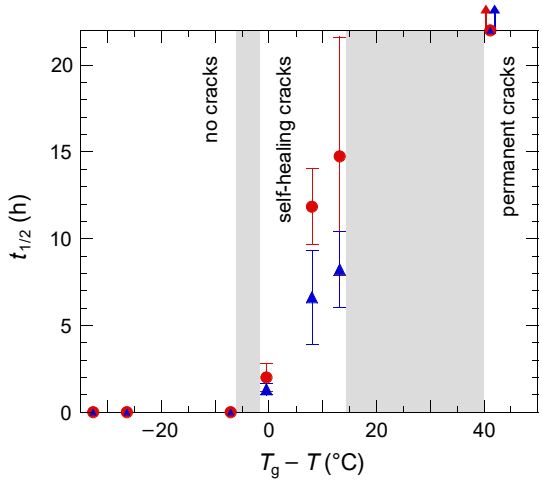

Figure 3.A.3. Time after which half of the small and intermediate cracks have healed ($t_{1/2}$), as derived from the intensity curves of crack healing, both for the edge (●) and centre (▲). These values are used in Equation (3.1) to fit the sigmoidal increase in $\bar{I}$. Each data point is the average of three measurements; the error bars represent the standard deviations. The grey vertical bars mark the transition regions between absence and presence of cracks, and between self-healing and permanent cracks, which are identical to those in Figure 3.8.

References

[1] B.-J. de Gans, P. C. Duineveld, U. S. Schubert. *Adv. Mater.* **16**, 203–213 (2004).

[2] D. A. Ansdell, *Paint and surface coatings: theory and practice* (Woodhead Publishing Ltd.: Cambridge, UK, 1999), chap. 10.10, pp. 461–472.

[3] P. A. Steward, J. Hearn, M. C. Wilkinson. *Adv. Colloid Interface Sci.* **86**, 195–267 (2000).

[4] R. D. Deegan, O. Bakajin, T. F. Dupont, G. Huber, S. R. Nagel, T. A. Witten. *Nature* **389**, 827–829 (1997).

[5] Á. G. Marín, H. Gelderblom, D. Lohse, J. H. Snoeijer. *Phys. Rev. Lett.* **107**, 085502 (2011).

[6] A. Crivoi, F. Duan. *Sci. Rep.* **4**, 4310 (2014).

[7] X. Chen, V. Boyko, J. Rieger, F. Reinhold, B. Reck, J. Perlich, R. Gehrke, Y. Men. *Soft Matter* **8**, 12093–12098 (2012).

[8] X. Chen, S. Fischer, Y. Men. *Langmuir* **27**, 12807–12814 (2011).

[9] J. C. Haley, Y. Liu, M. A. Winnik, W. Lau. *J. Coat. Technol. Res.* **5**, 157–168 (2008).

[10] Y. Zhang, Y. Qian, Z. Liu, Z. Li, D. Zang. *Eur. Phys. J. C* **37**, 14084 (2014).

[11] A. F. Routh, W. B. Russel. *Langmuir* **15**, 7762–7773 (1999).

[12] A. F. Routh, W. B. Russel. *Ind. Eng. Chem. Res.* **40**, 4302–4308 (2001).

[13] E. Gonzalez, M. Paulis, M. J. Barandiaran, J. L. Keddie. *Langmuir* **29**, 2044–2053 (2013).

[14] J. G. Brodnyan, T. Konen. *J. Appl. Polym. Sci.* **8**, 687–697 (1964).

[15] C. C. Roberts, L. F. Francis. *J. Coat. Technol. Res.* **10**, 441–451 (2013).

[16] M. S. Tirumkudulu, W. B. Russel. *Langmuir* **21**, 4938–4948 (2005).

[17] Y. M. Boiko, R. E. Prud'Homme. *Macromolecules* **30**, 3708–3710 (1997).

[18] D. Kawaguchi, K. Tanaka, T. Kajiyama, A. Takahara, S. Tasaki. *Macromolecules* **36**, 1235–1240 (2003).

[19] Y. M. Boiko, J. Lyngaae-Jørgensen. *J. Macromol. Sci., Part B: Phys.* **43**, 695–710 (2004).

[20] Y. M. Boiko, J. Lyngaae-Jørgensen. *Polymer* **45**, 8541–8549 (2004).

[21] Y. M. Boiko, A. Bach, J. Lyngaae-Jørgensen. *J. Polym. Sci., Part B: Polym. Phys.* **42**, 1861–1867 (2004).

[22] Y. M. Boiko. *Colloid Polym. Sci.* **289**, 1847–1854 (2011).

[23] J. Appel, S. Akerboom, R. G. Fokkink, J. Sprakel. *Macromol. Rapid Commun.* **34**, 1284–1288 (2013).

[24] J. M. Barton. *J. Polym. Sci., Part C* **30**, 573–597 (1970).

[25] H. M. van der Kooij, M. de Kool, J. van der Gucht, J. Sprakel. *Langmuir* **31**, 4419–4428 (2015). **(This chapter)**

[26] Y. Ma, H. T. Davis, L. E. Scriven. *Prog. Org. Coat.* **52**, 46–62 (2005).

[27] Y. O. Popov. *Phys. Rev. E* **71**, 036313 (2005).

[28] M. A. Winnik, J. Feng. *J. Coat. Technol. Res.* **68**, 39–50 (1996).

[29] F. T. Carter, R. M. Kowalczyk, I. Millichamp, M. Chainey, J. L. Keddie. *Langmuir* **30**, 9672–9681 (2014).

[30] H. Feng, J. Sprakel, D. Ershov, T. Krebs, M. A. Cohen Stuart, J. van der Gucht. *Soft Matter* **9**, 2810–2815 (2013).

[31] Q. Nawaz, Y. Rharbi. *Langmuir* **26**, 1226–1231 (2010).

[32] E. R. Dufresne, E. I. Corwin, N. A. Greenblatt, J. Ashmore, D. Y. Wang, A. D. Dinsmore, J. X. Cheng, X. S. Xie, J. W. Hutchinson, D. A. Weitz. *Phys. Rev. Lett.* **91**, 224501 (2003).

[33] W. P. Lee, A. F. Routh. *Langmuir* **20**, 9885–9888 (2004).

[34] L. Goehring, W. J. Clegg, A. F. Routh. *Phys. Rev. Lett.* **110**, 024301 (2013).

[35] M. S. Tirumkudulu, W. B. Russel. *Langmuir* **20**, 2947–2961 (2004).

[36] K. B. Singh, M. S. Tirumkudulu. *Phys. Rev. Lett.* **98**, 218302 (2007).

[37] J. Frenkel. *J. Phys. (Paris)* **9**, 385–391 (1945).

[38] R. E. Dillon, L. A. Matheson, E. B. Bradford. *J. Colloid Sci.* **6**, 108–117 (1951).

[39] J. L. Keddie, P. Meredith, R. A. L. Jones, A. M. Donald. *Macromolecules* **28**, 2673–2682 (1995).

[40] E. Gonzalez, C. Tollan, A. Chuvilin, M. J. Barandiaran, M. Paulis. *ACS Appl. Mater. Interfaces* **4**, 4276–4282 (2012).

[41] E. Odrobina, M. A. Winnik. *Macromolecules* **34**, 6029–6038 (2001).

[42] M. Doi, S. F. Edwards, *The theory of polymer dynamics*, vol. 73 (Clarendon Press, Oxford, 1988).

[43] G. C. Berry, T. G. Fox, *Advances in polymer science* (Springer, 1968), pp. 261–357.

Chapter 4

A mechanistic view of drying suspension droplets

This chapter is based on: Hanne M. van der Kooij, Gea T. van de Kerkhof and Joris Sprakel, 'A mechanistic view of drying suspension droplets', *Soft Matter* **12**, 2858–2867 (2016).

Abstract

When a dispersion droplet dries, a rich variety of spatial and temporal heterogeneities emerge. Controlling these phenomena is essential for many applications yet requires a thorough understanding of the underlying mechanisms. Although the process of film formation from initially dispersed polymer particles is well documented and is known to involve three main stages – evaporation, particle deformation and coalescence – it is impossible to fully disentangle the effects of particle deformation and coalescence, as these stages are closely linked. We circumvent this problem by studying suspensions of colloidal rubber particles that are incapable of coalescing. Varying the crosslink density allows us to tune the particle deformability in a controlled manner. We develop a theoretical framework of the main regimes and stresses in drying droplets of these suspensions, and validate this framework experimentally. Specifically, we show that changing the particle modulus by less than an order of magnitude can completely alter the stress development and resulting instabilities. Scanning electron microscopy reveals that particle deformability is a key factor in stress mitigation. Our model is the suspension equivalent of the widely used Routh–Russel model for film formation in drying dispersions, with additional focus on lateral nonuniformities such as cracking and wrinkling inherent to the droplet geometry, thus adding a new dimension to the conventional view of particle deformation.

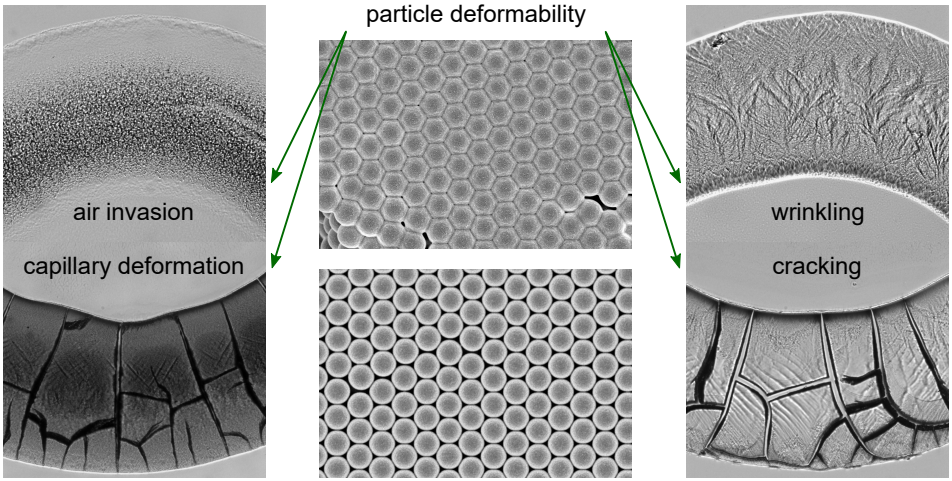

Particle deformability plays a central role in the mechanisms of suspension droplet drying.

4.1 Introduction

Water-based paints and inks are gaining ground on organic solvent-based formulations, as the low emission of volatile organic compounds from drying water-based coatings renders them more environmentally friendly and healthier for users. However, replacing the organic solvent with water complicates all stages of drying, thereby impeding the formation of a homogeneous film. The main complicating factor is the state of the polymeric binder. Because of the required water resistance of the dried coating, this binder phase, which provides cohesion to the final film, is inherently water-insoluble, implying that it can exist only as dispersed particles. In addition to mere concentration upon drying, as is the case for freely dissolved polymers, the dispersed particles must ultimately deform and coalesce to create a coherent film.[1–6] These requirements pose contradictory demands to the dispersion: on the one hand, it must be stable on the shelf and produce durable dry coatings, yet on the other hand, the particle stability and hardness must be sufficiently low to allow for rapid deformation and coalescence in the final drying stage. To meet these demands, it is imperative to have a clear understanding of the governing forces and their effects on the drying process.

Poor control over the subtle balance of forces in drying dispersions can be disastrous to the final film. Common types of failure are fracture and delamination,[7–12] wrinkling,[13] and undesired opacity by voids or particle flocculation.[14–16] Owing to the plethora of research on these phenomena, valuable descriptive and predictive models have been proposed that encompass the key parameters in dispersion drying.[17] Most notably, Routh and Russel have developed a theoretical framework for different regimes of film formation, based on the relative rates of evaporation and particle deformation.[18] Although their model has proven both fundamentally[19] and practically[19,20] effective, it lacks a clear distinction between deformation and coalescence of the binder particles. Indeed, these two processes are closely connected and occur partially simultaneously, precluding their disentanglement. Eliminating either of the two is required to fully uncover the mechanisms underlying the different stages of drying.

In addition to the temporal dependence of the above described processes, the drying of water-based dispersions has a strong spatial dependence. Local accumulation of particles or dissolved components may give rise to undesirable phenomena such as skin formation[21–23] and Marangoni flow-induced nonuniformities.[24] Because of their complexity, spatial heterogeneities are typically studied only in the vertical direction in large coatings.[17,21,25] For applications involving small quantities, however, horizontal heterogeneities are far from negligible. A widespread problem in inkjet printing and spray painting is the so-called 'coffee-ring effect':

small dispersion droplets that are pinned to the surface leave ring-shaped stains upon drying. This peculiar shape arises from a net outward flow of water and constituents, due to a high evaporation rate at the contact line combined with the constrained horizontal shrinkage of the droplet.[26] The coffee-ring effect causes not only height gradients in dried paint and ink droplets, but also gradients in particle packing,[22,27,28] particle deformation and coalescence,[29] and crack density (Chapter 3).[13,30,31] Although the droplet geometry adds extra difficulties to the drying process, it is of practical interest to elucidate the principal mechanisms by which these gradients develop in time and space.

A key parameter in all drying stages is the deformability of the binder particles. A typical way to tune the particle deformability is by changing the glass transition temperature (T_g) of the polymer (Chapter 3).[20,32,33] Upon increasing T_g beyond room temperature, the polymer phase transitions from a liquid melt into a solid glass, accompanied by a sharp rise in polymer viscosity. The main disadvantage of this strategy is the close correlation between the T_g dependence of particle deformability and that of coalescence. To study the effects of particle deformation alone on the different drying stages and stresses, the possibility of coalescence must be excluded.

In this chapter, we achieve complete disentanglement of particle deformation and coalescence by crosslinking the polymer phase. We vary the crosslink density to yield a wide range of such colloidal rubber particles with varying modulus. Using bright-field transmission microscopy, we examine drying droplets of these suspensions both qualitatively and quantitatively, and find that all drying phenomena show a marked transition around the same crosslink density. Scanning electron microscopy reveals that the governing factor in these transitions is the potential for particle deformation. We support our experimental findings by a theoretical framework describing the relation between particle modulus and four principal drying-induced stresses.

4.2 Theoretical considerations

To arrive at a complete description of drying suspension droplets, we start by establishing a theoretical foundation for the main drying stages and stresses. We consider suspensions of colloidal rubber particles with elastic moduli of 10^6 and 10^7 Pa, typical of sparsely and densely crosslinked polymer networks. We refer to these as 'soft' and 'hard' particles, respectively. The drying process of rubber suspensions can be subdivided into three main stages: (I) concentration, (II) air invasion, and (III) capillary deformation. These stages are depicted schematically in Figure 4.1a; the corresponding volume fractions of water (φ_w), polymer (φ_p)

and air (φ_a) are plotted versus time for soft and hard particles in Figure 4.1b and c, respectively. Here we consider a thin vertical slice of the drying droplet and neglect vertical heterogeneities. In the first stage of drying, the bulk of the water evaporates, transforming the suspension into a close packing of particles that is saturated with water. The decrease in φ_w equals the increase in φ_p. Further evaporation of water allows air to invade the packed bed of particles, creating interparticle interstices separated by pendular water bridges (stage II). Simultaneously, the capillary pressure generated by these bridges rises, causing the particles to gradually deform and form faceted polyhedra (stage III). The rate of capillary deformation depends on the ratio of the capillary stress to the particle modulus, which is considerably higher for soft particles and progressively increases upon thinning of the capillary bridges. Soft particles will ultimately form a void-free film with $\varphi_a \approx 0$ and $\varphi_p \approx 1$, whereas hard particles will not deform sufficiently to close all the voids, leaving φ_a at a non-negligible level.

In addition to the capillary stress, we distinguish three other major stresses that affect the droplet homogeneity. They are shown schematically in Figure 4.2a. Two are present directly at the start of drying: hydrodynamic stress (σ_h) and elasto-capillary stress (σ_{ec}). Hydrodynamic stress arises from the directional water flow caused by the coffee-ring effect, which transports particles to the edge and exerts a compressive force on the depositing particles.[26] The elasto-capillary

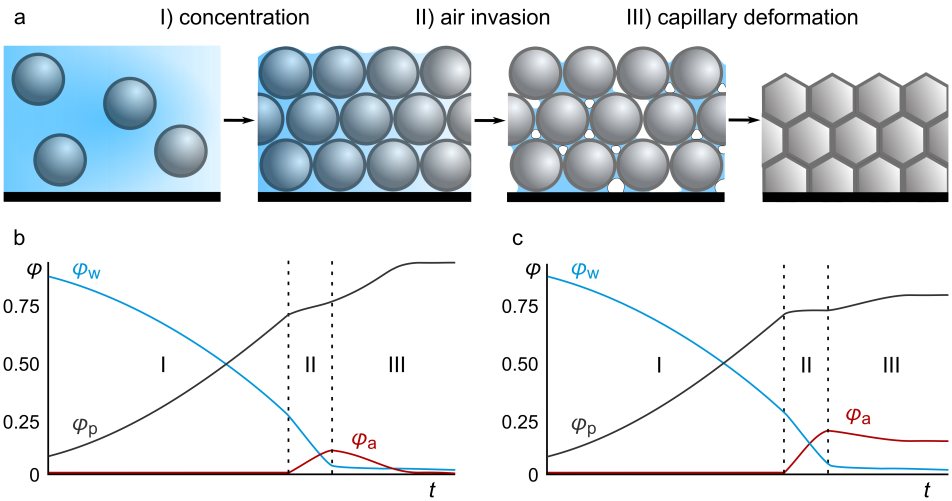

Figure 4.1. (a) Schematic of the principal stages during drying of a suspension of deformable colloids. Estimates for the volume fractions of water (φ_w), polymer (φ_p) and air (φ_a) throughout these stages are plotted for soft and hard particles in **(b)** and **(c)**, respectively.

stress also results from the coffee-ring effect: the central fluid domain attempts to minimize its surface energy and therefore pulls on the packed outer ring, effectively stretching the packed bed of particles inwards and potentially causing surface wrinkling.[13,34,35] Shrinkage stress (σ_s) and capillary stress (σ_c) dominate the last stages of drying. They do not apply to the droplet geometry alone, but to drying suspensions in general. Shrinkage stress arises after evaporation of the last bulk water, when continuing evaporation exerts a compressive force on the packed particles and induces a further increase in their volume fraction. Because the pinned contact line constrains the droplet shrinkage horizontally and thereby impedes relaxation of the shrinkage stress, cracks may form to relax σ_s alternatively. This is rapidly followed by air invasion and a rise of the capillary stress.

The magnitudes of these stresses relative to critical values determine the droplet homogeneity from the macroscopic to the microscopic level. For example, the

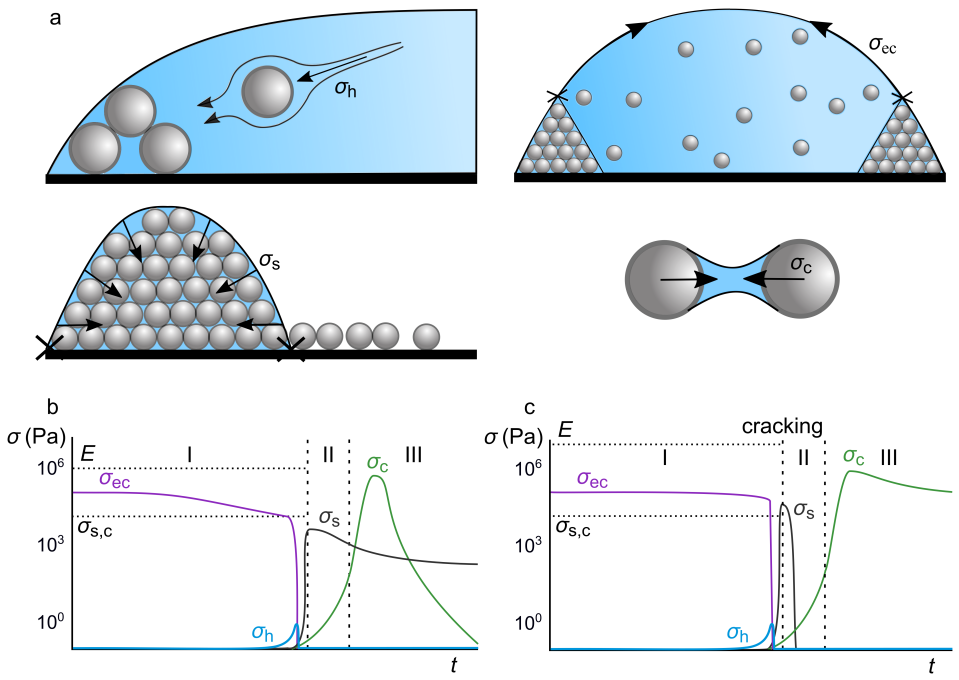

Figure 4.2. **(a)** Schematics of the four main stresses acting in a drying suspension droplet: hydrodynamic stress (σ_h), elasto-capillary stress (σ_{ec}), shrinkage stress (σ_s) and capillary stress (σ_c). Estimates for the time evolution of these stresses are plotted for soft and hard particles in **(b)** and **(c)**, respectively. The regimes I to III are identical to those in Figure 4.1. The horizontal dotted lines represent the elastic modulus of the particles (E) and the critical shrinkage stress ($\sigma_{s,c}$).

ratio of the shrinkage stress to the critical shrinkage stress sets the propensity for macroscopic cracking, and the ratios of the hydrodynamic and capillary stress to the particle modulus (E) determine the microscopic homogeneity. We therefore use scaling arguments to estimate the relative importance of the four stresses during droplet drying. The evolution of these stresses throughout the three aforementioned drying stages is plotted for soft and hard particles in Figure 4.2b and c, respectively.

The hydrodynamic stress on spherical particles equals the Stokes force divided by the particle surface area:

$$\sigma_{\mathrm{h}} = \frac{\xi\, v}{R^2} = \frac{6\pi\, \eta\, v}{R} \tag{4.1}$$

where ξ is the Stokes frictional coefficient, v is the approximate velocity of the particles, R is the particle radius, and η is the viscosity of the fluid. On the basis of earlier research, we estimate the radial particle velocity to start around 1 μm/s and rise to 10 μm/s near the end of drying, according to the rush-hour effect.[27,29] Using an order-of-magnitude approximation with R = 100 nm and η = 1 mPa·s gives a consequent increase of σ_{h} from 10^{-1} to 10^{0} Pa, before falling to zero when the bulk water has evaporated. Nevertheless, the maximum σ_{h} is still amply below the elastic moduli of the particles, and we therefore consider σ_{h} negligible.

The elasto-capillary stress is a surface phenomenon, acting only on the top layer of particles. Its horizontal component can be expressed as:

$$\sigma_{\mathrm{ec}} = \frac{\gamma\, \cos(\theta)}{d} \tag{4.2}$$

where γ is the liquid–air interfacial tension, θ is the contact angle between the droplet and the substrate, and d is the thickness of the top layer. Assuming $\theta = 45°$ and d = 1 μm gives $\sigma_{\mathrm{ec}} \approx 10^5$ Pa. The elasto-capillary stress has its maximum value immediately after the first particles have been deposited at the edge. In droplets of soft particles, the top layer will deform and wrinkle because the elasto-capillary stress is significant compared to the particle modulus, thereby relaxing σ_{ec} by an estimated order of magnitude. For hard particles, the two orders-of-magnitude difference between σ_{ec} and E will prevent wrinkling. The elasto-capillary stress vanishes abruptly when the last bulk water has evaporated.

The propensity for cracking is determined by the ratio of the shrinkage stress to the critical shrinkage stress ($\sigma_{\mathrm{s,c}}$). Using the classical Griffith's criterion for equilibrium crack propagation[36] combined with the Routh–Russel stress–strain relation for a network of identical elastic spheres[37] gives the following expression for $\sigma_{\mathrm{s,c}}$:[38]

$$\sigma_{s,c} = 0.3754 \left(\frac{2\gamma}{h}\right)^{2/3} \left(\frac{E\, M\, \varphi_{rcp}}{2}\right)^{1/3} \tag{4.3}$$

where h is the film thickness at cracking, M is the coordination number, and φ_{rcp} is the particle volume fraction at random close packing. The derivation of this equation is based on balancing the increase in surface energy upon cracking with the release of elastic energy, the latter of which involves not only relaxation of the film but also unfavourable shear deformation of particles around the cracks.[39] Both E and φ_{rcp} depend on the crosslink density. In our order-of-magnitude approximation, however, we consider the differences in φ_{rcp} negligible. Using $h = 10^2$ μm, $M = 10$ and $\varphi_{rcp} = 1$ gives $\sigma_{s,c} \approx 10^4$ Pa for both $E = 10^6$ and 10^7 Pa. Soft particles will deform to reduce the shrinkage stress and thereby prevent σ_s from reaching $\sigma_{s,c}$, whereas hard particles cannot deform sufficiently fast and cause $\sigma_s > \sigma_{s,c}$. As a result, macroscopic cracks emerge which allow rapid relaxation of σ_s to a negligible value, consistent with experimental observations.[39,40] The shrinkage stress in films of soft particles will decrease more gradually and to a lesser extent, limited by the degree of particle deformation.[40]

We calculate the maximum capillary stress by dividing the maximum capillary force between two identical spheres[41] by the contact area:

$$\sigma_c = \frac{4\pi\, \gamma\, \cos(\theta)}{3R} \tag{4.4}$$

Assuming complete wetting, i.e. $\theta = 0°$, gives $\sigma_c \approx 10^6$ Pa. This is of the same order of magnitude as the modulus of the soft particles, but lower than that of the hard particles. Soft particles will therefore gradually deform over time, relieving the capillary stress. Hard particles will not deform considerably on an experimental time scale, allowing relaxation of σ_c only by evaporation of the capillary bridges. This relaxation will be slow and incomplete because traces of water will remain associated with the film.

4.3 Experimental details

4.3.1 Particle synthesis

n-Butyl acrylate (*n*BA), ethylene glycol dimethacrylate (EGDMA), sodium dodecyl sulphate (SDS), and potassium persulphate (KPS) are purchased from Sigma-Aldrich. All chemicals are used as received. Poly(*n*BA) particles with varying crosslink density are synthesized by a one-step emulsion polymerization. In a 100 mL one-neck round-bottom flask containing a 2 cm oval magnetic stirring bar,

the following components are mixed: 62.5 g of Milli-Q water, 20 mg of SDS to stabilize the particles during the polymerization, and a total of 7.5 g of *n*BA and the crosslinker EGDMA. The mol% EGDMA is calculated as $n_{\mathrm{EGDMA}}/(n_{\mathrm{EGDMA}} + n_{n\mathrm{BA}})$. The flask is sealed with a rubber septum and flushed with dry nitrogen for 15 min while stirring at 250 rpm, followed by 5 min stirring at 250 rpm at 60 °C. Subsequently, a solution of 75 mg of the initiator KPS in 5 mL of Milli-Q water is injected quickly into the water phase, after which the nitrogen inlet and outlet are removed. The reaction mixture is left for approximately 20 h at 60 °C while stirring at 250 rpm. It is subsequently filtered and dialysed extensively against Milli-Q water for one week, yielding a dispersion with a solids concentration of ~8–9 wt%. The resulting particles are slightly aspherical, inherent to the synthesis procedure which causes the crosslinks to not be fully homogeneously distributed across the particles. This effect has been observed before for polymer particles with the same crosslinks.[42]

4.3.2 Characterization of particles

The hydrodynamic radii (R) of the particles are determined using dynamic light scattering (DLS). These measurements are performed on an ALV instrument equipped with an ALV-7002 external correlator and a Cobolt Samba 300 mW DPSS laser operating at a wavelength of 532 nm. The suspensions are diluted and measured at a detection angle of 90° and a temperature of 23 ± 1 °C. The hydrodynamic radii increase slightly and roughly linearly with increasing crosslink density, as shown in Figure 4.3.

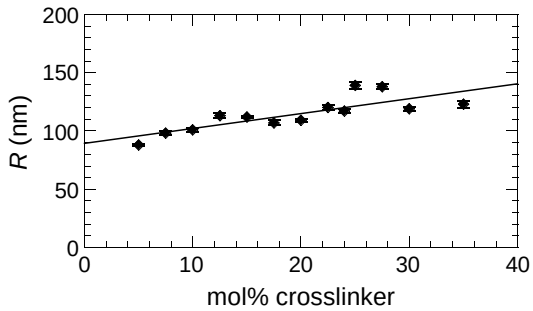

Figure 4.3. Hydrodynamic radii of the particles. The error bars represent the standard deviations, determined from 30 independent measurements per sample. The solid line is a linear fit to the data.

To enable complete elimination of coalescence, it is crucial that the fraction of non-crosslinked polymer chains in the particles is negligible. This fraction is determined for a suspension with 1 mol% crosslinker by Soxhlet extraction of the oven-dried polymer phase with chloroform. Overnight extraction at 75 °C gives a soluble polymer fraction of ~10%, implying that for all suspensions used in this study, with a minimum of 5 mol% crosslinker, the amount of non-crosslinked polymer is indeed negligible.

4.3.3 Drying of suspension droplets

Bright-field transmission microscopy

For analysis of the drying process, the suspensions are diluted to a concentration of 7 ± 0.5 wt%. 0.5 μL droplets are deposited on glass and dried in an enclosed, transparent chamber at a controlled temperature of 23 ± 1 °C and relative humidity of 40 ± 4%. The transmitted light intensity through the droplets is measured using a Nikon eclipse Ti-U inverted microscope in bright-field mode equipped with a CMOS camera (Thorlabs DCC1240C) and a 10× air objective (NA = 0.30, WD = 16.0 mm). The experiments for each suspension are performed in triplicate, with a frame rate of 10 fps and an exposure time of 30 ms. The resulting time-lapse image sequences are analysed by measuring the time evolution of the average transmitted intensity in a square area of 50×50 μm^2 at two locations: 100 μm from the contact line of the droplet, which we refer to as the 'edge', and 400 μm from the contact line, which we refer to as the 'centre'. We denote this pixel-averaged transmitted intensity as I. The square areas are consistently chosen to exclude cracks.

Because of the inherent delay involved in the sample deposition and camera focusing steps, the image acquisition cannot be started at exactly $t = 0$, with the delay ranging from 20 to 50 s. To allow for reliable averaging of the intensity curves of the different experiments per suspension, each curve is adjusted in two steps: first, from all t a single value is subtracted such that the local maxima of the curves recorded at the droplet edge overlap, thereby eliminating the variations in induction time. Second, all I are divided by the maximum intensity ($I_{\max}$) to account for variations in the initial transmission resulting from differences in the pre-acquisition drying of the samples and temporal variations in illumination power. The same transformations are performed to the curves recorded at the centre and edge of each sample.

Scanning electron microscopy

Dried droplets of the suspensions are analysed by scanning electron microscopy (SEM), 4 h after deposition. The samples are obtained by drying 0.5 μL of 7 ± 0.5 wt% droplets on silicon wafers with a natural oxide layer in an enclosed chamber at a controlled temperature of 23 ± 1 °C and relative humidity of 40 ± 4%. They are mounted on flat aluminium stubs with double-sided adhesive, conducting carbon tape. Charging of the samples is prevented by coating them with a 12 nm layer of iridium using a Leica EM SCD 500 sputter-coater. The SEM images are recorded on an FEI Magellan 400 field-emission SEM at an acceleration voltage of 5.0 kV.

4.4 Results and discussion

We validate and complement our theoretical framework by bright-field and scanning electron microscopy on drying suspension droplets. To achieve the desired range in particle modulus (E) from ~1 to 10 MPa, we use an inherently soft, low-T_g polymer that is crosslinked, resulting in submicron-sized rubber colloids. Upon increasing the crosslink density from 5 to 35 mol%, we find that the particles indeed transform from 'soft' to 'hard' on the time scale of drying. A side effect is a concomitant increase in particle radius of 1.5× (Figure 4.3), which likely results from a decrease in monomer solubility and proportionally lower number of particle nuclei in the reaction mixture. However, we assume that the effects from the seven-fold increase in particle modulus far outweigh possible effects from the particle size and therefore neglect the latter.

4.4.1 Drying stages and stresses

Typical time-lapse sequences of the transmitted intensity through droplets of soft and hard particles are shown in Figure 4.4a and b, respectively, with the corresponding full time series available as Supplementary Movies 1 and 2 in ref. 43. We clearly distinguish the three stages of concentration, air invasion and capillary deformation, as well as wrinkling and cracking instabilities dependent on the particle modulus. The drying process starts very similar for all suspensions: the coffee-ring effect causes transportation of the particles to the edge and their consequent packing, forming a consolidated outer ring surrounding the inner suspension.[3,26,28] The boundary manifests as a distinct, inward propagating front, which we refer to as the 'packing front' (Figure 4.4a, t1–2 and Figure 4.4b, t1, solid arrow).[37,44] The velocity of this front is initially constant at ~2 μm/s yet increases rapidly to ~50 μm/s near the end of stage I by the rush-hour effect.[27,29] The front velocity is independent of the crosslink density, confirming our hypothesis that

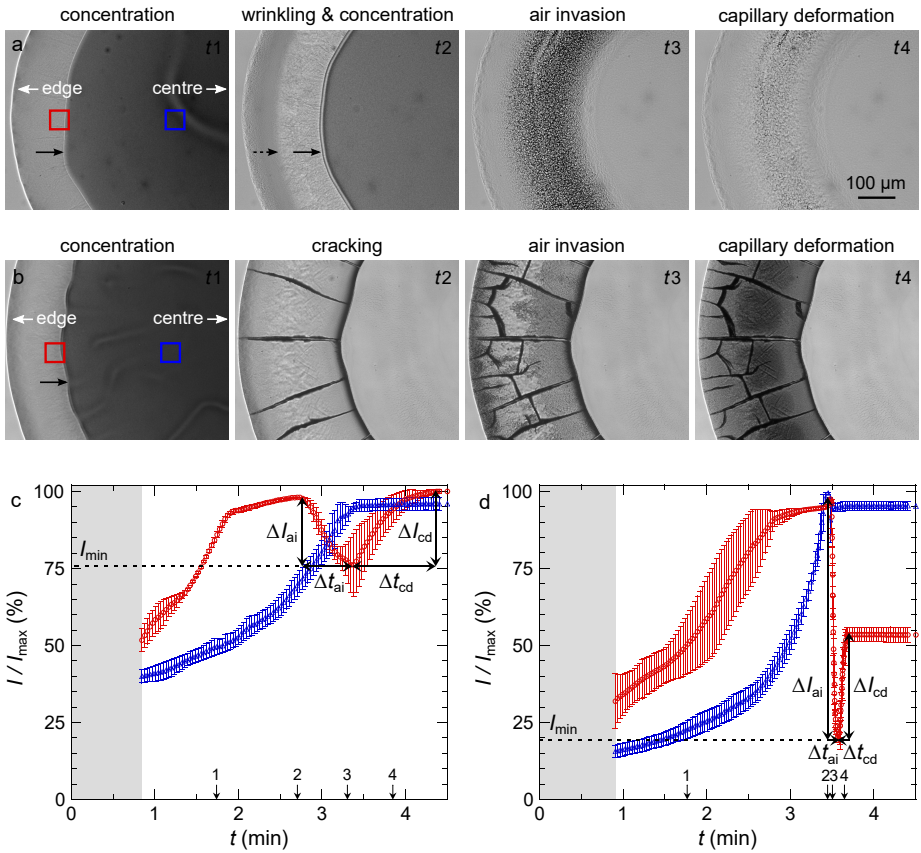

Figure 4.4. Time-lapse bright-field transmission micrographs of a drying droplet of particles with **(a)** 5 and **(b)** 35 mol% crosslinker. The scale bar applies to all micrographs. See Supplementary Movies 1 and 2 in ref. 43 for the full time series. The solid arrows point to inward propagating packing fronts, and the dashed arrow to a wrinkling front. The normalized intensity curves corresponding to (a) and (b) are plotted in **(c)** and **(d)**, respectively, averaged over the squares at the edge (●) and centre (▲), and averaged over three measurements. The error bars represent the standard deviations. The numbered arrows indicate the drying times for the micrographs. The grey vertical bars indicate the induction period between droplet deposition and onset of the measurement.

the hydrodynamic stress (σ_h) is negligible. Indeed, if σ_h would be significant compared to the particle modulus, it would deform the packing particles and lead to a consequent decrease of the evaporation rate. In that case, the propagation rate of the packing front should decrease with increasing particle deformability.[29,33]

Approximately 2 min after the start of drying, the elasto-capillary stress (σ_{ec}) comes into play and causes surface wrinkling. For soft particles, the wrinkles appear as a well-defined front that trails behind the packing front (Figure 4.4a, $t2$, dashed arrow), but with increasing mol% crosslinker the broadness of the front gradually increases and the extent of wrinkling decreases. This transition in the development of the wrinkles is likely due to changes in the ratio of σ_{ec} to the particle modulus. Surface wrinkling requires compression of the particles in the top layer, in order that this layer transforms from an assembly of discrete entities into a continuous structure.[45] Rigid particles do not deform considerably on the time scale of drying and hence reduce the potential for wrinkling. Soft particles do indeed deform sufficiently to allow wrinkling and consequent relaxation of σ_{ec}, in agreement with our theoretical predictions, yet the deformation is not instant and hence the wrinkling involves a lag time. This explains the appearance of the wrinkles as a distinct front behind the packing front.

The lack of deformation of hard particles also leads to the development of a high shrinkage stress (σ_s) near the end of stage I, inducing crack nucleation if σ_s exceeds the critical shrinkage stress (Figure 4.4b, $t2$–3). As a result, we find a sharp transition from absence to presence of cracks upon increasing the crosslink density from 17.5 to 20 mol%. Beyond 20 mol% crosslinker, the crack density is constant, similar to our findings in Chapter 3, Figure 3.5, where we varied the polymer T_g. Interestingly, the first cracks propagate radially (Figure 4.4b, $t2$), indicating the concentration of drying stresses along the direction of evaporation. Most secondary cracks join the existing cracks at angles close to 90° to relax the shrinkage stress most efficiently, as cracks release more energy perpendicular than parallel to their propagation direction[46,47] (Figure 4.4b, $t3$). Not surprisingly, the centre is largely devoid of cracks owing to the low film height. Only a few layers of particles adhere sufficiently strongly to the substrate to resist the coffee-ring effect and remain in the centre. The film thickness in the centre is therefore below the critical film thickness required for cracking.[48]

3 to 6 seconds after evaporation of the last bulk water, air invades the porous particle packing. The air fronts advance from the contact line and centre towards the top of the edge, displacing part of the water, which is clearly visible by the concomitant increase in refractive index fluctuations and consequent drop in transmitted light intensity (Figure 4.4a and b, $t3$). The pattern of front advancement is not homogeneous but is similar to invasion percolation.[11,49,50] In cracking

droplets, the fronts are particularly irregular owing to the enhanced air invasion from cracks.

Another consequence of the continued evaporation is the formation and thinning of capillary water bridges, giving rise to an increasing capillary stress (σ_c) that gradually deforms the particles and closes the air voids. This process of capillary deformation causes the transmitted light intensity to increase again (Figure 4.4a and b, $t4$). The deformation fronts trail behind the air invasion fronts, from the contact line and centre towards the top of the edge. If large cracks are present, they facilitate the capillary deformation locally by enhancing the evaporation rate, producing discrete dark 'islands' at the edge that rapidly shrink over time (see Figure 4.4b, $t4$, and Supplementary Movie 2 in ref. 43.)

4.4.2 Quantification of drying stages

Clearly, increasing the particle modulus seven-fold causes substantial changes in the drying process. To elucidate the governing mechanisms in more detail, we quantify these changes as a function of the crosslink density. We measure the time evolution of the transmitted light intensity both at the edge and centre of all droplets, averaged over a small area (see the squares in Figure 4.4a and b, $t1$), which we refer to as I. The resulting normalized intensity curves for particles with 5 and 35 mol% crosslinker are shown in Figure 4.4c and d, respectively. We clearly distinguish the different stages of drying, which are particularly prominent for the edge:

(I) Concentration. The first stage is very similar for all suspensions because of the negligible effects of the hydrodynamic stress. Upon evaporation of the bulk water, the droplet thickness decreases, giving rise to a gradual increase in the transmitted intensity. For the centre, this increase becomes progressively faster owing to the rush-hour effect; for the edge, it levels off when the wrinkling front passes.

(II) Air invasion. The displacement of interstitial water by air causes a drop in the transmitted light intensity, of which the magnitude and duration depend strongly on the crosslink density (compare Figure 4.4c with d). We measure the normalized decrease in intensity upon air invasion ($\Delta I_{ai}/I_{min}$) and the duration (Δt_{ai}) both for the edge and centre of all droplets. Interestingly, we identify two distinct regimes for the process of air invasion, with a crossover that coincides with the cracking transition (see • in Figure 4.5 for the edge and in Appendix Figure 4.A.1 for the centre). For soft particles, the amount of air invasion is very small and takes up to a minute to complete. This reflects their high deformability, which allows the particles to pack closely with low porosity, impeding the penetration of air.

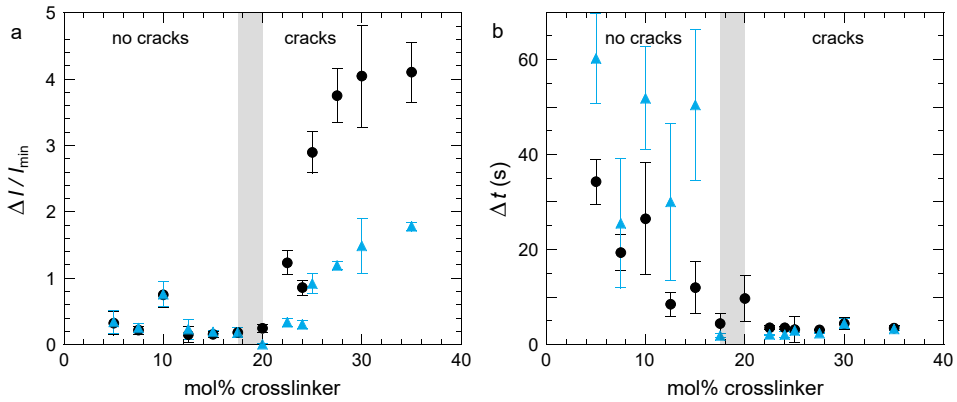

Figure 4.5. (a) Normalized decrease in transmitted light intensity due to air invasion ($\Delta I_{ai} / I_{min}$, •) and subsequent increase in intensity due to capillary deformation ($\Delta I_{cd} / I_{min}$, ▲) at the edge of droplets versus mol% crosslinker, averaged over three measurements. The error bars represent the standard deviations. **(b)** Duration of air invasion (Δt_{ai}, •) and capillary deformation (Δt_{cd}, ▲) for the same conditions as in (a). The grey vertical bars indicate the transition region between absence and presence of cracks.

For hard particles, the air invades in only a few seconds, even though the extent is considerably higher: up to 30-fold for the highest crosslink density. The rapidness of the air invasion results not only from the enhanced porosity, but also from the presence of cracks that provide extra surface area for air to enter. The trends for the centre are very similar (Appendix Figure 4.A.1), yet the absolute values are a factor 20 smaller due to the low film thickness in the centre.

(III) Capillary deformation. The invaded air is fully or partially expelled from the droplet during the last drying stage. For soft particles, the decrease in intensity upon air invasion is fully compensated by the subsequent increase in intensity upon capillary deformation, ΔI_{cd} (Figure 4.4c), whereas for hard particles it is only partially counterbalanced (Figure 4.4d). The transition between these two regimes thus marks a limit to the deformation beyond which the particles are too rigid to allow for complete closure of all the air voids. We quantify the amount of capillary deformation by normalizing the corresponding increase in intensity ($\Delta I_{cd}/I_{min}$). Remarkably, the transition from complete to partial capillary deformation overlaps with that corresponding to cracking and air invasion, emphasizing the governing role of the particle deformability (see ▲ in Figure 4.5 for the edge and in Appendix Figure 4.A.1 for the centre). Beyond this transition, the difference between ΔI_{ai} and ΔI_{cd} initially rises rapidly with increasing particle modulus yet levels off above

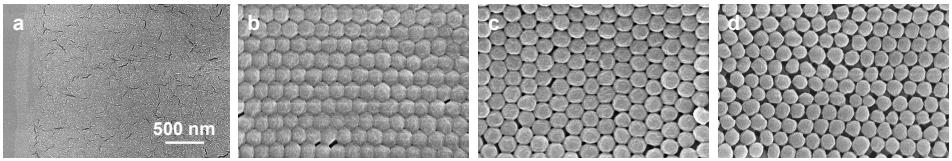

Figure 4.6. Scanning electron micrographs showing particle deformation at the edge of dried droplets with **(a)** 5, **(b)** 20, **(c)** 22.5, and **(d)** 30 mol% crosslinker. The scale bar applies to all images. For clarity, (a) displays the contact line. The tiny cracks are artefacts caused by the sputter-coating.

~30 mol%, implying that further increase of the crosslink density does not affect the particle deformation noticeably on an experimental time scale.

The duration of capillary deformation (Δt_{cd}) also shows the same trends as the duration of air invasion: for hard particles, the enhanced surface area in cracks allows rapid evaporation and a consequent rise in the capillary pressure, causing the capillary deformation to take only a few seconds. Below the transition region, Δt_{cd} increases with decreasing mol% crosslinker, which we argue arises from an increase in the final degree of deformation rather than from a decrease in the deformation rate. We note that these differences in duration are excluded from Figures 4.1b,c and 4.2b,c.

Zooming in to the edge of the dried droplets by SEM confirms that changes in particle deformability underlie the observed trends. Below the recurring transition of 20 mol% crosslinker, the particles are completely flattened onto the substrate (Figure 4.6a), whereas above it, the particle boundaries and air voids become progressively more visible (Figure 4.6b–d). The extent of deformation decreases with increasing crosslink density: particles near the soft–hard transition are highly faceted polyhedrons owing to the capillary stress (Figure 4.6b), whereas the hardest particles are only slightly deformed (Figure 4.6d). SEM magnifications of the centre reveal the same trends, but the crystallinity and packing density are lower due to the high rate of particle deposition resulting from the rush-hour effect[27] (Appendix Figure 4.A.2).

4.4.3 Wrinkling and cracking

The development of instabilities in drying suspensions is detrimental to the aesthetics and performance of the final coating. Above, we discussed the origin of wrinkles and cracks in relation to the elasto-capillary and shrinkage stress, respectively. To better understand the mechanisms underlying their formation, we

examine their structure and morphology in detail as a function of the crosslink density.

Surface wrinkles form for all crosslink densities, yet their extent clearly decreases with decreasing particle deformability while their wavelength increases (see Figure 4.7). The recurring transition of 20 mol% crosslinker also applies here: below this transition, the wrinkling is extensive and depends strongly on the crosslink density, whereas above it, the wrinkling is limited and weakly modulus-dependent. This indicates a critical E above which the particles do not deform sufficiently on the time scale of drying to allow their transformation into a continuous structure required for wrinkling.

The wavelength of the wrinkles (λ) scales with E and thus indirectly reflects the particle deformability. In addition, it scales with the film thickness (h) and the distance from the centre of the droplet (r) according to:[51]

$$\lambda \sim (B/\sigma_{ec})^{1/4}\, r^{1/2} \tag{4.5}$$

where B is the bending modulus of the film:

$$B = E\, h^3/12\left(1-\Lambda^2\right) \tag{4.6}$$

with Λ the Poisson ratio. Assuming that σ_{ec} and Λ are independent of crosslink density, it follows that $\lambda \sim E^{1/4}\, h^{3/4}\, r^{1/2}$. The scaling with E and h stems from the fact that stiffer and thicker films are more difficult to bend and stretch. The scaling with r reflects the increase in circumference with increasing distance to the droplet centre, due to which the elasto-capillary force is distributed over a larger area. All these relations are qualitatively visible in Figure 4.7. Foremost, λ increases with increasing crosslink density, confirming the positive correlation between mol% crosslinker and particle E. Second, the wavelength of the wrinkles is largest at the top of the edge where h has its maximum. Finally, the scaling with r causes an

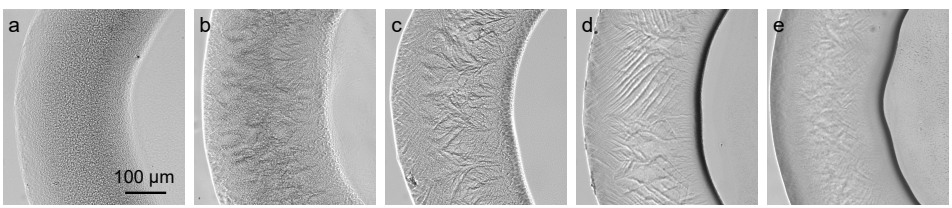

Figure 4.7. Bright-field transmission micrographs of wrinkles in coffee rings of particles with **(a)** 7.5, **(b)** 12.5, **(c)** 15, **(d)** 20, and **(e)** 35 mol% crosslinker. The images display the moment just after evaporation of the last bulk water. The scale bar applies to all images.

asymmetric distribution of λ across the edge, with smaller wavelengths near the centre–edge boundary.

Droplets of hard particles crack shortly after the wrinkling has completed. In addition to the sharp transition between absence and presence of cracks, the particle deformability gives rise to a second gradual transition in the crack morphology from ductile to brittle. Droplets of the softest particles that still allow cracking show a large number of arched, ductile cracks (Figure 4.8a,b), whereas droplets of hard particles show predominantly straight, brittle cracks (Figure 4.8c,d). The ductile mode is characterized by substantial plastic deformation of particles around the propagating crack tip, with part of the shrinkage stress relieved by viscous dissipation. The brittle mode involves straight cleavage of adjacent rows of particles by successive rupture of the connecting water films, with little plastic strain.[52] Because of the dissipative energy loss, the ductile cracks have considerably lower propagation rates[53] and are occasionally stopped in their tracks (Figure 4.8a,b).

Close comparison of Figure 4.8a with c reveals that the particle deformability influences not only the shape of the cracks but also their width. Cracks in droplets

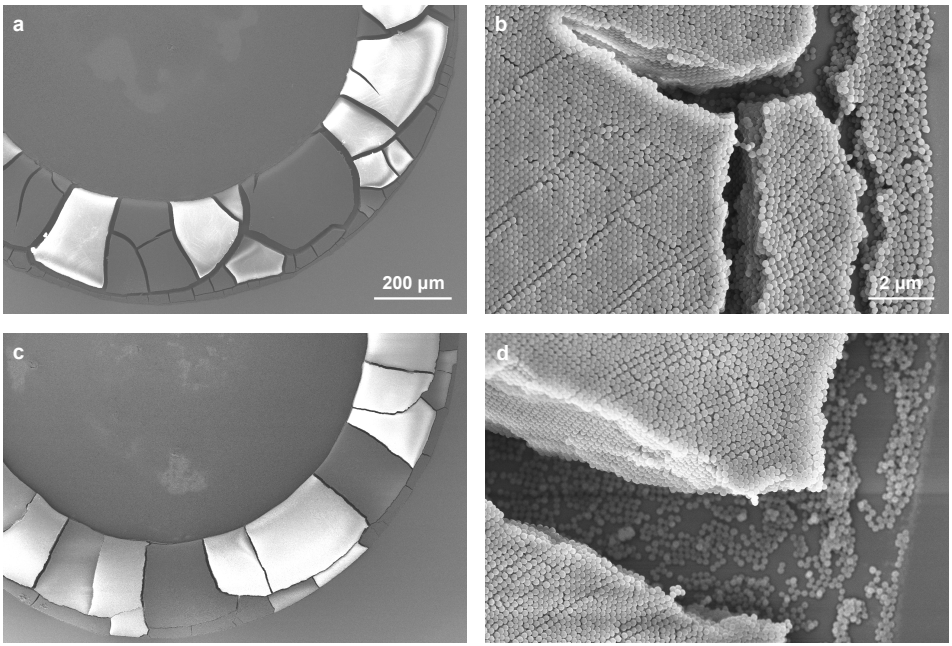

Figure 4.8. Scanning electron micrographs of cracks in dried droplets with **(a,b)** 20 and **(c,d)** 30 mol% crosslinker. (b) and (d) are magnifications of the contact line, which in (d) has delaminated from the substrate. The scale bars apply to both columns.

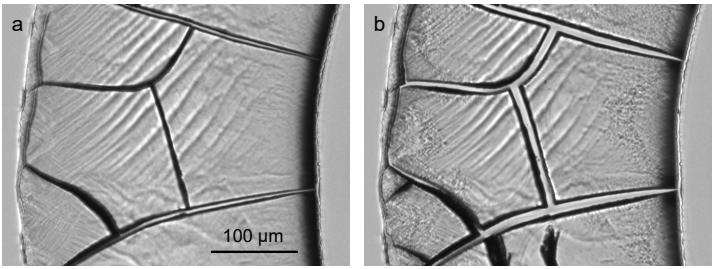

Figure 4.9. Crack widening by lateral particle deformation and compression at the edge of a drying droplet with 20 mol% crosslinker: **(a)** t = 195 s and **(b)** t = 198 s after droplet deposition. See Supplementary Movie 3 in ref. 43 for the full time series.

near the soft–hard transition expand to several times their width after nucleation as a result of lateral particle deformation and compression (Figure 4.9), whereas cracks in droplets of highly crosslinked particles hardly expand due to the limited capillary deformation (Figure 4.4b, t2–4). The crack widening takes only a few seconds and coincides with the air invasion (Figure 4.9b).

4.5 Concluding remarks

Despite the complexity of suspension droplet drying, the governing mechanisms depend strikingly similar on the particle deformability. Seemingly unrelated phenomena – wrinkling, cracking, air invasion and capillary deformation – share a common transition across which the properties change markedly. These changes coincide with the transition from complete to partial particle deformation on the time scale of drying. Theoretical predictions are in good agreement with experimental observations, confirming their validity and universality. Our model complements the Routh–Russel model for film formation in drying dispersions as it disentangles particle deformation from coalescence. Moreover, it extends the scope from the single-particle level to large-scale phenomena, including macroscopic heterogeneities specific to the coffee-ring geometry.

Acknowledgements

We thank the Wageningen Electron Microscopy Centre (WEMC) of Wageningen University & Research for access to their facilities.

4.A Appendix

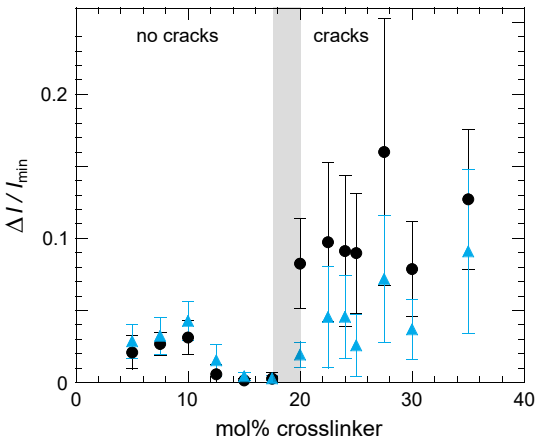

Figure 4.A.1. Normalized decrease in transmitted light intensity due to air invasion ($\Delta I_{ai} / I_{min}$, •) and subsequent increase in intensity due to capillary deformation ($\Delta I_{cd} / I_{min}$, ▲) in the centre of droplets versus mol% crosslinker, averaged over three measurements. The error bars represent the standard deviations. The grey vertical bar indicates the transition region between absence and presence of cracks.

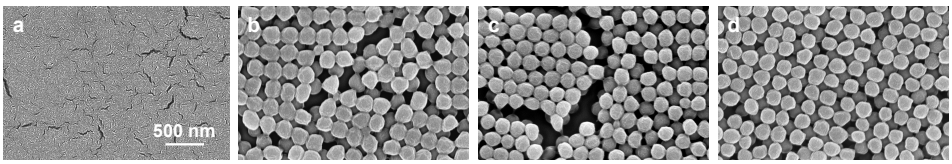

Figure 4.A.2. Scanning electron micrographs showing particle deformation in the centre of dried droplets with **(a)** 5, **(b)** 20, **(c)** 22.5, and **(d)** 30 mol% crosslinker. In (b–d), two layers of particles are visible with the substrate underneath. The scale bar applies to all images. The tiny cracks are artefacts caused by the sputter-coating.

References

[1] J. L. Keddie, A. F. Routh, *Fundamentals of latex film formation: processes and properties* (Springer, 2010).

[2] P. A. Steward, J. Hearn, M. C. Wilkinson. *Adv. Colloid Interface Sci.* **86**, 195–267 (2000).

[3] A. F. Routh. *Rep. Prog. Phys.* **76**, 046603 (2013).

[4] H. M. van der Kooij, J. Sprakel. *Soft Matter* **11**, 6353–6359 (2015). **(Chapter 2)**

[5] M. A. Winnik. *Curr. Opin. Colloid Interface Sci.* **2**, 192–199 (1997).

[6] J. L. Keddie. *Mater. Sci. Eng., R* **21**, 101–170 (1997).

[7] K. B. Singh, G. Deoghare, M. S. Tirumkudulu. *Langmuir* **25**, 751–760 (2009).

[8] K. I. Dragnevski, A. F. Routh, M. W. Murray, A. M. Donald. *Langmuir* **26**, 7747–7751 (2010).

[9] J. Qiao, J. Adams, D. Johannsmann. *Langmuir* **28**, 8674–8680 (2012).

[10] C. C. Roberts, L. F. Francis. *J. Coat. Technol. Res.* **10**, 441–451 (2013).

[11] J. Y. Kim, K. Cho, S. Ryu, S. Y. Kim, B. M. Weon. *Sci. Rep.* **5**, 13166 (2015).

[12] F. Giorgiutti-Dauphiné, L. Pauchard. *Soft Matter* **11**, 1397–1402 (2015).

[13] Y. Zhang, Y. Qian, Z. Liu, Z. Li, D. Zang. *Eur. Phys. J. C* **37**, 14084 (2014).

[14] J. L. Keddie, P. Meredith, R. A. L. Jones, A. M. Donald. *Langmuir* **12**, 3793–3801 (1996).

[15] A. Tzitzinou, J. L. Keddie, J. M. Geurts, A. C. I. A. Peters, R. Satguru. *Macromolecules* **33**, 2695–2708 (2000).

[16] Q. Nawaz, Y. Rharbi. *Langmuir* **26**, 1226–1231 (2010).

[17] A. Gromer, M. Nassar, F. Thalmann, P. Hébraud, Y. Holl. *Langmuir* **31**, 10983–10994 (2015).

[18] A. F. Routh, W. B. Russel. *Langmuir* **15**, 7762–7773 (1999).

[19] A. F. Routh, W. B. Russel. *Ind. Eng. Chem. Res.* **40**, 4302–4308 (2001).

[20] E. Gonzalez, M. Paulis, M. J. Barandiaran, J. L. Keddie. *Langmuir* **29**, 2044–2053 (2013).

[21] A. M. König, T. G. Weerakkody, J. L. Keddie, D. Johannsmann. *Langmuir* **24**, 7580–7589 (2008).

[22] K. L. Maki, S. Kumar. *Langmuir* **27**, 11347–11363 (2011).

[23] X. Chen, V. Boyko, J. Rieger, F. Reinhold, B. Reck, J. Perlich, R. Gehrke, Y. Men. *Soft Matter* **8**, 12093–12098 (2012).

[24] V. R. Gundabala, C.-H. Lei, K. Ouzineb, O. Dupont, J. L. Keddie, A. F. Routh. *AIChE J.* **54**, 3092–3105 (2008).

[25] A. F. Routh, W. B. Zimmerman. *Chem. Eng. Sci.* **59**, 2961–2968 (2004).

[26] R. D. Deegan, O. Bakajin, T. F. Dupont, G. Huber, S. R. Nagel, T. A. Witten. *Nature* **389**, 827–829 (1997).

[27] Á. G. Marín, H. Gelderblom, D. Lohse, J. H. Snoeijer. *Phys. Rev. Lett.* **107**, 085502 (2011).

[28] A. Crivoi, F. Duan. *Sci. Rep.* **4**, 4310 (2014).

[29] H. M. van der Kooij, M. de Kool, J. van der Gucht, J. Sprakel. *Langmuir* **31**, 4419–4428 (2015). **(Chapter 3)**

[30] D. Brutin, B. Sobac, B. Loquet, J. Sampol. *J. Fluid Mech.* **667**, 85–95 (2011).

[31] W. Bou Zeid, J. Vicente, D. Brutin. *Colloids Surf., A* **432**, 139–146 (2013).

[32] J. L. Keddie, P. Meredith, R. A. L. Jones, A. M. Donald. *Macromolecules* **28**, 2673–2682 (1995).

[33] F. T. Carter, R. M. Kowalczyk, I. Millichamp, M. Chainey, J. L. Keddie. *Langmuir* **30**, 9672–9681 (2014).

[34] B. Roman, J. Bico. *J. Phys. Condens. Matter* **22**, 493101 (2010).

[35] J. H. Weijs, B. Andreotti, J. H. Snoeijer. *Soft Matter* **9**, 8494–8503 (2013).

[36] A. A. Griffith. *Phil. Trans. R. Soc. A* **221**, 163–198 (1920).

[37] A. F. Routh, W. B. Russel. *AIChE J.* **44**, 2088–2098 (1998).

[38] K. B. Singh, M. S. Tirumkudulu. *Phys. Rev. Lett.* **98**, 218302 (2007).

[39] M. S. Tirumkudulu, W. B. Russel. *Langmuir* **21**, 4938–4948 (2005).

[40] M. S. Tirumkudulu, W. B. Russel. *Langmuir* **20**, 2947–2961 (2004).

[41] J. Sprakel, N. A. M. Besseling, M. A. Cohen Stuart, F. A. M. Leermakers. *Langmuir* **24**, 1308–1317 (2008).

[42] R. P. A. Dullens, E. M. Claesson, , W. K. Kegel. *Langmuir* **20**, 658–664 (2004).

[43] H. M. van der Kooij, G. T. van de Kerkhof, J. Sprakel. *Soft Matter* **12**, 2858–2867 (2016). **(This chapter)**

[44] Y. Ma, H. T. Davis, L. E. Scriven. *Prog. Org. Coat.* **52**, 46–62 (2005).

[45] P. Menut, S. Seiffert, J. Sprakel, D. A. Weitz. *Soft Matter* **8**, 156–164 (2012).

[46] S. Bohn, L. Pauchard, Y. Couder. *Phys. Rev. E* **71**, 046214 (2005).

[47] G. Gauthier, V. Lazarus, L. Pauchard. *EPL* **89**, 26002 (2010).

[48] R. C. Chiu, T. J. Garino, M. J. Cima. *JACS* **76**, 2257–2264 (1993).

[49] D. Wilkinson, J. F. Willemsen. *J. Phys. A: Math. Gen.* **16**, 3365–3376 (1983).

[50] L. Xu, S. Davies, A. Schofield, D. Weitz. *Phys. Rev. Lett.* **101**, 094502 (2008).

[51] J. Huang, M. Juszkiewicz, W. H. de Jeu, E. Cerda, T. Emrick, N. Menon, T. P. Russell. *Science* **317**, 650–653 (2007).

[52] S. Arif, J.-C. Tsai, S. Hilgenfeldt. *J. Rheol.* **56**, 485–499 (2012).

[53] S. Arif, J.-C. Tsai, S. Hilgenfeldt. *EPL* **92**, 38001 (2010).

Part II

Laser speckle imaging of drying realistic coatings

Chapter 5

Quantitative imaging of heterogeneous dynamics in drying and ageing paints

This chapter is based on: Hanne M. van der Kooij, Remco Fokkink, Jasper van der Gucht and Joris Sprakel, 'Quantitative imaging of heterogeneous dynamics in drying and aging paints', *Sci. Rep.* **6**, 34383 (2016).

Abstract

Drying and ageing paint dispersions display a wealth of complex phenomena that make their study fascinating yet challenging. To meet the growing demand for sustainable, high-quality paints, it is essential to unravel the microscopic mechanisms underlying these phenomena. Visualizing the governing dynamics is, however, intrinsically difficult because the dynamics are typically heterogeneous and span a wide range of time scales. Moreover, the high turbidity of paints precludes conventional imaging techniques from reaching deep inside the paint. To address these challenges, we apply a scattering technique, laser speckle imaging, as a versatile and quantitative tool to elucidate the internal dynamics, with microscopic resolution and spanning seven decades of time. We present a toolbox of data analysis and image processing methods that allows a tailored investigation of virtually any turbid dispersion, regardless of the geometry and substrate. Using these tools we watch a variety of paints dry and age with unprecedented detail.

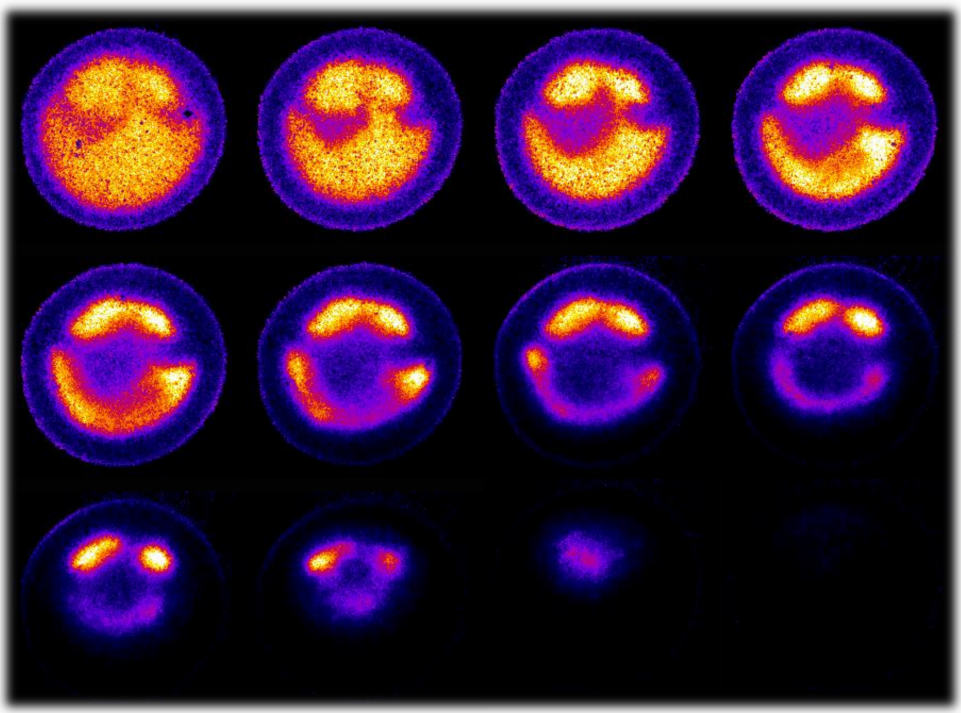

Time-lapse laser speckle images of a drying paint droplet, happy to be truly seen ◡̈

5.1 Introduction

During the drying of particulate dispersions, such as paints or inks, a rich diversity of thermodynamic, hydrodynamic and elastic stresses emerge which govern the fate of the system.[1,2] As stress heterogeneities develop in both space and time, a wide range of instabilities can occur, including fracture,[3–5] wrinkling,[6] and the formation of pinholes.[7] Even after full evaporation of the dispersing medium, paint films continue to evolve over time, for example due to chemical curing reactions, the reorganization of particles within the paint film[8] and the delamination of entire paint fragments from their substrate.[9] In some cases, instabilities occur almost simultaneously with the removal of solvent from the film, while in other cases they may take hours, days or even many years to become apparent; most notably, the continuous ageing of curing resins in artist oil paintings can lead to the development of surface defects centuries after the paint was applied.[10]

Clearly, understanding how the fluid and particle dynamics at the microscale govern the stability, aesthetics and longevity of a painted surface is difficult, as it involves a wide range of time and length scales. This is not only an important challenge for the preservation of painted surfaces and artworks, but also in the development of new sustainable coatings. With the increasing demand to eradicate volatile organic compounds (VOCs) from paints, due to their detrimental effects on the environment and the health of professional painters, developing water-based, solvent-free, alternatives has become urgent. Yet, the aforementioned instabilities are particularly severe for water-based paints, because all of the functional film-forming components are present as dispersed particles in water.[11] Arriving at a deeper understanding of the relationship between microscopic dynamics and the formation and ageing of a paint film is a crucial step in the endeavour towards sustainable coatings.[12] Moreover, establishing the generic origins of how drying dispersions become unstable is of fundamental importance in a much larger class of phenomena, ranging from the cracking of drying soils[13] to the inhomogeneous deposition of solutes from droplets,[14] e.g. in inkjet printing[15] or blood splatter.[16]

Connecting the wide range of time and length scales involved in this complex problem requires methods in which the rich spatiotemporal heterogeneities can be directly and quantitatively visualized. Conventional optical microscopy is rarely suited to this task as virtually all paint films are inherently turbid, leading to multiple scattering of light and low light transmission. By contrast, while turbidity is not an issue for resonant imaging methods such as MRI, these do not offer the spatiotemporal resolution to resolve the origin of such instabilities.

In this chapter, we adapt the medical imaging technique laser speckle imaging (LSI) to reveal and quantify the hidden dynamics deep within drying paint films

and droplets. This enables us to illuminate a complex array of dynamical processes which previously remained obscured, even for strongly scattering, light absorbing paints applied onto inhomogeneous and porous substrates such as paper or wood. In all these cases, we can extract quantitative information about flow velocities, diffusion rates and spatial correlations in heterogeneous dynamics with high spatial (micrometre) and temporal (millisecond) resolution.

5.2 Experimental details

5.2.1 Experimental set-up

LSI measurements are performed on the home-built set-up shown schematically in Figure 5.1a. The illumination source is a 532 nm solid-state laser (Cobolt Samba, 100 mW), whose intensity is regulated by passing the beam through a half-wave plate and polarizing beam splitter cube; the latter decomposes the beam into two perpendicular polarization components, one of which is directed into a beam dump. Adjustment of the rotation angle of the half-wave plate thus allows controlling the intensity of the transmitted component. After reflection by a mirror, the beam is expanded to a diameter of ~1 cm by a Galilean beam expander. The beam is then directed downward onto the sample via two mirrors, at a small angle with respect to the detection path to avoid intensity enhancement by coherent back-scattering.[17,18] The back-scattered light is reflected by a mirror onto a linear polarizer perpendicular to the polarization of the incident laser beam, to filter specular and low-order scattering paths. The multiply scattered light is then collected by a Qioptiq zoom lens and focused through an iris diaphragm and extension tubes onto a CCD camera. To ensure that the speckle statistics are independent of ℓ^*, the camera detects back-scattered photons from the centre of the illuminated area, and all our samples have a thickness $\gg \ell^*$.[19] The magnification of the imaging system is 1.8× and the depth-of-focus is ~0.1 mm. To optimize the spatial resolution whilst retaining a good signal-to-noise ratio, the speckle size is tuned by the diaphragm to be slightly larger than the pixel size, typically 2–3×.[20,21] Two cameras are alternately used: a HiSpec 1 camera (Fastec Imaging) for imaging at frame rates up to 1000 fps, and a Dalsa Genie camera (CR-GM00-H6400, Stemmer Imaging) for continuous streaming at frame rates of ~100 fps. The exposure time is adjusted to cover the full dynamic range of the camera. In parallel to the LSI measurements, a computer-controlled balance (Sartorius, model WZA224-NC) monitors the sample mass with 0.1 mg resolution and 1 Hz measurement frequency. In addition, the temperature and relative humidity are controlled by a home-built climate chamber enclosing the sample, which simultaneously eliminates air convection and stray light.

5.2.2 Data analysis

In traditional LSI, contrast is expressed by the level of speckle blurring, defined as the ratio of the standard deviation of the intensity to the mean intensity.[22,23] This ratio is reduced in areas with fast motion, or fast speckle fluctuations, which become blurred upon imaging with a finite exposure time. Although this analysis is well suited for temporally homogeneous systems, it falls short for systems whose dynamics vary strongly in both time and space. Revealing the latter requires measuring the intensity structure function, d_2 (Equation (5.1)), or the intensity autocorrelation function, g_2 (Equation (5.2)). In both equations, we use symmetric normalization, i.e. we normalize the numerators with the product of mean intensities at times t and $t + \tau$ instead of the square of the mean intensity, as this reduces artefacts by drift.

To enable true quantitative determination of the open time, it is crucial to have reasonable estimates for the two numerical constants β and γ. β is the spatial coherence factor that accounts for the number of speckles detected. In the ideal case, when each pixel detects fluctuations of only a single speckle, β equals 1.[24] As camera-based detection inevitably involves $\beta < 1$, we choose β such that $g_2(\tau) - 1 \to \beta$ for $\tau \to 0$. γ is a numerical prefactor which we have estimated at 1.5[25] by mapping diffusion coefficients of polystyrene particles in glycerol–water mixtures of different ratios measured by LSI onto those measured by dynamic light scattering (see Appendix 5.A.1 and Figure 5.A.1 for details).

5.2.3 Materials

All components of the LSI set-up are purchased from Thorlabs, unless specified otherwise. All paints are commercial water-based paints, except the sample in Figure 5.4 which is a dispersion of poly(styrene-*co*-butyl acrylate) particles (10 wt%, glass transition temperature $T_g = 36$ °C) whose synthesis is described in Chapter 3, Section 3.2.1. Glass substrates are obtained from ThermoScientific and used without further treatment. Printer paper is purchased from Pioneer (Ultra White office paper). 3 mm thick, untreated pine plywood is used as substrate for the measurements in Figure 5.5. These paints are applied with a coarse Storch AquaGel brush. The paints in Figure 5.2 are applied with a Quadruple Film Applicator (Erichsen) obtained from BYK–ALTANA.

5.3 Results and discussion

5.3.1 Laser speckle imaging

Laser speckle imaging (LSI) was first introduced in the 1980s as a non-invasive and cost-effective imaging technique to visualize subcutaneous and cerebral blood flow.[27–30] In recent years, its application has been extended to monitoring dynamical heterogeneities in synthetic soft materials,[20,31–34] food technology,[35,36] mechanical characterization of materials,[37–39] and analysis of processes on solid surfaces.[40–42] The technique relies on the illumination of a turbid material of interest with an expanded beam of a coherent light source (Figure 5.1a). As photons enter the scattering material, they undergo many scattering events before exiting the sample

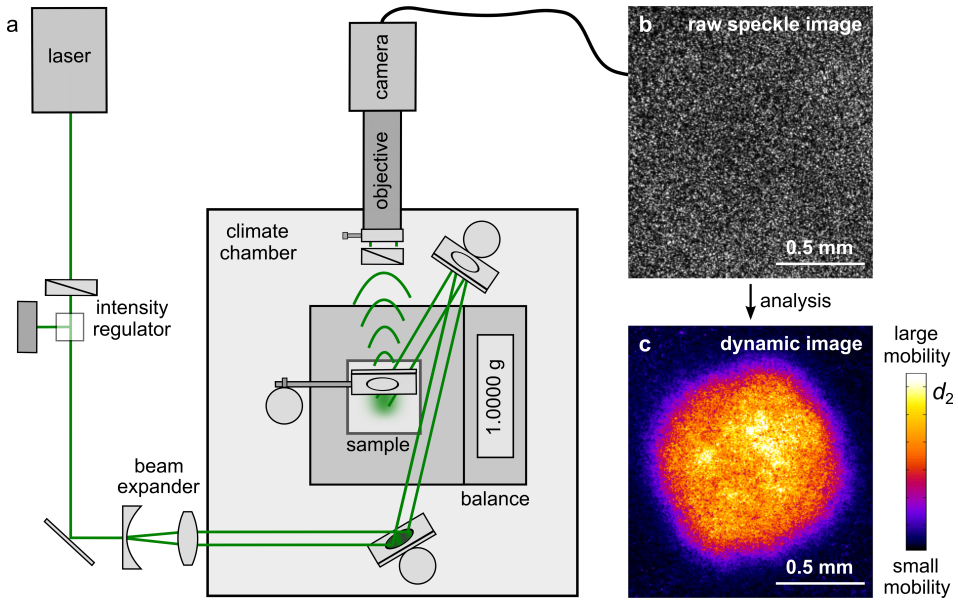

Figure 5.1. Schematic top view of the laser speckle imaging set-up and output. **(a)** The sample is illuminated with an expanded laser beam, and the back-scattered light is detected with a camera. This gives a speckled image of the sample **(b)**, here a drying white paint droplet on white paper. The contrast from the absolute intensity is too low to reveal the location of the droplet. Instead, LSI relies on fluctuations of the speckle intensity for its contrast, caused by motion of scattering objects (see Supplementary Movie 1 in ref. 26). These fluctuations are pixelwise translated into local dynamics via the autocorrelation function d_2 (Equation (5.1)), which encodes the mobility at a given time t, position x,y, and correlation time τ. The resulting d_2 images reveal dynamic heterogeneities **(c)**, here for the paint droplet at the onset of drying and $\tau = 20$ ms.

and reaching a camera. The many scattering events randomize the transport of the photons, resulting in a diffusion path of the photons through the material.[43] The typical randomization length is given by the transport mean free path ℓ^*, which can be deduced from Mie theory[44] or can be determined experimentally (see Chapter 11, Section 11.2.7 for more details).[18] The diffusion coefficient D_l of light in a multiple scattering medium is $D_\mathrm{l} = 3\ell^* c/n$, with $c = 3 \cdot 10^8$ m/s the speed of light in vacuum, n the refractive index of the medium, and ℓ^* typically of the order of 10–100 μm, giving $D_\mathrm{l} \simeq 10^3$–10^5 m^2/s.[45] By contrast, the diffusion rate of scatterers D_s, predicted by the Stokes–Einstein relation, is many orders of magnitude smaller, usually $D_\mathrm{s} = 10^{-10}$–10^{-15} m^2/s. This large separation in diffusion rates ensures that photons back-scattered to the detector essentially probe a static snapshot of the structure. Each photon will travel a different diffusion path through the multiple scattering medium; the resulting path length differences create an interference pattern known as a speckle pattern (Figure 5.1b).

As scatterers move within the sample, for instance by Brownian motion, fluid flow, or any other source of structural rearrangements, the speckle pattern changes. In LSI, temporal changes in the speckle intensity are analysed to create imaging contrast. Here we quantify the contrast by the intensity structure function:[46]

$$d_2(t,x,y,\tau) = \frac{\langle [I(t,x,y) - I(t+\tau,x,y)]^2 \rangle}{\langle I(t,x,y)\rangle \langle I(t+\tau,x,y)\rangle} \tag{5.1}$$

where averaging is over time and/or speckles. The structure function reflects changes in the intensity, with high values indicating decorrelation of the signal and hence enhanced mobility. Note that, when using d_2 as the image contrast, absolute speckle intensity values are irrelevant; even in samples with no contrast in the static structure (Figure 5.1b), contrast in local dynamics can emerge (Figure 5.1c). We consistently use d_2 to create spatial maps of the mobility, rather than the more common autocorrelation function g_2, given by

$$g_2(t,x,y,\tau) = \frac{\langle I(t,x,y) \cdot I(t+\tau,x,y)\rangle}{\langle I(t,x,y)\rangle \langle I(t+\tau,x,y)\rangle}, \tag{5.2}$$

because d_2 was shown both theoretically[46] and experimentally[47] to be less sensitive to low-frequency noise and drifts in the intensity. In the case of a stationary ergodic process with sufficient sample size, the two are directly related according to: $d_2(t,x,y,\tau) = 2(g_2(t,x,y,0) - g_2(t,x,y,\tau))$.[46]

The fact that dynamical heterogeneities in drying paints can be imaged based on temporal speckle correlations was first demonstrated by Zakharov and Scheffold.[32] However, to benefit from the wealth of previously unexplored quantitative inform-

ation captured in the speckle statistics, we aim to develop laser speckle imaging into a four-dimensional (x, y, t, τ) imaging tool that allows a more versatile and extensive analysis of coatings of all types. In particular, we show here that the correlation time τ acts as a tuning knob for creating image contrast. This parameter sets the time lag between images that are autocorrelated, and hence the typical time scale of the dynamics of focus. Computing d_2 for different correlation times allows distinguishing between different types of motion, because the image contrast is highest for dynamics occurring at the τ of choice. Additional information about the governing processes can be extracted from the specific shape of the $d_2(\tau)$ or $g_2(\tau)$ curves and the associated mean-square displacements $\langle \Delta r^2(\tau) \rangle$. For example, $\langle \Delta r^2 \rangle \propto \tau^2$ indicates pure ballistic (deterministic) motion, whereas $\langle \Delta r^2 \rangle \propto \tau$ indicates either pure diffusive (stochastic) motion or intermittent local structural changes.[48] Subdiffusive transport is characterized by a power-law exponent smaller than 1. Most practical applications involve a mixture of different types of motion, which are manifest as distinct scaling regimes in the mean-square displacement (Appendix 5.A.2 and Figure 5.A.2).

To quantify dynamics over a wide range of correlation and experimental times, access to long-term measurements at high frame rates is required. The lower-bound resolution to both t and τ is determined by the frame rate of the camera; the upper-bound resolution by the total measurement time. We have therefore implemented a real-time distribution feed to stream images of $>10^5$ pixels at 100 fps for many hours, yielding seven decades of dynamic range. Note that the lower-bound time resolution is increased when constructing d_2 maps without spatial averaging (e.g. Figure 5.1c), as this requires averaging the speckle fluctuations over a finite time interval $[t - \frac{n}{\text{frame rate}}, t + \frac{n}{\text{frame rate}}]$ with n a positive integer number of frames, effectively equating the time resolution to the width of this interval, $\frac{2n}{\text{frame rate}}$.

The spatial resolution is set by either ℓ^* or the speckle size on the camera chip divided by the image magnification M, depending on which is largest. The minimum speckle size is estimated as $r_s \approx 1.2\lambda(1 + M)d/a$, with λ the illumination wavelength, d the distance between camera chip and diaphragm, and a the aperture diameter.[49,50] In our experiments, $r_s/M = 5$–10 μm, implying that in many cases the transport mean free path is limiting to the resolution. Nevertheless, the amount of movement that can be detected, i.e. the displacement resolution, is many orders of magnitude smaller, at the nanometre scale, as multiple scattering amplifies the effects of small displacements.[43]

The effective penetration depth of light into the sample depends on the value of ℓ^*. For an isotropic sample in the back-scattering geometry, most photon paths do not exceed a few ℓ^*, because the path length (s) dependence of the photon flux $J(s)$ decays as $s^{-5/2}$ for large path lengths:

$$J(s) = (4\pi)^{-3/2}\, z_0\, D_l\, (s\,\ell^*/3)^{-5/2} \exp(-3\, z_0^2/4\, s\,\ell^*) \tag{5.3}$$

where $z_0 \propto \ell^*$ is the extrapolation length which contains information about the reflectivity at the sample surface.[51,52] The measured correlation functions are thus intensity-weighted convolutions of dynamics over the z-axis of the sample, in addition to the averaging in the x, y-plane dictated by the spatial resolution. ℓ^* is in turn a function of the wavelength of the laser. Near-infrared light can achieve penetration depths of millimetres and is most often used for medical imaging, for example to visualize subcutaneous blood perfusion.[53,54] By contrast, we use a laser source of 532 nm to achieve an effective penetration depth of the order of tens of micrometres.

5.3.2 Open time of paint films

We start by exploring a quantitative determination of the open time of paint films. The open time is defined as the time after application beyond which further reworking of the paint film results in visible surface defects. This open time is a crucial handling parameter for all paints, either protective or decorative, but of particular concern for the development of high-quality, sustainable, water-based formulations to replace solvent-based coatings. The eradication of all solvents from a formulation relying strictly on water as the suspending fluid directly causes a strong reduction in the open time, and hence in a loss of application flexibility.[55] Surprisingly, no standardized method exists to determine the open time without ambiguity, despite its importance in the handling properties of a paint. In fact, measurements performed by different operators or techniques often result in dissimilar values. Thus, accurately defining the open time is an important challenge.

To do so with LSI, we apply a homogeneous film of a commercial, pigmented water-based paint on a glass surface using a film applicator to establish the thickness. We then image the centre of the drying paint film, at a controlled temperature of 23 ± 1 °C and relative humidity of 41 ± 2%. As we observe no spatial heterogeneities (Appendix Figure 5.A.3a) we can average over all speckles in the field of view ($>10^5$) to obtain with excellent accuracy the intensity autocorrelation function $g_2(\tau)$ (Equation (5.2)) as a function of drying time. Additional time averaging is not necessary, implying that we compute a true ensemble average. Note that we here use g_2 instead of d_2, because the multi-speckle processing provides ample statistics and moreover, g_2 is more common and therefore offers a more intuitive interpretation.

As time progresses, and more water evaporates from the film (Appendix Figure 5.A.3b), the correlation function shifts to larger τ, indicative of a slowing

down of particle diffusion (see Appendix Figure 5.A.3c and d for $g_2(t,\tau)$ and $d_2(t,\tau)$ curves). We use the Siegert relation to compute the normalized field autocorrelation functions g_1 from g_2 and fit 600 of these correlation functions to a single-exponential decay, allowing us to extract the time evolution of the characteristic relaxation time τ_0:

$$g_1(t,\tau) = \frac{1}{\sqrt{\beta}}\sqrt{g_2(t,\tau)-1} = \exp\left[-\gamma[\tau/\tau_0(t)]^{\alpha(t)}\right] \tag{5.4}$$

where $\alpha(t)$ is the stretching exponent, and β and γ are numerical constants that we have experimentally determined (see Section 5.2.2 and Appendix 5.A.1).[24,43] Eight typical g_1 curves and fits are shown in Figure 5.2a. Each of the 600 fits is based on 4500 data points and has a sum of squared errors SSE below 0.06 (Appendix Figure 5.A.3e), enabling an accurate determination of the open time. Note that the characteristic time scale τ_0 is independent of the details of the experimental

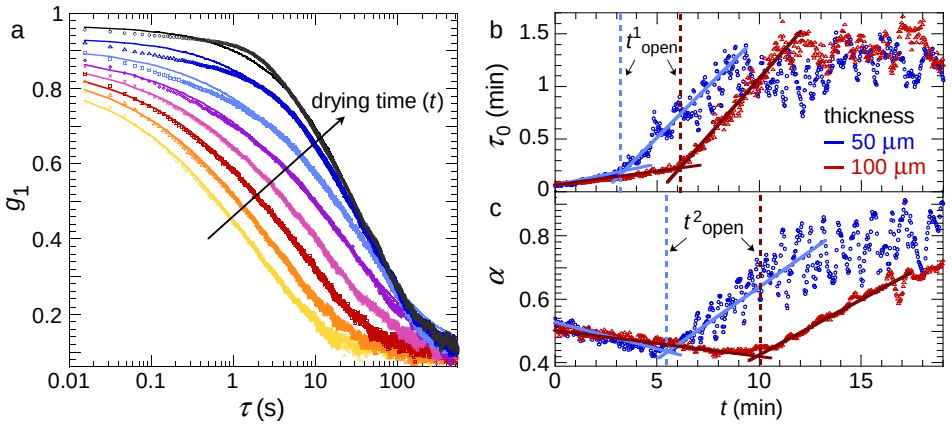

Figure 5.2. Unambiguous determination of the open time of paint films. **(a)** Evolution of the multi-speckle averaged field autocorrelation function during drying of a 100 µm thick film. For clarity, only a small subset of drying times is shown: t = 0 min (●), 3.3 min (▲), 6 min (■), 7.3 min (×), 9.3 min (♦), 11.5 min (■), 15 min (▲) and 20 min (●). The solid lines are fits to a single-exponential decay (Equation (5.4)), from which the typical time of particle relaxation $\tau_0(t)$ is obtained. **(b)** Evolution of τ_0 during drying of films of two different thicknesses. The kink in the τ_0 curve marks a transition from a weak to strong rise in viscosity, and hence provides a measure for the open time, t^1_{open}. **(c)** Stretching exponent α of the fits versus drying time. The minimum in the α curve marks a transition from Brownian to ballistic dynamics, indicating that particle diffusion is halted and evolves to advective compaction of a solid-like film. This time thus represents an upper bound to the workability of the film, which we denote by t^2_{open}.

set-up and requires no pre-existing knowledge of the properties of the sample as the ℓ^* dependence is lost in the back-scatter geometry. It thus allows a truly unambiguous and reproducible definition of the mobility of particles within the film.

A few minutes after applying the paint, a distinct change in the dynamics appears, which we quantify as a function of film thickness in Figure 5.2b. The τ_0 curves display a kink indicative of a transition from a weak to steep increase in film viscosity. Because the workability of a paint film is strongly dependent on viscosity, we can extract a measure for the open time t^1_{open} from the position of the kink, as illustrated in Figure 5.2b. Remarkably, also the curves of the stretching exponent α display two distinct regimes: in the first drying stage, the dynamics are predominantly Brownian, and gradually change from diffusive ($\alpha = 0.5$) to subdiffusive ($\alpha < 0.5$) (Figure 5.2c). In the subsequent stage, the particle transport is increasingly governed by advective processes ($\alpha \to 1$) arising from the evaporative flux which further concentrates the sample. This crossover from Brownian to advective dynamics signals the transition from a fluid paint film to one with semi-solid properties. Any defect created in a solid-like film can no longer spontaneously anneal; hence, the minimum in the α curve marks an upper bound to the workability and consequently a second unambiguous measure for the open time, t^2_{open}.

5.3.3 Stages in paint drying and ageing

In many cases, paint film drying is more complex, exhibiting not only a liquid–solid transition at the open time, but also spatiotemporal heterogeneities and instabilities beyond this point. Identifying these stages is an important step towards unravelling the microscopic mechanisms with which paints dry and become unstable over time. We exemplify this by the drying of a commercial water-based resin dispersion containing polymers that are glassy at room temperature (glass transition temperature $T_g = 45$ °C). LSI images created with d_2 as the contrast function show how the drying dynamics slow down, followed by the appearance of cracks[56–58] and distinct delamination events in which entire coating fragments detach from the glass substrate[9] (images a–f in Figure 5.3).

By choosing an intermediate value of the correlation time, $\tau = 16$ ms, we probe a mixture of diffusive and advective motion. The average value of the contrast function, $\langle d_2(\tau = 16\text{ ms})\rangle$, shows how transport slows down substantially during the first drying stage and arrests fully after approximately 60 min (red curve in Figure 5.3). At this stage, not yet all water has evaporated, but the suspension reaches a particle concentration of approximately 60 wt% corresponding to random

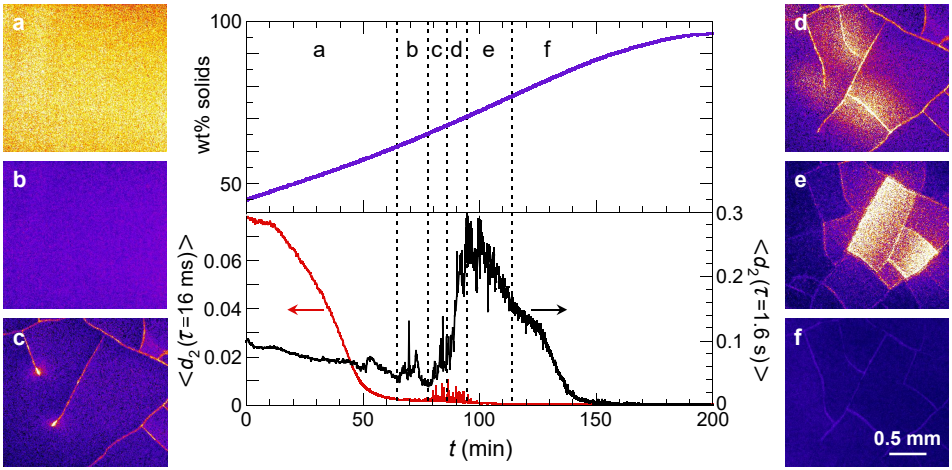

Figure 5.3. Drying and ageing stages of a non-film-forming polymer dispersion on glass, homogeneously coated as a 200 μm thick film. Images **(a)** to **(f)** show relatively fast dynamics, quantified by $d_2(\tau = 16$ ms), in the centre of the film in different stages: (a) evaporation, (b) stress build-up, (c) primary cracking, (d) secondary cracking, (e) delamination, and (f) relaxation. All images have the same colour scale and scale bar. See Supplementary Movies 2 and 3 in ref. 26 for the time evolution of cracking and delamination. The graphs show that the increase in wt% solids coincides with a shift from fast dynamics, $\langle d_2(\tau = 16$ ms$)\rangle$ (left ordinate), to slow dynamics, $\langle d_2(\tau = 1.6$ s$))\rangle$ (right ordinate). Note that the absolute d_2 values inherently increase with increasing τ.

close packing, beyond which particle diffusion and advection are halted. Further water evaporation has no significant effect on the value of d_2 for short τ. By contrast, selecting a τ two orders of magnitude larger at 1.6 s enables us to create contrast based on slow dynamics within a solid-like paint film, e.g. resulting from capillary deformation of the particles and the nucleation and growth of cracks. While these phenomena do not occur at times <60 min, a large burst of these slow ageing and cracking dynamics is visible after ~100 min. Finally, upon full evaporation of the water, all mobility in the film is quenched and a static state is reached.

These data illustrate how τ can be used as a spectral parameter to explore different processes and distinguish the successive stages of drying: (a) evaporation, (b) build-up of shrinkage stresses, (c,d) formation of primary and secondary cracks, (e) delamination, and (f) final relaxation of the film by particle deformation. Depending on the stages of interest, the value of τ can be fine-tuned to probe specific processes, thus allowing a tailored comparison of different samples or conditions.

5.3.4 Coffee-ring effect

Additional complexity arises when the geometry of drying is changed from a homogeneous film, in which boundary effects are negligible, to that of a droplet.[59] The drying of dispersion droplets is encountered in a wide variety of scenarios, ranging from spray painting[60] and inkjet printing[61] to the drying of blood splatter.[62] As the evaporative flux is higher at the pinned contact line of the droplet, a net flux is created from the centre of the droplet to its periphery. This fluid flow transports solutes to the outer edge, where they are deposited. This so-called coffee-ring effect was explored and explained in detail previously, but only for dilute suspensions to avoid multiple scattering and enable optical imaging (Chapters 3 and 4).[63–65] With LSI, we can study even the most opaque systems. We therefore image a concentrated droplet of latex particles during drying.

In our LSI images we clearly distinguish two key aspects of the coffee-ring effect (Figure 5.4a). First, we observe how a dense ring of colloids is deposited at the contact line of the droplet, evident as a depletion of mobility at the periphery, which grows inward as time progresses. While the short-time dynamics within this coffee ring are substantially quenched with respect to the liquid centre, where particles diffuse and flow freely, some particle motion is still visible which we attribute to low-frequency particle rearrangements and deformation due to capillary forces. Moreover, we observe a distinct gradient in particle mobility from the centre of the

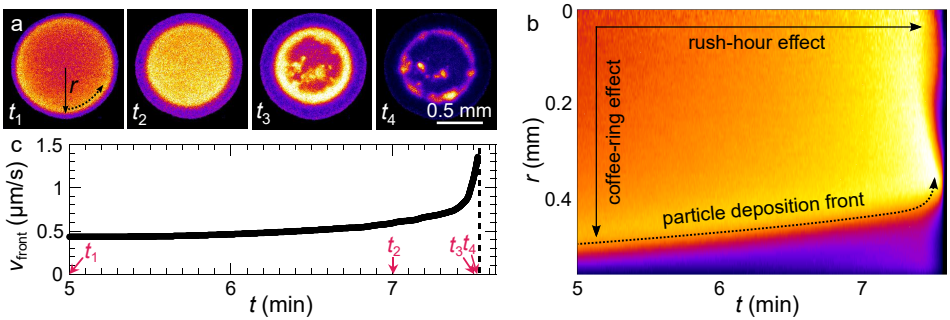

Figure 5.4. Spatial and temporal heterogeneities in a drying dispersion droplet on glass. **(a)** Time-lapse $d_2(\tau = 10$ ms) images of evaporation. All images have the same colour scale and scale bar. See Supplementary Movie 4 in ref. 26 for the full time series. **(b)** Kymograph of the azimuthally averaged d_2 versus distance from the centre of the droplet r (see (a)). The spatial divergence of d_2 by the coffee-ring effect and temporal divergence of d_2 by the rush-hour effect are indicated. **(c)** Velocity of the particle deposition front $v_{front} = \Delta r/\Delta t$ over time, derived from (b). The numbered arrows indicate the evaporation times displayed in (a).

droplet to the deposition front; this is clearly apparent in a plot of the azimuthally averaged value of d_2 as a function of distance to the centre r and time t (Figure 5.4b).

Secondly, the fluid flux to the contact line diverges near the end of drying, which was demonstrated and called the 'rush-hour effect' in previous work.[64] The origin of this effect is the increasing area-to-volume ratio of the droplet during drying, which diverges when the last bulk water evaporates and the water contact angle vanishes. We observe a proxy for this effect as a strong rise in the rate with which the coffee ring is deposited. To quantify the propagation velocity of the front, we determine the position of the dense particle deposit from the kymograph in Figure 5.4b, defined as the distance r where the gradient in d_2 is the largest. Indeed, the front velocity v_{front} is virtually constant in the early stages of drying but speeds up strongly as the last bulk water evaporates (Figure 5.4c).

Finally, we note that distinct heterogeneities in the particle dynamics emerge in the azimuthal direction mainly towards the end of drying, when the overall particle volume fraction within the droplet approaches the colloidal glass transition (Figure 5.4a, t_3 and t_4).

5.3.5 Paint application

In a drying droplet, spatiotemporal heterogeneities arise as a direct consequence of the droplet geometry. Yet, inhomogeneous dynamics may also result from the method of paint application; in many cases, both consumer and artist paints are applied by means of a paint brush. Since the hairs of a paint brush will not all be identical, this can result in subtle variations in local shear forces, depending on the application pressure, which will affect the drying process.

To explore the influence of the application method, we apply a commercial decorative woodtrim paint to a piece of untreated plywood using a hog bristle paint brush. Upon changing the application pressure, no visible changes occur in the appearance of the paint film, implying that variations in the thickness are at the microscopic level. However, when we use LSI to create contrast based on particle dynamics, rich spatial heterogeneities emerge (Figure 5.5a). Specifically, the inhomogeneity becomes more pronounced as the brush pressure is increased; this likely originates from an increase in the intra-film thickness variations. To quantify the typical length scale of such dynamical heterogeneities, we compute the spatial autocorrelation function of d_2, defined as $C_{d_2}(\Delta x, \tau) = \langle d_2(x,\tau) \cdot d_2(x+\Delta x,\tau)\rangle / \langle d_2(x,\tau)\rangle\langle d_2(x+\Delta x,\tau)\rangle$. Since brushing is a directional application method, we compute the correlation in the brush direction x, while averaging in the perpendicular direction. At short distances, the dynamics are correlated, yet the correlation decays with increasing Δx. From these functions we indeed conclude that the typical domain size grows with decreasing brush

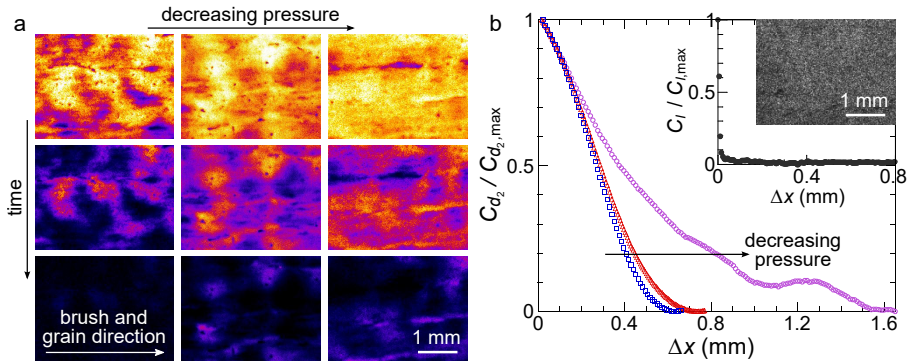

Figure 5.5. Drying of brush-applied woodtrim paint on plywood. **(a)** Time-lapse $d_2(\tau = 8$ ms) images of the centre of paints applied at three different brush pressures. From top to bottom, $t = 0$, 100 and 250 s after application. All images have the same colour scale and scale bar. See Supplementary Movies 5 and 6 in ref. 26 for the full time series. **(b)** Normalized spatial correlation of d_2 (see text) versus Δx for the measurements in (a). The **inset** shows a white-light photograph of the paint applied at intermediate pressure and the corresponding normalized spatial correlation of the raw intensity versus Δx.

pressure. We note that the same analysis performed on the absolute intensity of these samples under white-light illumination reveals no spatially correlated structure (Figure 5.5b, inset), thus highlighting the purely dynamic nature of these effects.

The dynamical heterogeneities resulting from the initial paint application persist throughout the drying process (Figure 5.5a), and also the spatial autocorrelation functions remain remarkably constant. Hence, the manner in which a paint film is applied must be taken into account to truly understand paint drying and its subsequent stability, for which aim LSI is ideally suited.

5.3.6 Real paints and surfaces

To demonstrate the versatility of laser speckle imaging, we explore three practical applications involving highly porous substrates. Interestingly, even if the paint itself is transparent, its dynamics can be inferred if the substrate participates in the drying process. Coatings applied on paper dry not only by evaporation, which is relatively slow, but also by imbibition of the solvent into the porous substrate.[66,67] This imbibition will cause the cellulose fibres which constitute the paper to swell and deform,[15] thus creating very small changes in the local structure that can be visualized by LSI. The propagation of such an imbibition front through a piece of paper is shown in Figure 5.6a. In sharp contrast to drying on a sealed substrate as

in Figure 5.4a, the propagation front is rough instead of smooth and its velocity is heterogeneous in time and space. LSI thus allows deducing the fluid dynamics both qualitatively and quantitatively from the substrate mobility.

In addition to transparent systems, we can go to the other extreme and study strongly pigmented systems. The drying dynamics of a just-applied droplet of carbon black ink on paper are revealed in Figure 5.6b. Even though the light absorption is strong, provided that sufficient light is multiply scattered we can analyse the drying process. The absolute scattered intensities clearly do not play a role, as $d_2^{\text{droplet}} \gg d_2^{\text{paper}}$ while $I^{\text{droplet}} \ll I^{\text{paper}}$ (Figure 5.6b). Due to the rapid drainage of water from the ink into the paper, the drying is highly heterogeneous and the porosity of the substrate projects in the d_2 image. The imbibition front displays a viscous finger-like pattern characteristic of fluid penetration through a porous material.[67–69]

Finally, we investigate how τ-resolved d_2 imaging can provide additional contrast and shed light onto the heterogeneous drying phenomena on paper. Even in scenarios where the raw speckle image is completely devoid of structural information, using LSI we can elucidate how the droplet dries and disentangle different types of processes (Figure 5.6c). We achieve this for a single raw speckle movie of a drying paint droplet on paper by computing d_2 images as a function of correlation time. With increasing τ, we shift our focus from fast diffusion and water flows inside the droplet, to intermediately fast processes such as coalescence of particles in the droplet, to very slow dynamics such as swelling of the paper fibres upon imbibition of the water (Figure 5.6c). Although the absolute d_2 values

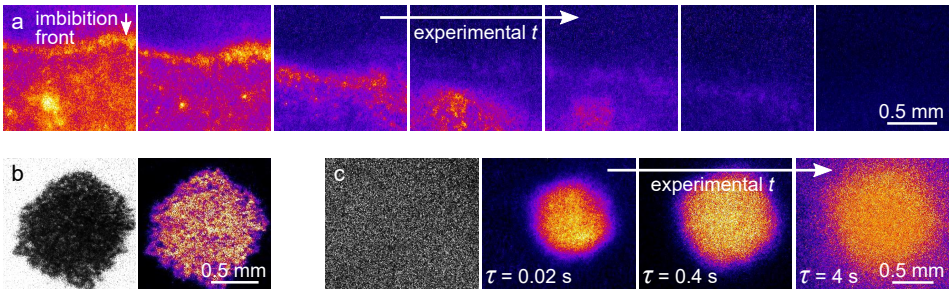

Figure 5.6. Examples of drying coatings on porous substrates. **(a)** Propagation of an imbibition front through paper. The total time from left to right is 2 min. See Supplementary Movie 7 in ref. 26 for the full time series. **(b)** Raw speckle image and $d_2(\tau = 10\text{ ms})$ image of a just-deposited black ink droplet on paper. **(c)** Raw speckle image and $d_2(\tau = 20\text{ ms})$ images of a white dispersion droplet on white paper, 1 min after deposition. The d_2 images display the mobility for different τ values, with the colour scales normalized to the highest d_2 of each image.

inherently increase with increasing τ, the spatially resolved d_2 mapping allows distinguishing relative differences in d_2 between different locations in the sample. We note that more thorough analysis of the specific shape of the $d_2(\tau)$ curves is required to differentiate paint dynamics from substrate dynamics, which is particularly relevant at the droplet periphery where the paint film is so thin that part of the photons will diffuse into the paper. This τ dependence thus adds an extra dimension to the three-dimensional raw data, providing a four-dimensional phase space of parameters to choose from, depending on the specific question.

5.4 Concluding remarks

In this chapter we have shown how laser speckle imaging is well suited to quantitatively visualize a plethora of complex phenomena that emerge during paint drying and ageing. This opens up many new possibilities for the rational and guided design of new sustainable alternatives to solvent-based paints, as well as for unravelling the origins of mechanical instabilities that threaten the longevity of protective coatings and works of art. The modular design of the LSI set-up enables its combination with other techniques; for example, complementing LSI with infrared spectroscopy will allow linking the occurrence of chemical reactions in a paint film, such as those causing artist oil paintings to cure and become brittle over time, to the mechanical stability of the painting. Not only the experimental set-up but also the data processing algorithms can be tailored according to the specific application. We have highlighted the largely unexplored potential of the correlation time τ as a spectral tuning knob to obtain image contrast. It is furthermore important to consider the type and extent of averaging: for qualitative imaging, the maximum spatial resolution can be pursued at the expense of temporal resolution, whereas for quantitative mapping, the spatial statistics must be included in the processing to ensure multi-speckle averaging and to suppress speckle noise. High-speed cameras and high speckle densities are desired in this respect – provided that the speckle size exceeds the pixel size – because the statistical noise, expressed by the variance $\sigma^2_{d_2}$ or $\sigma^2_{g_2}$, is inversely proportional to the acquired number N of independent values of $d_2(\tau)$ resp. $g_2(\tau)$.[21,47]

We believe that these initial results hold great promise for more in-depth studies of paints, including their spatially resolved viscoelastic properties, the effects of key parameters on drying and ageing, and the physics of fracture. LSI experiments are typically fast, non-destructive and well reproducible under controlled conditions. Moreover, the versatility of laser speckle imaging extends far beyond paints, making it a powerful technique for imaging dynamics of virtually any multiple scattering system.

5.A Appendix

5.A.1 Calibration of prefactor γ

To determine the open time of paint films, we extract the characteristic relaxation time τ_0 by fitting the field autocorrelation functions to a single-exponential decay: $g_1(\tau) = \exp\left[-\gamma(\tau/\tau_0)^\alpha\right]$, where γ is a numerical constant that we have calibrated. $\gamma = 1 + \Delta$ is the distance in units of transport mean free path after which the ballistic light impinging onto the sample is converted into diffusive light inside the sample. The value of Δ depends on factors including the polarization of the incident and detected light, particle size, and refractive index ratio between sample and surroundings. For isotropic scattering by particles dispersed in a medium whose refractive index equals that of the surroundings, the Milne theory predicts that $\Delta = 0.710$. However, most situations involve deviatory values of Δ and consequently of γ.[25]

Calibration of γ for highly concentrated, complex systems such as paints is unfeasible and therefore requires a different approach. To estimate the value of γ in our experiments, we measure the diffusion coefficients of polystyrene particles suspended in water–glycerol mixtures of different ratios, and fit the resulting D values to those measured by dynamic light scattering (DLS). The samples used for LSI contain 1 wt% of polystyrene and are enclosed in a sealed, glass chamber; the samples used for DLS contain $1 \cdot 10^{-3}$ wt% of polystyrene and are measured

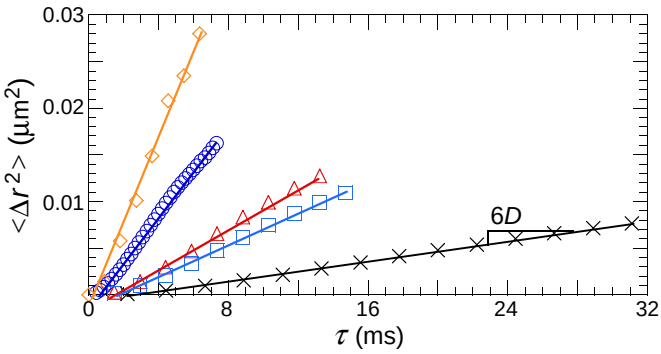

Figure 5.A.1. Mean-square displacements of polystyrene particles in water–glycerol mixtures with different viscosities, using $\gamma = 1.5$ (see text). The curves correspond to particles of 0.5 μm diameter in pure water (◇); and particles of 1 μm diameter in pure water (○), 25 wt% glycerol (△), 30 wt% glycerol (□), and 55 wt% glycerol (×). The solid lines are least-square fits to the function $\langle \Delta r^2 \rangle = 6D\tau$, from which the diffusion coefficients are obtained.

in standard polycarbonate capillaries of 1.9 mm diameter, on an ALV instrument equipped with an ALV-7002 external correlator and a Cobolt Samba 300 mW DPSS laser operating at a wavelength of 532 nm (detection angle = 90°, $T = 23 \pm 1$ °C).

We use two different sizes of the particles, 0.5 and 1 μm, density-matched in 45:55 H_2O–D_2O, and four different glycerol concentrations for the large particles: 0, 25, 30 and 55 wt%. For each sample we measure the multi-speckle averaged autocorrelation function using our LSI set-up and extract the mean-square displacement $\langle \Delta r^2(\tau) \rangle$ according to: $g_1(\tau) = \exp\left[-\gamma\, k_0 \sqrt{\langle \Delta r^2(\tau) \rangle}\right]$, where $k_0 = 2\pi n/\lambda_0$ is the wave vector, with λ_0 the laser wavelength in vacuum. The refractive indices n of the different water–glycerol mixtures are obtained from the literature. The resulting mean-square displacements versus the correlation time τ are shown in Figure 5.A.1. Their linear scaling confirms the absence of evaporation and sedimentation during the measurements, implying that Brownian motion is the only type of dynamics occurring, hence the diffusion coefficients can be determined by: $\langle \Delta r^2(\tau) \rangle = 6D\tau$. We fit these diffusion coefficients to the 'true' values measured using DLS, considering that $D_{\mathrm{LSI}} \propto 1/\gamma^2$, and find the optimal fit for $\gamma \approx 1.5$.

We note that this value is strictly valid only for samples of polystyrene particles in water–glycerol mixtures and will not apply perfectly to drying paint films. In fact, the strong heterogeneity of paint drying precludes using a single value of γ for the entire drying process. Nevertheless, the actual deviation of γ from 1.5 will be limited and will change only the absolute values of $\langle \Delta r^2(\tau) \rangle$ slightly.

5.A.2 Differentiation between different types of dynamics

For samples displaying a single type of motion, such as the polystyrene suspensions in sealed sample chambers shown in Figure 5.A.1, where Brownian motion is the only form of dynamics, interpreting the autocorrelation curves and associated mean-square displacements is relatively straightforward. Most practical applications, however, involve different types of processes in parallel. An example is the drying droplet in Figure 5.4. Evaporation of water from the droplet causes not only changes in the diffusion of particles but also a directional flow of particles to the contact line and droplet surface. We here demonstrate the differentiation between these processes in a drying polystyrene suspension droplet using a high-speed camera at 600 fps. The spatially resolved drying dynamics of this droplet are depicted in Figure 5.A.2a. The coffee-ring effect causes the deposition of a dense ring of colloids at the contact line of the droplet, which grows inward as time evolves. A distinct asymmetry appears in the coffee ring after approximately 10 min (t_2–t_4). The location where the last bulk water evaporates is delineated by a green circle. To elucidate the governing dynamics over time, we measure

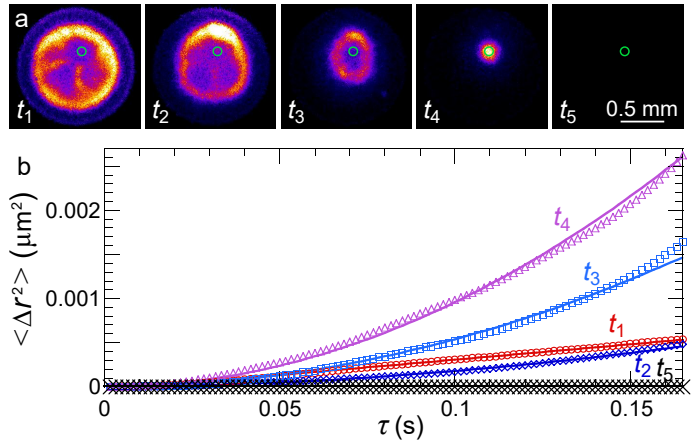

Figure 5.A.2. Drying of a polystyrene suspension droplet and quantification of the dynamics inside the green circular region. **(a)** Time-lapse $d_2(\tau = 1.7$ ms) images of evaporation. t_1 to t_5 represent increasing times after droplet deposition: 7 min (○), 11 min (◇), 13 min (□), 14.3 min (△), and 15.2 min (×). All images have the same scale bar of 0.5 mm and same colour scale except t_1, whose d_2 values are reduced 4×. **(b)** Mean-square displacements obtained by multi-speckle averaging over the 300 speckles inside the green circle, with additional time averaging over 0.40 s to improve the statistics. The labels correspond to the images in (a). The solid lines are least-square fits to the function: $\langle \Delta r^2 \rangle = 6D\tau + (v\tau)^2$.

the multi-speckle averaged mean-square displacements for the circular region (Figure 5.A.2b). The dependence of $\langle \Delta r^2 \rangle$ on τ shows a clear transition from linear (t_1), indicative of diffusive dynamics, to quadratic (t_3–t_4), indicative of ballistic motion. Intermediate times display a mixture of diffusive and ballistic transport (t_2). This shift signifies a decrease in D with increasing concentration and simultaneous increase in advective velocity v due to the coffee-ring effect. We fit the mean-square displacements to $\langle \Delta r^2(\tau) \rangle = 6D\tau + (v\tau)^2$, assuming that at t_1 the v term is negligible with respect to the D term, and vice versa at t_3–t_4. This gives a decrease in D from $6 \cdot 10^{-4}$ μm^2/s at t_1 to $4 \cdot 10^{-5}$ μm^2/s at t_2, while simultaneously v increases from 0.12 μm/s at t_2 to 0.21 μm/s at t_3 to 0.32 μm/s at t_4. After evaporation of the bulk water, all fast motion has vanished (t_5) and $\langle \Delta r^2 \rangle$ is negligible in the measured τ range.

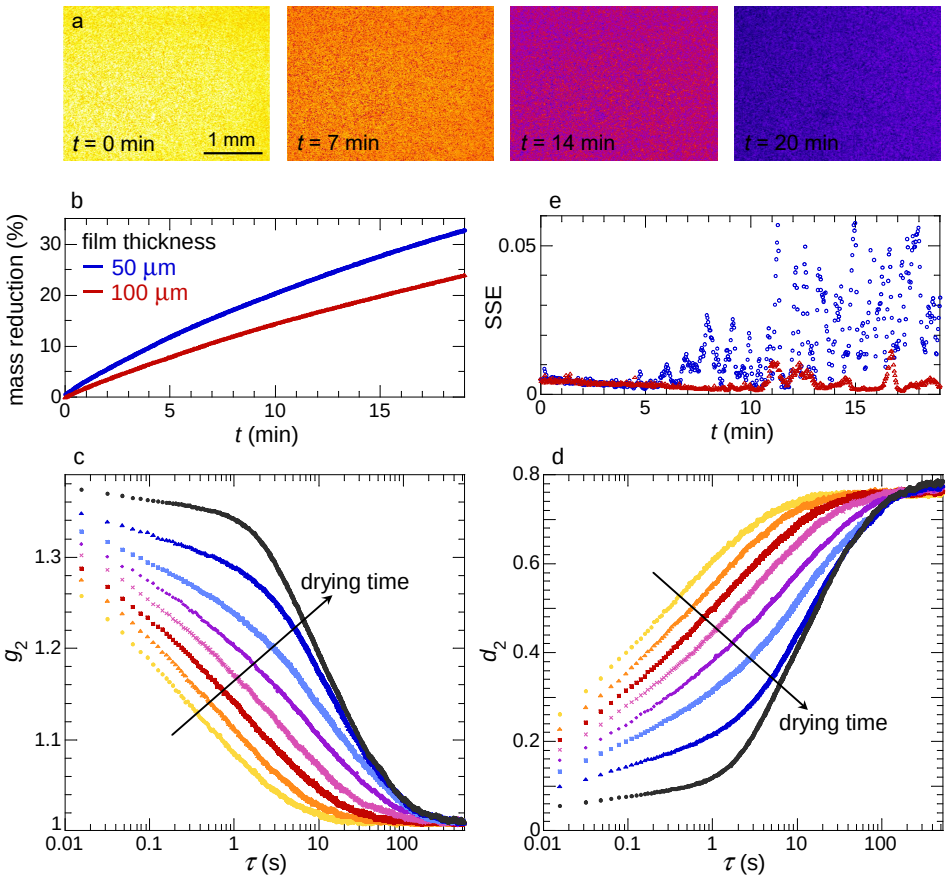

Figure 5.A.3. Open-time analysis; stexupplementary data for Figure 5.2. **(a)** Time-lapse $d_2(\tau = 16$ ms) images in the centre of a 100 µm thick homogeneous paint film. All images have the same colour scale. **(b)** Reduction of the film mass by water evaporation as a function of drying time for two different film thicknesses. At $t = t^1_{\text{open}}$ and t^2_{open} (see Figure 5.2b,c), still a considerable amount of water is present in the films. **(c)** Evolution of the multi-speckle averaged intensity autocorrelation function $g_2(\tau)$ and **(d)** intensity structure function $d_2(\tau)$ during drying of a 100 µm thick film. The two graphs display the same drying times as shown in Figure 5.2a: $t = 0$ min (●), 3.3 min (▲), 6 min (■), 7.3 min (×), 9.3 min (♦), 11.5 min (■), 15 min (▲) and 20 min (●). All g_2 curves converge towards the intercept $g_2(0) = 1.40 \pm 0.005$, which equals $\beta + 1$. **(e)** Sum of squared errors SSE corresponding to the single-exponential fits to the g_1 curves, defined as: $\text{SSE} = \sum_{i=1}^{m} \left[g_1(\tau_i) - f(\tau_i)\right]^2$ with $m = 4500$ the number of data points per g_1 curve, τ_i the i^{th} correlation time, $g_1(\tau_i)$ the i^{th} g_1 value to be predicted, and $f(\tau_i)$ the predicted value of $g_1(\tau_i)$.

References

[1] H. M. van der Kooij, G. T. van de Kerkhof, J. Sprakel. *Soft Matter* **12**, 2858–2867 (2016). **(Chapter 4)**

[2] A. Gromer, M. Nassar, F. Thalmann, P. Hébraud, Y. Holl. *Langmuir* **31**, 10983–10994 (2015).

[3] K. B. Singh, M. S. Tirumkudulu. *Phys. Rev. Lett.* **98**, 218302 (2007).

[4] L. Goehring, W. J. Clegg, A. F. Routh. *Phys. Rev. Lett.* **110**, 024301 (2013).

[5] A. F. Routh. *Rep. Prog. Phys.* **76**, 046603 (2013).

[6] Y. Zhang, Y. Qian, Z. Liu, Z. Li, D. Zang. *Eur. Phys. J. C* **37**, 14084 (2014).

[7] J. Domnick, D. Gruseck, K. Pulli, A. Scheibe, Q. Ye, F. Brinckmann. *Chem. Eng. Proc. Proc. Intens.* **50**, 495–502 (2011).

[8] T. Narita, C. Beauvais, P. Hébraud, F. Lequeux. *Eur. Phys. J. E* **14**, 287–292 (2004).

[9] F. Giorgiutti-Dauphiné, L. Pauchard. *Soft Matter* **11**, 1397–1402 (2015).

[10] F. Giorgiutti-Dauphiné, L. Pauchard. *J. Appl. Phys.* **120**, 065107 (2016).

[11] J. Keddie, A. F. Routh, *Fundamentals of latex film formation: processes and properties* (Springer, 2010).

[12] H. M. van der Kooij, J. Sprakel. *Soft Matter* **11**, 6353–6359 (2015). **(Chapter 2)**

[13] L. Goehring, R. Conroy, A. Akhter, W. J. Clegg, A. F. Routh. *Soft Matter* **6**, 3562–3567 (2010).

[14] H. M. van der Kooij, M. de Kool, J. van der Gucht, J. Sprakel. *Langmuir* **31**, 4419–4428 (2015). **(Chapter 3)**

[15] R. C. Daniel, J. C. Berg. *Adv. Colloid Interface Sci.* **123—126**, 439–469 (2006).

[16] D. Brutin, B. Sobac, B. Loquet, J. Sampol. *J. Fluid Mech.* **667**, 85–95 (2011).

[17] R. Lenke, G. Maret, *Scattering in polymeric and colloidal systems* (Gordon & Breach, 2000), chap. Multiple scattering of light: coherent backscattering and transmission, pp. 1–73.

[18] M. Verma, D. K. Singh, P. Senthilkumaran, J. Joseph, H. C. Kandpal. *Sci. Rep.* **4**, 7257 (2014).

[19] D. A. Weitz, J. X. Zhu, D. J. Durian, H. Gang, D. J. Pine. *Phys. Scr.* **1993**, 610–621 (1993).

[20] V. Viasnoff, F. Lequeux, D. J. Pine. *Rev. Sci. Instrum.* **73**, 2336–2344 (2002).

[21] S. E. Skipetrov, J. Peuser, R. Cerbino, P. Zakharov, B. Weber, F. Scheffold. *Opt. Express* **18**, 14519–14534 (2010).

[22] A. C. Völker, P. Zakharov, B. Weber, F. Buck, F. Scheffold. *Opt. Express* **13**, 9782–9787 (2005).

[23] P. Vaz, A. Humeau-Heurtier, E. Figueiras, C. Correia, J. Cardoso. *IEEE Rev. Biomed. Eng.* **9**, 106–120 (2016).

[24] P. Zakharov, F. Scheffold, *Light scattering reviews 4: single light scattering and radiative transfer* (Springer, Berlin, Heidelberg, 2009), chap. Advances in dynamic light scattering techniques, pp. 433–467.

[25] D. Bicout, G. Maret. *Phys. A* **210**, 87–112 (1994).

[26] H. M. van der Kooij, R. Fokkink, J. van der Gucht, J. Sprakel. *Sci. Rep.* **6**, 34383 (2016). **(This chapter)**

[27] C. Zhou, G. Yu, D. Furuya, J. H. Greenberg, A. G. Yodh, T. Durduran. *Opt. Express* **14**, 1125–1144 (2006).

[28] M. Draijer, E. Hondebrink, T. Leeuwen, W. Steenbergen. *Lasers Med. Sci.* **24**, 639–651 (2008).

[29] P. Zakharov, A. C. Völker, M. T. Wyss, F. Haiss, N. Calcinaghi, C. Zunzunegui, A. Buck, F. Scheffold, B. Weber. *Opt. Express* **17**, 13904–13917 (2009).

[30] D. Briers, D. D. Duncan, E. Hirst, S. J. Kirkpatrick, M. Larsson, W. Steenbergen, T. Stromberg, O. B. Thompson. *J. Biomed. Opt.* **18**, 066018 (2013).

[31] D. A. Sessoms, H. Bissig, A. Duri, L. Cipelletti, V. Trappe. *Soft Matter* **6**, 3030–3037 (2010).

[32] P. Zakharov, F. Scheffold. *Soft Mater.* **8**, 102–113 (2010).

[33] A. Amon, V. B. Nguyen, A. Bruand, J. Crassous, E. Clément. *Phys. Rev. Lett.* **108**, 135502 (2012).

[34] M. Z. Ansari, A. K. Nirala. *J. Opt.* pp. 1–7 (2015).

[35] M. Pajuelo, G. Baldwin, H. Rabal, N. Cap, R. Arizaga, M. Trivi. *Opt. Lasers Eng.* **40**, 13–24 (2003).

[36] O. P. Maksymenko, L. I. Muravsky, M. I. Berezyuk. *J. Biomed. Opt.* **20**, 095006 (2015).

[37] M. Erpelding, A. Amon, J. Crassous. *Phys. Rev. E* **78**, 046104 (2008).

[38] Z. Hajjarian, S. K. Nadkarni. *Sci. Rep.* **2**, 316 (2012).

[39] M.-Y. Nagazi, G. Brambilla, G. Meunier, P. Marguerès, J.-N. Périé, L. Cipelletti. *Opt. Laser Eng.* **88**, 5–12 (2017).

[40] T. Fricke-Begemann, G. Gülker, K. D. Hinsch, K. Wolff. *Appl. Opt.* **38**, 5948–5955 (1999).

[41] K. D. Hinsch, T. Fricke-Begemann, G. Gülker, K. Wolff. *Opt. Laser. Eng.* **33**, 87–105 (2000).

[42] N. H. Koshoji, S. K. Bussadori, C. C. Bortoletto, R. A. Prates, M. T. Oliveira, A. M. Deana. *PloS One* **10**, e0118429 (2015).

[43] D. J. Pine, D. A. Weitz, J. X. Zhu, E. Herbolzheimer. *J. Phys. France* **51**, 2101–2127 (1990).

[44] L. F. Rojas-Ochoa, D. Lacoste, R. Lenke, P. Schurtenberger, F. Scheffold. *J. Opt. Soc. Am. A* **21**, 1799–1804 (2004).

[45] M. P. van Albada, B. A. van Tiggelen, A. Lagendijk, A. Tip. *Phys. Rev. Lett.* **66**, 3132–3135 (1991).

[46] K. Schätzel. *Appl. Phys. B: Lasers Opt.* **42**, 193–213 (1987).

[47] G. F. Lorusso, A. Minafra, V. Capozzi. *Appl. Opt.* **32**, 3867–3870 (1993).

[48] D. J. Durian, D. A. Weitz, D. J. Pine. *Science* **252**, 686–688 (1991).

[49] A. E. Ennos, *Laser speckle and related phenomena* (Springer, 1975), pp. 203–253.

[50] O. Thompson, M. Andrews, E. Hirst. *Biomed. Opt. Express* **2**, 1021–1029 (2011).

[51] G. Popescu, A. Dogariu. *Opt. Lett.* **24**, 442–444 (1999).

[52] M. S. Patterson, B. Chance, B. C. Wilson. *Appl. Opt.* **28**, 2331–2336 (1989).

[53] J. D. Briers. *Physiol. Meas.* **22**, R35–R66 (2001).

[54] R. Bezemer, M. Legrand, E. Klijn, M. Heger, I. C. J. H. Post, T. M. van Gulik, D. Payen, C. Ince. *Opt. Express* **18**, 15054–15061 (2010).

[55] A. Overbeek, F. Bückmann, E. Martin, P. Steenwinkel, T. Annable. *Prog. Org. Coat.* **48**, 125–139 (2003).

[56] M. S. Tirumkudulu, W. B. Russel. *Langmuir* **21**, 4938–4948 (2005).

[57] Y. Xu, W. C. Engl, E. R. Jerison, K. J. Wallenstein, C. Hyland, L. A. Wilen, E. R. Dufresne. *Proc. Natl. Acad. Sci.* **107**, 14964–14967 (2010).

[58] Q. Jin, P. Tan, A. B. Schofield, L. Xu. *Eur. Phys. J. E* **36**, 13028 (2013).

[59] J. Y. Lee, J. W. Hwang, H. W. Jung, S. H. Kim, S. J. Lee, K. Yoon, D. A. Weitz. *Langmuir* **29**, 861–866 (2013).

[60] D. A. Ansdell, *Paint and surface coatings: theory and practice* (Woodhead Publishing Ltd.: Cambridge, UK, 1999), chap. 10.10, pp. 461–472.

[61] B.-J. de Gans, P. C. Duineveld, U. S. Schubert. *Adv. Mater.* **16**, 203–213 (2004).

[62] B. Sobac, D. Brutin. *Phys. Rev. E* **84**, 011603 (2011).

[63] R. D. Deegan, O. Bakajin, T. F. Dupont, G. Huber, S. R. Nagel, T. A. Witten. *Nature* **389**, 827–829 (1997).

[64] Á. G. Marín, H. Gelderblom, D. Lohse, J. H. Snoeijer. *Phys. Rev. Lett.* **107**, 085502 (2011).

[65] A. Crivoi, F. Duan. *Sci. Rep.* **4**, 4310 (2014).

[66] J. Bico, U. Thiele, D. Quéré. *Colloids Surf., A* **206**, 41–46 (2002).

[67] M. Alava, M. Dubé, M. Rost. *Adv. Phys.* **53**, 83–175 (2004).

[68] G. M. Homsy. *Annu. Rev. Fluid Mech.* **19**, 271–311 (1987).

[69] X. Cheng, L. Xu, A. Patterson, H. M. Jaeger, S. R. Nagel. *Nat. Phys.* **4**, 234–237 (2008).

Chapter 6

Quantifying the open time and film formation of water-borne coatings with laser speckle imaging

This chapter is based on: Slav A. Semerdzhiev, Hanne M. van der Kooij, Remco Fokkink, Jasper van der Gucht and Joris Sprakel, 'Quantifying the open time and film formation of water-borne coatings with Laser Speckle Imaging', *in preparation*.

Abstract

In drying water-borne coatings, the time span between the deposition of the liquid dispersion and the formation of a uniform solid harbours a procession of complex phenomena each of which carves the final properties of the dry paint film. One of the major challenges in the design of sustainable, water-based paints is to match or surpass the drying performance of their solvent-based counterparts. In particular, the so-called 'open time' – the time during which the coating remains wet and susceptible to alterations without affecting the aesthetics of the final film – is often much shorter in water-borne systems than in solvent-borne equivalents. Optimization and tailoring the open time would greatly benefit from methods capable of determining this critical parameter in a fast and unambiguous way. Yet, experimental access to the internal dynamics accompanying the drying process is challenging, as paints are often opaque and the drying phenomena usually populate a multitude of time and length scales. To address these obstacles, we deploy the optical technique laser speckle imaging (LSI), which allows probing nanoscale motions deep inside turbid paints. We apply this method to quantitatively and unambiguously determine the open time. We develop a set of scaling relations that accurately predict the experimentally measured open time as a function of key parameters governing the drying process. Additionally, we harness the wide temporal dynamic range of LSI to capture phenomena that inhabit the later drying stages, including deformation and coalescence of the polymer particles.

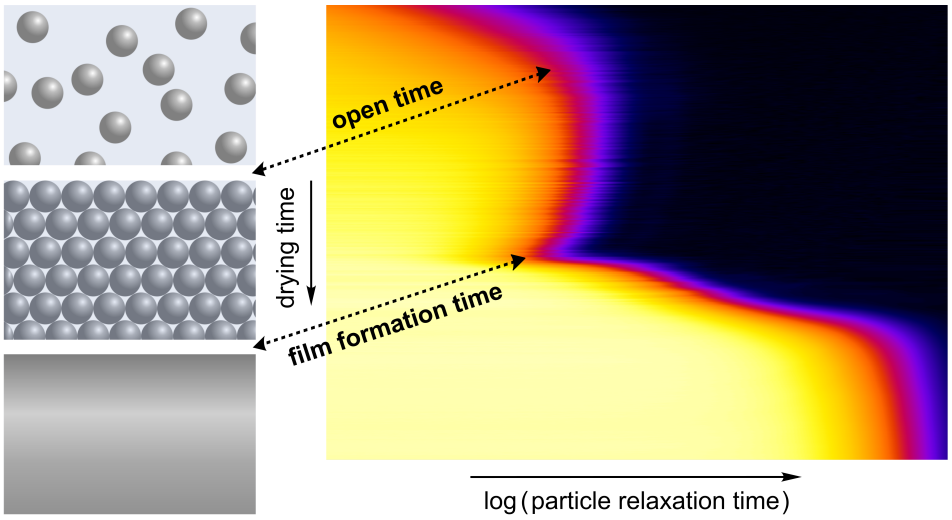

6.1 Introduction

The drying of aqueous colloidal coatings has been subject to scientific scrutiny for many decades. The entanglement of numerous accompanying phenomena such as hydrodynamics, colloidal interactions and mechanics renders the drying process highly complex and has prompted significant research efforts in pursuit of a better understanding. The need of such also has a practical genesis: drying composite colloidal coatings are of great importance for a variety of industrial fields such as food technology, inkjet printing and particularly coatings technology.[1–3] Solvent-based coatings emit volatile organic compounds (VOCs) which are very potent in amplifying the greenhouse effect and additionally are hazardous to the health of the consumer and the professional applying the coating.[4–7] These issues have prompted a transition from solvent-borne coatings to solvent-free or water-based (latex) systems. However, such a transition is far from trivial and offers many challenges. Water-based paints often dry much faster than their solvent-borne equivalents. This significantly shortens the time window in which the coating can be handled without leaving permanent topological defects; a crucial parameter for paints known as the open time. Moreover, in water-based coatings, the binder particles must coalesce to achieve phase inversion and film formation. The timing of this phase is also critical as it determines the properties of the final film.

The dynamics underlying the drying process shape the final state of the colloidal coating. The first step towards solving the challenges listed above is establishing the right tool to study and interpret these drying dynamics. Unfortunately, that is a challenge in itself. Studying the dynamics is notoriously difficult because they are often heterogeneous and span a wide range of time and length scales.[8] Additionally, the high turbidity of paints precludes investigations relying on conventional techniques such as microscopy (bright-field or fluorescence-based) and dynamic light scattering, which operate in the limit of sufficiently transparent samples. The limited availability of proper means to monitor and study paint drying obscures the progress in optimizing this process and makes it difficult to determine with high fidelity important quantities such as the open time and film formation time. Existing methods for open-time determination are typically rather qualitative and are applied manually by human operators, which introduces ambiguity and big spread in the obtained results. Other sophisticated MRI-based approaches are more precise and quantitative but very demanding in terms of equipment cost.[9,10]

In this chapter, we use laser speckle imaging (LSI) as a relatively inexpensive and straightforward approach to elucidate with microscopic resolution the dynamics inside drying opaque latex coatings, spanning seven orders of magnitude in time.

Access to these internal dynamics allows us to measure the open time of realistic paint formulations in a quantitative and unambiguous manner, and for a wide range of conditions. We validate our LSI findings by systematically comparing the experimentally determined open time as a function of different environmental parameters to predictions stemming from scaling relations based on the Hertz–Langmuir–Knudsen theoretical framework of evaporation. Finally, we further expand the application scope of LSI by demonstrating its ability to follow in detail the film formation in later drying stages. Not only can we readily detect the onset of phase inversion, but we can also track the dependence of this phenomenon on an important parameter such as the hardness of the latex particles. This method makes it possible to time-stamp critical stages in the drying of a latex coating with a high degree of accuracy, offering new handles for the rational design of improved water-based paint formulations.

6.2 Experimental details

6.2.1 Laser speckle imaging set-up

All measurements are performed on a custom-built instrument, which is represented schematically in Figure 6.1a. The sample holder is situated in an insulated chamber in which the temperature and relative humidity are maintained constant at the desired values. Unless specified otherwise, $T = 25\ ^\circ\mathrm{C}$ and $H_\mathrm{R} = 0.5$. The holder is coupled to a computer-controlled analytical balance (WZA224-NC, Sartorius), which allows for continuous monitoring of the sample mass. A 532 nm solid-state laser (Samba 1W, Cobolt) is used as the light source. The laser beam is first driven through a half-wave plate and then through a polarizing beam splitter to adjust the intensity. Subsequently, the light is guided through a beam expander to set the cross-section size of the beam to ~1 cm. The resulting beam is navigated via mirrors towards the sample. The back-scattered light from the sample first passes through a polarizer that filters the reflected photons and photons with short paths. Finally, the filtered back-scattered light is collected by a zoom lens (1.8×) and focused on a CCD camera (Dalsa Genie, CR-GM00-H640x, Stemmer Imaging). The speckle size is set 2–3 times bigger than the physical size of the camera pixels to ensure a good balance between spatial resolution and signal-to-noise ratio.[11] All speckle images are acquired at 100 fps with the exposure time optimized to exploit the full dynamic range of the camera.

6.2.2 Data analysis

To study the ongoing dynamics in the drying coatings, we compute the intensity structure function d_2, the intensity correlation function g_2, and the field correlation function g_1, using Equations (6.1), (6.2), and (6.3), respectively. The spatial correlation factor β ($0 < \beta \leq 1$), which accounts for the number of speckles per camera pixel, is chosen such that $g_2 - 1 \rightarrow \beta$ for $\tau \rightarrow 0$. A value of 1.5 is used for the numerical prefactor γ, which we have experimentally determined in Chapter 5, Appendix 5.A.1.

6.2.3 Materials

All measurements are performed on commercial water-based paints (acrylic–styrene copolymer emulsions). The effects of relative humidity and temperature are studied for 200 μm thick coatings deposited using a quadruple film applicator (Erichsen) that ensures well-defined dimensions (see Appendix 6.A.1 and Figure 6.A.1). The paint formulation includes 2.7 wt% butyldiglycol and texanol as coalescing aids, and 0.15 wt% TiO_2 (titania, $d = 316 \pm 8$ nm) as strongly scattering pigment. The initial water content is ~60 wt%. Film formation in the later drying stages is studied for 100 μm thick coatings with varying total coalescent concentrations of 2.7 wt%, 5.4 wt% and 7.2 wt% butyldiglycol plus texanol. The temperature and relative humidity are fixed at 23 ± 1 °C and 0.43 ± 0.02, respectively.

6.3 Results and discussion

6.3.1 Laser speckle imaging

LSI exploits multiple light scattering to evaluate, with both high temporal and spatial resolution, the dynamics inside opaque materials. This characteristic feature has encouraged the deployment of LSI in numerous fields such as biology, food technology and materials science.[12–20] In a turbid medium, light propagates via multiple scattering events. After a certain number of such events, the propagation direction of the photons is completely randomized (Figure 6.1a, inset). This allows to treat photon propagation in an opaque medium as a diffusive transport.[21] At the detector, the scattered photons emanating from the sample superpose and generate a speckle pattern (Figure 6.1b) due to the different paths that they have traversed. Since light diffuses orders of magnitude faster than any type of molecular or particle motion, the momentary realization of this interference pattern is directly related to the instantaneous arrangement of the scattering species within the sample. At

longer time scales, the speckle pattern changes because of the displacement of the scattering particles. LSI uses the diffusive nature of light propagation in turbid systems to extract information from these temporal changes in the speckle patterns about the movement of scattering species, and thus about the ongoing internal dynamics. See Chapter 1, Section 1.4, and Chapter 5 for a detailed description of the technique.

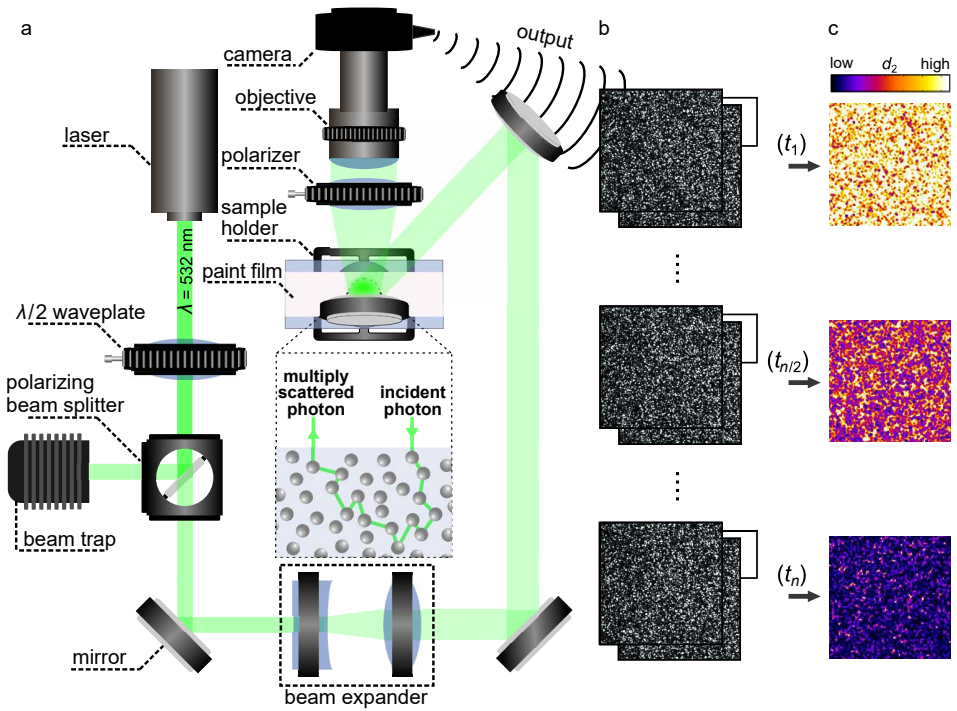

Figure 6.1. Laser speckle imaging set-up and output. **(a)** Schematic of the LSI instrument. The light is guided to the drying aqueous coating and impinges on it. After multiple scattering events, the propagation direction of photons in the sample is completely randomized (see inset). The multiply scattered light emanating from the sample is subsequently collected and projected onto a CCD camera chip. This yields a sequence recording of speckle patterns **(b)**. Correlating the raw speckle images using Equation (6.1) at a fixed correlation time τ for different time points t_i ($i = 1..n$) during the drying process translates the raw data into d_2 maps, which encode the spatially resolved mobility **(c)**. In the beginning of the drying process (t_1), the coating is populated with fast dynamics, while at the mid-drying stage ($t_{n/2}$) the dynamics have significantly slowed down due to the ongoing evaporation. At the end (t_n), all dynamics on the time scale of τ have come to a halt.

To quantify the speckle intensity fluctuations, we use the intensity structure function d_2, which reads:[22,23]

$$d_2(t,x,y,\tau) = \frac{\left\langle \left[I(t,x,y) - I(t+\tau,x,y)\right]^2 \right\rangle}{\left\langle I(t,x,y)\right\rangle \left\langle I(t+\tau,x,y)\right\rangle} \tag{6.1}$$

Here t is the time, x and y are the spatial coordinates, and τ is the correlation time which sets the time lag between two speckle patterns that are compared. High and low d_2 values indicate a large and small mobility, respectively (Figure 6.1c). d_2 is a convenient quantity that enables temporal and spatial mapping of the dynamics in a system of interest. Additionally, by choosing the appropriate τ we can resolve processes that take place at different time scales. The ability to construct spatio-temporal d_2 maps allows us to monitor the evolution of the dynamics and easily detect any dynamic heterogeneity that may occur within the sample under investigation. Visualizing such inhomogeneities is crucial for the next steps in our analysis in which we compute the intensity correlation function

$$g_2(t,x,y,\tau) = \frac{\left\langle I(t,x,y)\cdot I(t+\tau,x,y)\right\rangle}{\left\langle I(t,x,y)\right\rangle \left\langle I(t+\tau,x,y)\right\rangle} \tag{6.2}$$

that is closely related to d_2, and average it over all speckles in the field of view, provided that no discernible inhomogeneities are present. The spatially averaged $g_2(t,\tau)$ grants us access to the electric field correlation function $g_1(t,\tau)$ via the Siegert relation:

$$g_1(t,\tau) = \frac{1}{\sqrt{\beta}}\sqrt{g_2(t,\tau)-1} \tag{6.3}$$

where β is a numerical prefactor dependent on the experimental set-up (see Section 6.2.2).[21] Finally, we fit $g_1(t,\tau)$ using an exponential decay function:

$$g_1(t,\tau) = \exp\left(-\gamma[\tau/\tau_0(t)]^{\alpha(t)}\right) \tag{6.4}$$

where $\tau_0(t)$ is the characteristic relaxation time, $\alpha(t)$ is a stretching (or compressing) exponent, and γ is an experimental numerical constant that has been determined elsewhere (see Section 6.2.2). Both the relaxation time and stretching exponent are means to extract more quantitative information about the ongoing dynamics. For example, in the case of pure diffusion, the relaxation time is related to the diffusion coefficient D of the scatterers via $\tau_0 = 1/6\,{k_0}^2 D$, where $k_0 = 2\pi n/\lambda_0$ is the wave vector with n the refractive index of the medium and λ_0 the laser wavelength in vacuum. τ_0 thus provides information about the resistance or effective viscosity that the scatterers experience while moving. By contrast, the stretching exponent

α reflects the type of motion that the scattering particles undergo and as such serves as 'process identifier'. Since $g_1(\tau) = \exp\left(-\gamma k_0 \sqrt{\langle \Delta x^2(\tau) \rangle}\right)$ with $\langle \Delta x^2(\tau) \rangle$ the mean-square displacement, it follows that $\langle \Delta x^2(\tau) \rangle \propto \tau^{2\alpha}$. Values of $\alpha < 0.5$ thus imply sub-diffusive dynamics, $\alpha = 0.5$ signals Brownian dynamics, and $\alpha = 1$ indicates ballistic motion of the particles.[24,25] The complementary sensitivity of τ_0 and α to changes in the motion of the scattering particles renders these two quantities as appropriate tools for monitoring the dynamics in evolving systems such as drying water-borne coatings.

6.3.2 The open time of water-borne coatings

The drying of colloidal coatings is a complex phenomenon accompanied by a constellation of processes each of which is marked by its own characteristic dynamics, time scales and length scales.[11,26,27] For soft colloids, the drying process can be divided into four main stages (Figure 6.2a). We start with a liquid-like dispersion of freely diffusing particles. Due to solvent evaporation, in time the particles get concentrated and more densely packed. Upon close packing, capillary forces cause the particles to deform and – provided the glass transition temperature is sufficiently low – coalesce to yield a uniform film. The big temporal dynamic range of LSI allows us to capture different processes spanning multiple decades of time, and thus many of the events that take place during the drying of such dispersions (see Chapter 5).

First we focus on the early drying stages of water-borne paint systems. The dynamics in these early stages govern the open time (t_{OT}) of the drying coating, which is a crucial handling parameter not only for coatings but for any type of system containing an evaporating solvent. By definition, open time is the period after applying the paint in which the coating can still be reworked without leaving any visible and permanent topological irregularities. To demonstrate that we can determine the open time in a quantitative and unambiguous manner, we start by depositing a 200 μm thick coating of an acrylic–styrene copolymer emulsion on a glass substrate, and record a sequence of raw speckle images of the central section of the drying emulsion. The formulation contains TiO_2 nanoparticles of relatively low concentration yet sufficient to render the coating highly turbid and thus ensure optimal conditions for the deployment of LSI, i.e. multiple-scattering events. Since in such a setting the TiO_2 nanoparticles are the dominant scattering species, they can be considered as reporters of the ongoing dynamics in the coating, similarly to what is done in well-established microrheology approaches.[28] The resulting d_2 maps reveal spatially uniform evolution of the dynamics in time (Figure 6.1c), which allows us to compute the average field correlation curves $g_1(\tau)$

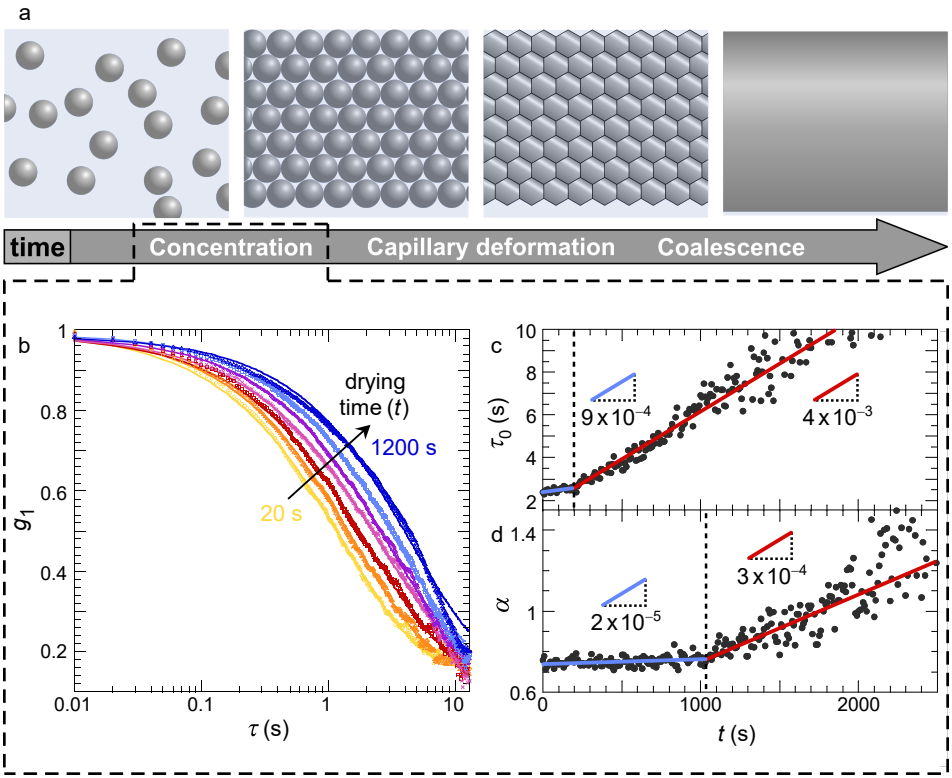

Figure 6.2. Open-time determination with LSI. **(a)** Simplified schematic of the main events taking place in a drying aqueous coating of soft colloidal particles. **(b)** Typical temporal evolution of the field correlation function g_1. The curves shift towards longer correlation times τ due to evaporation-induced particle concentration. The solid lines are fits to Equation (6.4). **(c)** Changes in the relaxation time τ_0 and **(d)** the process identifier α with the progression of the drying process. The temporal evolution of both parameters can be divided into two distinct regimes demarcated by a dashed line and coloured (solid lines) in blue or red. The slopes (⟋) $\mathrm{d}\tau_0/\mathrm{d}t$ and $\mathrm{d}\alpha/\mathrm{d}t$ are coloured in accordance with the corresponding regime. For $\tau_0(t)$ the dashed line marks the start of a sudden and more steep increase of the viscosity, and thus the onset of deterioration of the coating workability. In the case of $\alpha(t)$, the dashed line designates an abrupt change, signalling the formation of a semi-solid film. We consider this time point as the upper bound of t_{OT}.

with Equations (6.2) and (6.3). During water evaporation, the $g_1(\tau)$ curves shift towards longer correlation times (Figure 6.2b), which indicates retardation of the particle motion as a consequence of the increasing concentration. By examining the time evolution of the relaxation time τ_0 and the process identifier α, we can clearly discern different regimes in the dynamics. First we focus on the concentration stage, in which the $\tau_0(t)$ curve exhibits a sharp change in the slope $\mathrm{d}\tau_0/\mathrm{d}t$ (Figure 6.2c). This characteristic kink signals a transition from a slow to a faster increase in the viscosity of the coating. We interpret this time point as the onset of deterioration in the workability of the coating. Interestingly, the $\alpha(\tau)$ curve shows a similar sudden increase in the slope $\mathrm{d}\alpha/\mathrm{d}t$ (Figure 6.2d). This kink, however, is shifted to a later time point and has a different origin. The dynamics in the period preceding this time point $t < 1100$ s are more Brownian than advective ($\alpha \sim 0.7$) and barely change, whereas the subsequent period ($t > 1100$ s) gradually gets dominated by advective processes ($\alpha \rightarrow 1$) powered by the accelerating evaporative flux. The transition between these distinct regimes marks the transformation of the liquid dispersion into a quasi-solid. Such a coating with semi-solid properties cannot be further reworked without leaving permanent defects. Bearing that in mind, we define this characteristic time point as the upper bound for the coating workability and adopt it as a standard measure for the open time t_{OT} in the remainder of this chapter.

6.3.3 Open time versus coating thickness

Having established a quantitative determination of the open time of water-borne paints, we will couple this quantity to related physical phenomena using analytical models. Being successful in such an endeavour will not only validate our LSI findings, but will also provide predictive power for the open time as a function of key parameters influencing the drying process. Since water evaporation drives the concentration and packing of particles, it is logical to use the Langmuir–Knudsen equation, also known as the Hertz–Knudsen equation, as the starting point for the evaporative flux:[29–31]

$$\frac{\mathrm{d}M_A}{\mathrm{d}t} = (p_{\mathrm{s}} - p_{\mathrm{p}})\sqrt{\frac{m}{2\pi kT}} \tag{6.5}$$

where M_A is the mass of the evaporated water per unit area, p_{s} and p_{p} are the equilibrium (saturation) and partial vapor pressure of water, m is the mass of a water molecule, k is Boltzmann's constant, and T is the temperature. This expression is a convenient starting point, because $-\mathrm{d}M_A/\mathrm{d}t$ equals the mass change rate of the drying coating $\mathrm{d}M_A^{\mathrm{coating}}/\mathrm{d}t$. The latter can be obtained from the mass evolution measured in parallel with LSI (Figure 6.3a, top). As a first benchmark,

we will link t_{OT} to the starting thickness h_S of the wet coating. We multiply Equation (6.5) by the surface area of the coating A to get the total evaporation rate $Q = dM/dt$, which is a directly accessible quantity from the mass measurements. Since the evaporation rate is constant during the open-time period, integration is trivial and leads to:

$$M_S - M_{OT} = A(p_s - p_p)\sqrt{\frac{m}{2\pi kT}}\, t_{OT} \tag{6.6}$$

where M_S is the starting mass of the coating and M_{OT} is the mass at $t = t_{OT}$, derived from the characteristic kink in the corresponding $\alpha(t)$ curve (Figure 6.3a, bottom). This equation instructs that the mass flux and consequently the evaporation rate Q are independent of the starting thickness, which is experimentally confirmed by LSI measurements (Figure 6.3b). We also expect that the end of the open-time period occurs always at the same effective particle concentration regardless of the starting thickness of the wet coating. Thus, the relative mass at t_{OT}, $\phi_{OT} = M_{OT}/M_S$, is predicted to be constant for all coating thicknesses. To test the validity of this conjecture, we measure ϕ_{OT} for coatings with different h_S, which indeed does not depend on t_{OT} (Figure 6.3c). Subsequently, we rewrite the mass difference $M_S - M_{OT}$ as $M_S(1 - \phi_{OT})$. The dimensions of the coating are imposed by the used

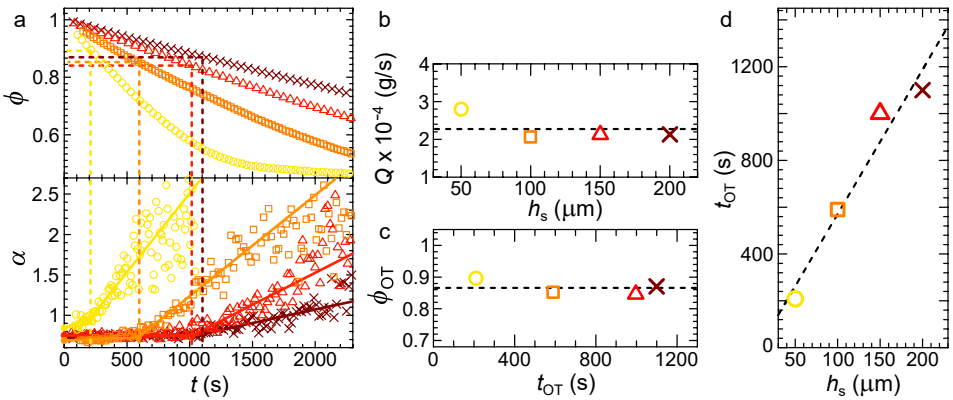

Figure 6.3. Open time as function of coating thickness. **(a)** Normalized coating mass (top) and process identifier (bottom) versus drying time for coatings with starting thickness h_S = 50 µm (○), 100 µm (□), 150 µm (△) and 200 µm (×). The dashed lines indicate the mass fractions at the end of the open-time period ϕ_{OT}. The solid lines guide the eye through the different regimes in the $\alpha(t)$ curves and designate the open time t_{OT}. **(b)** The evaporation rate Q and **(c)** the mass fraction ϕ_{OT} remain approximately constant for all coating thicknesses. Symbols represent the experimental data while the dashed lines are guides to the eye. **(d)** Open time versus coating thickness. The dashed line is a least-squares fit to the linear relation predicted by Equation (6.7).

deposition method (see Appendix 6.A.1 and Figure 6.A.1) and its width w and length l are the same for all experiments. Since the mass of the coating equals $M(t) = w\,l\,h(t)\,\rho(t) = A\,h(t)\,\rho(t)$ with $\rho(t)$ the density of the dispersion at time t, Equation (6.6) can be rewritten as:

$$t_{\mathrm{OT}} = \rho_{\mathrm{S}} \frac{(1-\phi_{\mathrm{OT}})}{(p_{\mathrm{s}} - p_{\mathrm{p}})} \sqrt{\frac{2\pi kT}{m}}\, h_{\mathrm{S}} = c_1 h_{\mathrm{S}} \tag{6.7}$$

where c_1 is an aggregate of all the constants. By omitting c_1 we obtain the scaling relation $t_{\mathrm{OT}} \propto h_{\mathrm{S}}$, which predicts a linear dependence of the open time with respect to the starting thickness of the coating, fully in line with our experimental findings (Figure 6.3d). This approach highlights the ability of a relatively simple but concise scaling relationship containing the governing physical parameters to provide remarkably good agreement with our LSI results. We will thus proceed with the same strategy and connect other important environmental parameters for the drying process with the behaviour of the LSI-determined open time.

6.3.4 Open time versus relative humidity

Humidity has a profound effect on the drying dynamics of aqueous systems, and hence, it strongly influences the open time of water-borne paints. To capture this effect in a quantitative manner using our LSI-based approach, the relative humidity needs to be incorporated as a parameter in the Langmuir–Knudsen equation. To that end we rewrite the latter as:

$$Q = (a p_{\mathrm{s}} - p_{\mathrm{p}})\, A \sqrt{\frac{m}{2\pi kT}} = (a - H_{\mathrm{R}})\, p_{\mathrm{s}}\, A \sqrt{\frac{m}{2\pi kT}} \tag{6.8}$$

where $H_{\mathrm{R}} = p_{\mathrm{p}}/p_{\mathrm{s}}$ is the relative humidity, and $a = p_{\mathrm{a}}/p_{\mathrm{s}}$ is a correction factor for the deviation of the water activity from ideal values due to the complex composition of our system, with p_{a} the actual saturation pressure. After integration and some algebra we arrive at:

$$t_{\mathrm{OT}} = \frac{c_2}{a - H_{\mathrm{R}}} \tag{6.9}$$

$$c_2 = \frac{M_{\mathrm{S}} - M_{\mathrm{OT}}}{p_{\mathrm{s}}\, A} \sqrt{\frac{2\pi kT}{m}} \tag{6.10}$$

Since $c_2 = \mathrm{const}$, the open time should scale with the relative humidity as $t_{\mathrm{OT}} \propto 1/(a - H_{\mathrm{R}})$. To test this prediction, we examine the temporal evolution of α for different values of H_{R}, and determine $t_{\mathrm{OT}}(H_{\mathrm{R}})$ from the characteristic kink in the $\alpha(t)$ curves (Figure 6.4a,b). We subsequently fit these experimental values to Equation (6.9), with a as the adjustable parameter (here $a = 0.8$). Interestingly, the

theoretical prediction holds for the upper range of relative humidities $H_R \geq 0.5$ but fails to accurately describe the experimental data in the lower range $H_R < 0.5$ (Figure 6.4b). Notably, the open time drops abruptly at $H_R \approx 0.48$ and barely changes below this humidity. This discontinuity in $t_{OT}(H_R)$ hints at the advent of an additional phenomenon that alters the drying dynamics. Indeed, lower relative humidities enhance the drying kinetics which in turn could (i) facilitate particle packing at a ϕ_{OT} value different from the value observed for more humid air,[32–35] or (ii) induce the formation of a thin solid-like layer called 'skin' at the dispersion–air interface.[10,36–38] Such a skin consists of accumulated, coalesced polymer particles and thus forms a barrier for water evaporation. The occurrence of both phenomena could account for the sudden drop and the subsequent constant value of the open time at low H_R.

To pinpoint the culprit for our experimental observations, we first identify a characteristic signature for each of the proposed phenomena. If a skin layer is formed at $H_R < 0.5$, the water transport through the dispersion–air interface

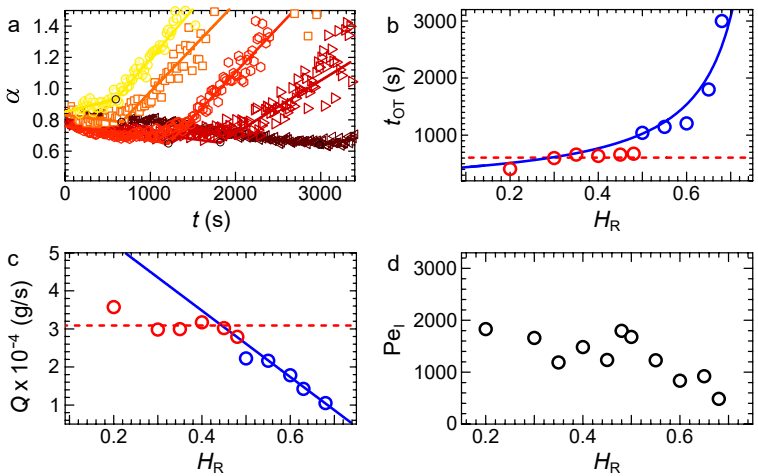

Figure 6.4. Open time as function of relative humidity. **(a)** Temporal evolution of α for 200 μm coatings at $H_R = 0.30$ (○), 0.45 (□), 0.50 (⬡), 0.60 (▷), and 0.68 (◁). The circles indicate the open times. **(b)** Open time versus relative humidity. The experimental data obtained for $H_R \geq 0.5$ (○) are in good agreement with the prediction according to Equation (6.9) (—). Due to skin formation, the open time exhibits a sharp drop and barely changes for $H_R < 0.5$ (○). **(d)** Evaporation rate versus relative humidity. The experimental results are in accordance with the expected scaling $Q = dM/dt \propto (a - H_R)^{-1}$ (—) for $H_R \geq 0.5$ (○) but attain a constant value at $H_R < 0.45$ (○), suggestive of skin formation. **(d)** Peclet number for freshly deposited coatings versus relative humidity.

should be significantly impeded by the presence of a semi-solid layer there. Hence, we would expect the change in the evaporation rate Q to exhibit different regimes at low and high humidities. By contrast, a different packing at ϕ_{OT} should not interfere with the water evaporation, as the size of the voids between the colloidal particles in a close-packing configuration is still much bigger than the size of water molecules. Thus, the water transport towards the dispersion–air interface should not be hindered and the change in Q should follow the same trend throughout the full range of experimental conditions used. Equation (6.8) instructs us that the evaporation rate should scale linearly with the relative humidity: $Q \propto (a - H_R)$. We indeed observe this experimentally for $H_R \geq 0.5$ (Figure 6.4c). However, for $H_R < 0.45$ the change in the experimentally determined evaporation rate deviates significantly from the linear regime at high humidities. In fact, the value of Q barely changes and remains close to constant at low H_R (Figure 6.4c). Such behaviour is in line with the scenario of skin formation. To further assess the likelihood of this scenario, we estimate the initial Peclet number Pe_I for the coatings at the beginning of the drying process (Appendix 6.A.2). The Pe_I values are larger than unity for the whole H_R range, implying that the system is predisposed to skin formation (Figure 6.4d). Nevertheless, our LSI measurements indicate that a skin is formed exclusively at $H_R \lesssim 0.5$. Most likely, only in this regime is the disjoining pressure overcome in the layer of accumulated particles, leading to coalescence (see Appendix 6.A.2 and Figure 6.A.2).[39] Both findings – the non-uniform dependence of the evaporation rate on relative humidity, and the high Peclet numbers – strongly suggest that skin formation is at the root of the discrepancy between the measured t_{OT} and the prediction of Equation (6.9).

6.4 Open time versus temperature

Temperature is another crucial environmental parameter that has strong effects on the drying of aqueous systems. To quantify these effects, we need to incorporate all contributions in the Langmuir–Knudsen equation. Considering solely the original form of Equation (6.5) leads to the relatively simple scaling $t_{OT} \propto \sqrt{T}$. However, the equilibrium vapour pressure p_s is strongly dependent on temperature and this needs to be accounted for. To that end we invoke the August–Roche–Magnus equation, which is widely used in atmospheric science and is a good empirical approximation of the Clausius–Clapeyron equation capturing the temperature dependence of p_s at standard atmospheric conditions:[40]

$$p_s = 6.1 \exp\left(\frac{17.3\,T}{T + 243.3}\right) \tag{6.11}$$

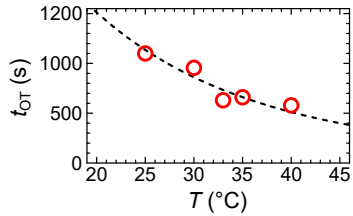

Figure 6.5. Open time as function of temperature. The symbols represent the experimental data while the dashed line shows the theoretical prediction according to Equation (6.12).

Substituting Equation (6.11) in Equation (6.8) and subsequent integration gives the following relation between temperature and the open time:

$$t_{OT} = c_3 \frac{\sqrt{T}}{\exp\left(\frac{17.3}{T+243.3}\right)} \tag{6.12}$$

where all the constants are absorbed in the factor c_3. Equation (6.12) predicts a non-trivial scaling between temperature and the open time $t_{OT} \propto \sqrt{T} \exp\left(\frac{-17.3}{T+243.3}\right)$. Remarkably, only adjusting the factor c_3 (free parameter in the fit) yields a prediction that perfectly falls in line with our experimental data for t_{OT} at different temperatures (Figure 6.5). The good agreement between the seemingly complicated scaling and our experimental results indicates that the most relevant effects are apparently captured by our LSI-based approach.

6.5 Beyond the open time

We have shown that LSI allows us to closely follow the dynamics in the early stages of drying colloidal coatings and determine accurately an important quantity such as the open time. However, other phenomena that populate the later drying stages are of equal importance for the terminal state of the paint film. The logical question now arises if LSI can also be used to monitor these later events. At the heart of film formation in water-based coatings is the process of phase inversion, in which the binder particles coalesce and give rise to a continuous polymer phase with any residual water dispersed in it as droplets. After the binder particles have attained close packing and undergone deformation, coalescence commences with the breakage of the thin water films that disjoin the highly deformed particles. This rupture is caused by the capillary forces which continuously grow with the ongoing solvent evaporation and at a certain point exceed the disjoining pressure that keeps the soft colloids apart. Once the thin film fails, the contents of the particles are free to intermix. In-situ methods to study the process of phase

inversion in a spatially resolved manner are scarce. It is challenging to detect coalescence events by simply looking for structural changes, since there is no clear macroscopic difference between strongly deformed and coalesced particles. In some cases, microscopy approaches have been deployed to monitor particle deformation and coalescence, but their application becomes limited if the studied system is opaque and once the size of the coalescing particles approaches the diffraction limit.[41–44].

To circumvent these challenges, we use LSI as an approach that relies on dynamics rather than structure to generate contrast, and follow in detail the film formation process in opaque latex coatings. We start by mapping the dynamics in drying acrylic–styrene copolymer emulsions with different concentrations of coalescing aids (see Section 6.2.3). The d_2 maps for a coating containing 2.7 wt% coalescent reveal a sudden enhancement in the dynamics long beyond the open time (Figure 6.6a,b). This enhancement manifests itself as a well-defined front (Figure 6.6c) and is followed by a rapid decrease in the mobility (Figure 6.6d). To dissect this sequence of events in a more quantitative manner, we compute the temporal evolution of the field correlation function over extended periods. As time progresses, $g_1(\tau)$ shifts to two orders-of-magnitude longer τ-values, indicating a significant retardation of the dynamics (Figure 6.6e). We subsequently extract the relaxation time τ_0 and process identifier α by fitting $g_1(\tau)$ to Equation (6.4).

Close examination of the resultant τ_0 curves allows us to identify four distinct drying stages for all coalescent concentrations (Figure 6.6f). Stage I is essentially the open-time period of the coating. Stage II is marked by a transient decrease of τ_0, implying enhanced motion. Most likely, the rising capillary pressure compresses and deforms the soft binder particles. This deformation translates into a macroscopic contraction of the coating, imposing a net translational motion to the TiO_2 particles downwards and towards the centre of the drying coating. Once the capillary pressure exceeds the disjoining pressure, the drying process advances to stage III, in which the interstitial water films rupture and phase inversion takes place. After particle coalescence, the TiO_2 particles inhabit a continuous polymer phase with a significantly higher viscosity, which is reflected by the steep rise in τ_0. Additionally, the motion of the particles shifts to a more diffusive mode. The onset of the rapid rise in the τ_0 curve marks the time point to which we refer as the film formation time t_{FFT}. In the final stage IV, the coalescing aids slowly evaporate from the film, causing the viscosity to gradually increase and the mobility of the TiO_2 particles to drop further. The resultant rise in τ_0 continues over many hours to days (Figure 6.6f, inset). Note that the associated high α values are likely artefacts without physical meaning.

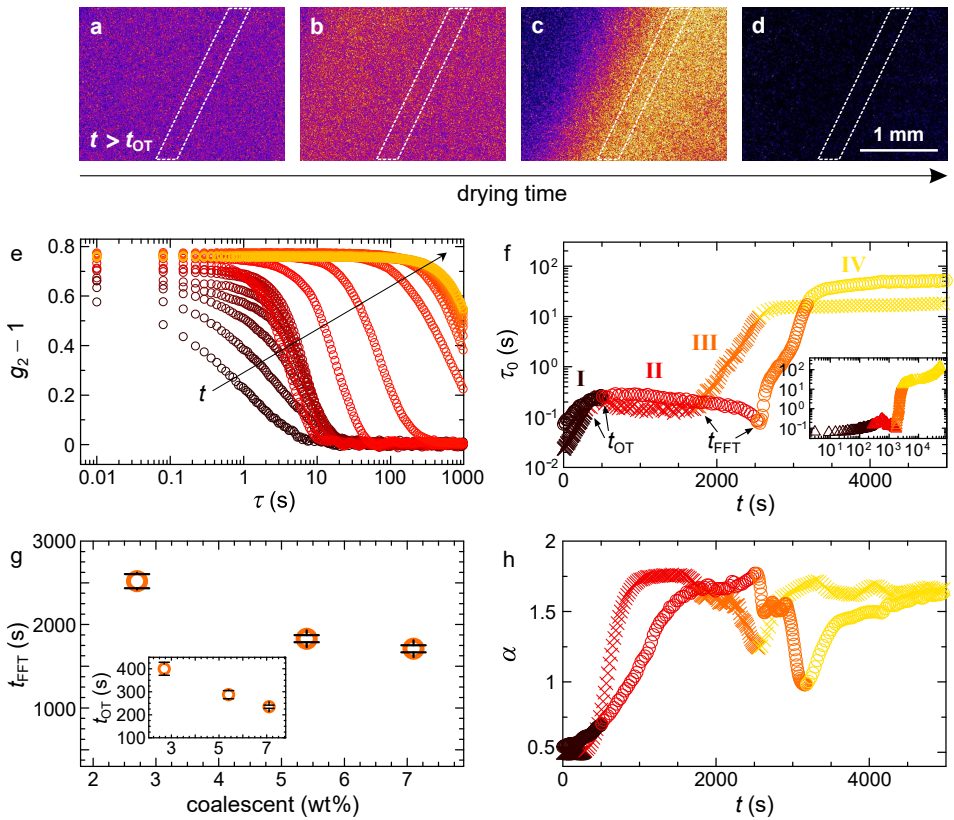

Figure 6.6. Quantification of film formation time and its dependence on coalescent concentration. **(a–d)** $d_2(\tau = 2\,\mathrm{s})$ maps of a 100 µm coating with 2.7 wt% coalescent at different time points beyond the open time, capturing the film formation dynamics: $t = 2545$ s **(a)**, 2550 s **(b)**, 2555 s **(c)** and 2563 s **(d)**. At $t = t_{\mathrm{FFT}} = 2555$ s, a clear coalescence front passes **(c)**. The dashed lines delineate the region of interest. The scale bar applies to all images. **(e)** Typical correlation functions over time for the coating containing 2.7 wt% coalescent, showing a distinct crossover and change of shape upon film formation. The time interval between consecutive curves is 5 min. **(f)** Temporal evolution of the characteristic relaxation time for 2.7 wt% (○) and 7.1 wt% (×) coalescent. The Roman numbers and colours designate the four drying stages described in the main text. The inset in (f) shows a long-term measurement of τ_0 for a coating with 5.4 wt% coalescent. **(g)** Film formation time and open time (inset) as a function of coalescent concentration. Each data point is the average of two measurements; the error bars represent the standard deviations. **(h)** Temporal evolution of the process identifier.

The temporal behaviour of τ_0 and the d_2 maps are well in agreement with each other. The rapid increase in τ_0 implies that coalescence must occur across a sharp front, as was found previously.[45–47] We indeed observe this clearly in the d_2 maps for the coating containing 2.7 wt% coalescent at $t = t_{FFT}$. A well-defined gradient in mobility (Figure 6.6c) traverses through the field of view. This front is truly a dynamic transition and cannot be identified on the basis of structural features, e.g. relying on absolute intensity (Appendix Figure 6.A.3a). Our interpretations are further supported by the $\alpha(t)$ curves: the significant increase of α in stage II implies a shift to (super-)ballistic dynamics (Figure 6.6h), which is in line with the stipulated collective translation of the particles caused by the contracting coating. High stretching exponents are relatively unusual but have previously been attributed to relaxation of internal stresses in jammed colloidal systems.[48,49] Interestingly, in stage III we observe a rapid drop in α after the film formation time (Figure 6.6h). This sharp decrease in α combined with the kink in τ_0 is consistent with our hypothesis that across the coalescence front, the TiO_2 particles shift from accelerating translation to more diffusive dynamics, which may well be the signature of coalescence in a coating.

Even though the overall shapes of the τ_0 and α curves are the same for different coalescent concentrations, they are clearly shifted along the time axis (Figure 6.6f,h). Surprisingly, adding coalescing aids considerably decreases the open time (Figure 6.6g, inset); this is an undesired effect which is important to take into account when formulating paints. We attribute this effect to the partitioning of coalescing aids into the polymer particles. As a consequence, the binder particles swell, and close packing is reached at an earlier time point. Dynamic light scattering measurements confirm this difference in particle sizes: the samples with 2.7 and 7.1 wt% coalescent exhibit particle diameters of 124 and 142 nm, respectively.

Fortunately, not only the open time decreases upon increasing the coalescent concentration, the film formation time decreases even more (Figure 6.6g), which is the intended result. Coalescing aids are commonly added to plasticize the binder particles by increasing the free volume of the polymer chains.[50–52] The earlier onset of coalescence is further enhanced by the swelling-induced increase in the volume fraction of the latex particles. Another consequence is the absence of a sharp coalescence front in the strongly plasticized coating (7.1 wt% coalescent), which instead is much more gradual and delocalized (compare Appendix Figure 6.A.3b with 6.A.3c). These observations are in agreement with previous work on drying surfactant-stabilized oil-in-water emulsions, which revealed two distinct modes of coalescence: 'front coalescence' at high surfactant concentrations (stable emulsions) versus 'bulk coalescence' at low surfactant concentrations (unstable emulsions).[53] In the first scenario, a steep gradient in the capillary pressure is required to induce

coalescence, which thus takes place at only at the drying end of the emulsion where the high capillary pressure condition is met. In the second scenario, a lower capillary pressure is already sufficient to induce coalescence, which thus occurs simultaneously at many locations in the bulk. These results are analogous to the findings in our work, where instead we have varied the particle resistance to coalescence by changing the coalescent concentration.

Since the characteristic shape of $\tau_0(t)$ and the dip in $\alpha(t)$ are reproducible in all measurements and also for other latex systems, these features may serve as a standard approach to extract the film formation time in drying water-borne coatings. The small standard deviations in t_{FFT} derived from the onset of the abrupt decrease in α highlight the robustness of this procedure (Figure 6.6g). Although the observed strong dependence of coalescence on the coalescent concentration is in line with expectations and earlier research,[50–52] we now have a straightforward and easily adaptable method to quantify the film formation time unambiguously.

6.6 Concluding remarks

In this study, we have introduced laser speckle imaging in the light of a versatile tool for a quantitative characterization of drying water-borne coatings. As such, LSI enables us to determine the open time of realistic paint formulations for a wide range of drying conditions. The excellent agreement between our experimental observations for the open time and the scaling predictions derived from well-established evaporation rate theory not only validates our LSI approach for open-time determination, but also allows accurate predictions for the behaviour of this quantity in the whole set of conditions used in this work. Furthermore, the advent of deviations from the expected behaviour permits the detection of undesired phenomena that might occur during drying, such as skin formation. We have shown how the wide temporal dynamic range of LSI makes it possible to extend our quantitative observations towards longer time scales populated by other relevant processes, namely the deformation of binder particles in later stages and their subsequent coalescence into a solid paint film. LSI allows us not only to accurately determine the time point at which phase inversion occurs but also to monitor the propagation of the coalescence front in a spatio-temporally resolved manner. These results highlight the potential role of this method in the detailed study of drying stages in water-based coatings, and could aid in the rational design of water-borne paints with a tailored drying profile.

Acknowledgements

We thank DSM Coating Resins in Waalwijk for providing us with the water-based paint formulations used in this work.

6.A Appendix

6.A.1 Paint deposition method

We apply a homogeneous coating of acrylic water-based paint on a glass substrate of 100×200 mm^2 using a film applicator (Figure 6.A.1a) that has some if its edges indented to an extent that ensures the casting of a coating with the desired thickness (Figure 6.A.1b). Once the paint is deposited, we transfer the sample into the LSI set-up and commence with the measurement.

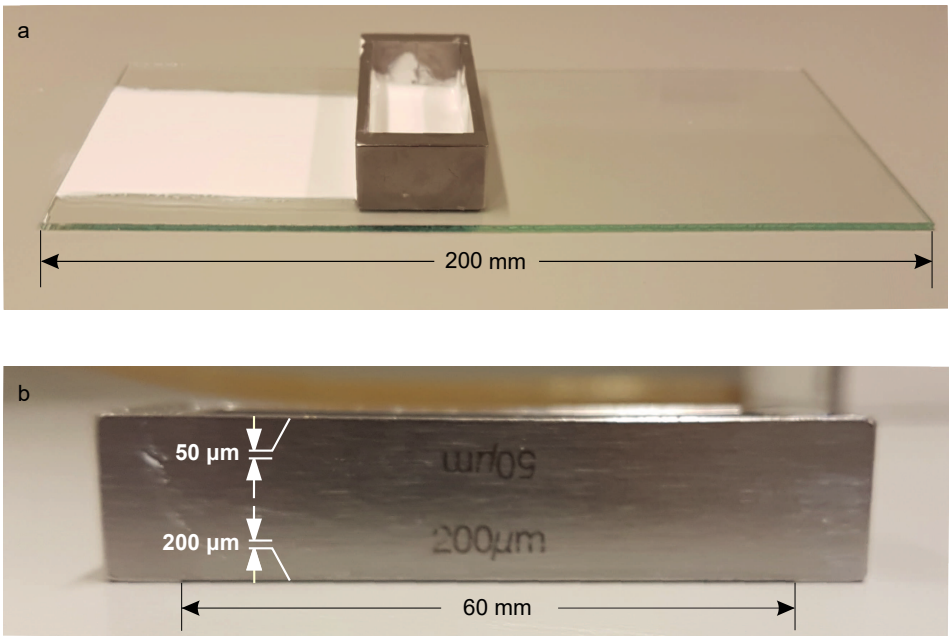

Figure 6.A.1. Paint deposition method. **(a)** Application of a coating onto a glass substrate by sliding the film applicator filled with paint to the right. **(b)** Close-up of the film applicator.

6.A.2 Peclet number estimation and skin formation

To further assess the susceptibility of our samples to skin formation, we estimate the initial Peclet number $\mathrm{Pe_I}$ for the different measurement conditions. In a colloidal dispersion with an evaporating continuous phase, there is an interplay between two types types of mass transport: (i) diffusive as a consequence of Brownian motion, and (ii) advective directed upwards due to the mass flux generated by the ongoing evaporation at the dispersion–air interface. The Peclet number estimates the balance between those two modes of mass transport and reads:

$$\mathrm{Pe_I} = \frac{h_\mathrm{s} v}{D} \tag{6.13}$$

where h_s is the starting thickness of the coating, v is the velocity with which the dispersion–air interface moves down ($|\mathrm{d}h/\mathrm{d}t|$) and D is the diffusion coefficient of the scattering TiO_2 nanoparticles. We have access to each of these quantities,

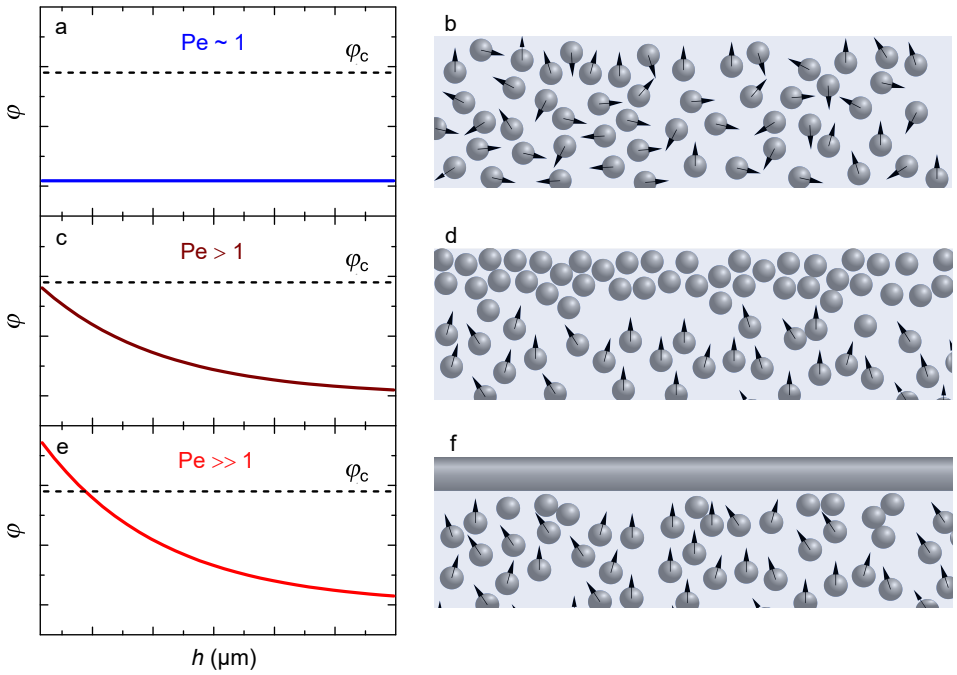

Figure 6.A.2. Peclet number and skin formation in drying dispersions of soft particles. Tentative particle volume fraction φ profiles for emulsions drying in different Pe regimes **(a,c,e)** and the corresponding schematics **(b,d,f)** representing the authors' impression of the accompanying phenomena. h is the distance from the dispersion–air interface.

which allows us to estimate Pe_I. The starting thickness h_s is known and fixed by the methodology used to deposit the paint. The velocity v can easily be calculated from the temporally resolved gravimetric measurements of the drying coating. Finally, from the LSI measurements we can compute the relaxation time τ_0 and calculate D through the relation: $\tau_0 = 1/6\, {k_0}^2 D$.

For Pe below unity, diffusive transport dominates and ensures a uniform particle distribution, resulting in a uniform pressure throughout the coating (Figure 6.A.2a,b). For Pe > 1, advective transport dominates, causing particles to accumulate at the dispersion–air interface and a concentration gradient to evolve, which gradually decays with increasing distance from the interface h (Figure 6.A.2c,d). High Pe is a necessary but not sufficient condition for skin formation to occur. In order for a semi-solid surface layer to form, a critical particle fraction φ_c needs to be attained, i.e. a pressure higher than the critical disjoining pressure, which will ensure the onset of coalescence (Figure 6.A.2e,f).

6.A.3 Coalescence

Coalescence events cannot be detected simply by analysing the absolute light intensity in the acquired raw speckle images (Figure 6.A.3a) but *can* be clearly identified in a d_2 image of the centre of a drying coating (Figure 6.A.3b). The coalescence front is narrow and well defined in the case of relatively rigid binder particles in a coating with 2.7 wt% coalescent (Figure 6.A.3b). By contrast, the highly plasticized coating with 7.1 wt% coalescent accommodates more gradual and delocalized coalescence events (Figure 6.A.3c).

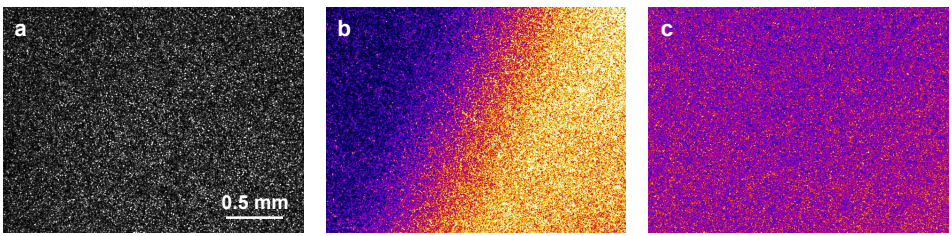

Figure 6.A.3. Coalescence in water-borne coatings. **(a)** Raw speckle image and **(b,c)** d_2 maps of a coalescing latex coating containing 2.7 wt% **(a,b)** and 7.1 wt% **(c)** coalescing aid. All time points equal t_{FFT}. The scale bar applies to all images.

References

[1] M. E. Embuscado, K. C. Huber, *Edible films and coatings for food applications* (Springer, 2009).

[2] S. D. Hoath, *Fundamentals of inkjet printing: the science of inkjet and droplets* (John Wiley & Sons, 2016).

[3] J. L. Keddie, A. F. Routh, *Fundamentals of latex film formation: processes and properties* (Springer, 2010).

[4] Z. W. Wicks, F. N. Jones, S. P. Peppas, *Organic coatings: science and technology* (John Wiley & Sons, Chichester, p. 259, 1992).

[5] L. A. Morrow, S. R. Steinhauer. *Biol. Psychiatry* **37**, 721–730 (1995).

[6] G. Triebig, J. Hallermann. *Occup. Environ. Med.* **58**, 575–581 (2001).

[7] I. Böckelmann, H. Lindner, B. Peters, E. A. Pfister. *Der Ophthalmologe* **100**, 133–141 (2003).

[8] A. Vagias, Q. Chen, G. H. ten Brink, D. Hermida-Merino, J. Scheerder, G. Portale. *ACS Appl. Mater. Interfaces* **1**, 2482–2494 (2019).

[9] J. M. Salamanca, E. Ciampi, D. A. Faux, P. M. Glover, P. J. McDonald, A. F. Routh, A. C. I. A. Peters, R. Satguru, J. L. Keddie. *Langmuir* **17**, 3202–3207 (2001).

[10] F. T. Carter, R. M. Kowalczyk, I. Millichamp, M. Chainey, J. L. Keddie. *Langmuir* **30**, 9672–9681 (2014).

[11] H. M. van der Kooij, R. Fokkink, J. van der Gucht, J. Sprakel. *Sci. Rep.* **6**, 34383 (2016). **(Chapter 5)**

[12] C. Zhou, G. Yu, D. Furuya, J. H. Greenberg, A. G. Yodh, T. Durduran. *Opt. Express* **14**, 1125–1144 (2006).

[13] P. Zakharov, A. C. Völker, M. T. Wyss, F. Haiss, N. Calcinaghi, C. Zunzunegui, A. Buck, F. Scheffold, B. Weber. *Opt. Express* **17**, 13904–13917 (2009).

[14] M. Draijer, E. Hondebrink, T. van Leeuwen, W. Steenbergen. *Lasers Med. Sci.* **24**, 639–651 (2009).

[15] M. Pajuelo, G. Baldwin, H. Rabal, N. Cap, R. Arizaga, M. Trivi. *Opt. Lasers Eng.* **40**, 13–24 (2003).

[16] O. P. Maksymenko, L. I. Muravsky, M. I. Berezyuk. *J. Biomed. Opt.* **20**, 095006 (2015).

[17] Z. Hajjarian, S. K. Nadkarni. *Sci. Rep.* **2**, 316 (2012).

[18] M. Erpelding, A. Amon, J. Crassous. *Phys. Rev. E* **78**, 046104 (2008).

[19] N. H. Koshoji, S. K. Bussadori, C. C. Bortoletto, R. A. Prates, M. T. Oliveira, A. M. Deana. *PLoS One* **10**, e0118429 (2015).

[20] H. M. van der Kooij, S. A. Semerdzhiev, J. Buijs, D. J. Broer, D. Liu, J. Sprakel. *Nat. Commun.* **10**, 3501 (2019). **(Chapter 9)**

[21] D. J. Pine, D. A. Weitz, J. X. Zhu, E. Herbolzheimer. *J. Phys. France* **51**, 2101–2127 (1990).

[22] E. O. Schulz-DuBois, I. Rehberg. *Appl. Phys.* **24**, 323–329 (1981).

[23] K. Schätzel. *Appl. Phys. B* **42**, 193–213 (1987).

[24] H. Guo, G. Bourret, R. B. Lennox, M. Sutton, J. L. Harden, R. L. Leheny. *Phys. Rev. Lett.* **109**, 055901 (2012).

[25] D. A. Weitz, D. J. Pine, P. N. Pusey, R. J. A. Tough. *Phys. Rev. Lett.* **63**, 1747–1750 (1989).

[26] J. L. Keddie. *Mater. Sci. Eng. R Rep.* **21**, 101–170 (1997).

[27] H. M. van der Kooij, G. T. van de Kerkhof, J. Sprakel. *Soft Matter* **12**, 2858–2867 (2016). **(Chapter 4)**

[28] T. G. Mason, K. Ganesan, J. H. van Zanten, D. Wirtz, S. C. Kuo. *Phys. Rev. Lett.* **79**, 3282–3285.

[29] I. Langmuir. *J. Am. Chem. Soc.* **54**, 2798–2832 (1932).

[30] M. Knudsen, *The kinetic theory of gases: some modern aspects* (Methuen & Company, 1950).

[31] H. Hertz. *Ann. Phys. (Berl.)* **253**, 177–193 (1882).

[32] A. F. Routh, W. B. Zimmerman. *Chem. Eng. Sci.* **59**, 2961–2968 (2004).

[33] Á. G. Marín, H. Gelderblom, D. Lohse, J. H. Snoeijer. *Phys. Rev. Lett.* **107**, 085502 (2011).

[34] K. Piroird, V. Lazarus, G. Gauthier, A. Lesaine, D. Bonamy, C. L. Rountree. *Europhys. Lett.* **113**, 38002 (2016).

[35] C. Noirjean, M. Marcellini, S. Deville, T. E. Kodger, C. Monteux. *Phys. Rev. Mater.* **1**, 065601 (2017).

[36] D. P. Sheetz. *J. Appl. Polym. Sci.* **9**, 3759–3773 (1965).

[37] A. M. König, T. G. Weerakkody, J. L. Keddie, D. Johannsmann. *Langmuir* **24**, 7580–7589 (2008).

[38] H. Wahdat, C. Hirth, D. Johannsmann, M. Gerst, M. Rückel, J. Adams. *Macromolecules* **51**, 4718–4726 (2018).

[39] H. Feng, J. Sprakel, J. van der Gucht. *Phys. Rev. E* **92**, 023011 (2015).

[40] O. A. Alduchov, R. E. Eskridge. *J. Appl. Meteorol.* **35**, 601–609 (1996).

[41] A. J. Mchugh, C. S. Tsay. *J. Appl. Polym. Sci.* **46**, 2011–2021 (1992).

[42] R. M. Charin, M. Nele, F. W. Tavares. *Langmuir* **29**, 5995–6003 (2013).

[43] E. Gonzalez, C. Tollan, A. Chuvilin, M. J. Barandiaran, M. Paulis. *ACS Appl. Mater. Interfaces* **4**, 4276–4282 (2012).

[44] T. Krebs, D. Ershov, C. G. P. H. Schroen, R. M. Boom. *Soft Matter* **9**, 4026–4035 (2013).

[45] Y. Ma, H. T. Davis, L. E. Scriven. *Prog. Org. Coat.* **52**, 46–62 (2005).

[46] J. C. Haley, Y. Liu, M. A. Winnik, W. Lau. *J. Coat. Technol. Res.* **5**, 157–168 (2008).

[47] H. M. van der Kooij, M. de Kool, J. van der Gucht, J. Sprakel. *Langmuir* **31**, 4419–4428 (2015). **(Chapter 3)**

[48] L. Cipelletti, L. Ramos, S. Manley, E. Pitard, D. A. Weitz, E. E. Pashkovski, M. Johansson. *Faraday Discuss.* **123**, 237–251 (2003).

[49] L. Cipelletti, L. Ramos. *J. Phys. Condens. Matter.* **17**, R253 (2005).

[50] W. F. Schroeder, Y. Liu, J. P. Tomba, M. Soleimani, W. Lau, M. A. Winnik. *J. Phys. Chem. B* **114**, 3085–3094 (2010).

[51] V. Divry, A. Gromer, M. Nassar, C. Lambour, D. Collin, Y. Holl. *J. Phys. Chem. B* **120**, 6791–6802 (2016).

[52] P. Berce, S. Skale, T. Razborşek, M. Slemnik. *J. Appl. Polym. Sci.* **134**, 45142 (2017).

[53] H. Feng, J. Sprakel, D. Ershov, T. Krebs, M. A. Cohen Stuart, J. van der Gucht. *Soft Matter* **9**, 2810–2815 (2013).

Part III

Laser speckle imaging of dynamic elastomers

Chapter 7

Laser speckle strain imaging reveals the origin of delayed fracture in a soft solid

This chapter is based on: Hanne M. van der Kooij, Simone Dussi, Gea T. van de Kerkhof, Raoul A. M. Frijns, Jasper van der Gucht and Joris Sprakel, 'Laser Speckle Strain Imaging reveals the origin of delayed fracture in a soft solid', *Sci. Adv.* **4**, eaar1926 (2018).

Abstract

Stresses well below the critical fracture stress can lead to highly unpredictable delayed fracture after a long period of seemingly quiescent stability. Delayed fracture is a major threat to the lifetime of materials and its unpredictability makes it difficult to prevent. This is exacerbated by the lack of consensus on the microscopic mechanisms at its origin, because unambiguous experimental proof of these mechanisms remains absent. Here we present an experimental approach to measure, with high spatial and temporal resolution, the local deformations that precipitate crack nucleation. We apply this method to study delayed fracture in an elastomer, and find that a delocalized zone of very small strains emerges as a consequence of strongly localized damage processes. This pre-fracture deformation zone grows exponentially in space and time, ultimately culminating in the nucleation of a crack and failure of the material as a whole. Our results paint a microscopic picture of the elusive origins of delayed fracture and open the way to damage detection well before it manifests macroscopically.

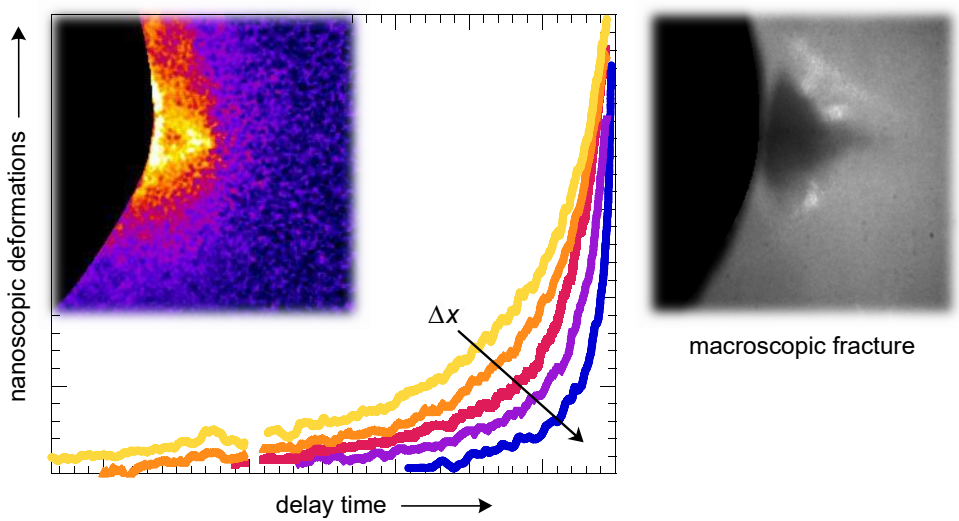

Nanostrain imaging predicts both the location and moment of unpredictable fracture.

7.1 Introduction

Loading a solid with a stress below its critical fracture stress does not mean that the solid is safe from catastrophic failure. In fact, subcritical stresses can lead to the sudden and unpredictable fracture of the material after a certain time delay, during which no precursors of the imminent failure are discernible by conventional imaging methods. Delayed fracture is observed in a wide variety of solids, ranging from brittle solids such as ceramics,[1] to ductile metals,[2] heterogeneous (porous) media,[3,4] plastics,[5] two-dimensional crystals,[6] and a range of soft materials.[7–11] Depending on the ratio of the applied load to the critical fracture stress, where crack nucleation is instantaneous, the delay time between loading and failure can vary from seconds to hours, days or even years.[1,9,10,12] The combination of the wide range of possible delay times and the absence of visible precursors to the failure makes delayed fracture difficult to predict. Consequently, this failure mode poses a significant threat to the operational safety and lifetime of a wide variety of common materials. And since the microscopic mechanisms governing the time delay between stress application and the moment of catastrophic failure remain elusive, its prevention has remained highly challenging.

Contrasting explanations have been put forth to explain delayed fracture. Explanations can be divided into two main categories. First, delayed crack nucleation has been hypothesized to be caused by the thermally-activated emergence of a flaw larger than the critical Griffith length.[3,4,7,13] By contrast, the erosion hypothesis to delayed fracture treats the nucleation of a crack as the result of a self-accelerating cascade of molecular damage processes at a site of stress localization. These damage processes erode the rigidity of the solid to zero upon which a crack can nucleate without an energy barrier.[8–10,14] In the first scenario, the scaling of the time delay τ_d between loading and failure is predicted to scale with stress σ as $\tau_d \propto \exp(-\sigma^4)$,[13] whereas the second theory predicts $\tau_d \propto \exp(-\sigma)$.[8,14] Because of the inherent time limitations of macroscopic mechanical experiments, distinguishing accurately between these two steep dependencies is virtually impossible. Rather, the definitive answer to the origins of delayed failure may be found microscopically: while the first scenario predicts no precursors to fracture, a cascade of damage processes and resultant damage-induced deformations to maintain a local force balance must precede crack nucleation in the second. To date, the lack of experimental approaches to assess these nanoscopic strains deep within a material at a locus of stress concentration in the moments before fracture has precluded the resolution of this debate.

In this chapter, we use laser speckle strain imaging (LSSI) to create highly resolved micromechanical maps of an elastomer in the moments before the

nucleation of a delayed crack. In this way, we quantitatively probe the small but distinct emergence of a zone of diverging strains that are the result of strongly localized bond rupture events. The deformation field is centred at the locus where a crack will nucleate once the damage is complete; the emergent strain zone is found to grow exponentially and reach macroscopic dimensions, until failure is inevitable. Our experiments provide strong evidence – supported by spring network simulations – for the erosion mechanism of delayed failure, in which crack nucleation is preceded by small-scale damage that results in large-scale strains in the pre-fracture zone.

7.2 Experimental details

7.2.1 Materials

We study delayed fracture in single-edge-notched, crosslinked poly(dimethylsiloxane) (PDMS) elastomers in which we embed 0.2 wt% of TiO_2 nanoparticles as scattering tracers. The elastomers are prepared by mixing PDMS Sylgard 184 (Dow Corning) prepolymer and crosslinking agent at a 5:1 weight ratio with 0.2 wt% TiO_2 nanoparticles (coated with silicone oil, ~30 nm diameter, US Research Nanomaterials); the low TiO_2 nanoparticle concentration ensures that particle–particle interactions are absent, while their coating with silicone oil precludes interactions with the PDMS matrix. Air bubbles are removed by centrifugation at $400g$ for 2 min. Subsequently, the mixture is poured into rectangular molds coated with a release agent (Universal Mold Release, Smooth-On). The molds are $60 \times 15 \times 5.0$ mm^3 ($l \times w \times h$) and feature a rectangular notch of $0.20 \times 10 \times 5.0$ mm^3 centred on the long edge. The samples are cured overnight at 65 °C, resulting in highly opaque elastomers that are macroscopically brittle, with fracture toughness $K_{\mathrm{Ic}} = 0.2$ MPa$\sqrt{\mathrm{m}}$ measured by dynamic mechanical analysis (see subsection below), and Young's modulus $E = 1.1 \pm 0.1$ MPa determined from the initial linear slope of a stress–strain curve (implying a mesh size on the order of $[k_{\mathrm{B}}T/E]^{1/3}$ = nanometres). The photon transport mean free path is measured by coherent back-scattering[15] to be $\ell^* = 50$ μm (see subsection below). It is important to note that Sylgard 184 contains at least 16 vol% of silica filler, in the form of ~100 nm aggregated silica particles,[16] added by the manufacturer to increase the tear strength. The mechanical properties and structure of silica-filled PDMS networks have been studied extensively.[16,17]

7.2.2 Forward-scatter LSSI

We create quantitative micromechanical maps with high spatiotemporal resolution using a custom-built laser speckle strain imaging set-up in the forward-scatter geometry. LSSI operates on the same optical principles as diffusing wave spectroscopy.[18] In our experiments, the sample is placed in a strain-controlled tensile tester and illuminated with an expanded coherent light beam (1.5 W, $\lambda = 532$ nm; Cobolt Samba), orthogonal to which the elastomer is strained (Figure 7.1b and Appendix Figure 7.A.1). The photons in the illumination beam are injected into the material and multiply scattered by the embedded nanoparticles. Because the sample thickness $h = 5.0$ mm is 100× larger than the transport mean free path $\ell^* = 50$ μm, the photons that exit the material in the forward-scattering direction have undergone numerous scattering events; consequently, they have traversed a diffusive rather than a ballistic trajectory within the sample. Each photon performs a unique random walk, giving rise to path length differences among the photons that cause random constructive and destructive interference in the scattered signal, which is recorded on the CMOS chip of a high-speed camera (HiSpec 1, Fastec Imaging, acquisition rate of 2000 Hz) as a speckle pattern of bright and dark spots. Both laser and camera are directed at the tip of the notch, where the tensile stresses are concentrated, dictating the site of eventual crack nucleation. Only the multiply-scattered light is detected, with transmitted and low-order scattering paths filtered by a linear polarizer perpendicular to the polarization of the incident laser beam.

As the embedded nanoparticles undergo thermal fluctuations, all photon path lengths change, causing the speckle pattern to change accordingly. The rate of these fluctuations is analysed on a pixel-by-pixel basis using the intensity structure function d_2 (Equation (7.1)), which provides access to quantitative information about the internal dynamics within the material. The angular brackets in Equation (7.1) denote averaging in time and/or space. Specifically, to create the d_2 images in Figure 7.1d, the speckle fluctuations are averaged over 100 frames = 50 ms in time and an additional 3×3 pixels = $7.8 \cdot 10^2$ μm^2 in space that acts as a sliding window. To compute the spatial and temporal $\langle d_2 \rangle$ and $\sqrt{f(\mathbf{U})}$ profiles in Figures 7.2a and 7.3, the speckle fluctuations are averaged over 5 ms in time and an additional 40 pixels = $3.5 \cdot 10^3$ μm^2 in space. Finally, the $\langle d_2(\tau) \rangle$ curves in Figure 7.2b are obtained by multi-speckle averaging over a rectangular area of 300×170 pixels = 4.5 mm^2, followed by time-averaging the resulting d_2 values over the first 2 s after application of the strain rate.

To allow computation of $\sqrt{f(\mathbf{U})}$ using Equation (7.2), the contrast function d_2 is first converted to the electric field correlation function g_1 by: $g_1(\tau) = \sqrt{1 - d_2(\tau)/2\beta}$.

Here the Siegert relation is applied, $g_1(\Delta t, \tau) = \sqrt{\left[g_2(\Delta t, \tau) - 1\right]/\beta}$, and the fact that $g_2(\Delta t, \tau) = g_2(\Delta t, \tau = 0) - d_2(\Delta t, \tau)/2$.[19] The g_2 function itself can be directly computed from the raw speckle patterns, yet in this work d_2 is consistently used as the starting point, since d_2 is more reliable than g_2 in cases of relatively poor statistics.[19] β is the spatial coherence factor that accounts for the number of speckles detected. It is chosen such that $d_2(\tau) \to 2\beta$ for $\tau \to \infty$. The mean-square displacement in Equation (7.2) is calculated by: $\langle \Delta r^2 \rangle = -6 \ln g_1 / [k_0\, h/\ell^*]^2$. The local strain acceleration rate constant $k(\epsilon, \Delta x)$ is obtained by least-squares fitting the differential strain intensity to an empirical, single-exponential equation: $\sqrt{f(\mathbf{U})}(\Delta t) = 1.7 \cdot 10^{-7} + 5 \cdot 10^{-6} \cdot \mathrm{e}^{k \Delta t}$.

7.2.3 Dynamic mechanical analysis

The macroscopic mechanical properties of the elastomers are measured using a dynamic mechanical analyser (Q800, TA Instruments). The samples are gripped using a film tension clamp with a clamp compliance of 0.24 μm/N, and uniaxial tensile tests are conducted at a controlled strain ramp rate of 20%/min. The Young's modulus E is obtained from the initial slope of the stress–strain curves. The fracture toughness is computed as $K_{\mathrm{Ic}} = \sigma_{\mathrm{c}} Y \sqrt{\pi a}$ with σ_{c} the critical fracture stress, $a = 10$ mm the notch length, and $Y = [1.12 + a(2.91a/w - 0.64)/w]/[1 - 0.93a/w] = 5.2$ the geometric configuration factor.

7.2.4 Coherent back-scattering

The transport mean free path $\ell^* = 50$ μm in the elastomers is estimated by measuring the decay of a coherent back-scattering cone. See ref. 15 for a detailed description of the method. In brief, the elastomer is illuminated with a 520 nm laser beam (Thorlabs MCLS1 4-Channel Laser Source), and a total of 500 images of the coherent back-scattering cone are acquired with an EM-CCD camera (Hamamatsu C9100-13) to ensure ample statistics. The image intensities are azimuthally averaged to obtain the radial intensity decay curve, which is fitted to extract ℓ^*, as detailed in ref. 15.

7.2.5 Spring network simulations

A network of linear elastic springs $f_i = \mu_i [l_i - l_0] = \mu_i \Delta l_i$ with identical stiffness μ and rupture force threshold f_{thr} is initially prepared by placing $N_x \times N_y$ nodes on a triangular lattice with spacing l_0 and featuring vertical bonds. A notch is placed in the network by removing the nodes inside a rectangular region (width w_x and height $2r_{\mathrm{notch}}$) with a circular end of radius r_{notch}. A step strain is applied to the network and all the nodes are displaced affinely. Nodes on the top, bottom and

right boundaries are kept fixed. The network is relaxed by minimizing the total elastic energy and the internal nodes are free to move off-lattice; the softening–breaking protocol is subsequently applied. The energy is minimized using the Fast Inertial Relaxation Engine (FIRE) algorithm[20] with tolerance $F_{\text{rms}} = 10^{-5}$ (in reduced units) and the other parameters as suggested in the original paper.

The weakest bond is identified as the one with the largest excess f_i/f_{thr_i} and undergoes softening $\mu_i \to \alpha\mu_i$. The energy is minimized again and the procedure is repeated. Each bond is allowed to soften a maximum of n_{soft} times before it is broken. After each softening, a new rupture threshold for the bond is randomly generated. In particular, after the j-th softening the threshold is uniformly picked in $\left(f_{\text{min}}^{(j)}, f_{\text{thr}}^{(0)}\right)$ with $f_{\text{min}}^{(j)} = \alpha^j f_{\text{thr}}^{(0)}$.

The simulation quantities are expressed in reduced units by setting the lattice spacing $l_0 = 1$, the initial spring constant $\mu = 1$ and by assuming a linear proportionality between rate constant r_i and excess force $f_i/f_{\text{thr}_i} > 1$ that sets the units for the simulation time t^*. The time evolution of the system is therefore dictated by the rate equation $R_{\text{tot}} = \sum_i r_i = \sum_i f_i/f_{\text{thr}_i}$ where the sum extends to all springs i with $f_i/f_{\text{thr}_i} > 1$. The time interval between two softening–breaking events is drawn randomly assuming exponentially distributed events: $\mathrm{d}t^* = -\ln(\text{rand}(0,1))/R_{\text{tot}}$.

We define $\langle \Delta x_{\text{dam}} \rangle = \left[\sum_{i=1}^{N_{\text{dam}}} \Delta x_i d_i\right] / N_{\text{dam}}$, with N_{dam} the number of damaged springs, $d_i = 1, \ldots, n_{\text{soft}}$ the number of times that spring i has undergone softening, and Δx_i its distance from the notch. The stiffness in the regions close to the notch is obtained by summing the spring constants in bins of width $3l_0 \times 5l_0$. The spring deformation rate is computed as $\left[\Delta l_i(t+\Delta t)^2 - \Delta l_i(t)^2\right] / \Delta t$, with Δt the time between snapshots that are 50 events apart. In Figure 7.4e–h, springs are coloured green when this rate exceeds the threshold $10^{-7} {l_0}^2/t^*$.

7.3 Results and discussion

7.3.1 Visualizing the strain precursors to crack nucleation

To resolve the local strains in a rubber en-route to delayed fracture, we create quantitative micromechanical maps using laser speckle strain imaging (LSSI) (see Section 7.2.2 for details).[21–27] We study a pre-notched, silica-filled silicone elastomer, which exhibits pronounced delayed failure after a period of apparent stability (Figure 7.1a). Some weak visco- and poro-elastic relaxation is observed just after application of a step strain, due to solvent migration and viscoelastic deformation.[11,28] As there is a clear separation of time scales between this relaxation and the delayed fracture, we treat these as independent phenomena. The nucleation

of a delayed crack occurs with no discernible precursors in the macroscopic mechanical signal. To probe whether precursors to the failure can be detected microscopically, we add 0.2 wt% of strongly scattering titania nanoparticles to the elastomer as tracers. We quantify the internal dynamics in the elastomer during the mechanical experiment in space and time by analysing the fluctuations of the speckle pattern created by multiply scattered photons (see Figure 7.1b,c and Supplementary Movie 1 in ref. 29), using the intensity structure function to create image contrast:[23,30–32]

$$d_2(x, y, \Delta t, \tau) = \frac{\langle [I(x, y, \Delta t) - I(x, y, \Delta t + \tau)]^2 \rangle}{\langle I(x, y, \Delta t) \rangle \cdot \langle I(x, y, \Delta t + \tau) \rangle} \tag{7.1}$$

where I is the speckle intensity at position (x, y) and at time to macroscopic fracture $\Delta t = t - t_f$, and τ is the correlation time. While the raw speckle images of

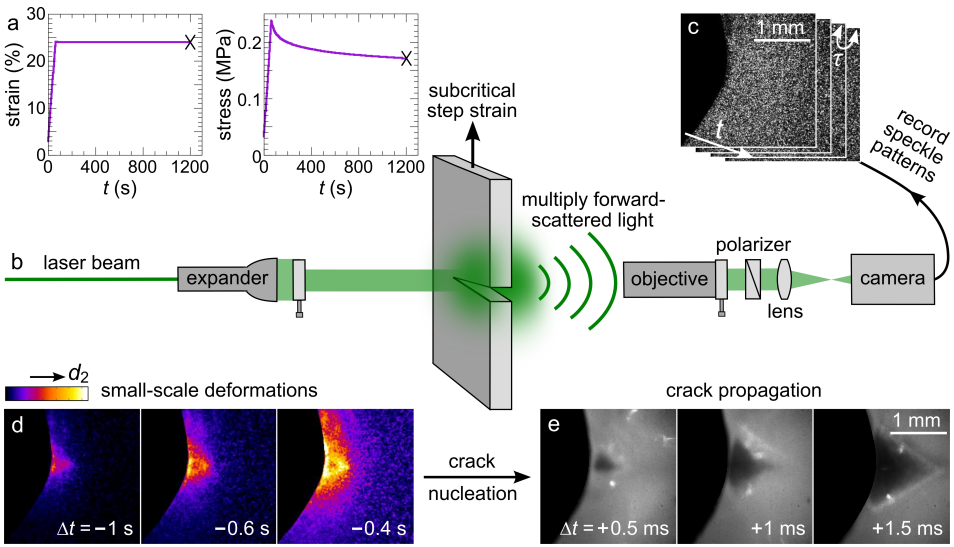

Figure 7.1. Imaging local pre-fracture deformations. **(a)** Macroscopic stress transient in a step-strained notched elastomer en route to delayed fracture (denoted by ×). **(b)** Schematic illustration of forward-scatter laser speckle strain imaging used to visualize strain precursors within the solid. The elastomer is illuminated with a coherent plane light wave, which is multiply scattered from TiO_2 nanoparticles embedded in the elastomer, giving rise to **(c)** speckle patterns on a camera on the opposite side. Spatiotemporal correlation of the speckle intensity fluctuations via the d_2 function (Equation (7.1)) is used to create image contrast, encoding the local dynamics. **(d)** The resulting mobility maps reveal a growing zone of nanoscopic deformations, culminating in **(e)** catastrophic failure and the nucleation of a brittle crack. The background is masked in all images.

a strained elastomer show no signs of precursors to failure (Figure 7.1c), images constructed using $d_2(\tau = 0.5\ \text{ms})$ as the contrast function reveal a localized region of enhanced dynamics close to the notch before crack nucleation, which occurs at $\Delta t = 0$ (Figure 7.1d). This zone of enhanced mobility, which exhibits a distinct wedge shape that is reminiscent of the process zone predicted by the Dugdale–Barenblatt model for ductile crack tips,[33,34] rapidly grows in amplitude and size as the moment of fracture approaches (see Supplementary Movie 2 in ref. 29). At this time t_f a macroscopic crack nucleates and propagates to destroy the sample (Figure 7.1e).

The contrast function d_2 encodes for the local dynamics within the material. The growth of a zone of high d_2 in space and time preceding crack nucleation may be caused by two different mechanisms. A first explanation could be the accumulation of damage via rupture of molecular bonds, which would lead to a decrease in the local rigidity and an enhancement of the vibration amplitude of the embedded nanoparticles. This scenario would involve a permanent enhancement of the dynamics. If true, then this weakened elasticity should remain detectable also after the sample has failed at the crack interface. However, post-mortem imaging of the fractured elastomer does not reveal any signs of damage other than the macroscopic crack. This is not surprising, because bond breakage is typically very localized in brittle elastomers such as the material under study and should not occur in a millimetre-sized zone, as shown previously using various methods.[35–37] Rather, the enhanced dynamics are emergent strains that result from the breaking of bonds at a very small locus below our imaging resolution. Stresses are concentrated near the notch, causing the scission of covalent bonds to initiate there; this bond breakage is highly anisotropic in filled rubbers.[16,38] Since the macroscopic strain is fixed, a change in the local elasticity due to bond rupture must require a redistribution of local stresses, hence local strains, to accommodate for the mechanical erosion that precedes nucleation. The emergent zone of enhanced and accelerating strains is thus a large-scale manifestation of the damage precursors, predicted by the erosion hypothesis,[8,9,14] that occur much more locally.

7.3.2 Validation of experimental methodology

Before we quantify the mechanical precursors to crack nucleation in more detail, we aim to establish the validity and accuracy of our interpretation of the measurement data. To do so, we perform several reference experiments. First we explore different contributions to the detected dynamics. Plots of contrast function d_2 as a function of distance from the notch Δx demonstrate that, at the correlation time that we use, $\tau = 0.5$ ms, the possible sources of speckle decorrelation are

well separated (Figure 7.2a): the noise threshold of our LSSI set-up is negligibly small (♦), while the intrinsic thermal fluctuations of nanoparticles in a quiescent and stable elastomer (■ and ▲) produce a significantly smaller decorrelation than the dynamics resulting from damage-induced deformations (●). Thus, the signal from the emergent strains that we probe is an order of magnitude larger than the background thermal fluctuations of the tracer particles and two orders of magnitude above the noise level.

Two types of particle motion contribute to signal decorrelation in these LSSI experiments. First, the embedded nanoparticles exhibit Brownian motion within the elastomer, characterized by diffusive statistics with a mean-square displacement $\langle \Delta r^2 \rangle$ that is limited because of the 'cages' imposed by the crosslinks.[39] Second, localized damage processes within the solid alter its elasticity and result in stress redistribution and resulting strains. In principle, the d_2 function measures a convolution of both types of motion. To disentangle these contributions, we first convert d_2 to the electric field correlation function g_1 (see Section 7.2.2), which we can subsequently express as:[26,40]

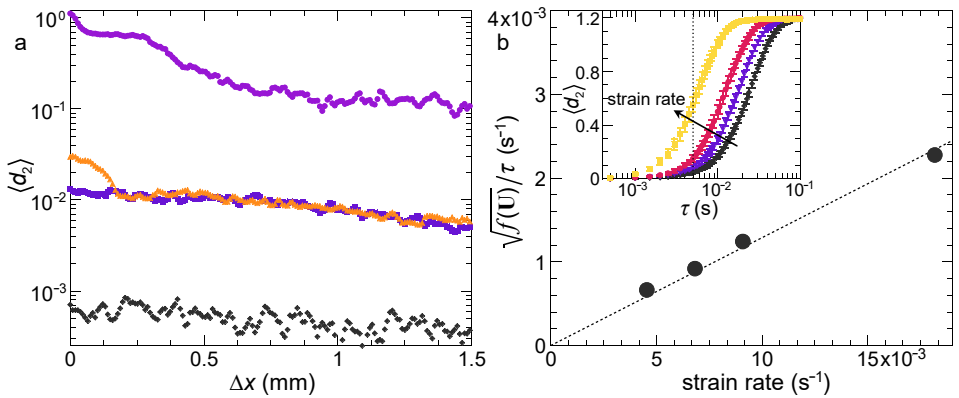

Figure 7.2. Set-up sensitivity and strain quantification. **(a)** Comparison of the average nanoparticle mobility $\langle d_2 \rangle$ in a thin horizontal strip in four different samples: an elastomer strained by 25% at $\Delta t = -1$ s (●); an elastomer strained by 3% (▲); the same elastomer in its quiescent, unstrained, state (■); and a static opaque medium, i.e. a piece of ground glass, in which no thermal speckle fluctuations occur (♦). The notch is located at $\Delta x = 0$. The angular brackets denote averaging over 40 pixels in the orthogonal direction. **(b)** Apparent local strain rate in the centre of an elastomer strained at a constant macroscopic rate. The dashed line is a predicted linear fit to the data, validating our analysis procedure. **Inset:** average $d_2(\tau)$ curves from which $\sqrt{f(\mathbf{U})}$ is computed, here at $\tau = 5$ ms marked by the dotted line. The error bars indicate the standard deviation of time-averaging d_2 over 2 s.

$$g_1 \approx \frac{k_0 h\sqrt{3f(\mathbf{U}) + \langle \Delta r^2 \rangle / \ell^{*2}}}{\sinh\left[k_0 h\sqrt{3f(\mathbf{U}) + \langle \Delta r^2 \rangle / \ell^{*2}}\right]} \tag{7.2}$$

where $k_0 = 2\pi n/\lambda_0$ is the wave vector with $n = 1.5$ the refractive index of PDMS and λ_0 the laser wavelength in vacuum; $h = 5$ mm is the sample thickness; $f(\mathbf{U}) \approx \frac{1}{15}\left[\mathrm{Tr}^2(\mathbf{U}) + 2\mathrm{Tr}(\mathbf{U}^2)\right]$ with $\mathbf{U}$ the strain tensor and Tr its trace; $\ell^* = 50$ μm is the photon transport mean free path determined independently by means of coherent back-scattering (see Section 7.2.4); and $\langle \Delta r^2 \rangle$ is the Brownian mean-square displacement of the tracer particles. We consider the latter constant (at fixed τ) and set it at the mean-square displacement of the nanoparticles in the quiescent material (see Section 7.2.2). Since elastomers are nearly incompressible, with Poisson's ratio $\nu \approx 0.5$, $\mathrm{Tr}(\mathbf{U})$ is negligible,[21] yielding $f(\mathbf{U}) \approx \frac{2}{15}\mathrm{Tr}(\mathbf{U}^2)$. The complexity of our experimental geometry precludes computation of the individual components of the strain tensor; therefore, we use $\sqrt{f(\mathbf{U})}$ as a measure for the differential strain between two correlated speckles,[40] here for the shortest possible correlation time $\tau = 0.5$ ms. Although this one-point correlation cannot provide an absolute measure for the strain, it provides a means to evaluate changes in the amplitude of the local deformation field with high resolution. In the remainder of this chapter, we will refer to $\sqrt{f(\mathbf{U})}$ as the 'differential strain intensity'.

The validity of this approach has been extensively demonstrated in earlier work,[21,26,40–42] yet only in the back-scatter geometry, which is biased towards surface strains. Our forward-scatter set-up offers two advantages: it probes the strains in the bulk of the material and offers a larger sensitivity to small deformations. As this method operates in the limit of multiple scattering, with a ratio of sample thickness h to ℓ^* of ~100, Ångström-scale motion of the scatterers already elicits a significant decorrelation of the speckle intensity. We estimate a minimum resolution of displacements that we can detect with reasonable accuracy as small as $\delta_{\mathrm{disp}} \approx 0.2$ nm. This excellent sensitivity gives us the ability to measure the extremely small differential strains preceding delayed fracture.

To further verify our method as a means to quantify local strains, we subject an unnotched elastomer to a constant tensile strain rate $\dot{\epsilon} = \mathrm{d}\epsilon/\mathrm{d}t$ and compute the differential strain intensity in the centre using Equation (7.2). Divided by the time separating the two correlated speckle patterns, here $\tau = 5$ ms, $\sqrt{f(\mathbf{U})}/\tau$ is analogous to the local strain rate. Indeed, we find a linear relationship between the measured local strain rate and that applied macroscopically (Figure 7.2b). The two are related by a geometry-dependent proportionality constant, which results from the fact that $f(\mathbf{U})$ is a scalar invariant of the strain tensor through a

combination of different components of the tensor. The validity of our analysis is further supported by the identical shapes of the $d_2(\tau)$ curves for different strain rates (Figure 7.2b, inset), which are only shifted on the time axis. Finally, we note that the accuracy of the measurement is good: the standard deviations of time-averaging d_2 over a constant-$\dot{\epsilon}$ period of 2 s are very small (Figure 7.2b, inset), and those of spatially averaging d_2 over an area of 4.5 mm^2 are also less than 10% in all cases.

For these reference samples subjected to a constant strain rate in the linear regime, the local deformation field is highly uniform. However, prior to a delayed fracture, we observe how a strongly heterogeneous deformation zone emerges (Figure 7.1d). To establish the accuracy of the d_2 images in Figure 7.1d, which we interpret as micromechanical maps of the elastomer during its mechanical perturbation, we must take into account the effects of spatial blurring. The measured signal in LSSI measurements is inherently a convolution of the local dynamics and the spatial distribution of photons in the material. Using random-walk simulations,[43,44] we find that the lateral blurring has a decay length of the order of the sample thickness (Appendix Figure 7.A.2). Thus, in these experiments we inevitably deal with a trade-off between spatial resolution and strain detection sensitivity: although the ratio of $h/\ell^* = 100$ provides high strain sensitivity, it also results in spatial blurring due to the long photon paths. Despite this spatial blurring, the observed changes in $f(\mathbf{U})$ with time are significant.

7.3.3 Quantification of local deformation field

Having established the validity and limits of our method, we now proceed to explore the pre-fracture deformation zone by plotting $\sqrt{f(\mathbf{U})}$ as a function of the time to fracture Δt in the last 7.7 s before fracture, for different distances Δx from the notch. These data clearly show the emergence of a growing deformation zone (Figure 7.3a), which starts at the notch, where the initial stress concentration reaches a maximum. The local differential strain grows more steeply as the moment of failure approaches, at which it converges to a single value for all locations in the field of view. The exponential growth of $\sqrt{f(\mathbf{U})}$, which is the consequence of the molecular damage at the notch that underlies the delayed crack nucleation, is evidence for the erosion hypothesis as it indicates a self-catalytic process that accelerates over time.

Interestingly, we observe the same kinetics for a (higher) strain of 30%, but on time scales that are two orders of magnitude shorter (Figure 7.3b), which is in line with the scaling of the delay time with the applied macroscopic stress or strain. This further confirms our theory that the pre-fracture deformation zone is

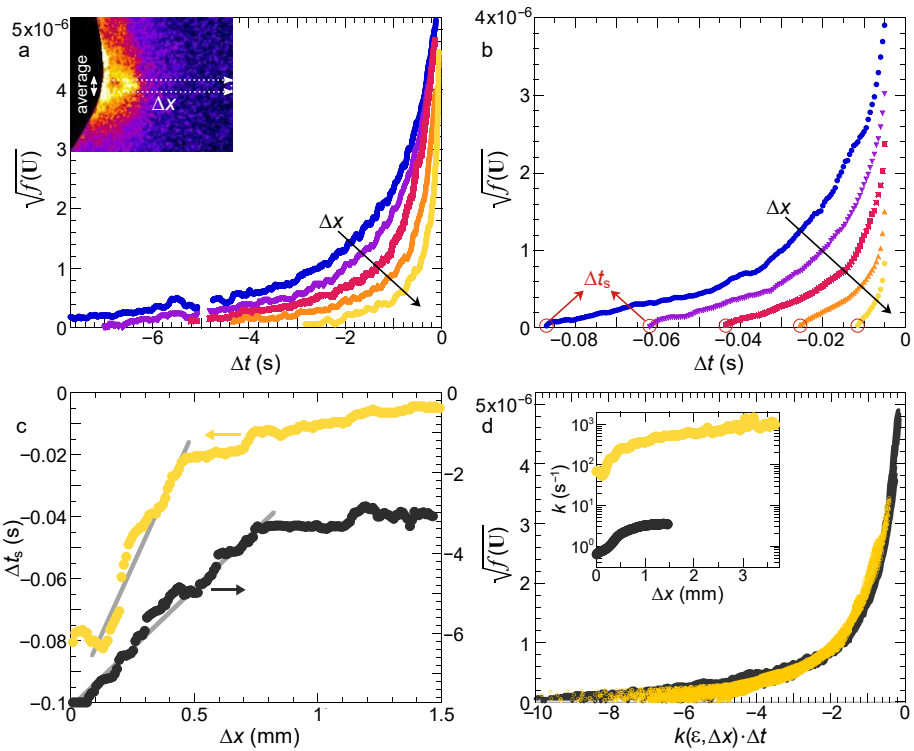

Figure 7.3. Localized growth of nanodeformations. **(a,b)** The local differential strain intensity $\sqrt{f(\mathbf{U})}$ increases exponentially towards the moment of crack nucleation $\Delta t = 0$, shown for an elastomer strained macroscopically by $\epsilon = 25\%$ **(a)** and 30% **(b)** as a function of the distance to the locus of highest stress concentration: $\Delta x = 0.1$, 0.28, 0.4, 0.55 and 1.5 mm. The angular brackets denote averaging over 40 pixels in the orthogonal direction (see inset in (a)). The expansion of the precursor zone is evidenced by the different starting points Δt_s of the $\sqrt{f(\mathbf{U})}$ curves. **(c)** Spatial dependence of Δt_s for a macroscopic strain of $\epsilon = 25\%$ (●, right ordinate) and 30% (●, left ordinate). The initial linear growth is marked by the fitted solid lines, whose slopes reveal growth velocities of 0.17 mm/s and 5.6 mm/s, respectively. **(d)** Collapse of all transient $\sqrt{f(\mathbf{U})}$ profiles, illustrating universality, through rescaling of the time axis with the local strain acceleration rate constant $k(\epsilon, \Delta x)$ (see **inset**). 10% of all data points are shown.

a slave of local damage processes: such a steep dependence on the macroscopic strain is in accord with the picture of bond rupture as a Kramers process, in which bond breaking is thermally activated and exponentially enhanced by a mechanical load.[8,12,45]

For both strains, our results illustrate how the precursors to crack nucleation expand in space at a constant rate but diverge steeply just before fracture. Specifically, by plotting the time at which the strain starts to rise Δt_s for different distances from the notch, we find a linear increase in the first growth stage (Figure 7.3c), whose slope is a measure for the spatial growth velocity of the deformation zone. It is interesting to note that these velocities – 0.17 and 5.6 mm/s for the 25 and 30% strained elastomer, respectively – are three orders of magnitude lower than the crack propagation rates – 0.7 and 10 m/s – which are again two to three orders of magnitude lower than the speed of sound in the material (~km/s).[46] Clearly, the damage processes that precede failure are governed by different physics than those that dictate the propagation rate of a nucleated crack.

The kinetic processes underlying the pre-nucleation damage and resultant deformations show a remarkably similar evolution at all distances Δx from the notch. Indeed, we are able to collapse all 550 measured differential strain $\sqrt{f(\mathbf{U})}$ profiles onto a single master curve through rescaling the time axis with a strain- and distance-dependent factor $k(\epsilon, \Delta x)$, which represents the rate with which the local strain accelerates (Figure 7.3d). The absolute values of k for the 25% and 30% strained elastomers differ by two orders of magnitude (Figure 7.3d, inset), in line with the picture of force-enhanced bond rupture and rigidity erosion. However, their dependence on Δx is nearly identical: with increasing Δx, k first increases and then reaches a plateau value far from the notch. This form is very robust and shows a negligible dependence on the extent of (orthogonal) spatial averaging up to ~40 pixels per bin, with low fit errors in all cases (Appendix Figure 7.A.3). The initial increase arises from the expansion of the deformation zone and acceleration of the damage processes at its origin, causing locations farther away from the notch to experience a faster rise of $\sqrt{f(\mathbf{U})}$ towards the moment of crack nucleation $\Delta t = 0$. Exactly at that time point, all the differential strains in the field of view converge, marking the transition from small-scale deformations to macroscopically detectable strains involved in the catastrophic failure.

7.3.4 Simulating delayed fracture

Finally, to strengthen the proposed connection between localized molecular damage and delocalized deformations, we perform simulations of a spring network model[47,48] subjected to a step strain. To describe damage accumulation, we irreversibly soften the bonds in the network when the force on them exceeds a critical rupture threshold f_{thr}. Each bond is allowed to soften a maximum of n_{soft} times before it is broken. The order in which the bonds are softened and ultimately broken is deterministic with the weakest bond damaging first, yet two stochastic rules are implemented in the simulations. (i) Local rearrangements are implicitly taken into account by randomly generating a new f_{thr} after each event,[48,49] according to the current stiffness μ of the bond. Softer regions have a higher probability to become weaker. (ii) The simulation time t^* is advanced in a stochastic fashion, while additionally assuming a total rate constant $R_{\mathrm{tot}} \sim 1/\mathrm{d}t^*$ that is proportional to the sum of the excess force (above f_{thr}) carried by all bonds.[50] Therefore, R_{tot} is a measure for the rate of damage accumulation, with a large R_{tot} implying fast damage dynamics, thus providing insight into the molecular bond scission processes.

In our simulations, we clearly observe the localization, accumulation and diffusion of damage preceding crack nucleation (Figure 7.4). Notably, the triangular shape of the damage zone (Figure 7.4a–c) resembles the shape of the deformation zone observed in experiments, and is independent of the choice of lattice topology and simulation parameters, within reasonable bounds (Appendix 7.A.4 and Figure 7.A.4). Despite the differences between simulations and experiments in the length scales, the number of bonds involved in the failure process, and in the network heterogeneity, our simulations provide further evidence that the deformations measured experimentally can be directly related to bond rupture events close to the notch. Bonds break as a direct result of the stress concentration imposed by the notch geometry; the consequent stress redistribution and growth of the damage zone cause deformations of springs progressively farther from the notch (Figure 7.4e–h). Future effort should be dedicated to improving the microscopic model to allow a quantitative comparison with experiments; for example, the delay time and the size of the damage zone can be tuned by subtly varying the softening–breaking protocol (see Appendices 7.A.5 and 7.A.6, and Figures 7.A.5 and 7.A.6).

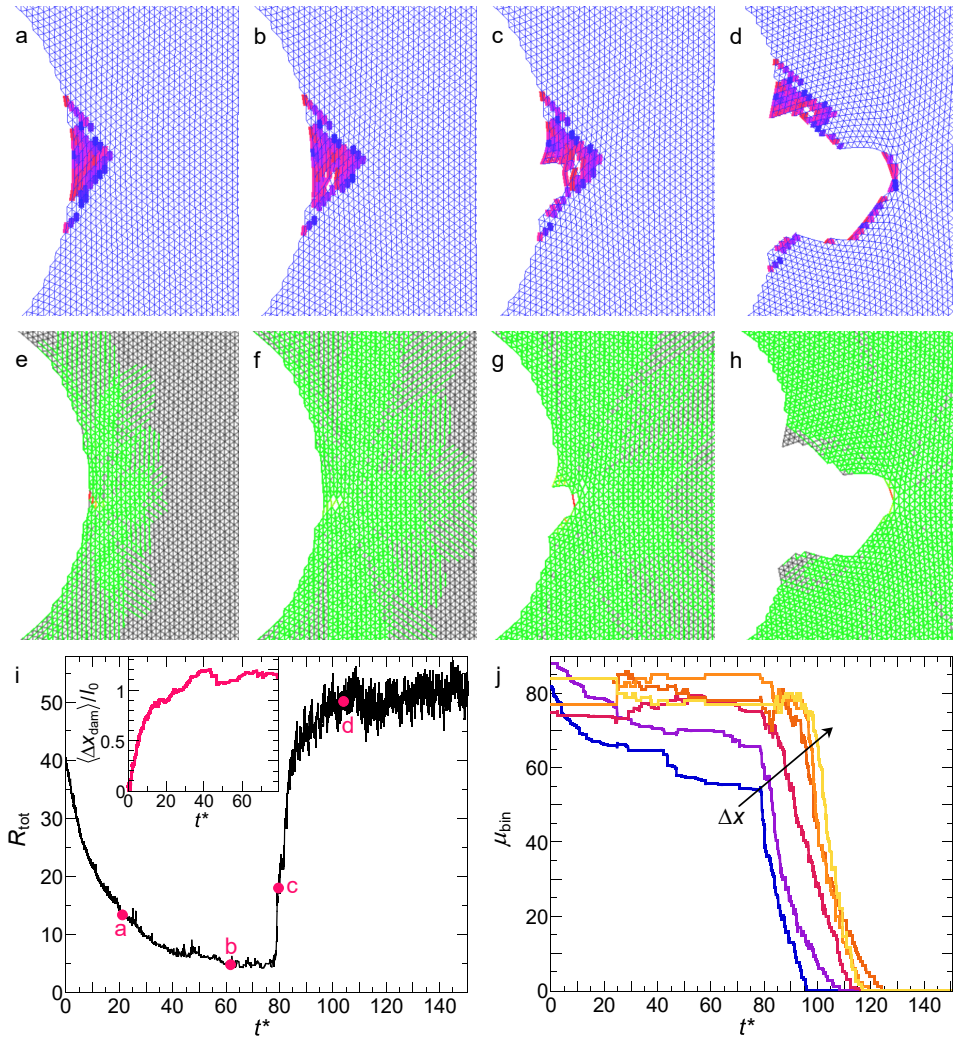

Figure 7.4. Spring network simulations of delayed fracture. **(a–h)** Time sequence of a fracture simulation at times $t^* \simeq 21.1$ (a,e), 61.7 (b,f), 79.7 (c,g) and 104 (d,h) (corresponding state points are indicated in (i)). In (a–d), bonds are colour-coded according to the amount of local damage, from blue to red indicating little to much damage. In (e–h), springs whose deformation rate exceeds a threshold are coloured green. **(i)** Total damage rate constant R_{tot} as a function of time, indicating different stages in the damage accumulation and rigidity loss that precipitate the macroscopic fracture. **Inset:** centre-of-mass position $\langle \Delta x_{\text{dam}} \rangle$ of the damage zone showing its growth towards the bulk until a crack nucleates. **(j)** Local stiffness μ_{bin} as a function of time at different distances from the notch: $\Delta x / l_0 = 1.5$, 4.5, 7.5, 10.5, 13.5 and 16.5. For these data, the simulation is parameterized as: $\epsilon = 25\%$, $f_{\text{thr}} = 0.35$, $r_{\text{notch}} = 20\, l_0$, $n_{\text{soft}} = 20$, $\alpha = 0.95$, $N_x \times N_y = 200 \times 100$, $w_x = 40\, l_0$ (see Section 7.2.5 and Appendices 7.A.4 and 7.A.5 for details).

7.4 Concluding remarks

Our results shed new light on a long-standing debate regarding the mechanisms of delayed failure, ruling out the hypothesis of subcritical crack nucleation as a sudden event without any precursors. Instead, we find that well before the fracture is macroscopically detectable, a distinct zone of small-scale deformations emerges at the exact locus of the ultimate crack nucleation. This local strain field grows exponentially in time and space and follows similar kinetics as the bond rupture cascade predicted by the erosion hypothesis. Because the resolution of LSSI is too low to directly visualize bond rupture, other techniques are required to provide conclusive evidence. Nevertheless, all our findings are in line with delayed fracture being the result of strongly localized damage accumulation which concomitantly causes delocalized deformations.

The originality of our methodology lies predominantly in the high deformation resolution, which far exceeds that of commonly used techniques to measure surface strains such as digital image correlation. In addition, LSSI not only provides information about the static deformation field, but also offers a wealth of dynamic information that allows different processes to be disentangled and quantified separately. The full capacity of this technique is still far from fully explored. For instance, the results in this chapter suggest that LSSI may pave the way to early detection of damage in existing materials well before its catastrophic effects become manifest. Moreover, it can provide a deeper understanding of the mechanisms of damage and dissipation in a much larger class of mechanical problems. Many challenging questions remain unanswered in the field of fracture and damage mechanics, in particular in those scenarios where the powerful continuum approach of linear elastic fracture mechanics breaks down,[51] for example experimentally probing the effects of heterogeneity, which are predicted to fundamentally alter the physics of mechanical instabilities.[52] Finally, with the emerging trend of ultratough solids through the molecular design of dissipative pathways[37,53,54] or self-healing capabilities (Chapter 8),[55,56] the need for techniques to elucidate the molecular dynamics underlying these unique mechanical properties has grown. Optical micromechanical mapping is a powerful tool to contribute to the rational design of tough and self-healing solids.[32]

7.A Appendix

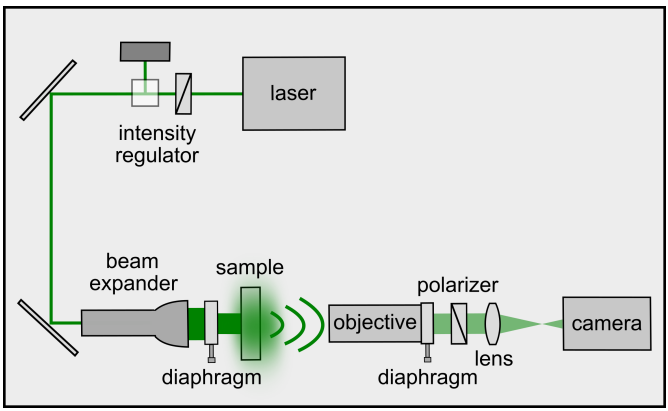

Figure 7.A.1. Schematic top view of laser speckle strain imaging in the forward-scatter geometry. The sample is illuminated with an expanded laser beam, whose intensity is regulated by passing the beam through a half-wave plate and polarizing beam splitter cube; the latter decomposes the beam into two orthogonal polarization components, one of which is directed into a beam dump. Adjustment of the rotation angle of the half-wave plate thus allows controlling the intensity of the transmitted component. After reflection by two mirrors, the beam is expanded to a diameter of 1.5 cm, of which the outer 0.2 cm are cut off by a diaphragm with circular aperture to ensure a uniform spatial intensity profile. The forward-scattered light is subsequently collimated by an infinity-corrected microscope objective (Mitutoyo Plan Apo, 2×, NA = 0.055), passed through an extension tube and second diaphragm onto a linear polarizer perpendicular to the polarization of the incident laser beam, which filters photons with low-order scattering paths. The unfiltered photons are collected by a converging lens and focused onto a CMOS camera (HiSpec 1, Fastec Imaging). The magnification of the imaging system is 1.5×. To optimize the spatial resolution while retaining a good signal-to-noise ratio, the speckle size is tuned by the diaphragm in the detection path to be slightly larger than the pixel size, typically 2–3×. The camera operates at a frame rate of 2000 Hz, and the exposure time is adjusted to cover the full dynamic range (typically ∼200 μs). A tailor-made enclosing chamber eliminates air convection and stray light. Partially adapted from Chapter 5.[31]

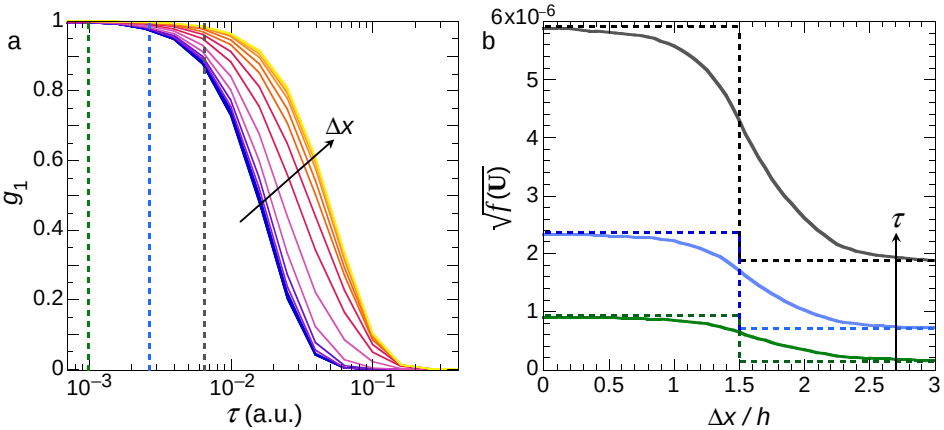

Figure 7.A.2. Spatial blurring in forward-scatter laser speckle strain imaging. To estimate the degree of lateral blurring in forward-scatter LSSI measurements, we perform random-walk simulations[43,44] of photon transport in a material with a thickness $h = 100\ell^*$. We evaluate the ability of the method to resolve non-uniform strains by considering a material with a step-wise decrease in shear rate $\dot{\gamma}$ of factor 10 at $\Delta x = 1.5h$. We collect statistics for 10^6 photons, which are launched one at a time in the $+z$-direction at different Δx-positions; the photons are allowed to perform a random walk until they leave the sample again at $z = h$. The step length is sampled from a Poisson distribution with mean ℓ^*, and we assume isotropic scattering, so that the direction of each step is random. For each step we calculate the transfer wave vector $\mathbf{q_i}$, and we record the accumulated phase shift $\langle \Delta\phi^2(\tau) \rangle = \sum_i (q_i \ell^*)^2 \, \Gamma_i$, with $\Gamma_i = (2/5)\,(\dot{\gamma}(\mathbf{r_i})\tau)^2$ the local strain intensity at the location of scattering event i at correlation time τ. The field correlation function $g_1(\tau)$ is obtained from this by averaging $\exp\left(-\left\langle \Delta\phi^2(\tau) \right\rangle/2\right)$ over all random walks.[43] Its variation with Δx is shown in **(a)**, where the two extreme curves would be the high- and low-$\dot{\gamma}$ scenarios in absence of spatial blurring. For three values of τ, indicated by the dashed lines in (a), $g_1(\Delta x)$ is converted in **(b)** to $\sqrt{f(\mathbf{U})}(\Delta x)$ to resemble the experimental output. From top to bottom: $\tau = 6.3 \cdot 10^{-3}$, $2.5 \cdot 10^{-3}$ and $1 \cdot 10^{-3}$. The dashed lines show the $\sqrt{f(\mathbf{U})}$ profiles in absence of lateral blurring, from which the deviation is considerable and similar for all τ values.

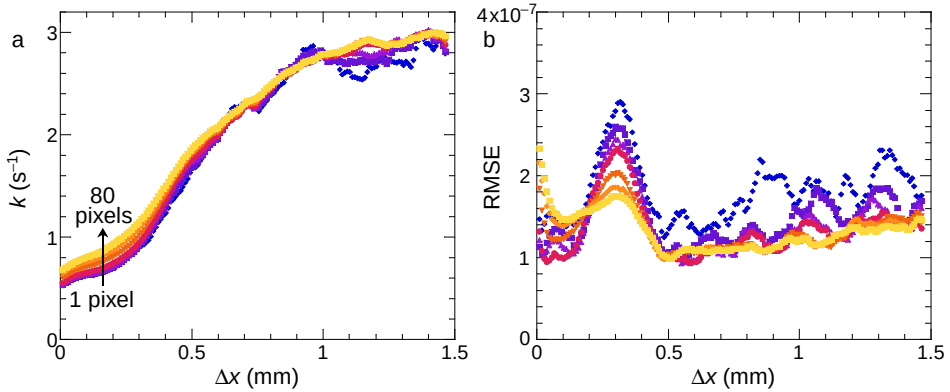

Figure 7.A.3. Robustness of the fitting procedure of the $\sqrt{f(\mathbf{U})}(\Delta t)$ profiles. **(a)** Effects of spatial averaging on the local strain acceleration rate constant k, obtained by fitting the $\sqrt{f(\mathbf{U})}(\Delta t)$ curves in Figure 7.3a to a single-exponential equation. Increasing the number of pixels per Δx bin (in the orthogonal direction) changes the k profile only to a small extent. The inset in Figure 7.3d is obtained by averaging over 40 pixels. **(b)** Root-mean-square errors corresponding to the fits. They are defined as: RMSE $= \left[\sum_{i=1}^{m}\left[\sqrt{f(\mathbf{U})}(\Delta t_i) - f(\Delta t_i)\right]^2 / [m-2]\right]^{1/2}$ with $m = 1546$ the number of data points per $\sqrt{f(\mathbf{U})}$ curve, Δt_i the i-th time point, $\sqrt{f(\mathbf{U})}(\Delta t_i)$ the i-th $\sqrt{f(\mathbf{U})}$ value to be predicted, and $f(\Delta t_i)$ the predicted value of $\sqrt{f(\mathbf{U})}(\Delta t_i)$.

7.A.4 Simulation protocol

A typical simulation setup is depicted in Figure 7.A.4a. Nodes on the top, bottom and right boundaries are kept fixed. The circular notch is placed closer to the centre of the simulation box in order to minimize left-boundary effects. When subjected to energy minimization, the nodes are free to move away from their initial lattice positions, different from the random fuse network simulations often used in fracture studies.[47] Nevertheless, lattice discretization and topology have unavoidable effects on the fracture process, especially on crack propagation. However, as we show in Figure 7.A.4 for some peculiar cases, we verify that the (triangular) shape of the damage zone is robust to variations in softening protocol, system size, notch radius, (subcritical) strain, lattice geometry and topology.

The softening–breaking protocol used in the simulations is illustrated in Figure 7.A.4b, where the force–displacement curve for a single spring is depicted. The linear spring is initialized with a spring constant $\mu^{(0)}$ and a rupture force threshold $f_{\text{thr}}^{(0)}$ (which is initially the same for all the springs in the network). Once the force reaches the threshold, the spring is softened $\mu^{(1)} = \alpha\mu^{(0)}$ and a new threshold $f_{\text{thr}}^{(1)}$ is (uniformly) randomly picked in the interval $(f_{\text{min}}^{(1)}, f_{\text{thr}}^{(0)})$ with

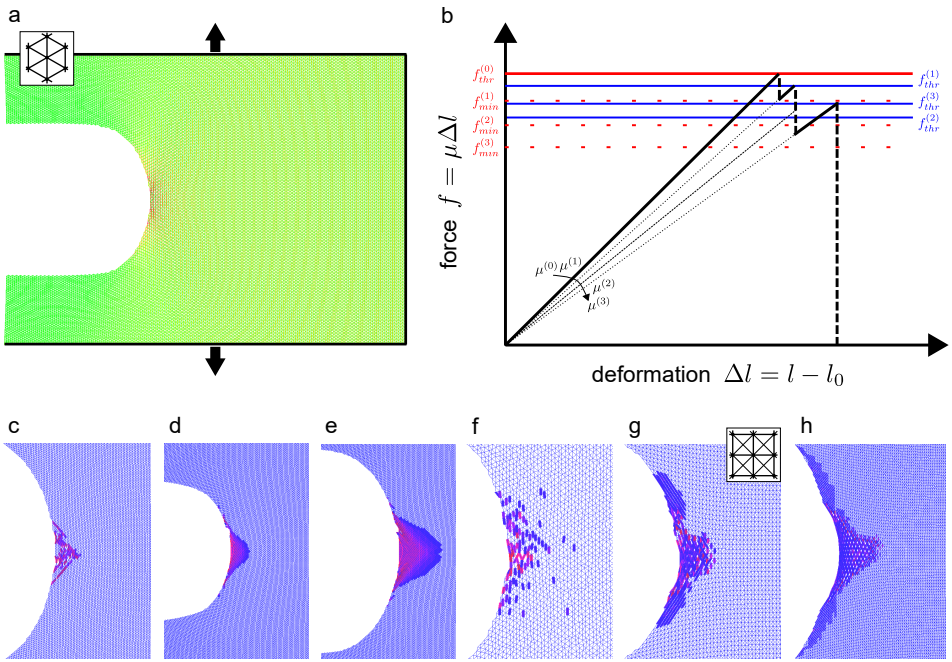

Figure 7.A.4. Simulation protocol and shape of damage zone. **(a)** Deformation field in a relaxed spring network after a step strain of 25%. Springs are coloured according to their deformation: from green to red, from less to more stretched. Clearly, the most stretched springs are close to the notch. The (intact) triangular network consists of $N_x \times N_y = 200 \times 100$ nodes. The circular notch has a radius $r_{\text{notch}} = 20\, l_0$ and it is shifted by $w_x = 40\, l_0$ towards the centre of the box. **(b)** Schematic example of the softening–breaking protocol: force as a function of deformation for a spring with initial stiffness $\mu^{(0)} = 1$, initial rupture threshold $f_{\text{thr}}^{(0)} = 0.35$, softening factor $\alpha = 0.9$, and softening times $n_{\text{soft}} = 3$. **(c–h)** Representative configurations (zoomed-in) of the damage zone before crack nucleation for different simulation parameters and network topology. Highlighted bonds are colour-coded according to the amount of damage: blue to red, low to high. All simulations have the same initial rupture threshold $f_{\text{thr}} = 0.35$. **(c)** $N_x \times N_y = 400 \times 200$, $r_{\text{notch}} = 40\, l_0$ ($w_x = 80\, l_0$), strain = 25%, $\alpha = 0.7$, $n_{\text{soft}} = 5$. **(d,e)** Fixed-threshold protocol, $N_x \times N_y = 400 \times 200$, strain = 30%, $\alpha = 0.9$, $n_{\text{soft}} = 10$, and notch radius **(d)** $r_{\text{notch}} = 20\, l_0$, **(e)** $r_{\text{notch}} = 40\, l_0$. **(f)** Triangular lattice with small positional disorder. $N_x \times N_y = 200 \times 100$, $r_{\text{notch}} = 20\, l_0$, strain = 25%, $\alpha = 0.9$, $n_{\text{soft}} = 10$. **(g,h)** Square lattice with next-nearest-neighbours interactions. $N_x \times N_y = 400 \times 200$, strain = 25%, $\alpha = 0.9$, $n_{\text{soft}} = 10$, and notch radius **(g)** $r_{\text{notch}} = 20\, l_0$, **(h)** $r_{\text{notch}} = 40\, l_0$.

$f_{\min}^{(1)} = \alpha f_{\text{thr}}^{(0)}$. The procedure is repeated n_{soft} times before the spring is irreversibly broken. According to this procedure, softer (damaged) regions have a higher probability of becoming weaker. Because of the stochastic nature of the softening protocol, the newly generated f_{thr} can be already below the current force (see for example $f_{\text{thr}}^{(2)}$ in Figure 7.A.4b) or significantly above it (see for example $f_{\text{thr}}^{(3)}$). In the first case, the spring is again a candidate for the next softening event. However, this does not imply that it will be immediately softened again, since the next softening–breaking event will occur to the weakest spring in the entire network. The competition between force redistribution (obtained by energy minimization) and the softening–breaking procedure can therefore be very subtle.

Nevertheless, within this framework, we obtain qualitatively consistent results. Indeed, in Figure 7.A.4c–h we observe that the shape of the damage zone is consistent across different simulations performed by varying some of the above protocol parameters, the system size, the notch radius, the lattice geometry and topology. In particular, in Figure 7.A.4d,e we use a different softening–breaking protocol in which the rupture threshold f_{thr} is kept constant. Clearly, this extreme protocol enhances the damage accumulation and it allows to clearly observe the triangular shape of the damage zone. In Figure 7.A.4f, we show a simulation snapshot obtained by using a triangular lattice with small positional disorder. In such a simulation, during network initialization each node is randomly displaced from its lattice position by at most $0.3l_0$ independently in both x and y, and the spring constants and rupture thresholds are assigned proportionally to the inverse of the rest length squared. Analogously, we show in Figure 7.A.4g,h simulation snapshots obtained with a different lattice topology. In this case, we use a square lattice with next-nearest-neighbours interactions in which the diagonal springs are initialized with $\mu/2$ and $f_{\text{thr}}/2$. We observe that for this topology, the damage is not only concentrated at the notch in a triangular fashion, but also slightly spread along the notch circumference.

7.A.5 Simulation time evolution

The time is introduced in the simulations by simply assuming a linear relationship between the excess forces carried by the bonds and the rates at which they soften/break. The larger the total rate constant R_{tot}, the faster the dynamics in the system. The intrinsically stochastic nature of the fracture process is illustrated in Figure 7.A.5a, where results from five equivalent simulations using the same softening–breaking protocol are shown. By construction, at $t^* = 0$ a large number of springs are stretched due to the applied step strain. The most stretched springs (close to the notch) quickly soften and R_{tot} decreases. Such a process continues

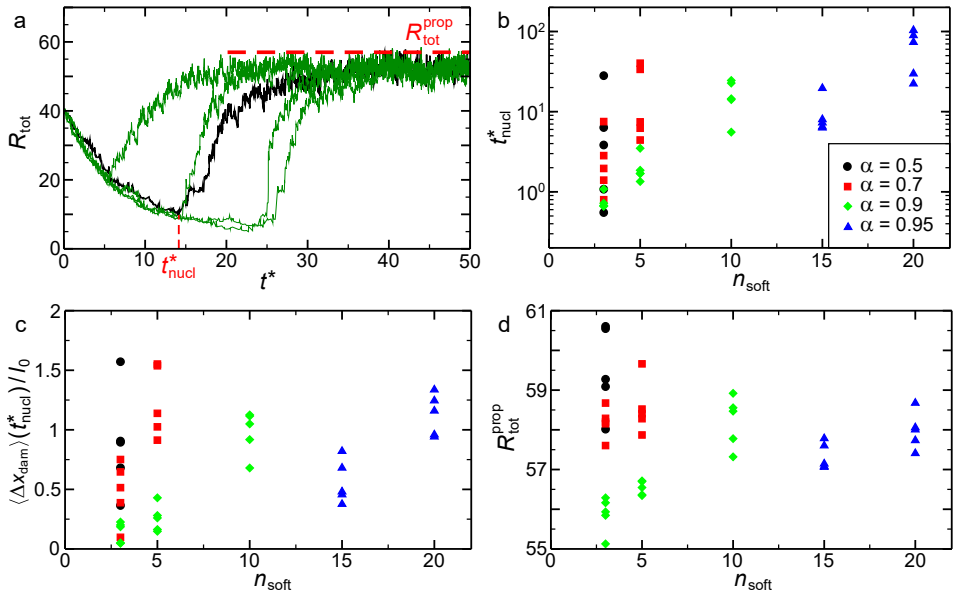

Figure 7.A.5. Tunability of the softening–breaking protocol. **(a)** Total rate constant R_{tot} as a function of reduced time t^* for five equivalent simulations obtained with α = 0.9 and n_{soft} = 10. A crack nucleates when $t^* = t^*_{nucl}$, which roughly corresponds to the minimum of R_{tot}, whereas the speed of the propagating crack is related to R^{prop}_{tot}. **(b)** Dependence of $t^* = t^*_{nucl}$ on n_{soft} for different α. **(c)** Dependence of the centre of mass of the damage zone at the moment of crack nucleation $\langle \Delta x_{dam} \rangle (t^*_{nucl})$ on n_{soft} for different α (see legend in (b)). **(d)** Dependence of R^{prop}_{tot} on n_{soft} for different α (see legend in (b)). All simulations in this figure are obtained with $N_x \times N_y = 200 \times 100$, $r_{notch} = 20\, l_0$, $f_{thr} = 0.35$, and strain = 25%. For each set of parameters, five equivalent simulations are performed.

slowly until the damage accumulated close to the notch is such that the first springs break (around t^*_{nucl}) and the dynamics accelerate. The crack nucleates and escapes from the damaged region while R_{tot} is increasing. Eventually, the crack propagates in the material at a speed that is roughly constant and related to R^{prop}_{tot}, defined as the maximum of R_{tot}. Intuitively, by increasing the number of softening events per bond n_{soft}, while keeping the softening factor α fixed, it is possible to increase (by a couple of orders of magnitude) the delay or nucleation time t^*_{nucl}, as shown in Figure 7.A.5b. However, in order to observe crack nucleation, a balance between α and n_{soft} is needed. Setting α too low and imposing n_{soft} too large results in a very softened/damaged zone close to the notch but does not allow bond-breaking and therefore prevents macroscopic crack nucleation and propagation. A similar increasing trend when increasing n_{soft} is observed for the extension of the damage zone, that is somehow related to $\langle \Delta x_{dam} \rangle$ at the moment

of crack nucleation (Figure 7.A.5c). The propagation speed of the macroscopic crack is only slightly affected by the variation of the softening–breaking parameters (as shown in Figure 7.A.5d, notice the y-axis scale), consistent with the fact that the crack propagation speed is mostly dictated by the properties of the undamaged material (i.e., the ratio between f_{thr} and the applied strain).

7.A.6 Simulation dependence on strain and notch radius

Finally, we study the effects of changing physical parameters, notably the imposed strain and the notch radius, on the nucleation time, damage diffusion and crack propagation (Figure 7.A.6). As expected, increasing the strain causes the delay time to decrease and the propagation speed to increase (by an order of magnitude for 10% increased strain). Varying the notch radius does not affect the propagation speed, but larger notches seem to have a broader distribution for the delay times at small strain. A clear trend for the width of the damage zone is difficult to identify.

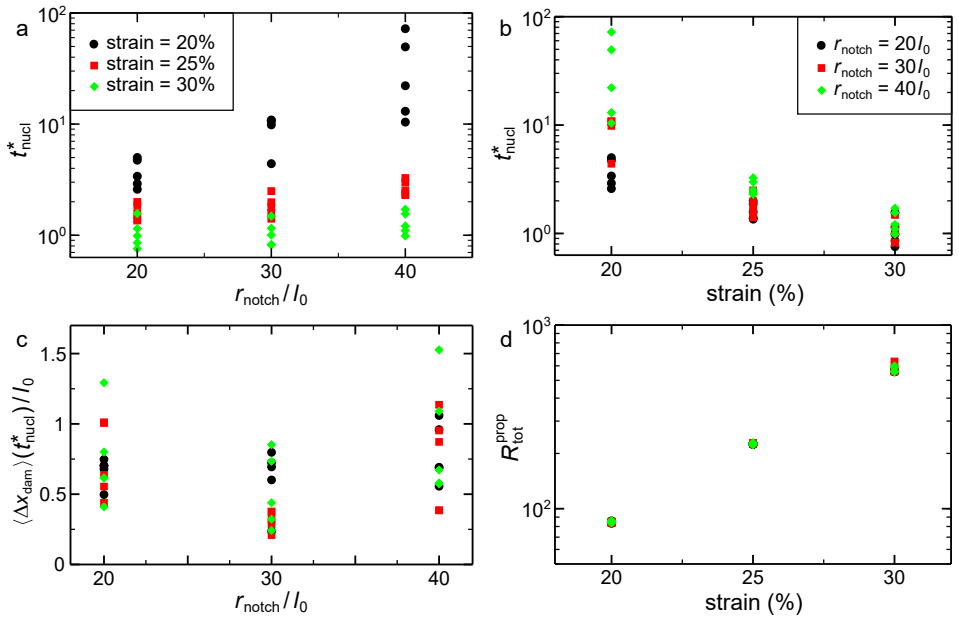

Figure 7.A.6. Simulations at different strains for various notch radii. All simulations in this figure are obtained with the same softening–breaking protocol (α = 0.9, n_{soft} = 10) and $N_x \times N_y = 400 \times 200$, $w_x = 80\,l_0$, f_{thr} = 0.35. For each set of parameters, five equivalent simulations are performed. **(a)** Delay time t^*_{nucl} as a function of notch radius for different strains. **(b)** Delay time as a function of strain for different notch radii. **(c)** Weighted centre of mass of damaged bonds at the moment of crack nucleation $\langle \Delta x_{\text{dam}} \rangle (t^*_{\text{nucl}})$ as a function of notch radius for different strains (see legend in (a)). **(d)** $R^{\text{prop}}_{\text{tot}}$ as a function of strain for different notch radii (see legend in (b)).

References

[1] S. Pearson. *Proc. Phys. Soc. B* **69**, 1293 (1956).

[2] N. J. Petch, P. Stables. *Nature* **169**, 842–843 (1952).

[3] A. Guarino, S. Ciliberto, A. Garcimartın, M. Zei, R. Scorretti. *Eur. Phys. J. B* **26**, 141–151 (2002).

[4] N. Shahidzadeh-Bonn, P. Vié, X. Chateau, J.-N. Roux, D. Bonn. *Phys. Rev. Lett.* **95**, 175501 (2005).

[5] O. Lengliné, R. Toussaint, J. Schmittbuhl, J. E. Elkhoury, J. P. Ampuero, K. T. Tallakstad, S. Santucci, K. J. Måløy. *Phys. Rev. E* **84**, 036104 (2011).

[6] L. Pauchard, H. Meunier. *Phys. Rev. Lett.* **70**, 3565–3568 (1993).

[7] D. Bonn, H. Kellay, M. Prochnow, K. Ben-Djemiaa, J. Meunier. *Science* **280**, 265–267 (1998).

[8] P. J. Skrzeszewska, J. Sprakel, F. A. de Wolf, R. Fokkink, M. A. Cohen Stuart, J. van der Gucht. *Macromolecules* **43**, 3542–3548 (2010).

[9] J. Sprakel, S. B. Lindström, T. E. Kodger, D. A. Weitz. *Phys. Rev. Lett.* **106**, 248303 (2011).

[10] S. B. Lindström, T. E. Kodger, J. Sprakel, D. A. Weitz. *Soft Matter* **8**, 3657–3664 (2012).

[11] X. Wang, W. Hong. *Soft Matter* **8**, 8171–8178 (2012).

[12] C. Ligoure, S. Mora. *Rheol. Acta* **52**, 91–114 (2013).

[13] Y. Pomeau. *C. R. Acad. Sci., Ser. IIb: Mec.* **314**, 553–556 (1992).

[14] M. K. Chaudhury. *J. Phys. Chem. B* **103**, 6562–6566 (1999).

[15] M. Verma, D. K. Singh, P. Senthilkumaran, J. Joseph, H. Kandpal. *Sci. Rep.* **4**, 7257 (2014).

[16] J. M. Clough, C. Creton, S. L. Craig, R. P. Sijbesma. *Adv. Funct. Mater.* **26**, 9063–9074 (2016).

[17] D. E. Hanson, M. Hawley, R. Houlton, K. Chitanvis, P. Rae, E. B. Orler, D. A. Wrobleski. *Polymer* **46**, 10989–10995 (2005).

[18] D. J. Pine, D. A. Weitz, J. X. Zhu, E. Herbolzheimer. *J. Phys. France* **51**, 2101–2127 (1990).

[19] K. Schätzel. *Appl. Phys. B: Lasers Opt.* **42**, 193–213 (1987).

[20] E. Bitzek, P. Koskinen, F. Gähler, M. Moseler, P. Gumbsch. *Phys. Rev. Lett.* **97**, 170201 (2006).

[21] M. Erpelding, A. Amon, J. Crassous. *Phys. Rev. E* **78**, 046104 (2008).

[22] D. A. Sessoms, H. Bissig, A. Duri, L. Cipelletti, V. Trappe. *Soft Matter* **6**, 3030–3037 (2010).

[23] P. Zakharov, F. Scheffold. *Soft Mater.* **8**, 102–113 (2010).

[24] Z. Hajjarian, H. T. Nia, S. Ahn, A. J. Grodzinsky, R. K. Jain, S. K. Nadkarni. *Sci. Rep.* **6**, 37949 (2016).

[25] M.-Y. Nagazi, G. Brambilla, G. Meunier, P. Marguerès, J.-N. Périé, L. Cipelletti. *Opt. Lasers Eng.* **88**, 5–12 (2017).

[26] A. Amon, A. Mikhailovskaya, J. Crassous. *Rev. Sci. Instrum.* **88**, 051804 (2017).

[27] T. Verho, P. Karppinen, A. H. Gröschel, O. Ikkala. *Adv. Sci.* **5**, 1700635 (2018).

[28] E. P. Chan, Y. Hu, P. M. Johnson, Z. Suo, C. M. Stafford. *Soft Matter* **8**, 1492–1498 (2012).

[29] H. M. van der Kooij, S. Dussi, G. T. van de Kerkhof, R. A. M. Frijns, J. van der Gucht, J. Sprakel. *Sci. Adv.* **4**, eaar1926 (2018). **(This chapter)**

[30] P. Zakharov, F. Scheffold, *Light scattering reviews 4: single light scattering and radiative transfer* (Springer, Berlin, Heidelberg, 2009), chap. Advances in dynamic light scattering techniques, pp. 433–467.

[31] H. M. van der Kooij, R. Fokkink, J. van der Gucht, J. Sprakel. *Sci. Rep.* **6**, 34383 (2016). **(Chapter 5)**

[32] H. M. van der Kooij, A. Susa, S. J. García, S. van der Zwaag, J. Sprakel. *Adv. Mater.* **29**, 1701017 (2017). **(Chapter 8)**

[33] D. S. Dugdale. *J. Mech. Phys. Solids* **8**, 100–104 (1960).

[34] G. I. Barenblatt. *Adv. Appl. Mech.* **7**, 55–129 (1962).

[35] A. K. Bhowmick. *J. Macromol. Sci., Part C* **28**, 339–370 (1988).

[36] Y. Akagi, H. Sakurai, J. P. Gong, U. Chung, T. Sakai. *J. Chem. Phys.* **139**, 144905 (2013).

[37] E. Ducrot, Y. Chen, M. Bulters, R. P. Sijbesma, C. Creton. *Science* **344**, 186–189 (2014).

[38] J. Diani, M. Brieu, P. Gilormini. *Int. J. Solids Struct.* **43**, 3044–3056 (2006).

[39] T. Narita, A. Knaebel, J.-P. Munch, M. Zrínyi, S. J. Candau. *Macromol. Symp.* **207**, 17–30 (2004).

[40] L. Djaoui, J. Crassous. *Granul. Matter* **7**, 185–190 (2005).

[41] M. Erpelding, B. Dollet, A. Faisant, J. Crassous, A. Amon. *Strain* **49**, 167–174 (2013).

[42] A. Le Bouil, A. Amon, J.-C. Sangleboeuf, H. Orain, P. Bésuelle, G. Viggiani, P. Chasle, J. Crassous. *Granul. Matter* **16**, 1–8 (2014).

[43] D. J. Durian. *Phys. Rev. E* **51**, 3350–3358 (1995).

[44] L. Vitomir, J. Sprakel, J. van der Gucht. *Sci. Rep.* **7**, 16879 (2017).

[45] E. Evans, K. Ritchie. *Biophys. J.* **72**, 1541–1555 (1997).

[46] K. Zell, J. I. Sperl, M. W. Vogel, R. Niessner, C. Haisch. *Phys. Med. Biol.* **52**, N475–N484 (2007).

[47] M. J. Alava, P. K. V. V. Nukala, S. Zapperi. *Adv. Phys.* **55**, 349–476 (2006).

[48] S. Zapperi, A. Vespignani, H. E. Stanley. *Nature* **388**, 658–660 (1997).

[49] F. Kun, S. Zapperi, H. J. Herrmann. *Eur. Phys. J B* **17**, 269–279 (2000).

[50] N. Yoshioka, F. Kun, N. Ito. *Phys. Rev. E* **91**, 033305 (2015).

[51] J. Fineberg, M. Marder. *Phys. Rep.* **313**, 1–108 (1999).

[52] A. Shekhawat, S. Zapperi, J. P. Sethna. *Phys. Rev. Lett.* **110**, 185505 (2013).

[53] M. Röttger, T. Domenech, R. van der Weegen, A. Breuillac, R. Nicolaÿ, L. Leibler. *Science* **356**, 62–65 (2017).

[54] X. Zhao. *Proc. Natl. Acad. Sci. U. S. A.* **114**, 8138–8140 (2017).

[55] S. R. White, N. R. Sottos, P. H. Geubelle, J. S. Moore, M. R. Kessler, S. R. Sriram, E. N. Brown, S. Viswanathan. *Nature* **409**, 794–797 (2001).

[56] J. F. Patrick, M. J. Robb, N. R. Sottos, J. S. Moore, S. R. White. *Nature* **540**, 363–370 (2016).

Chapter 8

Imaging the molecular motions of autonomous repair in a self-healing polymer

This chapter is based on: Hanne M. van der Kooij, Arijana Susa, Santiago J. García, Sybrand van der Zwaag and Joris Sprakel, 'Imaging the molecular motions of autonomous repair in a self-healing polymer', *Adv. Mater.* **29**, 1701017 (2017).

Abstract

Self-healing polymers can significantly extend the service life of materials and structures by autonomously repairing damage. Intrinsic healing holds great promise as a design strategy to mitigate the risks of damage by delaying or preventing catastrophic failure. However, experimentally resolving the microscopic mechanisms of intrinsic repair has proven highly challenging. The current work demonstrates how optical micromechanical mapping enables the quantitative imaging of these molecular-scale dynamics with high spatio-temporal resolution. This approach allows disentangling delocalized viscoplastic relaxation and localized cohesion-restoring rebonding processes that occur simultaneously upon damage to a self-healing polymer. Moreover, frequency- and temperature-dependent imaging provide a way to pinpoint the repair modes in the relaxation spectrum of the quiescent material. These results give rise to a complete picture of autonomous repair that will guide the rational design of improved self-healing materials.

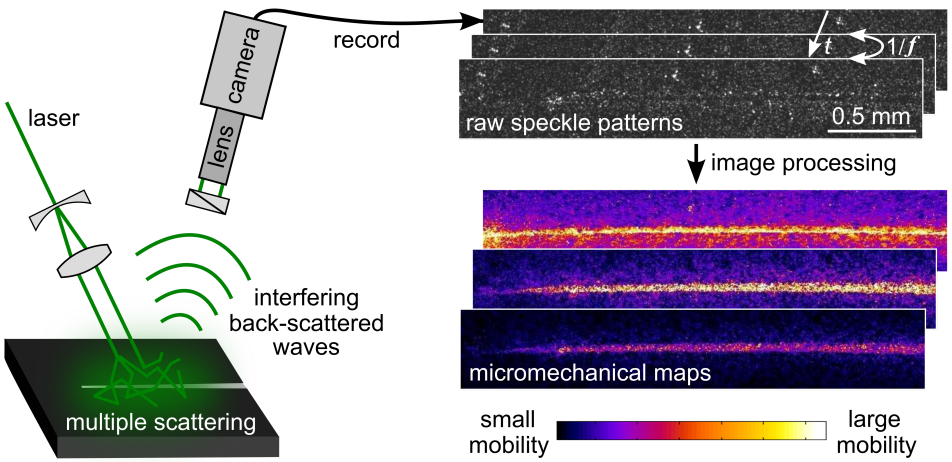

Laser speckle imaging illuminates the nanoscale motions via which self-healing polymers spontaneously restore damage. We use this method to construct micromechanical maps of repair in four dimensions (x, y, t, f).

8.1 Introduction

Functional materials inevitably suffer mechanical damage during their use, as a result of scratching, abrasion, fracture or impact.[1,2] Preventing material failure by managing the effects of damage is one of the foremost challenges in the design of high-performance materials.[3] Self-healing has emerged as a powerful approach to spontaneously repair damage before it can lead to catastrophic failure of the material as a whole.[4–6] Encoding self-healing capabilities in new materials is thus a promising strategy to enhance the durability and reliability of functional materials and coatings. A diversity of self-healing strategies has been developed in the past decades, ranging from extrinsic healing based on healing agents or capsules,[7,8] to intrinsic repair by the autonomous reformation of reversible chemical or physical bonds in the polymer itself.[9–11]

At its core, intrinsic self-healing is driven by the dynamics of polymer chains and supramolecular bonds at the molecular scale.[12–14] However, to date it remains a major challenge to experimentally unravel these dynamics in situ with appropriate spatial and temporal resolution. Although mechanochromic probes have been widely employed for real-time monitoring of bond failure,[15–17] methods to quantitatively visualize bond reformation are unavailable. Yet, such experiments are not only crucial to understand self-healing materials but could also aid in the rational design of new and improved materials. By definition, molecular mechanisms of repair act strongly confined to the site of damage, and may involve a wide range of characteristic relaxation time scales. Thus, to directly probe these mechanisms in situ with high resolution requires new methods that quantify microscopic polymer dynamics in both space and time.

In this chapter, we visualize for the first time the microscale dynamics governing the macroscopic repair of a polymer using the optical method laser speckle imaging (LSI).[18–20] We study autonomous healing in a thermoplastic, polyetherimide-based elastomer that exhibits excellent mechanical properties and spontaneous healing under ambient conditions.[21] By analysing the thermal motion of a small amount of embedded nanoparticles that act as tracers,[22] we extract the local dynamics within the material; we have confirmed that these nanoparticles do not significantly alter the properties of the polymer matrix (Figure 8.A.6c). This strategy allows us to create four-dimensional micromechanical maps of repair, as a function of two spatial coordinates, time and relaxation frequency. Using this in situ and non-invasive approach, we disentangle the combination of delocalized viscoplastic flow and localized cohesion restoration that occur after damage and during self-healing. Moreover, we show that frequency-dependent imaging[23] makes it possible to connect molecular relaxation spectra obtained using conventional

macroscopic measurements to the repair mechanisms occurring at the site of damage. These results provide unique insight into the molecular dynamics of repair and improve our understanding of their spatio-temporal scale in an intrinsic self-healing polymer.

8.2 Experimental details

8.2.1 Polymer variants

See Appendix 8.A.1 and Figures 8.A.1 and 8.A.2 for the materials and procedure used to prepare the polymers for this study. These thermoplastic elastomers are amorphous semi-aromatic polyetherimides prepared from an aromatic dianhydride and an aliphatic branched dimer diamine in different stoichiometric ratios. Table 8.1 summarizes their main characteristics. Both their mechanical integrity and self-healing ability arise predominantly from intermolecular Van der Waals interactions between the dangling branches of the diamines, which act as temporary crosslinks to create a transient supramolecular network.[21]

The polymers used in this study contain 0.5 wt% of iron(II,III) oxide nanoparticles to ensure strong multiple scattering and high LSI contrast. These nanoparticles are inert, do not interact and can be dispersed homogeneously. We have verified that at this low concentration, the presence of the nanoparticles affects the mechanical and self-healing properties only to a small extent (compare Figures 8.A.5 and 8.A.6 with ref. 21).

Table 8.1. Specifications of the polymers used in this study. Optimal healing temperature (T_{heal}), weight-average molecular weight (M_w), number-average molecular weight (M_n), polydispersity index (PDI), and glass transition temperature (T_g). T_{heal} is deduced from rheological temperature sweep measurements of tan(δ), see Figure 8.A.6d and ref. 21. M_w and M_n are determined using gel permeation chromatography with polystyrene as standard (1 mg/mL in THF). T_g is determined using differential scanning calorimetry, the second heating curve (10 °C/min in N_2 flow). See ref. 21 for a comprehensive characterization of the unfilled D-1.1 and D-0.9 polymers.

Polymer name	T_{heal} (°C)	M_w (kg/mol)	M_n (kg/mol)	PDI (-) (-)	T_g (°C)
B-D-1.0	n/a	26	14	1.9	19
D-1.1	24	35	15	2.3	8
D-0.9	30	18	11	1.6	17

8.2.2 Laser speckle imaging

The LSI method is based on the multiple scattering of light; it is essentially the imaging equivalent of diffusing wave spectroscopy.[24] See Chapter 1, Section 1.4, and Chapter 5 for a detailed description of the technique. In our experimental LSI set-up (Figure 8.A.3), we project an expanded and coherent laser beam (Cobolt Samba, 1 W, $\lambda = 532$ nm) onto the turbid sample of interest. The photons in the illumination beam become multiply scattered by the embedded nanoparticles in the sample. As a result of these many scattering events, the photons essentially perform a random walk within the sample, rather than a ballistic trajectory. Each photon traverses a different diffusive path; the resulting path length differences give rise to a random alternation of constructive and destructive interference, which is recorded on a camera as a random pattern of bright and dark spots called speckles. The camera (Dalsa Genie M640-1/2, Stemmer Imaging) is here placed in the back-scatter geometry. Specular and low-order scattering paths are filtered from the back-scattered light by a linear polarizer perpendicular to the polarization of the incident laser beam.

As the tracer particles move within the sample, for example by Brownian motion, viscoplastic relaxation of the polymer matrix, or rebonding processes, all photon path lengths change, reflected by changes in the speckle pattern. Analysing these temporal fluctuations in the speckle intensity allows us to extract information about the internal dynamics and accordingly create image contrast. In LSI, we quantify the rate with which the speckle intensity I of a speckle at time t and position (x, y) fluctuates by the intensity structure function d_2:[25]

$$d_2(x, y, t, \tau) = \frac{\langle [I(x, y, t) - I(x, y, t + \tau)]^2 \rangle}{\langle I(x, y, t) \rangle \cdot \langle I(x, y, t + \tau) \rangle} \tag{8.1}$$

If the tracer particles embedded in the polymer matrix are very mobile, the speckle intensity fluctuates rapidly, and d_2 reaches its maximum at short correlation time τ or high frequency $f = 1/\tau$. By contrast, if the particles move slowly, the speckle intensity varies more slowly and d_2 increases more gradually with increasing τ. Thus, by computing $d_2(x, y, t, \tau)$ we can determine how fast particles are moving at a certain time and location in the sample, which is a direct measure for the local polymer dynamics. We consistently use d_2 to create image contrast, rather than the commonly used absolute intensity I. Heterogeneities in absolute intensities are therefore irrelevant, while contrast from dynamic heterogeneities may emerge (see Figure 1 and Supplementary Movies 1 and 4 in ref. 26). More detailed information about the technique and data analysis are provided in Figure 8.3 and Appendix 8.A.1. In addition, Appendix 8.A.1 contains detailed descriptions of the freeze-

fracture method and characterization of the polymers in terms of self-healing performance, mechanical and rheological properties.

8.3 Results and discussion

Our experiments start by thermostating a slab of the thermoplastic elastomer and creating a through-cut with a scalpel. After reuniting the two cut surfaces (Figure 8.1, steps 1–2), we begin the LSI measurement. Laser speckle imaging involves the coherent illumination of the sample and detection of the back-scattered light, which here originates from photons multiply scattered by the nanoparticle tracers. Photon path length differences within the sample result in an interference, or speckle, pattern that is recorded on a camera (see Supplementary Movie 1 in ref. 26). A static snapshot of the speckle pattern contains no information about the healing process (Figure 8.1, step 4). Instead, we extract information from the raw data by analysing the temporal fluctuations in speckle intensity by means of the contrast function $d_2(x, y, t, \tau)$[27] (see Section 8.2.2 and Appendix 8.A.1). Within the microrheology approach,[22] the thermal motion of the nanoparticles, evaluated here as a function of spatial coordinates x, y, time after damage t and relaxation

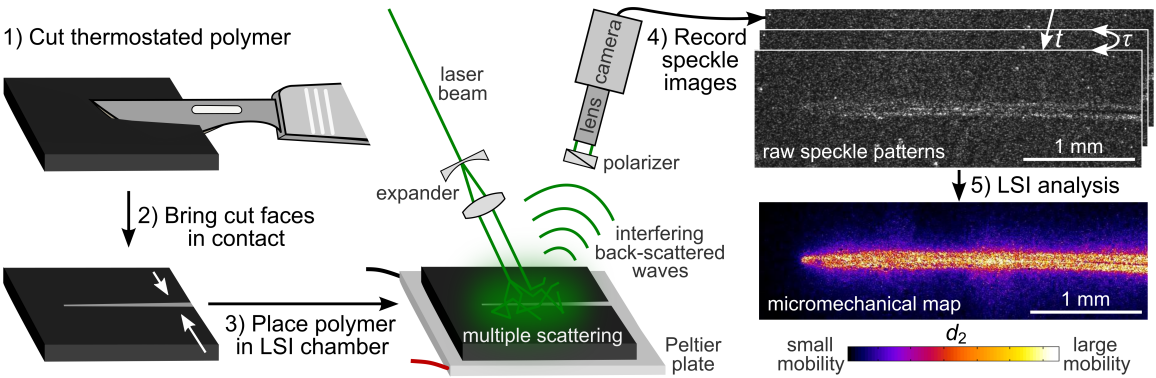

Figure 8.1. Visualizing the molecular dynamics of repair. **(1)** A thermostated slab of the polymer is cut through with a scalpel. **(2)** The cut surfaces are brought into contact and **(3)** probed using laser speckle imaging. The multiply scattered light is detected in back-scatter geometry as **(4)** a time sequence of speckle images of the damage zone. **(5)** The speckle fluctuations are quantified, pixel by pixel, by the contrast function d_2, which encodes the local molecular mobility at position (*x*,*y*), time after damage *t*, and characteristic frequency $f = 1/\tau$. The resulting time-lapse micromechanical maps reveal strong localization of dynamics near the cut, here at $t = 10$ s and $f = 1$ Hz.

frequency $f = 1/\tau$, can be directly related to the micromechanical properties of the polymeric medium.

A single LSI experiment yields a four-dimensional data set, from which we reconstruct spatio-temporal maps of the dynamics at some particular frequency (see Figure 8.1, step 5, and Supplementary Movie 1 in ref. 26).[28,29] These micromechanical maps, colour-coded by the local value of d_2, reveal localized molecular mobility at the cut. The correlation time τ acts as a tuning knob for the type of dynamics we aim to probe: low values of τ bring to light fast, high-frequency dynamics, bounded experimentally by the frame rate of acquisition, here $f_{max} = 64$ Hz; high values of τ enable the study of low-frequency processes, limited by the length of the image sequence, here $f_{min} = 10^{-3}$ Hz. Thus, each experiment harbors information about spatially and temporally resolved healing processes across almost five decades in relaxation frequency.

We start our study with a non-healing version of the thermoplastic elastomer (B-D-1.0, see Table 8.1), in which viscoplastic relaxation occurs but cohesion-

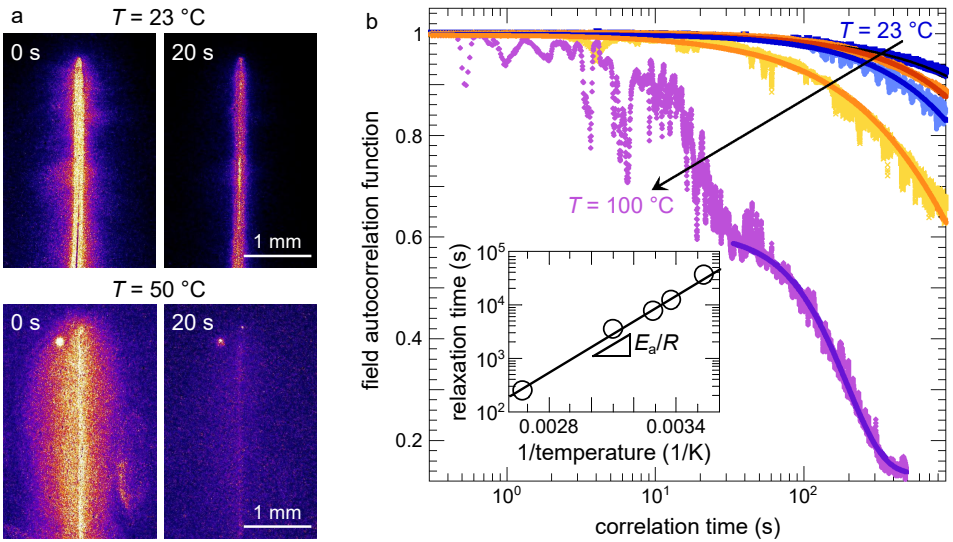

Figure 8.2. Viscoplastic relaxation around a cut in non-healing polymer B-D-1.0. **(a)** Time evolution of dynamics at two temperatures using $d_2(f = 1$ Hz) as the contrast function. **(b)** Measured field autocorrelation function $g_1(\tau)$ of the equilibrium polymer dynamics at $T = 10$, 23, 30, 50 and 100 °C (symbols), fitted to a stretched-exponential function (lines) to extract the thermal relaxation time τ_r, which obeys Arrhenius behaviour **(inset)** with an activation energy of 47 kJ/mol $\approx 19\, k_B T$. The fluctuations in the high-temperature correlation curves are not experimental noise but correspond to reproducible intermittent 'spikes' in the overall dynamics.

restoring processes are suppressed. Micromechanical maps reveal pronounced relaxation dynamics in a relatively large area around the cut (see Figure 8.2a and Supplementary Movies 1 and 2 in ref. 26). As time progresses, these delocalized relaxations subside until equilibrium is reached. We speculate that the rate of this viscoplastic relaxation is governed by the thermally activated reptation of polymer chains within the material. As expected, increasing the temperature leads to an increase in the rate at which these relaxations decay (Figures 8.2a and 8.A.4).

For a more quantitative test of our hypothesis, we determine the characteristic relaxation time of the material in equilibrium τ_r by computing the field autocorrelation function $g_1(\tau)$[24] in a region of interest (ROI) away from the damage zone. The field autocorrelation function is related to the contrast function d_2 as described in Appendix 8.A.1. At all temperatures, g_1 exhibits a terminal relaxation at large correlation times τ (Figure 8.2b). The characteristic relaxation time τ_r, extracted by fitting $g_1(\tau)$ to a stretched exponential decay, obeys the Arrhenius equation $\tau_\mathrm{r} \propto e^{E_\mathrm{a}/RT}$, with RT the thermal energy per mole and E_a the activation energy for relaxation of 47 kJ/mol $\approx$ 19 $k_\mathrm{B}T$ (Figure 8.2b, inset). Interestingly, from a single LSI experiment we can probe both the kinetic relaxation after cutting and the equilibrium relaxations of the material at rest.

In a self-healing version of this thermoplastic elastomer, similar viscoplastic relaxations are expected to occur, but simultaneously, strongly localized cohesion-restoring dynamics must take place at the cut interface. The polymer under study exhibits spontaneous repair at room temperature (D-1.1, see Table 8.1 and ref. 21), as evidenced from bulk mechanical and rheological analysis (Figures 8.A.5 and 8.A.6). After cutting, both stiffness and strength restore fully and autonomously within 10 days. Based on macroscopic testing, it was proposed that repair occurs through fast adhesion of the cut surfaces, by Van der Waals interactions between dangling chains, followed by slow polymer interdiffusion across the cut.[21] Although bulk measurements are valuable to establish the conditions and completeness of self-healing at the macroscopic scale, they do not provide direct insight into its microscopic origins. By contrast, micromechanical mapping with LSI allows us to shed light on these microscopic mechanisms.

Self-healing manifests as a zipper-like closure of the cut, from its tip inward, with a tangential closure velocity of ~30 μm/s (see Figures 8.3a, 8.A.7 and 8.A.8, and Supplementary Movie 3 in ref. 26). This zipping is driven by the inward tension on the cut which diverges at the tip, where the stress field exhibits a singularity.[30] These effects are further amplified by the gradient in width of the cut opening, which vanishes at the tip; the close proximity between the two surfaces at the cut tip allows for rapid adhesion and start of the interdiffusion process. This picture is corroborated by the absence of zipping, and homogeneous dynamics

when a cut surface is exposed to air (Figures 8.3b and 8.A.9). We confirm that the rate of polymer relaxation inherent to the material is a crucial step in the healing process by studying the recovery of the same polymer after a linear indentation, resulting in similar relaxation dynamics (Figure 8.A.10).

Repair requires cohesion to be restored across the cut interface. To disentangle these cohesion-restoring dynamics from the delocalized plastic relaxation inherent to a cut made in a ductile solid, we prepare a brittle crack in the same material by fracturing a pre-notched sample frozen in liquid N_2, thereby minimizing the degree of plastic deformation. Interestingly, the polymer exhibits excellent and fast

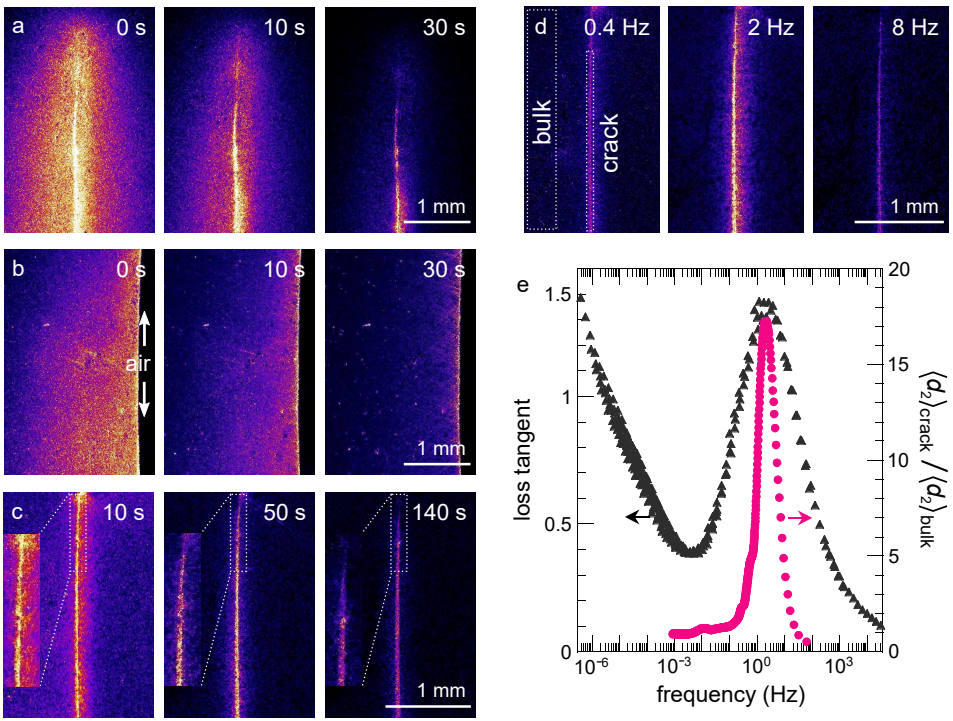

Figure 8.3. Resolving the mechanisms of repair. Time-lapse micromechanical maps for D-1.1, at $f = 1$ Hz, of **(a)** the self-healing of a cut made at room temperature, **(b)** viscoplastic relaxation at a cut–air interface, and **(c)** self-healing of a brittle freeze-fracture. **(d)** Frequency dependence of the self-healing mobility for the freeze-fracture at $t = 40$ s. The colour scales are normalized by the respective values of $\langle d_2 \rangle_{bulk}$ and all have the same limits. **(e)** Comparison between bulk rheology of the frequency dependence of the loss tangent $\tan(\delta)$ and the enhancement of self-healing mobility at the crack interface with respect to the bulk of the material, $\langle d_2 \rangle_{crack} / \langle d_2 \rangle_{bulk}$. The dotted lines in (d) indicate the ROIs in which these two properties are measured.

healing of the brittle fracture when reheated to room temperature (Figure 8.A.5c). In the absence of long-ranged plastic relaxation, we instead observe only localized dynamics at the fracture interface (see Figure 3c and Supplementary Movie 4 in ref. 26). We attribute these to the molecular motions involved in adhesion and subsequent intermixing of polymer chains. A close-up of the tip shows that also this brittle crack closes like a zipper, with a tangential closure velocity of ~5 μm/s (Figure 8.3c, insets). As this directional closure requires a tip where the crack width vanishes and stress field diverges, zipping motion is indeed absent for brittle fractures that traverse the entire sample and lack a distinct tip (Figure 8.A.11b).

These data illustrate that self-healing is a combination of delocalized viscoplastic flow (Figure 8.3b) and localized cohesion-restoring processes (Figure 8.3c), which raises the question how these dynamics are related to the linear relaxation spectrum of the material. To answer this question, we make use of the multidimensional nature of LSI to reconstruct frequency-dependent micromechanical maps during healing. Visual inspection of these maps at a brittle crack reveals that the self-healing dynamics are most pronounced and localized at a frequency of ~2 Hz (Figure 8.3d). To quantify this frequency dependence, we measure the average molecular mobility at the crack by means of the contrast function d_2, normalized by that in the bulk of the sample, $\langle d_2 \rangle_{\text{crack}} / \langle d_2 \rangle_{\text{bulk}}$, as a function of the relaxation frequency f. Indeed, the self-healing mobility displays a distinct peak at $f \approx 2$ Hz (see • in Figures 8.3e and 8.A.12). At frequencies below ~0.1 Hz and above ~100 Hz, localized repair dynamics vanish.

In linear bulk mechanical experiments, the frequency dependence of relaxation processes can for example be evaluated by means of the loss tangent $\tan(\delta)$, as a measure for the relative importance of viscous and elastic processes. Strikingly, a time–temperature superposition master curve of $\tan(\delta)$ from such macroscopic measurements, referenced to 25 °C, exhibits a peak at exactly the same frequency (Figure 8.3e, ▲). Thus, the local response to a strongly non-linear deformation, i.e. a brittle fracture, can be directly mapped onto the governing dissipative mechanisms of the material in equilibrium.

For a variant of this polymer which self-heals at 30 °C (D-0.9, see Table 8.1 and ref. 21), we observe a strong temperature dependence of the closure mode of the cut (Figures 8.4a and 8.A.13). We represent time series of these micromechanical maps as kymographs, in which the average values of d_2 in a strip along the cut are plotted as a function of time. Such kymographs in the space–time domain reveal three distinct closure modes (see Figure 8.4b and Supplementary Movies 5–7 in ref. 26). At 23 °C, the cut closes homogeneously, except at the tip itself. At the optimal healing temperature, 30 °C, a front of enhanced mobility advances away from the tip, closing the cut like a zipper. At much higher temperatures, where the rate

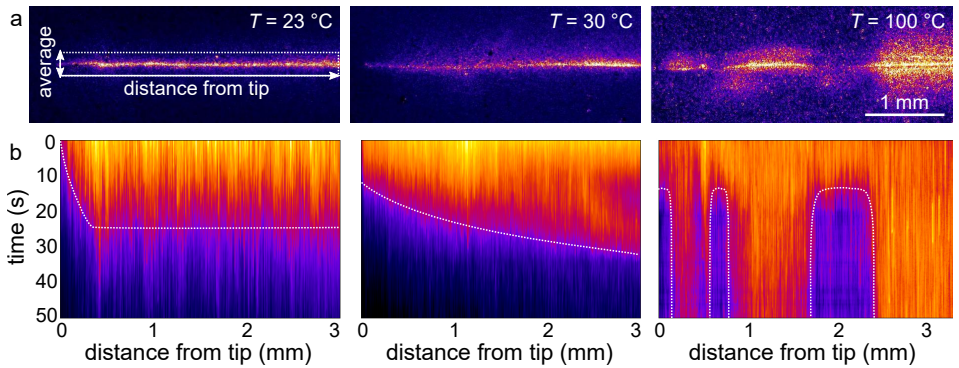

Figure 8.4. Modes of cut closure. **(a)** Micromechanical $d_2(f = 1\ \text{Hz})$ maps at $t = 25$ s after creating a cut in D-0.9 at different temperatures. All images have the same scale and colour coding. **(b)** Kymographs of the average mobility around the cut versus distance from the cut tip. With increasing temperature, the closure mode transitions from homogeneous relaxation (23 °C) to zipper-like closure (30 °C) and a fluid-like Rayleigh–Plateau instability (100 °C). The dotted lines are guides to the eye. All kymographs have the same scale.

of polymer reptation is strongly enhanced (Figure 8.2b), we observe rapid filling of the cut through a break-up process that is reminiscent of a Rayleigh–Plateau instability, driven by capillary pressure.[31]

8.4 Concluding remarks

These experiments give rise to a microscopic picture of repair in these self-healing polymers. Damaging the polymer results in both the breaking of cohesive interactions and viscoplastic deformations, which heal autonomously via: (i) slow flow of the material to fill the gap and bring the damaged surfaces into contact, allowing (ii) Van der Waals interactions to restore cohesion across the cut or crack, which involves (iii) a zipper-like motion in the presence of a distinct tip, and finally culminates in (iv) reptational intermixing and restoration of the material cohesion. Moreover, the latter process occurs at a distinct frequency that can be mapped onto the linear relaxation spectrum of the material.

Our results highlight how laser speckle imaging allows the optical micromechanical mapping of strongly non-linear processes, as a function of spatial coordinates, experimental time and relaxation frequency, with unprecedented detail. Due to the simplicity and non-invasive nature of the method, we envisage its extension to other materials, such as extrinsic self-healing systems, and to the study of different non-linear mechanical phenomena, such as the mechanisms of fracture and fatigue.

Illuminating and disentangling the rich convolution of diverse dynamics inherent to such strongly localized mechanics will not only deepen our insight into the physics of non-linear mechanics, but may ultimately enable the tailored design of high-quality self-healing materials.

8.A Appendix

8.A.1 Additional experimental details

Materials

The monomers used in this study are depicted in Figure 8.A.1. The aromatic monomers 4,4′-oxydiphthalic anhydride (ODPA) and 3,3′,4,4′-biphenyltetracarboxylic dianhydride (BPDA) are purchased from TCI Europe N.V. The fatty dimer diamine (DD1), derived from vegetable oil, is purchased from Croda Nederland B.V. N,N-dimethylacetamide (DMAc, 99.5% extra dry) is obtained from Acros Organics. Spherical iron(II,III) oxide nanoparticles sized 50–100 nm are obtained from Sigma-Aldrich.

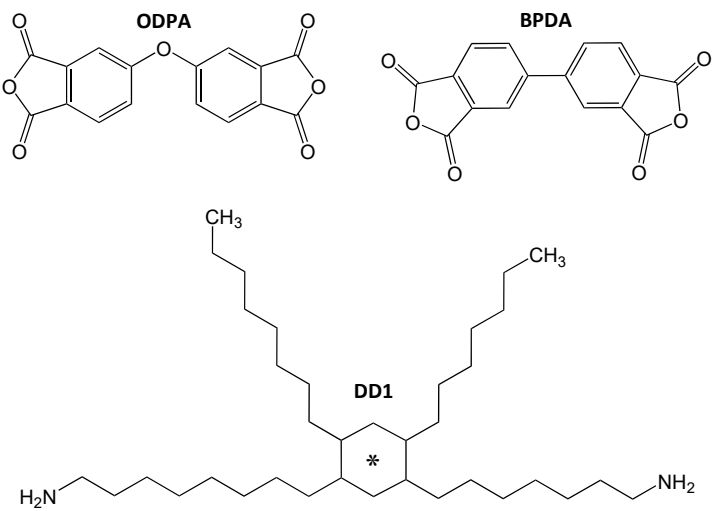

Figure 8.A.1. Monomers used for the polyetherimide syntheses. DD1 is actually a mixture of C-36 isomers with ∼95% saturated bonds and ∼5% double bonds, alycyclics and aromatics in the 'linker' (*).

Preparation of thermoplastic elastomers

Three different polyetherimides (PEIs) are synthesized using the two-step polymerization process outlined below and described in detail in a previous paper:[21] a non-healing reference polymer (B-D-1.0) composed of BPDA and DD1 in stoichiometric ratio; a polymer which self-heals around 24 °C (D-1.1) composed of ODPA and DD1 in a 1:1.1 molar ratio; and a polymer which self-heals around 30 °C (D-0.9) composed of ODPA and DD1 in a 1:0.9 molar ratio. The respective mass ratios are calculated using the molecular weights of the monomers (MW_{BPDA} = 294.2 g/mol, MW_{ODPA} = 310.2 g/mol and MW_{DD1} = 536.8 g/mol) and assuming all monomers are 100% difunctional.

The polymers are synthesized in the polar aprotic solvent DMAc with a total solids (monomers) content of 20 wt%. First, the diamine DD1 is dissolved in 2/3 (vol.) of the DMAc in a three-neck round-bottom flask, followed by the dianhydride (BPDA or ODPA) and the remainder of the solvent (1/3 (vol.)). The mixture is magnetically stirred at 200 rpm under nitrogen flow at room temperature and left to react until the solids are fully dissolved in the DMAc and the solution is clear and light yellow, suggesting the formation of the polyamic acid (PAA) (Figure 8.A.2a). Subsequently, the three-neck round-bottom flask containing the PAA solution is attached to a 10 mL Dean–Stark apparatus with reflux condenser. The reaction mixture is stirred at 150 rpm under nitrogen flow for 6 h at 160 °C and 1 atm to induce thermal imidization, yielding the polyetherimide (Figure 8.A.2a). The formed aqueous phase is removed in the Dean–Stark trap by azeotropic distillation with 10 wt% toluene.

To render the PEI multiply scattering, a dispersion of 20 wt% iron oxide nanoparticles in DMAc is subsequently added at a total nanoparticle concentration of 0.5 wt% by mixing the appropriate amount with the hot polymer solution (150 °C), and the mixture is immediately placed in an ice bowl. Once cooled down, the polymer is not soluble in DMAc anymore and consequently precipitates together with the nanoparticles (Figure 8.A.2b). The DMAc is decanted from the flask and the precipitate is transferred into a rectangular polytetrafluoroethylene (PTFE) mold of length = 70 mm, width = 20 mm, and thickness = 1 ± 0.5 mm. The samples in the molds are thermally post-treated in a vacuum oven at 150 °C for 12 h, after which they are allowed to cool down in air at room temperature overnight. This yields bulk polyetherimides with 0.5 wt% embedded tracer nanoparticles (Figure 8.A.2c) whose properties are summarized in Table 8.1.

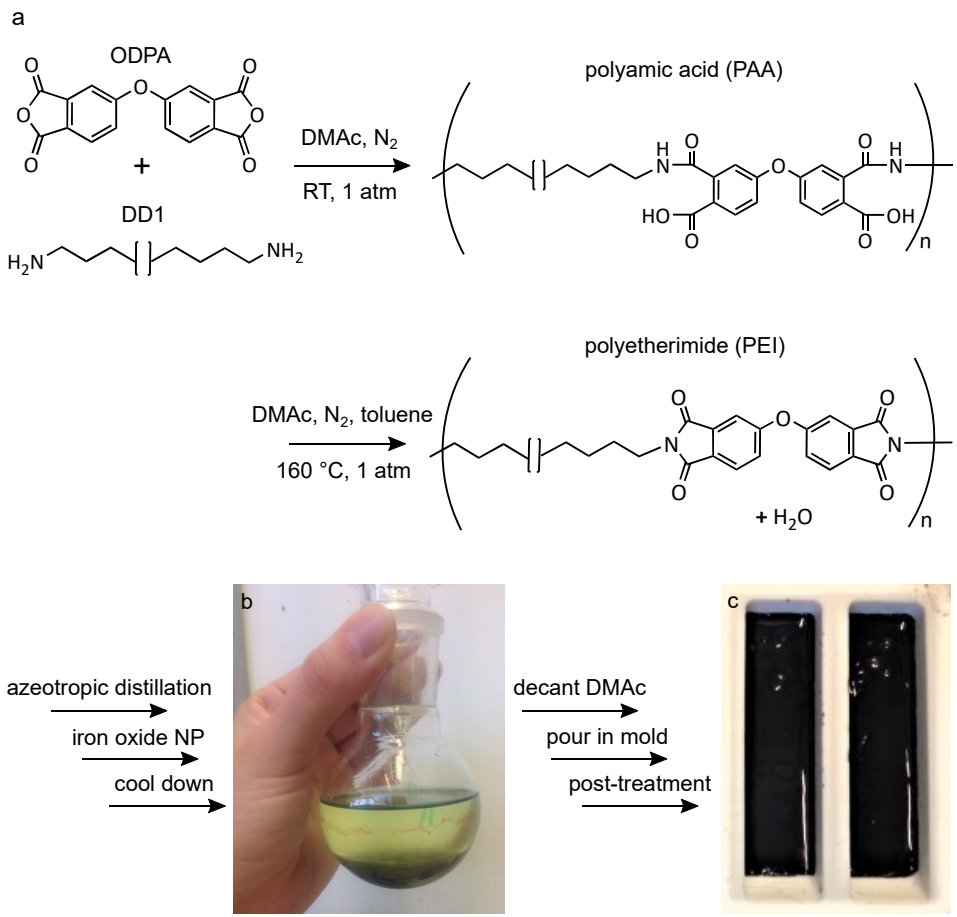

Figure 8.A.2. Preparation of the thermoplastic elastomers used in this study. **(a)** Schematic representation of the polyamic acid synthesis followed by cyclodehydration into a polyetherimide. The structure of DD1 is shown in a simplified way, with the brackets denoting the branched section that can be at different locations along the main C-18 chain. The reaction between BPDA and DD1 occurs analogously. **(b)** Insoluble PEI–nanoparticle precipitate with solvent DMAc on top, after bulk imidization and cooling down. **(c)** Final thermoplastic elastomers containing iron oxide tracer nanoparticles.

Freeze-fracturing

To avoid deformation during damage and subsequent viscoplastic recovery that might obscure the self-healing dynamics, we introduce a brittle freeze-fracture in the D-1.1 thermoplastic elastomer (Figure 8.3c–e). We study both a crack that halves the sample (Figures 8.A.5c and 8.A.11b) and a partial fracture that stops within the sample to circumvent separation and re-positioning of the two halves (Figure 8.3c–e). In both cases we first make a pre-notch, after which we either freeze the entire sample in liquid nitrogen at −196 °C, or only the pre-notched half. We subsequently fracture the sample by hand at the pre-notched location and reunite the two crack surfaces. In the partially frozen specimen, the crack invariably stops at the boundary of the frozen and unfrozen sections; after creating the crack, we freeze the entire sample to prevent asymmetric thermal stresses caused by different expansion rates of the two halves upon thawing. Finally, we tape a temperature sensor onto the specimen and monitor the dynamics at the crack tip using LSI.

Tensile mechanical and self-healing evaluation

Tensile mechanical tests are performed using dog-bone specimens according to the ASTM D1708 standard at 80 mm/min crosshead speed. To determine the self-healing performance, pristine samples are cut with a sharp razor blade at 23 °C. Subsequently, the two cut surfaces are carefully repositioned in the dog-bone PTFE mold, either immediately or after a delay of 24 h, and allowed to heal at 23 °C for 1, 5 and 10 days. The same is done for the freeze-fractured samples. All tests are performed in triplicate with excellent reproducibility.

Macroscopic rheology

The bulk linear viscoelastic properties of the polymers are measured using a Haake Mars III rheometer in the parallel-plate geometry, with a plate diameter of 8 mm. First, the linear viscoelastic range is determined by a 1 Hz oscillatory strain amplitude sweep at the highest and lowest temperature, from 0.001% to 10% strain. Frequency sweep measurements from 10 Hz to 0.1 Hz are subsequently performed from 110 °C to 10 °C in steps of 5 °C, at a shear strain amplitude of 0.5%. The master curves of the storage modulus G', loss modulus G'' and los tangent $\tan(\delta)$, at a reference temperature of 25 °C, are constructed from the acquired data by employing the time–temperature superposition (TTS) principle using Haake RheoWin software. All tests are performed in triplicate with excellent reproducibility.

LSI data processing

As described in Section 8.2.2, we consistently use the intensity structure function d_2 to create imaging contrast, rather than the more common intensity autocorrelation function g_2. In the case of a stationary ergodic process with large sampling size, the two are directly related by: $d_2(x, y, t, \tau) = 2[g_2(x, y, t, 0) - g_2(x, y, t, \tau)]$.[25] However, d_2 is less sensitive to noise and intensity drift and therefore preferred over g_2 in most practical applications.

To quantify the non-healing relaxation mode (Figures 8.2a and 8.A.4) in more detail, we compute the field autocorrelation function g_1 from d_2:

$$g_1(\tau) = \sqrt{1 - d_2(\tau)/2\beta} \tag{8.2}$$

where we have applied the Siegert relation $g_1(\tau) = \sqrt{(g_2(\tau) - 1)/\beta}$ and the fact that $\langle g_2(0) \rangle = \beta + 1$, with β the spatial coherence factor that accounts for the number of speckles detected. As camera-based detection inevitably involves $\beta < 1$, we choose β such that $g_2(\tau) - 1 \to \beta$ for $\tau \to 0$. The angular brackets $\langle\rangle$ here indicate a spatial, multi-speckle average, over a ~2 mm^2 section of the material sufficiently far from the cut. We do this at $t = 5$ min after the onset of self-healing to probe only the equilibrium and thermal relaxation modes of the material at rest. Thanks to the multi-speckle averaging, time averaging is not required; as a result, temporal heterogeneities in the dynamics, such as the distinct intermittency observed in Figure 8.2b, are conserved, which would be lost by averaging the intensity fluctuations over time. We subsequently extract the relaxation time τ_r by fitting the field autocorrelation functions to a stretched-exponential decay:

$$g_1(\tau) = \exp\left[-\gamma(\tau/\tau_r)^\alpha\right] \tag{8.3}$$

with α the stretching exponent and γ a numerical prefactor. In Chapter 5, Appendix 5.A.1, we have determined that for our experimental set-up, $\gamma \approx 1.5$.

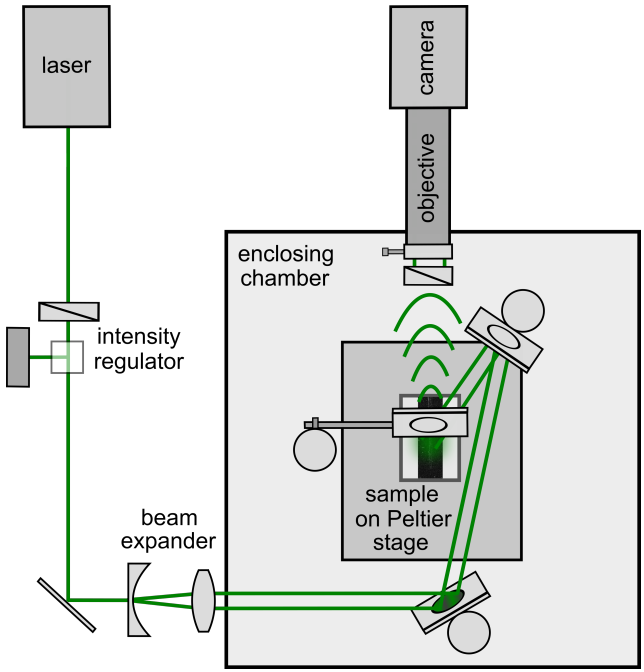

Figure 8.A.3. Schematic top view of the laser speckle imaging set-up in the back-scatter geometry. The sample is illuminated with an expanded laser beam, whose intensity is regulated by passing the beam through a half-wave plate and polarizing beam splitter cube; the latter decomposes the beam into two perpendicular polarization components, one of which is directed into a beam dump. Adjustment of the rotation angle of the half-wave plate thus allows controlling the intensity of the transmitted component. After reflection by a mirror, the beam is expanded to a diameter of $\sim$1 cm by a Galilean beam expander. The beam is subsequently directed downward onto the sample via two mirrors, at a small angle with respect to the detection path to avoid intensity enhancement by coherent back-scattering. The back-scattered light is reflected by a mirror onto a linear polarizer perpendicular to the polarization of the incident laser beam, which filters photons with low-order scattering paths. The transmitted photons are collected by a Qioptiq zoom lens and focused through an iris diaphragm and extension tubes onto a CCD camera. The magnification of the imaging system is $1.8\times$ and the depth-of-focus is $\sim$0.1 mm. To optimize the spatial resolution whilst retaining a good signal-to-noise ratio, the speckle size is tuned by the diaphragm to be slightly larger than the pixel size, typically 2–3$\times$. The camera operates at a frame rate of 64 Hz, and the exposure time is adjusted to cover the full dynamic range. A tailor-made enclosing chamber eliminates air convection and stray light. The polymers are placed on a Peltier stage with temperature controller (PE 94, Linkam Scientific Instruments), and the temperature is measured using an external thermistor probe (TSP01, Thorlabs). The entire set-up is mounted on an optical breadboard with an active vibration isolation system (Vario Basic 60, Accurion). Adapted from Chapter 5.[19]

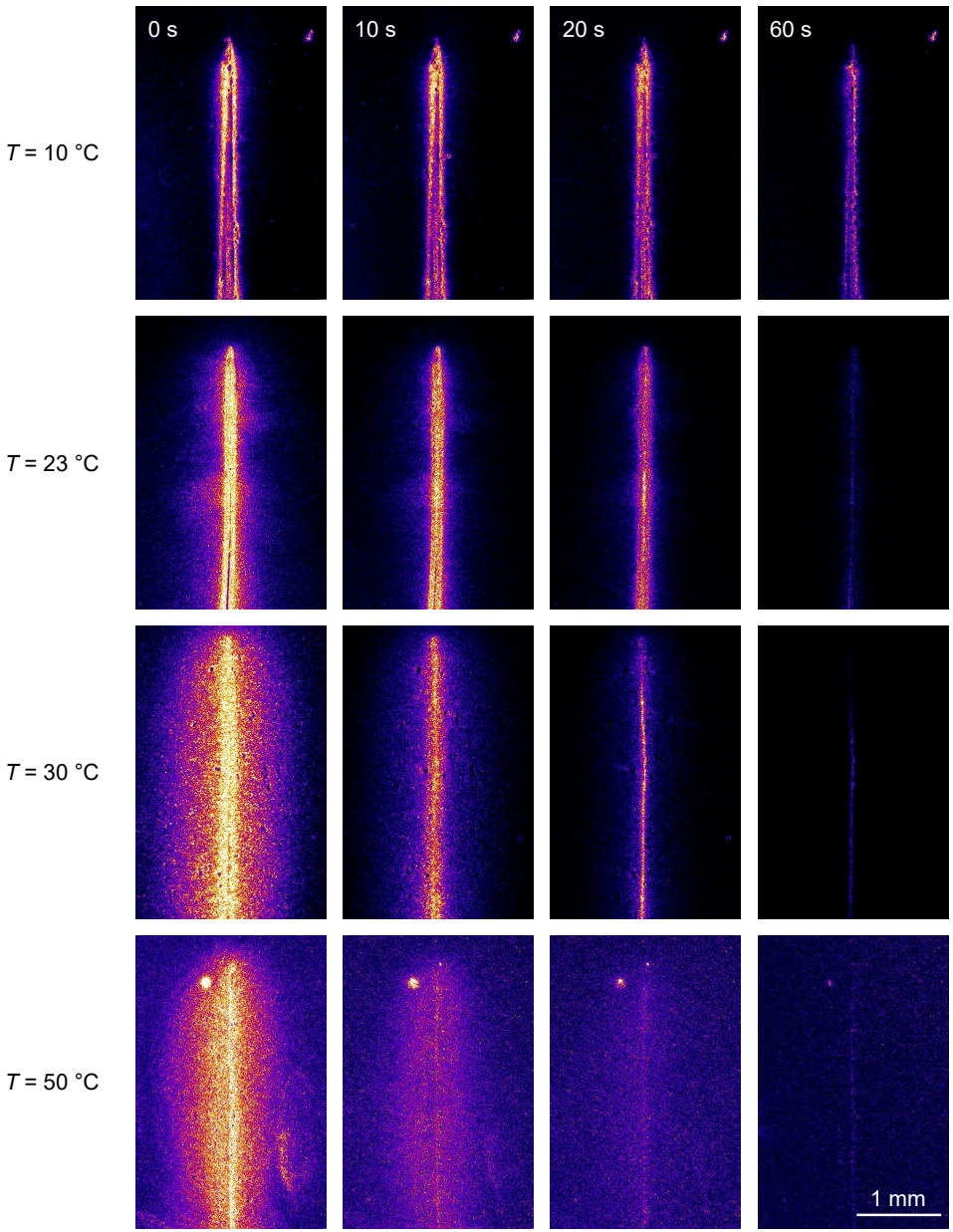

Figure 8.A.4. Viscoplastic relaxation around a non-healing cut. Time-lapse micromechanical maps for reference polymer B-D-1.0, as a function of temperature. $d_2(f = 1\ \text{Hz})$ is used as the contrast function. All images have the same scale bar and all rows display the same time points.

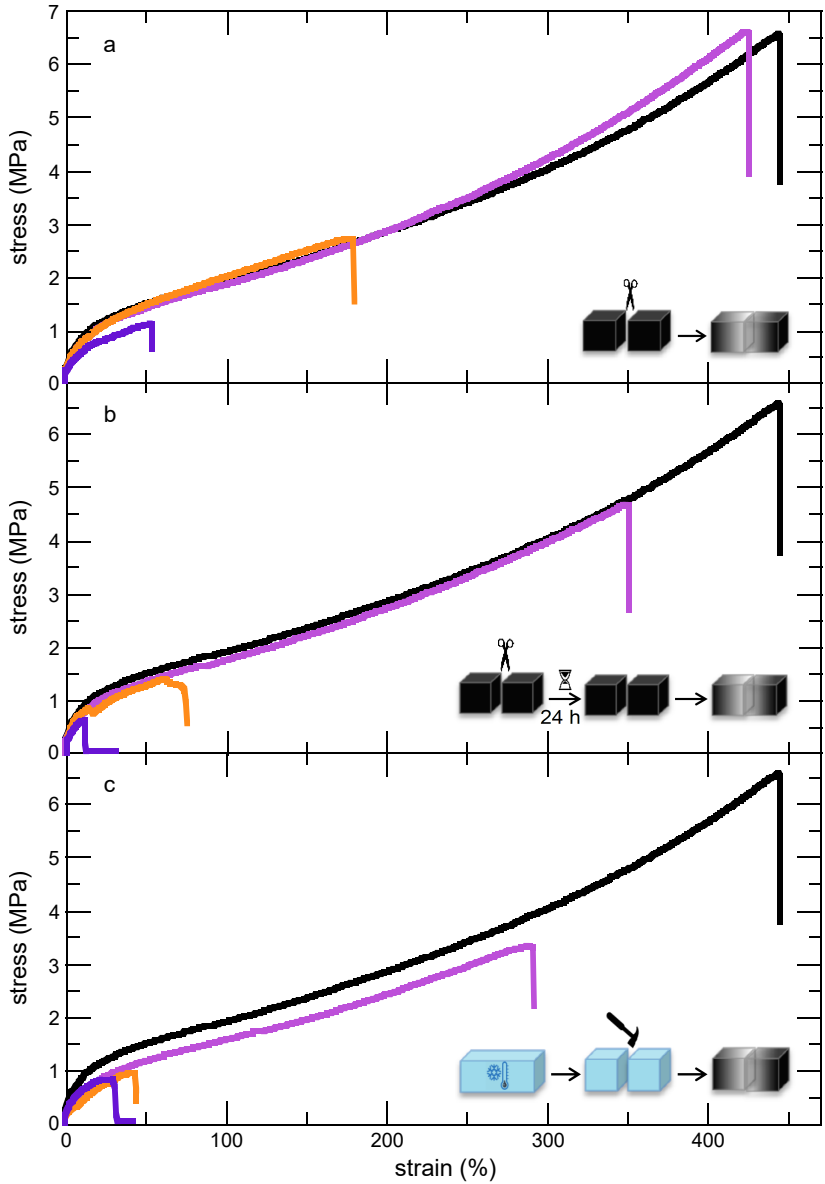

Figure 8.A.5. Tensile mechanical and self-healing performance of D-1.1 for different fracture modes: **(a)** blade-cut at 23 °C followed by immediate contact between the cut surfaces; **(b)** blade-cut at 23 °C followed by 24 h delay until contact; **(c)** brittle freeze-fracture at −196 °C followed by immediate contact between the crack surfaces. The pristine sample is indicated in each graph by —. All fracture modes are examined for three healing times: 1 day (—), 5 days (—) and 10 days (—). Stress–strain curves similar to (a) for D-1.1 without embedded nanoparticles can be found in ref. 21, Figure 6.

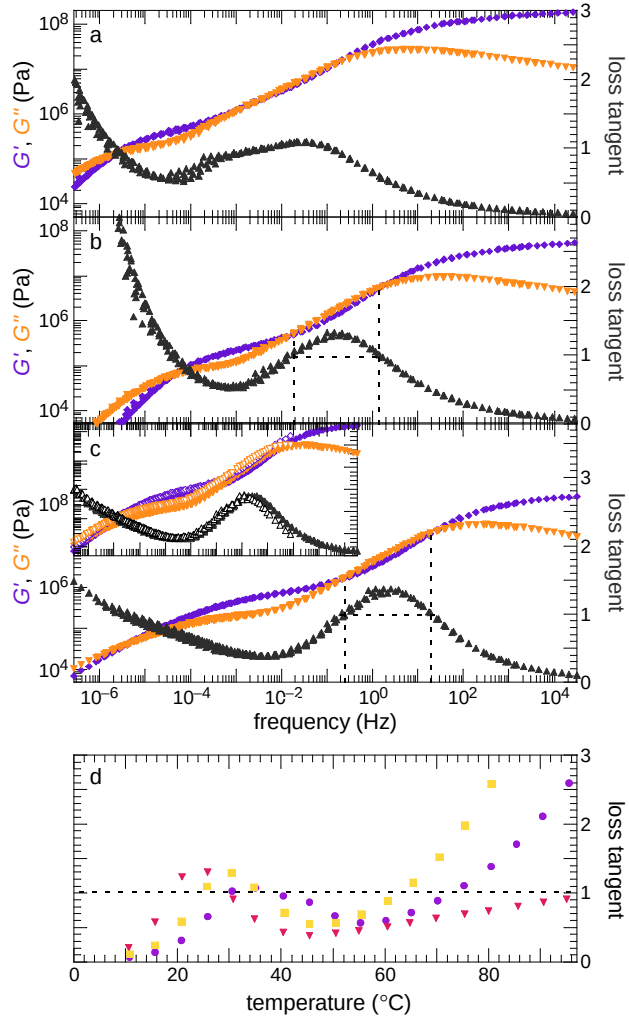

Figure 8.A.6. Bulk rheology of the linear viscoelastic properties of the three thermoplastic elastomers. **(a–c)** Time–temperature superposition master curves of the storage modulus G' (♦), loss modulus G'' (▼) and loss tangent $\tan(\delta) = G''/G'$ (▲), referenced to 25 °C, for **(a)** B-D-1.0, **(b)** D-0.9 and **(c)** D-1.1. The inset shows that the TTS curves of the unfilled D-1.1 polymer (open symbols) closely resemble those of the polymer with embedded nanoparticles (filled symbols). **(d)** Temperature dependence of $\tan(\delta)$ for B-D-1.0 (●), D-0.9 (■) and D-1.1 (▼). The dashed lines indicate the windows where viscous processes dominate and self-healing can proceed, determined by $\tan(\delta) > 1$. The non-healing polymer B-D-1.0 does not display such a window; D-0.9 exhibits the optimum loss tangent and healing capabilities at 30 °C, and D-1.1 at 24 °C. More extensive rheological characterization of D-0.9 and D-1.1 without embedded nanoparticles can be found in Figures 8.4 and 8.A.6 and in ref. 21.

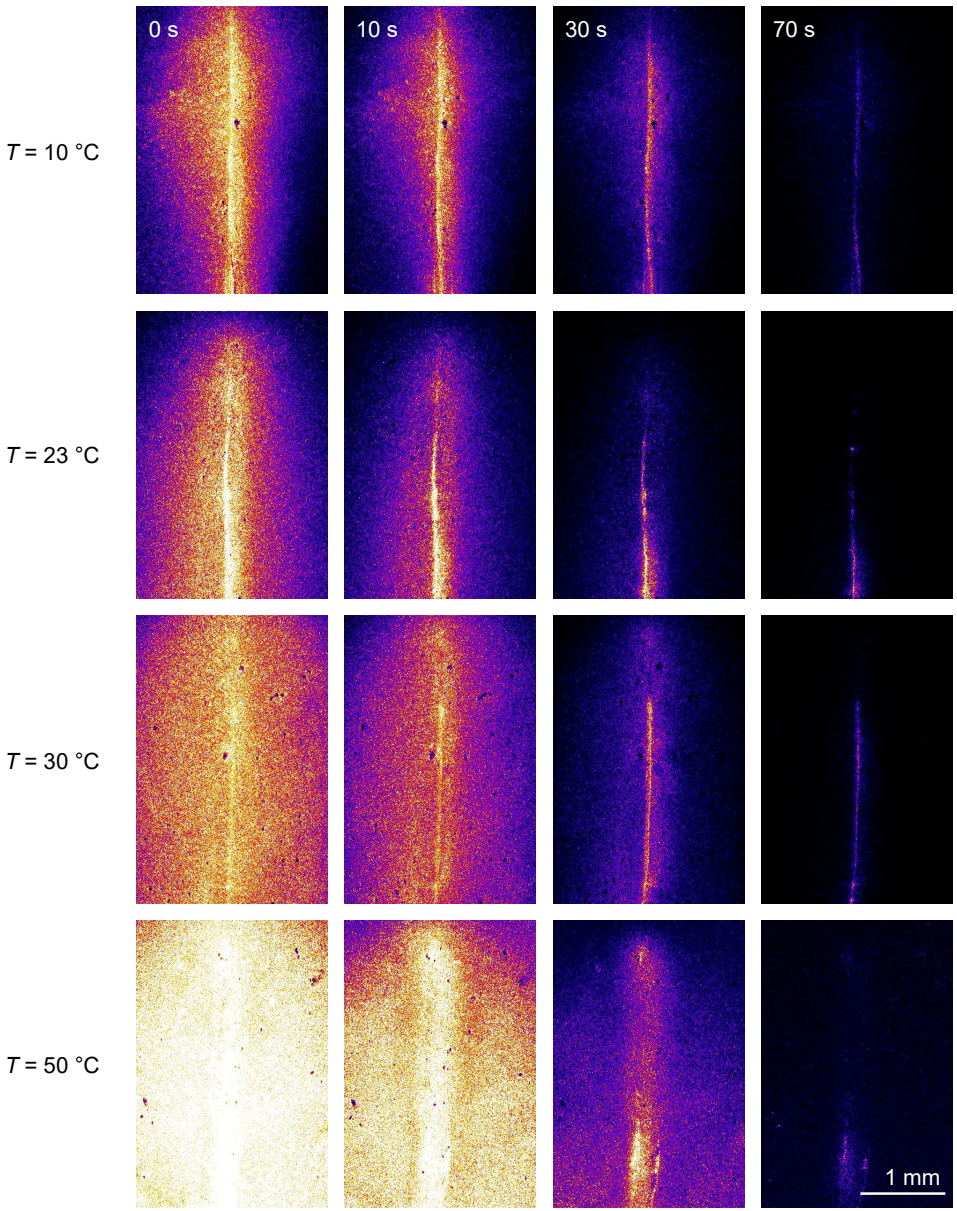

Figure 8.A.7. Time-lapse micromechanical maps for polymer D-1.1 at different temperatures. $d_2(f = 1\ \text{Hz})$ is used as the contrast function. All images have the same scale and colour coding, and all rows display the same time points. Only at 23 °C, the cut closes in a zipper-like manner and self-heals, implying that bond reformation is essentially dictated by kinetics: it is limited to a narrow temperature window, where rebonding across the cut is not too slow yet rebonding by backfolding of polymer chains is not too fast either.

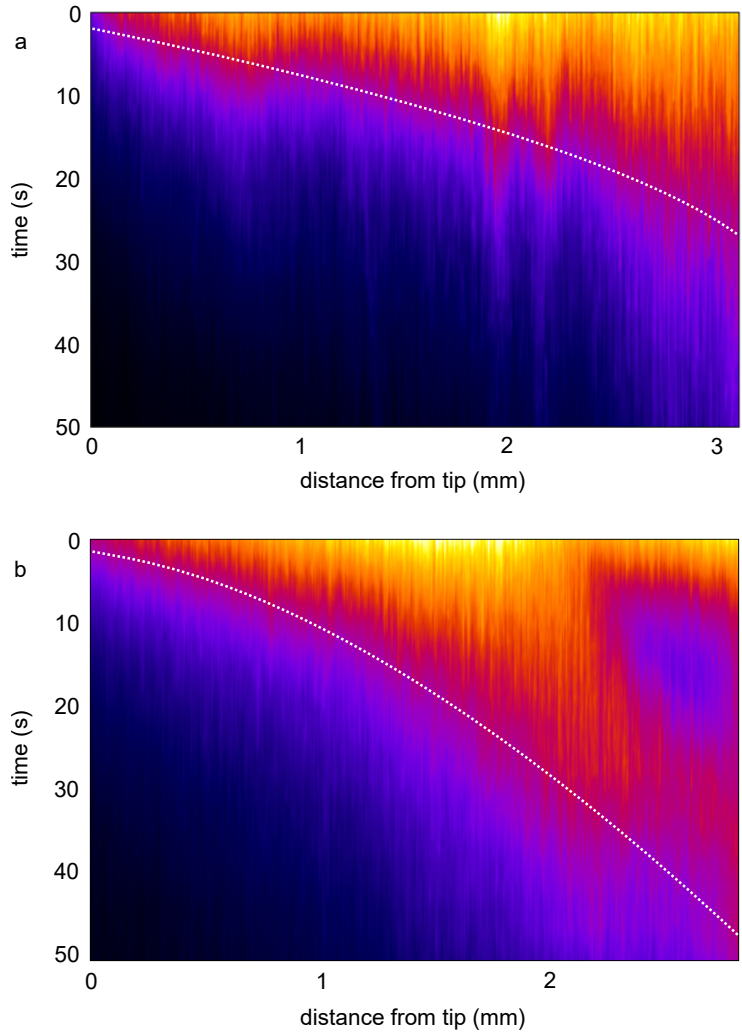

Figure 8.A.8. Kymographs of cut closure in D-1.1 at 23 °C. Horizontal cross-sections represent the molecular mobility along the cut, quantified by $\langle d_2(f = 1\text{ Hz})\rangle$ where averaging is over ∼50 pixels in the perpendicular direction. The kymograph in **(a)** corresponds to the time series in Figure 8.3a, and that in **(b)** to a second, independent measurement. Both feature a front of mobility which advances away from the tip, characteristic of a zipper-like closure. The dotted lines are guides to the eye.

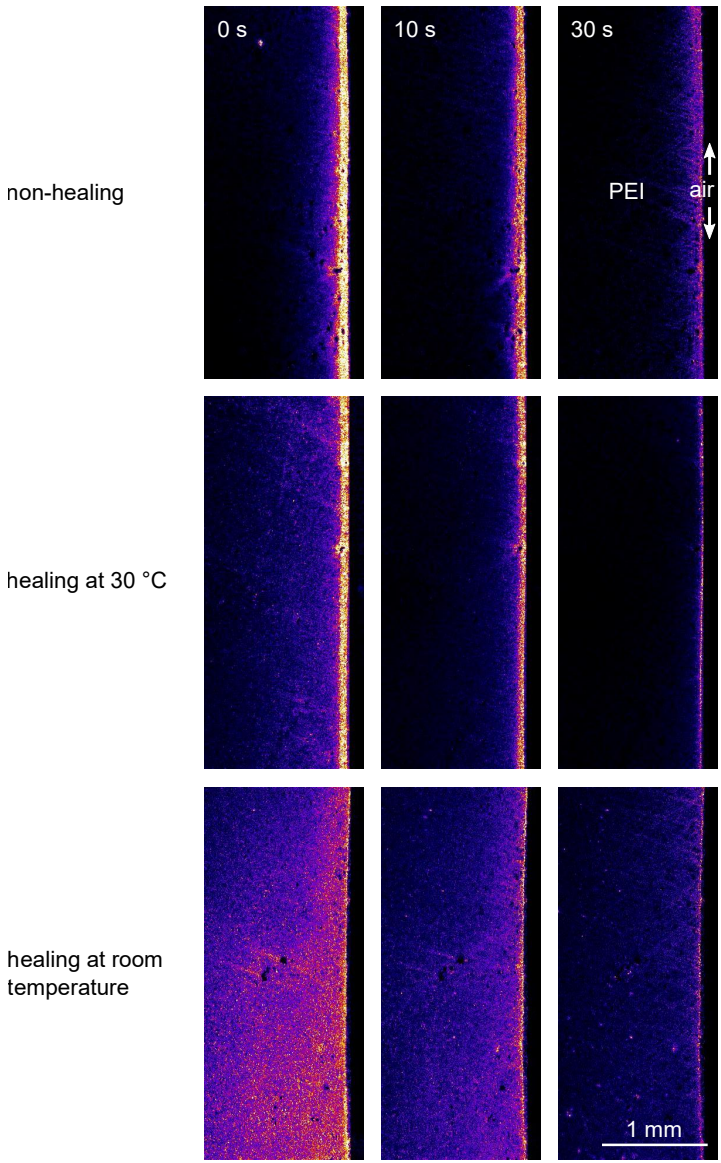

Figure 8.A.9. Time-lapse micromechanical maps of the viscoplastic relaxation at a cut–air interface, at 23 °C. $d_2(f = 1\ \text{Hz})$ is used as the contrast function. All images have the same scale bar and all rows display the same time points. Small amounts of noise in the air background are masked. Note that the dynamics are considerably longer-ranged for D-1.1, indicating stronger viscoplastic deformation during cutting due to a lower glass transition temperature ($T_g = 8$ °C for D-1.1 versus 19 °C for B-D-1.0 and 17 °C for D-0.9, see Table 8.1). We observe the same difference in spatial extent of the relaxation for reunited cut surfaces (compare Figures 8.A.4, 8.A.7 and 8.A.13).

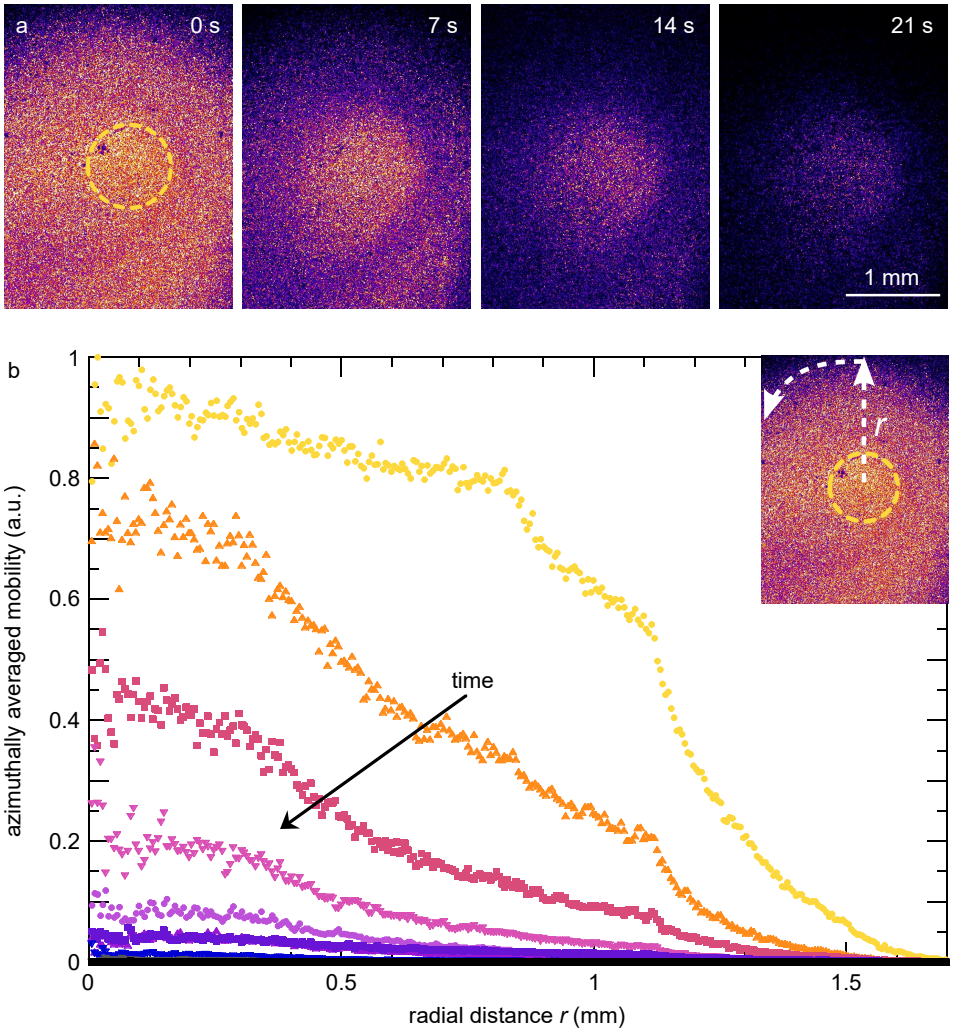

Figure 8.A.10. Viscoplastic relaxation dynamics in linear conditions. **(a)** Time-lapse micromechanical maps, at $f = 1$ Hz, of the viscoplastic recovery of D-1.1 after spherical indentation with small strain. The original location of the indenter is delineated with a dashed yellow line. See Supplementary Movie 9 in ref. 26 for the full time series. **(b)** Azimuthally averaged radial profiles from $t = 0$ s (●) to $t = 70$ s (■) after indentation, with 7 s intervals. The inset shows the definition of the radial distance r. This experiment confirms that the delocalized dynamics we observe in e.g. Figure 8.3a and b are purely viscoplastic relaxations as a result of local deformation of the material.

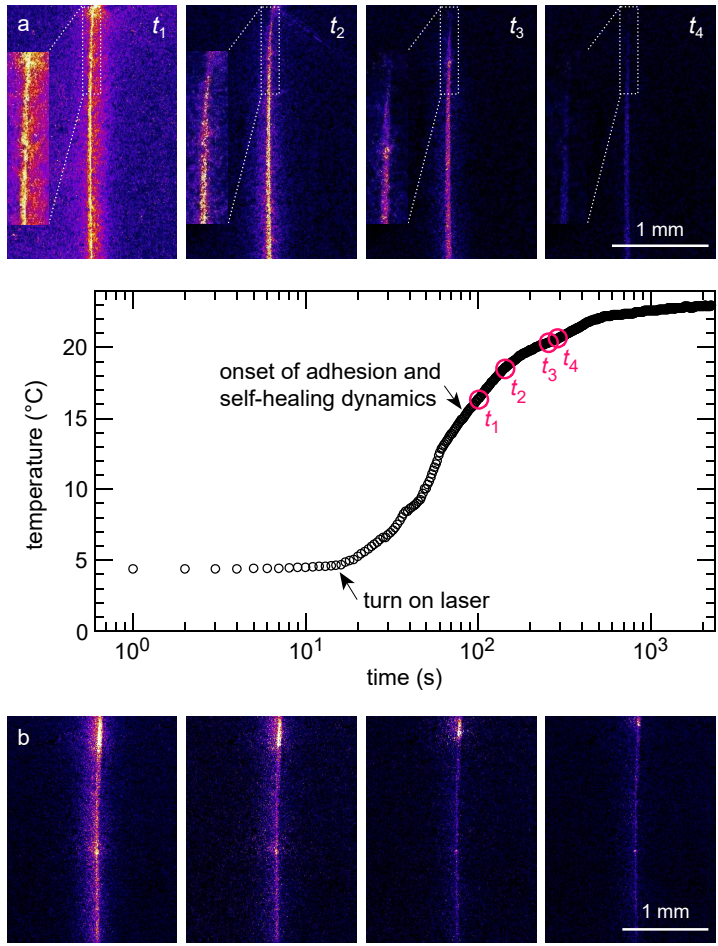

Figure 8.A.11. Temperature dependence and modes of freeze-fracture healing. **(a)** Evolution of the dynamics (top) and temperature (bottom) after freezing and semi-fracturing polymer D-1.1, elaborating on Figure 8.3c. The temperatures corresponding to times t_1 to t_4 are indicated in the graph, and are successively: 16.2, 18.6, 20.2 and 20.6 °C. Note that after switching on the laser, the sample heats up considerably faster due to light absorption. Because of the lower initial self-healing temperature compared to cuts made at 23 °C, the zipper propagates slower along the freeze-fracture and the instantaneous self-healing dynamics are weaker, yet they proceed longer (compare e.g. Figure 8.A.7). Furthermore, this brittle fracture is much straighter and smoother than the ductile cut made at room temperature, and exhibits more well-defined fracture planes. **(b)** A freeze-fracture that traverses the entire sample lacks a distinct tip and unidirectional zipper-like motion. Nevertheless, several locations of enhanced mobility are visible across the crack, which propagate and diminish over time.

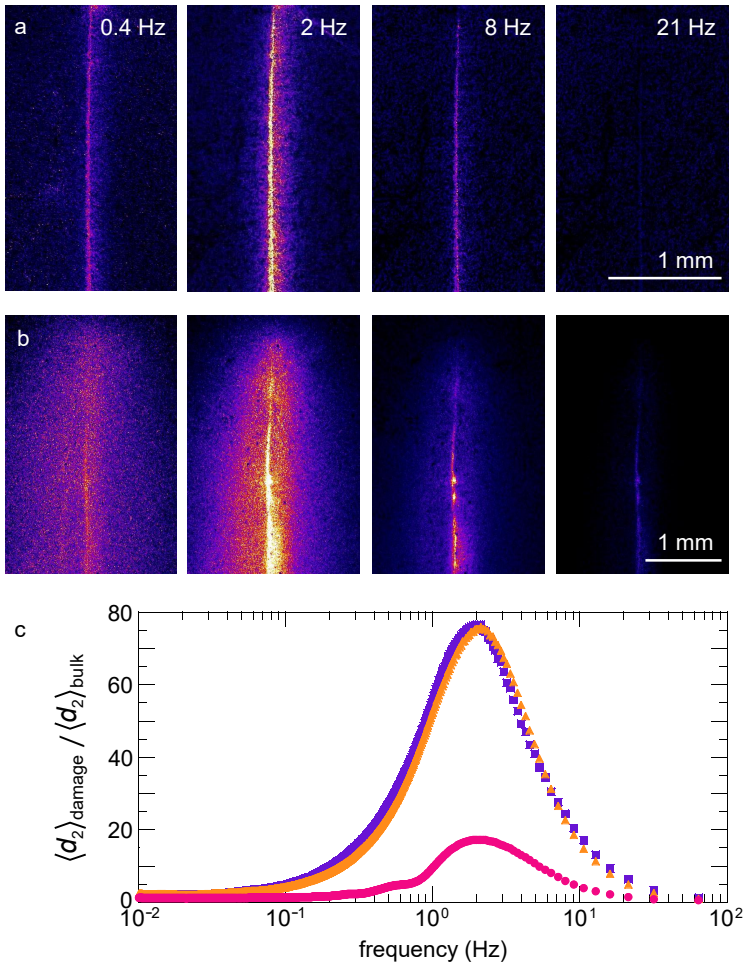

Figure 8.A.12. Reproducibility of frequency-resolved self-healing mobility. **(a)** Frequency dependence of the processes governing repair of a freeze-fracture, similar to Figure 8.3d, and of **(b)** a cut made at room temperature. The colour scales are normalized by the respective values of $\langle d_2 \rangle_{bulk}$ and all have the same limits. **(c)** Enhancement of self-healing dynamics at the damage interface with respect to the bulk of the material, $\langle d_2 \rangle_{damage} / \langle d_2 \rangle_{bulk}$, for the brittle fracture (●), the ductile cut (▲), and a second, independent measurement of a ductile cut made at room temperature (■). The peak for the freeze-fracture is considerably lower because the instantaneous self-healing dynamics are weaker in that case, being spread out over a longer time period (Figure 8.A.11a). Note that the widths of these self-healing peaks are narrower than the tan(δ) peaks in bulk rheological measurements (see Figures 8.3e and 8.A.6c); this is possibly due to kinetic broadening of the peaks in rheology due to finite frequency and temperature ramp rates.

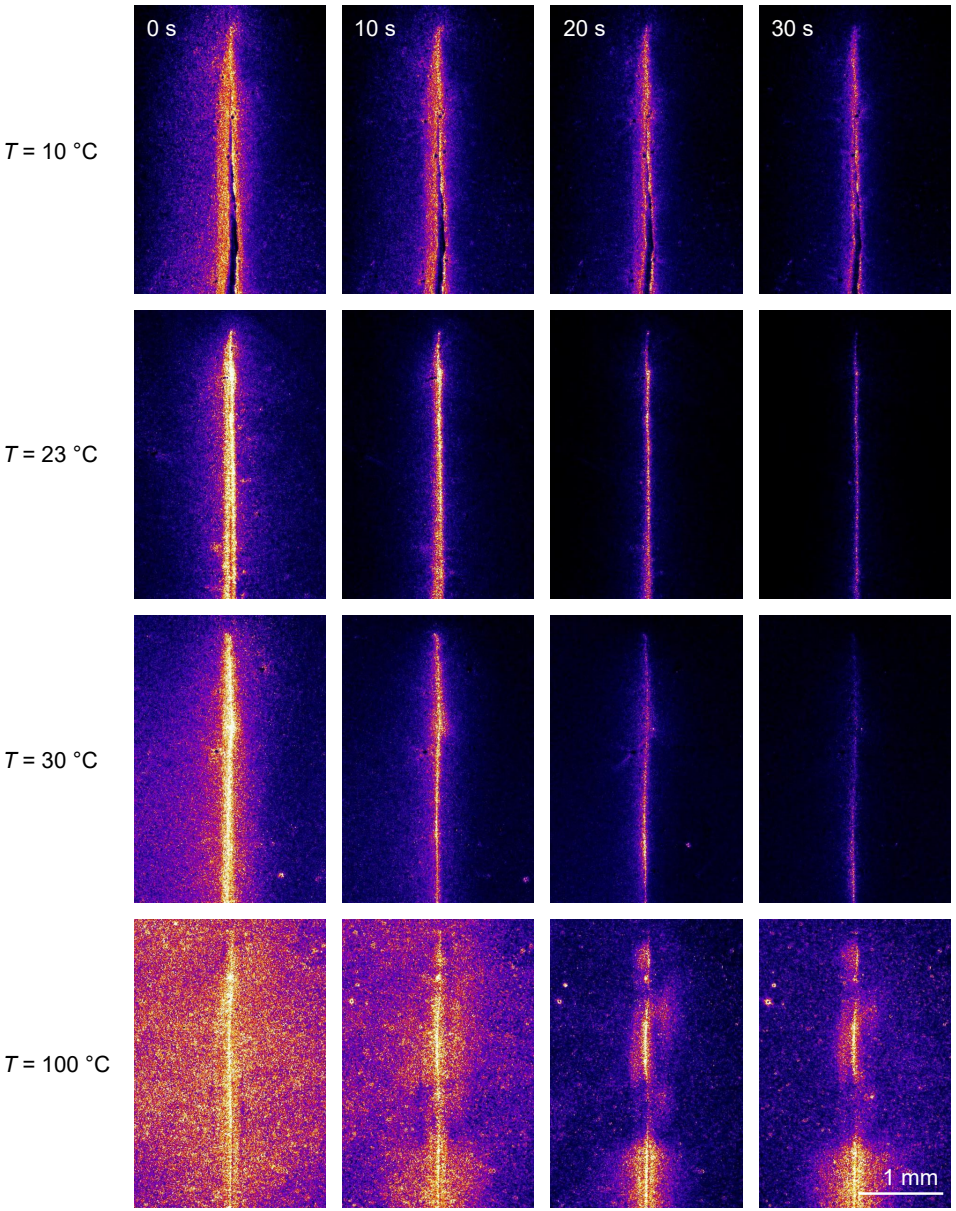

Figure 8.A.13. Time-lapse micromechanical maps for polymer D-0.9 at different temperatures. $d_2(f = 1\ \text{Hz})$ is used as the contrast function. Only at the optimal healing temperature of 30 °C the cut closes in a zipper-like manner. At 100 °C, a Rayleigh–Plateau instability develops. All images have the same scale and colour coding, and all rows display the same time points.

References

[1] B. Ghosh, M. W. Urban. *Science* **323**, 1458–1460 (2009).

[2] S. Gupta, Q. Zhang, T. Emrick, A. C. Balazs, T. P. Russell. *Nat. Mater.* **5**, 229–233 (2006).

[3] M. D. Hager, P. Greil, C. Leyens, S. van der Zwaag, U. S. Schubert. *Adv. Mater.* **22**, 5424–5430 (2010).

[4] B. J. Blaiszik, S. L. B. Kramer, S. C. Olugebefola, J. S. Moore, N. R. Sottos, S. R. White. *Annu. Rev. Mater. Res.* **40**, 179–211 (2010).

[5] A. B. W. Brochu, S. L. Craig, W. M. Reichert. *J. Biomed. Mater. Res., Part A* **96**, 492–506 (2011).

[6] Y. Yang, M. W. Urban. *Chem. Soc. Rev.* **42**, 7446-7467 (2013).

[7] S. R. White, N. R. Sottos, P. H. Geubelle, J. S. Moore, M. R. Kessler, S. R. Sriram, E. N. Brown, S. Viswanathan. *Nature* **409**, 794–797 (2001).

[8] Y. Zhao, J. Fickert, K. Landfester, D. Crespy. *Small* **8**, 2954–2958 (2012).

[9] P. Cordier, F. Tournilhac, C. Soulié-Ziakovic, L. Leibler. *Nature* **451**, 977–980 (2008).

[10] Y. Chen, A. M. Kushner, G. A. Williams, Z. Guan. *Nat. Chem.* **4**, 467–472 (2012).

[11] C. Wang, H. Wu, Z. Chen, M. T. McDowell, Y. Cui, Z. Bao. *Nat. Chem.* **5**, 1042–1048 (2013).

[12] S. Bode, L. Zedler, F. H. Schacher, B. Dietzek, M. Schmitt, J. Popp, M. D. Hager, U. S. Schubert. *Adv. Mater.* **25**, 1634–1638 (2013).

[13] S. Kupfer, L. Zedler, J. Guthmuller, S. Bode, M. D. Hager, U. S. Schubert, J. Popp, S. Grafe, B. Dietzek. *Phys. Chem. Chem. Phys.* **16**, 12422–12432 (2014).

[14] T. Yan, K. Schröter, F. Herbst, W. H. Binder, T. Thurn-Albrecht. *Sci. Rep.* **6**, 32356 (2016).

[15] D. A. Davis, A. Hamilton, J. Yang, L. D. Cremar, D. Van Gough, S. L. Potisek, M. T. Ong, P. V. Braun, T. J. Martínez, S. R. White, J. S. Moore, N. R. Sottos. *Nature* **459**, 68–72 (2009).

[16] F. Ciardelli, G. Ruggeri, A. Pucci. *Chem. Soc. Rev.* **42**, 857–870 (2013).

[17] E. Ducrot, Y. Chen, M. Bulters, R. P. Sijbesma, C. Creton. *Science* **344**, 186–189 (2014).

[18] A. K. Dunn, H. Bolay, M. A. Moskowitz, D. A. Boas. *J. Cerebr. Blood F. Met.* **21**, 195–201 (2001).

[19] H. M. van der Kooij, R. Fokkink, J. van der Gucht, J. Sprakel. *Sci. Rep.* **6**, 34383 (2016). **(Chapter 5)**

[20] M.-Y. Nagazi, G. Brambilla, G. Meunier, P. Marguerès, J.-N. Périé, L. Cipelletti. *Opt. Laser Eng.* **88**, 5–12 (2017).

[21] A. Susa, R. K. Bose, A. M. Grande, S. van der Zwaag, S. J. Garcia. *ACS Appl. Mater. Interfaces* **8**, 34068–34079 (2016).

[22] T. G. Mason, K. Ganesan, J. H. van Zanten, D. Wirtz, S. C. Kuo. *Phys. Rev. Lett.* **79**, 3282–3285 (1997).

[23] Z. Hajjarian, H. T. Nia, S. Ahn, A. J. Grodzinsky, R. K. Jain, S. K. Nadkarni. *Sci. Rep.* **6**, 37949 (2016).

[24] D. J. Pine, D. A. Weitz, J. X. Zhu, E. Herbolzheimer. *J. Phys. France* **51**, 2101–2127 (1990).

[25] K. Schätzel. *Appl. Phys. B: Lasers Opt.* **42**, 193–213 (1987).

[26] H. M. van der Kooij, A. Susa, S. J. García, S. van der Zwaag, J. Sprakel. *Adv. Mater.* **29**, 1701017 (2017). **(This chapter)**

[27] P. Zakharov, F. Scheffold, *Light scattering reviews 4: single light scattering and radiative transfer* (Springer, Berlin, Heidelberg, 2009), chap. Advances in dynamic light scattering techniques, pp. 433–467.

[28] D. A. Sessoms, H. Bissig, A. Duri, L. Cipelletti, V. Trappe. *Soft Matter* **6**, 3030–3037 (2010).

[29] A. Amon, V. B. Nguyen, A. Bruand, J. Crassous, E. Clément. *Phys. Rev. Lett.* **108**, 135502 (2012).

[30] J. R. Rice, G. F. Rosengren. *J. Mech. Phys. Solids* **16**, 1–12 (1968).

[31] P.-G. de Gennes, F. Brochard-Wyart, D. Quéré, *Capillarity and wetting phenomena: drops, bubbles, pearls, waves* (Springer, New York, 2004), chap. 5, pp. 107–138.

Chapter 9

Morphing of liquid crystal surfaces by emergent collectivity

This chapter is based on: Hanne M. van der Kooij, Slav A. Semerdzhiev, Jesse Buijs, Dirk J. Broer, Danqing Liu and Joris Sprakel, 'Morphing of liquid crystal surfaces by emergent collectivity', *Nat. Commun.* **10**, 3501 (2019).

Abstract

Liquid crystal surfaces can undergo topographical morphing in response to external cues. These shape-shifting coatings promise a revolution in various applications, ranging from haptic feedback in soft robotics or displays to self-cleaning solar panels. The changes in surface topography can be precisely controlled by tailoring the molecular architecture and mechanics of the liquid crystal network. However, the nanoscopic mechanisms that drive morphological transitions remain unclear. Here, we introduce a frequency-resolved nanostrain imaging method to elucidate the emergent dynamics underlying field-induced shape-shifting. We show how surface morphing occurs in three distinct stages: (I) the molecular dipoles oscillate with the alternating field (10 – 100 ms), (II) this leads to collective plasticization of the glassy network (~1 s), and (III) culminates in actuation of the topography (10 – 100 s). The first stage is universal in all explored LC geometries and governed by dielectric coupling. By contrast, network yielding and deformation rely on a delicate balance between liquid crystal order, field properties and network viscoelasticity.

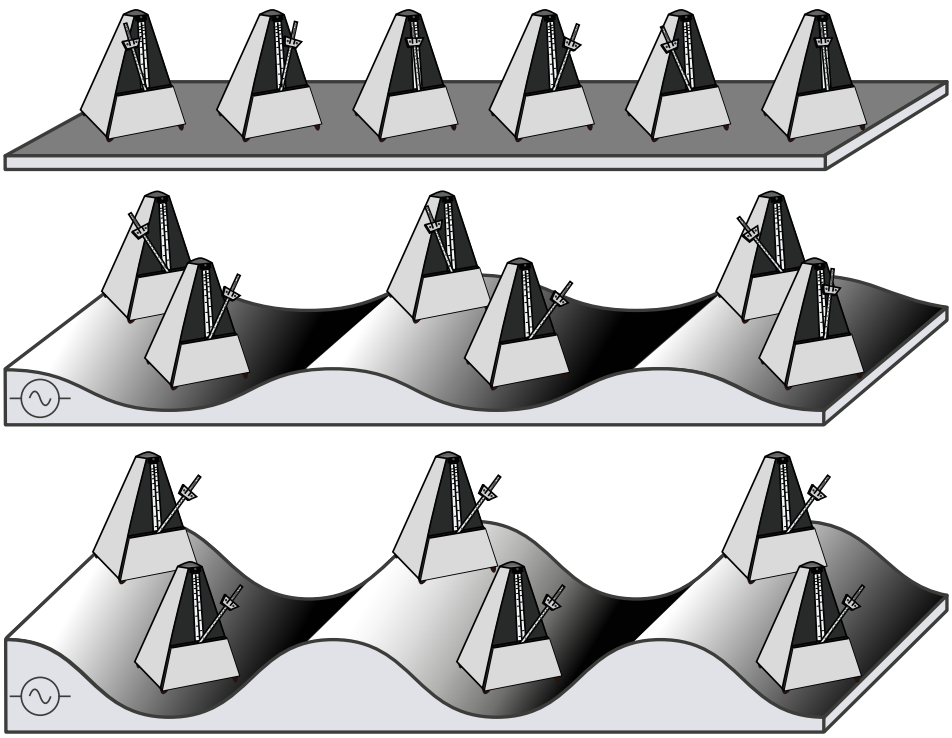

Surface morphing by collective synchronization of mesogens (symbolized by metronomes).

9.1 Introduction

In the pursuit of surfaces with programmable motility, coatings based on liquid crystal networks (LCNs) have emerged as a promising platform.[1] These coatings undergo topographical changes in response to external triggers, resulting in adaptable surface roughness, mechanics, wetting or adhesion in a pre-designed three-dimensional pattern.[2–11] Such shape-shifting LCNs have shown great potential as dynamic substrates for cell culture,[10,12] on-demand self-cleaning microstructures,[6,11,13] or bioinspired adhesives mimicking gecko locomotion.[4,14] To date, most attention has focused on light-actuated LC polymers, e.g. those functionalized with photoresponsive azobenzenes.[2,10,11,15–21] However, their thermal instability, low photomechanical conversion efficiency and photo-oxidative degradation have prompted the exploration of electrically active mesogens instead, which are widely employed in display panels with proven durability. The resulting polymers are capable of converting electrical energy into mechanical energy, typically in a spatially homogeneous manner or alternatively very localized.[12,22–26] To generate electrically switchable surface topographies, and thereby patterned surface properties, the electromechanical response must however be heterogeneous. Despite the large application potential of these coatings, only a handful have been developed in recent years.[3,5,6] Further advance of this unique class of materials would strongly benefit from a deeper understanding of the mechanisms governing topographical morphing. For example, it remains unclear how the application of an electric field sets in motion nanoscopic events that drive the ultimate microscopic shape-shifting.

Bridging the gap between the molecular level and large-scale collective motion requires a method with access to a wide range in time and length scales. While digital holography microscopy (DHM) has proven successful at visualizing surface morphing in real time with high spatial resolution,[5–9] it remains superficial with limited time resolution. By contrast, conventional (polarized) optical microscopy can be very fast, yet the structural changes of deforming LC surfaces are often too subtle to resolve in detail. We therefore propose a method based on laser speckle imaging (LSI). As described in previous chapters, LSI offers a nanometric motion-detection resolution and allows us to spectrally decompose the complex dynamic response in a single shot – up to frequencies exceeding 10 kHz. This technique was originally devised as a medical imaging platform to visualize blood flow,[27–30] and has emerged in recent years as a quantitative imaging tool to non-invasively probe the dynamics in a wide variety of complex materials.[31–39] Surprisingly, liquid-crystal based materials are still unexplored territory.

In this chapter, we establish a highly resolved view of the mechanisms underlying motility in electrically actuated liquid crystal networks. We use frequency-

resolved laser speckle imaging to elucidate the complex chain of events that ultimately culminates in shape-shifting: from molecular-scale interactions between the mesogens and external field, to the emergence of patterned network expansion at the microscale. This amplification of motion in space and time is driven by collective synchronization of the mesogens, which grows towards a critical weakening of the solid network in which they are embedded. We uncover how the spatiotemporal pattern of topographical morphing can be tailored by optimizing the liquid crystal alignment and electric field properties. These insights into the inner workings of shape-shifting coatings provide clear design guidelines for the next generation of morphing surfaces.

9.2 Experimental details

9.2.1 Materials

The monomers used in this study are depicted in Figure 9.1. Liquid crystal diacrylates **1** (1,4-bis-[4-{6-acryloyloxy-hexyloxy}benzoyloxy]benzene, CAS no. 125248-71-7) and **2** (1,4-bis-[4-{6-acryloyloxy-propyloxy}benzoyloxy]benzene, CAS

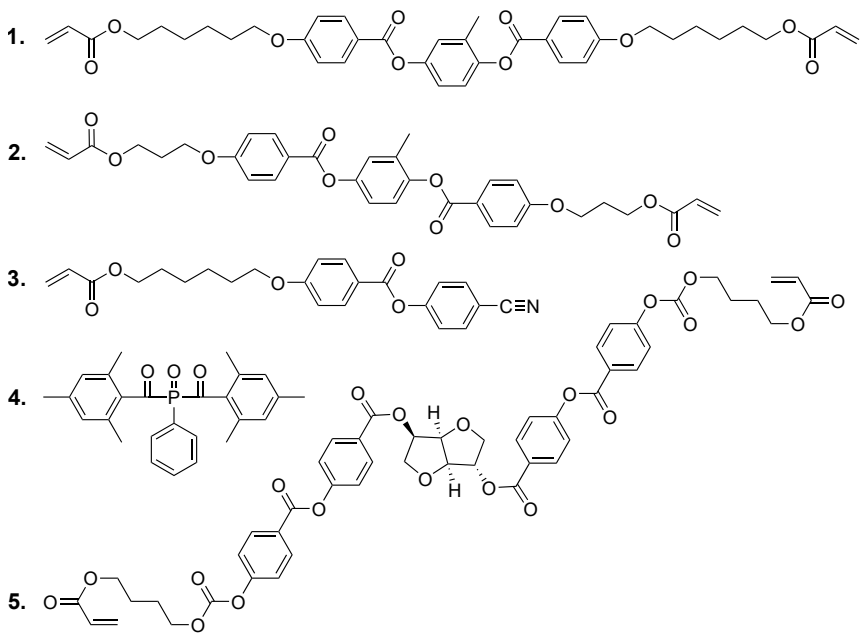

Figure 9.1. Chemical structures of the monomers used in the LCN syntheses.

no. 174063-87-7) form the polymer network. The cyano-capped LC monoacrylate **3** (4-[4-{6-[acryloyloxy]hexyloxy}benzoyloxy] 4-[cyano]benzoate, CAS no. 83847-14-7) couples effectively to the electric field by its large permanent dipole moment. Monomers **1** to **3** are obtained from Merck (UK). Photoinitiator **4** (phenylbis[2,4,6-trimethylbenzoyl]-phosphine oxide, CAS no. 162881-26-7) is purchased from BASF (Germany). Chiral dopant **5** (1,4:3,6-dianhydro-D-glucitol bis[4-[[4-[[[4-[{1-oxo-2-propenyl}oxy]butoxy]carbonyl]oxy]benzoyl]oxy]benzoate], CAS no. 223572-88-1) is obtained from Ciba (Switzerland) and added in small amount to induce a cholesteric (chiral nematic) phase with helical pitch of ~450 nm, only used for Figure 9.6c,d. All samples are prepared from a mixture of 24.75 wt% monomer **1**, 24.75 wt% monomer **2**, 49.5 wt% monomer **3** and 1.0 wt% photoinitiator **4**, dissolved in dichloromethane (CAS no. 75-09-2, purchased from Sigma-Aldrich, USA). Polyimide 7511L SUNEVER is obtained from Nissan Chemical Corporation (Japan), and polyimide AL-1051 from JSR Corporation (Japan). TiO_2 nanoparticles (~40 nm diameter, coefficient of variation ~40%, purity 99.5%) are purchased from US Research Nanomaterials (USA). All components of the LSI set-up are purchased from Thorlabs (Germany), unless otherwise specified.

9.2.2 Sample preparation

To establish the desired LC alignment, the glass substrates with patterned ITO are first cleaned and spin-coated with polyimide, followed by baking to yield a polyimide film thickness of ~30 nm. Polyimide 7511L is applied to obtain homeotropic alignment of the LC monomer mixture, and polyimide AL-1051 to achieve planar (i.e. parallel) anchoring to the substrate. The latter is additionally rubbed with a polyester cloth after baking to orient the nematic director along the y-direction i.e. perpendicular to the field lines. Subsequently, a thin film of the monomer mixture is formed by spin-coating from solution, and photopolymerized by UV light that excites photoinitiator **4**. The UV exposure is continued for 5 min under N_2 using a mercury lamp (OmniCure S2000, Lumen Dynamics Group Inc., Canada) at 26 °C to lock a (chiral) nematic orientation or at 70 °C to obtain an isotropic LCN. The samples are post-baked at 120 °C under N_2 to ensure complete cure of the acrylate monomers. The resulting LCNs are transparent and have order parameters between 0.6 and 0.7, with the exception of the disordered isotropic network. The nematic and isotropic networks show no domain formation between crossed polarizers. To render the coatings multiply scattering for LSI experiments, a thin layer of high-refractive-index TiO_2 (titania) nanoparticles is deposited onto the surface by spin-coating a 1 wt% aqueous TiO_2 suspension at 2000 rpm for 30 s. The suspension is sonicated for 10 min prior to spin-coating to ensure that

any aggregated particles are well-dispersed. The spin-coating conditions are fine-tuned to render the coating intermediately scattering, i.e. a well-developed speckle pattern is obtained through crossed polarizers implying that the scattered photons are sufficiently randomized, yet the TiO_2 coating is thin enough to not interfere with the surface morphing.

9.2.3 Characterization

An in-plane, sinusoidal electric field is generated by a function generator (TGA1241, TTi Inc., USA) connected to an amplifier (F20A, FLC Electronics, Sweden). Unless otherwise specified, the LCN coating is actuated at 25 °C at a peak-to-peak voltage of 70 V (i.e. a field strength of 14 V/μm) and a field frequency of 900 kHz. The output AC signal is monitored with an oscilloscope (TBS1022, Tektronix, USA). The surface profiles in Figure 9.2c are measured using digital holography microscopy (Lyncée Tec SA, Switzerland), as described extensively in ref. 5. The current-induced temperature change of the sample surface is measured using an infrared sensor (PCE-IR 51, PCE Instruments, Germany).

9.2.4 Laser speckle imaging

See Chapter 5 for a detailed description of the LSI method and our custom-built set-up, which we here operate in the intermediate scattering regime rather than in the strong multiple scattering limit. In brief: the active area of the LC surface is illuminated with an expanded coherent laser beam (Cobolt Samba, 1 W, λ = 532 nm, Cobolt, Sweden), whose photons are weakly multiply scattered by the TiO_2 nanoparticles on the surface. As a result of these scattering events, the photon paths approximate a diffusive rather than a ballistic trajectory. Each photon traverses a different, unique path, leading to path length differences among the photons that cause spatially random constructive and destructive interference in the scattered light pattern. This so-called speckle pattern is recorded on a camera which is here in the back-scatter geometry. Only the multiply scattered light is detected, with specular and low-order scattering paths filtered by a linear polarizer perpendicular to the polarization of the incident laser beam. Two cameras are alternately used: a Dalsa Genie CCD camera (CR-GM00-H6400, Stemmer Imaging, Netherlands) for continuous streaming at acquisition rates up to 200 fps, and a HiSpec 1 CMOS camera (Fastec Imaging, USA) for imaging at acquisition rates up to 40,000 fps.

As the surface-attached nanoparticles move, in response to internal sample dynamics, all photon path lengths change, causing the speckle pattern to change accordingly. The rate of these intensity fluctuations is quantified on a pixel-by-pixel

basis using the intensity structure function d_2:

$$d_2(x, y, \Delta t, 1/f) = \frac{\langle [I(x, y, \Delta t) - I(x, y, \Delta t + 1/f)]^2 \rangle}{\langle I(x, y, \Delta t) \rangle \cdot \langle I(x, y, \Delta t + 1/f) \rangle} \tag{9.1}$$

where I is the speckle intensity at position x, y and time after switching on or off the field Δt, and $f = 1/\tau$ with τ the time separating the two compared speckle patterns. The angular brackets denote averaging in time and/or space. If the surface is static over the lag time τ, the speckle pattern will be unaltered and hence d_2 is zero. The more dynamics have occurred during τ, the faster the speckle intensity fluctuates and the larger the numerator will be. The analysis frequency f thus serves as a means to distinguish processes occurring on different time scales. By using symmetric normalization in the denominator, the magnitude of d_2 becomes independent of the absolute speckle intensity and hence is universal regardless of the optical properties and geometry. Note that the intermediate scattering regime limits quantitative analysis beyond d_2, since rigorous theory is absent for this regime. Nevertheless, d_2 itself can be interpreted in a quantitative and reproducible manner. The intermediate scattering geometry moreover combines the best of both multiple and single scattering, unifying high sensitivity with applicability to thin films.

Fourier-transform LSI is a new, complementary approach that allows resolving the entire frequency spectrum exceptionally fast. It is based on the short-time fast Fourier transform (ST-FFT) of the temporal intensity signal.[40] Using a custom-written MATLAB routine, the power spectrum is computed for every pixel as a function of time and subsequently averaged over space. Although the absolute frequencies in the power spectrum and d_2 function cannot be compared one-to-one, the dependencies of power and d_2 on f are related, according to the Wiener–Khinchin theorem.[41] We therefore use the two interchangeably, with d_2 a well-established LSI parameter yet the power spectrum orders of magnitude faster in computing time. More detailed information about the Fourier analysis is provided in Appendix 9.A.1.

9.3 Results and discussion

9.3.1 Surface design and shape-shifting

We investigate the topographical morphing of well-established liquid crystal coatings which are homogeneous in chemical composition but heterogeneous in mechanical response.[5] We synthesize the LCNs by in-situ photopolymerization of a mixture of homeotropically aligned nematic liquid crystals. Half of the monomers

serve as crosslinkers, while the other half are pendant on the network chains and carry a cyano group whose large dipole moment couples strongly to the field (see Figure 9.2b and Section 9.2.1). The resulting network is 2.5–3 μm thick and optically transparent, with an elastic modulus of ~2 GPa and a glass transition range between 60–120 °C (Appendix Figure 9.A.2).[5] The LC coatings are applied on interdigitated indium tin oxide (ITO) electrodes, patterned onto a glass support (Figure 9.2a).

While these networks are rigid and glassy at room temperature, application of an alternating current (AC) rapidly transforms the material into one that is dynamic and motile.[5] When the field is perpendicular to the LC director, the polar mesogens experience a dielectric torque and attempt to align with the field – limited only by the elastic constraints imposed by the glassy network. This partial reorientation of the mesogens gives rise to induced linear birefringence of

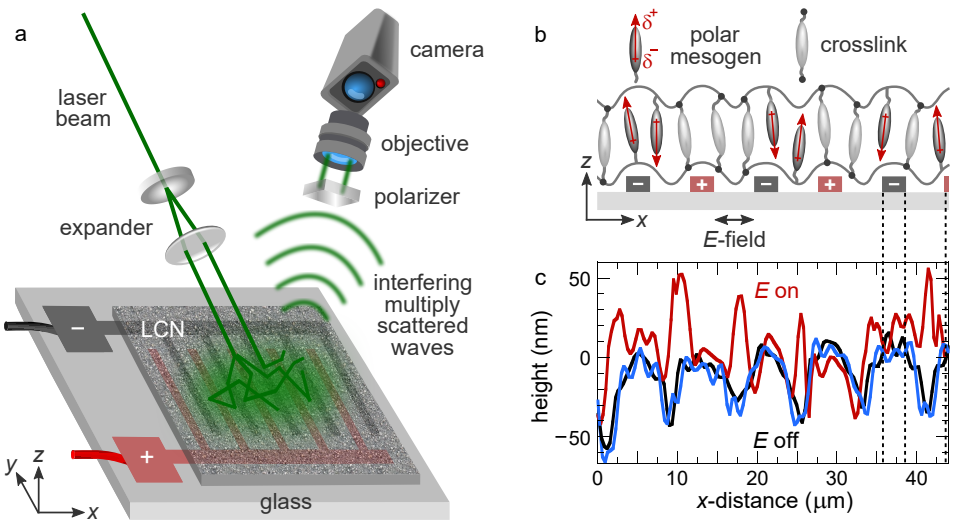

Figure 9.2. Nanoscale imaging of surface strains. **(a)** Schematic illustration of a laser speckle imaging (LSI) experiment. Photons from coherent plane-wave illumination, impinging on a LC device, are back-scattered by TiO_2 pigments on the surface, and detected by a high-speed camera. Motion of the surface results in fluctuations in the detected speckle pattern, which we analyse to uncover the nanoscopic surface dynamics. **(b)** Schematic of the LC device prior to expansion (not to scale). Half of the mesogenic units (in dark grey) possess a permanent dipole moment which can be torqued by the field, whereas the other half (in light grey) serve as crosslinkers. **(c)** Surface profiles measured by digital holography microscopy (DHM): initial field-off state (—), field-on steady state (—), and relaxed field-off state (—). Switching turns the minima into maxima in a fully reversible way.

~0.03. As the field vector continuously changes sign, it exerts an oscillatory torque on the dangling dipoles, causing them to pivot and induce dynamic disorder that generates free volume.[5,6] In response, the network expands, resulting in substantial height modulations. Moreover, the expansion pattern can be precisely tuned by the electrode arrangement.[5] We here use interdigitated electrodes, 3 μm wide with 5 μm gaps (Figure 9.2b). Surface profiling with digital holographic microscopy shows that prior to actuation, the coating is slightly corrugated with protrusions of ~50 nm that follow the contours of the electrodes (Figure 9.2c, —). 30 s after switching on the field, the surface topography is inverted (Figure 9.2c, —). The deformation persists as long as the AC field fuels it, and relaxes back to its original state within 30 s after the field is turned off (Figure 9.2c, —). Note that dielectric heating alone cannot cause this shape-shifting, as electrothermal expansion contributes to only ~8 nm of the total deformation, thus confirming free-volume effects as the main source[5] (Appendix Figure 9.A.3).

9.3.2 Nanoscopic imaging of surface motion

Although DHM reveals the amplitude and direction of surface deformation, its sensitivity and resolution are not sufficient to elucidate the nanoscopic mechanisms that underlie this shape-shifting behavior. We therefore apply a laser speckle imaging method to unravel the molecular origin of actuation in more detail. As elaborated in Chapters 1 and 5–8, LSI probes nanoscale motion using multiple scattering of coherent light. Since the network itself transmits nearly 100% of the visible light spectrum in both the off- and on-state,[6] we induce scattering from the surface by spin-coating a thin layer of high-refractive-index TiO_2 pigments, and illuminate the centre of the active area with a powerful laser (Figure 9.2a). We note that, due to the sample geometry, we operate in the limit of weak multiple scattering. As the photons impinge onto the sample surface, they are scattered several times, after which they travel to a camera detector. A linear polarizer filters out specular reflections and photons that have not undergone a sufficient number of scattering events. Path length differences between the photons result in an interference, or speckle, pattern on the detector. In the same experiment, we can probe both the surface expansion, derived from the absolute scattered intensity, and the surface motion, by analysing the temporal fluctuations in speckle intensity. As the method is based on an interferometric principle, we obtain a nanometric resolution of surface deformations.

To benchmark our approach, we first measure the spatially-resolved dynamics of the LC surface described above. As the surface topography morphs, the pigment coating will follow suit; this results in an alteration of the ensemble of scattering

paths and thus creates intensity fluctuations in the speckle pattern. The amplitude and rate of these fluctuations can be used to evaluate the extent and dynamics of the surface motility. We quantify these nanoscopic motions using the contrast function d_2 (Section 9.2.4). $d_2(x, y, \Delta t, f)$ is a four-dimensional function of the spatial coordinates x and y, time after switching on (or off) the field $\Delta t = t - t_{on}$, and a characteristic frequency $f = 1/\tau$ where τ is the lag time between correlated speckle patterns. We first fix f at 1 Hz and average over 100 s after switching. Indeed, this reveals a dynamic surface texture identical to the periodicity measured by DHM (compare Figure 9.3a, — to Figure 9.2c). Between electrodes, the field lines couple strongly to the dangling dipoles and induce a large expansion, whereas on top of electrodes, the dielectric coupling is negligible and the network remains unaltered (Figure 9.3a, —). To verify whether the measured periodicity is close to the expected 8 µm of the IDE design, we take the Fourier transform (FT) of the spatial motility signal. For the x-direction, this indeed shows a sharp peak at ~0.123 µm^{-1}, denoting a periodicity of 1/0.123 = 8.1 µm (Figure 9.3b, —). By

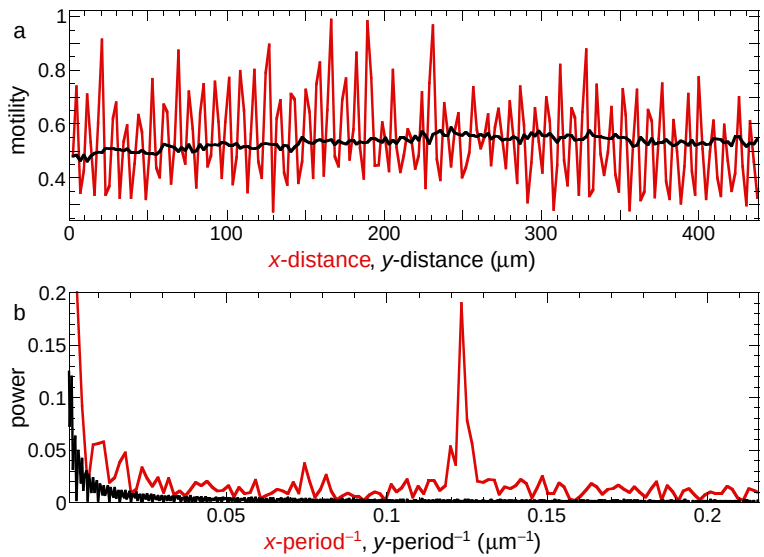

Figure 9.3. Spatial periodicity of surface motility. **(a)** Amplitude of the switching dynamics, probed with LSI, perpendicular (—) and parallel (—) to the electrodes. The motility is measured by $\langle d_2(f{=}1\text{ Hz})\rangle$ which is averaged over the orthogonal direction. The periodicity in d_2 matches the striated IDE pattern, as confirmed by corresponding power spectra **(b)**: for the x-direction, a sharp peak is visible at 1/8.1 µm^{-1}, representing the distance between electrodes. By contrast, the motility along electrodes lacks clear periodicity.

contrast, parallel to the electrodes d_2 is constant, reflected by the absence of peaks in the corresponding power spectrum (Figure 9.3b, —). These data confirm that the dynamic heterogeneity originates entirely from the field pattern imprinted by the electrode arrangement.

9.3.3 Elasticity-induced oscillations

In addition to probing surface motility, LSI yields complementary insight into the surface area of the coating. To first order, the scattering intensity is proportional to the surface concentration of TiO_2 particles, $I \propto c_s = n/A$, which we express as the reduced change in surface area $\tilde{A}(\Delta t) \equiv A(\Delta t)/A_0 = I_0/I(\Delta t)$. Thus, changes in intensity inversely reflect the amplitude of surface expansion. We here assume that the pigment particles adhere strongly to the network – an assumption corroborated by the fact that the original speckle pattern is largely retrieved after switching off the field, implying that surface morphing does not lead to significant rearrangement or displacement of the particles (Appendix Figure 9.A.4). We measure the change in surface area $\tilde{A}$ for different field frequencies f_{field} and, in full agreement with digital holography,[5] we find that the deformation grows with the field frequency (Figure 9.4a) and is completely reversible (Figure 9.4b). Moreover, the unique sensitivity of LSI brings to light a non-monotonic change in surface area, manifest

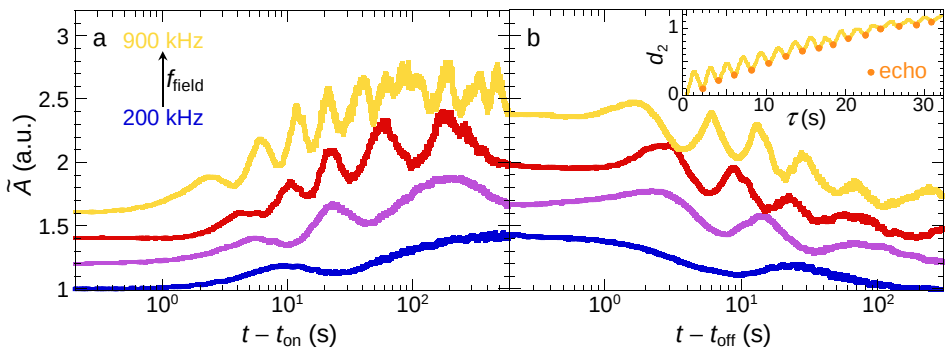

Figure 9.4. Kinetics of surface deformations. Change in surface area upon switching the field on **(a)** and off **(b)**, measured by the normalized change in scattering intensity, for field frequencies of 200, 300, 500 and 900 kHz. After an initial transient, the surface gradually expands **(a)** resp. contracts **(b)**, exhibiting elastic ringing. Both the undulation frequency and final deformation amplitude increase with increasing field frequency. For clarity, the curves are offset vertically by multiples of 0.2. **Inset:** intensity structure function d_2 versus lag time τ. In line with elastic recoil, d_2 displays clear echoes (●), implying that the surface recurrently falls back to an earlier position. $t - t_{\text{on}}$ = 100 s is chosen as reference point.

as pronounced undulations, whose frequency scales with the field frequency and decreases over time (note the logarithmic time axes and see Appendix Figure 9.A.4a,b). This phenomenon is reminiscent of elastic ringing. We hypothesize that upon deformation, the rigid network exerts an elastic restoring force that causes recoil and subsequent overshoot. A faster perturbation, in the form of a higher f_{field}, causes the surface to 'ring' at a higher frequency. This frequency decreases over time as the surface height converges to a steady state. We observe analogous oscillations when sweeping f_{field}, confirming the direct relationship between perturbing frequency and ringing frequency (Appendix Figure 9.A.5). Further evidence for the central role of surface viscoelasticity is found at elevated temperatures, where the network modulus drops[5] and accordingly the undulation period increases (Appendix Figure 9.A.6).

These results confirm that the overall surface area oscillates, yet to additionally prove ringing of the local surface topography, we take a closer look at the speckle pattern. Scrambling of this pattern directly reflects transformations of the surface topography. Indeed, the speckle pattern repeatedly changes and subsequently returns to almost the same texture, in an oscillatory fashion (Appendix Figure 9.A.7). This recoiling is also manifest as distinct echoes in the corresponding $d_2(\tau)$ traces (Figure 9.4b, inset). Superimposed onto the oscillations, there is however a net deformation of the network, causing the echoes to eventually be lost at long τ.

9.3.4 Probing high-frequency molecular interactions

Clearly, the surface morphing is determined by a complex interplay of network mechanics and dielectric interactions. To obtain a deeper understanding of the molecular mechanisms underlying the switching response, we use a novel analysis approach: Fourier-transform LSI (FT-LSI). The Fourier transform converts a signal from the time or spatial domain to the frequency domain.[28,40,41] Above, we used it to verify the periodicity of the motility in space; here, we apply the FT to the raw speckle intensity in time. This allows us to disentangle different temporal stages and identify dominant frequencies. We first validate our FT algorithm for a surface subjected to a linear sweep of the field frequency, which should give a well-defined and sharp signal in the intensity power spectrum. Indeed, we can exactly pinpoint the driving frequency at the expected Fourier frequency (Appendix Figure 9.A.8). FT-LSI thus enables us to resolve even the smallest effects of dielectric coupling between an electric field and molecular dipoles.

9.3.5 Temporal stages of surface morphing

Having established the validity and sensitivity of FT-LSI, we apply our method to a surface actuated at 900 kHz. This field frequency exceeds the frame rate of the camera and thus precludes direct detection, yet we can resolve the surface dynamics ensuing from this high-frequency AC field. We again compute the intensity power spectrum as a function of time, which in this case does not exhibit a single dominant frequency i.e. straight line (Appendix Figure 9.A.8), but instead has a more complex dependence on frequency and time (Figure 9.5a). Notably, while DHM points to a single, monotonic change in surface height,[5] LSI reveals three distinct dynamic stages (Figure 9.5a). Very likely, none of these stages arises from dielectric heating, since the electrothermal expansion is slow (<0.4 nm/s) and takes place at different time scales (Appendix Figure 9.A.3). Instead, emergent fast dynamics must be at the origin. A molecular cartoon of the three stages is shown in Figure 9.5b. (I) Within tens of milliseconds after activation, the field torques the polar mesogens, and their random motion changes to pivoting motion in line with the continuously shifting field vector. The corresponding deformation is small as the mesogens oscillate individually. (II) Since the AC frequency is tuned to network resonance frequencies,[5,42] the oscillations of the mesogens quickly become synchronized. This leads to cooperativity and amplification of the motion, resulting in plasticization of the network within a few seconds. The accompanying change in density causes a transient peak in motility. (III) The plasticized network allows the mesogens to pivot with ever-increasing tilt angle, which in turn makes the network progressively weaker. This positive feedback causes an increase in free volume and resultant microscopic expansion of the surface.[5,15]

Morphing of these coatings thus requires the emergence of collectivity on two levels: first, the individual motions of the dangling mesogens evolve into collective oscillations, orchestrated by the high-frequency AC field. Second, these oscillations concertedly plasticize the surrounding network, allowing also the crosslink mesogens to resonate, with steadily growing amplitude. This rising, dynamic collectivity of dangling and crosslink mesogens is amplified in both time and space, until the network elasticity brings the expansion to a halt.

To analyze the different stages in more detail, we take horizontal cross-sections of the two-dimensional power spectrum, at time points indicated by the dashed lines in Figure 9.5a. Low frequencies are intrinsically most prevalent in any signal, causing a decay of power versus f (Figure 9.5c). The shift of this decay along the frequency axis reflects the contribution of fast dynamics to the intensity signal. Clearly, stages I–III exhibit a large fraction of high-frequency components up to $>10^3$ Hz. By contrast, only frequencies below 10^{-1} Hz occur in an inert silica

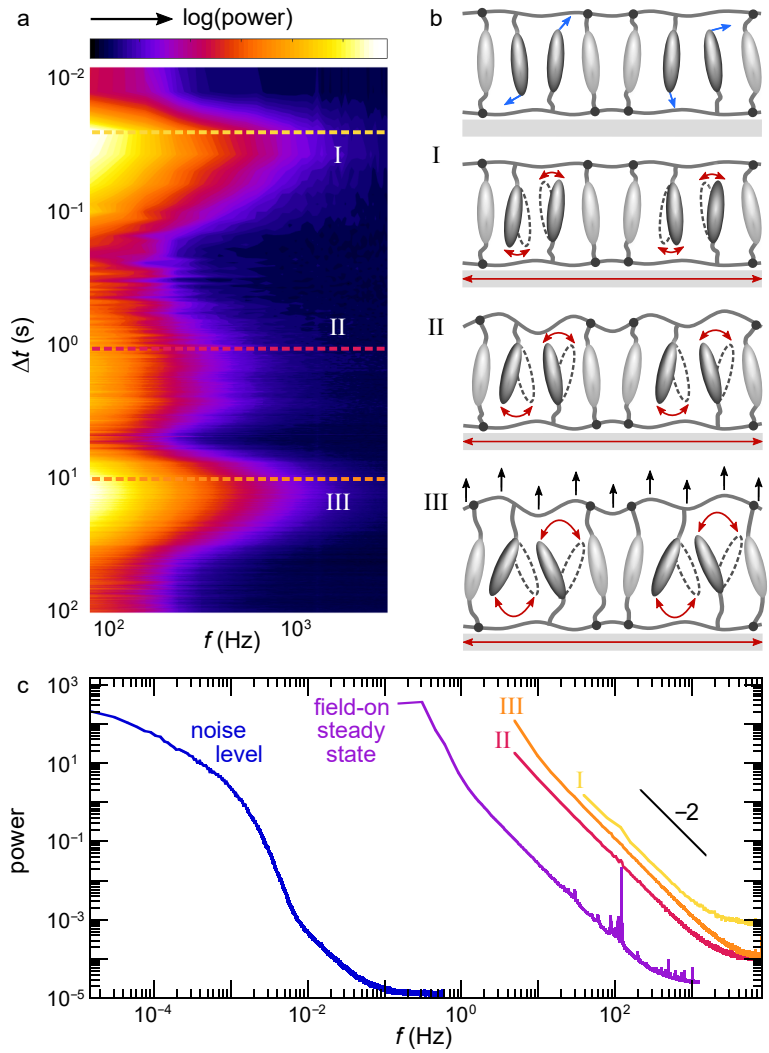

Figure 9.5. Frequency-resolved analysis of morphing kinetics. **(a)** Spectrogram of the dynamics after field switch-on at $\Delta t = 0$. Each horizontal strip represents one power spectrum of the temporal speckle intensity, averaged over 0.015 mm^2 surface. Three distinct dynamic stages can be identified. The colour scale ranges from −3 to −0.1. **(b)** Illustration of the field-off steady state (top) and morphing stages. Only the inter-electrode region is drawn. (I) Dielectric interactions drive the polar mesogens to oscillate along the AC field lines. (II) Under resonance conditions, the pendant and crosslink mesogens start moving cooperatively and plasticize the network. (III) A feedback loop of network weakening and increased oscillation amplitude causes amplification of the free volume, culminating in microscopic expansion. **(c)** Power spectra matching the indicated cross-sections in (a). All stages exhibit high-frequency motions that are ballistic in nature i.e. characterized by power law −2. By contrast, a static reference sample (—) obeys a complex f-dependence dominated by low modes, due to external noise rather than intrinsic material properties.

reference, likely due to external vibrations and slow drift. The signal we record from surfaces with emergent motility is thus more than four orders of magnitude above the noise level of our experimental set-up. Even in the steady state, 10^3 s after switching on the field, fast nanoscale motions persist (Figure 9.5c), governed by a continuous feedback loop between the field lines and dielectric properties of the network, which causes the resonance conditions to keep changing subtly. Also the shape of the power spectrum harbours information about the surface dynamics. While purely random motion would result in a power-law slope of $-3/2$, the measured slopes of -2 suggest ballistic motion, emphasizing the directional nature of all deformations.[43,44]

9.3.6 Quantification of dielectric response

We can use the same method to evaluate in detail how the surface motility evolves over time after switching on the AC field. We do so by invoking d_2 as the contrast function, since we have previously shown this provides quantitative insight into mechanical deformations (see Chapter 7). In this case, LSI directly measures an invariant of the surface strain tensor, i.e. the d_2 function represents a measure for the amplitude of the change in surface deformation as a function of time. We first compute d_2 for a high characteristic mechanical frequency of 100 Hz to probe the

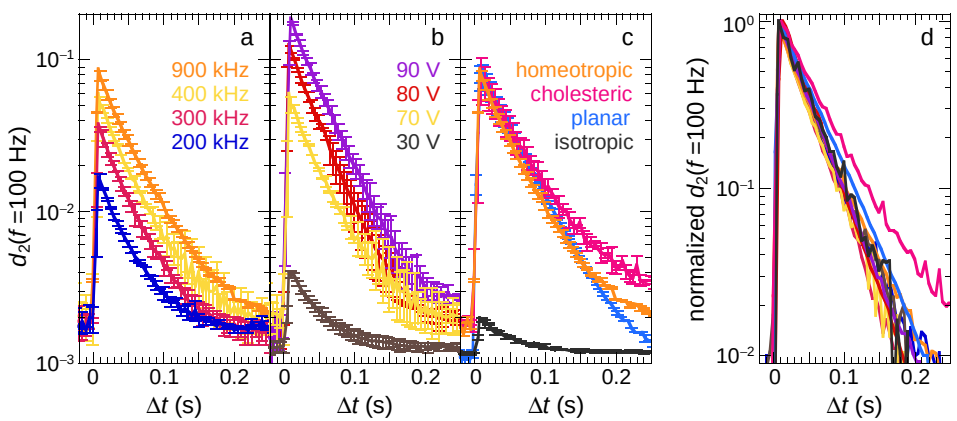

Figure 9.6. Stage I: Dielectric response. Fast transient of nanoscale motility as the field drives the polar mesogens into oscillation, whose amplitude depends on the field frequency **(a)**, voltage **(b)** and LC order **(c)**. The error bars represent standard deviations of the field-on/off average. Conditions: **(a)** homeotropic LCN at 70 V, **(b)** homeotropic LCN at 400 kHz, and **(c)** 70 V and 900 kHz. **(d)** Superposition of all curves through normalization highlights the dynamic signature of this stage.

fast, transient stage I. To increase the statistical accuracy of these data, we average both in space and between the on- and off-switching response, as these are identical and symmetric (Figure 9.6a–c). The dielectric origin of this stage is confirmed by the fact that its magnitude scales with the field frequency (Figure 9.6a) and voltage (Figure 9.6b). Moreover, its shape and rise–decay kinetics are remarkably universal for different LC topographies of similar chemical composition (Figure 9.6c): a cholesteric alignment with helical structure, a planar orientation with nematic director parallel to the substrate yet perpendicular to the field lines, and an isotropic phase without order. The latter gives a weak dielectric signal because most of the mesogens do not couple efficiently to the field. All measured field frequencies, voltages and LC geometries exhibit the same kinetics in stage I: d_2 peaks in only ~10 ms as the field tilts the polar mesogens almost instantaneously, and subsequently falls sharply over ~200 ms as the LCN relaxes to a local energy minimum. Indeed, we are able to collapse all profiles onto a single master curve through rescaling d_2 with its maximum (Figure 9.6d).

9.3.7 Quantification of morphing dynamics

Whereas stage I occurs under all conditions tested, the efficiency of the desired shape-shifting depends strongly on the LC orientation and field. In fact, for an isotropic LCN of the same chemical composition we detect no significant third stage (Figure 9.7a, —), highlighting the crucial role of collective synchronization which is inherently unattainable in a network without mesogen order. Below a field frequency of 40 kHz, also the homeotropic network dynamics vanish at all length scales accessible with our technique, i.e. they become sub-nanometric (Figure 9.7b, ▲). Beyond 40 kHz, the mesogen motility and surface expansion rise rapidly as the resonance conditions are increasingly satisfied. We here take advantage of the unprecedented sensitivity of LSI, which allows detecting significantly smaller deformations than DHM. At room temperature, digital holography cannot accurately measure height changes below $f_{\text{field}} \approx$ 600–700 kHz (Figure 9.7b, ●).[5] Moreover, while based on DHM the surface deformation seems complete after ~10 s,[5] LSI reveals that both the formation and relaxation of protrusions continue for hundreds of seconds (Figure 9.7a, —). Large deformations even take hours to fully relax (Appendix Figure 9.A.9). Clearly, the network viscoelasticity governs the morphing kinetics and dominates over dielectric interactions, which take place on orders-of-magnitude shorter time scales.[2,5]

We confirm these findings by morphing the surfaces via a different route. Instead of applying a constant 900-kHz field, we gradually increase f_{field} from 0 to 900 kHz over a period of 1000 s (Figure 9.7c). For the isotropic LCN, this again leads

to negligible surface deformation at all field frequencies tested (—). By contrast, the homeotropic network expands rapidly with increasing f_{field} (—), consistent with Figure 9.7b, ▲. Interestingly, we find exactly the same threshold frequency of 40 kHz, highlighting the exceptional sensitivity of LSI which is independent of the precise morphing kinetics and sample history.

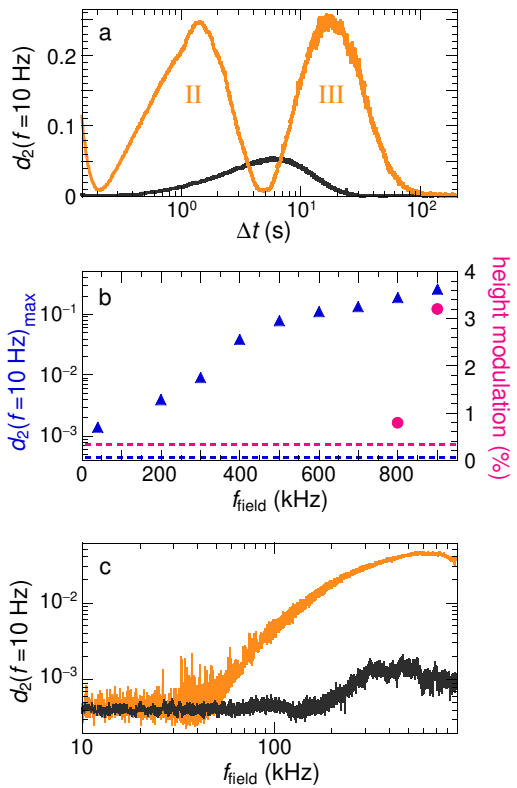

Figure 9.7. Stages II–III: Network plasticization and deformation. **(a)** In a homeotropic LCN (—), the emergence of concerted mesogen dynamics (stage II) leads to efficient surface motility (stage III), whereas an isotropic network (—) lacks the final deformation stage. **(b)** Peak motility in stage III (▲) and % height change measured by DHM (●) versus field frequency. Both techniques show an increase in surface expansion with increasing f_{field}, yet the relatively lower noise level of LSI compared to DHM (dashed lines) allows probing over an order-of-magnitude lower field frequencies (down to ~40 kHz versus ~800 kHz). **(c)** Field frequency sweep from 0 to 900 kHz at 0.9 kHz/s for a homeotropic network (—) and isotropic network (—), confirming the extraordinarily high displacement sensitivity of LSI.

9.4 Concluding remarks

In this chapter, we have shown how a frequency-resolved nanomechanical imaging technique can illuminate the hierarchical cascade of events that leads to surface morphing in liquid crystal network coatings. We uncover how an initially weak, yet measurable, dielectric response of individual mesogens to the field, amplified in time by the synchronization of pivoting motions, causes softening of the polymer matrix and finally results in network expansion and the emergence of surface topography. These experiments thus provide fundamental insights into the operational mechanisms by which artificial shape-shifting occurs in liquid crystal materials. Our approach paves the way to exploring how changes in molecular chemistry, mesogen alignment and device architecture influence the emergent collectivity, to ultimately optimize and amplify the shape-shifting response. Moreover, the method is readily amenable to probe these effects also in bulk materials, where similar effects can give rise to actuation and locomotion.[12–14,16–25,45]

9.A Appendix

9.A.1 Fourier-transform laser speckle imaging

The following Matlab routine is used to compute one-dimensional power spectra and two-dimensional spectrograms of speckle intensity fluctuations. First, for each time step, a set of images is loaded into memory. The total number of time steps and number of images per step are tailored to the question at hand and the frame rate employed. The set of images is normalized on a pixel-by-pixel basis by subtracting the time-average intensity from the temporal intensity signal, so that the intensity fluctuates around zero. The power spectrum is subsequently obtained by taking the squared modulus (i.e. absolute value) of the output of the Matlab fft function. The result is a 3D matrix of power values as a function of the two spatial dimensions x and y and frequencies f, which is spatially averaged over all pixels to yield a single power spectrum. This algorithm is iterated over consecutive time steps to produce a power spectrogram.

The highest frequency that can be resolved using Fourier transform is half of the sampling rate – called the Nyquist frequency[40] – which in LSI is half of the camera frame rate. The lowest frequency is determined by the number of images in a set, implying that the frequency range can be extended to lower values at the cost of time resolution, or vice versa the time resolution can be improved at the expense of frequency scope.

The power spectrum and $d_2(\tau)$ are closely related. Specifically, the power spectrum and the electric field correlation function $g_1(\tau)$ are a Fourier pair, which means that the two can be interconverted using the (inverse) Fourier transform.[41] g_1 is directly related to d_2 via: $g_1(\tau) = \sqrt{1 - d_2(\tau)/2\beta}$. Here, β is a numerical constant that accounts for the number of speckles detected per pixel (see Chapter 5, Section 5.2.2).

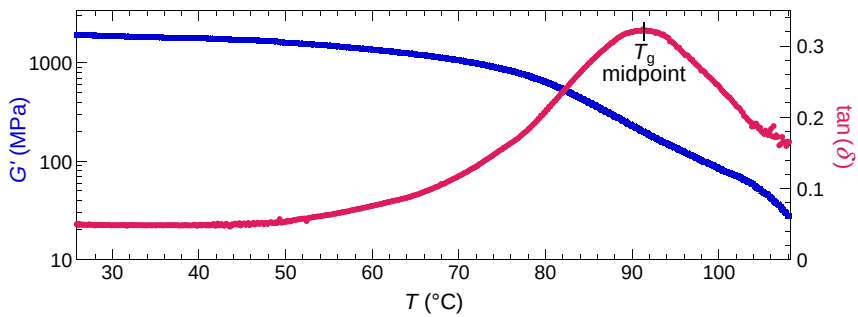

Figure 9.A.2. Thermomechanical properties. Storage modulus G' (■) and loss tangent $\tan(\delta)$ (●) versus temperature for a free-standing, homeotropic LCN film, measured using dynamic mechanical thermal analysis (DMTA) (Q800, TA Instruments, USA). The glass transition is quite broad, ranging from ∼60 °C to >110 °C, and centred around 91 °C (peak of loss tangent). The experiment is conducted in tensile mode at a heating rate of 3 °C/min and oscillation frequency of 1 Hz, with the stretching direction perpendicular to the nematic director.

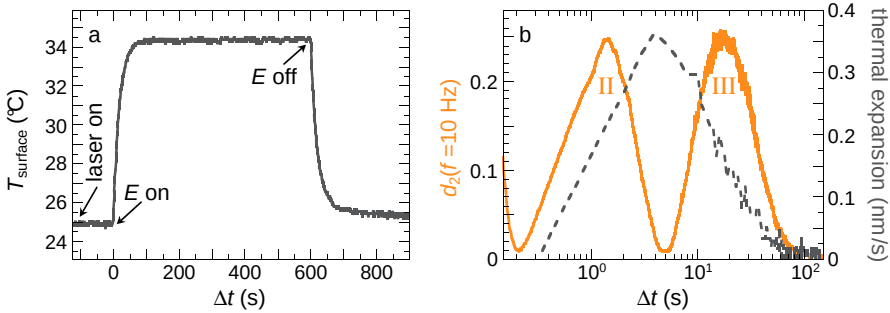

Figure 9.A.3. Electrothermal effects. **(a)** Changes in the surface temperature of a homeotropic LCN actuated at 900 kHz and 70 V, measured using an infrared sensor. Dielectric heating causes a rise of 9.5 °C within 80 s after switching on the field (at $\Delta t = 0$ s), followed by a plateau where the heat generation and heat exchange with the surroundings are in equilibrium. The kinetics of cooling after switching off the field (at $\Delta t = 600$ s) are very similar. Turning on the laser (at $\Delta t = -100$ s) results in negligible heating, because the sample absorbs virtually no 532-nm light. Throughout the experiment, the surface temperature remains far below the glass transition range. **(b)** Network deformations (—, left ordinate) and electrothermal expansion rate (- -, right ordinate) computed from (a) assuming a thermal expansion coefficient[46] of $3 \cdot 10^{-4}$ K^{-1}. The cumulative electrothermal expansion is ~8 nm. Clearly, dielectric heating does not underlie the three dynamic stages, as the time scales are incompatible. Further evidence is found in the large mismatch of frequencies: the three stages are characterized by frequencies >10 Hz, yet the thermal expansion in 1/10 s is <0.04 nm i.e. below the detection limit of LSI. The measured motility thus cannot result from electrothermal effects.

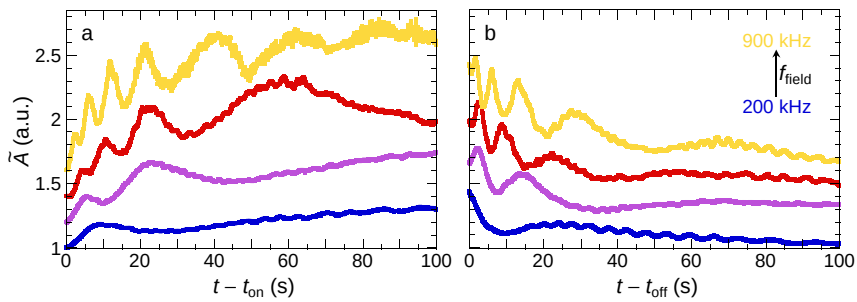

Figure 9.A.4. Kinetics and reversibility of surface deformations. **(a,b)** Zooms of Figure 9.4 on linear time axes, to highlight the decrease in undulation frequency over time. Note that the last 500 s of (a) and the last 200 s of (b) are omitted for clarity.

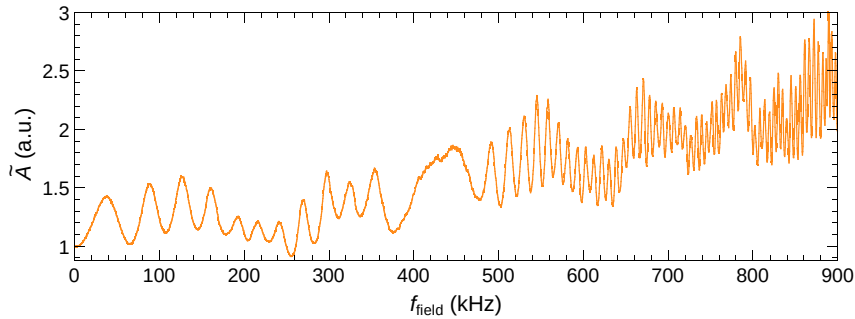

Figure 9.A.5. Frequency dependence of surface deformations. Change in surface area of a homeotropic LCN during a field frequency sweep from 0 to 900 kHz at 3 kHz/s. The surface expansion grows with the driving frequency and exhibits undulations with decreasing period, as the dielectric interactions between the field and LCN keep changing during the sweep. The speckle fluctuations are averaged over 250 μm^2 surface.

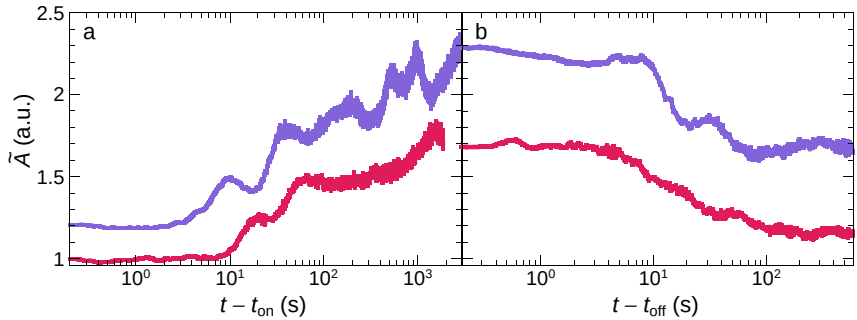

Figure 9.A.6. Temperature dependent kinetics of surface deformations. Change in surface area of a homeotropic LCN upon switching the field on **(a)** and off **(b)** at temperatures of 45 °C (●) and 65 °C (●). For clarity, the upper curve is offset vertically by 0.2. Some elastic ringing is observed, yet the extent is considerably smaller than at 25 °C (see Figure 9.4, ●). Particularly at 65 °C, where the LCN is in its glass transition regime, the oscillations almost vanish. These results confirm that network elasticity is at the origin of the surface undulations.

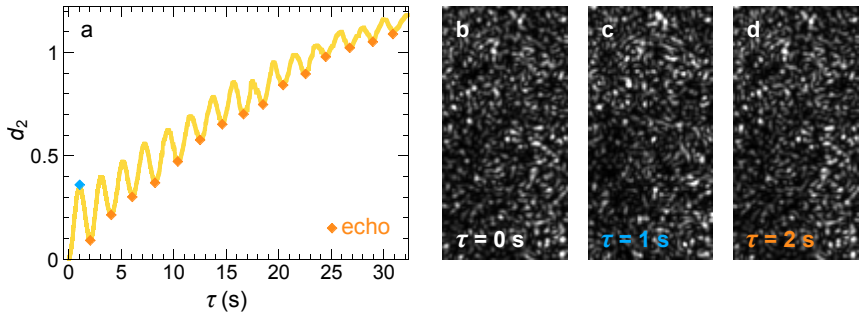

Figure 9.A.7. Speckle echoes by elastic ringing. **(a)** Intensity structure function $d_2(\tau)$ identical to the inset in Figure 9.4b, displaying distinct echoes (orange diamonds). At these echoes, the speckle pattern reverts to an earlier pattern, reflecting elastic recoil of the surface. Indeed, the pattern at $\tau = 0$ s **(b)** is almost identical to that at $\tau = 2$ s **(d)**. By contrast, between echoes the surface shows an overshoot, causing the speckle pattern to transiently change considerably. Pattern **(c)** at $\tau = 1$ s clearly deviates from both (b) and (d). These features are characteristic of elastic ringing. The oscillations of $d_2(\tau)$ are indeed quite unique, since usually d_2 increases monotonically with increasing lag time τ. The speckle patterns cover 0.015 mm^2 surface area.

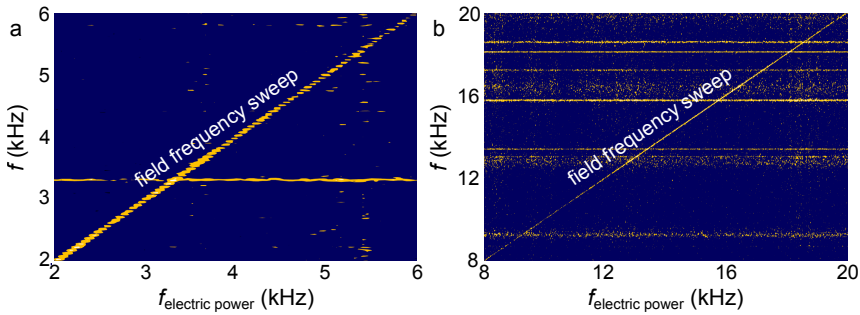

Figure 9.A.8. Detecting the driving field frequency. Spectrally resolved dynamics (vertical axis) during linear sweeps of the driving frequency (horizontal axis), from 2 to 6 kHz **(a)** and from 8 to 20 kHz **(b)**. Each vertical strip represents one power spectrum of the temporal speckle intensity, averaged over 0.0030 mm^2 surface. For clarity, the low-frequency noise is excluded. The horizontal lines correspond to electrical artefacts. Although these driving frequencies are too low to elicit significant surface deformation, pronounced diagonal signals are visible, corresponding to minute dielectric interactions between the field and molecular dipoles. We note that the horizontal axes do not represent f_{field} i.e. the frequency of the electric current I and voltage V, but rather the frequency of the electric power P, which is twice as high. Since $P(t) = I(t)V(t)$, it indeed follows that for an AC field, $f_P = 2f_I = 2f_V \equiv 2f_{\text{field}}$ for all possible phase angles between current and voltage. Clearly, it is the electric power which dictates the material response. In view of consistency with previous work, we adhere to f_{field} in the rest of the text.

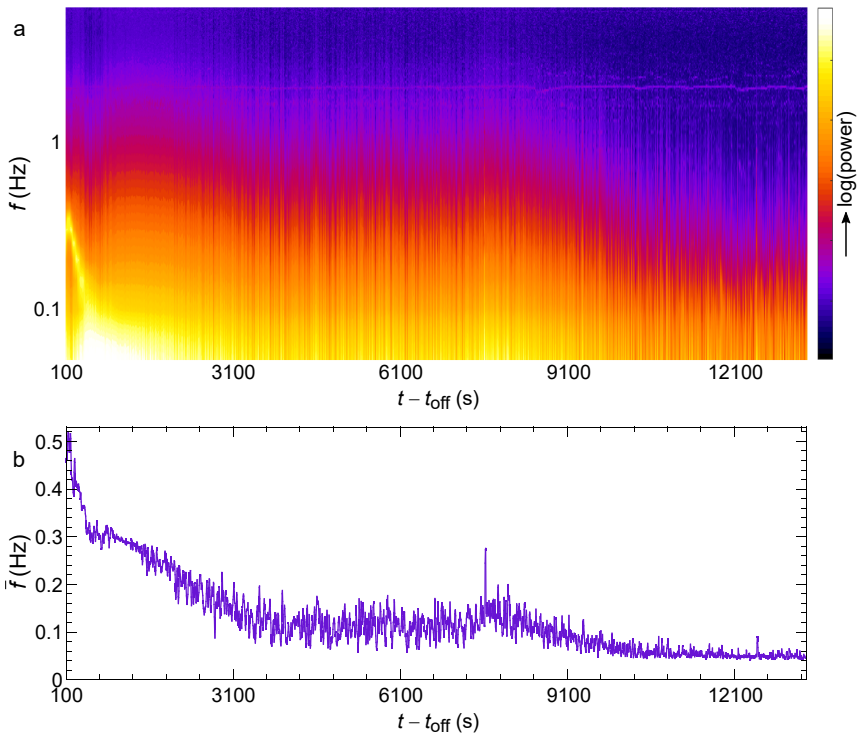

Figure 9.A.9. Long-term relaxation dynamics. **(a)** Spectrogram of the surface motility of a homeotropic LCN after switching off the field. Each vertical strip represents one power spectrum of the temporal speckle intensity, averaged over 0.57 mm^2 surface. Since the network is glassy, complete relaxation takes hours and is characterized by low frequencies (note the different f-axis compared to Figure 9.5a). **(b)** Mean frequency of the spectrogram in (a), computed as $\bar{f} = \sum_{i=1}^{n} f_i P_i$, to highlight the gradual slowing down of the network dynamics in time. The f-axis is logarithmic in (a) yet linear in (b).

References

[1] T. J. White, D. J. Broer. *Nat. Mater.* **14**, 1087–1098 (2015).

[2] D. Liu, D. J. Broer. *Nat. Commun.* **6**, 8334 (2015).

[3] E. M. Akinoglu, L. T. de Haan, S. Li, Z. Xian, L. Shui, J. Gao, G. Zhou, M. Giersig. *ACS Appl. Mater. Interfaces* **10**, 37743–37748 (2018).

[4] D. Liu, D. J. Broer. *Soft Matter* **10**, 7952–7958 (2014).

[5] D. Liu, N. B. Tito, D. J. Broer. *Nat. Commun.* **8**, 1526 (2017).

[6] W. Feng, D. J. Broer, D. Liu. *Adv. Mater.* **30**, 1704970 (2018).

[7] M. K. McBride, M. Hendrikx, D. Liu, B. T. Worrell, D. J. Broer, C. N. Bowman. *Adv. Mater.* **29**, 1606509 (2017).

[8] G. Babakhanova, T. Turiv, Y. Guo, M. Hendrikx, Q.-H. Wei, A. P. H. J. Schenning, D. J. Broer, O. D. Lavrentovich. *Nat. Commun.* **9**, 456 (2018).

[9] G. Babakhanova, H. Yu, I. Chaganava, Q.-H. Wei, P. Shiller, O. D. Lavrentovich. *ACS Appl. Mater. Interfaces,* **11**, 15007–15013 (2019).

[10] G. Koçer, J. ter Schiphorst, M. Hendrikx, H. G. Kassa, P. Leclère, A. P. H. J. Schenning, P. Jonkheijm. *Adv. Mater.* **29**, 1606407 (2017).

[11] A. H. Gelebart, D. Liu, D. J. Mulder, K. H. J. Leunissen, J. van Gerven, A. P. H. J. Schenning, D. J. Broer. *Adv. Funct. Mater.* **28**, 1705942 (2018).

[12] A. Agrawal, H. Chen, H. Kim, B. Zhu, O. Adetiba, A. Miranda, A. Cristian Chipara, P. M. Ajayan, J. G. Jacot, R. Verduzco. *ACS Macro Lett.* **5**, 1386–1390 (2016).

[13] H. Shahsavan, S. M. Salili, A. Jákli, B. Zhao. *Adv. Mater.* **27**, 6828–6833 (2015).

[14] H. Shahsavan, S. M. Salili, A. Jákli, B. Zhao. *Adv. Mater.* **29**, 1604021 (2017).

[15] H. Finkelmann, E. Nishikawa, G. G. Pereira, M. Warner. *Phys. Rev. Lett.* **87**, 015501 (2001).

[16] M. Camacho-Lopez, H. Finkelmann, P. Palffy-Muhoray, M. Shelley. *Nat. Mater.* **3**, 307–310 (2004).

[17] C. L. van Oosten, C. W. M. Bastiaansen, D. J. Broer. *Nat. Mater.* **8**, 677–682 (2009).

[18] M. E. McConney, A. Martinez, V. P. Tondiglia, K. M. Lee, D. Langley, I. I. Smalyukh, T. J. White. *Adv. Mater.* **25**, 5880–5885 (2013).

[19] S. Iamsaard, S. J. Aßhoff, B. Matt, T. Kudernac, J. J. Cornelissen, S. P. Fletcher, N. Katsonis. *Nat. Chem.* **6**, 229 (2014).

[20] A. H. Gelebart, D. J. Mulder, M. Varga, A. Konya, G. Vantomme, E. W. Meijer, R. L. B. Selinger, D. J. Broer. *Nature* **546**, 632–636 (2017).

[21] Y. Liu, B. Xu, S. Sun, J. Wei, L. Wu, Y. Yu. *Adv. Mater.* **29**, 1604792 (2017).

[22] W. Lehmann, H. Skupin, C. Tolksdorf, E. Gebhard, R. Zentel, P. Krüger, M. Lösche, F. Kremer. *Nature* **410**, 447–450 (2001).

[23] A. Fukunaga, K. Urayama, T. Takigawa, A. DeSimone, L. Teresi. *Macromolecules* **41**, 9389–9396 (2008).

[24] C. Ohm, M. Brehmer, R. Zentel. *Adv. Mater.* **22**, 3366–3387 (2010).

[25] T. Okamoto, K. Urayama, T. Takigawa. *Soft Matter* **7**, 10585–10589 (2011).

[26] L. T. de Haan, G. Zhou. *J. Phys. Chem. Solids* **122**, 36–40 (2018).

[27] H. Bolay, U. Reuter, A. K. Dunn, Z. Huang, D. A. Boas, M. A. Moskowitz. *Nat. Med.* **8**, 136–142 (2002).

[28] P. Zakharov, A. C. Völker, M. T. Wyss, F. Haiss, N. Calcinaghi, C. Zunzunegui, A. Buck, F. Scheffold, B. Weber. *Opt. Express* **17**, 13904–13917 (2009).

[29] D. A. Boas, A. K. Dunn. *J. Biomed. Opt.* **15**, 011109 (2010).

[30] A. Nadort, K. Kalkman, T. G. van Leeuwen, D. J. Faber. *Sci. Rep.* **6**, 25258 (2016).

[31] M. Erpelding, A. Amon, J. Crassous. *Phys. Rev. E* **78**, 046104 (2008).

[32] A. Amon, V. B. Nguyen, A. Bruand, J. Crassous, E. Clément. *Phys. Rev. Lett.* **108**, 135502 (2012).

[33] Z. Hajjarian, S. K. Nadkarni. *Sci. Rep.* **2**, 316 (2012).

[34] H. M. van der Kooij, R. Fokkink, J. van der Gucht, J. Sprakel. *Sci. Rep.* **6**, 34383 (2016). **(Chapter 5)**

[35] A. Amon, A. Mikhailovskaya, J. Crassous. *Rev. Sci. Instrum.* **88**, 051804 (2017).

[36] M.-Y. Nagazi, G. Brambilla, G. Meunier, P. Marguerès, J.-N. Périé, L. Cipelletti. *Opt. Lasers Eng.* **88**, 5–12 (2017).

[37] H. M. van der Kooij, A. Susa, S. J. García, S. van der Zwaag, J. Sprakel. *Adv. Mater.* **29**, 1701017 (2017). **(Chapter 8)**

[38] H. M. van der Kooij, S. Dussi, G. T. van de Kerkhof, R. A. M. Frijns, J. van der Gucht, J. Sprakel. *Sci. Adv.* **4**, eaar1926 (2018). **(Chapter 7)**

[39] T. Verho, P. Karppinen, A. H. Gröschel, O. Ikkala. *Adv. Sci.* **5**, 1700635 (2018).

[40] G. D. Bergland. *IEEE Spectrum* **6**, 41–52 (1969).

[41] W. Lu, N. Vaswani. Preprint at https://arxiv.org/abs/0904.0602 (2009).

[42] H. W. Broer. *Acta Appl. Math.* **120**, 61–86 (2012).

[43] S. Takesue, T. Mitsudo, H. Hayakawa. *Phys. Rev. E* **68**, 015103 (2003).

[44] J. Mo, A. Simha, S. Kheifets, M. G. Raizen. *Opt. Express* **23**, 1888–1893 (2015).

[45] T. H. Ware, M. E. McConney, J. J. Wie, V. P. Tondiglia, T. J. White. *Science* **347**, 982–984 (2015).

[46] D. Liu, C. W. M. Bastiaansen, J. M. J. den Toonder, D. J. Broer. *Macromolecules* **45**, 8005–8012 (2012).

Chapter 10

Electroplasticization of liquid crystal polymer networks

This chapter is based on: Hanne M. van der Kooij, Dirk J. Broer, Danqing Liu and Joris Sprakel, 'Electroplasticization of liquid crystal polymer networks', *ACS Appl. Mater. Interfaces* **12**, 19927–19937 (2020).

Abstract

Shape-shifting liquid crystal networks (LCNs) can transform their morphology and properties in response to external stimuli. These active and adaptive polymer materials can have impact in a diversity of fields, including haptic displays, energy harvesting, biomedicine and soft robotics. Electrically driven transformations in LCN coatings are particularly promising for application in electronic devices, in which electrodes are easily integrated and allow for patterning of the functional response. The morphing of these coatings, which are glassy in the absence of an electric field, relies on a complex interplay between polymer viscoelasticity, liquid crystal order and electric field properties. Morphological transformations require the material to undergo a glass transition that plasticizes the polymer sufficiently to enable volumetric and shape changes. Understanding how an alternating current can plasticize very stiff, densely crosslinked networks remains an unresolved challenge. Here, we use a nanoscale strain detection method to elucidate this electric-field-induced devitrification of LCNs. We find how a high-frequency alternating field gives rise to pronounced nanomechanical changes at a critical frequency, which signals the electrical glass transition. Across this transition, collective motion of the liquid crystal molecules causes the network to yield from within, leading to network weakening and subsequent nonlinear expansion. These results unambiguously prove the existence of electroplasticization. Fine-tuning the induced emergence of plasticity will not only enhance the surface functionality but also enable more efficient conversion of electrical energy into mechanical work.

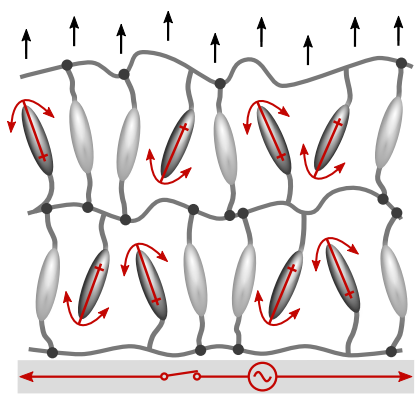

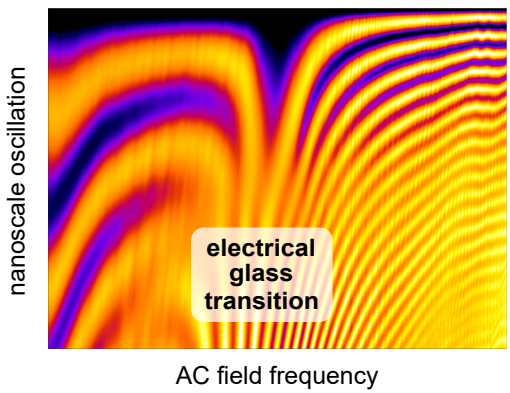

10.1 Introduction

Liquid crystal polymers have emerged in the past decade as a powerful platform to create active materials with unique functional responses.[1] These materials synergistically combine the high anisotropy and stimuli-responsiveness of liquid crystals with the tuneable viscoelasticity of polymers. The liquid crystal polymer chains are typically crosslinked into a glassy liquid crystal network (LCN) or flexible liquid crystal elastomer (LCE) to impart mechanical strength and shape reversibility while retaining the liquid-crystal organization.[2,3] Triggered by external cues such as light,[4–13] heat,[14–16] humidity,[17–19] gas[19,20] or an electric field,[21–27] these materials can undergo pre-programmed changes in shape or properties via local adjustment of the liquid crystal order and dynamics. A virtually infinite range of three-dimensional spatiotemporal variations in roughness, motility, wetting or adhesion can thus be realized. Responsive liquid crystal polymer networks have shown great potential in advanced application fields, including surfaces with adjustable friction for use on robotic fingers,[26,28,29] on-demand dry self-cleaning coatings for next-generation solar cells,[25,30,31] membranes with tuneable permeability for regulated gas transport,[16] interactively deforming haptic interfaces for Braille displays,[32–34] and dynamic biointerfaces to guide cell behaviour.[10,23]

Irrespective of the area of application, the common denominator is that functionality arises from a complex competition between solid mechanics on the one hand and the intrinsic desire of liquid crystals to align with external fields on the other. Despite tremendous advances in engineering these 'smart' materials, the precise nanomechanics governing shape transformation have remained elusive. Paradoxically, liquid crystal networks are typically glassy and static in the off-state, whereas surface morphing requires the emergence of substantial mobility across different length scales. Topographical deformation *must* therefore involve field-induced network plasticization.

Increasing the temperature beyond a critical value, denoted as T_g, is the most obvious way to cross the glass-to-rubber transition. However, heating is unsuitable for most practical applications and difficult to program in a spatially varying manner to create switchable surface topographies. Inspired by the phenomenon of athermal photofluidization in non-crosslinked azo-polymer films,[35–39] light-driven LCNs have thus been developed, which locally plasticize upon illumination. The light responsiveness of these materials stems from incorporated azobenzene moieties. Upon UV exposure, azobenzenes isomerize from a rod-like *trans* form to a bent *cis* conformation, which is reversed by blue-light illumination. Simultaneous excitation of both the *trans* and *cis* isomers via dual-wavelength illumination thus leads to continuous *trans*↔*cis* cycling of the azobenzene moieties at kHz

rate.[40] When embedded in an LCN, these oscillatory switching and reorienting azobenzenes exert large internal collective forces on the polymer network, which in turn devitrifies the glassy solid. Experimental evidence for the resultant macroscopic network softening was found in a photoinduced decrease in the elastic modulus of up to two orders of magnitude.[41,42] Combined optical and mechanical analysis confirmed the direct correlation between photoisomerization of the azobenzene moieties, photoinduced change in birefringence (i.e. liquid crystal alignment), and photogenerated macroscopic stress.[43–45] The use of light as a trigger has the advantage of contactless, remote control over the shape-shifting response. Yet, photoresponsive polymers also suffer from several drawbacks, such as low light conversion efficiency, thermal instability, and photo-oxidative degradation.

By contrast, electric actuation allows for direct addressing of the material, facile spatial patterning and easy integration into portable devices.[24,26] Analogous to heat and light, an alternating electric field imposed on mesogens with a large dipole moment can also induce molecular vibrations. These vibrations inside a glassy network are speculated to render the material malleable and dynamic at temperatures far below its T_g.[24–26] The fact that an electric field can cause mechanical changes and result in pronounced shape-shifting, suggests the existence of a field-induced glass-to-rubber transition. However, conclusive evidence for this 'electroplasticization' in liquid crystal polymer networks is lacking. To improve the energy conversion efficiency of electric-field-driven LCNs and minimize dissipation as heat or by plastic deformations, nanoscale insights into the network mechanics at and across this transition are essential. Macroscopic rheology is inherently unsuited to this task, because the electrodes and connected LCN coating are not free-standing but surface-constrained. Moreover, the electroplasticization occurs very locally in a spatially heterogeneous manner. While nano-indentation and atomic force microscopy do provide the desired local mechanical information,[35,37,46,47] these techniques are invasive and limited by their temporal resolution. Clearly, an experimental method is needed that allows dynamic nanomechanical analysis of the network in situ and with high spatiotemporal resolution.

In this chapter, we employ laser speckle imaging to evidence and study electric-field-induced devitrification of LCNs. As demonstrated in previous chapters, this method offers a quantitative analysis of surface strains in these materials, and allows in a single experiment to obtain nanomechanical information spanning six decades in time. LSI was originally developed in the medical field for non-invasive imaging of blood flow,[48–51] but has attracted increasing interest of material scientists and proven powerful for probing the nanoscopic mechanics and dynamics of a diversity of complex materials.[52–58] In Chapter 9, we used LSI to shed more light

on the mechanisms underlying shape-shifting of electrically actuated liquid crystal networks. We revealed how the transformation of surface topography occurs in three distinct hierarchical stages, from the molecular scale upwards and from milliseconds to minutes. Here, we extend our previous work by proposing an approach to disentangle elastic and plastic deformations during LCN actuation, providing direct evidence for dissipative processes characteristic of network plasticization. We uncover a complex, nonlinear coupling between the driving electric field and surface dynamics, mediated by induced molecular oscillations. Pronounced changes in the oscillation frequency and plasticity occur within a narrow field frequency window, which is dictated by the network nanomechanics. These results not only conclusively evidence the existence of electroplasticization, but can also help tailor and optimize the morphological response of these materials.

10.2 Experimental details

10.2.1 Materials

The liquid crystal monomers used in this study are depicted in Figure 10.1b. LC diacrylates **1** (1,4-bis-[4-{6-acryloyloxy-hexyloxy}benzoyloxy]benzene, CAS no. 125248-71-7) and **2** (1,4-bis-[4-{6-acryloyloxy-propyloxy}benzoyloxy]benzene, CAS no. 174063-87-7), and cyano-capped LC monoacrylate **3** (4-[4-{6-[acryloyloxy]-hexyloxy}benzoyloxy] 4-[cyano]benzoate, CAS no. 83847-14-7) are purchased from Merck (UK). Photoinitiator **4** (phenylbis[2,4,6-trimethylbenzoyl]-phosphine oxide, CAS no. 162881-26-7) is obtained from BASF (Germany). Polyimide 7511L SUNEVER is purchased from Nissan Chemical Corporation (Japan). The reaction solvent dichloromethane is obtained from Sigma-Aldrich (USA). TiO_2 (titania) nanoparticles (~40 nm diameter, coefficient of variation ~40%, purity 99.5%) are purchased from US Research Nanomaterials (USA). All components of the LSI set-up are obtained from Thorlabs (Germany), unless otherwise specified.

10.2.2 Sample preparation

1.5×1.5 cm^2 glass substrates are patterned with interdigitated indium tin oxide (ITO) electrodes, 3 μm wide with 5 μm gaps, covering a total area of 0.5×0.5 cm^2. The substrates are cleaned using acetone and isopropanol. To induce spontaneous homeotropic alignment of the mesogens, a ~30 nm thick film of polyimide 7511L is spin-coated onto the glass and baked at 200 °C for 1 hour. Subsequently, the LCN monomers (Figure 10.1b) are mixed in a ratio of 24.75 wt% monomer **1**, 24.75 wt% monomer **2**, 49.5 wt% monomer **3** and 1.0 wt% photoinitiator **4**, and dissolved in dichloromethane. The solution is spin-coated onto the baked polyimide film and

photopolymerized using UV light from a mercury lamp (OmniCure S2000, Lumen Dynamics Group Inc., Canada) for 5 min under N_2 at 26 °C to lock a nematic orientation. The coating is post-cured at 120 °C under N_2 to ensure complete conversion of the monomers. Finally, a thin layer of high-refractive-index TiO_2 nanoparticles is deposited onto the surface by spin-coating a 1 wt% aqueous TiO_2 suspension at 2000 rpm for 30 s, to render the coating multiply scattering for LSI. The TiO_2 suspension is sonicated for 10 min prior to spin-coating to disperse any aggregated nanoparticles. The spin-coating conditions are optimized to fulfil the intermediate-scattering requirements, implying that well-developed speckle patterns are obtained (i.e. the scattered photons are randomized), yet the TiO_2 coating is sufficiently thin to not alter the surface morphing.

10.2.3 Electric actuation

An in-plane, sinusoidal electric field is produced by a waveform generator (TGA1241, TTi Inc., USA) connected to an amplifier (F20A, FLC Electronics, Sweden). Unless otherwise specified, actuation occurs at 25 °C at a peak-to-peak voltage of 70 V (i.e. a field strength of 14 V/μm). The output AC signal is monitored using an oscilloscope (TBS1022, Tektronix, USA).

10.2.4 Laser speckle imaging

LSI experiments are performed in the back-scatter geometry on a custom-built set-up described in detail in Chapter 5. An LSI measurement involves illumination of the area of interest with an expanded coherent laser beam (Cobolt Samba, 1 W, λ = 532 nm, Cobolt, Sweden) and detection of the multiply scattered photons by a camera. Because the coatings in this study are optically transparent during all stages of actuation, the incident photons are predominantly back-scattered from TiO_2 nanoparticles on the surface. Only multiply scattered photons are detected, as specular and low-order scattering paths are filtered by a linear polarizer perpendicular to the original laser polarization. This results in a so-called speckle pattern on the camera: a spatially random pattern of dark and light 'blobs' arising from destructive and constructive interference, respectively. Our camera (Dalsa Genie CCD, CR-GM00-H640x, Stemmer Imaging, Netherlands) allows for continuous streaming of these speckle patterns at frame rates up to 200 fps.

While the absolute speckle intensity provides information about the surface area, the main power of LSI is its measurement of *changes* in the speckle intensity over time to gain highly resolved insight into the surface dynamics. The rate of these speckle fluctuations is computed for every pixel using the intensity structure function d_2:

$$d_2(x, y, t, \tau) = \frac{\langle [I(x, y, t) - I(x, y, t + \tau)]^2 \rangle}{\langle I(x, y, t) \rangle \cdot \langle I(x, y, t + \tau) \rangle} \tag{10.1}$$

where I is the speckle intensity at position x, y and time after switching on or off the field, t; and τ is the time separating two speckle patterns. In this study, the angular brackets denote averaging over a large number of independent speckles i.e. pixels in space, and contrary to earlier work no time averaging is applied to achieve maximum temporal resolution.

10.3 Results and discussion

10.3.1 Liquid crystal network design and functionality

We study a liquid crystal polymer network whose functional response has been characterized in Chapter 9 and ref. 24. The network is attached to a glass support patterned with interdigitated electrodes and coated with a ~30 nm polyimide film to ensure homeotropic alignment (Figure 10.1a). We synthesize the LCN by in-situ photopolymerization of a mixture of monomers **1** to **4** (Figure 10.1b) in a weight ratio of 1:1:2:0.04. Monomers **1** and **2** are liquid crystal diacrylates that serve as crosslinkers, while additionally their rigid core exhibits thermotropic liquid-crystalline behaviour. Monomer **3** is a liquid crystal monoacrylate capped with a cyano group, whose large dielectric anisotropy allows for efficient coupling with an external field. The monomers self-assemble into a nematic phase at room temperature, which is subsequently 'frozen' via photopolymerization, initiated by photoinitiator **4**. This yields a 2.5–3 μm thick, optically transparent, monodomain liquid crystal network with order parameter of 0.6–0.7.[24,59] A simplified cross-section is shown in Figure 10.1c.

At room temperature in the field-off state, the LCN is stiff and glassy, with an elastic modulus of ~2 GPa and a thermal glass transition range from 60 to 120 °C (see Chapter 9, Appendix Figure 9.A.2). Remarkably, switching on a high-frequency alternating current (AC) rapidly plasticizes the network and has a profound effect on both the individual mesogen dynamics and network mobility as a whole. It is crucial that the field lines are perpendicular to the nematic director, so that the dangling polar mesogens experience the maximum dielectric torque and are forced to align with the field. Although this alignment is largely prohibited by the high crosslink density, the dangling dipoles can collectively exert a substantial force on the LCN in which they are embedded, giving rise to yielding of the solid at a critical field strength and frequency. The yield point can be regarded as a stress-induced glass-to-rubber transition, which is common in soft and granular materials.[60–62]

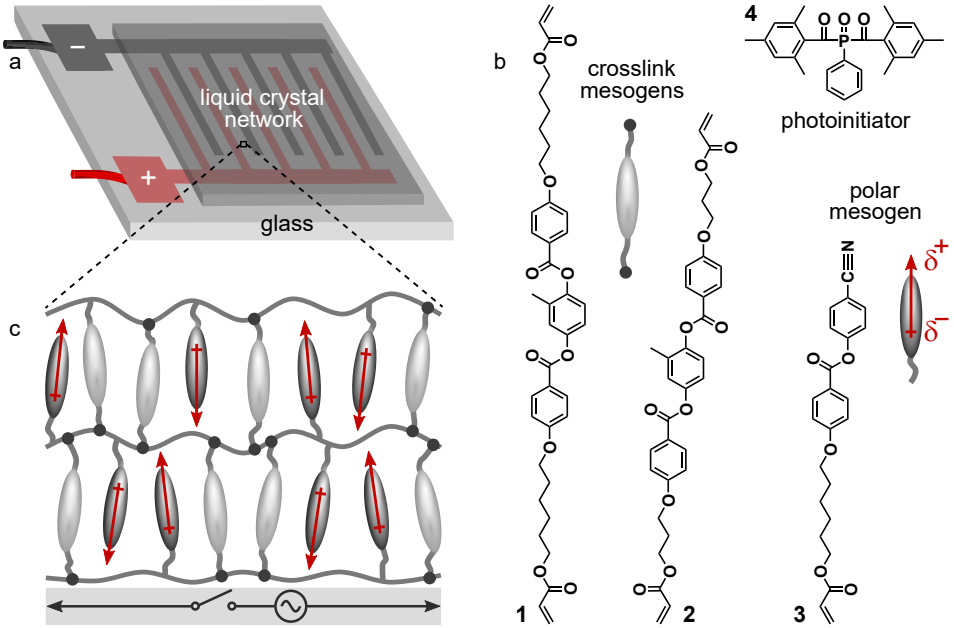

Figure 10.1. LCN device composition. **(a)** Schematic of a liquid crystal network coating with embedded interdigitated electrodes, patterned onto a glass support. **(b)** Chemical structures of the monomers used in the photopolymerization reaction. The two crosslink mesogens and polar mesogen occur in a 1:1:2 ratio in the network. **(c)** Schematic zoomed-in cross-section of a homeotropically aligned LCN between two electrodes. In the field-on state, the AC field lines are perpendicular to the nematic director. The light grey mesogens are electrically inactive crosslinks, whereas the dark grey mesogens are permanent dipoles that couple strongly to the field. The dimensions are not to scale.

At low stress, the material response is largely elastic, whereas exceeding the yield point involves irreversible plasticity. Yielding and plasticization are typically evoked by an external mechanical perturbation, yet here the forces are generated from within.

These effects are particularly prominent because the AC field vector continuously changes sign and causes the polar mesogens to pivot in a synchronized, oscillatory manner. By tuning the field frequency i.e. oscillation frequency to natural frequencies of the LCN, the pivoting motion not only plasticizes the network but also generates molecular disorder and associated free volume. These dynamic voids decrease the overall network density[63] and lead to significant surface expansion. The possible shape-shifting patterns and dimensions are virtually endless, as the switchable features are not a material property but instead are determined

by the electric field configuration. In our device geometry (Figure 10.1a), the electric field is maximum between electrodes; hence, the field-induced expansion manifests as local protrusions (see Chapter 9, Figure 9.2).[24]

In the previous chapter, we have used laser speckle imaging to establish a detailed description of the stages leading to surface morphing. We have shown how a hierarchical chain of events, initiated by an AC field, can ultimately give rise to patterned network expansion and shape-shifting. Molecular cooperativity in space and synchronization in time have proven central in this process, which can be divided into three distinct successive stages: (I) The polar mesogens couple to the alternating field and start to oscillate. (II) Collectively, the mesogens generate large oscillatory stresses, which are the origin of network softening or 'electroplasticization'. (III) These internal mechanical forces put the network under tension, while simultaneously free volume is formed around the dangling mesogens, jointly leading to network expansion. The resultant height modulation can reach hundreds of nanometres.[24–26]

10.3.2 Local measurement of nanodeformations

While previous work has elucidated the nature of the first and last stages, the second and crucial stage in which the glassy network devitrifies has remained elusive to date. In this chapter, we focus on unambiguously evidencing the existence of the proposed electric-field-induced glass transition in these coatings. LSI was originally devised for highly turbid materials,[64] yet we demonstrated in Chapter 9 that relevant, semi-quantitative results can also be acquired in the intermediate scattering regime, rendering LSI applicable to thin films coated with high-refractive-index nanoparticles. We thus spin-coat a thin layer of TiO_2 pigments onto the LCN surface and illuminate the centre with a coherent, collimated laser beam. The laser photons are scattered several times inside the TiO_2 layer before travelling back and reaching the camera detector. Although we operate in the limit of weak multiple scattering because of the thin-film geometry, we filter photons that have undergone no or too few scattering events by a linear polarizer in front of the camera. All of the remaining photons have travelled different path lengths and have thus accumulated phase shifts, resulting in a random interference pattern on the camera called speckle pattern. Changes in this pattern reflect displacements of the TiO_2 nanoparticles, which in turn must ensue from deformations of the network surface because the pigments are firmly attached.

The characteristic time scale of speckle intensity fluctuations is directly related to the rate of surface deformations, and the fluctuation amplitude is related to the amount of deformation. Surface strains of the order of nanometres are

detectable, as cumulative nanometric changes in scattering events rapidly add up to measurable variations in the speckle pattern. We quantify the surface motion using the structure function d_2 (Section 10.2.4). $d_2(x, y, t, \tau)$ is a four-dimensional function of spatial coordinates x and y; time after switching the field on or off, t; and lag time between correlated speckle patterns, τ. As highlighted in Chapters 5–9, computing d_2 as a function of τ allows us to spectrally resolve processes occurring on different time scales. For example, stage I is very fast and thus requires analysis at short $\tau = 0.01$ s to prevent loss of temporal resolution (Figure 10.2a), whereas stages II–III benefit from analysis at longer $\tau = 0.2$ s to obtain sufficient speckle decorrelation (Figure 10.2b). We previously used the imaging power of LSI to create spatial representations of the dynamics. In this chapter, we average over a small area (0.040 mm^2) to further enhance the signal-to-noise ratio.

10.3.3 Temperature dependence of morphing stages

We first focus on unravelling the combined effects of heat and electricity, both of which enhance molecular vibrations. However, while heat causes random reorientation of the mesogens and a concomitant decrease in molecular order,[23,35] an AC field involves anisotropic angular displacement of the mesogens.[22] In fact, switching on a 900 kHz field even causes some in-plane birefringence to build up, due to the biased reorientation of mesogens along the field lines. The change of birefringence is, however, only ~0.03, implying that the mesogens vibrate with small amplitude and that their orientational redistribution upon actuation is limited.

To test if the field-induced directional changes dominate over the heat-induced loss of order, we measure the dielectric response (stage I) at three temperatures. Our samples are thermostated to the desired temperature well before electric induction. We quantify the local, nanoscale surface deformation using the above described d_2 structure function. Molecular displacements inside the liquid crystal network, such as tilting of the polar mesogens, will cause a small but detectable deformation of the surface. d_2 reflects the magnitude of these surface strains and thus indirectly measures the degree of internal network perturbations.

In Chapter 9, we found that the deformation kinetics during the dielectric response are strikingly universal for our class of LCNs. This observation is confirmed at different temperatures: d_2 peaks within 10–15 ms after field switch-on as the field torques the polar mesogens, followed by exponential relaxation of the network over ~200 ms (Figure 10.2a). Conversely, the *amount* of surface deformation depends strongly on the mesogen–field interactions. We previously uncovered a distinct positive relationship between the deformation amplitude and

field frequency, voltage, and angle between the molecular dipoles and field lines (see Chapter 9, Figure 9.6). At elevated temperature, the network permittivity and dielectric interactions are larger;[24] this indeed enhances the mesogen alignment and consequent LSI signal (Figure 10.2a). Moreover, the network weakens with increasing temperature,[24,59] allowing the polar mesogens to pivot with greater amplitude. Clearly, these anisotropic phenomena far outweigh the randomizing effects of heat.

Also the final height modulation in stage III increases with rising temperature, thanks to the larger network mobility and permittivity (Figure 10.2b). Note that the surface temperature remains below the polymer T_g (60–120 °C) in all experiments, since dielectric heating is only ~10 °C, as measured using an infrared sensor

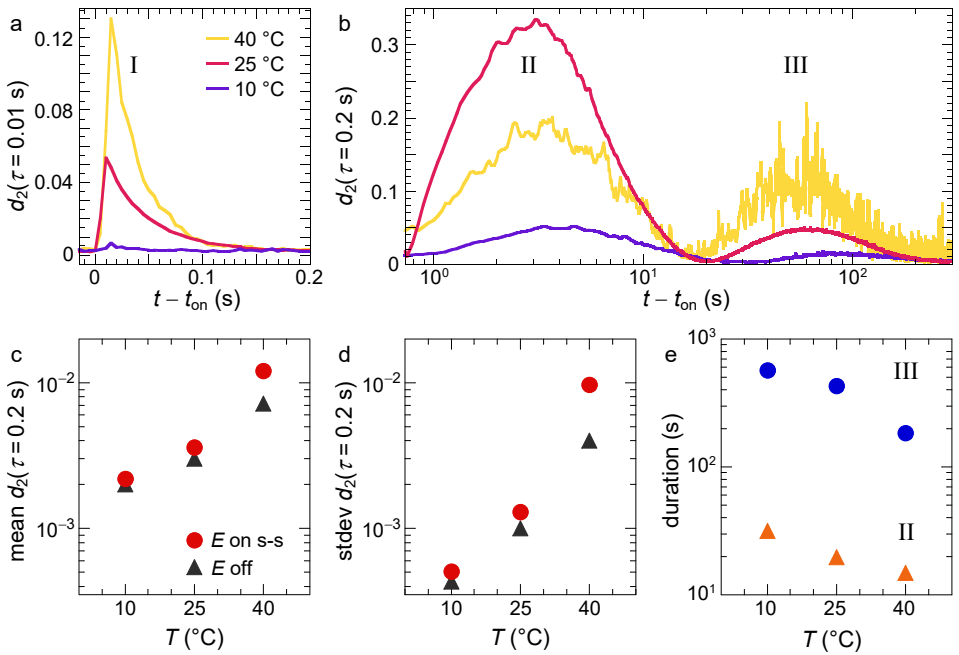

Figure 10.2. Temperature dependence of electrically driven surface morphing. **(a,b)** Three distinct stages underlie shape-shifting, as described in detail in Chapter 9: (I) fast alignment of the polar mesogens, (II) network plasticization, and (III) gradual deformation. The amplitudes increase monotonically with increasing temperature, except for the electroplasticization stage. **(c,d)** Nanoscale surface fluctuations in the field-on steady-state (s-s) and field-off state. Both the average motility **(c)** and its standard deviation **(d)** i.e. intermittency rise with increasing temperature. **(e)** Temperature-dependent kinetics of stages II and III. See Appendix Figure 10.A.3 for the measurement procedure.

(see Appendix A9.2 of Chapter 9). This limited temperature rise is one of the key differences between electroplasticization and the well-established process of high-frequency welding (see Appendix 10.A.1 for details).[65,66] Temperature gradients in the coating are negligible, thanks to its small thickness (2.5–3 μm) and attachment to a relatively thick glass substrate (1 mm) which dissipates heat from the LCN by acting as a heat sink.

Qualitatively, stages I–III are highly similar for the three temperatures, confirming how nanoscale motions are amplified in time and space in a step-wise manner (Figure 10.2a,b). Even for a different (cholesteric[67]) alignment of identical chemical composition, we find the same three stages (Appendix Figure 10.A.2). Nevertheless, quantitative comparison reveals important differences. First evidence for electroplasticization is found in stage II, whose amplitude does not increase monotonically with increasing T analogous to the other stages, but instead is smaller at 40 °C than at 25 °C. This observation is perfectly in line with the fact that closer to the network T_g, less electrical plasticization is required to yield the solid matrix, even though the subsequent expansion is larger. Other effects of the temperature are relatively modest, yet can still be well identified using LSI. For example, the mean surface motility in the field-off state (▲) and in the field-on steady-state (●, 500 s after field switch-on) both show a clear positive dependence on temperature (Figure 10.2c). The difference between 10 and 40 °C remains however within an order of magnitude. Equivalently, the standard deviation of d_2 – a measure for the intermittency of the surface fluctuations – also grows with increasing temperature (Figure 10.2d). This intermittency is clearly visible in the 40 °C curve in Figure 10.2b and indicates that a softer network responds more chaotically to the mesogen oscillations. These surface fluctuations are e.g. beneficial for dirt removal applications,[25] favouring operation of this device at elevated temperature, in addition to achieving larger height modulations. Moreover, heat accelerates the kinetics of plasticization and expansion, as evident from a slight decrease in the duration of stages II and III (Figure 10.2e and Appendix Figure 10.A.3).

10.3.4 Disentangling elastic and plastic strains

We have shown how a 900 kHz AC field activates three well-defined hierarchical dynamic stages over a range of temperatures. However, at each temperature, a critical field frequency exists below which no significant surface morphing occurs. According to digital holography microscopy (DHM) measurements, the desired functionality of the LCN emerges only at field frequencies (f_{field}) of 500 kHz and above (see Figure 3d in ref. 24). Efficient plasticization is crucial in this regard. At low f_{field}, the surface deformation is largely elastic and reversible, limited by the

glassy nature of the network. At sufficiently high field frequencies, the surface expansion becomes nonlinear, with concomitant irreversible rearrangements inside the coating. During such a plastic response, not only is energy dissipated but the material also adopts a new shape, as depicted schematically in Figure 10.3a–c. The network microstructure will change non-affinely to accommodate for these plastic strains. In order to shed more light on the phenomenon of electroplasticization, distinguishing local elastic from plastic strains is key. LSI is a highly sensitive, versatile and effective means to identify elastic–plastic transitions in LCNs.

From a single LSI experiment, we can not only extract the surface motility d_2, which quantifies the *changes* in scattered intensity, but also the surface area, which relates to the *absolute* scattered intensity. More precisely, the average speckle intensity $\langle I \rangle$ is proportional to the surface concentration of nanoparticles $c_s = n/A$, with A the surface area (defined in Figure 10.3a). We can thus compute the reduced change in surface area over time: $\tilde{A}(t) \equiv A(t)/A_0 = I_0/I(t)$. Interestingly, at low field frequency (200 kHz), the increase in $\tilde{A}$ upon field switch-on is exactly reversed upon field switch-off and displays remarkably little hysteresis (Figure 10.3d). By contrast, the surface *structure* will not fully recover to its initial value after an on–off cycle and will exhibit plastic rearrangements. These rearrangements do not alter the overall shape of the coating, nor the surface roughness, but manifest themselves as irregular nanoscale changes of the surface, which are fixed when the coating re-solidifies (see Figure 10.3c in blue).

To quantify this plasticity, we focus on the entire speckle pattern i.e. the structure function d_2 rather than on the average speckle intensity. We start from the same reference point as in Figure 10.3d, which is the last speckle pattern before induction at $t = t_{on}$. As the network expands over time, the surface structure and corresponding speckle pattern will change gradually and incrementally with respect to the reference pattern, leading to a progressive rise of d_2. The lag time τ here equals the time after electric induction. Switching off the field at $t - t_{on} = 600$ s allows the surface to slowly return to its original shape, thus causing a decrease in d_2 as the shape recovery is largely elastic. Remarkably, while the change in surface area is symmetric between field switch-on and -off (Figure 10.3d), the surface structure does not follow the same route upon expansion and contraction (Figure 10.3e). This hysteresis is clearly apparent from the finite d_2 plateau at long τ, which reflects plastic rearrangements. In a perfectly elastic system, each surface-attached TiO_2 nanoparticle would return exactly to its initial position after shape recovery, since the nanoparticles adhere strongly to the network and display negligible lateral displacement; hence, the original unperturbed speckle pattern would be regained, with $d_2 \to 0$. The height of the plateau at long τ is thus a measure for the fraction of the surface undergoing irreversible deformation. At

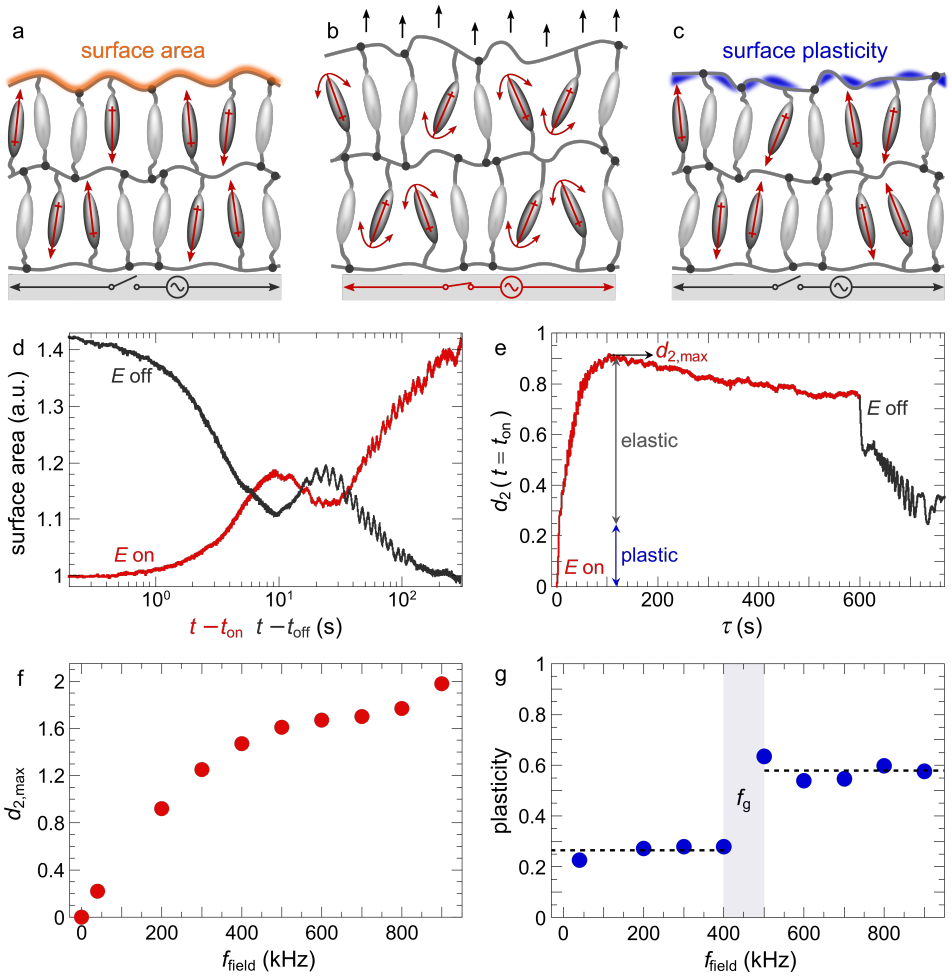

Figure 10.3. Shape-shifting elasticity and plasticity. **(a–c)** Schematic cross-sections of a liquid crystal polymer network in the field-off state **(a)**, after switching on a high-frequency AC field **(b)**, and after field switch-off and relaxation **(c)**. The electric field drives the polar mesogens into oscillation, causing local network plasticization and expansion. After field switch-off, elastic displacements are restored, yet plastic deformations (in blue) remain. The dimensions are not to scale. **(d)** Change in $\tilde{A}$ after switching a 200 kHz AC field on (—) and off (—), which are fully symmetric. **(e)** The corresponding surface structure function, referenced to $t = t_{on}$, shows hysteresis between field switch-on (—) and -off (—). The drop in d_2 measures the reversible, elastic deformation, whereas the plateau at long τ measures plastic strains. **(f)** Maximum d_2, reflecting total elastic plus plastic deformation, versus field frequency. **(g)** Unrecovered fraction of the surface structure change. A sharp transition from 400 to 500 kHz signals a sudden rise in plasticity, corresponding to a field-induced glass transition around the critical frequency f_g.

200 kHz, this height is approximately a quarter of the maximum d_2 ($d_{2,\max}$, Figure 10.3e).

Although the plasticity is relatively small at low field frequency, we must take into account that the total surface expansion is also rather limited. Digital holography even fails to detect any deformation,[24] implying that the height modulation is less than 10 nm. This is confirmed by the relatively small $d_{2,\max}$, which equals 0.9 instead of the intrinsic maximum value of 2. Indeed, the maximum d_2 is a good gauge of the total deformation amplitude; in agreement with DHM and simulations,[24] we find that $d_{2,\max}$ rises rapidly with increasing f_{field} at low field frequencies and reaches an optimum around 900 kHz (Figure 10.3f). The reduced change in surface area $\tilde{A}$ displays a very similar trend (Appendix Figure 10.A.4a). By contrast, the plasticity has a strikingly different dependence on f_{field}, showing two regimes with an abrupt transition around 400–500 kHz (Figure 10.3g and Appendix Figure 10.A.4b). We have estimated this plasticity from the ratio between the long-τ plateau ($d_{2,\min}$) and $d_{2,\max}$. Although this approach does not provide absolute values for the amount of plasticity, it offers a means to compare the relative plasticity with high resolution. Clearly, surface morphing occurs for all field frequencies with only partial recovery (Figure 10.3g). At low f_{field}, this deformation is small and largely in the linear elastic region, i.e. the field induces few irreversible structural changes. Beyond a critical frequency of 400–500 kHz, there is a sharp crossover towards significantly enhanced local plasticization. Analogous to the thermal glass transition (T_g) of the LCN, this critical frequency may signal the electrical glass transition f_g.

10.3.5 Electroplasticization by high AC frequency

If the critical field frequency is truly an electrical glass transition, we expect a peak in energy dissipation around f_g that accompanies the yielding process. To investigate this, we subject the LCN to a linear field sweep from 0 to 900 kHz at 3 kHz/s. Interestingly, the surface does not expand linearly with increasing field frequency, but instead exhibits pronounced undulations, as the dielectric interactions between the field and LCN keep changing during the sweep (Figure 10.4a). This oscillatory motion is reminiscent of elastic ringing. The 'ringing' of this coating is a complex phenomenon: not only does the field frequency change over time, but also the network modulus and density fluctuate strongly in response to the field, thus causing recoil and overshoot of the surface as it fails to meet the rapidly changing resonance conditions. In Chapter 9, Figure 9.4, we uncovered that the ringing frequency is proportional to the field frequency when a constant f_{field}

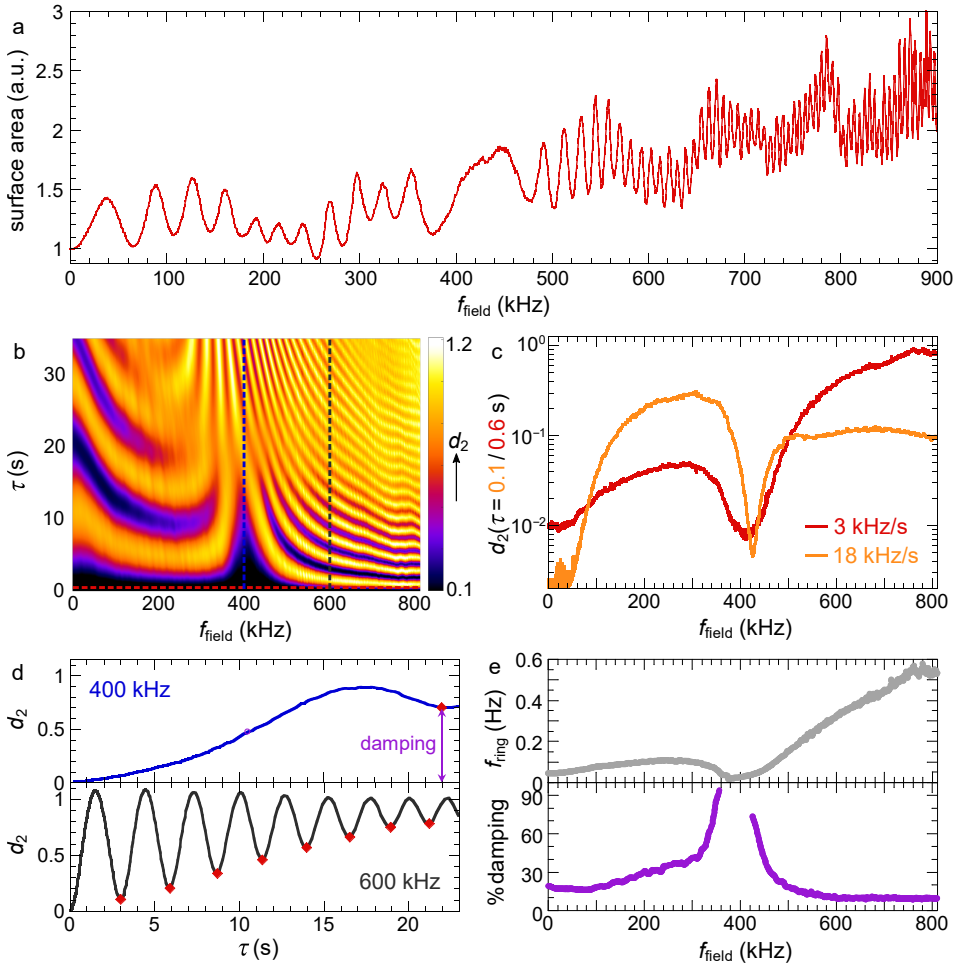

Figure 10.4. Electroplasticization by high-frequency AC field. **(a)** Change in $\tilde{A}$ and **(b)** d_2 spectrum during a field frequency sweep at 3 kHz/s. The surface expands with increasing f_{field} and exhibits undulations with decreasing period. A pronounced divergence of the period around critical frequency $f_g = 400$ kHz coincides with **(c)** a drop in the surface motility, signalling energy dissipation characteristic of a glass transition. The colours indicate different sweep rates. Note that a six-fold higher τ is used to compute d_2 for the six-fold slower sweep. **(d)** Vertical cross-sections through the spectrum in (b) at 400 and 600 kHz. Distinct elastic ringing is evident at 600 kHz: the surface does not expand monotonically with increasing lag time τ, but recurrently returns to an earlier position, manifest as a train of 'echoes' marked by ♦. **(e)** Field frequency dependence of the ringing frequency (top) and percent damping per period (bottom), extracted from the $d_2(\tau)$ curves. Both show a crossover at 400 kHz. While the ringing frequency vanishes at f_g, dissipation-induced damping diverges.

is applied. A similar trend is visible during this sweep, although a discontinuity appears between 400 and 500 kHz (Figure 10.4a).

To gain more insight into the origin of this discontinuity, we again revert to the structure function d_2, which we compute as a function of both f_{field} and τ (Figure 10.4b). A striking array of periodic undulations emerges, confirming that the surface repeatedly expands and contracts to an earlier position in an oscillatory manner. However, the oscillation frequency does not increase monotonically, but instead diverges around 400 kHz, suggesting a decoupling of the field and network expansion. This critical transition – also observed in Figure 10.3g – recurs in the one-point d_2 (Figure 10.4c, —) which is essentially a horizontal cross-section through Figure 10.4b. It is likely not governed by kinetics but predominantly thermodynamic in origin, since the crossover occurs after >100 s of sweeping the field, much longer than typical dielectric and relaxation time scales of the material. Moreover, a highly similar transition is visible for a faster f_{field} sweep of 18 kHz/s (Figure 10.4c, —). For very low sweep rate, the response is somewhat different, as elaborated in Appendix Figure 10.A.5.

10.3.6 Nanomechanical insight from surface oscillations

The periodicity of the $d_2(\tau)$ functions offers an opportunity to extract nanomechanical information from the ringing frequency and damping. While a typical d_2 curve increases continuously with increasing τ, we here observe a train of 'echoes' at integral multiples of the oscillation period. These echoes are particularly well visible when taking vertical cross-sections through Figure 10.4b, as shown for f_{field} = 400 and 600 kHz in Figure 10.4d. At 400 kHz, the ringing frequency f_{ring} is very low, yet at 600 kHz, $d_2(\tau)$ displays a nearly perfect sinusoidal undulation. The amplitude of the echoes (♦) gradually diminishes with increasing τ because each oscillation involves additional rearrangements. Note that the speckle fluctuations are averaged only over space, without any time averaging or smoothing, highlighting the remarkable sensitivity of LSI.

For each field frequency, we determine the ringing frequency from the position of the first $d_2(\tau)$ maximum. In line with our earlier observations, we do not find a linear relationship between f_{ring} and f_{field}, but rather a highly non-monotonic dependence (Figure 10.4e, top). The discontinuity around 400 kHz signifies a transient rise in energy dissipation indicative of a glass transition, with electrical energy converted into molecular rearrangements instead of powering surface undulations. Fourier transform of the raw intensity signal yields an identical trend (Appendix Figure 10.A.6), verifying the robustness of our method. Further validation is obtained when comparing the amount of damping at different field

frequencies (Figure 10.4d): while at 400 kHz the oscillation is almost fully damped after a single period, at 600 kHz the damping per period is only 9%. We estimate the percent damping as the ratio between the first d_2 minimum (i.e. echo) and maximum. Plotted versus f_{field}, this again reveals two distinct regimes centred at 400 kHz (Figure 10.4e, bottom). The percent damping can be considered analogous to the loss tangent $\tan(\delta)$ used in macroscopic mechanical analysis – a measure for the relative importance of dissipative and elastic processes. Indeed, a peak in $\tan(\delta)$ is a signature of a thermal glass transition.[41]

10.3.7 Thermal shift of electrical glass transition

The final support for our hypothesis is found in the temperature dependence of f_g. Thermally and electrically induced plasticization are closely connected, as already found in Figure 10.2b, stage II. Specifically, heat is expected to lower the field frequency at which electroplasticization occurs. We thus measure the surface deformation at $T = 40$ °C, which indeed displays a sharp discontinuity at a reduced f_{field} of ~200 kHz (Figure 10.5a). Taking a horizontal cross-section through the spectrum at $\tau = 0.6$ s, equivalent to Figure 10.5c, confirms the downward shift of f_g (Figure 10.5b). Interestingly, also the d_2 regime at low f_{field} is shifted towards longer time scales, and consequently the short-τ d_2 curve does not show two clear regimes. A likely explanation is a decreased amount and frequency of elastic deformations compared to viscous dissipation. Note that the d_2 intermittency is again much stronger than that at 25 °C (compare Figure 10.5b with Figure 10.4c),

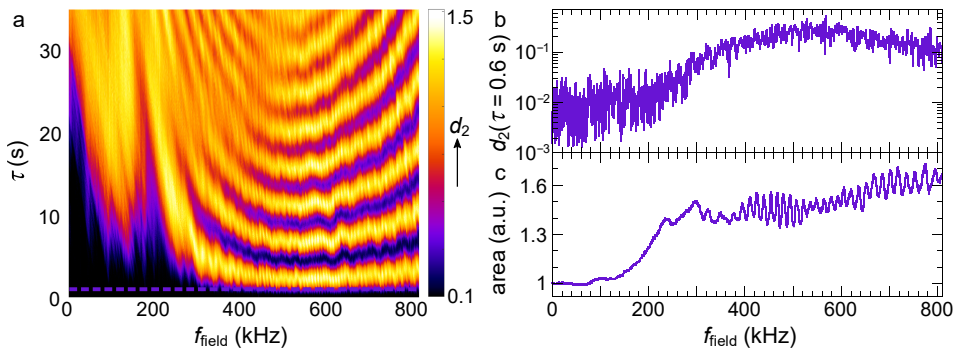

Figure 10.5. Thermal shift of f_g. **(a)** d_2 spectrum, **(b)** surface motility, and **(c)** change in $\tilde{A}$ during a field frequency sweep at 3 kHz/s and $T = 40$ °C. The discontinuity around ~200 kHz indicates an earlier onset of electroplasticization than at 25 °C. Note also the considerably reduced undulation frequency in (a) compared to Figure 10.4b.

indicating a more chaotic response of the LCN to the field, characteristic of the higher thermal energy. Also the change in surface area $\tilde{A}$ during the field sweep corroborates the faster onset of electroplasticization: while at 25 °C, significant surface expansion starts only around 400 kHz (Figure 10.4a), at 40 °C a rapid rise in $\tilde{A}$ is manifest already at 200 kHz (Figure 10.5c).

10.3.8 Microscopic interpretation

Our results reveal the existence of a true electric-field-induced devitrification of the LC polymer network at a critical field frequency of several hundreds of kHz. This raises the question what microscopic mechanisms inside the material underlie this glass transition.

The alternating electric field induces a pivoting motion of the dangling mesogens. Since these molecular oscillations are constrained and frustrated by the rigid environment of the glassy and crosslinked network, it is likely that they exhibit substantial disorder, which induces non-affinity in the thermal motions. In other rigid soft materials, both ordered[68] and glassy,[69,70] it was shown that increasing the amplitude of thermal non-affinities leads to a loss of material rigidity and possibly a solid-to-liquid transition, akin to the one we observe here. Moreover, the dynamic disorder created by the field-induced oscillations inside the LCN causes a volumetric expansion,[24,40,63] which reduces the material density and increases the effective distances between mesogens. This necessarily reduces the strength of the van der Waals interactions between neighbouring mesogens and provides an additional mechanism for the rigidity loss that must accompany devitrification. Rigidity in our LCN derives from both covalent bonds between monomers in the network and supramolecular interactions between mesogens, probably of the van der Waals type. The covalent network is most likely unaffected by the actuation, since the observed shape and volumetric changes are fully reversible.[24] The electroplasticization must therefore relate to a reduction of the supramolecular van der Waals interactions.

Finally, the question remains why devitrification in our experiments occurs at frequencies of hundreds of kHz. These frequencies are far too small to reflect natural dipolar resonances at the molecular level. By contrast, resonator-related vibrations that link to sample dimensions, such as the electrode distances, are much slower. Rather, these frequencies probably reflect the excitation of collective modes of motion of many mesogens in tandem, analogous to the excitation of phonons in an ordered lattice. We thus postulate that the critical field frequency to cross the glass transition is governed by long-ranged molecular vibrations related to intermolecular interactions. At present, there is insufficient knowledge of the

vibrational spectrum of collective modes in liquid crystal materials to provide a clear explanation for the values we have found. Since it appears that these collective effects are crucial to explain plasticization and actuation of active LCNs at a microscopic level, theoretical efforts in this area are highly needed.

10.4 Concluding remarks

Research into the engineering of active LCNs to date has relied on the fundamental premise that oscillating molecular dipoles cause plasticization of the network,[24–26,59] which ultimately enables the shape-shifting response from which these materials derive their appeal. We here provide the first conclusive evidence for this hypothesis, by revealing how LCN coatings are 'electroplasticized' by a high-frequency AC field. Using a nanoscale strain detection method based on laser speckle imaging, we uncover how small oscillatory forces, generated by embedded responsive mesogens, collectively induce an athermal glass transition. Molecular synchronization is crucial in this regard, as plasticity emerges only beyond a critical field frequency of 400–500 kHz. Around this frequency, we find pronounced discontinuities in strain nonlinearity, oscillation frequency and damping. These phenomena have interesting analogies with mechanical yielding processes observed in a variety of soft materials, ranging from yield stress fluids[60,71] to polymeric solids[61,72] and granular media,[62,73] where mechanical stress can induce a solid-to-liquid transition. In this study, the mechanical disturbance underlying the field-induced glass transition is not applied from the outside, but generated from within by the frustrated motion of polar mesogens in response to an electric field.

Our results not only support the existence of an electrical glass transition, but also provide new insights into optimization of the surface functionality. For example, fine-tuning the oscillation frequency to match human tactile perception allows for more efficient dynamic Braille interfaces.[32–34] In the context of biointerfaces, the spatiotemporal nanomechanics are key in signalling and regulating cell behaviour.[10,23] Most practical applications will benefit from reduced field frequencies, which involve less complex device configurations and lower power consumption. On the basis of the measured equivalence between T and f_{field}, we thus recommend lowering the network T_{g}, e.g. by extending the alkyl spacer length or by decreasing the crosslink density.

10.A Appendix

10.A.1 Differences between electroplasticization and HF welding

The electroplasticization described in this work has some resemblance with the phenomenon known as high-frequency (HF) welding or dielectric sealing.[65,66] In this process, an alternating electric field in the range of radio or microwave frequencies is used to generate heat inside a polar material, thus melting it and enabling weld formation. The rise in temperature is caused by intermolecular friction due to imperfect alignment of the chemical dipoles with the field. In other words, the electric current alternates so rapidly that the molecular dipoles pivot out of phase, inducing energy dissipation. Although both electroplasticization and high-frequency welding result from polarization of polar moieties by a high-frequency AC field, there are various fundamental differences:

- Dielectric heating forms the basis of HF welding, rendering the polar material very hot, whereas it plays only a limited role in our experiments. Real-time monitoring of the LCN surface temperature using an infrared sensor has demonstrated moderate heating of ~10 °C upon actuation at room temperature (see Chapter 9, Appendix Figure 9.A.3). This is insufficient to reach the thermal glass transition at 60–120 °C. The concomitant electrothermal expansion is estimated to be only ~8 nm rather than the actual 50–100 nm measured using DHM (see Chapter 9, Figure 9.2c).[24] The primary contribution to plasticization must therefore be mechanical in origin, allowing for a glass-to-rubber transition well below the original T_g.

- LSI reveals plasticization down to a field frequency of 40 kHz, which is three orders of magnitude below the radio frequencies typically used in HF welding (10–100 MHz). The molecular dipoles in our experiments will thus more easily stay in phase with the electrical current and minimize the intermolecular friction and heat production.

- We previously found that the surface expansion decreases beyond an overall sample temperature of ~60 °C, where the enhanced network mobility causes free volume to be filled rapidly.[24] Both the plasticization signal (stage II) and the volumetric expansion (stage III) *increase* with increasing field frequency (Chapter 9).[24] These findings confirm that the local dielectric heating is insufficient to cause thermal plasticization, which underlies HF welding, since otherwise a rise in dielectric heating would entail a reduction in free volume formation.

- High-frequency welding is applied to thermoplastics, while our LCNs are densely crosslinked.

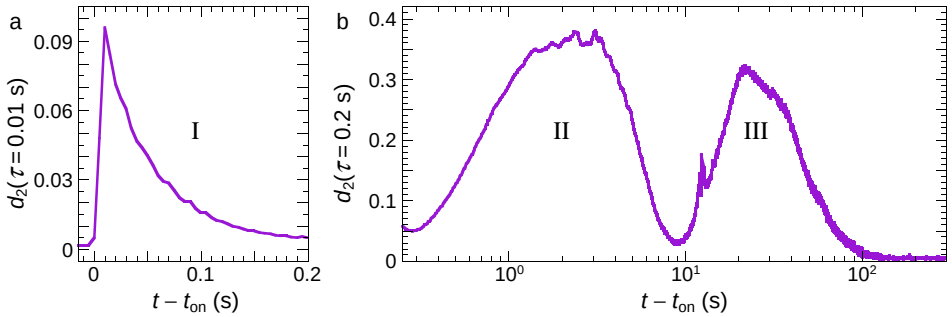

Figure 10.A.2. Morphing stages for a cholesteric alignment. The three stages in Figure 10.2a,b are not unique for a homeotropic alignment, but are highly similar for a cholesteric LCN of the same chemical composition. **(a)** Fast dielectric response to a 900 kHz AC field, and **(b)** successive network plasticization and deformation. The cholesteric (chiral nematic) phase is induced by adding a small amount of chiral LC diacrylate to the monomer mixture prior to photopolymerization. The resulting helical axis is perpendicular to the glass substrate, with helical pitch of ∼450 nm. The chiral dopant, 1,4:3,6-dianhydro-D-glucitol bis[4-[[4-[[[4-[{1-oxo-2-propenyl}oxy]butoxy]carbonyl]-oxy]benzoyl]oxy]benzoate], is obtained from BASF.

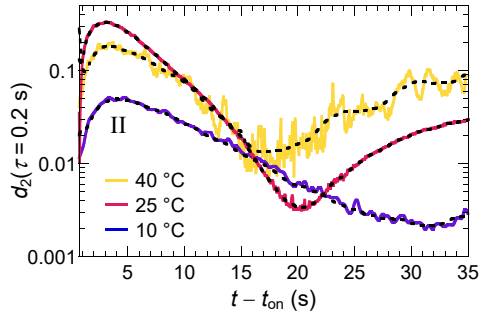

Figure 10.A.3. Zoom-in of Figure 10.2b. The electroplasticization stage II is plotted on a log–lin scale for clarity. To quantify the duration unambiguously, we first smooth the d_2 data using a moving average over 2.5 s (dashed black lines), followed by finding the minima around stage II. The time difference between these minima equals the duration, which decreases with increasing temperature (Figure 10.2e). The same procedure applies to stage III.

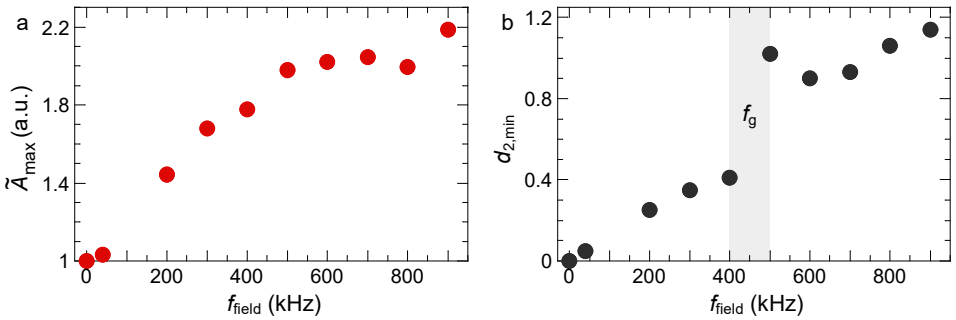

Figure 10.A.4. Extension of Figure 10.3. **(a)** Field frequency dependence of the maximum reduced surface area $\tilde{A}$ after field switch-on. Analogously to $d_{2,max}$ in Figure 10.3f, $\tilde{A}_{max}$ measures the total deformation amplitude and hence shows a similar positive trend. **(b)** Long-τ d_2 plateau after field switch-off, representing field-induced plastic rearrangements. The ratio between $d_{2,min}$ and $d_{2,max}$ gives the plasticity in Figure 10.3g. The grey vertical bar marks the electrical glass transition frequency.

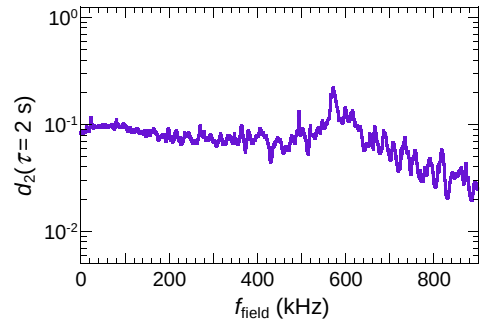

Figure 10.A.5. Surface motility during a field frequency sweep at 0.9 kHz/s. One-point d_2 function, similar to Figure 10.4c, yet for a very low sweep rate. Since the total sweep takes 1000 s in this case, the energy dissipation and elastic deformation are so gradual that clear regimes separated by f_g cannot be distinguished. Note that the τ values used to compute d_2 are chosen inversely proportional to the sweep rate, i.e. τ = 0.1, 0.6 and 2 s for sweep rates of 18, 3 and 0.9 kHz/s, respectively, to allow for direct comparison of the different sweeps.

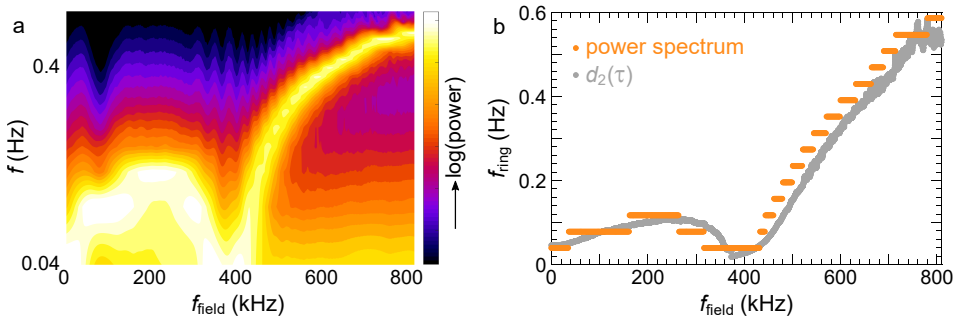

Figure 10.A.6. Field frequency dependence of the ringing frequency measured by Fourier transform (FT). **(a)** Frequency-domain equivalent of Figure 10.4b, computed using Fourier analysis of the raw speckle images. See Chapter 9 and ref. 58 for a detailed description of FT-LSI. **(b)** Comparison between the ringing frequency obtained from the d_2 spectrum in Figure 10.4b (identical to Figure 10.4e-top) and f_{ring} obtained from the power spectrum in (a). The latter is determined for every f_{field} as the frequency at which the power has a local maximum. Both curves show a highly similar trend, confirming the robustness of our method, yet f_{ring} from the power spectrum is inherently discrete.

References

[1] T. J. White, D. J. Broer. *Nat. Mater.* **14**, 1087–1098 (2015).

[2] F. Ge, Y. Zhao. *Adv. Funct. Mater.* p. 1901890 (2019).

[3] T. H. Ware, M. E. McConney, J. J. Wie, V. P. Tondiglia, T. J. White. *Science* **347**, 982–984 (2015).

[4] H. Finkelmann, E. Nishikawa, G. G. Pereira, M. Warner. *Phys. Rev. Lett.* **87**, 015501 (2001).

[5] Y. Yu, M. Nakano, T. Ikeda. *Nature* **425**, 145 (2003).

[6] M. Camacho-Lopez, H. Finkelmann, P. Palffy-Muhoray, M. Shelley. *Nat. Mater.* **3**, 307–310 (2004).

[7] M. E. McConney, A. Martinez, V. P. Tondiglia, K. M. Lee, D. Langley, I. I. Smalyukh, T. J. White. *Adv. Mater.* **25**, 5880–5885 (2013).

[8] S. Iamsaard, S. J. Aßhoff, B. Matt, T. Kudernac, J. J. L. M. Cornelissen, S. P. Fletcher, N. Katsonis. *Nat. Chem.* **6**, 229 (2014).

[9] H. K. Bisoyi, Q. Li. *Chem. Rev.* **116**, 15089–15166 (2016).

[10] G. Koçer, J. ter Schiphorst, M. Hendrikx, H. G. Kassa, P. Leclère, A. P. H. J. Schenning, P. Jonkheijm. *Adv. Mater.* **29**, 1606407 (2017).

[11] A. H. Gelebart, D. J. Mulder, M. Varga, A. Konya, G. Vantomme, E. W. Meijer, R. L. B. Selinger, D. J. Broer. *Nature* **546**, 632–636 (2017).

[12] X. Pang, J.-a. Lv, C. Zhu, L. Qin, Y. Yu. *Adv. Mater.* p. 1904224 (2019).

[13] M. Chen, B. Yao, M. Kappl, S. Liu, J. Yuan, R. Berger, F. Zhang, H.-J. Butt, Y. Liu, S. Wu. *Adv. Funct. Mater.* p. 1906752 (2019).

[14] H. Shahsavan, S. M. Salili, A. Jákli, B. Zhao. *Adv. Mater.* **29**, 1604021 (2017).

[15] G. Babakhanova, T. Turiv, Y. Guo, M. Hendrikx, Q.-H. Wei, A. P. H. J. Schenning, D. J. Broer, O. D. Lavrentovich. *Nat. Commun.* **9**, 456 (2018).

[16] A. Cao, R. J. H. van Raak, X. Pan, D. J. Broer. *Adv. Funct. Mater.* **29**, 1900857 (2019).

[17] Y. Liu, B. Xu, S. Sun, J. Wei, L. Wu, Y. Yu. *Adv. Mater.* **29**, 1604792 (2017).

[18] O. M. Wani, R. Verpaalen, H. Zeng, A. Priimagi, A. P. H. J. Schenning. *Adv. Mater.* **31**, 1805985 (2019).

[19] R. Lan, J. Sun, C. Shen, R. Huang, L. Zhang, H. Yang. *Adv. Funct. Mater.* **29**, 1900013 (2019).

[20] J. E. Stumpel, C. Wouters, N. Herzer, J. Ziegler, D. J. Broer, C. W. M. Bastiaansen, A. P. H. J. Schenning. *Adv. Opt. Mater.* **2**, 459–464 (2014).

[21] W. Lehmann, H. Skupin, C. Tolksdorf, E. Gebhard, R. Zentel, P. Krüger, M. Lösche, F. Kremer. *Nature* **410**, 447–450 (2001).

[22] C. Ohm, M. Brehmer, R. Zentel. *Adv. Mater.* **22**, 3366–3387 (2010).

[23] A. Agrawal, H. Chen, H. Kim, B. Zhu, O. Adetiba, A. Miranda, A. C. Chipara, P. M. Ajayan, J. G. Jacot, R. Verduzco. *ACS Macro Lett.* **5**, 1386–1390 (2016).

[24] D. Liu, N. B. Tito, D. J. Broer. *Nat. Commun.* **8**, 1526 (2017).

[25] W. Feng, D. J. Broer, D. Liu. *Adv. Mater.* **30**, 1704970 (2018).

[26] W. Feng, D. J. Broer, D. Liu. *Adv. Funct. Mater.* p. 1901681 (2019).

[27] Z. S. Davidson, H. Shahsavan, A. Aghakhani, Y. Guo, L. Hines, Y. Xia, S. Yang, M. Sitti. *Sci. Adv.* **5**, eaay0855 (2019).

[28] D. Liu, D. J. Broer. *Angew. Chem., Int. Ed.* **53**, 4542–4546 (2014).

[29] D. Liu, D. J. Broer. *Soft Matter* **10**, 7952–7958 (2014).

[30] H. Shahsavan, S. M. Salili, A. Jákli, B. Zhao. *Adv. Mater.* **27**, 6828–6833 (2015).

[31] A. H. Gelebart, D. Liu, D. J. Mulder, K. H. J. Leunissen, J. van Gerven, A. P. H. J. Schenning, D. J. Broer. *Adv. Funct. Mater.* **28**, 1705942 (2018).

[32] C. J. Camargo, H. Campanella, J. E. Marshall, N. Torras, K. Zinoviev, E. M. Terentjev, J. Esteve. *Macromol. Rapid Commun.* **32**, 1953–1959 (2011).

[33] C. J. Camargo, H. Campanella, J. E. Marshall, N. Torras, K. Zinoviev, E. M. Terentjev, J. Esteve. *J. Micromech. Microeng.* **22**, 075009 (2012).

[34] N. Torras, K. Zinoviev, C. J. Camargo, E. M. Campo, H. Campanella, J. Esteve, J. E. Marshall, E. M. Terentjev, M. Omastová, I. Krupa, P. Teplický, B. Mamojka, P. Bruns,

B. Roeder, M. Vallribera, R. Malet, S. Zuffanelli, V. Soler, J. Roig, N. Walker, D. Wenn, F. Vossen, F. M. H. Crompvoets. *Sens. Actuators, A* **208**, 104–112 (2014).

[35] P. Karageorgiev, D. Neher, B. Schulz, B. Stiller, U. Pietsch, M. Giersig, L. Brehmer. *Nat. Mater.* **4**, 699–703 (2005).

[36] G. J. Fang, J. E. Maclennan, Y. Yi, M. A. Glaser, M. Farrow, E. Korblova, D. Walba, T. E. Furtak, N. A. Clark. *Nat. Commun.* **4**, 1521 (2013).

[37] N. Hurduc, B. C. Donose, A. Macovei, C. Paius, C. Ibanescu, D. Scutaru, M. Hamel, N. Branza-Nichita, L. Rocha. *Soft Matter* **10**, 4640–4647 (2014).

[38] J. Vapaavuori, A. Laventure, C. G. Bazuin, O. Lebel, C. Pellerin. *J. Am. Chem. Soc.* **137**, 13510–13517 (2015).

[39] H. Zhou, C. Xue, P. Weis, Y. Suzuki, S. Huang, K. Koynov, G. K. Auernhammer, R. Berger, H.-J. Butt, S. Wu. *Nat. Chem.* **9**, 145–151 (2017).

[40] D. Liu, D. J. Broer. *Nat. Commun.* **6**, 8334 (2015).

[41] K. Kumar, A. P. H. J. Schenning, D. J. Broer, D. Liu. *Soft Matter* **12**, 3196–3201 (2016).

[42] K. Kumar, C. Knie, D. Bléger, M. A. Peletier, H. Friedrich, S. Hecht, D. J. Broer, M. G. Debije, A. P. H. J. Schenning. *Nat. Commun.* **7**, 11975 (2016).

[43] A. Shimamura, A. Priimagi, J.-i. Mamiya, T. Ikeda, Y. Yu, C. J. Barrett, A. Shishido. *ACS Appl. Mater. Interfaces* **3**, 4190–4196 (2011).

[44] Y. Yue, Y. Norikane, R. Azumi, E. Koyama. *Nat. Commun.* **9**, 3234 (2018).

[45] M. Pilz da Cunha, E. A. J. van Thoor, M. G. Debije, D. J. Broer, A. P. H. J. Schenning. *J. Mater. Chem. C* **7**, 13502–13509 (2019).

[46] K. G. Yager, C. J. Barrett. *Macromolecules* **39**, 9320–9326 (2006).

[47] J. M. Harrison, D. Goldbaum, T. C. Corkery, C. J. Barrett, R. R. Chromik. *J. Mater. Chem. C* **3**, 995–1003 (2015).

[48] H. Bolay, U. Reuter, A. K. Dunn, Z. Huang, D. A. Boas, M. A. Moskowitz. *Nat. Med.* **8**, 136–142 (2002).

[49] P. Zakharov, A. C. Völker, M. T. Wyss, F. Haiss, N. Calcinaghi, C. Zunzunegui, A. Buck, F. Scheffold, B. Weber. *Opt. Express* **17**, 13904–13917 (2009).

[50] A. Nadort, K. Kalkman, T. G. van Leeuwen, D. J. Faber. *Sci. Rep.* **6**, 25258 (2016).

[51] W. Heeman, W. Steenbergen, G. M. van Dam, E. C. Boerma. *J. Biomed. Opt.* **24**, 080901 (2019).

[52] M. Erpelding, A. Amon, J. Crassous. *Phys. Rev. E* **78**, 046104 (2008).

[53] A. Amon, A. Mikhailovskaya, J. Crassous. *Rev. Sci. Instrum.* **88**, 051804 (2017).

[54] M.-Y. Nagazi, G. Brambilla, G. Meunier, P. Marguerès, J.-N. Périé, L. Cipelletti. *Opt. Lasers Eng.* **88**, 5–12 (2017).

[55] H. M. van der Kooij, A. Susa, S. J. García, S. van der Zwaag, J. Sprakel. *Adv. Mater.* **29**, 1701017 (2017). **(Chapter 8)**

[56] H. M. van der Kooij, S. Dussi, G. T. van de Kerkhof, R. A. M. Frijns, J. van der Gucht, J. Sprakel. *Sci. Adv.* **4**, eaar1926 (2018). **(Chapter 7)**

[57] T. Verho, P. Karppinen, A. H. Gröschel, O. Ikkala. *Adv. Sci.* **5**, 1700635 (2018).

[58] J. Buijs, J. van der Gucht, J. Sprakel. *Sci. Rep.* **9**, 13279 (2019).

[59] H. M. van der Kooij, S. A. Semerdzhiev, J. Buijs, D. J. Broer, D. Liu, J. Sprakel. *Nat. Commun.* **10**, 3501 (2019). **(Chapter 9)**

[60] D. Bonn, M. M. Denn. *Science* **324**, 1401–1402 (2009).

[61] H. G. H. van Melick, L. E. Govaert, H. E. H. Meijer. *Polymer* **44**, 2493–2502 (2003).

[62] E. I. Corwin, H. M. Jaeger, S. R. Nagel. *Nature* **435**, 1075–1078 (2005).

[63] D. Liu, C. W. M. Bastiaansen, J. M. J. den Toonder, D. J. Broer. *Macromolecules* **45**, 8005–8012 (2012).

[64] D. J. Pine, D. A. Weitz, J. X. Zhu, E. Herbolzheimer. *J. Phys. France* **51**, 2101–2127 (1990).

[65] J. G. Drobny, *Handbook of thermoplastic elastomers* (Elsevier, 2014), chap. 4.12.2.6 High frequency (RF) welding.

[66] S. Hollande, J.-L. Laurent, T. Lebey. *Polymer* **39**, 5343–5349 (1998).

[67] H. K. Bisoyi, T. J. Bunning, Q. Li. *Adv. Mater.* **30**, 1706512 (2018).

[68] J. Sprakel, A. Zaccone, F. Spaepen, P. Schall, D. A. Weitz. *Phys. Rev. Lett.* **118**, 088003 (2017).

[69] A. Zaccone, E. Scossa-Romano. *Phys. Rev. B* **83**, 184205 (2011).

[70] A. Zaccone, E. M. Terentjev. *Phys. Rev. Lett.* **110**, 178002 (2013).

[71] P. Coussot, Q. D. Nguyen, H. T. Huynh, D. Bonn. *Phys. Rev. Lett.* **88**, 175501 (2002).

[72] A. D. Printz, A. V. Zaretski, S. Savagatrup, A. S.-C. Chiang, D. J. Lipomi. *ACS Appl. Mater. Interfaces* **7**, 23257–23264 (2015).

[73] J. A. Dijksman, G. H. Wortel, L. T. H. van Dellen, O. Dauchot, M. van Hecke. *Phys. Rev. Lett.* **107**, 108303 (2011).

Chapter 11

General discussion

"It is indeed an endless cycle of imagination and concentration,
of divergence and convergence,
of playing and thinking
that determines the rhythm of science and scholarship."
– Prof. Robbert Dijkgraaf (1960–)

In this thesis, we have focused and expanded on many aspects of the title. Here, we will end with one last cycle of convergence and divergence. We will first unite all chapters, reflect upon the central themes, and identify potential blind spots. Finally, we will scatter and diffuse our attention by broadening the perspectives of laser speckle imaging.

11.1 Quantitative imaging of nanodynamics in polymer materials

Designing sustainable polymer materials with advanced properties from the bottom up is becoming increasingly important – whether it concerns water-borne paints, high-performance elastomers, or other materials of the future. Given the dwindling natural resources and ever-growing demand for multi-purpose applications, material development cannot solely rely on trial and error or serendipitous discoveries. Rather, we must strive to gain a deep understanding of the mechanisms underlying the emergence of functionality. This knowledge begins at the nanoscale, where single colloids and polymer chains are constantly moving. In isolation, these motions may be fairly simple and well understood. Yet, together in a larger aggregate, all sorts of feedback and surprising effects may develop, which render the system highly complex and give rise to unforeseen collective phenomena. Grasping the core of these collective effects is pivotal in the design and control of novel sophisticated materials.

An extra level of complexity emerges when external forces come into play that drive the material out of equilibrium, which is a central thread in this thesis. Examples are a gradient in chemical potential that causes evaporation (Chapters 2–6); a strain field that induces heterogeneous deformations (Chapter 7); surface tension that prompts self-healing (Chapter 8); and an electric field that actuates shape-morphing (Chapters 9 and 10). In all these cases, the macroscopic behaviour is more a function of collective properties than of the underlying details of individual polymer chains and colloids. Instrumentation to visualize the collective dance of the nanoscale building blocks is therefore indispensable.

In this thesis, we have endeavoured to develop imaging methods optimally suited for this task. We have established an extensive experimental toolbox to unravel the nanoscale dynamics and mechanics of various complex polymer

dispersions and elastomers, focusing on the most crucial period in their lifetime: the drying of paints (Chapters 2–6); the fracture and self-healing of elastomers (Chapters 7 and 8); and the morphing of liquid crystal polymer networks (Chapters 9 and 10). Our quest has been quite challenging, since the collective 'dance moves' often span a wide range of length and time scales. Moreover, even the minutest motions matter.

To address this challenge, we have employed a two-pillar approach. In Part I of this thesis, we have synthesized semi-transparent model paints with well-defined properties, and used traditional bright-field microscopy to investigate drying phenomena across multiple scales. In conjunction with theoretical calculations for a quantitative analysis, and scanning electron microscopy for nanoscale information, this approach has resulted in a quite comprehensive mechanistic understanding. In Parts II and III of this thesis, we have adapted and improved a relatively unexplored optical method, laser speckle imaging (LSI), to reveal the hidden dynamics in non-transparent polymer systems. By tapping into the exceptionally broad temporal range of LSI and its potential to resolve nanometric deformations, we have seen things never seen before in paints and elastomers. These views are more than subjective, as we have extracted an additional wealth of quantitative information from our raw data using tailor-made image processing algorithms.

11.2 Limitations of LSI

"To light a candle is to cast a shadow." – Ursula K. Le Guin (1929–2018)

There is no light without darkness. While a candle illuminates most of its surroundings, it inevitably leaves parts in the dark. Analogously, every technique has its flaws, and LSI is no exception. Here we describe these limitations and illustrate them with examples from our own research.

11.2.1 Optical transparency

The most obvious drawback of LSI is its inapplicability to transparent materials, for which the prerequisite of multiple scattering breaks down. In those cases, the incident photons will primarily be transmitted rather than scattered, and the resultant signal thus cannot be properly interpreted using the formalism of diffusing wave spectroscopy (DWS).[1,2] This will lead to serious imaging artefacts if neglected. For instance, the drying of a clearcoat, i.e. a non-pigmented paint, is almost invisible in an LSI experiment, and will therefore remain underexposed. Cracks in such a coating *do* strongly scatter the light (Figure 11.1a) and consequently appear as erroneous localized regions of activity (Figure 11.1b–d).

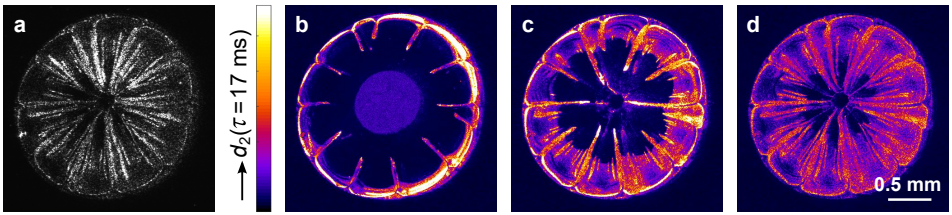

Figure 11.1. Limitation of LSI: insufficient scattering to allow for reliable analysis. **(a)** Raw speckle pattern of a pigment-free paint droplet dried on glass, at t = 320 s after deposition. The cracks scatter considerably more than the intermediate regions. **(b–d)** Time-lapse d_2 maps of the preceding crack propagation. **(b)** t = 210 s after deposition. The dynamics in the central wet region are greatly underestimated because of the low scattering intensity i.e. high transparency. **(c)** t = 280 s, and **(d)** t = 320 s (corresponding to (a)). The colour coding and scale bar apply to all d_2 images.

A relatively straightforward solution is to introduce inert scatterers into a transparent material, e.g. titania or silica nanoparticles. Less than 2 vol% of nanoparticles generally suffices to render the material turbid without altering the properties of the pristine material noticeably. We have used this strategy in Chapters 6–10.

While DWS analysis of transparent samples is indisputably wrong, a more difficult scenario concerns translucent samples that are neither transparent nor opaque, for which the suitability of LSI and resultant data interpretation are not clear-cut. The intermediate-scattering regime represents the most challenging situation, as no rigorous theory can be applied.[3] In this cross-over regime between single and highly multiple scattering, the laser photons experience a complex mixture of single, double, triple etc. and frequent scattering, and hence the interpretation of the intensity correlation function becomes significantly complicated. Theoretical efforts in this regard generally fall short and are strongly sample dependent. Two possible workarounds are: (i) elimination of the *non*-singly scattered light to permit dynamic light scattering (DLS) analysis;[4–6] or conversely, (ii) suppression of the weakly scattered light to enable DWS-based interpretation. We have adopted the latter strategy in Chapters 9 and 10. Indeed, the contribution of low-order scattering paths can considerably be reduced by extracting the depolarized light alone, which we have realised in all chapters of this thesis by means of a linear polarizer in the detection path. Scattering has the useful feature that it decreases the light polarization. More precisely, the degree of polarization falls off exponentially with the number of scattering events.[7] Single scattering by perfectly spherical objects preserves the degree and state of polarization. Although selective detection

of depolarized light cannot fully eliminate weakly scattered photons, it strongly shifts the detected path length distribution towards longer paths, thus allowing for semi-quantitative LSI analysis.

11.2.2 Two-dimensionality

In its current form, LSI provides a two-dimensional projection of processes occurring in three dimensions. This projection is a highly complex convolution of the dynamics at different depths inside the material, in addition to the inevitable lateral averaging (see Section 11.2.3). More specifically, the locally measured correlation function is a weighted average over all detected photon path lengths and dynamics probed by those photons. This convolution is further complicated by gradients in the scatterer concentration and concomitant gradients in the transport mean free path ℓ^*, which is the step length in the diffusive photon path (see Section 11.2.7). Especially in drying coatings, such gradients are unavoidable, as the latex particles accumulate at the air–water interface. Moreover, ℓ^* usually evolves over time, hence the depth probed is both spatially and temporally nonuniform.

Even a relatively simple system, e.g. a drying droplet containing only polystyrene colloids on a glass substrate, entails an abundance of spatio-temporal variations in ℓ^* and the internal dynamics (Figure 11.2a–d). These dynamics are not only heterogeneous in time and the x, y-plane, which we *can* resolve using LSI, but also in the depth direction, which is not directly accessible. For instance, in Figure 11.2 we clearly discern the coffee-ring effect[8,9] and rush-hour effect,[10] yet we cannot identify the underlying hydrodynamic vortices in the z-direction. Furthermore, the particles not only accumulate at the outer periphery, but also at the upper air–water interface, which cannot be explored. The origin of the stripes along the

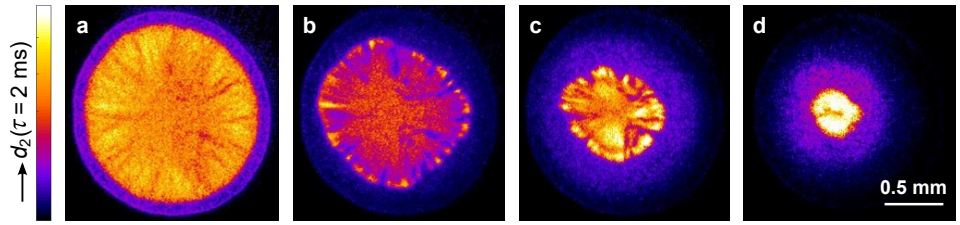

Figure 11.2. Limitation of LSI: depth-averaging. **(a–d)** Time-lapse 2D d_2 images of an evaporating polystyrene latex droplet on glass. While the coffee-ring and rush-hour effects are evident, the underlying complex 3D fluid flows remain obscured. (a) t = 120 s after deposition, (b) t = 125 s, (c) t = 126.5 s, and (d) t = 127.5 s. The colour coding and scale bar apply to all images.

azimuth also remains elusive. Most likely, these striations represent alternating regions of more and less densely packed particles, but insight into the governing hydrodynamic instabilities requires access to the third spatial dimension. While the d_2 function is ideal for exposing lateral variations in local mobility, it cannot yet reveal heterogeneities in depth and ℓ^* which are closely connected. Depth-resolved LSI strategies are highly recommended in this regard (see Section 11.4.1).

11.2.3 Spatial blurring

One of the key foundations of DWS and LSI is photon diffusion. An undesired yet inevitable side effect is spreading of the photons across dynamic boundaries: the location where a photon enters a turbid material generally deviates from the point where this photon exits, since it diffuses inside the sample before egressing from the surface, instead of merely reflecting off the surface. As a result, the output scattered light distribution is always a blurred version of the illumination pattern. The real dynamics underlying all d_2 images in this thesis are therefore sharper than they appear. We have modelled, discussed and quantified these effects for the forward-scatter geometry in Chapter 7, Appendix Figure 7.A.2. A comprehensive theoretical and numerical treatment for back-scatter LSI is given in ref. 11. In non-steady-state experiments, it is difficult to quantify the spatial extent of the blurring, as ℓ^* is continuously evolving and spatially non-uniform.

A clear example of convoluted lateral blurring and a mobility gradient is visible around propagating crack tips in a partially-dried latex coating. Interestingly, LSI allows us to not only see the cracks themselves – as other, conventional microscopy techniques do – but also the deforming area around the crack tips (Figure 11.3a). Each tip is surrounded by a pronounced zone of plastic deformation, known as the process zone, where particles are being rearranged and pushed aside as the crack advances. In Section 11.3.2, we benefit from these distinct zones to extract information about the film properties, and to learn how cracks can be stopped in their tracks – or even better, prevented from appearing in the first place. It is however challenging to disentangle the contribution of spatial blurring from the real strain gradient. An indication that the latter dominates in Figure 11.3a is the d_2 anisotropy around the tips, which is biased towards the direction perpendicular to the propagation direction. Indeed, cracks are known to release more stress normal to their edges than along their growth direction.[12,13]

Also in the case of delamination events, spatial blurring is evident (see Figure 11.3b and Chapter 5, Figure 5.3e). After cohesive cracking, fragments of the coating successively lose their adhesion to the glass substrate, manifest as delineated bursts of activity. Although the delaminating fragment is quite sharply demarcated, the

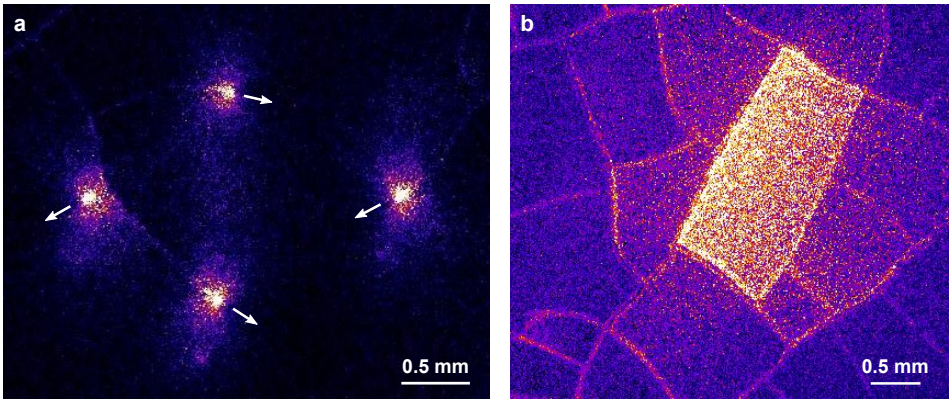

Figure 11.3. Limitation of LSI: spatial blurring of dynamics. **(a)** d_2 map of advancing crack tips in a ~100 μm thick water-saturated coating of rigid colloids. The arrows indicate the propagation directions. The d_2 gradients around the tips are likely convolutions of true strain gradients and blurring by diffusive photon transport. Computed for $\tau = 16$ ms. **(b)** d_2 map of delamination (adhesive failure) in a different coating of similar composition to (a). The sheets surrounding the detaching plane also light up, which is more likely a blurring artefact than due to mechanical connection. Computed for $\tau = 40$ ms.

surrounding sheets also light up to a smaller extent. This seemingly long-ranged mobility is more likely due to long-distance photon diffusion than arising from mechanical connection between the fragments.

A potential solution to the blurring artefact is currently being designed and implemented in our group in a follow-up project, conducted by PhD student Jesse Buijs. Instead of using wide-field illumination, the essence of this approach is point illumination of the sample of interest, in which case both the photon entry and exit points are known.[14,15] Images can be reconstructed by scanning a focused light source over the sample and recording the back-scattered pattern for every illumination point. In Section 11.4.1, we explain how this strategy may improve LSI in another major area, namely by providing depth information. An obvious disadvantage is the relatively long time required to build images for multiple illumination points, implying that this method is suitable only for slowly evolving, steady-state, or equilibrium systems. Further technical details are beyond the scope of this thesis.

11.2.4 Limited structural information

Strictly speaking, LSI provides insight into dynamics alone and does not uncover the local structure, because the spatial averaging and granularity of the speckle pattern scramble all structural features smaller than a few speckles (~10–100 μm). In practice, however, some structural information can still be indirectly inferred from the dynamics. Examples in this thesis are: visualizing the roughness of brush-applied paint on plywood (Chapter 5, Section 5.3.5); differentiating coalesced particles from deformed particles (Chapter 6, Section 6.5); and deducing heterogeneities in particle packing from crack patterns (Section 11.3.2). To some extent, even direct access to the local structure is attainable by measuring variations in the average scattering intensity. Examples in this thesis are: changes in the surface texture of liquid crystal networks (Chapters 9 and 10); crack locations (Figure 11.1a); and sintering of powder coatings (Section 11.3.1). Nevertheless, LSI is certainly not the method of choice when it comes to structural details. Its non-invasive nature does allow for direct correlation with complementary techniques. For instance, the studied sample can afterwards be transferred to a scanning electron microscope or atomic force microscope to scrutinize the nanoscopic surface morphology, or to a magnetic resonance or X-ray tomography facility to probe the three-dimensional microstructure. The nanoscale dynamics and ensuing structure could thus be accurately linked, even for the same field of view.

11.2.5 Light absorption

Each LSI measurement will involve a certain degree of light absorption by the material. In this thesis, we have considered these effects negligible, as most of our studied materials absorb only a small fraction of 532-nm light. The incident laser light is consequently scattered rather than transformed into heat. In other words, $\ell^* \ll \ell_a$, with ℓ_a the characteristic absorption length – defined as the distance over which the intensity of light in a material decreases by a factor of e^{-1} due to absorption. For dark materials, absorption must certainly be taken into account. The consequences thereof are twofold: (i) the incident light will locally heat the material, and (ii) absorption will change the path length distribution $P(s)$. Specifically, long paths are attenuated more strongly than short paths,[14] thus suppressing the correlation decay at short τ. The simplest way to incorporate these effects is by assuming that absorption exponentially attenuates paths according to their path length,[2] so that $P(s)$ can be replaced by $P(s) \exp(-s/\ell_a)$ in the fundamental equation for $g_1(\tau)$ (see Chapter 1, Section 1.4.2):

$$g_1(\tau) = \int_0^\infty P(s)\, \exp\left(-s/\ell_a\right) \exp\left(-s{k_0}^2 \left[\ell^* f(\mathbf{U}) + \langle \Delta r^2(\tau)\rangle / 3\ell^*\right]\right) \mathrm{d}s$$

$$= \int_0^\infty P(s)\, \exp\left(-s{k_0}^2 \left[\ell^* f(\mathbf{U}) + \langle \Delta r^2(\tau)\rangle / 3\ell^* + 1/{k_0}^2\ell_a\right]\right) \mathrm{d}s \qquad (11.1)$$

The field correlation function for the back-scatter geometry can then be written as:

$$g_1(\tau) \approx \exp\left(-\gamma\, k_0 \sqrt{3\ell^{*2} f(\mathbf{U}) + \langle \Delta r^2(\tau)\rangle + 3\ell^*/{k_0}^2\ell_a}\right) \qquad (11.2)$$

In the forward-scatter geometry, the full expression becomes:

$$g_1(\tau) \approx \frac{k_0\, h \sqrt{3f(\mathbf{U}) + \langle \Delta r^2(\tau)\rangle/\ell^{*2} + 3/{k_0}^2\ell_a\ell^*}}{\sinh\left[k_0\, h \sqrt{3f(\mathbf{U}) + \langle \Delta r^2(\tau)\rangle/\ell^{*2} + 3/{k_0}^2\ell_a\ell^*}\right]} \qquad (11.3)$$

Equation (11.3) bears purely theoretical relevance. In practice, if absorption is sufficiently strong to affect g_1 significantly, the forward-scattering signal will anyhow be too low for reliable measurements. Substantial absorption thus renders forward-scatter LSI unusable per se. In the back-scatter geometry, by contrast, the effects can be measurable and profound. Quantification of ℓ_a is important in those cases, especially at short correlation times, when the decay of g_1 is dominated by the last term in Equation (11.2).

We have first-hand experienced the effects of absorption while measuring asphaltic bitumen (Figure 11.4a). In collaboration with Greet Leegwater from the section Pavement Engineering at the TU Delft, we aimed to study the healing of notched bitumen using LSI.[16] Unfortunately, the impact of a 1 Watt laser beam caused the pitch black specimen to melt, because the temperature locally increased to 60 °C (Figure 11.4b). Not only was the resultant smell not very pleasant – a notorious phenomenon on hot summer days in traffic – but also was the quiescent state of the bitumen disturbed, precluding accurate measurements of the processes of interest. The viscoelastic properties of bitumen are strongly temperature dependent,[17] and temperature gradients due to differential heating are therefore undesired. Indeed, flow towards the notch was greatly enhanced under the high laser power (Figure 11.4c).

The easiest solution would be to remove excess heat by connecting the sample to a heat sink. Alternatively, in the case of bitumen, one could also apply the time–temperature superposition principle. According to this principle, dynamics at elevated temperatures are essentially the same as those at low temperatures, yet occurring on shorter time scales. Another option is to choose a different

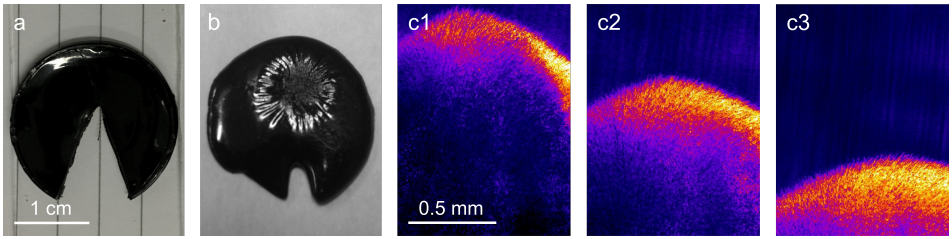

Figure 11.4. Limitation of LSI: light absorption and consequent sample heating. **(a)** Bitumen specimen prior to an LSI measurement. Image courtesy of Greet Leegwater. **(b)** Specimen after illuminating the notch tip with a 1 Watt laser beam for 18 hours. The laser-induced heating greatly accelerated closure of the notch, and additionally damaged the bitumen surface. **(c1–c3)** Time-lapse d_2 images of heating-assisted healing of bitumen, computed for $\tau = 0.1$ s. The time steps are 40 s.

illumination wavelength at which the material does not absorb significantly. For bitumen, this means longer wavelengths.[18] Simply reducing the laser power and increasing the camera exposure time will often not suffice; in the experiment above, the exposure time was already at its maximum of 0.1 s, thus limiting the frame rate to <10 fps. Strong light absorption inherently necessitates a higher laser power to achieve sufficient scattered signal at the detector, which further aggravates the absorption and heating problems.

11.2.6 Scrambling of length scales and anisotropy

LSI provides no direct means of relating dynamics to a single length scale or local anisotropy. Because the photons have been scattered numerous times when reaching the detector, they have lost all information about directionality and angular dependence. In fact, ℓ^* can be physically interpreted as the average distance a photon has to travel before its direction is completely randomized (see Section 11.2.7).[2] Each photon path typically constitutes many random-walk steps of length ℓ^*. Hence, the detection angle θ in LSI does not possess the same significance as it does in the single-scattering limit, such as in dynamic light scattering (DLS). This angle is defined as the angle of detection with respect to the direction of the incident laser beam. In DLS experiments, it provides a quantitative measure of the scale of observation, and can thus be varied to scan different spatial scales. More precisely, $1/q$ sets the length scale at which motion is probed, with q the scattering vector, defined as $q = 4\pi n \sin(\theta/2)/\lambda_0$. Here, n is the refractive index of the medium and λ_0 is the laser wavelength in vacuum. The field correlation function can subsequently be related to the mean-square displacement of the scatterers via: $g_1(q,\tau) = \exp\left(-q^2\langle\Delta r^2(\tau)\rangle/6\right)$.[19]

The appearance of k_0 instead of q in Equations (11.1) to (11.3) emphasizes the absence of a well-defined scattering angle in LSI. Fortunately, this also means that the precise detection angle is not critical, since the multiply-scattered light exits almost equally in all directions. Meticulous alignment of the optical components, as vital in DLS, is therefore unnecessary. Moreover, the typical displacement resolution or length scale of focus *can* be tuned to some extent by changing the LSI geometry, i.e. back- or forward-scatter. Generally stated, forward-scatter LSI is more sensitive to small displacements because of the larger number of scattering events N involved. In this geometry, N is determined by the ratio between sample thickness h and ℓ^*, which in turn sets the effective length scale that is probed and consequently influences the signal decorrelation time. A larger h/ℓ^* implies a higher sensitivity to smaller length scales, and this ratio can thus be varied to gain some scale-resolved insight – either by changing the sample thickness, or by adjusting ℓ^* through the scatterer density or illumination wavelength.

In regard to polydisperse paints, we recommend contrast-variation LSI for discriminating between different particle populations.[20] This strategy involves the synthesis of two latices with different particle sizes, which can be blended to form a bidisperse latex. By refractive-index-matching only one of the two batches, selective sensitivity to the other population is attained, and vice versa. This allows to alternately interrogate the two particle species and thereby decouple their individual dynamics. Although this method is somewhat laborious, index-matching of the small particles is likely not necessary if the size ratio is large, as large particles scatter significantly more than the small ones. The largest particles will thus dominate the scattering signal and render the contribution of the small ones negligible.

To solve the lack of anisotropy-resolved information in a standard LSI measurement – inherent to the depolarized detection – we propose a novel (hypothetical) strategy in Section 11.4.2.

11.2.7 Unknown ℓ^*

As described above, light propagation in a strongly scattering material is characterized by the transport mean free path ℓ^* and the typical absorption length ℓ_a. Determining ℓ^* and ℓ_a is, however, not trivial, as their effects on the light scattering statistics are intertwined. For many materials, neither these two quantities nor the internal dynamics are known a priori, yielding at least three unknown parameters.[21] Moreover, ℓ^* and ℓ_a may be spatio-temporally heterogeneous. Fortunately, for most samples $\ell_a \gg \ell^*$, and hence the effects of absorption can be considered

insignificant. We will therefore focus on the origin and measurement of ℓ^* in this section.

The photon transport mean free path is related to the photon mean free path ℓ, which equals the average distance that a photon travels between successive scattering events. For a uniform distribution of non-interacting and non-light-absorbing particles, the photon mean free path is given by $\ell = 1/\rho\sigma$, with ρ the number density of particles and σ the scattering cross-section of a single particle. The latter can be derived explicitly in the Rayleigh regime, but must be evaluated numerically in the Mie regime. Rayleigh and Mie scattering are the two predominant forms of (quasi-)elastic light scattering – implying that the photon energy, and thus the wavelength, does not change substantially upon scattering. Scattering in the Rayleigh regime occurs for particles much smaller than the laser wavelength; it is strongly wavelength dependent and mostly isotropic (Figure 11.5a). Scattering in the Mie regime applies to particles with sizes of the same order as the laser wavelength; it depends more intricately on λ and is anisotropic, occurring preferentially in the forward direction (Figure 11.5b). We deal with both types of scattering in this thesis.

According to Lord Rayleigh's famous equation, short wavelengths are far more scattered than long wavelengths. Specifically, the Rayleigh scattering cross-section of a perfect sphere is given by:

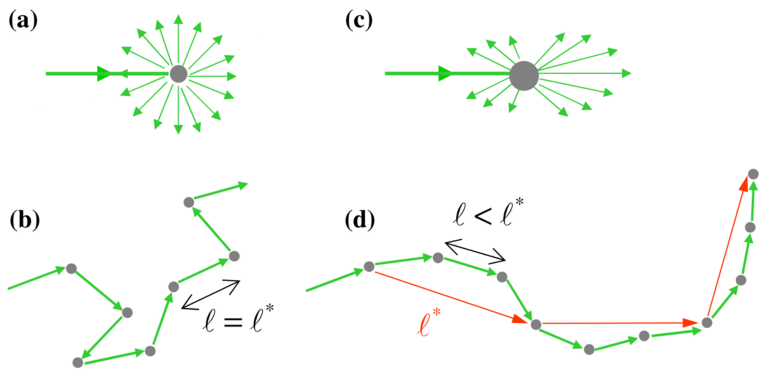

Figure 11.5. Elastic-scattering regimes and light propagation in the multiple-scattering limit. Reprinted from ref. 22, with the permission of AIP Publishing. **(a)** Isotropic (Rayleigh) scattering involves **(b)** a mean free path ℓ that equals the random-walk step length ℓ^*. **(c)** Anisotropic (Mie) scattering is biased towards the forward direction, featuring an average scattering angle $0° < \langle\theta\rangle < 90°$ and hence an anisotropy factor $0 < \langle\cos\theta\rangle < 1$. **(d)** As a result, many scattering events are needed for a photon to completely 'lose memory' of its initial orientation, i.e. $\ell < \ell^*$ (see text).

$$\sigma = \frac{2\pi^5 d^6}{3\lambda^4}\left(\frac{m^2-1}{m^2+2}\right)^2 \tag{11.4}$$

where d is the particle diameter and $m = n_\mathrm{p}/n_\mathrm{m}$, with n_p and n_m the refractive index of the particle and medium, respectively. In the Mie regime, the solution is considerably more complicated than the Rayleigh approximation.[23] An elaborate description of Mie theory is beyond the scope of this thesis.

The intrinsic anisotropy of Mie scattering implies that photons require many scattering events to fully 'forget' their direction of incidence. Specifically, the randomization of the photon propagation direction occurs over a distance $\ell^* = \ell/[1 - \langle\cos\theta\rangle]$, where $\langle\cos\theta\rangle$ is the ensemble-averaged anisotropy factor – a measure for the directionality of elastic light scattering.[24] In the case of isotropic scattering, $\langle\cos\theta\rangle$ vanishes, and $\ell^* = \ell$ (Figure 11.5b).

Insight into the light transport properties of a multiply-scattering material is important for two main reasons. First of all, these properties determine the photon path length distribution, and consequently the scattering statistics. The typical light penetration depth (in back-scatter LSI) and length scales probed (in forward-scatter LSI) depend sensitively on ℓ^* in particular. Secondly, the photon transport properties harbour relevant information about the local internal structure and its evolution over time. This capacity remains relatively underexposed. Below, we outline the manifold ℓ^* measurement methods that have been established over the years. We concentrate on ℓ^* rather than on ℓ_a, as light absorption is often negligible compared to scattering, yet most of the listed methods can be adapted or extended to determine ℓ_a as well.

- **Reference with known ℓ^*.** The most straightforward way to determine ℓ^* is by comparing the diffuse optical transmission to a calibration sample with known light transport properties.[25] The average transmitted intensity $\langle I_\mathrm{T}\rangle$ scales as $\ell^*/[h + 4\ell^*/3]$.[1,26] Considering the multiple-scattering limit $h \gg \ell^*$, this equation reduces to: $\langle I_\mathrm{T}\rangle \propto \ell^*/h$. At fixed sample thickness h, the transport mean free path of the investigated sample can thus be determined via: $\ell^* = \ell^*_\mathrm{ref}\,\langle I_\mathrm{T}\rangle/\langle I_\mathrm{T}\rangle_\mathrm{ref}$. When using this strategy, it is important that the optical properties of the reference and investigated sample are comparable, notably ℓ^* and the refractive-index discontinuities at the boundaries. These requirements often do not hold, and a reference sample may not be readily available. In recent years, several more universal, less error-prone approaches have therefore emerged, rendering a calibration sample obsolete.

- **Thickness variation.** In the forward-scatter geometry, the correlation function has a clear relation to the sample thickness, as evident from Equation (11.3).

Specifically, increasing h shifts g_1 towards shorter time scales. Measuring a systematic series of correlation functions as a function of sample thickness thus allows to calibrate ℓ^* by fitting all experimental curves simultaneously to Equation (11.3), with ℓ^* and the internal dynamics as constant fitting parameters, and h as the variable yet known parameter.

- **Oblique-angle illumination.** One of the simplest and quickest approaches to measure ℓ^* is by impinging a narrow laser beam at an oblique angle on the sample of interest, and recording the back-scattered pattern. Because of the tilted illumination, the centre of the diffuse scattering pattern will be shifted with respect to the point of incidence. This distance is geometrically defined as $\Delta r = \ell^* \sin \alpha / n$, with α the angle between the tilted beam and the surface normal. While originally applied in one dimension,[27] extra information about the in-plane anisotropy can be obtained from two-dimensional images.[28,29] The major difficulty of this method is correctly identifying the centre of the diffuse scattering profile, which is inevitably convoluted with the speckles. The true profile is therefore partially obscured. To accurately resolve Δr, high-resolution images taken with different exposure times are imperative.

- **Structured illumination.** Also without tilt angle, ℓ^* can be deduced from the detailed optical response to a known illumination pattern. The exact spatial structure of the back-scattered pattern depends sensitively on the incident intensity distribution, which may be spatially uniform,[30] modulated,[31] or random.[32,33] The transport mean free path can be derived by comparing the output patterns with theoretical predictions.

- **Coherent back-scattering.** This strategy takes advantage of the weak-localization effect of light. When illuminating a sample with a narrow laser beam, the back-scatter intensity is enhanced in the beam centre, and decays in a cone-like fashion with increasing radial distance from the beam.[34,35] The experimentally measured conical profile can be fitted by known equations to estimate ℓ^*. Specifically, the width of the cone is dictated by the in-plane component of the transport mean free path.[36] Nevertheless, obtaining a well-resolved coherent back-scatter cone is rather challenging due to various experimental hindrances.[34]

- **Photon time-of-flight distribution.** All equations in this thesis so far are based on continuous-wave laser illumination and detection of the entire distribution of photon path lengths.[37] Instead of integrating over all path lengths, an alternative is to selectively gather photons with specific time-of-flight (TOF), e.g. only early-arriving photons that have travelled short paths inside the material, or vice versa,

only late-arriving photons. The optical transport properties are contained in the full distribution of photon travel times.[38] By fitting the measured distribution of TOFs, ℓ^* can thus be precisely quantified.[39] Even more rigorous solutions are attainable using intensity-modulated light of varying frequency (order 100 MHz to 100 GHz).[40,41] Upon scattering, the modulation amplitude is attenuated and its phase is shifted, to an extent dictated by the light transport properties. In practice, however, these procedures are quite expensive and involved, since an ultrafast and pulsed laser is pivotal to enable gated detection of photons by their time-of-flight.

- **Laser wavelength modulation.** In standard LSI experiments, speckle patterns are correlated over time at a fixed laser wavelength. A quite robust methodology to quantify ℓ^* is through correlating speckle intensities at different wavelengths. Modulation of the incident wavelength introduces a variation in the optical path lengths, and consequently a change in the scattering intensity, which is superimposed onto the phase shifts caused by the material dynamics.[42] The corresponding intensity correlation function can be defined as: $g_2(\Delta\lambda/\lambda) = \langle I(\lambda) \cdot I(\lambda + \Delta\lambda)\rangle / \langle I\rangle^2$. Subsequently, g_1 can be computed via the Siegert relation, and expressed as a function of λ, $\Delta\lambda$, and the fit parameter ℓ^*. Adjustment of the laser wavelength can be achieved by tuning the cavity length.[42,43] Interestingly, this method can be readily adapted for heterogeneous samples, by dividing the field of view into meta-pixels to provide spatially resolved insight into ℓ^*.[42]

In this thesis, we have devoted relatively little attention to the measurement of ℓ^*, since most of our LSI experiments have been performed in the back-scatter geometry. Equation (11.2) shows that in the absence of a deformation field and absorption, ℓ^* drops out of the equation. The exact value of this quantity is in those scenarios not required for correct data analysis, but is relevant only for knowledge of the approximate depths probed. The magnitude of ℓ^* *is* crucial in forward-scatter LSI. We have addressed this geometry in Chapter 7, where we have used the coherent back-scattering approach to measure the transport mean free path.

11.2.8 Non-ergodicity

In a perfectly ergodic system, the time-averaged correlation function is identical to its ensemble-averaged analogue.[44] Yet, such scenarios are rare in practice. Most systems are out-of-equilibrium, non-steady-state, and/or slowly ageing. As a result, the temporal intensity statistics are not equivalent to the ensemble statistics,[45] and furthermore the relationship between d_2 and g_2 as given in Equation (1.6) also

breaks down. d_2 considerably outperforms g_2 if a sample features a non-ergodic component. While d_2 is unaltered by a non-fluctuating component in the scattered light – since image subtraction cancels out constant intensities – the presence of immobile scatterers causes g_2 to decay only partially to a finite plateau.[46] The power spectrum obtained by Fourier transform (Chapters 9 and 10) is directly related to g_2 according to the Wiener–Khinchin theorem.[47] Hence, a similar reasoning applies, and the power spectrum is likewise affected by static scatterers.

How can the condition of ergodicity still be fulfilled in those cases, and a valid relationship between d_2, g_2 and the power spectrum be restored? Traditionally, light-scattering analysis was entirely based on temporal statistics, but single-pixel time traces are insufficient to obtain a correct signal for non-ergodic materials. In the 1990s, multi-speckle i.e. spatial averaging was therefore established as a substitute for single-pixel time correlations.[48,49] In multi-speckle DWS, the many camera pixels serve to provide ample statistically independent intensity values. Usually, all pixels of the camera chip were incorporated in the multi-speckle average, yet with modern, high-resolution cameras, this yields unnecessarily abundant statistics. In Chapter 7, we have instead presented a combined strategy of multi-speckle and temporal averaging. By simultaneously averaging speckle correlations over small sliding windows in both space and time, a substantial increase in statistics can be realised, without considerably compromising spatial or temporal resolution. For example, to create Figure 7.1d, we have averaged the intensity correlations simultaneously over 9 pixels in space and 100 points in time, equivalent to 900 correlations in total.

11.2.9 Vibration sensitivity

The greatest strength of laser speckle imaging is also one of its greatest weaknesses. LSI is extraordinarily sensitive to minute displacements, which grants access to previously hidden nanoscale dynamics, but also introduces undesired sensitivity to vibrations in the equipment, building and air. We have therefore implemented active vibration isolation elements underneath our set-up (Vario Basic 60, Accurion) to eliminate external motions with frequencies higher than a few Hz. The contribution of unwanted vibrations beyond those frequencies has indeed proven negligible in our experiments, as evidenced by measuring correlation functions for static reference samples (see e.g. Chapter 9, Figure 9.5c). It is practically impossible to suppress lower-frequency motions *during* the measurement, which must thus be filtered from the signal afterwards. Nevertheless, low frequencies are usually well separated from the dynamics of interest, and hence pose no problem in practice.

11.3 New horizons for LSI

"Somewhere, something incredible is waiting to be known." – Carl Sagan (1934–1996)

For many polymer materials, each of the above described limitations is surmountable. No single technique is flawless, and every method is based on (implicit) assumptions. We believe that the power of LSI to solve hard problems in soft matter is virtually limitless. The insights obtained in this thesis open up numerous ideas for further experimentation, and several promising foundations are laid below.

11.3.1 Film formation in powder coatings

Water-based paints are the best alternative to solvent-based formulations for everyday applications. However, when it comes to treating bare metal, the most cost-effective coatings are powder-based, which account for 15–20% of all coatings worldwide.[50] Powder coatings are commonly used as protective and decorative finishes in the automotive industry,[51] on household appliances, electronic and industrial devices, bicycle and boat parts, steel construction materials, and farming equipment.

Powder coatings, as the name states, are powders rather than liquid paints. The fraction of volatile organic compounds is therefore intrinsically very low. These coatings are applied as dry powder particles, of size ~2–70 μm, and subsequently heated to induce film formation. Two main categories can be distinguished: thermosets and thermoplastics.[52] We here focus on the thermosetting variant, which is cured upon heating through crosslinking, to form a solid network. The corresponding powder particles consist of thermosetting resins, curing agents, pigments, fillers, and other additives. Thanks to the curing reaction, the resulting finish is typically harder and stronger than conventional coatings. By contrast, thermoplastic powder coatings do not undergo any chemical reactions during the baking process; they merely liquefy and flow to form a film, which finally resolidifies upon cooling.

Despite the widespread use of powder coatings, the scientific literature on the physics governing film formation is remarkably scarce. At present, insight into the heating and curing stages is acquired almost exclusively via bulk and surface techniques. Yet, spatially resolving and quantifying the physical phenomena that lead to film formation is not only fundamentally intriguing, but also necessary to further improve this emerging technology.

We have therefore used LSI to obtain a more thorough picture of the mechanisms at work in commercial powder coatings, in an industrially relevant setting. We

have performed our experiments in direct partnership with Leendert Molhoek and Jan Bongaerts from DSM Coating Resins in Zwolle. We have thankfully received various powder coatings, electrostatically sprayed onto aluminium panels ('Q-panels', $w \times l = 100 \times 150$ mm^2). Since the used resins yield a transparent film upon curing, 2.5 wt% of TiO_2 nanoparticles was incorporated to ensure strong multiple scattering and a reasonably constant ℓ^* throughout all stages. The motion that we detect using LSI originates primarily from these pigment particles, rather than from the polymer chains themselves. Nevertheless, the pigment dynamics closely reflect the mobility of the surrounding polymer matrix.

To render our LSI set-up applicable to powder coatings, we include an adjustable hot plate as heating element. In parallel with the LSI measurements, a computer-controlled infrared sensor (PCE-IR 51, PCE Instruments) records the surface temperature of the coating with 1% error at a 10 Hz frequency. Linking the instantaneous coating temperature to the local mobility allows to identify and quantify (i) the different heating stages, and (ii) shrinkage upon cooling. We elaborate on these phenomena in the following sections.

Heating stages

Upon heating a powder coating, the powder particles undergo different transformations, to ultimately culminate in a homogeneous, coherent and rigid film. The core of successful curing comprises two key steps: first, with increasing temperature, the initially solid particles must liquefy and sinter i.e. coalesce; and second, at even higher temperatures, network formation i.e. curing must occur in a complete way. These different stages are well-known and have been analysed by a.o. rheometry and differential scanning calorimetry (DSC). However, most conventional techniques apply only to bulk materials and do not provide any spatially resolved information. Moreover, the extraordinary displacement sensitivity of LSI can provide more detailed insight into the different processes, as it allows detection of even the most subtle dynamics which previous remained obscured.

We have applied back-scatter LSI to a series of semi-crystalline powder coatings that we have gratefully received from DSM Coating Resins in Zwolle. These powders are largely amorphous but contain some crystalline domains. The corresponding heating profile exhibits three important temperatures (Figure 11.6a): a glass transition temperature (T_g), a melting temperature (T_m), and a cure temperature (T_{cure}). In practice, these processes occur over a range of temperatures because of the polymer polydispersity.

We first compute the average scattering intensity and mobility over the field of view (5.8 mm^2). Although the pigment particles ensure a relatively constant

scattering efficiency, we find that the coating turbidity decreases by a total of ~30%, as quantified by the normalized change in intensity $\Delta I/I_0$ (Figure 11.6b). The largest change in turbidity occurs from approximately 60–80 °C, which is preceded by a rapid rise in the mobility $d_2(\tau = 0.2\ \text{s})$ (Figure 11.6c, note the logarithmic axes). Spatially resolved d_2 maps reveal that the powder particles sinter in this temperature window (Figure 11.7a–d): the individual particles liquefy and consequently merge into a continuous, more homogeneous film with somewhat reduced scattering power.

While the turbidity curve is relatively featureless except for the sintering-related decay (Figure 11.6b), the d_2 curve exhibits a wide range of distinct kinks and transitions (Figure 11.6c). We here choose a τ value of 0.2 s, which appears to

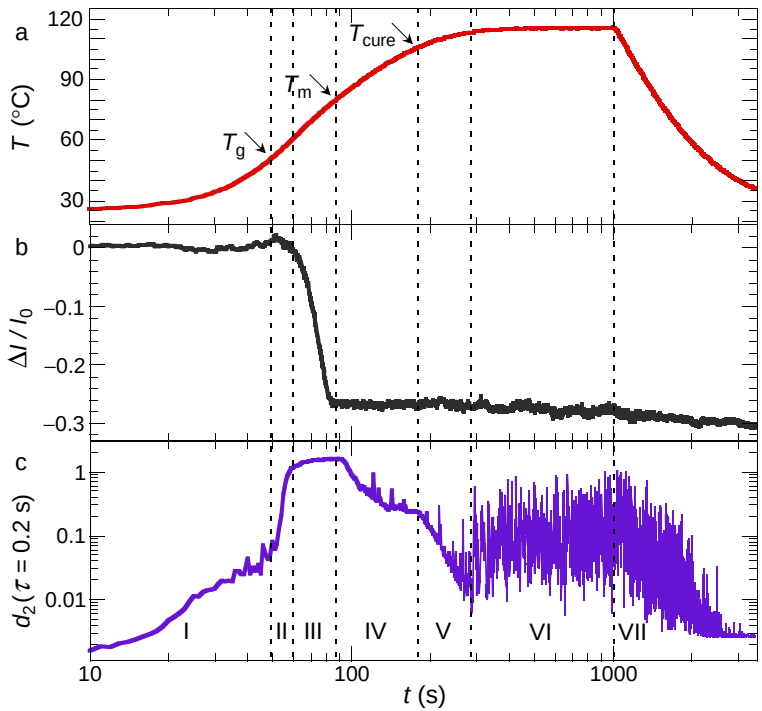

Figure 11.6. Heating stages in a powder coating. **(a)** Temporal evolution of the surface temperature during heating and subsequent cooling. The glass transition, melting, and cure temperature are indicated. **(b)** Change in coating turbidity, expressed as the normalized change in back-scattered intensity. Particle sintering in stage III leads to a small rise in homogeneity and a consequent decrease in turbidity. **(c)** Evolution of the mobility, which displays well-defined transitions (see text). The data in (b) and (c) are averaged over 5.8 mm^2.

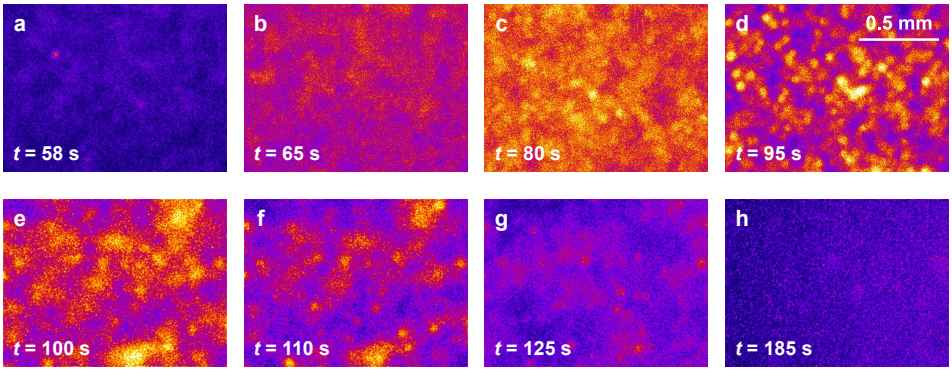

Figure 11.7. Time-lapse d_2 maps of particle sintering in stage III **(a–d)** and coating levelling in stage IV **(e–h)**. The scale bar applies to all images. Images (a–d) are computed for $\tau = 5$ ms, and (e–h) for $\tau = 200$ ms.

most optimally separate the different stages. We can now combine the information captured in this curve with our spatially resolved d_2 images and DSC data from DSM, which provides evidence for the following seven stages:

I. Upon heating below the T_g, the mobility gradually rises, indicating thermal expansion of individual powder particles.

II. At the glass transition, d_2 displays a sharp kink and a sudden acceleration of the dynamics, as the glassy polymer phase transitions into a liquid-like phase with rapidly decreasing viscosity.

III. The polymer viscosity continues to decrease with increasing distance to the T_g, allowing the largely liquefied powder particles to sinter sequentially (Figure 11.7a–d).

IV. At T_m, the crystalline fraction of the semi-crystalline resin melts. This enables flow and levelling of the coating as it liquefies further, thus eliminating spatial inhomogeneities to a large extent (Figure 11.7e–h).

V. Beyond the cure temperature, the dynamics slow down according to an apparent power law, due to the progressive formation of a rigid, crosslinked network.

VI. When the curing process has finalized and a solid film has formed, the coating starts to display long-ranged, intermittent contractions, visible as shifts of the entire speckle pattern (see the next section). These deformations likely

arise from heterogeneous tensions in the network due to curing-induced chemical shrinkage.

VII. After 1000 s we switch off the hot plate, allowing the dynamics to gradually slow down and return to a static baseline state.

As briefly discussed above, d_2 is not only temporally variable but also spatially heterogeneous, especially during sintering and levelling (Figure 11.7). Interestingly, the individual powder particles liquefy and coalesce at considerably different times: it takes over 30 s for all particles to lose their identity, during which they light up consecutively (Figure 11.7d). This temporal separation probably arises from a combination of three factors: (i) a temperature gradient across the coating thickness; (ii) a range in powder particle sizes; and (iii) intrinsic chemical heterogeneity. These observations emphasize the importance of imaging, to reveal features that spatial averaging lacks access to.

To examine the robustness and validity of our results, we repeat the experiment for a similar powder coating with slightly reduced crystalline fraction. The d_2 and $\Delta I/I_0$ curves for both coatings are plotted versus temperature in Figure 11.8. Indeed, we retrieve exactly the same stages, but the glass and melting transitions occur at higher T in the second coating (represented by the light-coloured curves). These observations are perfectly in line with DSC measurements performed by

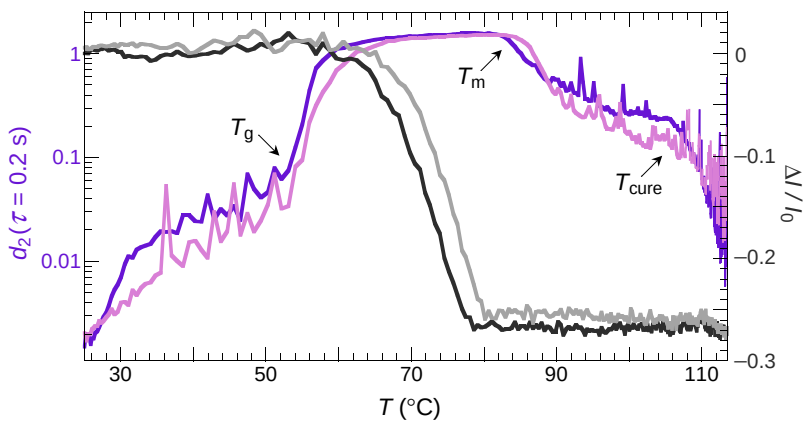

Figure 11.8. Comparison of different formulations of a powder coating. The dark-coloured curves (— and —) are identical to those in Figure 11.6b and c, yet plotted as a function of temperature. The light-coloured curves (— and —) represent the mobility and turbidity, respectively, of a coating with somewhat lower crystallinity. All stages in the second coating are highly similar, only shifted to marginally higher temperatures.

Jan Bongaerts at DSM, according to which the T_g and T_m of the second coating are several °C elevated. In addition, the mobility of the second coating is somewhat lower in the molten state, which is consistent with rheological measurements that indicate a higher viscosity above T_m (data not shown).

Cooling-induced shrinkage

Shrinkage upon cooling of powder coatings is undesirable yet inevitable. This phenomenon is one of the main culprits of poor coating adhesion to the substrate, and hence, it is crucial to quantify the extent and time evolution unambiguously. Since lateral shrinkage occurs predominantly towards the coating centre, we have focused our LSI set-up on a corner, where the shrinkage direction is most evident. Subsequently, we have analysed the raw speckle patterns using a routine based on digital image correlation (DIC) and particle image velocimetry (PIV).[53,54] These image processing algorithms are well established for tracking spatial displacement and velocity fields. Usually, DIC is performed on a surface-sprayed speckle pattern, and PIV on tracer particles, yet here the tracked speckle pattern originates from inside the coating. Application of cross-correlation methods to back-scattered speckle patterns is relatively rare, despite their potential. A few notable exceptions on weakly scattering systems[55–59] and in the multiple-scattering limit[21] have indeed proven successful.

Advantages of this method are its non-invasive nature, great displacement sensitivity, and access to sub-surface displacements. The main disadvantage is its unsuitability when the internal dynamics are highly non-affine, which causes the speckle pattern to be scrambled without directionality. The affine part of the displacement field must therefore dominate over non-affine dynamics.[58] At the end of the curing stage, our coatings are indeed sufficiently solid to minimize speckle scrambling. We can quantify the long-range displacement field surprisingly well. A typical vector field at a corner is shown in Figure 11.9a, representing a temperature decrease of 110 °C. The vector lengths reflect the total local displacement magnitude of ~110 μm in this case. Clearly, the coating shrinks laterally towards the centre in a spatially uniform manner, in line with expectations. We generate these displacement maps using the MATLAB-based open-source software PIVlab.[60] From this toolbox, we apply the fast Fourier transform (FFT) algorithm, which we run on square interrogation windows in multiple passes, without providing any input regarding the expected direction. This algorithm is based on standard space correlation methods to determine the displacement of each square between times t and $t + \tau$. The multi-pass interrogation – with step-wise decreasing window size – further allows to increase the signal-to-noise ratio.

Since the vector field is spatially uniform, we can average the vector magnitude over the entire field of view, and plot this as a function of time to quantify the evolution of thermal shrinkage. We define the average displacement i.e. lateral shrinkage during each time interval as $\langle\delta\rangle = \sum_{i=1}^{N} \left({\delta_{x,i}}^2 + {\delta_{y,i}}^2\right)^{1/2} / N$, where $\delta_{x,i}$ and $\delta_{y,i}$ are the horizontal and vertical components of the displacement of the i^{th} interrogation window, respectively, and N is the total number of windows.[55] Plotting the cumulative lateral shrinkage δ as a function of decreasing temperature yields an approximately linear relationship (Figure 11.9b, left ordinate). The total cooling-induced shrinkage in this field of view amounts to ~4%, which far exceeds the thermal shrinkage arising from the aluminium panel of ~0.3%.

We note that non-affine internal dynamics are still clearly present at the onset of thermal shrinkage, as quantified by $d_2(\tau = 0.2\text{ s})$ (Figure 11.9b, right ordinate). Thanks to the large amplitude of the (superimposed) rigid shift, and its long-range homogeneity, these two types of motion can still be quite well disentangled. The magnitude and intermittency of d_2 both decrease during cooling, in a roughly logarithmic fashion, until a static baseline is reached below 40 °C. We believe that these findings warrant more detailed investigation in future studies.

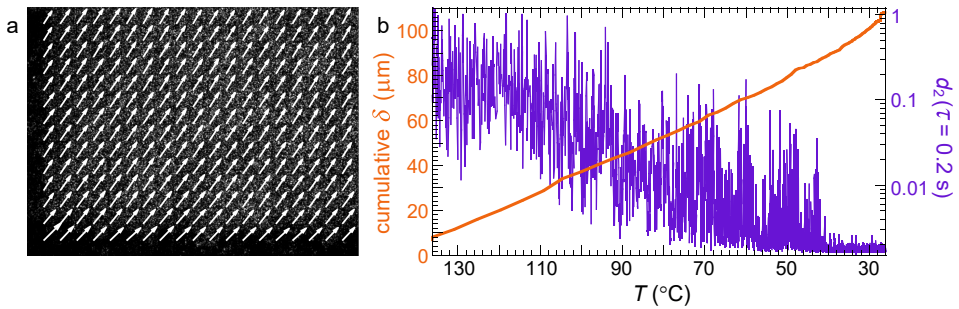

Figure 11.9. Quantification of thermal shrinkage. **(a)** Cumulative displacement field at the corner of a cured coating after cooling, obtained using DIC/PIV-based analysis on the raw speckle patterns. The vector length δ represents the local displacement magnitude, here totalling ~110 μm (drawn to scale) over a temperature drop of 110 °C. The vectors point towards the direction of shrinkage, which is the coating centre. Because the coating is longer vertically than horizontally (15 cm versus 10 cm), the vertical shrinkage is larger than the horizontal shrinkage, hence $\delta_y > \delta_x$. The dark background is the aluminium substrate. **(b)** Cumulative lateral shrinkage (left ordinate) and non-affine dynamics (right ordinate) during cooling. These two types of motion can be well separated thanks to their distinct time and length scales.

11.3.2 Crack propagation in drying paint films

"There is a crack in everything. That's how the light gets in." – Leonard Cohen (1934–2016)

While crack patterns in nature can be fascinating, fractures in paint films are highly undesired, as they are detrimental to the coating performance and appearance. Cracks must therefore be prevented at all costs. In Figure 11.3a, we have shown that LSI can sensitively probe the propagation of cracks, specifically the damage front which moves ahead of and around crack tips. The extent and directionality of this deformation zone are closely related to the local microstructure and strain field. Analysing these so-called 'process zones' may thus cast more light on the nanoscopic origins of fracture, which can be directly linked to the macroscopically observable crack pattern.

Not only individual cracks offer useful information, but LSI also reveals crack tip interactions that have not been reported before. While interactions with the film edge may be expected (Figure 11.10a), interactions with other tips (Figure 11.10b) and local heterogeneities (Figure 11.10c) are largely unexplored. These

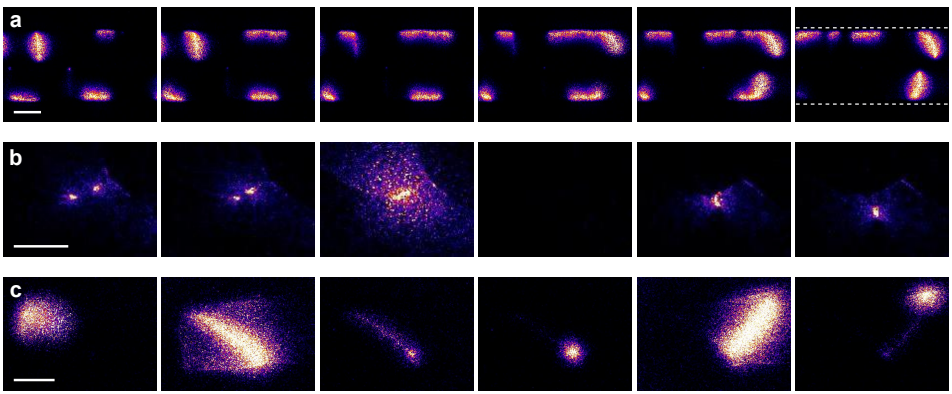

Figure 11.10. Crack tip interactions. Time-lapse d_2 images of propagating crack tips in ~100 μm thick water-saturated coatings of rigid colloids. Note that fast tips appear elongated because of temporal averaging. All images are computed for $\tau = 35$ ms. The scale bars represent 0.5 mm. **(a)** Tip–edge interactions. The crack tips, propagating at ~5 mm/s, bend upon reaching the film edge (demarcated in the last image), and subsequently follow the contour. **(b)** Tip–tip interactions. Two crack tips, moving towards each other in a ductile manner at ~0.05 mm/s, 'collide' upon meeting, which is accompanied by a burst of activity. 3 s after the collision, a new crack nucleates from the same location. **(c)** Tip–microstructure interactions. A brittle crack, advancing at ~5 mm/s, 'bounces off' a heterogeneity in the paint film. Subsequently, it continues its track at an angle of ~90°.

interactions are fundamentally interesting, as they suggest that the cracks sense each other's stress fields and the coating microstructure over a relatively long distance. Moreover, they may provide practical insight into fracture mitigation strategies. The addition of mechanically dissipative components, such as low-T_g water-soluble polymers or laponite nanoclay, will likely suppress failure by relieving built-up stresses, and thereby enhance the fracture toughness of the coating. These effects can be mapped with high displacement resolution using LSI. By complementing the nanoscopic dynamics with scanning electron microscopy of the local nanostructure – possibly at exactly the same location – we intend to arrive at a deeper understanding of the importance of stress dissipation, particle packing, particle deformability, and film heterogeneity on the propensity to fracture.

Finally, we are able to track the propagating crack tips and determine their velocity distribution. Preliminary results suggest an unexpectedly broad distribution, indicative of pronounced heterogeneities in the microstructure and stress field. In many cases, we find two distinct propagation modes within a single film, exhibiting signs of both ductile and brittle fracture. Figures 11.3a and 11.10 highlight the wide variety of propagation modes that we have encountered, even for the same latex under approximately constant drying conditions.

11.3.3 Microchannel flow

Microfluidics is an ever-evolving scientific discipline that offers many benefits to chemical and biological research. In contrast to laboratory-scale analyses, microfluidic devices require a substantially reduced amount of sample and allow more sensitive, high-throughput detection.[61] Laser speckle imaging and microfluidics are an excellent match, as demonstrated in refs. 62–65, where microchannels serve as mimics of the human microvasculature and as well-controlled in-vitro platforms for screening of blood flow anomalies.

A relatively quick approach to measure flow velocities in microchannels is based on the speckle contrast analysis described in Chapter 1, Section 1.4.1. We have applied this strategy for the first time to synthetic soft matter. Together with PhD students Ties van de Laar and Ruben Higler from our group, we have explored the potential of LSI to reproduce flow profiles in a well-defined geometry, namely a glass capillary with rectangular cross-section (VitroCom, USA). As a model system, we use a suspension of 1 wt% monodisperse, 1 μm diameter polystyrene particles density-matched in H_2O/D_2O. We flow this suspension through the capillary at a controlled pressure, and subsequently compute the speckle contrast $K = \sigma_I/\mu_I$, where σ_I and μ_I are the standard deviation and mean of the intensity, respectively. By averaging all pixels in the longitudinal direction, this allows us to generate the

cross-sectional contrast from a single speckle pattern. As explained Chapter 1, a lower contrast indicates more speckle blurring and hence a higher flow velocity. We have recorded speckle images at five different exposure times, yielding the K^2 profiles in Figure 11.11a1. Note that these profiles are projections of the dynamics in the depth direction, which is 10× smaller than the lateral direction, i.e. 0.70 mm.

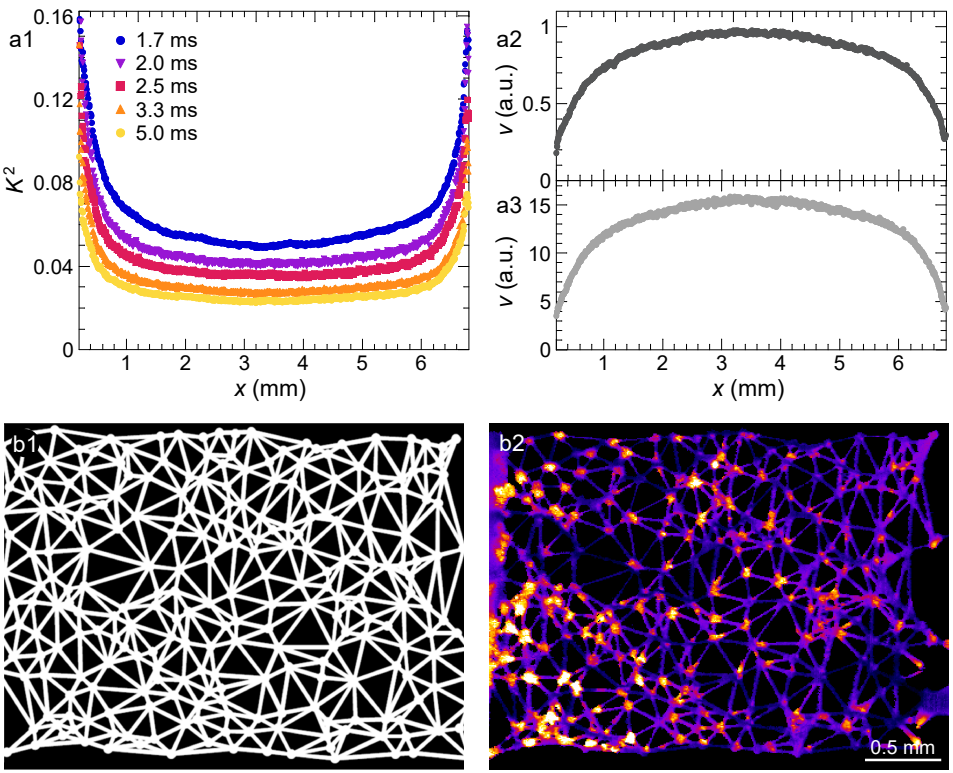

Figure 11.11. Particle flow through microchannels. **(a)** Pressure-driven Poiseuille flow in a 70×7.0×0.70 mm^3 rectangular capillary. Computation of the cross-sectional speckle contrast for different exposure times **(a1)** allows determination of the relative flow velocities via Equation (11.5), yielding the cross-sectional velocity profile in **(a2)**, and for a ∼15× higher pressure drop across the channel in **(a3)**. Note that 0.2 mm of both edges is excluded because of artefacts related to the slightly tilted detection angle. **(b)** Complex flow in a disordered geometry mimicking a porous medium. **(b1)** Two-dimensional design, with the inlet on the left. All channels are 50 μm deep. The pore bodies are 50 μm in diameter, and the pore throats are 20 μm wide. Reproduced with permission from ref. 66. **(b2)** d_2 map, computed for τ = 25 ms, showing highly inhomogeneous dynamics.

To estimate the relative flow velocities, we use the approximate relation between K and the exposure time T:[67,68]

$$K^2(v,T) \approx \frac{1}{2BvT}\left[2 - \frac{1-\exp(-2BvT)}{BvT}\right] \tag{11.5}$$

where v is the flow velocity and B is a proportionality constant. Multi-exposure LSI thus allows semi-quantification of flow velocities by fitting $K^2(v,T)$ to the above equation, with v constant for different exposure times and T constant in space. The resultant flow profile corresponding to Figure 11.11a1 is shown in Figure 11.11a2, and that for a ~15× higher pressure in Figure 11.11a3. Since several assumptions underlie Equation (11.5), v should be considered as a relative indicator of the flow velocity, rather than as an absolute measure. Nevertheless, we can accurately infer the shape of the cross-sectional flow profile, which for both pressures resembles the expected Poiseuille profile.

We can take LSI one step further and measure particle flow in a complex microfluidic device. The design of this device is depicted in Figure 11.11b1, where open pores are white and the inlet is on the left side. Such a disordered geometry may aid in unravelling the mechanisms by which particulate flows permeate porous structures. Ties van de Laar has fabricated this channel from polydimethylsiloxane (PDMS) using standard soft lithography methods, as described in detail in ref. 66. We flow the aforementioned polystyrene suspension through this micromodel at a constant applied pressure of 5 mbar, and subsequently compute $d_2(\tau = 25\text{ ms})$ (Figure 11.11b2). This clearly reveals a considerably higher mobility in the nodes (pore bodies), where the dynamics are more chaotic compared to the connections (pore throats). Moreover, we observe a decreasing mobility gradient from the inlet to the outlet, in line with expectations. Although these findings are preliminary, they highlight LSI as a powerful tool to visualize heterogeneous flows in microfluidic devices.

11.3.4 Portability and complementarity

The limited number of components needed for laser speckle imaging makes this technique well suited for portability. In recent years, various hand-held and low-cost variants have therefore seen the light;[65,69–73] based on a webcam[74] or camera-phone;[75] integrated into a commercial microscope;[76,77] or incorporated in an endoscope to sense blood flow in deep tissues.[78,79] Thanks to these developments, LSI is expanding beyond niche applications in universities and academic hospitals towards diverse clinical settings, industry, and even art conservation.[69,80] Also in

our group, a tablet-controlled hand-held instrument has been developed (Figure 11.12a),[81] in addition to several semi-portable set-ups (Figure 11.12b).

Other assets of laser speckle imaging are its flexibility and ease of hyphenation with complementary methods. In recent years, LSI variants have been combined with infrared thermal imaging,[84] optical coherence tomography,[79,85] shear wave elastography,[86,87] magnetic resonance imaging,[88] and multispectral imaging of absorbance and reflectance.[62,89,90] We also envisage coupling of LSI with spectroscopic methods such as infrared and Raman spectroscopy, to link the local nanomobility to chemical processes; or with electrochemical impedance spectroscopy, to study the dynamics of coating delamination and corrosion in more detail. A third recommendation is the use of two back-scatter cameras in parallel, on opposite sides of a sample. This will enable the imaging of different interfaces in a single experiment, such as the substrate–water interface of a coating, where delamination takes place, and the air–water interface, where particles accumulate and skin formation may occur. An alternative is simultaneous forward- and back-scatter LSI. These two points of view may facilitate unravelling the interplay between motions at different depths and length scales.

For polymer networks in particular, we expect substantial progress by coupling LSI to optical read-out of molecular-level force sensors or mechanophores, which yield an optical signal upon mechanochemical activation.[91,92] Mechanophores have been widely incorporated in elastomers in the last decade.[93] In Chapter 7 of this thesis, we could not provide direct insight into the molecular origin of the detected damage. Although our findings hint strongly at a cascade of bond breaking before crack nucleation, conclusive evidence can be found only by visualizing molecular rupture events.

Finally, we see great potential in the combination of LSI with bulk mechanical testing, to simultaneously acquire information about local nanoscale deformations and the macroscopic strain, fracture or fatigue response. For example, we have aligned our portable LSI installation with a tensile tester constructed by the Novel Aerospace Materials group of the TU Delft. While straining a natural rubber specimen, we were thus able to in situ probe the spatially resolved nanostrains ensuing from a zone of stress concentration (Figure 11.13). A zoom lens allowed us to flexibly adjust the magnification (compare Figure 11.13a with b–e). Clearly, long-range deformations spread in an asymmetric manner, and ultimately give rise to fracture once they cover the entire sample. Remarkably pronounced post-fracture relaxations are also apparent in Figure 11.13e.

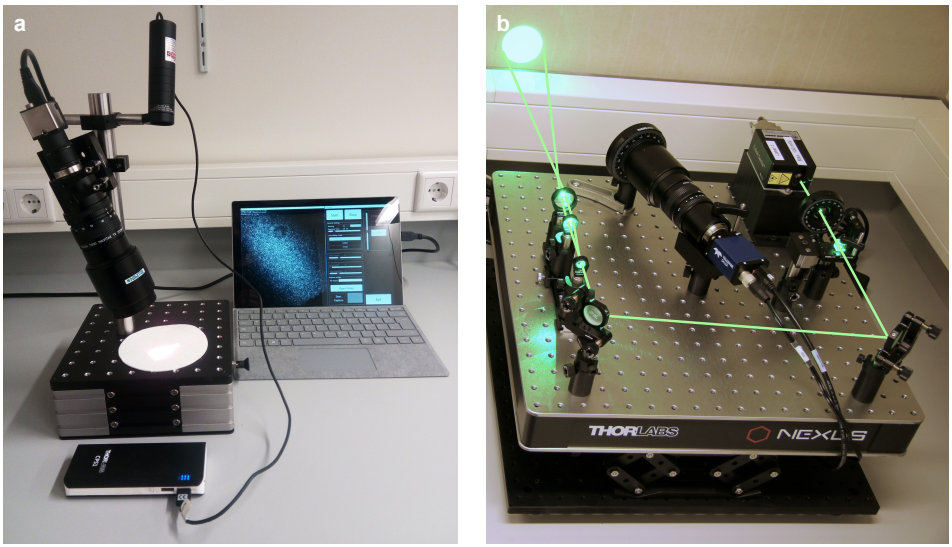

Figure 11.12. Portable LSI instruments. **(a)** Photograph of a wireless, compact set-up that is controlled by a tablet (right) and charged by a power bank (bottom). The supporting platform provides active vibration reduction. Adapted with permission from ref. 81. **(b)** Semi-portable, high-resolution LSI equipment, mounted on height-adjustable lab jacks. The illuminating laser beam path is depicted schematically. The images in Figure 11.13 are generated using this set-up, directed towards a tensile test in action.

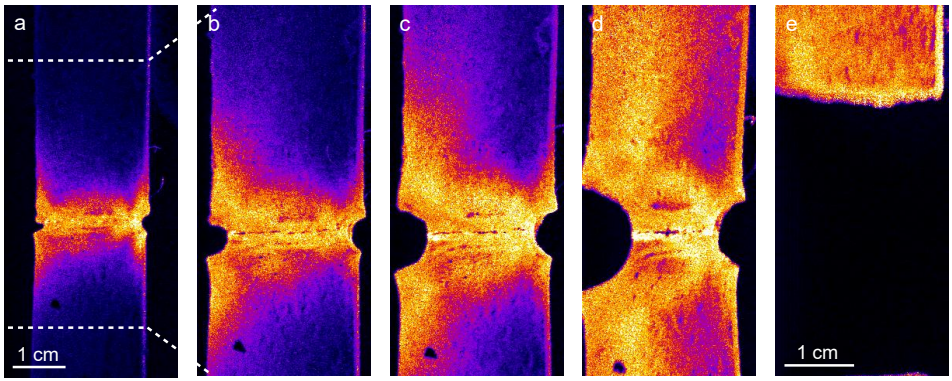

Figure 11.13. Combination of portable LSI with tensile testing. **(a–d)** Time-lapse $d_2(\tau = 16\ \text{ms})$ maps of the straining of a self-healed natural rubber,[82,83] until **(e)** catastrophic fracture. The time steps are 9 s. Both the material and tensile tester were prepared by the Novel Aerospace Materials group of the TU Delft, directed by Prof. Sybrand van der Zwaag. The scale bar in (e) applies to (b–e).

11.4 New variants of LSI

"There's light enough for what I've got to do." – Charles Dickens (1812–1870)

There are plenty of future opportunities for LSI that would ease its adoption as a standard laboratory method. The modularity and versatility described in the previous section also imply facile adaptation of the method itself. We are eager to shift the boundaries and the reader's imagination in the following sections. With the development of ultrafast lasers and the increase in computation power, these dreams may soon be within reach.

11.4.1 Five-dimensional imaging

The grand LSI challenge is imaging in three spatial dimensions, thus introducing depth information. A makeshift solution is to vary the pigment concentration and thereby ℓ^*, while keeping all other sample properties constant. This approach allows the systematic interrogation of different effective depths. Nevertheless, it is rather time-consuming and labour-intensive, and requires modification of the investigated material. We propose to alleviate these experimental constraints by developing a five-dimensional LSI set-up, with access to the z-dimension in addition to x, y, t and τ. Below, we recommend three ways to implement this fifth dimension. The details of these ideas are largely conceived by colleagues in our group. The three concepts can be applied individually, or combined to further improve the depth information. In our group, Jesse Buijs is currently realising the first LSI instrument capable of five-dimensional data acquisition, on the basis of both scanning-point-illumination and time-gated detection.

- **Wavelength tuning.** The first approach relies on encoding depth information through multi-wavelength acquisition of laser speckle images. The effective photon penetration depth is of the order of a few ℓ^*,[11] which in turn is a function of the illumination wavelength (see Section 11.2.7). The characteristic distance over which the light intensity decays inside a sample can thus be tuned by adjusting the laser wavelength. Generally, increasing λ allows greater depths to be probed. The use of (near-)infrared light in medical LSI applications is founded on this principle, since light penetration well beyond the skin surface is required for blood flow imaging in deep tissues.

  Multi-wavelength illumination can obviously be attained by using multiple lasers. An alternative, more flexible and versatile strategy is to use a pulsed white-light laser, and switch between narrow spectral bands by means of an acousto-optic tuneable filter (AOTF).[94] The multiply back-scattered light can

be captured on a hyperspectral camera, which allows recording sequential speckle patterns at different wavelengths within a single exposure time. From these depth-dependent slices, three-dimensional spatial information about the material dynamics can be extracted during post-processing, e.g. by iteratively solving the relevant equations over all spectral slices within a tomographic stack.

Despite the intricate acquisition scheme, the temporal resolution of this method can be rather high, thanks to the use of an AOTF. This monochromator involves no mechanical actuation, as switching between spectral slices is electronically controlled. The switching time is typically of the order of 10 µs.[95] The rate-limiting step is therefore the camera exposure time T, which equals the cumulative acquisition time for all spectral slices in a stack. T depends strongly on the laser power, scattering efficiency and total number of slices, but it will likely be less than 0.1 s. The depth resolution is inversely proportional to the spacing between spectral slices. Under optimal conditions, we expect this to be several micrometres.

- **Point illumination.** A second strategy is based on scanning-point-illumination, which we have introduced in Section 11.2.3 in the context of reducing blurring artefacts. By projecting a narrow laser beam onto the sample, and scanning it in a raster-like fashion using electronic mirrors, spatially resolved point-spread functions can be measured. Combination of adjoining point-spread functions allows reconstruction of the three-dimensional sample dynamics. This concept thus improves conventional LSI by significantly enhancing the spatial resolution, while simultaneously providing depth information.[14,15]

- **Time gating.** Both the lateral and depth resolution can be improved even further by selecting specific path lengths through time gating. With increasing photon time-of-flight, the average lateral diffusion distance increases, and the probability distribution of the penetration depth shifts towards deeper layers.[15,96,97] Instead of indiscriminate detection of photons, TOF-selective photon detection thus allows deconvolving the spatial blurring and resolving the probed depths. A common way to measure path-dependent correlation functions is by means of a gating scheme based on a pulsed laser, an optical delay line, and a nonlinear crystal.[37,97] More detailed technical specifications are outside the scope of this thesis.

11.4.2 Anisotropy-resolved imaging

In Section 11.2.6, we have discussed the lack of anisotropy-resolved information in LSI data. This shortcoming seems unavoidable when it comes to depolarized light detection – an absolute requirement for valid data interpretation. Yet, while the detected light has inevitably lost its polarization due to multiple scattering, adjusting the polarization of the *incident* beam may still provide some insight into orientational effects. This potential is yet to be tapped into.

If a material is intrinsically anisotropic, the scattering efficiency will be a function of both the alignment axis of the material and the polarization of the incoming light. Either of the two could be varied, but changing the laser polarization is in most cases the easiest and most reliable approach. This essentially boils down to rotating the laser polarization and detection polarizer simultaneously, to ensure that low-order scattering paths are consistently eliminated. The intensities corresponding to the two principal, orthogonal rotation angles are denoted by I_{hv} and I_{vh}, where the first subscript indicates the polarization direction of the incident beam (horizontal or vertical), and the second subscript that of the detected light. For an anisotropic sample, $I_{\mathrm{hv}} \neq I_{\mathrm{vh}}$, since ℓ^* is a function of the scattering anisotropy. The dynamics parallel and perpendicular to the sample director may thus be distinguished from each other. How exactly and to what extent this principle works is still unclear, but the practical implementation is well feasible and relatively easy. Only minor optical and hardware modifications to the LSI set-up are needed to effectuate synchronized adjustment of the incident and detected polarization directions. The resulting set-up could be calibrated using reference samples with known orientation.

The potential applications of this LSI variant are manifold. A first example concerns drying polymer dispersions, which generally display evolving local anisotropy, especially during directional drying.[98–100] Such anisotropy strongly influences the mechanical and optical properties of the final dry coating, rendering this analysis also industrially relevant. The same reasoning applies to drying-induced instabilities, such as cracks and shear bands, whose development is closely related to the local anisotropy.

A second application regards oriented semi-crystalline polymers, which contain partially aligned crystallites.[101–104] Although the molecular orientation has a great impact on the macroscopic mechanical behaviour of the polymer, the anisotropy-resolved nanodynamics and crack growth remain largely unexplored. We also expect that orientational anisotropy substantially influences self-healing and shape-shifting functionalities, which this novel LSI method might capture nicely and uniquely.

11.5 Conclusions and outlook

"Imagination will often carry us to worlds that never were, but without it we go nowhere." – Carl Sagan (1934–1996)

We hope to have sparked the reader's imagination, interest and curiosity in this thesis. Future LSI studies are recommended to address the many areas in which we are still left in the dark. We strongly encourage more common use of laser speckle imaging, and we hope that this thesis opens the way for other researchers to transform LSI into a technique tailored to their specific question. The methods that we have developed can readily be applied to quantitatively probe a virtually endless variety of (nonlinear) nanomechanical phenomena that govern the dynamics of polymer materials.

The results in this thesis shed new light on the nanoscopic mechanisms behind complex and ill-understood macroscopic phenomena in drying polymer dispersions and dynamic elastomers. To the best of our knowledge, LSI is one of the few techniques that allows bridging the gap, in a single experiment, from millisecond motions at the nanoscale to ultraslow, collective ageing processes. Visualization and spectral deconvolution of these multi-scale dynamics, inherent to most polymer systems, will not only deepen our fundamental knowledge, but may ultimately enable more targeted development and improvement of high-quality materials.

Because of the simplicity, versatility and modularity of LSI equipment, we envision its extension to a much wider range of materials than discussed in this thesis. Indeed, LSI-related methods are rapidly diffusing into fields other than medicine and synthetic polymers. In recent years, diverse applications have emerged in food technology,[105–107] plant development,[108–112] graphology,[113] and microbiology.[114,115] Peculiarly, the local mobility is in these fields often denoted as the 'biospeckle activity', and speckle fluctuations as the 'biospeckle phenomenon'. We have yet to discover the fundamental difference between a biospeckle and a regular speckle.

We can let our minds wander further. There is no reason to limit ourselves to the visible and sensible (infrared) regions of the light spectrum, and more exotic LSI analogues spring to mind. Larger wavelengths such as microwaves might unravel deep processes in strongly scattering materials. In fact, the microwave laser or so-called 'maser' is a forerunner of the laser.[116] Until recently, an insurmountable bottleneck in the application of masers was their exclusive operation at extremely low temperatures or under high vacuum. With the advent of continuous-wave

room-temperature masers,[117] 'maser speckle imaging' has become a feasible and tempting technology.

Alternatively, we can shift our perspective to shorter wavelengths such as X-rays. While LSI provides nanoscopic displacement resolution, its spatial resolution is ultimately limited by the wavelength of light. In Chapter 1, we have introduced the X-ray equivalent of dynamic light scattering: X-ray photon correlation spectroscopy (XPCS).[118,119] This technique uses high-brilliance synchrotron radiation to illuminate the dynamics inside a sample, yet its imaging capabilities are far from fully realised. The significantly smaller wavelength of X-rays – in the range of 10 pm to 10 nm – evidently outperforms photons with respect to the spatial resolution.

Finally, instead of light we could divert to electrons, which also exhibit (sub-)nanometric de Broglie wavelengths. A particularly thought-provoking method utilizes a coherent electron beam to spatio-temporally resolve Ångström-scale dynamics. Only a single, intriguing paper has been published on this technique, termed 'dark-field electron correlation spectroscopy' by the authors, who implemented it into a modern transmission electron microscope.[120] This method can thus make us see even sharper than laser-like focus. With so many promising vistas ahead, we believe that the future is bright.

Light ***S***hines ***I***nfinitely...

References

[1] D. J. Pine, D. A. Weitz, P. M. Chaikin, E. Herbolzheimer. *Phys. Rev. Lett.* **60**, 1134–1137 (1988).

[2] D. J. Pine, D. A. Weitz, J. X. Zhu, E. Herbolzheimer. *J. Phys. France* **51**, 2101–2127 (1990).

[3] P. Zakharov, F. Scheffold, *Light scattering reviews 4: single light scattering and radiative transfer* (Springer, Berlin, Heidelberg, 2009), chap. Advances in dynamic light scattering techniques, pp. 433–467.

[4] G. D. J. Phillies. *J. Chem. Phys.* **74**, 260–262 (1981).

[5] K. Schätzel. *J. Mod. Opt.* **38**, 1849–1865 (1991).

[6] J. M. Schmitt, A. H. Gandjbakhche, R. F. Bonner. *Appl. Opt.* **31**, 6535–6546 (1992).

[7] D. Bicout, C. Brosseau. *J. Phys. I* **2**, 2047–2063 (1992).

[8] R. D. Deegan, O. Bakajin, T. F. Dupont, G. Huber, S. R. Nagel, T. A. Witten. *Nature* **389**, 827–829 (1997).

[9] D. Mampallil, H. B. Eral. *Adv. Colloid Interface Sci.* **252**, 38–54 (2018).

[10] Á. G. Marín, H. Gelderblom, D. Lohse, J. H. Snoeijer. *Phys. Rev. Lett.* **107**, 085502 (2011).

[11] L. Vitomir, J. Sprakel, J. van der Gucht. *Sci. Rep.* **7**, 16879 (2017).

[12] A. Groisman, E. Kaplan. *Europhys. Lett.* **25**, 415–420 (1994).

[13] L. Goehring, S. W. Morris. *Phys. Today* **67**, 39–44 (2014).

[14] D. A. Boas, A. G. Yodh. *JOSA A* **14**, 192–215 (1997).

[15] J. Sutin, B. Zimmerman, D. Tyulmankov, D. Tamborini, K. C. Wu, J. Selb, A. Gulinatti, I. Rech, A. Tosi, D. A. Boas, M. A. Franceschini. *Optica* **3**, 1006–1013 (2016).

[16] G. Leegwater, T. Scarpas, S. Erkens. *Transp. Res. Rec.* **2574**, 124–130 (2016).

[17] D. Lesueur. *Adv. Colloid Interface Sci.* **145**, 42–82 (2009).

[18] A. M. Hung, E. H. Fini. *Fuel* **242**, 408–415 (2019).

[19] B. J. Berne, R. Pecora, *Dynamic light scattering: with applications to chemistry, biology, and physics* (Courier Corporation, 2000).

[20] R. Higler, R. A. M. Frijns, J. Sprakel. *Langmuir* **35**, 5793–5801 (2019).

[21] M.-Y. Nagazi, G. Brambilla, G. Meunier, P. Marguerès, J.-N. Périé, L. Cipelletti. *Opt. Lasers Eng.* **88**, 5–12 (2017).

[22] A. Amon, A. Mikhailovskaya, J. Crassous. *Rev. Sci. Instrum.* **88**, 051804 (2017).

[23] H. C. van de Hulst, *Light scattering by small particles* (Dover Publications, New York, 1981).

[24] P. E. Wolf, G. Maret, E. Akkermans, R. Maynard. *J. Phys.* **49**, 63–75 (1988).

[25] C. Zhang, M. Reufer, D. Gaudino, F. Scheffold. *Korea-Aust. Rheol. J.* **29**, 241–247 (2017).

[26] A. Ishimaru, *Wave propagation and scattering in random media* (Academic Press, New York, 1978).

[27] L. Wang, S. L. Jacques. *Appl. Opt.* **34**, 2362–2366 (1995).

[28] T. Lindbergh, M. Larsson, I. Fredriksson, T. Strömberg, *Proc. SPIE* (2007), vol. 6435, p. 64350I.

[29] O. H. A. Abildgaard, F. Kamran, A. B. Dahl, J. L. Skytte, F. D. Nielsen, C. L. Thomsen, P. E. Andersen, R. Larsen, J. R. Frisvad. *Appl. Spectrosc.* **69**, 1096–1105 (2015).

[30] C. Baravian, F. Caton, J. Dillet, J. Mougel. *Phys. Rev. E* **71**, 066603 (2005).

[31] D. J. Cuccia, F. P. Bevilacqua, A. J. Durkin, F. R. Ayers, B. J. Tromberg. *J. Biomed. Opt.* **14**, 024012 (2009).

[32] F. Scheffold, I. D. Block. *Opt. Express* **20**, 192–200 (2012).

[33] P. Jain, S. E. Sarma. *Sci. Rep.* **9**, 11157 (2019).

[34] C. M. Aegerter, G. Maret. *Prog. Optics* **52**, 1–62 (2009).

[35] M. Verma, D. K. Singh, P. Senthilkumaran, J. Joseph, H. C. Kandpal. *Sci. Rep.* **4**, 7257 (2014).

[36] G. Jacucci, O. D. Onelli, A. De Luca, J. Bertolotti, R. Sapienza, S. Vignolini. *Interface Focus* **9**, 20180050 (2018).

[37] A. G. Yodh, P. D. Kaplan, D. J. Pine. *Phys. Rev. B* **42**, 4744 (1990).

[38] J. M. Drake, A. Z. Genack. *Phys. Rev. Lett.* **63**, 259–262 (1989).

[39] M. Pagliazzi, S. Konugolu Venkata Sekar, L. Colombo, E. Martinenghi, J. Minnema, R. Erdmann, D. Contini, A. Dalla Mora, A. Torricelli, A. Pifferi, T. Durduran. *Biomed. Opt. Express* **8**, 5311–5325 (2017).

[40] V. Toronov, E. D'Amico, D. Hueber, E. Gratton, B. Barbieri, A. Webb. *Opt. Express* **11**, 2717–2729 (2003).

[41] H. K. Kim, U. J. Netz, J. Beuthan, A. H. Hielscher. *Opt. Express* **16**, 18082–18101 (2008).

[42] A. Mikhailovskaya, J. Fade, J. Crassous. *Eur. Phys. J. Appl. Phys.* **85**, 30701 (2019).

[43] J. Crassous, M. Erpelding, A. Amon. *Phys. Rev. Lett.* **103**, 013903 (2009).

[44] P. N. Pusey, W. van Megen. *Physica A* **157**, 705–741 (1989).

[45] P. Zakharov. *Opt. Lett.* **42**, 2299–2301 (2017).

[46] P. Zakharov, A. Völker, A. Buck, B. Weber, F. Scheffold. *Opt. Lett.* **31**, 3465–3467 (2006).

[47] W. Lu, N. Vaswani. Preprint at https://arxiv.org/abs/0904.0602 (2009).

[48] A. P. Y. Wong, P. Wiltzius. *Rev. Sci. Instrum.* **64**, 2547–2549 (1993).

[49] S. Kirsch, V. Frenz, W. Schärtl, E. Bartsch, H. Sillescu. *J. Chem. Phys.* **104**, 1758–1761 (1996).

[50] S. Kumari, Global paints and coatings market (2019). www.medium.com/@savitrics.96/global-paints-and-coatings-market-global-industry-analysis-and-forecast-2018-2026-by-resin-by-13585a3ce06f.

[51] C. Conesa, K. Saleh, A. Thomas, P. Guigon, N. Guillot. *KONA Powder Part. J.* **22**, 94–106 (2004).

[52] Z. Du, S. Wen, J. Wang, C. Yin, D. Yu, J. Luo. *J. Mater. Sci. Chem. Engineer.* **4**, 54–59 (2016).

[53] T. C. Chu, W. F. Ranson, M. A. Sutton, W. H. Peters. *Exp. Mech.* **25**, 232–244 (1985).

[54] C. E. Willert, M. Gharib. *Exp. Fluids* **10**, 181–193 (1991).

[55] O. Lieleg, J. Kayser, G. Brambilla, L. Cipelletti, A. R. Bausch. *Nat. Mater.* **10**, 236–242 (2011).

[56] L. Cipelletti, G. Brambilla, S. Maccarrone, S. Caroff. *Opt. Express* **21**, 22353–22366 (2013).

[57] N. Ali, D. C. D. Roux, L. Cipelletti, F. Caton. *Meas. Sci. Technol.* **27**, 125902 (2016).

[58] A. Pommella, A.-M. Philippe, T. Phou, L. Ramos, L. Cipelletti. *Phys. Rev. Appl.* **11**, 034073 (2019).

[59] J. Alvarado, L. Cipelletti, G. H. Koenderink. *Soft Matter* **15**, 8552–8565 (2019).

[60] W. Thielicke, E. Stamhuis. *J. Open Res. Softw.* **2**, e30 (2014).

[61] N. Convery, N. Gadegaard. *Micro Nano Engineer.* (2019).

[62] E. Yeom, S. J. Lee. *Biomicrofluidics* **9**, 024110 (2015).

[63] Q. Wu, W. Ren, Z. Yu, E. Dong, S. Zhang, R. X. Xu. *J. Biomed. Opt.* **20**, 121308 (2015).

[64] Y. Yang, A. Lü, W. Li, Z. Qian. *AIP Advances* **9**, 015003 (2019).

[65] D. D. Patel, D. M. Lipinski. *Sci. Rep.* **10**, 7177 (2020).

[66] T. van de Laar, *Sticky, squishy & stuck: a soft matter approach to membrane failure*, Ph.D. thesis, Wageningen University & Research (2018).

[67] D. D. Duncan, S. J. Kirkpatrick. *JOSA A* **25**, 2088–2094 (2008).

[68] A. Rege, K. Murari, A. Seifert, N. V. Thakor, A. P. Pathak. *J. Biomed. Opt.* **16**, 056006 (2011).

[69] A. J. Pérez, R. J. González-Peña, R. Braga Jr, Á. Perles, E. Pérez-Marín, F. J. García-Diego. *Sensors* **18**, 190 (2018).

[70] A. Rege, S. I. Cunningham, Y. Liu, K. Raje, S. Kalarn, M. J. Brooke, L. Schocket, S. Scott, A. Shafi, L. Toledo, O. J. Saeedi. *Transl. Vis. Sci. Technol.* **7**, 7 (2018).

[71] S. K. Nadkarni, *Seminars in thrombosis and hemostasis* (Thieme Medical Publishers, 2019), vol. 45, pp. 264–274.

[72] B. Lertsakdadet, C. Dunn, A. Bahani, C. Crouzet, B. Choi. *Biomed. Opt. Express* **10**, 5149–5158 (2019).

[73] Z. Hajjarian, S. K. Nadkarni. *J. Biomed. Opt.* **25**, 050801 (2020).

[74] L. M. Richards, S. M. Shams Kazmi, J. L. Davis, K. E. Olin, A. K. Dunn. *Biomed. Opt. Express* **4**, 2269–2283 (2013).

[75] I. Remer, L. F. Pierre-Destine, D. Tay, L. M. Golightly, A. Bilenca. *J. Biophotonics* p. e201800098 (2018).

[76] C.-Y. Lee, B.-H. Huang, W.-J. Chen, J.-Y. Yi, M.-T. Tsai. *OSA Continuum* **3**, 1129–1137 (2020).

[77] A. Mangraviti, F. Volpin, J. Cha, S. I. Cunningham, K. Raje, M. J. Brooke, H. Brem, A. Olivi, J. Huang, B. M. Tyler, A. Rege. *Sci. Rep.* **10**, 7614 (2020).

[78] R. C. Bray, K. R. Forrester, J. Reed, C. Leonard, J. Tulip. *J. Orthop. Res.* **24**, 1650–1659 (2006).

[79] J. Wang, M. Hosoda, D. M. Tshikudi, Z. Hajjarian, S. K. Nadkarni. *Biomed. Opt. Express* **8**, 137–150 (2017).

[80] L. Baij, J. Buijs, J. J. Hermans, L. Raven, P. D. Iedema, K. Keune, J. Sprakel. *Sci. Rep.* **10**, 10574 (2020).

[81] J. Buijs, J. van der Gucht, J. Sprakel. *Sci. Rep.* **9**, 13279 (2019).

[82] M. Hernández, A. M. Grande, S. van der Zwaag, S. J. García. *ACS Appl. Mater. Interfaces* **8**, 10647–10656 (2016).

[83] M. Hernández, A. M. Grande, W. Dierkes, J. Bijleveld, S. van der Zwaag, S. J. García. *ACS Sustain. Chem. Engineer.* **4**, 5776–5784 (2016).

[84] T. Suzuki, N. Oishi, H. Fukuyama. *J. Biomed. Opt.* **24**, 031014 (2018).

[85] O. I. Baum, V. Y. Zaitsev, A. V. Yuzhakov, A. P. Sviridov, M. L. Novikova, A. L. Matveyev, L. A. Matveev, A. A. Sovetsky, E. N. Sobol. *J. Biophotonics* p. e201900199 (2019).

[86] P.-Y. Chao, P.-C. Li. *Opt. Express* **24**, 18860–18871 (2016).

[87] P.-Y. Chao, W.-W. Liu, S.-F. You, P.-C. Li. *Sci. Rep.* **8**, 14470 (2018).

[88] A. M. König, T. G. Weerakkody, J. L. Keddie, D. Johannsmann. *Langmuir* **24**, 7580–7589 (2008).

[89] P. B. Jones, H. K. Shin, D. A. Boas, B. T. Hyman, M. J. Moskowitz, C. Ayata, A. K. Dunn. *J. Biomed. Opt.* **13**, 044007 (2008).

[90] J. W. Kim, H. Jang, G. H. Kim, S. W. Jun, C.-S. Kim. *J. Biomed. Opt.* **24**, 076001 (2019).

[91] E. Ducrot, Y. Chen, M. Bulters, R. P. Sijbesma, C. Creton. *Science* **344**, 186–189 (2014).

[92] J. M. Clough, C. Creton, S. L. Craig, R. P. Sijbesma. *Adv. Funct. Mater.* **26**, 9063–9074 (2016).

[93] M. Stratigaki, R. Göstl. *ChemPlusChem* **85**, 1–10 (2020).

[94] S. Krause, C. Cerretani, T. Vosch. *Chem. Sci.* **10**, 5326–5331 (2019).

[95] K. B. Yushkov, V. Y. Molchanov. *J. Biomed. Opt.* **22**, 066017 (2017).

[96] F. Martelli, T. Binzoni, A. Pifferi, L. Spinelli, A. Farina, A. Torricelli. *Sci. Rep.* **6**, 27057 (2016).

[97] L. Colombo, M. Pagliazzi, S. K. V. Sekar, D. Contini, A. Dalla Mora, L. Spinelli, A. Torricelli, T. Durduran, A. Pifferi. *Neurophotonics* **6**, 035001 (2019).

[98] P.-C. Kiatkirakajorn, L. Goehring. *Phys. Rev. Lett.* **115**, 088302 (2015).

[99] B. Yang, J. S. Sharp, M. I. Smith. *ACS Nano* **9**, 4077–4084 (2015).

[100] L. Goehring, J. Li, P.-C. Kiatkirakajorn. *Phil. Trans. R. Soc. A* **375**, 20160161 (2017).

[101] L.-B. W. Lee, R. A. Register, D. M. Dean. *J. Polym. Sci. B: Polym. Phys.* **43**, 97–106 (2005).

[102] D. Mi, C. Xia, M. Jin, F. Wang, K. Shen, J. Zhang. *Macromolecules* **49**, 4571–4578 (2016).

[103] M. Mirkhalaf, J. A. W. van Dommelen, L. E. Govaert, J. Furmanski, M. G. D. Geers. *J. Polym. Sci. B: Polym. Phys.* **57**, 378–391 (2019).

[104] M. Hegde, L. Yang, F. Vita, R. J. Fox, R. van de Watering, B. Norder, U. Lafont, O. Francescangeli, L. A. Madsen, S. J. Picken, E. T. Samulski, T. J. Dingemans. *Nat. Commun.* **11**, 830 (2020).

[105] S. Kumari, A. K. Nirala. *Laser Phys.* **26**, 115601 (2016).

[106] A. Rahmanian, S. A. Mireei, S. Sadri, M. Gholami, M. Nazeri. *Postharvest Biol. Tec.* **162**, 111118 (2020).

[107] R. Pandiselvam, V. Mayookha, A. Kothakota, S. Ramesh, R. Thirumdas, P. Juvvi. *Trends Food Sci. Tech.* **97**, 1–13 (2020).

[108] R. A. Braga, L. Dupuy, M. Pasqual, R. R. Cardoso. *Eur. Biophys. J.* **38**, 679–686 (2009).

[109] A. Zdunek, A. Adamiak, P. M. Pieczywek, A. Kurenda. *Opt. Laser. Eng.* **52**, 276–285 (2014).

[110] M. Z. Ansari, A. Mujeeb, A. K. Nirala. *Laser Phys.* **28**, 065608 (2018).

[111] P. Singh, A. Chatterjee, V. Bhatia, S. Prakash. *Comput. Electron. Agric.* **169**, 105212 (2020).

[112] C. Schott, J. Steingroewer, T. Bley, U. Cikalova, B. Bendjus. *Eng. Life Sci.* **20**, 287–295 (2020).

[113] Y. Kuznetsov, A. Sdobnov, I. Meglinski, A. Harmelin, V. Kalchenko. *Laser Phys. Lett.* **16**, 115601 (2019).

[114] M. Z. Ansari, E. E. Ramírez-Miquet, I. Otero, D. Rodríguez, J. G. Darias. *J. Biomed. Opt.* **21**, 066006 (2016).

[115] E. E. Ramírez-Miquet, H. Cabrera, H. C. Grassi, E. de J. Andrades, I. Otero, D. Rodríguez, J. G. Darias. *Lasers Med. Sci.* **32**, 1375–1386 (2017).

[116] J. P. Gordon, H. J. Zeiger, C. H. Townes. *Phys. Rev.* **99**, 1264–1274 (1955).

[117] J. D. Breeze, E. Salvadori, J. Sathian, N. M. Alford, C. W. M. Kay. *Nature* **555**, 493–496 (2018).

[118] O. Bikondoa, *X-ray photon correlation spectroscopy for the characterization of soft and hard condensed matter*, X-ray and neutron techniques for nanomaterials characterization (Springer, 2016), chap. 3, pp. 95–156.

[119] A. R. Sandy, Q. Zhang, L. B. Lurio. *Annu. Rev. Mater. Sci.* **48**, 167–190 (2018).

[120] P. Zhang, J. J. Maldonis, Z. Liu, J. Schroers, P. M. Voyles. *Nat. Commun.* **9**, 1129 (2018).

Summary

In light of the ever-growing societal demand for high-performance, sustainable products, it is of utmost importance to unravel the inner machinery of future's materials. This pursuit is particularly relevant for polymer materials, which are highly complex yet ubiquitous. Synthetic polymer materials come in all shapes and sizes, including plastics, paints, adhesives, elastomers and gels. They play an essential role in everyday life. Yet, the Earth's diminishing resources and growing population set increasingly stringent limits on the possibilities. Modern societies must therefore make a transition from short-lifetime, polluting products to durable, environmentally friendly alternatives. Examples in this thesis are water-based paints as substitutes for organic-solvent-based systems, and sophisticated materials such as self-healing and self-cleaning polymers. The high complexity of these materials calls for more than trial-and-error testing alone. Rather, researchers must seek to gain a deeper understanding of the polymer dynamics and mechanics on all scales involved.

The legendary Nobel physicist Richard Feynman (1918–1988) once wrote on his blackboard: *"What I cannot create, I do not understand."* However, this truth does not imply that we *do* understand what we *can* create. Resolving the multitude of issues we encounter today, and are about to face in the (near) future, requires fundamental insight into the nanoscopic processes driving polymer behaviour. Remarkably, this nanoscale is generally not the primary scale of interest when developing new polymer materials.

In this thesis, we cast new light on the nanoscale dynamics and mechanics inside complex polymer materials. We herein focus on polymer dispersions and networks, specifically drying water-borne coatings (Parts I and II) and dynamic elastomers (Part III). Reaching down to the very core of these materials is an ambitious task, as the smallest length scales are unreachable to conventional imaging methods that operate using visible light. Indeed, the wavelength of visible light equals hundreds of nanometres, thus precluding interaction with nanometric objects.

We overcome these limitations in two ways in this thesis. In **Part I**, we simplify matters by creating model polymer dispersions representative of water-based paints. We unleash the full power of bright-field microscopy to elucidate the various mechanisms at work. Although this method is not truly nanometric, we complement it in three ways to still realise a comprehensive picture of the governing processes down to the nanoscale: (i) we systematically vary the dispersion

parameters to allow for nanoscopic insight through deduction; (ii) we examine the nanoscale surface structure in detail using electron microscopy; and (iii) we establish multi-scale theoretical frameworks to underpin our experimental results in a quantitative manner.

This three-pillar approach has proven successful for semi-transparent systems, yet it severely fails for non-transparent, turbid materials – which most everyday polymers are. For those cases, a more specialized microscopy technique is optimally suited: laser speckle imaging (LSI). This technique has its roots in the biomedical field, where it was pioneered in the 1980s and gained renewed attention in the early 2000s with the advent of powerful digital cameras and computers. We introduce an advanced version of LSI, and apply it to drying polymer dispersions in **Part II** of this thesis. Laser speckle imaging allows us to cut through the fog of opaque samples with exceptional sensitivity. In this method, we shine a powerful laser beam on the material of interest, which diffuses through the cloudiness. Subsequently, we capture the light that returns, and use dedicated computer algorithms to acquire an abundance of quantitative information about hidden phenomena deep inside the material.

Not only do we use LSI to probe the inner dynamics of coatings, but we also open up a whole new world of applications related to dynamic elastomers in **Part III**. We quantitatively visualize various collective 'dances' of nanoscale building blocks in high-tech materials for the first time. We uncover the molecular path to catastrophic fracture, where – analogous to a flashmob dance – a rapidly growing number of molecules participate until a climax is reached. We show how polymer damage can be completely healed, because – like a moshpit – molecules spontaneously move in collective patterns with net directionality. Finally, we reveal how molecular collaboration can result in unique, long-ranged shape transformations – similar to synchronized ballet.

First and foremost, these nanoscopic glances beneath the surface of coatings and elastomers are fundamentally interesting. Yet, we hope they will also expedite the development of sustainable polymer materials with increased lifetime. We summarize our main findings and their implications in the following paragraphs.

Part I: Drying model coatings

It is impossible to imagine society without coatings. They are practically omnipresent on man-made products, such as walls, cars, furniture, appliances, airplanes and countless more. Chances are that the reader has at least once painted something. Most likely, the used paint was water-based, since this type of paints has gained increasing popularity compared to paints based on organic solvents, which

strain the environment and the consumer's health. Nevertheless, water-based 'latex' coatings cannot yet compete with their solvent-based counterparts in terms of final film homogeneity, gloss, water repellency, chemical resistance and durability. The foundations of these differences are laid during drying; the internal drying dynamics decisively determine the final film appearance and performance.

While painting, have you ever wondered how the liquid-like coating dries and eventually forms a solid-like uniform film? This process seems simple, but in reality it is highly complex. If the paint ingredients or drying conditions are not optimal, a variety of problems can therefore occur during and/or after drying. Think of crack formation, detachment from the surface, thickness inhomogeneities, or permanent brush marks. These instabilities threaten the lifetime of both protective and decorative coatings. In many cases, the instabilities are clearly visible at the macroscopic scale with the naked eye, yet they are in fact caused by subtle heterogeneities in the dynamics at much smaller scales. To understand why these complications arise and how we can prevent them, more knowledge about the drying process of water-borne paints is needed. Specifically, it is essential to illuminate how the nanoscopic and microscopic dynamics relate to the macroscopic evolution of a paint film. In the first chapters of this thesis, we investigate principal parameters that govern this dynamic route to coating film formation, with the ultimate aim to improve the quality of 'green' paints.

Unfortunately, this quest is complicated by the fact that commercial paints contain many dozens of components. To accurately elucidate the mechanisms underlying the various drying phenomena, we have to simplify our systems and eliminate many factors, so that the effects of key parameters can be uncovered. In the chapters of Part I, we focus entirely on such 'model coatings'.

Chapter 2

In Chapter 2, we provide a critical introduction to major themes in the field of paint drying. We highlight that the study of latex film formation is not only relevant for practical applications, but also intrinsically intriguing. At the macroscopic level, people consider watching paint dry as the most boring thing to do – the idiom exists for good reason! Yet, at the microscopic level, not only is it interesting, it is even exciting. We review the literature to showcase that drying paints are a true playground for soft matter scientists, featuring remarkable phenomena on many time and length scales: from individual particle pairs, to collective effects in complex dispersions, to potential complications of this collectivity in the form of large-scale instabilities. We address different methods to characterize the coating morphology during and after drying, either directly (via microscopy) or indirectly

(via scattering). We hope to convince readers that a seemingly boring, mundane and tedious process, when approached from the right angle, can be absolutely fascinating.

Chapter 3

In Chapter 3, we present a study of the effects of particle softness on the drying and ageing of polymer dispersion droplets. Well-controlled film formation in drying droplets is central to a variety of applications, such as spray painting and inkjet printing, where a homogeneous coating is highly desired. However, the particles often end up in a nonuniform deposit due to the coffee-ring effect, and severe cracks may emerge. A crucial determinant of good film formation is the particle softness. Not only for humans, but also for latex particles, being *soft matters*! Using tailored synthesis procedures, we systematically vary this parameter by adjusting the glass transition temperature (T_g) of the polymer phase, from -10 °C to 64 °C. We apply bright-field microscopy and scanning electron microscopy to this well-defined series to bridge time scales from sub-seconds to days, and length scales from a few nanometres to the millimetre.

This chapter focuses on three important yet complex phenomena: coalescence, cracking, and crack healing. We show both qualitatively and semi-quantitatively that the particle softness greatly influences the relative time scales and interplay of these key processes, and hence the final film morphology and properties. Specifically, as the polymer phase becomes softer – i.e. the T_g is lowered with respect to room temperature – coalescence proceeds; by contrast, as the particles become harder, distinct cracks develop. Perhaps most surprisingly, we provide evidence for self-healing of cracks. This peculiar potential has not been reported before. The onset of coalescence and crack healing is found when the particles are still glassy, up to thought-provoking T_g values of 13 °C above room temperature. After a few days of ageing, these droplets reach the same homogeneity as low-T_g droplets shortly after drying. This applies to all investigated length scales, from the single-particle level (coalescence) to the macroscopic level (healed cracks). The formation of a continuous, crack-free film from a latex droplet can thus occur along two distinct paths: upon drying ($T_g - T < -5$ °C) or by crack self-healing (-5 °C $< T_g - T \lesssim 30$ °C).

Chapter 4

A disadvantage of varying the glass transition temperature is that changes in particle softness are inherently accompanied by a solid-to-liquid transition: the polymer phase is either soft and liquid-like at low T_g, or hard and solid-like at

high T_g. The effects of softness and phase behaviour are intimately linked, and jointly influence the stages of particle deformation and coalescence during film formation. Hence, it is challenging to disentangle their individual effects. To study exclusively the effects of particle deformability on the drying stages and mechanisms, in Chapter 4 we switch off coalescence by synthesizing crosslinked latex particles. The resultant colloidal rubber particles are completely solid and therefore incapable of coalescing. By crosslinking the polymer phase with different densities, we tune the particle modulus in a controlled manner from approximately 1 to 10 MPa. Similarly to Chapter 3, we dry small droplets of these suspensions, and combine bright-field and scanning electron microscopy to analyse the effects of particle deformability from the macroscopic to the particle scale. Moreover, we complement our experiments with a theoretical framework of the main mechanical stresses at play during the different stages of droplet drying and film formation. Using scaling arguments, we derive the relative importance of these stresses, and their contribution to nanoscale phenomena (particle packing and deformation) as well as macroscopic instabilities (wrinkles and cracks).

Both experimentally and theoretically, we identify the same three drying stages for all studied rubber suspensions: (I) concentration, (II) air invasion, and (III) capillary deformation. While the first stage is universal within this series, the particle softness strongly influences both the duration and extent of the last two stages. We find distinct transitions at a recurring crosslink density of 20 mol%. Remarkably, these transitions exactly coincide with pronounced changes in the wrinkle wavelength and crack density, emphasizing the central role of the particle deformability. This knowledge may contribute to the mitigation or even prevention of complications during dispersion drying.

Part II: Laser speckle imaging of drying realistic coatings

To obtain a deeper understanding of film formation in polymer dispersions, we adopt a bottom-up approach in this thesis. In Part I, we have started our research on relatively simple latices that serve as models for water-borne paints. In Part II, we gradually increase their complexity to finally arrive at 'real', practical coating systems. The primary enhancement is the addition of strongly scattering pigment particles, which are present in all paints intended to cover the surface underneath. These pigments render the coating opaque, thus requiring laser speckle imaging for analysis of the internal, sub-surface dynamics, at depths where conventional optical methods cannot reach.

Decoding the recorded laser speckle images is quite challenging. These so-called 'speckle patterns' do not directly reflect the sample structure; rather, they are

interference patterns wich indirectly represent millions of small particles inside the sample. More precisely, speckle patterns are generated by countless scattered photons that have travelled numerous random walks through the sample. Thanks to prior research by experts in the field and our own unique implementation of LSI, we can extract a wealth of quantitative information from these complex raw data, with millisecond temporal resolution and nanometric displacement resolution.

In the chapters of Part II, we showcase the versatility of LSI and its applicability to a variety of realistic coating systems. Often, different drying phenomena occur simultaneously, over a wide range of characteristic time scales, and spatially heterogeneously. The method we present allows connecting up to seven decades of time scales in a spatially-resolved manner, and thus forms a stepping stone towards understanding the fundamental drying mechanisms and ultimately preventing paint films from undergoing failure.

Chapter 5

In Chapter 5, we report the first thorough application of laser speckle imaging to complex coating systems, relevant to both the uninitiated and experts in the field. The primary aim of this chapter is to provide readers with a toolbox of data analysis methods that can easily be extended to other material science applications. We apply these methods to a diversity of drying scenarios, and implement a quantitative interpretation of our results which goes beyond standard routines. Notably, we introduce an entirely new use of the correlation time τ to create image contrast, which adds a new dimension to the LSI technique. We harness the τ-dependence to disentangle fast and slow dynamics and to probe the processes of interest most sensitively.

This chapter follows an order of increasing heterogeneity: from (i) a uniformly applied paint film; to (ii) heterogeneities caused by statistical processes (i.e. cracking and delamination); (iii) extra inhomogeneity induced by the sample geometry (i.e. a droplet geometry which triggers the coffee-ring effect and consequent anisotropy of all dynamics); (iv) induced heterogeneity by the application method (i.e. brush application); and finally (v) additional fluctuations by porosity of the substrate.

Chapter 6

In Chapter 6, we address an important question that emerged from industry. One of the key handling parameters of a coating system is the open time; defined as the time after application beyond which re-modelling of the paint film will result in permanent defects, such as brush marks. With the increasing regulatory pressure to remove all volatile organic solvents from water-based paints, controlling the

open time, in particular extending it, has become imperative. Surprisingly, despite its importance in handling a paint, no standardized method exists to determine the open time without ambiguity. In fact, measurements performed by different operators often result in different values that depend strongly on the method that is used. To aid in the development of water-based paints with a desirable handling character, this chapter aims to describe an experimental method to determine the open time unambiguously.

We apply laser speckle imaging to an industrially relevant, pigmented acrylic paint system. Using tailored image processing algorithms, we show how to quantify the characteristic time constant of the pigment dynamics as well as a proxy for the nature of their motion. These two parameters enable the extraction of two unique measures for the open time, without any assumptions and without externally perturbing the paint film. In addition, we develop an in-depth theoretical framework of the factors influencing the open time. By establishing a set of scaling relations, we are able to accurately predict the experimental results as a function of film thickness, humidity and temperature.

Finally, we show how LSI can be used to shed more light on the process of film formation at the end of drying, when a continuous and uniform film must be formed through coalescence. We pinpoint a signature of coalescence that is universal within the investigated series of coatings. Furthermore, we quantify the effects of the concentration of plasticizers, whose eradication is an important theme in coatings research.

Part III: Laser speckle imaging of dynamic elastomers

Having established LSI as a powerful technique to dissect the inner workings of complex polymer dispersions, in Part III we highlight how the same method can unveil the internal dynamics and mechanics of advanced polymer networks. In all cases, we induce strong scattering from the networks by embedding a small amount of probe nanoparticles, which serve the same purpose as pigment particles in paints. Motion at the molecular level directly affects the dynamics of the probe particles. Deciphering and quantifying these dynamics thus allows us to resolve some of the dance moves of the polymer molecules.

Chapter 7

Fracture is the major cause of polymer failure. To date, considerable research effort has been devoted to understanding crack propagation, yet understanding how the crack appeared in the first place remains largely uncharted territory. In Chapter 7,

we therefore use LSI to make (seemingly) unpredictable fracture predictable. We provide the first experimental proof of the mechanisms of crack nucleation in a strained elastomer, thus resolving a long-standing debate on the nature of delayed fracture of polymer networks.

We quantitatively analyse our experimental data to create spatially-resolved maps of the local nanodeformations prior to catastrophic failure, with unprecedented temporal and mechanical resolution. Our findings reveal that delayed failure is preceded by a dramatic acceleration of high-frequency motions – right at the locus of ultimate fracture. Although we do not detect the breaking of bonds directly, we bring to light a long-ranged zone of deformations resulting from very localized network weakening. This zone grows exponentially in space and time, reflecting a self-catalytic cascade of damage processes, until fracture is inevitable and instantaneous. Computer simulations are in good qualitative agreement with the spatial and temporal trends found in our experiments. These newly acquired insights settle a lingering controversy in the fracture physics community, and may aid in safeguarding polymers from failure.

Chapter 8

As discussed in Chapter 7, one way to ensure that damage is not the beginning of the end, is by stopping it in its track before a tipping point is reached. An alternative, novel strategy is to develop polymers with the fascinating capability to spontaneously repair damage *after* it has formed, just like the human skin. This approach can significantly enhance polymer longevity. In Chapter 8, we use LSI to visualize, quantify, unravel and explain the molecular motions of autonomous repair. Self-healing polymers, which spontaneously repair damage from scratching, cutting, fracture or abrasion, offer tremendous potential for a new generation of robust and durable coatings. Although the development of these polymers has taken flight in the past decades, it is still largely unknown how specific molecular motions are at the origin of self-healing. Elucidating these motions is indeed very challenging: they occur only at the site of damage, and typically encompass a wide range of relaxation modes and frequencies. The lack of a true understanding of autonomous repair in turn precludes the rational design and encoding of self-healing functionality in polymers.

In this chapter, we create four-dimensional micromechanical maps of *in situ* self-healing phenomena across almost six decades in frequency. Our results reveal how polymer molecules perform a collective dance to slowly repair cuts and cracks, closing the opening like a zipper. We show that autonomous repair is essentially a combination of two key processes: (i) strongly localized supramolecular rebonding,

which restores the material cohesion at the locus of damage; and (ii) delocalized viscoplastic relaxation, which recovers the original shape of the polymer. The localized activity is most pronounced at a characteristic frequency of 2 Hz, surprisingly similar to typical frequencies found using bulk rheology. Since self-healing polymers are expected to increase the safety and sustainability of materials throughout society, our results may have implications for the development of more reliable building materials, aircraft and medical implants.

Chapters 9 and 10

The polymers of the future are not only durable and self-healing, but they are also active, adaptive and interactive. In the past decades, a wide variety of active materials based on liquid crystal polymer networks (LCNs) have materialized, capable of bio-inspired morphing, sensing, transport or locomotion. These materials can undergo programmed changes in shape or properties in response to external cues. However, the precise mechanisms of this complex behaviour have remained unclear. The absence of this fundamental knowledge impedes the design of functional liquid-crystal structures from the bottom up. In Chapters 9 and 10, we use LSI to fill parts of this knowledge gap. We study surface morphing in a prominent class of liquid-crystal-based active materials: shape-shifting coatings. We activate the LCNs by a high-frequency alternating electric field, which causes embedded responsive molecules to oscillate. Subsequently, we probe nanoscale changes in the local dynamics and mechanics of the material en route to shape-shifting. We analyse our data using recently developed mathematical algorithms based on the Fourier transform. In addition to being exceptionally fast, these algorithms allow us to spectrally decompose the dynamic response in a single shot, thus providing a highly resolved view of the mechanisms underlying motility in liquid crystal polymer networks.

In Chapter 9, we show how the switching of surface topography, and thereby e.g. wetting or frictional properties, occurs in a distinct hierarchical pattern: from molecular-scale interactions between liquid crystal molecules and the external field, to the emergence of large-scale collective motion. This chain of events is initiated by switching on an electric field, which triggers a small – but detectable and quantifiable – dielectric response of the liquid crystal molecules to the field. We uncover how this motion amplifies in time through collective synchronization, leading to a critical weakening of the solid network in which the responsive molecules are embedded, and ultimately gives rise to patterned network expansion and surface transformation.

At the heart of this functional response must be a field-induced glass-to-rubber transition. For many years, it was indeed hypothesized that the polymer network is plasticized under the action of a high-frequency alternating current. Without such 'electroplasticization', as we term it, the initially static and glassy material cannot undergo substantial shape changes. However, conclusive evidence was never provided, nor were the detailed mechanisms elucidated. In Chapter 10, we report the first experimental observation of a true electrical glass transition in liquid crystal polymer networks. Through systematic exploration, we find that frustrated, collective oscillations of responsive molecules cause a mechanical disturbance inside the network, inducing a distinct elastic-to-plastic transition. This transition occurs only beyond a critical field frequency, which scales with the temperature gap to the thermal glass transition. We anticipate that these findings may have implications for the molecular engineering of new 'smart' and active polymer materials.

Chapter 11

This thesis concludes in Chapter 11 with a general discussion of all chapters. We connect the dots and focus on the bigger picture of our work. Furthermore, we critically evaluate laser speckle imaging and highlight that this method is by no means picture perfect, alike any other technique. We end by identifying new lights on the LSI horizon. We extend our method to a wider range of material science applications, and describe potential new exciting variants. We believe that this thesis paints a bright future.

List of publications

This thesis

- Hanne M. van der Kooij and Joris Sprakel, 'Watching paint dry; more exciting than it seems', *Soft Matter* **11**, 6353–6359 (2015). **(Chapter 2)**
- Hanne M. van der Kooij, Marleen de Kool, Jasper van der Gucht and Joris Sprakel, 'Coalescence, cracking, and crack healing in drying dispersion droplets', *Langmuir* **31**, 4419–4428 (2015). **(Chapter 3)**
- Hanne M. van der Kooij, Gea T. van de Kerkhof and Joris Sprakel, 'A mechanistic view of drying suspension droplets', *Soft Matter* **12**, 2858–67 (2016). **(Chapter 4)**
- Hanne M. van der Kooij, Remco Fokkink, Jasper van der Gucht and Joris Sprakel, 'Quantitative imaging of heterogeneous dynamics in drying and aging paints', *Sci. Rep.* **6**, 34383 (2016). **(Chapter 5)**
- Slav A. Semerdzhiev, Hanne M. van der Kooij, Remco Fokkink, Jasper van der Gucht and Joris Sprakel, 'Quantifying the open time and film formation of waterborne coatings with Laser Speckle Imaging', *in preparation*. **(Chapter 6)**
- Hanne M. van der Kooij, Simone Dussi, Gea T. van de Kerkhof, Raoul A. M. Frijns, Jasper van der Gucht and Joris Sprakel, 'Laser Speckle Strain Imaging reveals the origin of delayed fracture in a soft solid', *Sci. Adv.* **4**, eaar1926 (2018). **(Chapter 7)**
- Hanne M. van der Kooij, Arijana Susa, Santiago J. García, Sybrand van der Zwaag and Joris Sprakel, 'Imaging the molecular motions of autonomous repair in a self-healing polymer', *Adv. Mater.* **29**, 1701017 (2017). **(Chapter 8)**
- Hanne M. van der Kooij, Slav A. Semerdzhiev, Jesse Buijs, Dirk J. Broer, Danqing Liu and Joris Sprakel, 'Morphing of liquid crystal surfaces by emergent collectivity', *Nat. Commun.* **10**, 3501 (2019). **(Chapter 9)**
- Hanne M. van der Kooij, Dirk J. Broer, Danqing Liu and Joris Sprakel, 'Electroplasticization of liquid crystal polymer networks', *ACS Appl. Mater. Interfaces* **12**, 19927–19937 (2020). **(Chapter 10)**

Other work

- Hanne M. van der Kooij, Evan Spruijt, Ilja K. Voets, Remco Fokkink, Martien A. Cohen Stuart and Jasper van der Gucht, 'On the stability and morphology of complex coacervate core micelles: from spherical to wormlike micelles', *Langmuir* **28**, 14180–14191 (2012).

- Ahu Gümrah Dumanlı, Gen Kamita, Jasper Landman, Hanne M. van der Kooij, Beverley J. Glover, Jeremy J. Baumberg, Ullrich Steiner and Silvia Vignolini, 'Controlled, bio-inspired self-assembly of cellulose-based chiral reflectors', *Adv. Opt. Mater.* **2**, 646–650 (2014).

- Ahu Gümrah Dumanlı, Hanne M. van der Kooij, Gen Kamita, Erwin Reisner, Jeremy J. Baumberg, Ullrich Steiner and Silvia Vignolini, 'Digital color in cellulose nanocrystal films', *ACS Appl. Mater. Interfaces* **6**, 12302–12306 (2014).

- Jeroen Appel, Niek de Lange, Hanne M. van der Kooij, Ties van de Laar, Jan-Bart ten Hove, Thomas E. Kodger and Joris Sprakel, 'Temperature controlled sequential gelation in composite microgel suspensions', *Part. Part. Syst. Charact.* **32**, 764–770 (2015).

- Merve Cetintas, Joris de Grooth, Anton H. Hofman, Hanne M. van der Kooij, Katja Loos, Wiebe M. de Vos and Marleen Kamperman, 'Free-standing thermo-responsive nanoporous membranes from high molecular weight PS-PNIPAM block copolymers synthesized via RAFT polymerization', *Polym. Chem.* **8**, 2235–2243 (2017).

- Merve Mocan, Hares Wahdat, Hanne M. van der Kooij, Wiebe M. de Vos and Marleen Kamperman, 'Systematic variation of membrane casting parameters to control the structure of thermo-responsive isoporous membranes', *J. Membr. Sci.* **548**, 502–509 (2018).

Acknowledgements

"There is light at the end of the tunnel." – Many people ☺

Light both directly and indirectly permeates this thesis in front of you. In the title, on the cover, in quotes, in light-related terminology, in the literal light that forms the basis of our experimental set-ups, and in the figurative light that we have shed on manifold questions. Moreover, this chapter is full of metaphorical lights, in the form of all the people who have contributed to the completion of this thesis. The fact that you are reading this section probably implies that you have played a role in lightening up my PhD adventure. Thank you for that! You have made the proverbial tunnel as bright as the light at the end. These acknowledgements are for everyone who has supported me during my PhD years. Each of them has thus 'let light be'. The order below does not necessarily reflect my gratitude.

Joris, you are the main reason I started this PhD in the first place. On my birthday, 7.5 years ago, we already signed my first contract. It turned out to be the best birthday gift of my life. The research topic fitted me like a glove, and I could not have wished a better supervisor in you! We connected both on a scientific and personal level. We have had countless good conversations, about the deep and light aspects of research and life. Anything you say is crystal clear. Your positive attitude encouraged me to start and finish projects, believe in myself, and keep thoroughly enjoying research. You provided me with support and advice whenever needed, while at the same time allowing me the freedom and independence to explore my own path. Thank you for challenging me to move beyond my self-imagined limits, which has helped me build self-confidence. You even motivated me to step out of my comfort zone and venture into the *terra incognita* of laser speckle imaging. I cannot wait to explore and conquer more exciting research areas with you in the future!

Jasper, thank you for welcoming me into your group, and for allowing me to work on such a great variety of research topics. You orchestrate PCC so well! Thank you for your seemingly boundless positivity, patience and analytical depth. You can reach to the core of the (soft) matter like no other. I am grateful for all the freedom and opportunities you have given me to develop myself. You have a very natural way of approaching research and people, which has always made me feel at ease. I have learned a lot from you! Your office door was always open for good scientific conversations, but also to join coffee breaks and chat about the more mundane aspects of life. Thank you for the many insightful and enjoyable work meetings. I cannot recall one meeting that did *not* last longer than scheduled ☺.

I would like to greatly acknowledge the **Dutch Polymer Institute (DPI)**, for giving me the unique opportunity to embark on this PhD journey. Thank you for the financial support and for facilitating the industrial interest in our work. I also wish to express my sincere gratitude to all industrial participants in our DPI coatings cluster. Without your funding, this thesis and laser speckle imaging would not exist. Listening and talking to you has sparked my curiosity and interest in coatings even more. Thank you for your feedback at the many progress meetings. It has been very insightful to learn about the practical implementation and (im)possibilities of my research. **BYK-Chemie**, **Lawter** and **Saint-Gobain**, I have greatly appreciated your scientific and financial contributions, our fruitful contact and exchange of knowledge.

I especially want to express my gratitude to **Ronald Tennebroek**, **Tijs Nabuurs** and **Matthew Gebhard** (DSM Coating Resins, Waalwijk) for your continuous involvement in my project. Many thanks for the good and regular contact, and for readily providing us with fascinating latex dispersions and TiO_2 pigment paste. Tijs, thank you for inviting me at your facility in the beginning of my PhD, offering me a tour and a useful introduction to particle synthesis, both theoretically and in practice.

Leendert Molhoek and **Jan Bongaerts** (DSM Coating Resins, Zwolle), thank you particularly for your interest in exploring the application potential of laser speckle imaging to powder coatings. You generously provided us with a large number of powder coatings, which you carefully transported to Wageningen. Performing preliminary LSI measurements with you was a pleasure and insightful, as well as our multiple discussions and correspondence afterwards.

Keimpe van den Berg (AkzoNobel), you have been at virtually all progress meetings, invariably full of useful questions. Thank you for showing sincere interest in my project and always providing relevant feedback!

DPI Coatings Technology programme area coordinators, **Monique Bruining** and **Ronald Korstanje**, thank you for your valuable input and support during the progress meetings and beyond.

Many thanks go to our academic collaborators, who have significantly enriched my PhD experience. It was a great privilege and an honour to work with you! Thank you for providing us with your fascinating materials so generously. You are leading lights in materials science. **Sybrand van der Zwaag**, **Santiago García** and **Arijana Susa** (Novel Aerospace Materials group, TU Delft), what a joy to unleash LSI on your beautiful self-healing polymers! Chapter 8 of this thesis would not have existed otherwise. I have greatly enjoyed our meetings, which were always full of new insights. **Sybrand**, as the scientific director of DPI, you recognized the potential of laser speckle imaging and initiated a 'marriage' between LSI and

your intriguing materials. You have an eye for seeing the unseen in scientific results, and bringing them to a new level by clever experiments, analysis and interpretation. You always have a fresh angle on topics and you can connect the dots like no other. Thank you in particular for your very useful, detailed and sharp comments on my propositions, which have helped me significantly to improve them. **Santiago**, you are as dynamic yet strong as your polymers! Thank you for your inexhaustible enthusiasm, energy and support. **Arijana**, you are a bright, caring, enthusiastic, beautiful young lady. Thank you for introducing me into the chemistry and properties of your wonderful samples! Your emails were always very thoughtful and clear, full of relevant information and details. Thanks for all the positive vibes ◡̈.

Dick Broer and **Danqing Liu** (Laboratory of Stimuli-Responsive Functional Materials and Devices, TU Eindhoven), I cannot express enough how grateful I am for you opening a whole new world to us, which has culminated in Chapters 9 and 10 of this thesis. **Dick**, after chairing a DPI meeting you approached us for a potential collaboration. What we originally expected to be a small side project has transformed into far more than we ever imagined. You are an example to other researchers, by showing that excellent scientists can also be extremely kind, dedicated to helping others, and unhurried. Thank you for all your useful ideas and feedback. **Danqing**, you are such a powerful and beautiful young lady! I am greatly impressed about your research skills and capabilities. During your times in Wageningen, you demonstrated exceptionally quick thinking and experimental expertise, while also being a very easy-going, fun and friendly person. I am certain that your scientific journey will move along many beautiful and uphill paths!

I wish to express my sincere thanks to the four distinguished persons in my jury for taking part in this special day. **Prof. Schroën**, **Prof. Keddie**, **Prof. Katsonis** and **Dr. Ellenbroek**, I am very grateful for your willingness to read my thesis critically and thoroughly, and for your enthusiam to challenge me with interesting questions, allowing me to defend.

I would like to acknowledge the **Wageningen Electron Microscopy Centre (WEMC)** of Wageningen University, where I received all the possibilities and freedom to perform the SEM measurements in Chapters 1–4. Special thanks in particular to **Marcel Giesbers** for allowing me to perform the SEM training, for assistance with the SEM equipment, and for optimal arrangements even after the coronavirus outbreak.

I want to express special thanks to the talented MSc and BSc students working with me on this project. **Marleen**, **Gea** and **Thijmen**, supervising you was a great pleasure and privilege! I myself learned a lot from working with you, discussing mysterious results, and answering your clever questions. I wish you all the best in

your future careers, which I am sure will be joyful and successful. **Marleen**, we connected during our first lab trip at PCC, after which you approached me for a thesis project. I had just started my PhD and was still exploring the direction of my scientific voyage, but your active and hands-on mentality gave us a kick-start. It has even led to important parts of Chapter 3. I still vividly remember the countless conversations we had about paints and microscopy, and the fun SEM sessions together, gazing in awe at your beautiful particles. You showed me that coalescence is a better love story than Twilight ;-)! **Gea**, you are such a good and reliable researcher. Your projects were far from easy, but you always remained enthusiastic and optimistic – even after dozens of particle synthesis problems or radical changes of plan. Thank you for doing both your BSc and MSc theses with me! I owe significant parts of Chapters 4 and 7 to you. All the best finishing your PhD in Cambridge! **Thijmen**, many thanks for your great BSc thesis work, which you performed diligently and positively. You have even helped lay the foundations of a future publication! I am sure that a bright path is ahead of you.

What a joy to be part of the **Sprakel team**! The atmosphere in the Sprakel group is very inspiring. **Joris**, thank you for creating meetings that are scientifically in-depth and effective while also being uniquely fun and humorous. **Ruben**, we go back a long way. I have really enjoyed studying with you, sharing our MSc thesis joys and struggles at PCC, meeting in Cambridge (luckily we had exactly one day there ◡̈), and continuing for many more years as fellow PhDs. You have a vast knowledge and expertise in a wide variety of subjects. Thanks for sharing this freely and eagerly! Chapter 11, Section 11.3.3 is a typical example where your ideas and helping hand have been valuable. **Ties**, thank you for the numerous nice and useful conversations! You are a very easy-going, social and kind person. Always willing to help unselfishly, and pro-actively think along. It was fun to organize the Sprakel–Voets BBQ together with you! Special thanks for your significant contributions to Chapter 11, Section 11.3.3, and for your tips regarding the thesis writing stage. **Jan Maarten**, thank you for your abundant optimism and deep thoughts about manifold scientific questions. I always felt enlightened after conversations with you. I particularly enjoyed our train trip to Physics@FOM, talking about good food, science and playing the piano. You are super kind and approachable. I look forward to building on the impressive foundations that you have laid for the optical tweezers! **Maarten**, it was a pleasure working, talking and laughing with you. We struggled so much to find sponsors for the PhD trip, but I enjoyed every minute because we did it together. You have an exceptional eye for detail, with a swiftness and seemingly effortless energy for making important decisions. Thank you for the nice Koningsdag in Utrecht! It always feels like coming home when talking with you. **Gosia B.**, you are so kind

and caring. Thank you for always bringing a peaceful, joyful, authentic atmosphere with you. **Hélène**, thank you for the nice chats in and outside the synthesis lab. You are a vibrant young lady, and I wish you all the best in your personal life and professional career! **Hande**, many thanks for your encouragements and energy. I also really enjoyed our drive to the Voets–Sprakel meeting, during which we had very good and pleasant chats. **Huanhuan**, thank you for your kindness and encouraging attitude. **Jesse**, thank you that I could and can always count on you. You are as stable as (most of) the lasers that you are working with ◡̈. Thank you for the brilliant, clever and thorough Fourier-transform LSI algorithms. They form an important part of Chapter 9. **Slav**, you are a very easy-going and intelligent person, and I have greatly enjoyed working together with you! Your optimism and energy are contagious and uplifting. I have loved our many (non-)scientific conversations. Thank you in particular for your major contributions to Chapters 6 and 9, and for your shared interest in the amazing yet mysterious 'crackticles'. Whenever I really needed you input – even last-minute – you provided this ultra-quickly, cheerfully and thoroughly. Last but not least, presenting at the 'Chemische Kring Zwolle' would not have been nearly as fun without you! **Raoul**, thank you for your kindness and listening ear! I especially enjoyed our car trips to and from the P(h)D weekend in 2018, with you as the driver. The long distance seemed negligible thanks to our good conversations. Moreover, you contributed considerably to Chapter 7, with very well-executed and valuable experiments. Thanks for that! **Jochem**, you are one of the most genuinely interested persons I know. Thank you for always bringing an atmosphere of playfulness intermixed with wisdom. I enjoy our nice ad hoc conversations, and look forward to more of them! **Anja**, thanks for the good conversations, and for introducing me to the wonderful world of Pickering emulsions! **Lucile**, I think you do not realise your own talents. I have enjoyed our lively talks, sharing our joys and doubts, our highlights and struggles. You are a brilliant and beautiful young lady! **Inge B.**, thank you for showing continued interest in my work. You are one of the most friendly, pure and reliable persons I know. It always feels comfortable being around you. Thanks for the positive vibes! **Riccardo**, thank you for the chats about great science, notably LSI and drying coatings! Your warm greetings in the hallways and labs always make me smile. **Ellard**, thank you for the many nice conversations! I am glad to have found a fellow coating enthusiast in you. I feel honoured to be your advisor in the coming years, and I am very confident that you will excel and thrive. **Martijn**, when meeting or working with you it is impossible to *not* become enthusiastic and motivated. You are extraordinarily talented, and your work and thoughts seem almost effortless and always fun! Thank you for the great scientific discussions, which I look forward to continuing. **Jessica**, thank you for your warm smiles, and

for our lovely and pleasant chats. I wish you all the best in Switzerland. **Tingting**, **Gomathi**, **Prathap** and **Ping**, it has been a joy to know you and discuss great science with you!

To my lovely office mates throughout the years. **Jeroen**, we had a really fun time together. Your advice and experience regarding particle synthesis were very useful in my starting period, when synthesis was still somewhat daunting to me. You always approach people and situations with a cool head but a warm heart. I am grateful for all your clever remarks and down-to-earth mentality. **Pieter**, unfortunately we have been office mates only very briefly. Your exceptionally impressive working hours in the lab did not help in this regard ;-) but I really enjoyed the short period that we shared our office! You are a very pure, interested, honest and kind person. **Qimeng**, we met in our fresh office shortly after the move to Helix. We had a nice chat, and I have felt a connection ever since. Except in one area... My sincere apologies for all the light in and on this thesis ;-) Best of luck with finishing your PhD journey, I am already so proud of you! I look forward to calling you Dr. Wu. **Fabiola**, thank you for radiating an atmosphere of warmth, positivity and calm to everyone. I was lucky to have my desk next to you ◡̈. Also many thanks for inviting me to your wedding. **Justin**, I think we are quite like-minded, which I have always appreciated and enjoyed. I have received an incredible amount of positive support from you. Every day you were a source of new ideas and insights. You are very social and often asked how my research and I were doing, followed by helpful and generous advice. Thank you also for critically and thoroughly reading my thesis Introduction! Your comments were really useful. **Dana**, thanks for the cheerful, open and interactive atmosphere that you create. Your presence always made our office more fun and bright. I am glad you have found your way in your PhD, which will surely be a successful way! **Preeti**, you are such a kind, creative and composed person. I have greatly enjoyed the time sitting next to you, talking about a diversity of topics. You are a hard and efficient worker, which will certainly pay off.

Support staff, you may be the most important and indispensable persons in the group. Thank you for keeping PCC running so smoothly. **Remco**, I thoroughly enjoyed designing, developing and building the DWS–ESI set-up together. You have turned me from someone who hardly knew the difference between a nut and a bolt, into a person who confidently tackles optical and mechanical equipment. Together with your >2 right hands, we formed a great team. Your golden hands, infinite creative ideas and patience, and willingness to help any moment have been very valuable to me. You have a talent for explaining things in an exceptionally clear and understandable manner. Thank you for all your inventive and immediate solutions, and for being at the completion of my PhD adventure as my paranymph!

Mara, thank you for mastering and excelling at our group's administration on many levels. Thank you also for the numerous lovely chats we have had! Your positive energy and laughter are always uplifting. I think we are on the same wavelength and really have a connection. I look forward to invading your office every now and again for many more years to come. **Josie**, thank you for offering me a listening ear and arranging manifold things, while actively thinking along and providing well-thought-through advice. You are very quick in reaching to the core of situations and expressing this clearly. You truly care for other people's well-being, and are one of least judgemental and most understanding people I know. You have a talent for pinpointing the beauty in people, which no one else would recognize. Thank you for continuing our nice tea times also after your time at PCC! I look forward to many more joyful and insightful conversations in the years to come. **Anita**, thank you for your superb and ultra-fast arrangements concerning my appointment all those years! You were always perfectly on top of the financial situation of my project and our group as a whole, for which you have a rare talent. You executed adaptations to my contract flawlessly and faster than the speed of light. Also on a personal level, I still remember your genuine interest in my personal situation, which never ceased. Especially during the period of my mother's illness, I greatly appreciated your warmth and authentic care for me. Thank you for even joining my mother's farewell ceremony. **Hannie**, you are a caring, understanding, reliable, and all-round person. Thank you for the many valuable conversations we have had. Your trust in me has helped me overcome my fear of inadequacy. Your encouraging words and good advice have been very useful to me! In addition, many thanks for your excellent and patient technical support at the start of my PhD, when you and your clear labjournal notes helped me to operate the bright-field microscope and the SEM at ORC. **Diane**, you always offer a helping hand for lab-related and other issues. A big thank you for your commitment and dedication! You are so kind, cheerful, positive and genuinely interested, and I keep being impressed about your efficient and action-oriented mentality. **Lennart**, **René**, **Anton K.**, **Ronald**, **Bert**, **Dirk** and **Leonie**, thank you for patiently and generously sharing your expertise and helping hands throughout the years, as well as for the many nice conversations.

Marleen, **Peter** and **Frans**, you re-introduced me into the fascinating world of thermodynamics. **Marleen**, you are such a friendly, positive and approachable person. I have really enjoyed teaching Driving Forces with you, and even more the nice conversations we had during the breaks. Or stuck in the wrong train ;-) I know you are genuinely modest, but you are truly an excellent and all-round researcher in many ways. Thank you for allowing me to co-author two papers with you! I wish you all the best and warmth in the cold North. **Peter**, your

logical reasoning and broad knowledge of thermodynamics are truly inspiring. Thank you for your dedication to teaching and always approaching people with a warm smile. Thank you also for managing the finances of PCC so well. **Frans**, you are very generous with your energy, time and knowledge. Thank you for contributing to the family-like spirit of PCC, and for your frequent feedback on presentations! You have a talent for spotting the beauty in scientific results. I also greatly appreciate your joining of the PhD trip to England!

To the other great scientific staff of PCC. **Mieke**, thank you for your scientific feedback during group meetings and your frequent participation in social activities. Your altruistic, intelligent, calm and wise character is an example to many. You genuinely care about people and you have a passion for helping, regardless of whether a professor or bachelor student is in front of you. **Renko**, you are an all-round great person to work with. Thank you for your scientific input during group meetings and for being such a pleasant colleague! **Joshua**, thanks for the nice chats we had from time to time, and for joining the PhD trip to England. Thank you also for reviving and elevating the journal club meetings. The ease with which you explain complex phenomena is impressive. You can express your thoughts very well, both in speech and in writing. You have humour, intelligence and a hard-working attitude, which will bring you far! **Tom**, a big thank you for always being willing to help, and for giving lots ot good advice after presentations. I believe your mind is full of creative and clever ideas. You are genuinely dedicated to supporting and guiding people, often without self-interest. Thanks for providing me with various new insights! **Siddharth**, your enthusiasm and positive outlook are contagious. I am very glad that you joined PCC recently, and I look forward to many collaborations in the future!

I might never have started my PhD if it weren't for the fellow students during my MSc thesis at PCC. **Ilse**, **Joanne**, **Nadine** and **Andrea**, thank you for being such dear friends. Thank you for the countless hours of discussing research, personal chats, laughs, and delicious brunch-lunch-high-teas (which invariably turned into dinner ;-). I am thankful for sharing both the serious and light sides of life and work with you! You are highly talented young ladies.

Many thanks to all dear fellow PhD students and postdocs. **Simone**, it was a privilege and pleasure working together on the delayed fracture paper. You are a highly dedicated, intelligent, meticulous and hard-working researcher, which will bring you far. Thank you for not being too frustrated when our joint manuscript had to undergo a 'slight' transformation ;-) without any fault on your part. Instead, you actively helped in good spirits to make that publication a success! **Merve**, you are one of the kindest persons I know. You truly care about other people's well-being, and you are so warm and approachable. I feel very honoured to

co-author two beautiful papers with you! We first got to know each other during the VLAG PhD week, when we were roomies. You are the easiest roommate imaginable. I particularly remember our stargazing together, celebrating our shared astrophilicity ◡̈. **Aljosha**, it has been a pleasure to roam through so many realms of conversation space over the years. No questions of life were too complex to discuss. You always made me laugh and feel understood, making me look forward to our next discussion. Night and day, bright ideas are bubbling up in your mind, which you are eager to share and put into practice. You are a brilliant and artistic researcher, with exceptionally sharp and strong analytical skills. I wish you the best of luck finishing your thesis! **Sabine**, thank you for the many pleasant chats and for keeping an eye on me when my mom was very ill. I still have your (mother's) sweet knitted keychain. I will never forget that you took care of me and encouraged me after I collapsed a bit during a Sprakel meeting. You are so kind, considerate and creative. Warm wishes! **Johan**, you have a heart of gold. Thank you for the nice walks and talks about a diversity of topics. You are a very special, friendly, honest, interested and loyal person. I wish you all the best and courage, have confidence in yourself! **Maarten**, **Wolf**, **Gosia W.** and **Natalia**, thank you for co-organizing the PhD trip to England! Our many meetings were always pleasant and mostly efficient, and I have learned a lot from each of you throughout the process. **Niek** and **Lione**, thank you for organizing the awesome P(h)D weekend in 2018 so well! **Niek**, we also organized SinteFysko together, which went almost flawlessly. Your relaxed yet focused attitude was super helpful. **Lione**, special thanks for the many nice ad hoc chats that we had! Furthermore, in no particular order, I would like to thank **Armando**, **Marc**, **Katarzyna**, **Inge S.**, **Nadia**, **Céline**, **Surender**, **Bram**, **Harke**, **Kris**, **Kamuran**, **Juan**, **Monika**, **Yunus**, **Thao**, **Soumi**, **Ran**, **Prachi**, **Rojman**, **Christian**, **Duc**, **Jacob**, **Antsje**, **Marcel**, **Marco**, **Anbu**, **Anton H.**, **Bob**, **Aurélie**, **Ram**, **Raisa**, **Sven**, **Nicolò**, **Vahid**, **Huy**, **Xiufeng**, **Riahna** and **Rob**, for making PCC such a great place to work! You have all co-created the social, unique and family-like environment that PCC is famous for. **Ali**, **Akankshya**, **Ralph**, **Ketan**, **Zohreh**, **Chandan**, **Larry** and **Richard**, you joined our group relatively recently. I look forward to getting to know you better.

BioNT group, I belong to the lucky 'generation' that has experienced your presence at close proximity. **Aldrik**, **Vittorio**, **Anton**, **Junyou**, **Rui**, **Jan Bart**, **Maria**, **Camilla**, **Gerben**, **Stan** and **Julia**, thank you for your positive vibes, creativity and research expertise! It was great to have you around.

Ook mijn vrienden en familie ben ik zeer erkentelijk voor hun steun. Allereerst, lieve **Tom**, ik kan jou nooit genoeg bedanken voor je niet-aflatende support, hulp en advies in de afgelopen jaren. Het meest tastbare bewijs in dit proefschrift zijn de samenvattende afbeeldingen voor Hoofdstukken 2 en 9, die we echt als top-team ontworpen hebben, met vooral héél veel uren en werk van jouw kant. Maar veruit jouw meeste bijdragen zijn onzichtbaar. Bedankt voor je oneindige geduld, acceptatie en positivisme. Bedankt voor de mega tas vol chocoladerepen om mijn laatste proefschrift-schrijf-fase te overleven. Bedankt voor je honderden appjes met bemoedigingen. Bedankt voor je check-check-double-checks van mijn laatste proefschrift versies. Je bent tot 3 uur 's nachts wakker gebleven op mijn inleverdatum. Het was zo bijzonder om dat moment samen te beleven via de app! We zijn bijzonder goed op elkaar afgestemd, kunnen alles met elkaar delen, en voelen elkaar feilloos aan. Ik kan me geen betere vriend wensen ♡.

Jasper, in de eerste plaats bedankt dat je zo'n goede vriend bent! Ik geniet altijd van praten met jou en **Marte**, of we nou discussiëren over gave wetenschap of kletsen over meer persoonlijke dingen. Onze tijd in Cambridge was een groot avontuur, dat we hebben voortgezet in onze PhD's. Ik kan je niet genoeg bedanken voor de grandioze cover van dit proefschrift. Je kunt toveren met een camera en de belichting, en onmogelijke situaties mogelijk maken. De fotoshoot was een hele bijzondere belevenis. Ik kijk uit naar de vele jaren als collega's die voor ons liggen, en die ongetwijfeld vol zullen zijn met interessante gesprekken en samenwerkingen.

Lidwina, dankjewel voor jouw tomeloze positieve energie en vertrouwen! Je hebt me geleerd om meer te ontspannen, genieten, lummelen, lachen en zelfs dansen en acteren. Dit maakt elke samenkomst met jou onvergetelijk ◡̈. Of we nou een feestje vieren, aan een wijnproeverij deelnemen, Bossche Bollen en andere verrukkelijke dingen creëren, in Jasper's fotoshoots stralen, op jouw filmset staan, of gewoonweg heerlijk kletsen en eten! Je bent een prachtige persoon en geweldige vriendin. Dankjewel dat je me toont dat ik waardevol ben, no matter what. En je geweldige man, **Bas**, bedankt voor je steun en oprechte interesse in mij. Ik kan altijd bij jullie terecht voor een luisterend oor en wijze raad.

Marije, dankjewel voor je geweldige support gedurende alle jaren. Je hebt me nooit opgegeven, ook al duurde het soms wel errug lang ;-). Bedankt voor de heerlijke, persoonlijke, diepe-maar-luchtige, urenlange gesprekken die nooit zijn opgehouden sinds onze fietstochtjes naar NSW. Je helpt me dingen te relativeren, met humor, advies en een oprecht luisterend oor. Ik ben ontzettend blij met jou als vriendin!

Yu, by sheer coincidence we met during a course, in which your professional and loving coaching attitude struck me right away. Later you became my dear

friend, for which I am still grateful! You have been a constant source of inspiration and support, and you always ask exactly the right questions. You have a heart of gold.

Lydia, wat was het gezellig in de jaren dat ik bij je woonde, eerst met Ilona en toen samen. Ik ben heel dankbaar dat we zulke goede vriendinnen gebleven zijn! Je bent één van de meest optimistische, krachtige en dappere personen die ik ken, met daarnaast een hart van goud. Bedankt voor de vele fijne gesprekken gedurende de jaren, die me altijd weer opladen met hernieuwde energie. Ik kijk uit naar meer terrasjes en dagjes bij jullie thuis, met Dominggus en jullie prachtige kids!!

Dirk, we zien elkaar niet regelmatig, maar we kletsen altijd heerlijk verder! Het is zo gezellig met jou, dankjewel daarvoor. En we delen duidelijk onze interesse in algemene kennis en quizzen. Superfijn dat ik daarin niet alleen sta ;-). De pubquiz is voor herhaling vatbaar!

Sue, bedankt voor de vele telefoontjes en afspraakjes vol waardevolle gesprekken! Het was ontzettend fijn om mijn zorgen, slaapproblemen en PhD-perikelen met jou te kunnen delen, zonder veroordeling en met veel begrip van jouw kant. Ik heb ook genoten van jouw tientallen tot honderden (!!) repen chocola. We zitten echt op dezelfde golflengte, zo bijzonder! Dankjewel voor jouw begrip en tomeloze interesse in mij ♡. Onze vriendschap betekent veel voor mij.

Sanne, dankzij puur toeval waren we roomies tijdens de Han-sur-Lesse winterschool. Al meteen de eerste avond was het zo gezellig samen! We hebben daar veel fijne en goede gesprekken gehad, die nooit zijn opgehouden. Je bent nu mijn lieve vriendin, en ik geniet enorm van onze gezellige (bel)gesprekken. Je bent een ontzettend pure, begripvolle, vrolijke, eerlijke en mooie persoon. Ik wens je veel goeds in België!

Linda, **Vincent**, **Nadine**, **Sven**, **Lisa**, **Jasper** en **Robert Jan**, bedankt voor onze heerlijke kletsmomenten, spelletjesmiddagen en etentjes! Jullie gezelligheid en betrokkenheid zijn heel waardevol geweest tijdens mijn PhD. Ik ben dankbaar dat ik altijd met jullie kan meerijden, wat een luxe :). Ik kijk uit naar veel meer fijne samenkomsten, hopelijk gauw in mijn appartementje *in spe*. En **Carel**, ook van een afstand zijn jouw positieve vibes duidelijk voelbaar! Superfijn dat je altijd betrokken bent gebleven bij mij en mijn onderzoek, dankjewel.

Lieve **Celeanum vriendinnen! Anna**, **Eline**, **Marloes**, **Lisanne**, **Titia**, **Marijke** en **Eleonore**, bijzonder dat we na zoveel jaren nog steeds blijven afspreken. Bedankt voor al jullie support! Onze vriendschap betekent veel voor mij. Ook al zien we elkaar niet heel vaak, het voelt altijd vertrouwd en als thuiskomen bij jullie. We kletsen gewoon lekker verder waar we gebleven waren ☺.

Lieve **oma Knoelie**, het is lang geleden dat ik deze naam gebruikt heb, maar ik ben dankbaar dat ik nog steeds jouw Knoelie ben! Je hebt altijd in mij geloofd. Ik geniet enorm van onze telefoontjes, waarin je me adviezen voor alle vlakken van het leven meegeeft. Jouw enthousiasme omtrent mijn belevenissen is enorm waardevol voor mij. Ik ben heel blij dat ik het verdedigen van mijn proefschrift met jou kan delen.

Lieve **oma Poppedijne**, het voelt goed om je nu zo te noemen, met zo'n dierbare naam. Dankjewel voor al je liefde, wijze adviezen, bemoedigende woorden en positivisme. Ik ben altijd blij na een gesprek met jou. Bedankt dat je zo goed voor mijn moeder hebt gezorgd, zodat ik me minder zorgen hoefde te maken. Ik vind het ongelofelijk bijzonder dat jij op je 90^{e} nog bij mijn promotie bent.

Lieve **Ludo**, wat missen we Marianne! Ik ben nog steeds dankbaar voor haar nuchtere blik, die mijn PhD-perikelen steevast in een ander daglicht zette. Ik vind het geweldig dat jij altijd mijn geïnteresseerde oom geweest bent, en dat we recent nog dichter naar elkaar gegroeid zijn. Je bent een hele oprechte, getalenteerde en mooie persoon!

Lieve **Annelies**, bedankt voor de fijne telefoontjes en je oprechte interesse! Ik heb veel gehad aan jouw wijze en nuttige adviezen. Ik ben altijd welkom bij jou en word dan helemaal in de watten gelegd, o.a. met verrukkelijke maaltijden. Dankjewel dat je in mij bent blijven geloven, en me helpt ook in mijzelf te geloven. Je bent een schat!!

Lieve **Hanneke**, **Herman**, **Liza**, **Demi**, **Nouschke**, **Ralph** en **PP**, bedankt dat ik altijd bij jullie terecht kan! Jullie hebben me vaak met goede raad en (gezellige) daad terzijde gestaan, o.a. door me te helpen relativeren en wat minder serieus te zijn :). Ik hoop in de toekomst meer tijd met jullie door te brengen, in ontspannen uitjes, fijne gesprekken en heerlijke etentjes. Jullie energie en opgewektheid zijn aanstekelijk! Bedankt dat jullie gewoon om mij geven, met of zonder PhD.

Dear **Finnish family**, rakas perhe! **Timo**, **Elsa**, **Leena**, **Helmi** and **Riku**, I am so thankful for your coming into my life. You always bring positive vibes and a good atmosphere. Serious and relaxed when needed, fun and lively when possible. You are all beautiful persons and I would love to get to know you better!

Dear **Hanna**, you are a very special, vibrant and beautiful lady. Thank you for being such a good wife to my father! I am grateful for you as my step mom. You fully accept me the way I am, and always adapt to create the best home for me. I can always count on you. I am so glad that we are on the same wavelength and can talk about nearly everything. I look forward to getting even closer and connected on a deeper level. Rakkaudella!

Lieve **Ralf**, ik ben heel blij dat jij tot onze familie bent gaan behoren, en dat je zo geweldig voor mijn zus zorgt! Bedankt voor je steun de afgelopen jaren, je

interesse in mij en je wijsheid. Je bent enorm all-round getalenteerd, en je gaat het vast nog ver schoppen. Dankjewel voor je gezelligheid en enthousiasme. Je geeft me altijd het gevoel thuis te komen, ook al kennen we elkaar nog niet zo lang.

Lieve **Renée**, geweldige zus. Ik ben zo trots op ons!! Dankjewel voor je geloof in mij al deze jaren, voor je lieve woorden, cadeaus en bloemen, voor de vele goede en waardevolle gesprekken, voor je meeleven, meedenken en eerlijkheid. Ik voel me vereerd dat jij me als paranimf terzijde staat op mijn moment suprème. Ik hoop dat we nog heel veel meer mooie momenten samen mogen delen ♡♡.

Lieve **mam**, ik houd zoveel van jou! Ik mis je gigantisch, maar ik geloof dat je nog steeds mijn grootste fan bent. Ik blijf je voor altijd dankbaar voor alle levenslessen, zowel op persoonlijk als intellectueel vlak.

Lieve **pap**, bedankt dat je nooit een seconde aan me getwijfeld hebt. Jouw vertrouwen in mij en onvoorwaardelijke liefde zijn rotsvast. Bedankt voor je niet-aflatende steun, eerlijkheid, onuitputtelijke enthousiasme en optimisme, vuur en humor. En dankjewel dat je zoooo goed voor mama gezorgd hebt ♡. Je bent altijd een geweldige steunpilaar voor mij geweest, in fijne gesprekken vol goede adviezen, praktische hulp, telefoontjes zelfs midden in de nacht, en volledige acceptatie van wie en hoe ik ben. Ik ben je voor altijd dankbaar!

Hanne – Wageningen, 2020

About the author

Hanne Maria van der Kooij was born on 6 December 1989 in Zwolle, the Netherlands. She lived in Katowice, Poland, during the first six months of her life. After travelling and moving for the next two years, she and her parents finally settled in Dronten, the Netherlands.

In 2007, Hanne received her high-school diploma from the Gymnasium Celeanum in Zwolle. She then went on to study Molecular Life Sciences at Wageningen University. Hanne obtained both her BSc and MSc degrees *cum laude*, specializing in physical chemistry. As an integral part of her master's studies, Hanne conducted a research project at the Laboratory of Physical Chemistry and Colloid Science of Wageningen University, under the supervision of Dr. Evan Spruijt and Prof. Martien Cohen Stuart, using a variety of scattering methods to illuminate polymeric micelles. She also completed a research internship at the University of Cambridge, England, in the group of Prof. Ullrich Steiner, Dr. Ahu Gümrah Dumanlı and Dr. Silvia Vignolini, on the chiral self-assembly of cellulose nanocrystals.

Hanne started pursuing her PhD in 2013 at the Laboratory of Physical Chemistry and Soft Matter of Wageningen University, under the supervision of Prof. Joris Sprakel and Prof. Jasper van der Gucht. This thesis is the culmination of a 6.5-year (part-time) journey. As from May 2020, Hanne has embarked on a new scientific adventure, working as a Staff Scientist in the same research group.

Overview of completed training activities

Discipline-specific activities

- Workshop 'New Horizons in Polymer Characterisation', DPI, Eindhoven, 2014.
- Advanced Chemistry Graduate Course, VLAG, Wageningen, 2014–2015.
- Physics@FOM, FOM, Veldhoven, 2015.†
- Workshop 'Bubbles and Droplets', FPE & FPH & PCC, Wageningen, 2015.†
- CHAINS, NWO, Veldhoven, 2015.†‡
- Han-sur-Lesse Winterschool, Han-sur-Lesse (BE), 2016.
- Workshop 'Scattering Methods', ICMS TU/e, Eindhoven, 2016.†
- International Soft Matter Conference, SoftComp, Grenoble (FR), 2016.‡
- Physics@FOM including masterclass, FOM, Veldhoven, 2017.‡
- Drying Days Conference, CNRS & University of Toulouse, Toulouse (FR), 2017.‡
- SoftComp Annual Meeting, SoftComp, Venice (IT), 2017.†
- CHAINS, NWO, Veldhoven, 2017.†
- Physics of Drying Conference, École des Ponts ParisTech & Saint-Gobain, Paris (FR), 2018.†‡
- Workshop 'Nano-Characterisation', 4TU.HTM, Utrecht, 2019.†

General courses

- VLAG PhD week, VLAG, Baarlo, 2013.
- Symposium 'How to write a world-class paper', WUR Library, Wageningen, 2013.
- PhD Peer Consultation, WGS, Wageningen, 2014.
- PhD Competence Assessment, WGS, Wageningen, 2014.
- MATLAB masterclasses, MathWorks, Wageningen, 2014.
- Scanning electron microscopy training (theory & practice), WEMC, Wageningen, 2014.
- Journal Club, PCC & VLAG, 2014–2019.

Optionals

- Preparation of research proposal, PCC, Wageningen, 2013.
- Discussion and implementation of digital labjournal pilot, PCC, Wageningen, 2013.
- Scientific colloquium at AkzoNobel, AkzoNobel, Sassenheim, 2014.†
- Organization committee of PhD study trip to England, PCC, 2014–2015.
- PhD study trip, PCC, England (UK), 2015.††
- Scientific Voets–Sprakel colloquium, ICMS TU/e & PCC, Eindhoven, 2016.
- Scientific Sprakel–Voets colloquium including organization, PCC & ICMS TU/e, Wageningen, 2017.†
- Lindau Nobel Laureate Meeting, KNAW, Lindau (DE), 2017.
- Invited lecture at Océ, Océ, Venlo, 2018.†
- Invited lecture at the 'Chemische Kring Zwolle', KNCV, Zwolle, 2018.†
- Invited lecture at NVVT symposium, Dutch Association of Paint Technicians, Nieuwegein, 2018.†
- Group meetings and colloquia, PCC, Wageningen, 2013–2019.†
- Dutch Polymer Institute meetings, DPI, Arnhem & Eindhoven & Wageningen & Paris (FR), 2013–2019.†‡

---

† oral presentation

‡ poster presentation

Cover design by Jasper Landman || www.bobfzbl.com

Printed by ProefschriftMaken || www.proefschriftmaken.nl

This work forms part of the research programme of the Dutch Polymer Institute (DPI), project #781, P.O. Box 902, 5600 AX Eindhoven, The Netherlands